

THÈSE DE L'UNIVERSITÉ DE LYON

Délivrée par

L'UNIVERSITÉ CLAUDE BERNARD LYON I

ÉCOLE DOCTORALE MEGA

(Mécanique, Énergétique, Génie civil, Acoustique)

présentée par

Yann PELTIER

pour obtenir le titre de **Docteur en Mécanique des Fluides**

(arrêté du 7 août 2006)

Titre:

MODÉLISATION PHYSIQUE DES ÉCOULEMENTS DÉBORDANTS EN PRÉSENCE D'UN ÉPI PLACÉ DANS LA PLAINE D'INONDATION

soutenue publiquement le 06 septembre 2011

JURY

M. Michel LANCE
M. Eric BARTHÉLÉMY
M. Olivier EIFF
Mme. Nicole GOUTAL
M. André PAQUIER
M. Koji SHIONO
M. Sébastien PROUST
M. Nicolas RIVIÈRE

Prof. Université Lyon I
Prof. INPG-ENSE³
Prof. INPT-ENSEEIH
Ingénieur-Chercheur EDF-LNHE
ICPEF Cemagref de Lyon
Prof. Université de Loughborough
CR Cemagref de Lyon
Prof. INSA de Lyon

Président du jury
Rapporteur
Rapporteur
Examinateur
Directeur de thèse
Directeur de thèse
Encadrant de thèse
Encadrant de thèse

*To Anne-Sophie,
To my family,
To my friends*

Acknowledgement

Ce manuscrit de thèse marque l'aboutissement de trois années et demie de recherche et de formation. Bien que la thèse soit principalement un travail personnel, sans l'aide et le soutien d'un grand nombre de personnes, je n'aurais jamais pu l'accomplir. Je tiens donc ici à remercier celles et ceux qui m'ont permis de mener à son terme ce grand projet.

Je voudrais tout d'abord remercier les membres du jury qui ont accepté de participer à toutes la procédure de soutenance. Merci à Michel LANCE qui a accepté de présider mon jury de thèse. Merci à Eric BARTHELEMY et à Olivier EIFF qui m'ont fait l'honneur de rapporter ma thèse, malgré la longueur et la densité de mon manuscrit. Vos conseils m'ont été d'une grande aide pour préparer la soutenance et pour améliorer le dit-manuscrit. Merci enfin à Nicole GOUTAL qui a accepté de faire parti de mon jury de thèse et qui a montré un grand intérêt quant à l'application de mon travail d'un point de vue opérationnel.

Je voudrais ensuite remercier mes directeurs de thèse. Merci André d'avoir pris le temps de travailler avec moi alors que tu avais bien d'autres étudiants à voir et projets à mener. Ton flegme m'a montré qu'en s'énervant, on n'allait pas plus vite. Thank you Koji for having supervised my work, the distance was sometimes an obstacle for communicating, but everytime I came in Loughborough and everytime you came in Lyon my work suddenly won three months. Your great experience in the compound channel field and in experimental sciences was really helpful.

Que serait ce travail de thèse sans mes Encadrants. Sébastien, ta rigueur, ta soif de connaissance, ta manière de remettre en cause mes affirmations injustifiées ont été un des moteurs de mon travail. Je me suis démené pour prouver, démontrer, infirmer mes intuitions, car c'est cela et quelques PETITES choses de plus qui font que l'on peut dire que l'on est un chercheur; j'y suis presque, encore quelques PETITS articles et je pourrai voler de mes propres ailes. Nicolas, tes connaissances et ta rigueur en sciences expérimentales m'ont permis de développer les miennes. Je me sens capable maintenant de monter ma propre expérience de A à Z. Je tiens aussi à te remercier pour ta patience, tu m'as subi pendant 3 ans dans ton bureau ou dans le hall hydraulique; j'ai chanté, parlé, je me suis énervé pour rien quand mon ordinateur saturait alors que j'avais lancé 20 calculs en même temps et pourtant tu as toujours été patient et tu n'as jamais rechigné à me filer un coup de main quand je saturais, merci.

Un grand merci aussi aux mercenaires de la sciences qui m'ont accompagné tout le long de la thèse: Benoit CAMENEN, Jérôme LE-COZ, Emmanuel MIGNOT, Benoit TERRIER. Travailler avec vous a vraiment été enrichissant. J'ai découvert que le travail en équipe dans un laboratoire ou entre plusieurs laboratoires ou simplement entre potes était une des facettes les plus intéressantes de la recherche. Merci à Benoit C. et Jérôme de m'avoir fait découvrir le Japon. Merci à Benoit T. de m'avoir accueilli en Angleterre. Merci à Manu d'avoir passé autant de temps avec moi pour faire de la science.

Je ne peux pas continuer ces remerciements sans remercier l'équipe de métrologie du Cemagref: Fabien THOLLET, Mickaël LAGOUY et Guillaume DRAMAIS. Un grand merci en particulier à Fabien sans qui ma thèse ne serait toujours pas finie. Rappelle toi ces séances mémorables de montage de la manip' par huit degrés puis trente-six degrés dans le hall hydraulique.

Merci à Anne EICHOLZ et à Hélène FAURANT-PHILIPPE d'avoir été derrière moi pour me rappeler quand j'avais encore une fois de plus oublié de faire une tâche administrative. Mais surtout merci pour votre gentillesse.

Merci à biquet, biquette et chouquette de m'avoir supporté dans le bureau, c'était énooorme. En plus on arrivait à travailler, sauf quand les chaises couinaient et les claviers claquaient et que 16h arrivait. Merci aussi pour les pures soirées que l'on a passé ensemble. Biquet, j'ai toujours pas fait le barbeuk chez vous!

Merci J.M. et Stéphane pour m'avoir sorti la première année et m'avoir fait découvrir les nuits lyonnaises.

Merci à Anne-Laure, Audrey, Bruce, Élodie, Aziz, Clotaire, Benj, Jean-Phi, Sandra, Éric, Romain, Stéphanie, Judicaël, Lionel P., Marina, Jérôme, Flora, Benoit C., Claire, Aurélien, Mathieu, M. Pouic Pouic et à tous les autres que je n'ai pas cités et qui veulent bien se reconnaître pour ces bons moments de détente au coin café, au Wallace, aux Berthom, en montagne... J'aurais presque envie de recommencer la thèse rien que pour revivre ça.

Un grand merci à mes potes de Belfort et de Toulouse qui me soutiennent depuis toujours. Vous m'avez permis de garder les pieds sur terre. Guillaume, Titi, Maxime et Tacha on va peut être pouvoir remonter en montagne maintenant. $\pi 7$ foreveeeer!!

Merci à mes colloques officiels et officieux Stéphanie, Lionel, Maxime, Gillian, Audrey et Bruce.

Mes remerciements vont aussi à tout l'équipe du LMFA basée à l'INSA de Lyon qui m'a accueilli au cours de mon ATER et à l'équipe de l'UFR de mécanique de l'université Lyon I. Vous m'avez permis de terminer ma thèse dans de très bonnes conditions. Un grand merci à Nicolas, Emmanuel, Valéry et Delphine pour avoir travaillé avec moi sur la soutenance.

Thanks to all my Bro' in England, Milo, Daan, Steeve. We had some really great moments all together!!

Je ne sais toujours pas parler Japonais, alors merci à Baba San et Nakagawa sensei pour leur accueil au Japon et dans le laboratoire de Ujigawa.

Merci aux geeks qui pullulent sur la toile et qui m'ont permis de maîtriser les subtilités de Latex, LabVIEW et Matlab.

Merci à Asimov, Simmons, Herbert, Silverberg, Tolkien, Gemmel, Abnett...

Je terminerai enfin par remercier ma famille. Vous me soutenez depuis que je suis petit, j'aurais pu m'arrêter une bonne douzaine de fois depuis ces neuf dernières années, mais vous m'avez toujours poussé pour me dépasser. Pas si feignant que ça en fait le Yann!!

Anne-Sophie, tu es en grande partie responsable de ma réussite, tu m'as soutenu quand je n'arrivais plus à rédiger, tu m'as encouragé, tu as pris en charge notre couple les deux derniers mois de la thèse. Sache que je serai là pour toi ma puce quand ça sera ton tour.

Lille, le 14/09/2011

Résumé étendu

Au cours de fortes crues, le lit mineur de la rivière peut déborder dans les plaines d'inondations contiguës. Ces écoulements dits “en lit composé” sont caractérisés par de fortes interactions turbulentes entre lits qui conduisent à une réduction de la débitance totale de la rivière.

Si, généralement, les variations de sections en travers des rivières naturelles ou anthropisées sont progressives et continues, au droit de certains biefs, des obstacles transversaux et discontinus (naturels ou artificiels) peuvent partiellement ou totalement bloquer les plaines d'inondation. L'écoulement dans la plaine d'inondation est dès lors contracté par l'obstacle qui promeut le développement de zones de recirculation de part et d'autre de l'obstacle. Dès lors la section d'écoulement est réduite ce qui génère des échanges de masse entre lits qui viennent se superposer aux interactions turbulentes.

Ces écoulements sont caractérisés par de fortes variations des paramètres hydrauliques. Nous nous sommes intéressés à la modélisation physique de ces écoulements et nous avons particulièrement étudié les distorsions introduites par l'obstacle sur la turbulence dans l'écoulement. Ce travail est basé sur de nouvelles expériences menées dans deux canaux à lit composé. Deux configurations ont ainsi été étudiées: l'une sans obstacle (état de référence) et la seconde avec obstacle.

La compréhension de l'hydrodynamique des débordements au voisinage d'un obstacle bloquant transversalement la plaine d'inondation est primordiale pour les modélisateurs. L'estimation précise de la crue avec une période minimale de retour de cent années fait partie intégrante de la conception d'autoroutes insubmersibles et de remblais de chemin de fer. En outre, dans le cadre de la mise en place des Plans de Préventions des Risque d'Inondations, les zones inondables au droit d'un obstacle doivent être déterminées avec un minimum d'incertitudes afin d'évaluer avec précision les dangers pour les biens et les personnes.

Le premier résultat de cette thèse est d'avoir construit un jeu complet de données d'écoulements rapidement variés en présence d'un épi dans la plaine d'inondation. À terme, cet ensemble de données sera utilisé pour l'analyse comparative de modélisations numériques existantes et la création de nouveaux modèles numériques.

Le second résultat de cette thèse réside dans l'analyse des effets sur les paramètres hydrauliques de la superposition des deux problématiques que sont (i) les écoulements en géométrie en lit composé et (ii) les écoulements rapidement variés au voisinage d'un obstacle.

Le dernier résultat de cette thèse est finalement d'avoir exprimé les processus physiques en fonction des paramètres hydrauliques mesurés en utilisant une équation de quantité de mouvement à deux dimensions basée sur les équations de Saint-Venant. À terme, ces comparaisons permettent de définir les zones de dominance de certains phénomènes physiques par rapport aux autres dans les écoulements rapidement variés. Ces zones devront être traitées avec prudence par les modélisateurs pour créer des cartes d'inondation précises et des modèles numériques de prévisions de crues pertinents.

Mots-clés : inondations, lit composé, écoulement rapidement varié, obstacle, zones de recirculation, turbulence, transferts de quantité de mouvement.

Abstract

During strong flood events the river main channel may overflow in its contiguous floodplains. These flows in “compound channel” are characterised by strong turbulent interactions between the flow in the main channel and the ones in the floodplains, resulting in a reduction of the channel conveyance.

If in natural or anthropized rivers, the river cross-section generally gradually and continuously varies, transversal and discontinuous obstacles either natural or artificial may partially or totally block off floodplains. The flow in the floodplain is therefore contracted by the obstacle that promotes the development of two recirculation zones, one upstream of the obstacle and one downstream. It results in a reduction of the flow section and then in the generation of strong mass exchange between channels that superimposes to the turbulent interaction.

These flows are rapidly varied and are characterised by strong changes in the distributions of the hydraulic parameters. We were interested in the physical modelling of these flows and we especially investigated the distortions introduced by the obstacle on the turbulence. This study is based on new experiments conducted in two different compound channels. Two configurations were studied: one without obstacle (reference state) and the second with obstacle.

Understanding of the hydrodynamics of overbank flows in the vicinity of a transversal obstacle blocking off the floodplain are paramount for flow modellers. The accurate estimation of the flood with a minimum returning period of one hundred year is a necessary part of the designing of unsinkable motorway and railway embankments. Moreover, as part of the establishment of the flood hazards prevention plans, flooded area in the vicinity of embankments must be determined with minimal uncertainties in order to accurately evaluate the danger.

The first result of this thesis is thus to build a complete set of data of rapidly varied flows in the vicinity of a groyne set on the floodplain of a compound channel. To term, this data set will be used for benchmarking of existing numerical modelling and for creating new modelling.

The second result of this thesis is to analyse effects on the hydraulic parameters of the superimposition of the two problems that are (i) flow in compound geometry and (ii) rapidly varied flow in the vicinity of a thin obstacle.

The last result of this thesis is to express the physical processes as a function of the measured parameters using a two-dimensional momentum equation based on the Saint-Venant equations. To term, these comparisons enable to define zone of dominance in the flow for certain processes that modellers must then treat or model with care for producing robust flood mappings or relevant prevision model.

Keywords: flood, compound channel, rapidly varied flows, obstacle, recirculation zones, turbulence, momentum transfer.

Contents

Acknowledgement	I
Résumé étendu	III
Abstract	V
Notation	XVII
General introduction	XXI
I Physics and fundamental equations	1
1 Physics of compound channel flows: a literature review	3
1.1 Technical jargon of the compound channel	4
1.1.1 Main geometrical parameters in a straight compound channel	4
1.1.2 Compound channel flow classification	4
1.2 Shallow uniform flow in straight compound open-channels	5
1.2.1 Velocity and depth	6
1.2.2 Horizontal shear layer in compound open-channels	6
1.2.3 Boundary shear stress	13
1.2.4 Secondary currents of Prandtl's second kind	14
1.3 Gradually varied flows in compound channel	15
1.4 Flows in the vicinity of a thin obstacle	17
1.4.1 Sudden enlargement in single open-channels	17
1.4.2 Groyne in single open-channels	19
1.4.3 Groyne in the floodplain of a compound open-channel	22
1.5 Partial conclusion	23
2 Fundamental equations for flow description in compound open-channel	25
2.1 Introduction	25
2.2 The Navier-Stokes equations for incompressible flows	26
2.3 Reynolds-Averaged Navier-Stokes equations: RANS method	27
2.3.1 Reynolds decomposition	27
2.3.2 Equation of the mean motion	27
2.3.3 Equations of the fluctuating motion	28
2.4 2D-H equations of Barré de Saint-Venant	28
2.4.1 Definition of the boundary conditions	29
2.4.2 Conservative form of the continuity equation	30
2.4.3 Conservative form of the momentum equations	30
2.5 Identification of physical processes using a 2D-H equation	32
2.6 Approximation of physical processes using modelling	33
2.6.1 Friction	33
2.6.2 Turbulence	35
2.6.3 Secondary currents of Prandtl's second kind	39
Conclusion of Part I	41
II Material and Method	43
3 Experimental set-up and metrology	45
3.1 Introduction	45
3.2 Experimental flume (LMFA)	45
3.2.1 Main characteristics of the flume	45
3.2.2 Topography of the flume	46
3.2.3 Upstream and downstream boundary conditions	47

3.2.4	Pumps and flow-meters	49
3.3	Measuring devices	50
3.3.1	Traversing device, data acquisition and measuring mesh	50
3.3.2	Measurement of water depth	52
3.3.3	Measurements of water level: definition of a reference plan	53
3.3.4	Measurement of mean velocity and turbulence	54
3.3.5	Preston tube	61
3.3.6	Large Scale Particle Imaging Velocimeter (LSPIV)	63
3.4	Experimental data-set	66
3.4.1	Method for constructing the data-set	66
3.4.2	Resulting data-set	68
4	Data post-processing	71
4.1	Introduction	71
4.2	Uncertainty computation	71
4.2.1	Errors	71
4.2.2	Uncertainty estimations	72
4.2.3	Estimation of random uncertainties	73
4.2.4	Propagation of uncertainties	74
4.2.5	Consideration of the systematic errors in the uncertainty calculation	74
4.2.6	Device uncertainty	74
4.3	Large Scale Image Particles velocimetry	75
4.3.1	Validity of measurements	75
4.3.2	Extraction of the geometry of recirculation zones	76
4.4	Integration schemes	78
4.4.1	Vertical integration: depth averaging	79
4.4.2	Lateral integration: discharge computation	80
4.5	Despiking the ADV data	81
4.5.1	The Phase-Space Thresholding Method	81
4.5.2	Differences with the method developed by Goring and Nikora (2002)	82
4.6	Repositioning the angles of ADV data	83
4.6.1	Problem of the angle repositioning	83
4.6.2	Rotation matrix	84
4.6.3	Impacts of wrong angles on the velocity	84
4.6.4	Impacts of wrong angles on Reynolds stresses	85
4.6.5	Methods to correct a bad angle orientation	86
4.7	Spectral analysis of the turbulence	89
4.8	Correction of the systemic error on micro-propeller measurements	92
4.8.1	Sources of errors	92
4.8.2	Correction for reference flows	93
4.8.3	Corrections for Groyne-case flows	96
	Conclusion of Part II	99
III	Experiments and analyses	101
5	Reference flows	103
5.1	Introduction	103
5.2	Setting up of the flow conditions for the reference flows	104
5.3	Effects on the flow of the flume set-up	107
5.3.1	Effects of boundary conditions on depths and velocities in a subsection	107
5.3.2	Effects of the bottom topography	108
5.3.3	Mass exchange	109
5.4	Detailed description of a reference flow: RF300L	109
5.4.1	Main flow features	110
5.4.2	Analysis of the turbulence	111
5.4.3	Boundary shear stress	117
5.5	Effects of a change in the total discharge	120
5.5.1	Main flow features	120
5.5.2	Analysis of the turbulence	121
5.5.3	Boundary shear stress	124
5.6	Criteria for flow establishment	128
5.6.1	Segments of establishment	128
5.6.2	Definition of the criteria	128

5.7	Partial conclusion	129
6	Impacts of the introduction of a groyne in a developing flow in compound channel	131
6.1	Introduction	131
6.2	Geometry of recirculation zones	132
6.2.1	Longitudinal length	132
6.2.2	Spanwise length of the downstream recirculation zone	133
6.3	Main flow features	134
6.3.1	Effects of recirculation zones on the flow	134
6.3.2	Impacts on the flow of backwater effects	136
6.4	Mass exchange	138
6.5	Analysis of the turbulence	138
6.5.1	Geometrical characteristics of the mixing layer developing at the interface between channels	139
6.5.2	Turbulence in the mixing layer at the interface between channels	140
6.5.3	Mixing layer developing at the tip of the groyne in the floodplain	141
6.5.4	Turbulence out of the mixing layers	142
6.5.5	Coherent structures in the two mixing layers	144
6.6	Distribution of boundary shear stress	148
6.6.1	Boundary shear stress out of the mixing layers	149
6.6.2	Boundary shear stress in mixing layers	150
7	Impacts of a change in the groyne length or total discharge in a groyne-case flow	151
7.1	Introduction	151
7.2	Influence of the groyne length	151
7.2.1	Main flow features	153
7.2.2	Mass exchange	156
7.2.3	Analysis of the turbulence	156
7.2.4	Distribution of boundary shear stress	164
7.3	Influence of the total discharge	165
7.3.1	Main flow features	165
7.3.2	Mass exchange	168
7.3.3	Analysis of the turbulence	168
7.3.4	Distribution of boundary shear stress	175
8	Discussion on momentum transfer in compound channel	177
8.1	Introduction	177
8.2	Asymptotic regimes for recirculation zones?	178
8.3	Dispersion on the vertical of the horizontal velocities	179
8.3.1	Dispersion for reference flows	179
8.3.2	Dispersion for groyne-case flows	181
8.3.3	Momentum coefficients for reference flows	183
8.3.4	Momentum coefficients for groyne-case flows	183
8.4	Dominance of physical processes: momentum calculations	184
8.4.1	Reference flows	185
8.4.2	Groyne-case flows	187
8.4.3	Advices to flow modellers	193
	Conclusion of Part III	195
IV	General conclusions and prospects	199
	General conclusion	201
	Prospects	205
	Bibliography	209
V	Appendices	219
A	1D St-Venant Equations and conveyance modelling	221
A.1	One-dimensional equations	221
A.1.1	Equations in a subsection	222
A.1.2	Equations in the total cross-section	223
A.1.3	The momentum coefficient	224

A.2	1D-modelling of flows: conveyance modellings	224
A.2.1	The concept of resistance to flow	225
A.2.2	The single channel method (SCM): Manning (1889)	226
A.2.3	The divided channel method (DCM): Lotter (1933)	226
A.2.4	The corrected DCM	227
A.2.5	The Exchange Discharge Model (EDM): Bousmar and Zech (1999)	230
A.2.6	The Independent Subsection Method (ISM): Proust <i>et al.</i> (2009)	232
A.3	Conclusion	234
B	Experiments at the open-laboratory of Ujigawa	235
B.1	Introduction	235
B.2	Presentation of the experiment and measurements	236
B.2.1	Flume characteristics and experimental set-up	236
B.2.2	Velocity measurements using LSPIV technique	236
B.2.3	Test cases carried out	238
B.3	Results from the LSPIV	239
B.3.1	An estimation of the bed evolution	239
B.3.2	Results for an impermeable spur dyke	239
B.3.3	Results for a permeable spur dyke	243
B.4	Discussion	243
B.5	Conclusion	244
B.6	Acknowledgement	245
C	Devices uncertainties	247
C.1	Water depth and water level: ultrasonic probe	247
C.2	Mean velocity and turbulence	248
C.2.1	Micro-propeller:	248
C.2.2	Pitot tube:	248
C.2.3	ADV:	248
C.3	Preston tube	249
C.4	LS-PIV	249
C.5	Derived quantities	249
C.5.1	Froude number	249
C.5.2	Dispersion on the vertical of the horizontal components of the velocity	250
C.5.3	Vertical momentum coefficient	250

List of Figures

1	Flood hazard mapping near Sainte-Foy l'Argentière	XXIV
1.1	Photograph of a compound open-channel in Japan	3
1.2	Definition sketch of the geometrical parameters in a compound open-channel	4
1.3	Physical phenomena in a straight compound channel (uniform flow)	5
1.4	Example of isovel profiles in a compound channel	6
1.5	Developing mixing layer in a single or in a compound open-channel	7
1.6	Photograph and sketch of a mixing layer under uniform flow conditions	7
1.7	Turbulent spectrum of shallow shear flow in a single channel	9
1.8	Turbulent co-spectrum and phase relation of shallow shear flow in a single channel	9
1.9	Sketch of a vortex moving on an uneven bottom	10
1.10	Secondary currents and mixing layer interactions: impact of the floodplain depth	11
1.11	Lateral variation of depth-averaged Reynolds shear stress for various water depths	12
1.12	Boundary shear stress distribution in symmetrical compound channel	13
1.13	Boundary shear stress distribution in asymmetrical compound channel	14
1.14	(\bar{v}, \bar{w}) components in a secondary current under uniform flow conditions	15
1.15	Top view of a recirculation zone downstream of a sudden enlargement	17
1.16	Dimensionless recirculation length as a function of the friction number for various expansion ratio	19
1.17	Horse-shoe vortex system in the upstream recirculation zone	20
1.18	Lengths of recirculation zones as a function of the friction number	21
2.1	Definition sketch of the axis directions and velocity components	26
3.1	Definition sketch and photographs of the flume in the LMFA	46
3.2	Topography of the LMFA flume	47
3.3	Photograph of the boundary conditions at the LMFA	48
3.4	Grundfos pump SP125-1-A	49
3.5	Photographs of the flow-meters and of the discharge regulator	50
3.6	Procedure of data acquisition using LabVIEW	51
3.7	Measurement meshes of LMFA experiments	51
3.8	Scheme of operating principle of an ultrasonic probe	52
3.9	Convergence of the cumulative mean and standard deviation of ultrasonic measurements	53
3.10	Reference plan and bottom level in the floodplain	54
3.11	'Nixon Flowmeters' micro-propeller	55
3.12	Cumulative mean and standard deviation of the micro-propeller measurements	56
3.13	Cumulative mean and standard deviation of the Pitot tube measurements	58
3.14	ADV working principle scheme	59
3.15	Cumulative mean velocity, STD and CPSD of ADV measurements for GC230L	61
3.16	Preston tube scheme	62
3.17	Two positions of the video-camera for LSPIV technique	64
3.18	Image orthorectification	65
4.1	Respective roles of random and systematic errors	72
4.2	Interrogation and research area size for LSPIV optimization	76
4.3	Spanwise length of recirculations for three groyne-cases	77
4.4	Random motion of the stagnation point	78
4.5	Trapezoidal integration used for the depth-averaged velocity	79
4.6	Trapezoidal integration used for the total discharge	80
4.7	Spiked ADV data: impact of spikes on the variance of the signal	81
4.8	Application of the Phase-Space Thresholding Method: effects on the spikes	82
4.9	Correction of the method developed by Goring and Nikora (2002)	83
4.10	Impacts of wrong angles on ADV measurements: velocities	85
4.11	Impacts of wrong angles on ADV measurements: Auto-covariance	86
4.12	Impacts of wrong angles on ADV measurements: Cross-covariance	86
4.13	Observation of lateral velocities in a secondary current under uniform flow conditions	87
4.14	(U_d, V_d, T_{xy}) after an angle correction using the local method	88
4.15	Denoising of a power spectrum density	91

4.16	Micro-propeller recalibration laws for reference flows	94
4.17	Corrected depth-averaged velocities for reference flows	96
4.18	Corrected depth-averaged velocities of the groyne-case flows	97
5.1	Depth-averaged velocity fields of reference flows	103
5.2	Mean water depths in a subsection for reference flows	106
5.3	Discharge ratio in the floodplain for reference flows	106
5.4	Velocities in a subsection for the reference flows	107
5.5	Levels of the bottom of the LMFA flume	108
5.6	Local Froude number distribution for RF300L	110
5.7	Depth-averaged velocities for RF300L: mixing layer development	111
5.8	Mixing layer widths and centres for reference flows	112
5.9	Reynolds shear stress at one elevation for RF300L	113
5.10	Depth-averaged Reynolds stresses at the interface for reference flows	114
5.11	Lateral distribution of depth-averaged Reynolds stress for reference flows	115
5.12	Autocorrelation function of lateral velocity in and out of the mixing layer for RF300L	116
5.13	Spectral analysis for RF300L in the centre of the mixing layer	117
5.14	Spanwise distribution of boundary shear stresses for RF300L	118
5.15	Isolines of longitudinal velocities in four cross-sections for RF300L	118
5.16	Local Froude number distribution for RF200L and RF400L	120
5.17	Depth-averaged velocities for RF200L and RF400L	121
5.18	Reynolds shear stress and lateral gradient of longitudinal velocity for RF200L and RF400L	122
5.19	Turbulence intensity for RF200L and RF400L	123
5.20	Autocorrelation function of lateral velocity in the mixing layer for RF200L and RF400L	123
5.21	Spectral analysis for RF200L and RF400L	124
5.22	Spanwise distribution of boundary shear stresses for RF200L and RF400L	125
5.23	Streamwise distribution of boundary shear stresses in a subsection for reference flows	126
5.24	[Isolines of longitudinal velocities in four cross-sections for RF200L and RF400L	127
6.1	Depth-averaged velocity fields for RF300L and GC330L	131
6.2	Lateral expansion of the downstream recirculation zones for groyne-case flows	133
6.3	Angle of deviation relative to the streamwise direction for GC330L	134
6.4	Water levels and depth-averaged longitudinal velocity for $Q_t = 24.7$ l/s and $d = 0.3$ m	135
6.5	Froude number distribution for groyne-case flow $Q_t = 24.7$ l/s and $d = 0.3$ m	136
6.6	Scheme of the various sources of backwater effects for groyne-case flow GC330L	137
6.7	Flow depths in a subsection for RF300L and GC330L	137
6.8	Discharge distribution for GC330L	138
6.9	Width and centre of the mixing layer for RF300L and GC330L	139
6.10	Depth-averaged Reynolds shear stress distribution at the interface for GC330L	141
6.11	Reynolds stresses in the vicinity the downstream recirculation zone for GC330L	142
6.12	Distribution of depth-averaged Reynolds stress for GC330L	143
6.13	Turbulence intensity for GC330L	144
6.14	Autocorrelation function of lateral velocity at the interface for RF300L and GC330L	145
6.15	Power spectrum densities in the centre of the mixing layer for GC330L and RF300L	145
6.16	Cross power spectrum densities in the centre of the mixing layer for GC330L and RF300L	146
6.17	Data coordinates in the vicinity of the recirculation zone used for spectral analysis for GC330L	146
6.18	Autocorrelation function of lateral velocity along the separation line for GC330L	147
6.19	PSD, CPSD and phase relation along the separation line for GC330L	148
6.20	Boundary shear stress distribution for RF300L and GC330L	149
6.21	Boundary shear stress distribution for GC330L compared to RF300L	149
7.1	Depth-averaged velocity fields of groyne-case flows	152
7.2	Angle of deviation relative to the streamwise direction for GC330L and GC350L	153
7.3	Water levels and depth-averaged longitudinal velocity for $Q_t = 24.7$ l/s and $d = 0.5$ m	154
7.4	Froude distribution for $Q_t = 24.7$ l/s, with $d = 0.3$ m and $d = 0.5$ m	154
7.5	Water levels in a subsection for RF300L, GC330L and GC350L	155
7.6	Scheme of the various sources of backwater effects for groyne-case flows	156
7.7	Discharge distribution for GC350L	156
7.8	Width and centre of the mixing layer for GC330L and GC350L	157
7.9	Depth-averaged Reynolds shear stress distribution at the interface for GC330L and GC350L	158
7.10	Link between Reynolds shear stress and lateral gradient of longitudinal velocity GC350L	158
7.11	Reynolds shear stress in the vicinity of the downstream recirculation zone for GC350L	159
7.12	Reynolds stresses distribution and link with velocity for GC350L	160
7.13	Turbulence intensity for GC330L and GC350L at the interface	160
7.14	Autocorrelation function of lateral velocity at the interface for GC330L and GC350L	161

7.15	Power spectrum densities in the centre of the mixing layer for GC330L and GC350L	161
7.16	Cross power spectrum densities in the centre of the mixing layer for GC330L and GC350L	162
7.17	Autocorrelation function of lateral velocity along the separation line for GC330L and GC350L	163
7.18	PSD, CPSD and phase relation along the separation line for GC350L	163
7.19	Boundary shear stress distribution for GC330L and GC350L	164
7.20	Boundary shear stress distribution for GC350L compared to GC330L	165
7.21	Angle of deviation relative to the streamwise direction for GC230L and GC430L	165
7.22	Water levels and depth-averaged longitudinal velocity for GC230L and GC430L	166
7.23	Froude distribution for GC230L, GC330L and GC430L	167
7.24	Discharge distribution for GC230L, GC330L and GC430L	168
7.25	Width and centre of the mixing layer for increasing total discharge	169
7.26	Depth-averaged Reynolds shear stress distribution at the interface for GC230L and GC430L	170
7.27	Reynolds stresses distribution and link with velocity for GC430L	170
7.28	Reynolds stresses in the vicinity of the downstream recirculation zone for GC230L and GC430L	171
7.29	Turbulence intensity for GC230L and GC430L	172
7.30	Autocorrelation function of lateral velocity at the interface for GC230L and GC430L	172
7.31	Power spectrum densities in the centre of the mixing layer for GC230L and GC430L	173
7.32	Cross power spectrum densities in the centre of the mixing layer for GC230L and GC430L	173
7.33	PSD, CPSD and phase relation along the separation line for GC230L and GC430L	174
7.34	Boundary shear stress distribution for GC230L and GC430L compared to GC330L	175
8.1	Length of recirculation zone and friction number: present experiments	178
8.2	Depth-averaged vertical dispersion X_{xx} and X_{xy} for reference flows	180
8.3	Depth-averaged vertical dispersion X_{xx} for groyne-case flows	181
8.4	Depth-averaged vertical dispersion X_{xy} for groyne-case flows	182
8.5	Scheme of the mesh for calculating gradients	185
8.6	Momentum balances for reference flows	186
8.7	Momentum balances for GC330L	188
8.8	Momentum balances for GC350L	190
8.9	Momentum balances for GC230L	191
8.10	Momentum balances for GC430L	192
A.1	Ackers' method (1993), discharge adjustment fac. and coherence fac. vs relative depth	229
A.2	Solving an abrupt floodplain contraction with 1D-models	234
B.1	Characteristics and schematic view of the flow around a spur dyke	237
B.2	Photograph of the experimental set-up	237
B.3	Normalized recirculation length measured in the lee of a spur dyke	240
B.4	Velocity and bed-load transport for case Hr02d24i	241
B.5	Dimensionless bed evolution for two critical velocities	242
B.6	Dimensionless bed evolution for three test cases	242
B.7	Corrected velocity from LSPIV measurements for the test case Hr04d24i	243
B.8	Effect of permeable spur dyke	243

List of Tables

3.1	Mean characteristics of the experimental flume at the LMFA	45
3.2	Listing of the parameters used for solving the II-Theorem	67
3.3	Experimental data-set of experiments at the LMFA	68
4.1	Summary of the different sources of devices uncertainties	74
4.2	Devices uncertainties in LMFA experiments	75
4.3	Longitudinal length of recirculation zones	78
4.4	Standard deviation using the original and modified data despiking method	83
4.5	Original values of velocities and Reynolds stresses before rotation	85
4.6	Angles of rotation computed with the method of local rotation	87
4.7	Percentage of Q_t^{inj} , computed using micro-propeller and ADV LMFA data	92
4.8	Mean Residues and correlations of reference flow fits	95
4.9	% of Q_t^{inj} , computed using the corrected micro-propeller data of the reference flows	95
4.10	Micro-propeller recalibration coefficients for groyne-case flows	97
4.11	% of Q_t^{inj} for the groyne cases after using the groyne-case calibration	98
5.1	Fits of water levels and fits of the bottom under reference conditions	105
5.2	Boundary shear force and gravity force in the total cross-section for RF300L	119
5.3	Boundary shear force and gravity force in the total cross-section for RF200L and RF400L	126
5.4	Established hydraulic parameters for reference flows	128
6.1	Longitudinal lengths of the downstream recirculation zones for groyne-case flows	132
8.1	Effects of a groyne on the momentum balance compared to the reference	189
8.2	Effects of an increase in the groyne length or in the total discharge	193
B.1	Description of the experiments carried out in Japan	238

Notation

Mathematical operator

$\overline{(-)}$	Ensemble mean
$\langle - \rangle_{j,k,l}$	Spatial averaging along the directions j,k,l
$(-)_d$	Depth averaging operator: $(-)_d = \frac{1}{h} \langle - \rangle_z$
$\ - \ $	Quadratic norm
$FT(-)$	Fourier Transform
$(-)'$	Operator of fluctuation

Subscripts or superscripts

b	Bottom
cr	Critical
fp	Floodplain
hpr	Horizontal plan of reference
inj	Injected
int	Interface
l	Left
mc	Main channel
p	Parietal
r	Right
rec	Recirculation
ref	Reference flow
s	Surface
t	Total
w	Wall
ws	Water surface

Principal symbols

Roman letters

A	m^2	Total cross-sectional area of compound the channel
A_i	m^2	Cross-sectional area of subsection i
A_a	m^2	Apparent area perpendicular to the flow direction
ACC	USI	Accuracy on measurements
B	m	Total width of the compound channel
B_i	m	Width of subsection i
C_d	m	Drag force coefficient
C_j	USI	Calibration coefficient or constant
d	m	Groyne length

D_1	rad	Rotation angle 1 for correcting ADV data
D_2	rad	Rotation angle 2 for correcting ADV data
$D_{p,i}$	m	Distance between the ultrasonic probe and the surface i to be measured (i = ws or i = b)
e	m	Groyne thickness
f	Hz	Frequency
F_e	N	External force acting on the fluid
F_d	N	Drag force
$Fr(x, y)$	-	Local Froude number at position (x, y)
Fr_i	-	Froude number in the subsection i
F_s	Hz	Sampling frequency
g	m/s ²	Gravitational acceleration ($g = 9.81$ m ² /s)
$h(x, y)$	m	Time-averaged local water depth
H_{bf}	m	Bank-full height
H_i	m	Width-averaged water depth in the subsection i
H_r	-	Relative water depth ($H_r = H_{fp}/H_{mc}$)
I_k	-	Turbulence intensity in energy
I_x	-	x-wise turbulence intensity
I_y	-	y-wise turbulence intensity
k	m ⁻¹	Wave number calculated with the longitudinal velocity
\bar{k}	J/kg	Kinetic energy of the mean motion per unit of mass
\bar{k}'	J/kg	Mean turbulent kinetic energy per unit of mass
k_s	m	Surface roughness height
$K_{s,i}$	m ^{1/3} /s	Strickler's coefficient in the subsection i
l	m	Turbulent length-scale
l_m	m	Turbulent mixing length
L	m	Length of the flume
L_x	m	Streamwise length of the recirculation
$L_y(x)$	m	Spanwise length of the recirculation at station x
n_i	s/m ^{1/3}	Manning's coefficient in the subsection i
N	-	Number of samples in a series
p	Pa	Instantaneous pressure: $p = p(x, y, z, t)$
p_o	-	Porosity of the fictional mobile bed
P	m	Wetted perimeter in the total cross-section
P_i	m	Wetted perimeter in the subsection i
Pr	-	Prandtl number
q_x^i	m ² /s	Longitudinal discharge per unit of length $U_d \times h$
q_y^i	m ² /s	Lateral discharge per unit of length $V_d \times h$
Q_i	m ³ /s	Discharge in the subsection i
R_d^2	-	Least squares method determination coefficient
R_i	m	Hydraulic radius in subsection i
R_{ii}	-	Autocorrelation function of the velocity in the direction i
$R_{img,i}$	m/pixel	Image resolution after orthorectification for LSPIV measurements (i = longitudinal or lateral direction)
Re_i	-	Reynolds number in a subsection i: $Re_i = U_{d,i} \times 4R_i/\nu$
Re_{*i}	-	Turbulent Reynolds number in a subsection i: $Re_{*i} = u_{*i} \times k_{s,i}/\nu$
RY	USI	Reproducibility
S	-	Friction number ($S = \lambda \times d/8H$)
S_{ii}	m ² /s ² /Hz	Power (S_{xx}, S_{yy}) or cross-power spectrum density (S_{xy})
$S_{e,x,i}$	-	x-wise Slope of energy in subsection i
$S_{f,x,i}$	-	x-wise Slope of friction in subsection i
$S_{o,i}$	m/m	Bottom mean slope in the i-wise direction

$S_{ws,i}$	m/m	Free surface mean slope in the i-wise direction
t	s	Time
$T_{b,i}$	Pa	Boundary shear stress averaged on the wetted perimeter of subsection i
$T_{ij,k}$	Pa	Depth-averaged Reynolds stress at the position k (k = interface for instance)
u_*	m/s	Local friction velocity ($u_* = \sqrt{\tau_b/\rho}$)
u	m/s	Instantaneous longitudinal velocity ($u = u(x, y, z, t)$)
u_i	m/s	Instantaneous velocity in the i direction
$U_{*,i}$	m/s	Friction velocity in a subsection i: $U_{*,i} = \sqrt{T_{b,i}/\rho}$
U_d	m/s	Time and depth-averaged longitudinal velocity
U_i	m/s	Longitudinal mean velocity in the subsection i
U_s	m/s	Time-averaged longitudinal surface velocity
v	m/s	Instantaneous lateral velocity ($v = v(x, y, z, t)$)
V_n	m/s	Norm of the velocity
V_o	V	Voltage
V_s	m/s	Time-averaged lateral surface velocity
w	m/s	Instantaneous vertical velocity ($w = w(x, y, z, t)$)
$W_{r,i}$	-	Shallowness ratio in subsection i
x	m	Streamwise direction
X_{ij}	m ² /s ²	Depth-averaged dispersion on the vertical in the direction (i,j)
y	m	Spanwise direction
z	m	Vertical direction
$z(x, y)$	m	Local level of the free surface or of the bottom relative to a reference frame
Z_i	m	Level in a subsection of the free surface or of the bottom relative to a reference frame

Greek letters

β_{ij}^v	-	Vertical momentum coefficient in the i and j direction
χ_{ij}	m ³ /s ²	Vertical dispersion term of direction (i,j)
ϵ	m ² /s ²	Turbulent dissipation rate
ϕ	rad	Phase relation
κ	-	Von Karman constant ($\kappa = 0.41$)
λ	-	Darcy-Weisbach friction factor
λ_E	-	Elder coefficient
λ_S	-	Student coefficient
λ_U	-	Universal threshold
μ	N.s/m ²	Dynamic viscosity of water ($\mu = 1.002 \times 10^{-3}$ N.s/m ² at 20°C)
μ_t	N.s/m ²	Turbulent dynamic eddy viscosity
ν	m ² /s	Kinematic viscosity of water ($\nu = 1.004 \times 10^{-6}$ m ² /s at 20°C)
ν_t	m ² /s	Turbulent kinematic eddy viscosity
ρ	kg/m ³	Water density ($\rho = 998$ at 20°C)
τ	s	Turbulent time-scale
τ_a	Pa	Apparent shear stress at the interface
τ_b	Pa	Local boundary shear stress
$\tau_{ij,k}$	Pa	Reynolds stress at the position k
τ_t	Pa	Total stress (viscous + turbulent)
θ	deg	Angle between the ADV and the flume reference frames

Abbreviations

<i>ADV</i>	Acoustic Doppler Velocimeter
<i>CPSD</i>	Cross-Power spectrum density
<i>DCM</i>	The Divided Channel Method
<i>DNS</i>	Direct Navier-Stokes Simulation
<i>EDM</i>	The Exchange Discharge Model
<i>FP</i>	Floodplain
<i>GRPs</i>	Ground Reference Points
<i>ISM</i>	The Independent Subsection Method
<i>LMFA</i>	Laboratoire de Mécanique des Fluides et d'Acoustique
<i>LSPIV</i>	Large Scale Particle Imaging Velocimeter
<i>LES</i>	Large Eddy Simulation
<i>MC</i>	Main channel
<i>PSD</i>	Power spectrum density
<i>RANS</i>	Reynolds-Averaged Navier-Stokes equations
<i>SCM</i>	The Single Channel Method
<i>SKM</i>	The Shiono and Knight Method
<i>SERC FCF</i>	Science and Engineering Research Council Flume Channel Facility

General introduction

Historic background

With the industrial revolution in the 18th–19th centuries, the massive rural exodus and the resulting urbanization, engineers thought that the control of rivers was within their reach. The rivers were converted, diverted and channelled in order to promote the production, trade and industrial developments. The fantasy that flooding events were controllable was grown by building dikes and dams ever larger for containing the excess water. This policy therefore allowed an acceleration of the settlement and industrialization of the floodplains [[Arnould, 2005](#)].

If the beginning of the 20th was “quite calm” because of the economic crisis and the two world wars, from 1945 until the end of the seventies, with the decline of the rural society, mass urbanization of floodplains started up again. The need of space quickly and easily urbanizable pushed to build everywhere. Floodplains were occupied by businesses, industries, individual and collective housing. In cities, thousands of kilometres of rivers, torrents and streams were dried, covered by streets, car-parks, businesses and administrative buildings. This urbanization suppressed the capacity of absorption of the water by the ground, therefore promoting the rapid flow of water towards rivers. Floods were therefore increased by additional contributions due to excess runoffs: ordinary floods became more devastating for people and goods [[Arnould, 2005](#)]. The first responses for floodplain and cities protection against flood consisted in heavy alleviation works, such as dikes, detention reservoirs and dams set along rivers. The dikes channelled the excess flow in the main channel by artificially increasing the height of the river banks and the detention reservoirs enabled to temporary store the excess water that would overflow from the river channelled by dikes. Dams were used for regulating the downstream river hydrology. Nevertheless, these flood counter-measures resulted in moderate or poor outcomes, due among other things (1) to unanticipated morphological responses of the rivers, (2) to the dike working-principle itself: dikes accelerate river flow and do not attenuate the maximum of flood-discharge [[Lefort and Tanguy, 2009](#)], (3) to bad designing of the hydraulic work and (4) in worst cases to dike breaches.

In addition to developments in cities and floodplains, the number of transit facilities increased in the floodplains as well. With the motorways, railways and the other transport infrastructures, hundreds of bridges and transversal embankments (unsinkable and designed for a minimum of one hundred year return period) were then constructed for crossing rivers and floodplains [[Arnould, 2005](#)]. These constructions, occupying floodplains, reduced the flow section, increasing therefore the flow-velocity downstream and generating a backwater curves with rising water depths just at the upstream of the obstacle cross-section. Indeed, upstream of the bridge pier or transversal embankment, a flow contraction is generated (for bottom made of erodible materials, scours occur in the vicinity of the obstacle tip). The flow then diverges downstream of the obstacle. In the diverging zone, the kinetic energy of the flow is partly dissipated and the rest is converted into potential energy until the flow is no more perturbed by the upstream obstacle [[Lefort and Tanguy, 2009](#)]. As a consequence, bridges and embankments were responsible for increasing the flooded area upstream of the obstacle, but they attenuated the maximal flood-discharge.

Since the eighties and especially from the nineties, governments, international organizations, scientists and engineers have realized the risks associated with the massive development of flood-

plains. They realized that although the development of the floodplains is absolutely necessary for our economic and social needs, such developments cannot be done despite the watershed ecosystem. The development must be carried out in a rational way to maximize the economic and social welfare in an equitable manner without compromising the sustainability of vital ecosystems [*Programme associé de gestion des crues*, 2004]. “River engineers are therefore more and more solicited to mitigate flood impacts in sustainable ways: more space is allocated to rivers, respecting or reconstituting their natural floodplains by withdrawing dikes and abandoning possible settlements areas or using them only seasonally” [*Bousmar*, 2002]. However these sustainable solutions are often applicable on areas with low anthropization only. In large anthropized areas, “damages” are often too large to be easily and quickly corrected using sustainable ways and alternative solutions must be applied for limiting the risks in such areas, as upstream dry dams built in region with low interests for protecting the high-valued zones.

Scientific background

Engineers’ challenge regarding the flood management is a twofold challenge: (1) river restoration, (2) people and goods protections. To achieve this, hydraulics engineers need robust and accurate tools for modelling the relationship between the river hydrology and the hydraulic parameters. Thanks to hydrological models that provide the discharge corresponding to a given rain by estimating as well as possible the percentage of the precipitation that runoffs for a given watershed (weakly or largely anthropized, restored or not), hydraulic models must be capable to accurately predict the water levels, the velocities in the flooded urbanized areas, the flood propagation and the morphological consequences of the floods. One of the main difficulty lies in the complexity of the modelling of overbank flows.

During a flood event, the river main channel (MC) may overflow in its contiguous floodplains (FP). As a result, the flow in the main channel, faster and deeper, interacts with the flow in the floodplain, which is slower and shallower. In such a configuration, the river is generally modelled as a two-stage channel and the resulting flow is called “compound channel flow”.

Under uniform flow conditions (no streamwise variation in the hydraulic parameters and water surface slope is parallel to the bottom slope of the river), in addition to bed and wall frictions, a zone of intense shearing at the junctions between the main channel and the floodplains is generated because of the difference in velocity between channels. This zone, the so-called “mixing layer”, is characterized by strong momentum transfer due to turbulent exchanges between channels and is a source of turbulent dissipation. This dissipation results in a reduction in the river conveyance [*Knight and Demetriou*, 1983].

As uniform flows in compound channel are quite uncommon in the field, mainly due to changes in the topography of floodplains and main channels, new works were then conducted on configurations where the river flow or the river geometry progressively and continuously vary. These flows are called “gradually varied” flows. Three types of gradually varied flows were studied:

1. Gradually varied flow in prismatic geometry: disequilibrium in the upstream discharge distribution [*Bousmar et al.*, 2005; *Proust et al.*, 2011].
2. Non prismatic geometry with continuously varying floodplain with a constant overall width for the flume (skewed compound channels [*Chlebek and Knight*, 2008; *Elliot and Sellin*, 1990; *Sellin*, 1993]; meandering two-stage channels [*Shiono and Muto*, 1998]).
3. Non prismatic geometry with a variable overall width for the flume (symmetrically converging floodplains [*Bousmar et al.*, 2004]; symmetrically diverging floodplains (divergence

angle smaller than 4° , *i.e.* no development of recirculation zones) [Proust, 2005] [Bousmar *et al.*, 2006; Proust *et al.*, 2010]; compound channel with an abrupt floodplain contraction (convergence angle of 22°) [Proust *et al.*, 2006]).

In non prismatic channels, each channel either yields or receives water from its contiguous channel(s) [Bousmar, 2002; Proust, 2005]. These mass exchanges are characterized by non-negligible lateral velocities which may generate additional momentum transfer if longitudinal velocities between channels are different. As a consequence, depending on the geometry, either diverging or converging for instance, the momentum transfer due to mass exchange may become dominant relative to the momentum transfer due to turbulent exchange. Previous effects are also observed in prismatic channels, where an unbalanced upstream discharge distribution induces an over- or an under-feeding of the floodplain (the contrary for the main channel). In such a flow, measurements seem to also indicate a strong correlation between mass exchange and momentum transfer due to turbulent exchange, but further experiments are still necessary for well establishing these dependencies. Nevertheless, previous experiments in non-prismatic and prismatic channels changed the way the flow can be described using theoretical modelling; the modeller must be aware of the weight of each encountered phenomenon in order to provide a proper modelling of gradually varied flows.

If in natural or anthropized rivers, the river cross-section generally gradually and continuously varies, transversal and discontinuous obstacles either natural (hill on a floodplain, rock slide, ...) or artificial (embankments for railways and motorways, ...) may partially or totally block off floodplains. The flow in the floodplain is therefore contracted by the obstacle that promotes the development of two recirculation zones, one upstream of the obstacle and one downstream. It results in a reduction of the flow section and in the generation of strong mass exchange between channels. In addition, the longitudinal slope of the water surface at the tip of the obstacle is at least one order of magnitude steeper than the bottom slope: such a flow is therefore considered as “rapidly varied” [Ancey, 2009; Chow, 1959]. Although really common on the fields (See Figure 1, flood hazard mapping in Sainte-Foy l’Argentière near Lyon in France; red circles represent transversal embankments), the hydrodynamics of overbank flows with an obstacle set on the floodplain has been rarely studied. Studies rather dealt with recirculating flows without a particular interest for compound geometries. Thus, in the literature we mostly found studies on scours and scours-countermeasures in single and compound channels [Melville *et al.*, 2006] and [Zhang and Nakagawa, 2008; Zhang *et al.*, 2009], on hydrodynamic considerations for recirculating flows in single channel [Carrasco and Vionnet, 2004; Koken and Constantinescu, 2008] and on recirculating flows behind isles or sudden enlargement [Babarutsi *et al.*, 1989; Chu *et al.*, 2004]. To the author knowledge, Proust [2005, Chap. 9] is the only author who experimentally studied overbank flows with an obstacle set on the floodplain. He investigated three flows in an asymmetrical compound channel with a thin embankment (or **groyne**) set against the right floodplain-bank, perpendicular to the streamwise direction. These experiments showed a correlation between the longitudinal length of the recirculation zones, the length of the obstacle and the bottom friction. On the other hand, few information were available regarding the turbulence and boundary shear stress distributions within and between subsections. In the sequel, the three previous flows were numerically modelled using Rubar20 (2D-H St-Venant equations with no transport equations for the turbulence [Paquier, 1995]). The results indicated that the numerical modelling has some difficulty for capturing recirculating flows and the role of the turbulence was still not completely understood. The author concluded that additional detailed measurements and theoretical developments were therefore necessary.

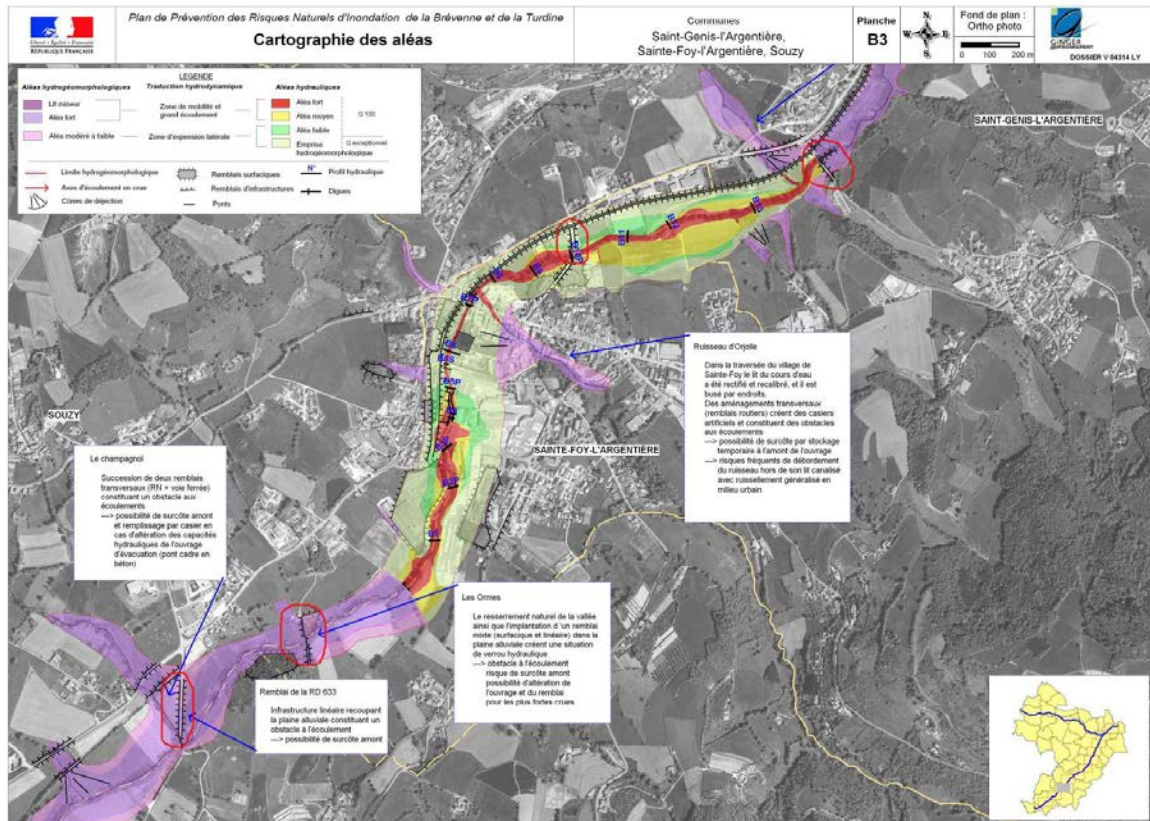


Figure 1 – Flood hazard mapping near Sainte-Foy l'Argentière in France; red circles represent transversal embankments. (source: www.rhone.equipement.gouv.fr/.../B3_ALEAS_St-Genis-L-Argentiere_Ste-Foy-l-Argentiere_Souzy_cle21e593.pdf)

Scope of this work

Given the previous historic and scientific backgrounds, the understanding of overbank flows in compound channel in the vicinity of a transversal obstacle blocking off the floodplain is paramount for flood modellers. The accurate estimation of the flood with a returning period of one hundred year is a necessary part of the designing of unsinkable motorway and railway embankments [Lefort and Tanguy, 2009]. Moreover, as part of the establishment of the flood hazards prevention plans (in French PPRI: Plan de Prévention des Risques d'Inondations), flooded area in the vicinity of embankments must be determined with minimal uncertainties (see Figure 1 for an example of flood mapping). Moreover, the danger can be evaluated through a vulnerability parameter proportional to the product of the velocity by the water depth in a considered area [Dimitrov and Pin, 2006]. Accurate measurements of mean hydraulic parameters, turbulence and boundary shear stresses are therefore required for improving our understanding of overbank flows in the vicinity of transversal embankment.

The first objective of this thesis is thus to build a complete set of data of rapidly varied flows in the vicinity of a groyne set on the floodplain of a compound channel. Experiments were conducted in two **asymmetrical** compound channels. The first one is located at the Laboratoire de Mécanique des Fluides et d'Acoustiques (LMFA), in Lyon, France and the second is located at the open-Laboratory of Ujigawa (Kyoto University, Japan). In France, the effects of variations in the groyne length and total discharge were investigated for six groyne-case flows. Four were fully detailed. Depth, velocity, turbulence, boundary shear stress and geometry of recirculation zones were measured; two were partially detailed: the turbulence and boundary shear stresses were not measured. In Japan, the effect of the permeability of the groyne were investigated for ten groyne-case flows. Five were conducted with impermeable groyne and five

were conducted with a permeable groyne. These flows were partially described: the turbulence and boundary shear stresses were not measured. In addition to the work done in this PhD-thesis, this data-set will be used later to make a benchmarking of existing numerical models in the case of rapidly varied flows.

The second objective of this thesis is to analyse effects on the hydraulic parameters of the superimposition of the two problems that are (i) flow in compound geometry and (ii) rapidly varied flow in the vicinity of a thin obstacle. We answer to the question: “what are the impacts of groyne on the physical processes typically encountered in compound channels?”. To achieve this, three flows without groyne and close to uniform flow conditions were investigated in the LMFA flume. They were used as reference state to be compared with the groyne-case flows previously measured in the LMFA flume. Mass exchanges and mixing layers characteristics were notably evaluated for each flow cases.

The last objective of this thesis is to express the physical processes as a function of the measured parameters using a two-dimensional momentum equation based on the Saint-Venant equations. The weight of each process is then evaluated and compared together. To term, these comparisons enable to define zone of dominance in the flow for certain processes that modellers must then treat or model with care for producing robust flood mappings or prevision model.

Contents Outline

The main body of the thesis is divided into three parts and exclusively deals with experiments performed at LMFA. Experiments in Japan are presented in appendix [B](#). The first part of the main body then presents a state of the art of the physics of flows in straight compound open-channels, together with the fundamental equations and the modellings we used for identifying the flow processes. The second part deals with the experimental set-up at the LMFA laboratory and the different methods used for post-processing measurements. The third part finally presents the data-set we measured and explores the physical processes associated with the presence of a groyne set onto the floodplain.

The first chapter deals with a state of the art on the physics of flows in compound open-channels with a **straight main channel**. Physical phenomena of flows under uniform flow conditions are first discussed; the first aim, here, is to make a statement of the additional phenomena that are present in compound geometry with comparison to single channel flows. Then additional phenomena for gradually varied flows in compound channel are highlighted. Eventually, the physics of recirculating flows in both single and compound channels is presented; the lack of information concerning the physical processes in flows occurring in the vicinity of an obstacle in compound channel is pointing out.

In the second chapter, the fundamental equations, as their simplifications used for modelling overbank flows, are described. The purpose of this chapter is to show that physical processes encountered in a compound channel whether under uniform flow conditions or under non uniform flow conditions can be described using a special 2D-H momentum equation based on the Saint-Venant Equation. The modelling usually used in compound channel are also presented. They are used in absence of enough good measurements of the parameters contained in the momentum equation. Nevertheless none of them have been developed for recirculating flows.

In the third chapter, the experimental flume and its equipment we improved are presented. The topography of the asymmetrical flume, the new filling equipments, the new boundary condition settings and the automatic traversing devices we designed are described. The new measuring devices we adapted for this thesis as the old one, their operating principles and their uncertainties are also presented.

In the fourth chapter, the data post-processing we used for correcting measurements are described. The LSPIV technique and the method for assessing the geometry of the recirculation zones is first exposed. The necessity of correcting the Doppler data and the velocity measurements is then discussed. The protocol for spectral analysis of the turbulence is also given.

The fifth chapter is devoted to the study of three reference flows (without groyne set on the floodplain). These flows are developing flows, but they can be considered **as established in a segment located in the centre of the flume**. We thus show that despite the shortness of the flume, an establishment can be reached thanks to particular inlets and outlets we used in the flume for this thesis.

In the sixth chapter and in the seventh chapter, we study the superimposition of the compound channel problem with the recirculating flow problem. Geometries of the recirculation zones that develop of both sides of the groyne are first presented. We then compare one groyne-case flow to its corresponding reference flow (Chapter 6). The purpose here is to understand what are the influences of the groyne on the flow parameters we previously described in Chapter 5. To finish, the various groyne-case flows are compared together (Chapter 7); the purpose is to evaluate (1) the influences of the groyne length at a given total discharge and (2) the influence of the total discharge at a given groyne length. We analyse in details the recirculation zones, the mean flow parameters, the friction, the turbulence and the coherent structures developing in mixing layers.

The last chapter is devoted to the estimation of the weight of each physical process that occurs in the flows we measured (reference and groyne-case flows). We first show that the theory developed for sudden enlargements by *Babarutsi et al.* [1989] and *Rivière et al.* [2004] does not enable to easily identify which phenomenon from the turbulence and the friction dominates the development of the recirculation zones downstream of the groyne in the groyne-cases we studied. Dominances are therefore estimated through the use of a **dispersive** 2D momentum equation. It results that if mass exchange and the associated momentum transfer are the dominant phenomena for flows with a groyne set onto the floodplain whatever are the groyne length and the total discharge, the turbulence in mixing layers and the friction effects are not negligible.

The conclusion finally gives an overview of the main results of this thesis and some prospects are proposed for future studies.

Notice that in appendix, one is devoted to the experiment performed in Japan. Impact of impermeable and permeable groynes on a flow in a compound channel and considerations on bed-load transports are presented [*Baba et al.*, 2010]. Changes in the bottom slope are also investigated. Finally effects of the length of the flume on the longitudinal length of the recirculation zones is analysed.

Part I

Physics and fundamental equations

1

Physics of compound channel flows: a literature review

In a natural or engineered river, the flow is usually contained in the main channel, limited in each side by banks. During snow melting or significant rainfalls, the river main channel (MC) cannot conserve all the runoff. The river consequently overflows in its contiguous floodplains (FP). “The term “two-stage channel” or “compound channel” covers channel cross-sections having berms or floodplains that come into action at high flows but which are normally dry (Figure 1.1).” [Ackers, 1993]. In such a flow configuration, the flow in the main channel, faster and deeper, interacts with the flow in the floodplain, which is slower and shallower. It results in momentum transfer between channels, associated to the development of large coherent vortices at the interfaces separating the channels. These momentum transfers are at the origin of the reduction of the main channel conveyance and of the increase in the floodplain conveyance [Knight and Demetriou, 1983; Sellin, 1964].



Figure 1.1 – Photographs of a compound open-channel in Japan near the open-laboratory of Ujigawa.

The purpose of this chapter is to make a comprehensive statement of the basic physics of overbank flows in straight compound open-channels with smooth floodplains. For a question of conciseness, the other types of compound channels that are not used in this thesis are not presented (rough floodplains, meandering, curvilinear channels, ...); a description of these flows can be found in Ikeda and McEwan [2009].

1.1 Technical jargon of the compound channel

1.1.1 Main geometrical parameters in a straight compound channel

The geometrical description of the compound channels uses simple geometrical parameters (Figure 1.2). B is the total width of the channel, B_{fp} is the width of the floodplain and B_{mc} is the width of the main channel. H represents the local water depth, H_{bf} the bank-full height and H_{fp} (resp. H_{mc}) the local water depth in the floodplain (resp. in the main channel). Finally $S_{o,i}$ ($i = x$ or $i = y$) is the average slope in the i -wise direction.

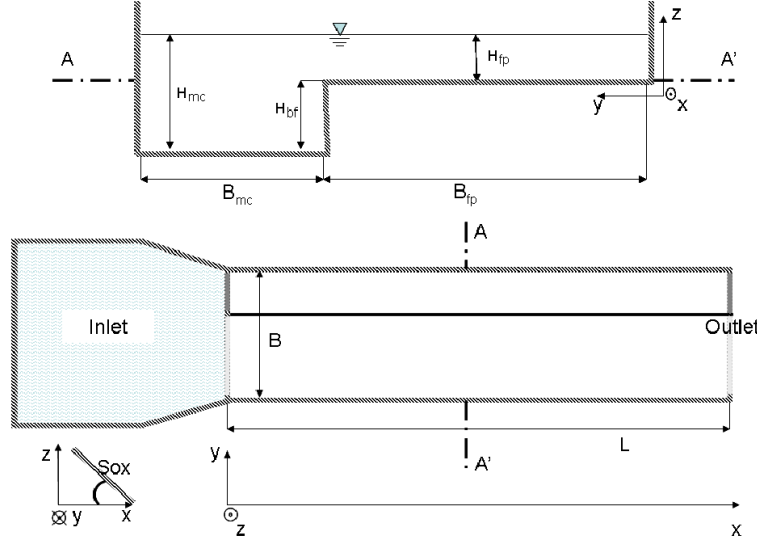


Figure 1.2 – Definition sketch of the geometrical parameters in an asymmetrical compound open-channel.

The significance of a flood is quantified by the modellers using the “relative flow depth” which writes:

$$H_r = \frac{\langle \bar{h}_{fp} \rangle}{\langle \bar{h}_{mc} \rangle} = \frac{\langle \bar{h}_{mc} \rangle - H_{bf}}{\langle \bar{h}_{mc} \rangle} \quad (1.1)$$

where $\langle \bar{h}_i \rangle = H_i$ is the spatial-averaged depth in the subsection i (floodplain or main channel).

An other convenient way exists to characterize an overbank flow, some engineers use the “relative hydraulic radius”. It is expressed as following in a compound channel [Nicollet and Uan, 1979]: $R_r = R_{fp}/R_{mc} = A_{mc}/A_{fp} \times P_{fp}/P_{mc}$, where A_i is a wetted subsection area and P_i is the associated wetted perimeter. In this case, the width of the subsections are taken into account in this ratio.

1.1.2 Compound channel flow classification

According to Chow [1959], the hydraulics parameters in a flow are variables of time and space. The flow can be therefore steady or unsteady (hydraulic parameters depend on the time) and can be (1) uniform (no streamwise variations of hydraulic parameters) or (2) gradually varied (low streamwise variations of hydraulic parameters) or (3) rapidly varied (high streamwise variations of hydraulic parameters).

In addition with the previous classification, a flow can either be considered as shallow or deep. In the shallow case, the flow is bounded by both the bottom and the free surface and is a layered turbulent flow in a domain for which the dimensions in the streamwise and spanwise directions

greatly exceed the third dimension (*i.e.* the water depth) [Jirka and Uijttewaal, 2003]. The turbulent motion is then separated between a small-scale three-dimensional turbulence (characteristic length smaller than the depth) and a large-scale turbulence (characteristic length greater than the water depth) bounded in an horizontal plan, because the vertical motion is restricted by the water depth. By contrast, in the deep case, the turbulent motion is restricted in any direction.

Whether for shallow or deep configurations, the kinetic energy of the turbulent macro-structures is transformed – across the Kolmogorov cascade – in internal energy by the micro-structures in order to respect the energy conservation. The limit of size of the smallest structures is linked to the dissipative effects (the Kolmogorov scale), while the macro-structures are limited by the geometry of the flow (size of obstacle, pipe diameter, water depth, ...). Nevertheless, for shallow cases, the biggest turbulent structures are not the most energetic structures, some intermediate structures indeed concentrate a lot of energy and transfer this energy to the biggest structures through an inverse cascade as well as to the smallest structures through the classical cascade [Batchelor, 1969; Kraichman, 1967].

NB – According to Chassaing [2000a] the classical cascade of energy is always associated to an inverse cascade, but excepted for shallow flow configurations, this inverse cascade is generally negligible.

1.2 Shallow uniform flow in straight compound open-channels

At the river scale, straight (or prismatic) compound geometry does not exist and therefore uniform flow - in stricto sensu - cannot exist. But at the reach scale, the flow can be approximated as uniform, because of the very low spatial variations. By contrast, such flows are quite frequent in many research or industrial applications. The absence of longitudinal variations of the flow parameters [Ancey, 2009] enables to easily identify the physical processes in such a flow configuration. The flow processes can be therefore more easily modelled or mastered by the operators. The study of such flows has enabled the understanding of the basic physics of overbank flows.

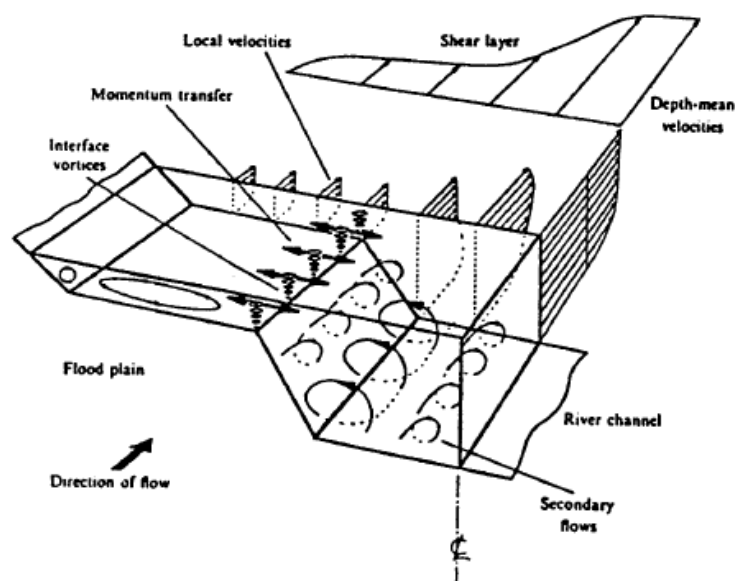


Figure 1.3 – Uniform flow in a straight compound channel: physical phenomena [Shiono and Knight, 1991].

The Figure 1.3 highlights the various encountered physical processes in a straight compound open-channel when the flow is uniform.

- Horizontal planform vortices in the mixing layer developing at the interface between the main channel and the floodplain,
- Frictions due to the presence of solid boundaries (bottom and lateral banks),
- Helical secondary currents of Prandtl's second kind due to the presence of the lateral banks.

These three phenomena obviously interact together which complicates the understanding of the physics of flows in compound channels. Notice that the interaction between the free surface and the air is generally neglected.

1.2.1 Velocity and depth

The variations in flow depth between the main channel and the floodplain has a strong influence on the vertical profiles of mean velocity. As shown in Figure 1.4 (isolines of longitudinal velocity), whether in symmetrical or in asymmetrical compound channel, in the floodplain(s), where the depth is shallow, the velocity is slow, while in the main channel, where the depth is deeper, the velocity is higher.

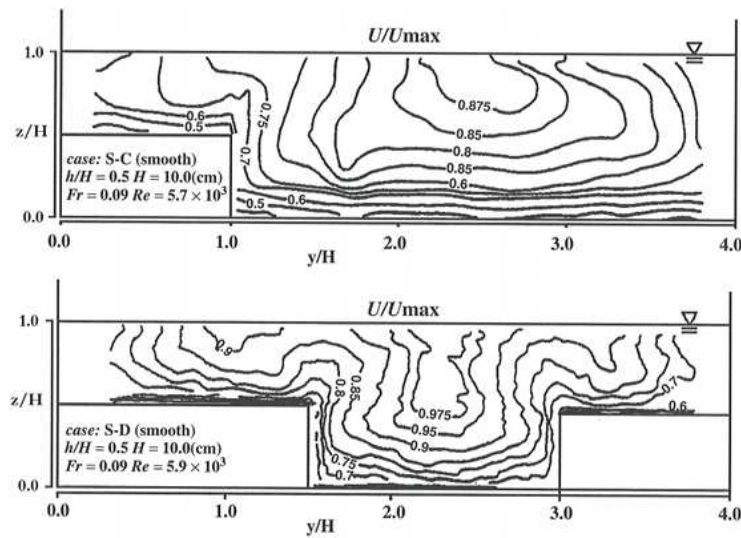


Figure 1.4 – Isovel profile of the longitudinal velocity in a compound channel. Asymmetrical and symmetrical flumes [Ikeda and McEwan, 2009].

In addition, as highlighted by the Figure 1.5, the lateral profile of longitudinal depth-averaged velocity in an asymmetrical compound channel can be approximated by an hyperbolic tangent profile, while in symmetrical channel, the profile is more or less fitted by an hyperbolic sinus profile [Chu et al., 1991].

1.2.2 Horizontal shear layer in compound open-channels

After Chu et al. [1991], two kind of shear layers or mixing layers exist depending on the geometry of the flume or on the hydraulic characteristics of the flow (Figure 1.5). In a single channel, given a constant water depth, the mixing layer is due to a difference in the roughness across the river-bed or is due to the flow interaction at the confluence between two rivers. For overbank flows, the main channel flow, faster and deeper and the floodplain flow, slower and shallower interact

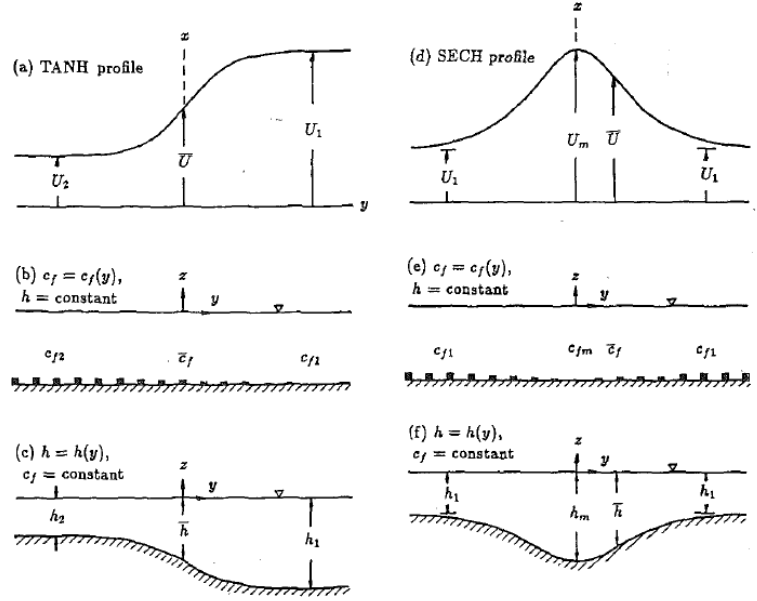


Figure 1.5 – Typical lateral evolution of a mixing layer in single channel and in compound channel. [Chu et al., 1991]

along the interface between both channels and thus generate the mixing layer. Whether in single channel or in compound channel flow, the velocity gradient induced by the velocity difference between each flow leads to generation of organized planform vortices centred on the inflectional point, as illustrated in Figure 1.6 for compound channel. These planform vortices are responsible for momentum transfer between channels.

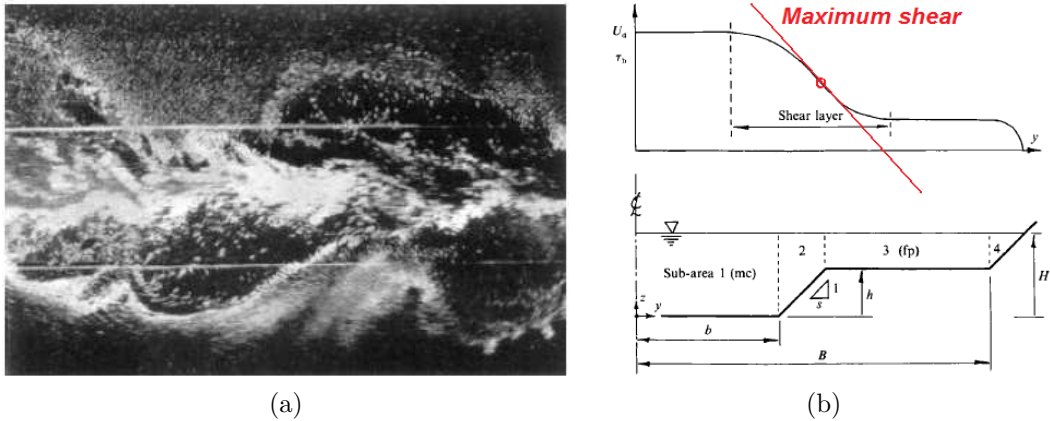


Figure 1.6 – (a) Top view of macro-structures developing at the interface MC/FP. The interface is indicated by the white stripes [Sellin, 1964] (b) Typical spanwise distribution of longitudinal depth-averaged velocity under uniform flow conditions in a compound channel [Shiono and Knight, 1991].

1.2.2.1 Shear layer in single channel

Before presenting the horizontal shear layer in a compound channel, it is interesting to recall the physics of the mixing layers in single channel, which are the most studied situations in the literature.

Deep shear layer

After *Uijtewaal and Booij* [2000], under deep flow conditions (*i.e.* $W_{r,i} = \langle \bar{h}_i \rangle / B_i > 2\%$), whether in a river or in a flume, the difference in velocity between two streams and the associated velocity gradient generate a zone of turbulence production. In first instance, 2D coherent structures are generated, then through the vortex-pairing mechanism, the structures grow until they become unstable and disintegrate into 3D turbulence.

From the theory of the self-similar mixing layer (transversal profiles of longitudinal velocity can be fitted with the same law) and from experiments it was deduced that the width δ of the mixing layer can be written as below:

$$\delta = \frac{U_1 - U_2}{MAX(\frac{\partial U_d}{\partial y})} \quad (1.2)$$

where U_1 is the cross-sectional velocity out of the mixing layer in the fast region, U_2 is the cross-sectional velocity out of the mixing layer in the slow region and $MAX(\partial U_d / \partial y)$ is the maximum gradient of depth-averaged velocity (*i.e.* gradient at the inflection point). Moreover notice that U_1 and U_2 are constant.

These mixing layers have a growth rate (Equation 1.3) that is proportional to $\lambda_M = (U_1 - U_2) / (U_1 + U_2)$:

$$\frac{d\delta}{dx} = \alpha_{dw} 2\lambda_M \quad (1.3)$$

where, according to *Uijtewaal and Booij* [2000] the factor α_{dw} (dw denotes “deep water”) has an empirically determined constant value of about 0.09 in most cases. Exceptions to the rule are: forced mixing layers, mixing layers with laminar boundary layers at the splitter plate [*Chu and Babarutsi*, 1988] and shallow mixing layers.

Shallow shear layer

After *Uijtewaal and Booij* [2000] and *van Prooijen et al.* [2005], under shallow flow conditions (*i.e.* $W_{r,i} < 2\%$), the additional friction caused by the presence of the bottom is responsible for the decrease in the growth rate of the mixing layer. In a such flow configuration, conditions of self-similarity on the velocity profile are not fulfilled and the velocity difference between both sides of the mixing layer is not constant anymore. Moreover the water depth restricts the turbulence motion in the vertical direction (turbulent eddies with dimensions larger than the water depth can only move in the horizontal plane). As a result the mixing layer width is no more the only characteristic turbulent length-scale.

Effects of shallowness and bottom friction on the development of a shear layer are expressed using the wake stability parameter or the friction number S [*Chu et al.*, 1983]. After *Chu et al.* [1991], this number compares the stabilizing effect of the friction (dissipation of turbulent kinetic energy) with the destabilizing effect of transverse shear (production of turbulent kinetic energy). For the shallow mixing layer the friction number is defined as:

$$S = \frac{\lambda \delta}{8H\lambda_M} \quad (1.4)$$

where λ is the Darcy-Weisbach coefficient, δ the width of the mixing layer, $\lambda_M = (U_1 - U_2) / (U_1 + U_2)$ and h the water depth.

Stability analysis proved the existence of a critical value S_c , which is ranging from 0.06 to 0.12 [*Alavian and Chu*, 1985; *Chu et al.*, 1983]. For $S \ll S_c$, the bottom friction has weak effects on the mixing layer and the latter is unstable because the 2D-macro-vortices are disintegrated

in 3D turbulence. For $S > S_c$ the growth of the instability is impeded by the bottom friction that generates an additional dissipation in the flow. As written by *Uijttewaal and Booij* [2000], “The bottom friction has a two-fold influence on the large scale structures. First, the bottom friction is responsible for dissipation of large scale energy which is transferred directly from the 2D large scale structures to 3D small scale bottom-generated turbulence without interaction of intermediate scales. Second, the bottom friction has a stabilizing influence on the generation of large scale structures and thereby reduces the growth of the mixing layer (see in Figure 1.7)”.

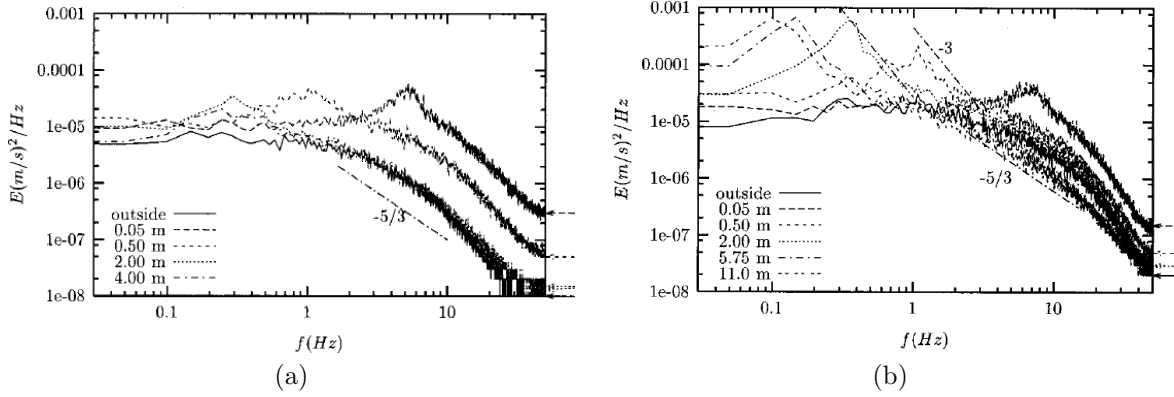


Figure 1.7 – Power-density spectra of spanwise velocity fluctuations in the centre of a mixing layer developing in single channel at various downstream positions. (a) $h = 42$ mm, (b) $h = 67$ mm [*Uijttewaal and Booij*, 2000].

Streamwise evolution of power spectrum densities are displayed in Figure 1.7 for the lateral velocity measured in the centre of two shallow mixing layers investigated by *Uijttewaal and Booij* [2000]. For the “less shallow” case ($h = 67$ mm in Figure 1.7.b), the spectral densities exhibit a peak with a slope of -3 at their high-frequency side, which indicates that the large coherent structures possess two-dimensional characteristics [*Batchelor*, 1969]. In addition, the frequency of the peaks shift towards lower frequency with downstream position, therefore highlighting a growth in the structures sizes. With increasing the shallowness, the peak reduces and the -3 slope vanishes after few meters. The shallowness and therefore the bottom friction have destroyed the 2D horizontal structures that have then degenerated into 3D structures.

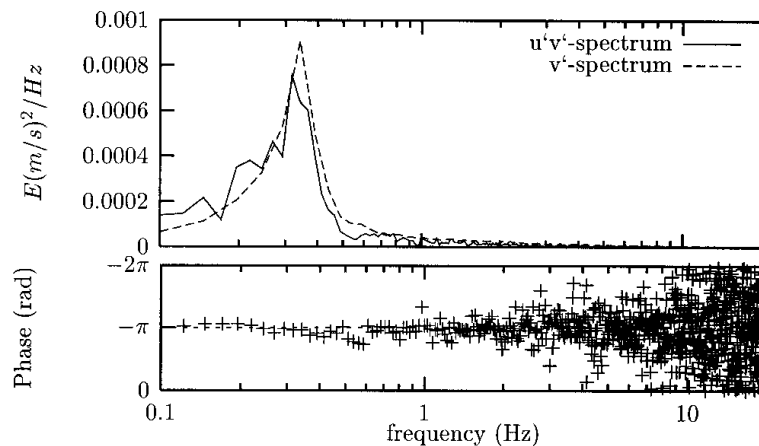


Figure 1.8 – Cross-power-density spectrum (upper panel) for velocity fluctuations and phase relation (lower panel) for the u' and v' components: $h = 67$ mm, $x = 2$ m, single channel [*Uijttewaal and Booij*, 2000].

Finally linking the power-spectrum of the spanwise velocity fluctuations v' with the cross-power spectrum and the phase relation between u' and v' (Figure 1.8) highlights that the peak of the power-spectrum and the peak of the cross-power spectrum collapse, *i.e.* the momentum transfer is mainly carried out by the coherent structures at low frequencies. The phase relation

between u' and v' is equal to $-\pi$ until the descending edge of the peak in the cross-power spectrum density (at low frequencies); after [Tennekes and Lumley \[1972\]](#) this phase of $-\pi$ indicates a positive turbulent production, *i.e.* the turbulent structures are coherent and energetic. As soon as the phase becomes random (beyond the high-frequency side of the peak), the structures lose their coherency and therefore become dissipative [[Pope, 2000](#)].

1.2.2.2 Shear layers in compound channel

In the last decade, new experimental studies by [Nezu et al. \[1999\]](#), [Bousmar \[2002\]](#) and [van Prooijen et al. \[2000, 2005\]](#) have highlighted the complex physics and characteristics of the shear layers in compound channels. It was shown that the lateral variations in water depth have considerable consequences for the large scale vortices. As demonstrated by [van Prooijen et al. \[2005\]](#) because of the difference in depth between the main channel and the floodplain, the vortices in the mixing layer are asymmetric. The lateral velocity component of the large vortices is inversely proportional to $1/H_i(y)$ in front of the structure and by continuity is directly proportional at the rear. The flow is therefore decelerated upstream of the large vortex and is accelerated downstream (Figure 1.9.a). As a consequence the vortex is stretched in the upstream direction and the centre of the recirculation is located in the downstream part of the vortex.

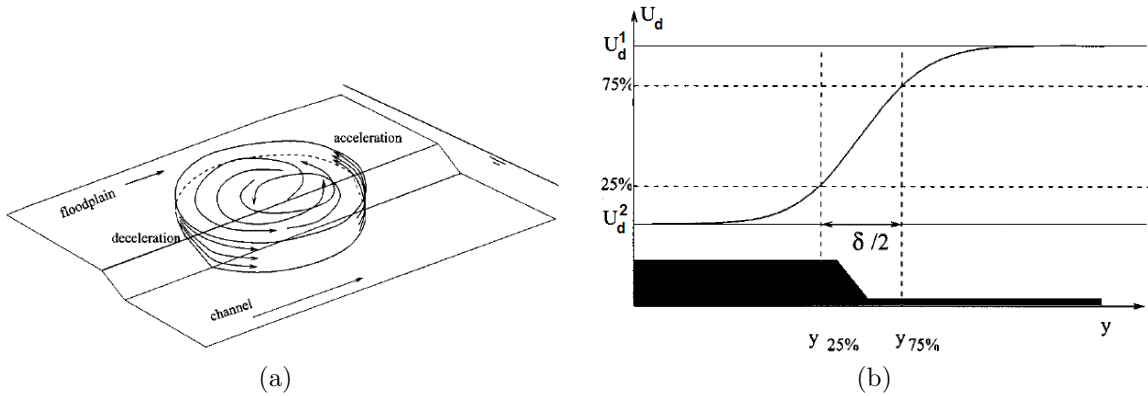


Figure 1.9 – (a) Sketch of a vortex moving on an uneven bottom. Transverse velocity increases at front and decreases at back of vortex [[van Prooijen et al., 2005](#)]. (b) Notation used by [van Prooijen et al. \[2005\]](#) for defining the velocity distribution in a mixing layer developing in a compound channel.

[van Prooijen et al. \[2005\]](#) adapted the physical modelling of the mixing layer proposed for single channels by [Uijtewaal and Booij \[2000\]](#). They proposed a new definition for the centre and the width of the mixing layer for taking into account the asymmetry in the lateral profile of longitudinal velocities (Figure 1.9.b). The centre of the mixing layer y_c thus corresponds to the location where $U_d(y_c) = U_2 + 0.5(U_1 - U_2)$, with U_1 the cross-sectional velocity in the main channel outside the mixing layer and U_2 the cross-sectional velocity in the floodplain outside the mixing layer (see scheme in Figure 1.9.b for notations) and the width of the mixing layer writes:

$$\delta = 2(y_{75\%} - y_{25\%}) \quad (1.5)$$

where $U_d(y_{25\%}) = U_2 + 0.25(U_1 - U_2)$ and $U_d(y_{75\%}) = U_2 + 0.75(U_1 - U_2)$.

Like mixing layers in single channels, the shear layers developing in a compound channel can also be shallow or deep. Yet, the mixing layer also depends on the relative flow depth (Figure 1.10).

Thanks to measurements of instantaneous velocity profiles and vorticity fields below the free surface at various relative flow depths in an asymmetrical compound channel, [Nezu et al. \[1999\]](#)

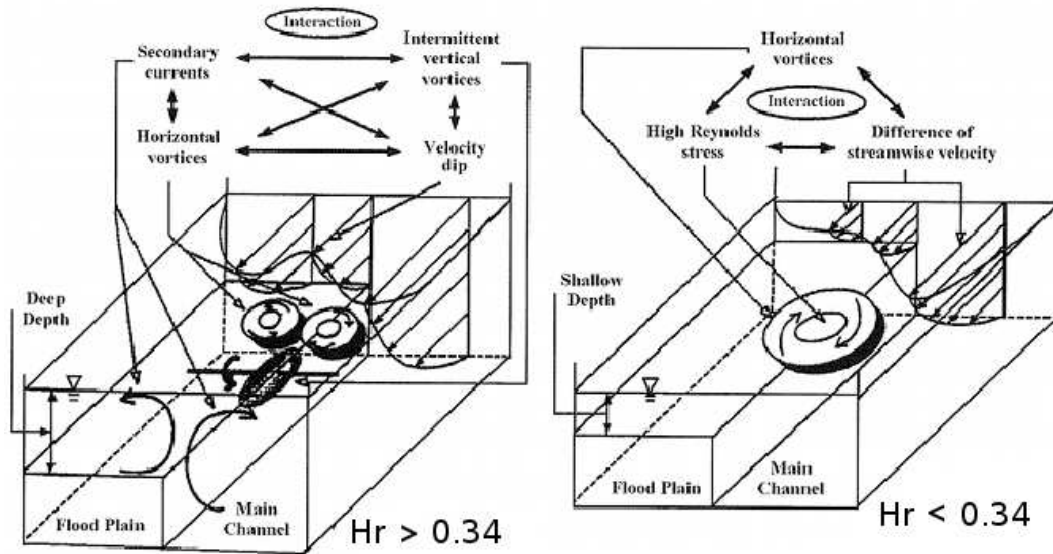


Figure 1.10 – Interactions between secondary currents and mixing layer: impact of the flood-plain depth [Nezu *et al.*, 1999]. Left figure: high relative flow depth, right figure: low relative flow depth.

proposed an additional classification for the mixing layers in compound channel. As schematized in Figure 1.10:

- At low relative flow depth ($H_r \leq 0.34$), because of the lateral shear between channels, clockwise vortices appear (*i.e.* vorticity > 0) and evolve downstream. The vortex street between channels is generated because of the inflection in the velocity profile, like in classical mixing layers in single channels. As a result, the boundary shear stress on the floodplain increases towards the junction, due to the interaction between the FP and MC flow.
- At high relative flow depths ($H_r > 0.34$), secondary flows coming from the junction between channels govern the 3D structures. These secondary flows are generated by the turbulence anisotropy in the shear layer between the main channel and the floodplain. Low momentum and energy are transported from the junction through these secondary currents. As a result, the horizontal distribution of depth-averaged velocity has a valley feature near the junction as also has the turbulence. As a consequence, the vorticity sign changes between the main channel and the floodplain: clockwise vortices appear in the main channel and counter-clockwise vortices appear in the floodplain. The periodic planform vortices are weaker than the ones at low relative flow depth and active intermittent boils coming from the junction between channels are observed.

NB – Notice that in both cases, depending on the depth (especially in the flood-plain), the developing structures may be restricted or not by the friction.

In the case of a symmetric compound channel, two vortex streets are generated along the main channel which leads to the generation of a Karman vortex street. In such a flow configuration, the depth-averaged lateral Reynolds shear stress is maximum for a ratio $B_{mc}/H_{mc} = 5$. Each street interacts with each other until the ratio $B_{mc}/H_{mc} = 8$, beyond this ratio, at a given H_{mc} , the lateral shear stress is a constant [Ikeda and McEwan, 2009].

To finish, in most of the studies carried out on mixing layers developing in compound channels [Sellin, 1964; Shiono and Knight, 1991; van Prooijen *et al.*, 2000, 2005], the momentum transfer due to turbulent interaction was also examined in addition to the flow structures. They were examined by varying the channel geometry and the relative flow depth as well.

In mixing layers developing in compound channels, the momentum transfer associated to the large vortices developing at the interface between channels is responsible for the decrease in the main channel conveyance and for the increase in the floodplain(s) conveyance. As the mixing layer is also a source of dissipation, some part of the transferred energy between channels is dissipated; as a result the total conveyance of the compound channel, relative to a single channel of same hydraulic radius, is reduced [Knight and Demetriou, 1983; Knight and Hamed, 1984; Knight et al., 1984]. Nevertheless, as shown in Figure 1.11 where lateral variations of depth-averaged Reynolds shear stress for various water depths are displayed ($H = 0.169 \text{ m} \Rightarrow H_r = 0.110$ and $H = 0.200 \text{ m} \Rightarrow H_r = 0.250$), the Reynolds shear stress in the mixing layer which is extreme, decreases with increasing water depths, therefore indicating that the loss of conveyance reduces.

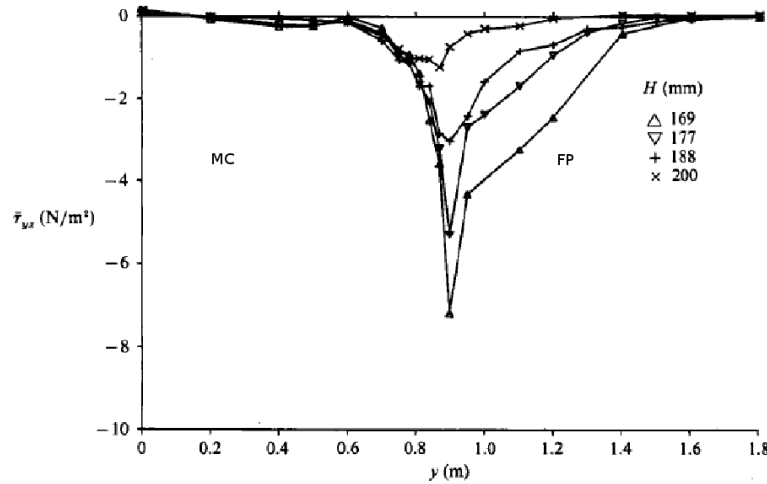


Figure 1.11 – Lateral variation of depth-averaged Reynolds shear stress for various water depths in a straight compound channel [Shiono and Knight, 1991].

Knight and Hamed [1984] investigated the flow interaction between the main channel and the floodplain under uniform flow conditions through the calculation of an “apparent shear force” at the vertical interface of a prismatic compound channel with symmetrical floodplains. The apparent shear force, equal to the subtraction of the gravity force in the floodplain by the shear force in the floodplain, enabled to determine momentum transfer due to turbulent exchange between channels; analyses highlighted that the apparent shear force at the interface could reach 20 % of the boundary shear force in the floodplain at low relative depth ($H_r \approx 0.05$). Turbulence must be therefore taken into account for having a good estimation of boundary shear stress in absence of measurements.

Shiono and Knight [1991] showed that in addition to bed friction and momentum transfer due to turbulent exchange at the interface, momentum transfer due to secondary currents across the total cross-section must be taken into account under uniform flow conditions. Through the use of a depth-averaged equation for the longitudinal streamwise component of momentum (see Equation 2.46), the authors showed that the contribution of secondary currents to momentum transfer is not negligible at high relative depth ($H_r \geq 0.3$); at $H_r = 0.4$, secondary current term in the vicinity of the interface can indeed reach 50 % of the measured apparent shear stress.

Bousmar [2002]; Bousmar and Zech [1999] finally showed that the consideration of turbulent exchange in momentum equations is paramount for correctly estimating stage-discharge curves and discharge distributions between channels. Thus, by explicitly considering momentum transfer due to turbulent exchange in the modelling (EDM: Exchange Discharge Model, see §A.2.5), the mean errors on the total discharge estimation performed on the data of the FCF Wallingford [Knight, 1992] and on other data sets [Asano et al., 1985; Ghosh and Jena, 1971; Knight and Hamed, 1984; Wormleaton et al., 1982] is reduced by 400 % with comparison to a Single Channel Method (SCM) – mean error SCM $\approx 20 \%$, mean error EDM $\approx 5 \%$ – and is reduced by 300

% with comparison to a Divided Channel Method (DCM) – mean error DCM ≈ 15 % – (see definition of methods in Appendix A). Results also emphasized that discharge distributions between the main channel and floodplains are better modelled with the EDM.

1.2.3 Boundary shear stress

Boundary shear stresses enable to quantify effects of solid boundaries in contact with the flow. They are also useful for studying sediment (bed-load) transport. In the literature, many studies therefore deal with boundary shear stress measurements (and modelling) in symmetrical or in asymmetrical compound channels [Afzalimehr and Rennie, 2009; Knight and Hamed, 1984; Knight et al., 1994].

In a wide prismatic single channel far from the lateral banks the boundary shear stress is equivalent to $\rho ghS_{o,x}$. By contrast, in a compound channel, the mixing layer developing at the interface between the main channel and the floodplain is responsible for an increase in the boundary shear stress magnitudes in the floodplain (especially near the interface, where the flow is locally accelerated by the mixing layer) and for a decrease in magnitude of the boundary shear stresses in the main channel. As shown in Figure 1.12, where boundary shear stress in a symmetrical compound channel are plotted relative to $\rho ghS_{o,x}$, the boundary shear stresses are 25 % smaller than $\rho ghS_{o,x}$ in the main channel and 25 % greater in the main channel. According to Shiono and Knight [1991], “the boundary shear stress differs from the standard two-dimensional value, owing to transverse gradients in the additional shear stresses arising from secondary flow and lateral shear effects”.

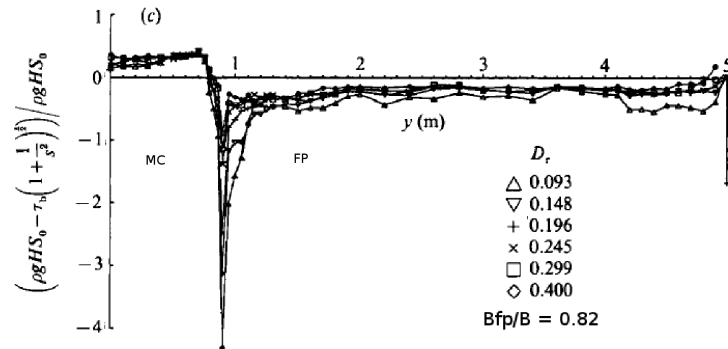


Figure 1.12 – Boundary shear stress distribution in symmetrical compound channel [Shiono and Knight, 1991]. Only one floodplain and half the main channel are displayed.

A typical boundary shear stress distribution in asymmetrical compound channel is displayed in Figure 1.13. This diagram comes from Holden and James [1989]. Experiments were performed in a 16 m long and 0.92 m wide asymmetrical compound channel with a mean slope of 1/1000 and a trapezoidal cross-section (angle of the bank between the main channel and the floodplain, 30°, 60° and 90°). The relative flow depths H_r of experiments B(60°) displayed in Figure 1.13 vary between 0.11 (B12) and 0.41 (B80). Boundary shear stresses are named τ_c in the main channel, τ_p in the floodplain and they are normalized by the data at the junction between the main channel and the floodplain $\tau_{cj} = \tau_{pj}$.

As shown in Figure 1.13, in asymmetrical compound channel, the maximum of boundary shear stress is measured in the vicinity of the centre of the main channel. By contrast, according to Ikeda and McEwan [2009, p. 98] and as displayed in Figure 1.12, in symmetrical compound channel, two maxima of boundary shear stress are observed of both sides of the centre of the main channel and a local minimum is measured in the centre; this shape is due to the secondary-current cells that develop in the main channel. In asymmetrical configuration the double-shaped

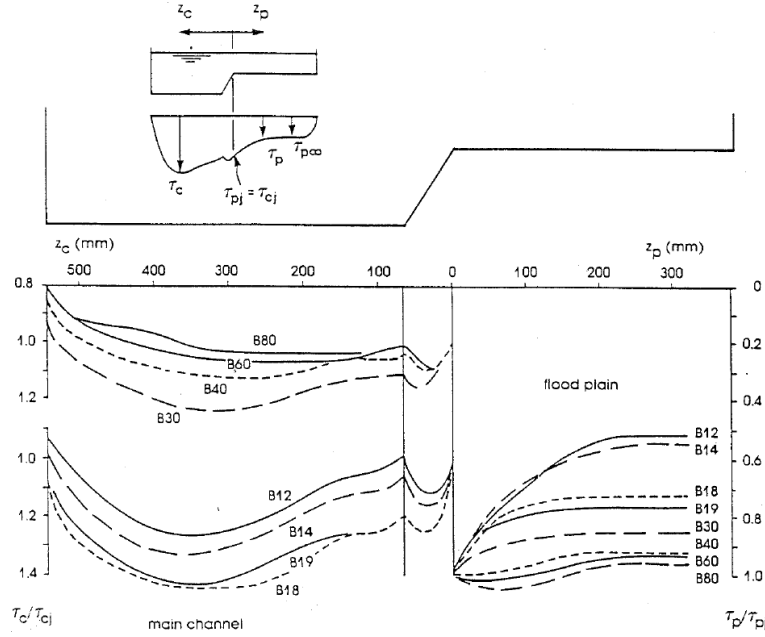


Figure 1.13 – Boundary shear stress distribution in asymmetrical compound channel [Holden and James, 1989].

maximum is not observed, because of the main channel side-wall that has a greater influence on boundary shear stress than the secondary-cells.

Finally, measurements of the effects of the bank / side slope at the junction between the main channel and the floodplain indicate that a vertical interface generates more friction in the flow than an inclined junction for relative depth greater than $H_r = 0.15$ [Rhodes and Knight, 1994]. By contrast, for relative depths smaller than 0.15 and an inclination of 60° , the friction is the strongest.

1.2.4 Secondary currents of Prandtl's second kind

After Nezu and Nakagawa [1993], two main sources of secondary currents are identified. The first kind, the so-called “secondary currents of Prandtl's first kind” are driven by centrifugal force and they are observed in non-uniform flows in curvilinear channels [Ikeda and McEwan, 2009] and in meandering channels [Einstein and Li, 1958; Morvan et al., 2002; Shiono and Muto, 1998]. In straight compound open-channel, either in uniform flow or in non-uniform flows, an intermittent upward flow motion at the interface between the main channel and the floodplains is observed. This flow motion is induced by the imbalance of the Reynolds normal stresses originating from the complex nature of the channel cross-section [Nezu et al., 1999]. This phenomenon is closely related to the “secondary currents of Prandtl's second kind”, which are most of the time observed in the form of streamwise-axis helical vortices (Figure 1.14) [Shiono and Feng, 2003; Shiono and Knight, 1991; Tominaga and Nezu, 1991]. These vortices are due to the anisotropy of the turbulence in the vicinity of the mixing layer developing between the main channel and the floodplain and they affect the boundary shear stress distribution and the mixing layer at the interface between channels.

Some example of secondary currents developing in an asymmetrical compound channel for various relative flow depths and floodplain widths are displayed in Figures 1.14.a and 1.14.b. At least two counter-rotative cells are observed in the main channel. In the floodplain, measurements are often not enough accurate for capturing more than one secondary-cell. The secondary currents are sensitive to the width of the channels and to the water depth Ikeda and McEwan [2009]:

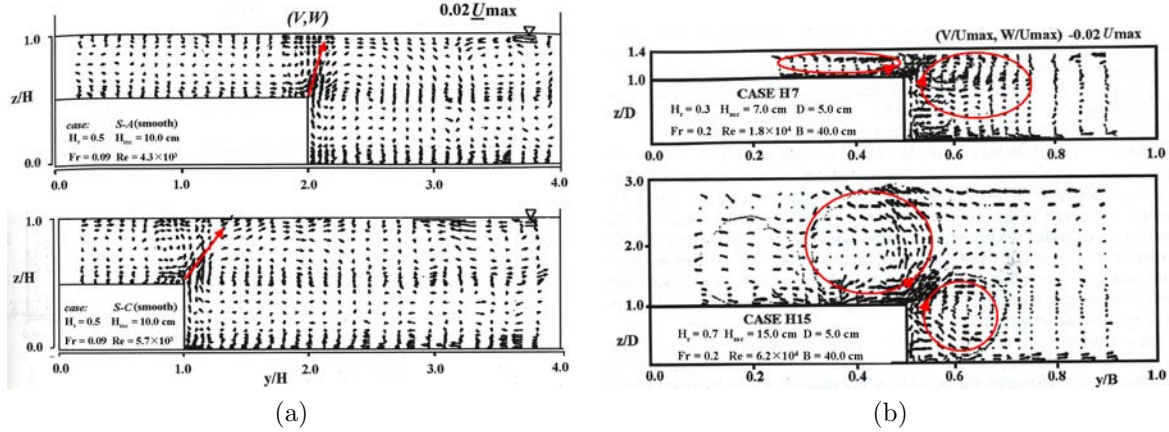


Figure 1.14 – Velocity components (\bar{v}, \bar{w}) in secondary currents of Prandtl’s second kind for uniform flow conditions in an asymmetrical compound channel (After, [Ikeda and McEwan \[2009\]](#); [Nezu et al. \[1999\]](#)).

- At a given relative flow depth, the decrease in the floodplain width increases the up-flow from the junction between the main channel and the floodplain towards the free surface (spread of the floodplain secondary current in the main channel part: see large red arrows at the tip of the floodplain step in Figure 1.14.a). An increase in the roughness of the floodplain attenuates the up-flow effects at the junction between MC and FP.
- In addition to secondary currents in the floodplain and in the main channel, an increase in the relative flow depth, at a given floodplain width, initiates the development of a secondary cell just above the junction between the main channel and the floodplain. As a consequence, the vortex developing below the bank-full height in the main channel (“bottom vortex”) is weakened by a “free surface vortex” (see in Figure 1.14.b close to the bank-full height).

To finish, because of the secondary currents, the maximum of longitudinal velocity is located below the free surface in the middle of the main channel in symmetrical compound channel and in asymmetrical compound channel with wide main channel [[Tominaga and Nezu, 1991](#)]. In the case of a narrow main channel, the maximum is still below the free surface, but is slightly shifted towards the main channel bank [[Ikeda and McEwan, 2009](#)].

1.3 Gradually varied flows in compound channel

As uniform flows in compound geometries are uncommon on the field, focus was then put on gradually varied flows. Three types of flow configurations were progressively investigated [[Proust et al., 2010](#)]:

1. Gradually varied flow in prismatic geometry: disequilibrium in the upstream discharge distribution [[Bousmar et al., 2005](#); [Proust et al., 2010, 2011](#)].
2. Non prismatic geometry with continuously varying floodplain width and constant overall width for the flume (skewed compound channels [[Chlebek and Knight, 2008](#); [Elliot and Sellin, 1990](#); [Sellin, 1993](#)]; meandering two-stage channels [[Shiono and Muto, 1998](#)]),
3. Non prismatic geometry with a variable overall width for the flume (symmetrically converging floodplains [[Bousmar et al., 2004](#)]; symmetrically diverging floodplains (divergence angle smaller than 5.8° , *i.e.* no development of recirculation zones) [[Bousmar et al., 2006](#); [Proust, 2005](#)]; compound channel with an abrupt floodplain contraction (convergence angle of 22°) [[Proust et al., 2006](#)]),

These experiments showed that mass exchange between subsections may generate additional momentum transfer that superimposes to the momentum transfer due to turbulence usually found in prismatic geometries.

NB – For flow configurations with constant overall width, mass exchange between channels generates low variation (but not nil) in flow depth along the longitudinal axis. Contrariwise, for flow configurations without constant overall width, gradient of depth are marked [Proust et al., 2010].

Bousmar [2002] and Bousmar et al. [2004] first showed that in addition to momentum transfer due to turbulent exchange at the interface between the main channel and the floodplain, effects of mass exchange between channels must be explicitly modelled. Comparisons between the Single Channel Method (SCM), The Divided Channel Method (DCM) and the Exchange Discharge Method (EDM) (see descriptions of the method in §A) in a skewed channel [Bousmar, 2002] and in converging channels ([Bousmar et al., 2004]) emphasized that the EDM – the only method that explicitly consider mass exchange between subsections – is the only method that well fits the measured stage-discharge data (total discharge); the two other methods over or under-estimate the total discharge (maximal error of 50 %) and the modelled water depths are generally lower than the measured data (maximal error of 15 %).

In the sequel, Proust et al. [2010, 2011], thanks to a method that solves three 1D-momentum equations, one in each subsection, coupled to a mass conservation equation in the total cross-section (Independent Subsection Method, see §A.2.6), estimated the weight of each physical phenomenon depending on the flume geometry and depending on the position in the flume (floodplain, main channel, ...). The purpose was to assess in which situation the flow is driven by turbulent effects or is driven by advection effects. It then results that:

- In gradually varied flow conditions, the two predominant physical phenomena that influence the water levels and the sub-sectional velocities are the bed friction and the momentum transfer due to mass exchange within a subsection (mass conservation).
- For a fixed angle of divergence/convergence between the floodplain lateral-walls and the axis of the main channel, converging floodplains enhance turbulent exchange at the interface compared to diverging floodplains, while diverging floodplains accentuate momentum transfer due to mass exchange between channels compared to converging floodplains.
- With an increasing angle of divergence/convergence, the relative weight of momentum transfer due to mass exchange between channels increases while the relative weight of momentum transfer due to turbulent exchange decreases.

Thus, Proust et al. [2010] showed that in a converging floodplain (maximal semi-angle of convergence is equal to 11.3°), the head loss due to turbulent exchange at the interface can reach 70 % of the head loss due to friction, while the head loss due to mass exchange is only equal to 10 % of the friction head loss ($H_r = 0.2$). In a diverging floodplain (maximal semi-angle of divergence is equal to 5.7°), head loss due to mass exchange can reach 200 % of the head loss due to friction; in the same time, head loss due to turbulence at the interface is at maximum equal to 60 % of the friction head loss.

These results showed that the correct estimation of the lateral mass exchange is paramount for well modelling momentum transfer due to mass exchange between channels, but the good assessment of the turbulence cannot be avoided as well.

The question, now, is to know how the flow characteristics are impacted when a groyne is set on the floodplain. In some parts of such a flow configuration, the “angle of divergence/convergence” of the flow is indeed greater than those presented in Proust et al. [2010, 2011].

1.4 Flows in the vicinity of a thin obstacle

In natural or anthropized rivers, transversal and discontinuous obstacles either natural (hill on a floodplain, rock slide, ...) or artificial (embankments for railways and motorways, ...) may partially or totally block off floodplains. During a flood event, the flow in the floodplains is therefore contracted by the obstacle and two recirculation zones develop upstream and downstream. It results in a reduction of the flow section and in the generation of strong mass exchange between channels. In addition as measured by [Proust \[2005\]](#) and [Bourdat \[2007\]](#), the longitudinal slope of the water surface at the tip of the obstacle is at least one order of magnitude steeper than the bottom slope: such a flow is therefore considered as “rapidly varied” [[Ancey, 2009](#); [Chow, 1959](#)].

1.4.1 Sudden enlargement in single open-channels

Understanding of flows with a groyne set on the floodplain first requires the understanding of a more simple flow configuration as displayed in Figure 1.15: flow in the vicinity of a sudden enlargement.

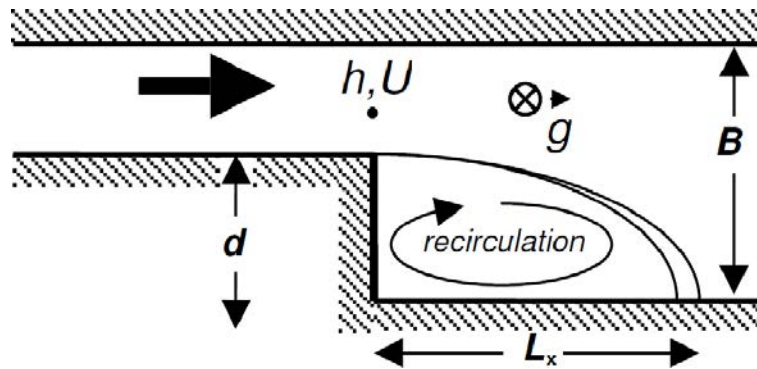


Figure 1.15 – Top view of a recirculation zone downstream of a sudden enlargement [[Rivière et al., 2008](#)].

In such a flow configuration, only one recirculation zone develops downstream of the enlargement. Moreover, as the approaching velocity is collinear to the lateral wall, the maximal lateral expansion of the recirculation zone cannot be greater than the length d of the obstacle.

The turbulence inside this recirculating flow is characterized by the competition and the interaction of two turbulent motion-scales [[Babarutsi et al., 1989](#); [Chu et al., 2004](#)]:

- A large-scale turbulent motion at vertical axis, of characteristic length comparable to the length of the obstacle. This turbulent motion is produced all along the separation line (the virtual boundary between the main flow and the recirculation zone) by the transverse shear induced by the presence of the sudden enlargement in the flow.
- A small-scale turbulent motion at horizontal axis, of characteristic length equivalent to the water depth H . This turbulent motion is produced by the bottom friction and have a stabilizing effect on the development of the recirculation zone [[Babarutsi et al., 1989, 1996](#)].

By stability consideration on the mixing layer developing along the separation line, [Chu et al. \[1983, 2004\]](#) and [Babarutsi et al. \[1989, 1996\]](#) ([McGill University](#)) proposed the so-called bed friction number S for comparing the turbulent length scales responsible for the streamwise development of the recirculation zones; the horizontal turbulent length-scale ($l_1 = d$) was thus

compared to the bed friction length-scale ($l_2 = 8H/\lambda$) as follows:

$$S = \frac{\lambda d}{8H} \quad (1.6)$$

where λ is a cross-sectional Darcy-Weisbach coefficient and H is a cross-sectional water depth; H is measured in the cross-section just upstream of the expansion. λ is calculated in the cross-section just upstream of the expansion and represents the friction that would occur in a flow without expansion that has the same depth as the flow with an expansion.

NB – In the studies performed at the McGill University, [Babarutsi et al., 1989, 1996; Chu et al., 1983, 2004], it is assumed (but never explicitly shown) that the water depth is constant within the zone containing the recirculation zone. This hypothesis is required by the theory of the stability number S , initially developed by Chu et al. [1983].

Using this friction number, Babarutsi et al. [1989] in a flume of 7 m long with a sudden enlargement occupying the half-width of the flume, then emphasized the presence of two asymptotic regimes in the recirculating flows. Thus for $S < 0.05$ (non-frictional regime), the turbulence is only driven by the length of the enlargement. As a result, the streamwise length L_x of the recirculation zone writes:

$$L_x = 8d \quad (1.7)$$

Contrariwise, for $S > 0.1$ (frictional regime), the turbulence is driven by the turbulence generated by the bottom and the streamwise length of the recirculation zone is then proportional to the water depth and to the friction:

$$L_x = \frac{4.8H}{\lambda} \quad (1.8)$$

Given Equations 1.7 and 1.8 and the fact that $H < d$, the recirculation zones in the frictional regime drastically reduce compared to the ones in the non-frictional regime. According to Rivière et al. [2008, 2011], this difference between regime must be related to the ability of the flow out of the recirculation zone to pull along water in the recirculation zone. Indeed, in the case of a frictional recirculating flow, turbulent structures developing along the separation line are restricted by the bottom friction to not widely spread in the horizontal direction. The resulting velocity profiles induce a strong velocity shear between the flows in and out of the recirculation zone, which indicates a great capacity to pull along the water in the recirculation zone. By contrast, in the case of a non-frictional recirculating flow, the turbulent structures can widely develop in the horizontal direction. It then results that the velocity shear between the recirculation zone and the main flow has reduced and the main flow therefore needs a longer distance to pull along the water in the recirculation zone.

Rivière et al. [2008, 2011] showed that the streamwise length of the recirculation zone also depends on the expansion ratios $B/(B-d)$ (B the total width of the flume, see Figure 1.15). As shown in Figure 1.16, the lengths of the recirculation zones decrease with decreasing $B/(B-d)$. This effect provides information on the capacity of the main flow to maintain its ability to pull along the water in the recirculation zone. With increasing the length of the enlargement, the main flow loses its ability to conserve its initial velocity (measured upstream of the enlargement) once the enlargement has occurred; the velocity in the main flow decreases and consequently the main flow loses its ability to pull along the water in the recirculation zone. These results emphasize that the regression found by Babarutsi et al. [1989] are not universal.

By contrast, according to Rivière et al. [2008], the flow conditions in the cross-section just upstream of the obstacle, highlighted by calculation of Froude numbers, has low influence on the recirculation zone development.

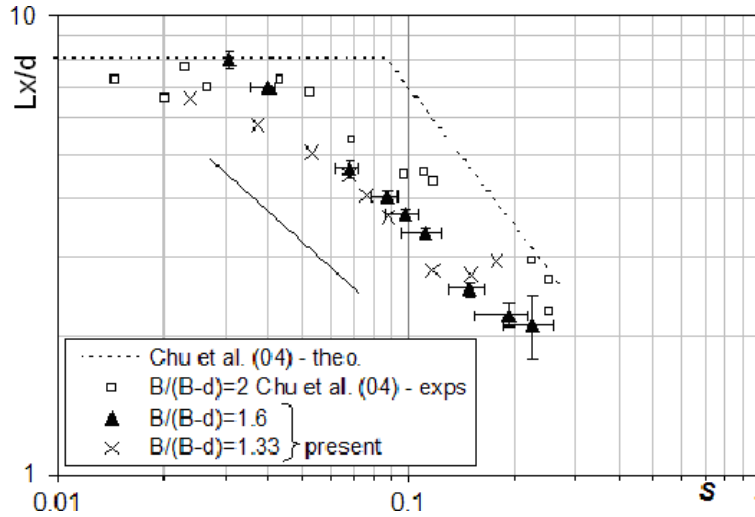


Figure 1.16 – Dimensionless recirculation length L_x/d as a function of the friction number S for different expansion ratios $B/(B-d)$ [Rivière et al., 2011].

1.4.2 Groyne in single open-channels

To the author knowledge, the literature mainly deals with flows in the vicinity of a groyne set in a single channel. The studies generally deal with counter measures against scouring at vertical abutments [Melville et al., 2006], or with sediment transport in the vicinity of a groyne [Zhang and Nakagawa, 2008; Zhang et al., 2009] or with groyne-field flows [Weitbrecht et al., 2008]. Studies also deal with scale-effects around a spur-dike in flat-bed channels and with the predictions of the lengths of the recirculation zones developing in clear water [Ettema and Muste, 2004; Rivière et al., 2004]. The field of exploration is quite wide and such flows still need complementary experiments for understanding the complexity of their physics.

1.4.2.1 Effect of the groyne on the surrounding flow

Unlike to sudden enlargement, the groyne is responsible for a flow contraction upstream of the groyne cross-section that implies a flow acceleration [Molinas et al., 1998], this, especially near the bottom. In the vicinity of the groyne, the flow becomes strongly three-dimensional; a plunging flow is indeed observed in the vicinity of the upstream face of the obstacle and affects the water surface by strongly reducing the depth around the tip of the groyne. This plunging flow also interacts with the horizontal recirculating flow in the upstream recirculation zone, resulting in the creation of the so-called “horse-shoe vortex system”. The horse-shoe vortex develops along the upstream face of the groyne (Figure 1.17) and is then bent by the main flow at the tip of the groyne. According to Carrasco and Vionnet [2004] and Koken and Constantinescu [2008], the horse-shoe vortex is responsible for the strong increase in boundary shear stress at the tip of the groyne and is partly responsible for scour. In the groyne cross-section, the velocity is still increasing and the water depth strongly decreases. Unlike in a sudden enlargement, velocities are deflected towards the opposite wall to the groyne and their modules vary depending on the distance to the obstacle [Martinez-Monclus, 2005]. Once the groyne is passed, the velocity deflection progressively reduces and vanishes in the contraction zone, where the lateral extent of the recirculation zone is maximum. Downstream of this contraction, the flow is deflected towards the wall of the groyne. The velocity progressively decelerates and the water depth progressively rises. The return to an equilibrium depends on several geometrical and hydraulic parameters and scale effects [Ettema and Muste, 2004].

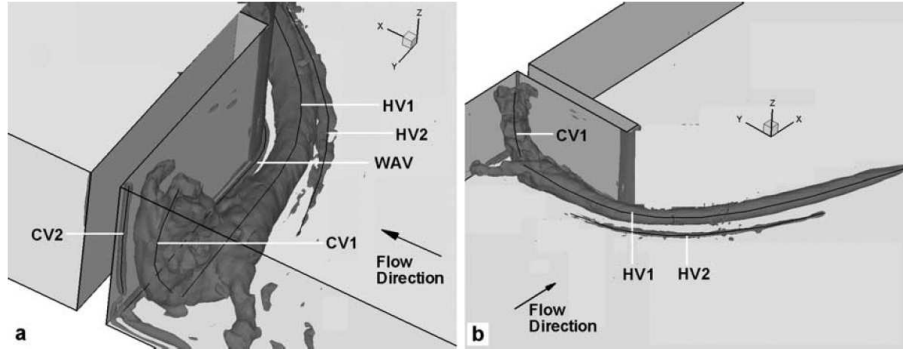


Figure 1.17 – Visualization of vortical structure of the mean flow using Large Eddy Simulation (LES). HV: Horse-Shoe Vortex, CV: Corner Vortex [Koken and Constantinescu, 2008]. (a) coherent structures located upstream of the spur dike. (b) Horse-shoe Vortex system (HV).

Figure 1.17 emphasizes the complexity of the flow in the upstream recirculation zone. “The quantity Q is the second invariant of the velocity gradient tensor resolved in LES ($Q = -0.5 \partial u_i / \partial x_j \times \partial u_j / \partial x_i$) and represents the balance between the rotation rate and the strain rate. Positive Q isosurfaces isolate areas where the strength of rotation overcomes the strain, thus making those surfaces eligible as vortex envelopes.” [Koken and Constantinescu, 2008]. The corner vortices (CV) at vertical axes feed the horse-shoe vortices (HV) at horizontal axis. It results in rise in the turbulence near the bottom, hence the increase in boundary shear stress observed by several authors.

1.4.2.2 Prediction of the lengths of the recirculation zones

The prediction of the lengths of the recirculation zones that develop of both sides of the groyne is paramount for engineers and scientists. Like for sudden enlargement, the various parameters that act on the recirculation zones must be characterised.

Upstream recirculation zone

The position of the separation point on the side-wall upstream of the groyne depends on the position of the groyne relative to the inlet and on the size of the groyne. In experiments of Ettema and Muste [2004], the groyne is placed at 2.6 m of the inlet in the baseline flow and the streamwise length of the upstream recirculation zone is approximately equal to $2d$. In experiments of Koken and Constantinescu [2008], the groyne is placed in a fully developed flow (*i.e.* the groyne is placed at least at 10 or 12 m from the inlet) and the streamwise length is equal to $0.7d$. To the author knowledge, no precise formula has been found for positioning the separation point. Nevertheless, it seems that the closer is the groyne to the inlet and the longer is the upstream recirculation zone.

The position of the stagnation point is also problematic. In the literature, it is located at the upstream face of the groyne and corresponds to the maximal extent of the recirculation zone. Depending on the streamwise length of the upstream recirculation length (also denoted L_x), the stagnation point is either located at the upstream corner of the tip of the groyne ($L_x > d \Rightarrow \max(L_y(x)) = d$) or is located on the upstream face of the groyne ($L_x \leq d \Rightarrow \max(L_y(x)) \leq d$).

For the downstream recirculation zone

The theory of the McGill University (see §1.4.1) was applied on experiments performed in the LMFA laboratory by *Rivière et al.* [2004] and *Martinez-Monclus* [2005]. Purpose was to test if this theory can be applied on flows in the vicinity of groyne. Results emphasizes that although the two asymptotic regimes and the transition zone were observed, the regression law proposed by *Babarutsi et al.* [1989] did not match very well with measurements (see red markers in Figure 1.18). As a consequence, new fits were proposed. The non frictional regime was found for $S < 0.02$ and the streamwise length of the recirculation zone follows:

$$L_x = 12d \quad (1.9)$$

The frictional regime was found for $S > 0.07$ and the length of the recirculation zone writes:

$$L_x = \frac{5.4H}{\lambda} \quad (1.10)$$

According to *Rivière et al.* [2004], changes in the fit laws are mainly due to the fact that the recirculation zones developing in the lee of the groyne have a shape that differs from the one generated in a sudden enlargement. Unlike to sudden enlargements, the maximal lateral expansion of recirculation zones in the lee of a groyne may be indeed greater than the groyne length and the flow is then strongly deviated towards the opposite wall to the groyne. This deviation induces a reduction of the “initial velocity” in the groyne cross-section which affects the ability of the main flow to pull along the water in the recirculation zone, hence the longer recirculation zone. *Ettema and Muste* [2004], for instance, observed that L_x/d can be equal to 14, *i.e.* approximately two time greater than what observed *Babarutsi et al.* [1989] in sudden enlargement.

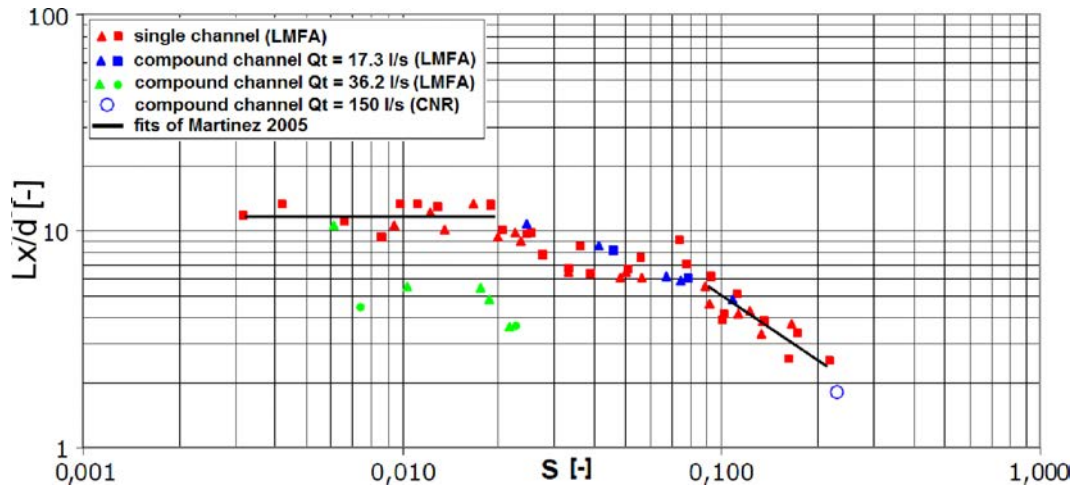


Figure 1.18 – normalized Lengths L_x/d of recirculation zones as a function of the friction number S [*Martinez-Monclus*, 2005; *Proust*, 2005].

In addition, as observed by *Rivière et al.* [2008] for sudden enlargements, measurements in single channels performed by *Francis et al.* [1969] and completed by *Rivière et al.* [2004] emphasized a strong dependency of the streamwise length of the recirculation zone (L_x) with the expansion ratio $B/(B - d)$. The presence of the opposite wall limits the lateral expansion of the recirculation zone and therefore impacts the streamwise length by increasing the latter.

After *Ettema and Muste* [2004], some scale-effects must also be taken into account in the determination of the geometry of the recirculation zone. Recirculation zones are sensitive to the surrounding depth in the flume. A decrease in the water depth implies a decrease in the streamwise recirculation length. The streamwise length is also dependent on the length of the flume, *i.e.* the backwater curve coming from the tailgates tempts to reduce the streamwise

length of the recirculation zone. The same dependency is observed for the maximal lateral extent ($\max(L_y(x))$). A decrease in the depth and in the length of the flume implies that $\max(L_y(x)) = d$. According to [Ettema and Muste \[2004\]](#), these scale-effects can be related to the nature of the turbulence that is generated in the groyne cross-section.

Finally it is interesting to notice that the inclination of the groyne in the flow has no impact on the shape of the recirculation zone. [Francis et al. \[1969\]](#) indeed showed that for angles within the range 60° and 150° , only the projected length on the spanwise direction affects the shape of the recirculation zone.

NB – The question of the validity of the use of the friction number S for flows with a groyne must be asked. The friction number is indeed defined for a constant water depth in the obstacle cross-section with a cross-sectional Darcy-Weisbach coefficient [[Chu et al., 1983, 1991](#)]. If the hypothesis of constant depth is acceptable in a sudden enlargement [[Rivière et al., 2011](#)], the distribution of the water depth is three-dimensional for flows with a groyne. Moreover a strong variation of the Darcy-Weisbach coefficient is also observed between cross-sections containing the recirculation zone; as a consequence, choosing the Darcy-Weisbach coefficient in the groyne-cross-section may be not representative of the flow conditions without perturbations (the groyne).

1.4.3 Groyne in the floodplain of a compound open-channel

The literature is mainly focused on the downstream recirculation zone [[Bourdat, 2007](#); [Peltier et al., 2008](#); [Proust, 2005](#)].

Experiments were performed in a compound channel with a groyne set on the floodplain [[Bourdat, 2007](#); [Martinez-Monclus, 2005](#); [Proust, 2005](#)]. Results of experiments are partially displayed in Figure 1.18, in which the measured recirculation lengths are plotted as a function of the friction number S . Blue markers ($Q_t = 17.3$ l/s) and green markers ($Q_t = 36.2$ l/s) represent measurements in compound channels (LMFA and CNR: Compagnie Nationale du Rhône). The lengths of the recirculation zones at low total discharge follow the fit proposed by [Rivière et al. \[2004\]](#) for groynes in single channels (Equations 1.10 and 1.9). By contrast, at high total discharge, the measured lengths are largely smaller than the fit. This behaviour was attributed to a transition to a supercritical regime that occurred in the contraction cross-section in the floodplain. The flow stayed supercritical at least until the reattachment point and in the same time, the water depth strongly decreased until the end of the recirculation zones. As a result, the friction effects were enhanced [[Chow, 1959](#)] and the turbulent structures in the recirculation zones were limited, hence the reduction in length of the recirculation zones.

The authors of the previous studies concluded that the prediction of lengths of recirculation zones in the lee of a groyne – using Equations 1.10 and 1.9 – is operational for frictional recirculating flows, since variations of water depths are low. By contrast, the method has tremendous difficulties for getting the lengths in non-frictional regime and transitional regime, especially at high total discharge, since water depths strongly vary. The strong variations in depths invalidate the use of S , because in the calculation of S , it assumes that the depth H is constant in the vicinity of the recirculation zone [[Chu et al., 1983](#)].

The authors of the previous studies also highlighted the role of the interface between the main channel and the floodplain. The interface between the main channel and the floodplain plays the role that played the opposite wall to the obstacle in single channel. The expansion ratio $B/(B - d)$ in single channel therefore becomes $B_{fp}/(B_{fp} - d)$ in compound channel. However, as this interface is not a solid boundary, but is a zone of strong momentum transfer between the main channel and the floodplain, the effect of the expansion ratio is in competition with

an antagonist effect. The interface is indeed a zone where momentum is transferred from the main channel towards the floodplain. Thus with increasing $B_{fp}/(B_{fp} - d)$, the floodplain loses its ability to pull along the water in the recirculation zone, hence an increase in the streamwise length of the recirculation zone, but in the same time momentum transfer is performed between the main channel and the floodplain, therefore resulting in an increase in the “initial velocity” in the groyne cross-section, which induces a decrease in the streamwise length of the recirculation zone [Proust, 2005; Rivière et al., 2004].

1.5 Partial conclusion

In this chapter, the main flow features of the compound channel flows were exposed. The distributions of the velocity, turbulence and boundary shear stress under uniform flow conditions were given. We then showed that in gradually varied flows, mass exchange and momentum transfer due to mass exchange superimpose to the other phenomena, which modifies their distribution.

Using the literature, we showed that putting a groyne in the floodplain of a compound channel is a good mean for generating strong mass exchange between channels. Nevertheless, the generated recirculation zone in the lee of the groyne cannot be estimated, *a priori*. As a consequence, they must be experimentally observed in order to accurately evaluate their impact on the flow. In addition, all the phenomena we previously described were observed in prismatic geometries or in gradually varied flows. It then remains a lot of questions regarding their behaviours in compound channel with a groyne set on the floodplain. We have notably no idea of the shape of the boundary shear stress and turbulence distributions in such a flow.

In order to guide the experimenters in the choice of the parameters to measure, the following chapter (Chapter 2) sets out the equation.

A general conclusion is finally given for these two chapters.

2

Fundamental equations for flow description in compound open-channel

2.1 Introduction

In this PhD-thesis, we mainly analyse the phenomena that are responsible for lateral mass exchange and momentum transfer in the horizontal directions of the flow in a compound channel, *i.e.* recirculating flow in the floodplain and mixing layer at the interface between the main channel and the floodplain (see Chapter 1). Although flows in compound channels are three-dimensional (secondary currents, boils), several authors showed that consistent descriptions of such horizontal phenomena can be made by only considering the horizontal components of the velocity [*van Prooijen et al.*, 2005] and hydraulic parameters coming from 2D depth-averaged momentum equations [*Bousmar*, 2002]. As a consequence, we decide to only measure the horizontal components of the velocity and the hydraulic parameters used in the terms of the 2D-H dispersive St-Venant equations. In addition to observations in the literature, the choice to work with parameters present in the 2D-H St-venant equations rather with other types of momentum equations was also driven by several other reasons:

1. Parameters coming from 1D momentum equations (see Appendix A) are not sufficient for describing the mixing layer and the recirculation zones in the spanwise direction.
2. Parameters coming from 3D momentum equations obviously give more information. Nevertheless given the number of terms in such equations (Equations 2.2 or 2.5 and 2.7), their measurements would require too much time for finally resulting in a description similar to those obtained with parameters coming from the 2D-H St-venant equations. Moreover, the vertical component of the velocity could not be measured or was only partially measured on the vertical (1) because of the velocity measuring devices or (2) because of the shallow depth in the floodplain. It results that few direct information on secondary-currents were available during experiments.
3. The use of the 2D x-wise momentum equation proposed by *Shiono and Knight* [1991] (see Equation 2.46, Shiono and Knight Model) was not possible. This model was developed for flows under uniform flow conditions and it has not been yet adapted for flows with recirculation zones.

In this chapter, we present the 2D-H dispersive momentum equations from which are extracted the parameters used for identifying the physical phenomena present in experiments. The general Navier-Stokes equations for an incompressible flow are first presented; no distinction is made between single and compound channels. From these equations, using the “Reynolds decompositions” and the ensemble-mean operator, the 3D-mean motion equations and the fluctuating motion equations are then worked out. We show that the ensemble-averaging of the Navier-Stokes equations explicitly reveal the effects of the turbulence on the flow. In the sequel, from

the depth-averaging of the 3D-mean motion equations, we deduce the 2D-H dispersive Saint-Venant equations, also called 2D-H dispersive shallow water equations. There we show that the depth-averaging of the 3D-mean motion equations enables to identify the physical phenomena present in our experiments:

1. lateral mass exchange,
2. momentum transfer due to mass exchange between channels,
3. the friction induced by the presence of a solid boundary in the flow,
4. stresses due to the turbulence,
5. notably, the turbulent shear initiated by the mixing layers at the interface between channels and along the separation line of the recirculation zone in the floodplain,
6. and indirectly, the secondary currents through measurements of the dispersion on the vertical of the horizontal components of the velocity.

To finish, we discuss about some modelling of the phenomena we identified.

2.2 The Navier-Stokes equations for incompressible flows

The dynamics of a fluid is described by the non-linear partial differential equations of Navier-Stokes developed in the 19th century. The general solution of these equations is unknown and their direct simulation is only possible at low Reynolds numbers with very simplified geometries [Estivalezes, 2005]. Most of the time, these equations need to be simplified or reduced in order to be solved.

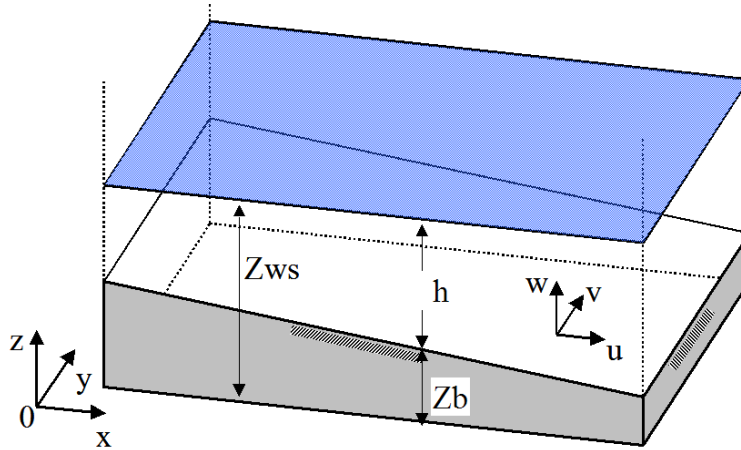


Figure 2.1 – Definition sketch of the axis directions and velocity components

Let consider an **incompressible flow** in a Cartesian reference frame $(0, x, y, z)$ where the velocity and the pressure are considered as random functions of space and time (Figure 2.1); the local mass conservation is expressed as following:

$$\frac{\partial u_i}{\partial x_i} = 0 \quad (2.1)$$

and the instantaneous momentum equations is written:

$$\frac{\partial u_i}{\partial t} + \frac{\partial u_i u_j}{\partial x_j} = -\frac{1}{\rho} \frac{\partial p}{\partial x_i} + \nu \frac{\partial^2 u_i}{\partial x_j \partial x_j} + \frac{F_{e,i}}{\rho} \quad (2.2)$$

where u_i are the instantaneous velocity in the i -wise direction ($i = x, y, z$), p is the instantaneous pressure and $F_{e,i}$ are the external forces that act on the system.

Since these equations are really complicated and the general analytical solutions are still unknown, different methods for solving/simplifying these equations were proposed. According to [Chassaing \[2000a\]](#), these methods can be classified following five generations:

1. Fits and charts: empirical considerations,
2. Boundary layer methods,
3. Reynolds Averaged Navier-Stokes method (RANS), statistic method, Probabilistic method,
4. Large Eddy simulation (LES),
5. Direct Navier-Stokes Simulation (DNS).

In the subsequent sections, we only consider the RANS method for simplifying the Navier-Stokes equations in order to express the physical phenomena in the flow as function of the measured hydraulic parameters.

2.3 Reynolds-Averaged Navier-Stokes equations: RANS method

2.3.1 Reynolds decomposition

In the RANS method (Reynolds Average Navier-Stokes Equations), the velocities and the pressure are considered as random functions of time and space and they are decomposed using the “Reynolds decomposition” (Equation 2.3):

$$\begin{aligned} u_i(x, y, z, t) &= \overline{u_i}(x, y, z, t) + u'_i(x, y, z, t) \\ p(x, y, z, t) &= \overline{p}(x, y, z, t) + p'(x, y, z, t) \end{aligned} \quad (2.3)$$

$\overline{(-)}$ is an operator of statistical mean or ensemble mean. This operator verifies the property of linearity and independence relative to the operator of time and space derivation [[Chassaing, 2000a](#)]. the variable $(-)'$ represents the fluctuations of the velocity around the average value and is centred by definition $(\overline{(-)'}) = 0$.

2.3.2 Equation of the mean motion

By applying the Reynolds decomposition and an ensemble-mean on the general equations of Navier-Stokes, the ergodicity principle enables the writing of the mean motion equations [[Bousmar, 2002](#); [Chassaing, 2000a](#)]. The mass conservation of the mean motion is then written,

$$\frac{\partial \overline{u_i}}{\partial x_i} = 0 \quad (2.4)$$

and the momentum equation has the following formulation:

$$\frac{\partial \overline{u_i}}{\partial t} + \frac{\partial \overline{u_i u_j}}{\partial x_j} = -\frac{1}{\rho} \frac{\partial \overline{p}}{\partial x_i} + \nu \frac{\partial^2 \overline{u_i}}{\partial x_j \partial x_j} - \frac{\partial \overline{u'_i u'_j}}{\partial x_j} + \frac{\overline{F_{e,i}}}{\rho} \quad (2.5)$$

This system of equations describes the 3D mean-motion of a fluid and is generally complex to solve without application of hypotheses. The appearance of a fluctuating term in these equations

should be noticed; this term is written $-\overline{\rho u'_i u'_j}$ and is called Reynolds stresses and represents the additional stress imposed by the fluctuations – the turbulence – on the mean motion of the fluid.

The ensemble-averaging of the Navier-Stokes equations induces a loss of information and opens the system of equations. The share of lost information relating to the fineness of the statistical description must be reconstructed and fed back to close the system. This closure occurs through turbulence models more or less elaborate depending on the desired accuracy for numerical modelling. Turbulence is typically modelled using the model of mixing length of Prandtl. But it can also be modelled by adding new equations to the basic system; these equations are either transport equations of turbulence (transport of turbulent kinetic energy or turbulent dissipation) or transport equations of Reynolds stresses, *a fortiori*, the best existing closures for RANS method [Chassaing, 2000a; Estivalezes, 2005].

2.3.3 Equations of the fluctuating motion

It should be noticed that the transitions from the instantaneous equations of Navier-Stokes to the mean motion equations induces a loss of information. Thus, the term to term difference of both equations, in absence of volume force fluctuations, is not equal to zero; the difference emphasizes a dynamic of the fluctuations (Equation 2.6 and Equation 2.7):

$$\frac{\partial u'_i}{\partial x_i} = 0 \quad (2.6)$$

$$\frac{\partial u'_i}{\partial t} + u'_j \frac{\partial \bar{u}_i}{\partial x_j} + u_j \frac{\partial u'_i}{\partial x_j} + u'_j \frac{\partial u'_i}{\partial x_j} - \frac{\partial \overline{u'_j u'_i}}{\partial x_j} = -\frac{1}{\rho} \frac{\partial p'}{\partial x_i} + \nu \frac{\partial^2 u'_i}{\partial x_j \partial x_j} \quad (2.7)$$

By using these new equations (Equation 2.6 and Equation 2.7), it is possible to recover all or partly the information lost because of the averaging of the general equations of Navier-Stokes. Nevertheless, the use of these equations is really complicated; for solving this new system, we indeed need to know at least three new initial conditions and twelve boundary conditions of the fluctuating fields. It demands a lot of accurate measurements.

Resulting equations (Equations 2.4, 2.5, 2.6 and 2.7) are still too complicated for describing or numerically solving flows of our experiments. They required too many measurements for the flow description and too many boundary conditions for the flow resolution. In order to have information on the physical phenomena in our experiments, equations of the mean motion (Equations 2.4 and 2.5) must be still simplified.

2.4 2D-H equations of Barré de Saint-Venant

Most of the river flows can be considered as 2D flows [Jirka and Uijttewaal, 2003], as one dimension in the flow (the depth) is largely smaller than the two others: river flows are generally considered as shallow flows since the water depth is negligible in front of the longitudinal and transversal directions. In such flow conditions, the three-dimensional equations of the mean motion can be depth-averaged and become the 2D-H Saint-Venant equations or the 2D-H shallow water equations. These equations describe the behaviour of a purely 2D open-channel flow using hydraulic depth-averaged parameters. In order to obtain these equations, it is assumed that:

- the pressure distribution on the vertical is hydrostatic, *i.e.* in Equation 2.5 ($i = 3$) all the terms are negligible in front of the pressure term and gravity term and the depth-averaging of the resulting equation gives the classical result: $\bar{p} = \rho g(Z_w - z) + p_a$, where p_a is the atmospheric pressure.

- The vertical velocities are negligible; the velocity is aligned with the bottom: $\bar{w} = 0$.
- The diffusion due to viscosity is negligible in front of the turbulent diffusion. As a consequence, the total stress in the flow is equal to the Reynolds stress τ_{ij} .
- The tangential stress at the free surface is negligible in front of the other stresses in the flow.

These new equations are shorter compared to the original system of Navier-Stokes and enable a better identification of the mathematical expressions that correspond to the phenomena we present in Chapter 1. The simplification of the 3D mean motion equations indeed leads emergence of new parameters modelling effects of the physical phenomena on the mean flow.

1. Effects of lateral mass exchange and momentum transfer due to mass exchange are thus expressed through the advection terms and the pressure gradients.
2. Effects of the turbulence and of the shear layers are expressed through the Reynolds stress terms.
3. Effects of the solid boundary are expressed through the boundary shear stress.
4. Effects of the secondary-currents are indirectly expressed through the dispersion on the vertical of the horizontal components of the velocity.

2.4.1 Definition of the boundary conditions

2.4.1.1 Free surface

When the deformations of the free surface are weak (no breaking), a particle captured by the free surface at a given time, remains on the free surface. According to [Bousmar \[2002\]](#), this property defines the free surface boundary condition. Thus, by considering that the free surface can be written:

$$S(x, y, z, t) = Z_{ws} - z = 0 \quad (2.8)$$

where ws means water surface, Z_{ws} is the water free surface level and z an altitude, the boundary condition becomes:

$$\begin{aligned} \frac{DS(x, y, z, t)}{Dt} &= \frac{\partial (Z_{ws} - z)}{\partial t} + \bar{u}_{ws} \frac{\partial (Z_{ws} - z)}{\partial x} + \bar{v}_{ws} \frac{\partial (Z_{ws} - z)}{\partial y} + \bar{w}_{ws} \frac{\partial (Z_{ws} - z)}{\partial z} \\ &= \frac{\partial Z_{ws}}{\partial t} + \bar{u}_{ws} \frac{\partial Z_{ws}}{\partial x} + \bar{v}_{ws} \frac{\partial Z_{ws}}{\partial y} - \bar{w}_{ws} = 0 \end{aligned} \quad (2.9)$$

2.4.1.2 Static bottom condition

In this thesis, only pure water was used (no sediment). The bottom is static and the bottom boundary condition is written as following [[Bousmar, 2002](#)]:

$$\bar{u}_b \frac{\partial Z_b}{\partial x} + \bar{v}_b \frac{\partial Z_b}{\partial y} - \bar{w}_b = 0 \quad (2.10)$$

where b means bottom, Z_b is the level of the bottom and $(\bar{u}_b, \bar{v}_b, \bar{w}_b)$ are the velocities on the bottom.

2.4.2 Conservative form of the continuity equation

Using the notations below,

$$\begin{aligned} U_d &= \frac{1}{h} \int_{Z_b}^{Z_{ws}} \bar{u} dz \\ V_d &= \frac{1}{h} \int_{Z_b}^{Z_{ws}} \bar{v} dz \end{aligned} \quad (2.11)$$

where the depth $h = Z_{ws} - Z_b$ and (U_d, V_d) are the longitudinal and the lateral depth-averaged velocities and using the boundary conditions previously defined, the application of the Leibniz rule to the depth-averaged continuity equation (Equation 2.4) gives:

$$\frac{\partial h}{\partial t} + \frac{\partial h U_d}{\partial x} + \frac{\partial h V_d}{\partial y} = 0 \quad (2.12)$$

2.4.3 Conservative form of the momentum equations

2.4.3.1 Projection in the x-wise direction

Using hypotheses of 2D flows, the depth-averaged momentum equation in the x-wise direction is first written:

$$\begin{aligned} \int_{Z_b}^{Z_{ws}} \left(\frac{\partial \bar{u}}{\partial t} + \frac{\partial \bar{u}\bar{u}}{\partial x} + \frac{\partial \bar{u}\bar{v}}{\partial y} + \frac{\partial \bar{u}\bar{w}}{\partial z} \right) dz = \\ - \frac{1}{\rho} \int_{Z_b}^{Z_{ws}} \frac{\partial \bar{p}}{\partial x} dz - \int_{Z_b}^{Z_{ws}} \left(\frac{\partial \bar{u}'u'}{\partial x} + \frac{\partial \bar{u}'v'}{\partial y} + \frac{\partial \bar{u}'w'}{\partial z} \right) dz \end{aligned} \quad (2.13)$$

Using the Leibniz rule, the left hand-side acceleration term of 2.13 for a static bottom is written:

$$\int_{Z_b}^{Z_{ws}} \frac{\partial \bar{u}}{\partial t} dz = \frac{\partial h U_d}{\partial t} - \bar{u}_{ws} \frac{\partial Z_{ws}}{\partial t} \quad (2.14)$$

As previously noticed, the depth-averaging of the mean-motion equations implies a loss of information and generates the dispersion terms. For instance, in the first advection term, the depth-integration of \bar{u}^2 is different from the square of the depth-averaged velocity. The introduction of the vertical momentum coefficient β_{ij}^v enables to take into account this difference [Henderson, 1966]: $\int_{Z_b}^{Z_{ws}} \bar{u}^2 dz = \beta_{xx}^v U_d^2 h$. However, in order to simplify the resolution, this coefficient is often set equal to 1, because most of the authors considers that the dispersion is negligible. Nevertheless, in the present demonstration, the dispersion terms are explicitly expressed and using identities $\bar{u} = U_d + (\bar{u} - U_d)$ and $\bar{v} = V_d + (\bar{v} - V_d)$ proposed by Bousmar [2002], the advection terms in Equation 2.14 therefore become:

$$\int_{Z_b}^{Z_{ws}} \frac{\partial \bar{u}^2}{\partial x} dz = \frac{\partial U_d^2 h}{\partial x} + \frac{\partial}{\partial x} \int_{Z_b}^{Z_{ws}} (\bar{u} - U_d)^2 dz - \bar{u}_{ws}^2 \frac{\partial Z_{ws}}{\partial x} + \bar{u}_b^2 \frac{\partial Z_b}{\partial x} \quad (2.15)$$

$$\int_{Z_b}^{Z_{ws}} \frac{\partial \bar{u}\bar{v}}{\partial y} dz = \frac{\partial U_d V_d h}{\partial y} + \frac{\partial}{\partial y} \int_{Z_b}^{Z_{ws}} (\bar{u} - U_d)(\bar{v} - V_d) dz - \bar{u}_{ws} \bar{v}_{ws} \frac{\partial Z_{ws}}{\partial y} + \bar{u}_b \bar{v}_b \frac{\partial Z_b}{\partial y} \quad (2.16)$$

$$\int_{Z_b}^{Z_{ws}} \frac{\partial \bar{u}\bar{w}}{\partial z} dz = \bar{u}_{ws} \bar{w}_{ws} - \bar{u}_b \bar{w}_b = 0 \quad (2.17)$$

From Equation 2.17, we then define the depth-averaged vertical dispersion on the vertical of the horizontal components of the velocity X_{ij} :

$$\begin{aligned} X_{xx} &= \frac{1}{h} \int_{Z_b}^{Z_{ws}} (\bar{u} - U_d)^2 dz \\ X_{yy} &= \frac{1}{h} \int_{Z_b}^{Z_{ws}} (\bar{v} - V_d)^2 dz \\ X_{xy} &= \frac{1}{h} \int_{Z_b}^{Z_{ws}} (\bar{u} - U_d) (\bar{v} - V_d) dz \end{aligned} \quad (2.18)$$

In the sequel, since the pressure distribution is hydrostatic, the pressure head in the right-hand side member of Equation 2.13 becomes:

$$\begin{aligned} \frac{1}{\rho} \int_{Z_b}^{Z_{ws}} \frac{\partial \bar{p}}{\partial x} dz &= \frac{g}{2} \frac{\partial h^2}{\partial x} + gh \frac{\partial Z_b}{\partial x} \\ &= \frac{g}{2} \frac{\partial h^2}{\partial x} - gh S_{o,x} \end{aligned} \quad (2.19)$$

where $S_{o,x} = -\partial Z_b / \partial x$ is the longitudinal slope of the bottom

Concerning the Reynolds stress terms, considering that Reynolds stresses at the free surface are negligible in front of the other stresses in the flow and using the following notation,

$$\begin{aligned} \frac{T_{xx}}{\rho} &= -\frac{1}{h} \int_{Z_b}^{Z_{ws}} \overline{u'u'} dz \\ \frac{T_{xy}}{\rho} &= -\frac{1}{h} \int_{Z_b}^{Z_{ws}} \overline{u'v'} dz \end{aligned} \quad (2.20)$$

the depth-averaging of the Reynolds stresses gives:

$$\begin{aligned} \int_{Z_b}^{Z_{ws}} \left(\frac{\partial \overline{u'u'}}{\partial x} + \frac{\partial \overline{u'v'}}{\partial y} + \frac{\partial \overline{u'w'}}{\partial z} \right) dz &= -\frac{1}{\rho} \frac{\partial h T_{xx}}{\partial x} - \frac{1}{\rho} \frac{\partial h T_{xy}}{\partial y} \\ &\quad - \overline{u'u'}_b S_{o,x} - \overline{u'v'}_b S_{o,y} - \overline{u'w'}_b \end{aligned} \quad (2.21)$$

where the three last terms in Equation 2.21 represents the stress exerted by the solid boundaries on the flow; these terms are not equal to zero, because the total stress is maximal at the bottom and the viscous stresses have been neglected (see in §2.6.1). The stresses at the bottom write as follow:

$$-\overline{u'u'}_b S_{o,x} - \overline{u'v'}_b S_{o,y} - \overline{u'w'}_b = \frac{1}{\rho} (T_{xx,b} S_{o,x} + T_{xy,b} S_{o,y} + T_{xz,b}) \quad (2.22)$$

NB – $T_{xy,b} S_{o,y} \approx T_{xx,b} S_{o,x} \ll T_{xz,b}$, because $S_{o,y} \approx S_{o,x} \ll 1$. The notation $T_{xz,b} = \tau_b$ is then adopted (τ_b , the boundary shear stress). On the lateral banks, the boundary shear stress should be multiplied by $\sqrt{1 + S_{o,y}^2}$ in order to take into account the inclination of the walls [*Shiono and Knight, 1989*].

Using the previous equations (Equation 2.14, 2.15, 2.16, 2.19 and 2.21) and the boundary equations (Equation 2.9 and 2.10) the conservative form of the momentum equation in the

x-direction is finally equal to:

$$\begin{aligned} \frac{\partial h U_d}{\partial t} + \frac{\partial}{\partial x} \left(h U_d^2 + \frac{g}{2} h^2 \right) + \frac{\partial h U_d V_d}{\partial y} = & + g h S_{o,x} - \frac{\tau_{b,x}}{\rho} + \frac{1}{\rho} \frac{\partial h T_{xx}}{\partial x} + \frac{1}{\rho} \frac{\partial h T_{xy}}{\partial y} \\ & - \frac{\partial}{\partial x} \int_{Z_b}^{Z_{ws}} (\bar{u} - U_d)^2 dz - \frac{\partial}{\partial y} \int_{Z_b}^{Z_{ws}} (\bar{u} - U_d) (\bar{v} - V_d) dz \end{aligned} \quad (2.23)$$

2.4.3.2 Projection in the y-direction

By following the same procedure of simplification of the mean motion equation in the y-wise direction, the 2D-H momentum equation in the y-wise direction is equivalent to Equation 2.23:

$$\begin{aligned} \frac{\partial h V_d}{\partial t} + \frac{\partial h U_d V_d}{\partial x} + \frac{\partial}{\partial y} \left(h V_d^2 + \frac{g}{2} h^2 \right) = & + g h S_{o,y} - \frac{\tau_{b,y}}{\rho} + \frac{1}{\rho} \frac{\partial h T_{yx}}{\partial x} + \frac{1}{\rho} \frac{\partial h T_{yy}}{\partial y} \\ & - \frac{\partial}{\partial x} \int_{Z_b}^{Z_{ws}} (\bar{u} - U_d) (\bar{v} - V_d) dz - \frac{\partial}{\partial y} \int_{Z_b}^{Z_{ws}} (\bar{v} - V_d)^2 dz \end{aligned} \quad (2.24)$$

This equation is complementary to Equation 2.23 and gives some additional information about the physical processes, this, especially in the y-wise direction of the flow. Nevertheless, in this thesis, we only are interested in the study of the terms in the x-wise momentum equation (Equation 2.23), because (1) the parameters in it give the best information about the flow processes and (2) most of the measured parameters in Equation 2.24 have variations that are not significant for having consistent information on flow processes (uncertainty on the lateral velocity is close to 50 %).

2.5 Identification of physical processes using a 2D-H equation

Considering that flows in our experiments are steady, the first terms in Equations 2.12, 2.23 and 2.24 can be shunted. The mass conservation then gives:

$$\frac{\partial h U_d}{\partial x} = - \frac{\partial h V_d}{\partial y} \quad (2.25)$$

and the second and the third terms in Equation 2.23 using Equation 2.25 become:

$$\frac{1}{gh} \frac{\partial}{\partial x} \left(h U_d^2 + \frac{g}{2} h^2 \right) = \frac{\partial h}{\partial x} + \frac{U_d^2}{gh} \frac{\partial h}{\partial x} + \frac{1}{g} \frac{\partial U_d^2}{\partial x} \quad (2.26)$$

$$\frac{1}{gh} \frac{\partial h U_d V_d}{\partial y} = \frac{q_y}{gh} \frac{\partial U_d}{\partial y} - \frac{U_d^2}{gh} \frac{\partial h}{\partial x} \quad (2.27)$$

with $q_y = V_d h$ the lateral unit-discharge.

Replacing the terms 2.26 and 2.27 in Equation 2.23 finally results in a new formulation for the x-wise momentum equation, in which the physical processes in the flow can be easily identified:

$$\begin{aligned} \frac{\partial h}{\partial x} + \frac{1}{2g} \frac{\partial U_d^2}{\partial x} + \frac{q_y}{gh} \frac{\partial U_d}{\partial y} = & S_{ox} - \frac{\tau_{b,x}}{\rho gh} + \frac{1}{\rho gh} \frac{\partial h T_{xx}}{\partial x} + \frac{1}{\rho gh} \frac{\partial h T_{xy}}{\partial y} \\ & - \frac{1}{gh} \frac{\partial h X_{xx}}{\partial x} - \frac{1}{gh} \frac{\partial h X_{xy}}{\partial y} \end{aligned} \quad (2.28)$$

where:

- $\frac{\partial h}{\partial x}$ is the hydrostatic pressure gradient,

- $\frac{1}{2g} \frac{\partial U_d^2}{\partial x}$ is the streamwise variation of the longitudinal kinetic energy; it results from the streamwise variation of the mass in the flume,
- $\frac{q_y}{gh} \frac{\partial U_d}{\partial y}$ represents the momentum transfer due to lateral mass exchange,
- $S_{ox} - \frac{\tau_{b,x}}{\rho gh}$ represents balance between the friction in the flow and the streamwise slope of the channel,
- $\frac{1}{\rho gh} \frac{\partial h T_{xx}}{\partial x}$ gives information about effects of the additional stress in the streamwise direction that creates the turbulence on the mean motion,
- $\frac{1}{\rho gh} \frac{\partial h T_{xy}}{\partial y}$ indicates effects on the flow of a potential lateral velocity/turbulence shear in the flow,
- $-\frac{1}{gh} \frac{\partial h X_{xx}}{\partial x}$ gives information about the dispersion on the vertical of the longitudinal component of the velocity; this dispersion is due to the bottom friction that is responsible for the non-uniformity on the vertical of the longitudinal velocity \bar{u} ,
- $-\frac{1}{gh} \frac{\partial h X_{xy}}{\partial y}$ gives information about the dispersion on the vertical of the longitudinal and lateral component of the velocity; this dispersion is due to the bottom friction for \bar{u} and is due to the secondary-currents for the lateral velocity \bar{v} [Bousmar, 2002].

NB – The flow parameters that are used in Equation 2.28 were accurately measured for 7 flows among the 9 investigated during our experiments in France (LMFA: see flow-cases in Table 3.3). For the two others (GC250L and GC420L), the boundary shear stress and the turbulence were not measured. Concerning flows in Japan (Appendix B), the boundary shear stress and the turbulence were not measured either.

2.6 Approximation of physical processes using modelling

The left hand-side member of Equation 2.28 can be directly evaluated with measurements, but concerning terms in the right hand-side member, some of them must be modelled, either because their measurements were inaccurate or because they were simply not measured because of an absence of devices for measuring it. In the following section, we then discuss different solutions for modelling the friction, the turbulence and the dispersion on the vertical of the horizontal components of the velocity.

NB – Most of the modelling we present can be either used in single or in compound geometry. When a modelling is specific to the compound geometries, we specify it in the text.

2.6.1 Friction

2.6.1.1 Boundary shear stress and its experimental characterisation

The depth-averaging of the 3D-mean motion equations leads emergence of a new term to measure or model: the boundary shear stress τ_b which expresses the effects of the presence of a solid boundary on the flow. The boundary shear stress (or bed shear stress) is a general appellation regrouping the bottom shear stress measured along the horizontal bottom and the wall shear stress measured on the lateral banks of the flume [Knight and Hamed, 1984]. Boundary shear stress is generally measured with a Preston tube (see §3.3.5).

As shown in Equation 2.22 under hypotheses of the 2D-H Saint-Venant equations (viscous diffusion \ll turbulent diffusion, ...), in absence of Preston tube, the boundary shear stress is related to the vertical Reynolds shear stress measured close to the bottom ($\tau_{xz,b}$ in the streamwise direction and $\tau_{yz,b}$ in the spanwise direction). This relationship is however a crude simplification of what exactly happens near the bottom. Strictly speaking, the boundary shear stress is related to the total stress at the bottom. For a 2D-uniform flow (*i.e.* $\partial/\partial t = 0$, $\partial\bar{u}_i/\partial x = 0$, condition of symmetry in the y-wise direction, $\bar{u} = \bar{u}(z)$ and $\bar{w} = 0$), the total stress at the bottom in the streamwise direction has the following expression.

$$\lim_{z \rightarrow Z_b} \tau_{t,x}(z) = \lim_{z \rightarrow Z_b} \left[\left(\mu \frac{\partial \bar{u}}{\partial z} - \rho \overline{u'w'} \right) \right]_z^{Z_{ws}} = \tau_{b,x} \quad (2.29)$$

After [Schlichting and Gersten \[2000\]](#) and [Chassaing \[2000a\]](#) the Reynolds shear stress τ_{xz} is null at $z = Z_b$. As a consequence, $\tau_{t,x}(z = Z_b) = \tau_b = \mu \partial \bar{u} / \partial z|_{z=Z_b}$. However, the vertical gradient of the longitudinal velocity near the bottom is quite difficult to be well measured; this gradient is indeed located in the viscous sub-layer of the boundary layer that develops from the bottom to the free surface and this sub-layer is quite thin, especially for smooth flow conditions. [Cheng and Castro \[2002\]](#), among other authors, noticed that the maximum of the vertical Reynolds shear stress τ_{xz} in the log-region of the boundary layer is close to the value of the total shear stress in the viscous sub-layer. As a consequence the boundary shear stress is generally approximate using the subsequent relationship:

$$\lim_{z \rightarrow Z_b} \left[\left(\mu \frac{\partial \bar{u}}{\partial z} - \rho \overline{u'w'} \right) \right]_z^{Z_{ws}} = \lim_{z \rightarrow z \text{ where } \tau_{xz} \text{ is maximum}} \left(-\rho \overline{u'w'}(z) \right) = \tau_b \quad (2.30)$$

2.6.1.2 Modeling of the boundary shear stress

In absence of detailed measurements of Reynolds shear stress on the vertical or of Preston tube measurements, an alternative solution is to use modelling. Only semi-empirical formula widely used by practitioners and engineers are proposed in this paragraph.

It is convenient to express the effects of the boundary shear stress on the flow as energy slopes ($S_{f,x}$ and $S_{f,y}$) of the head loss due to friction [[Bousmar et al., 2004](#); [Proust et al., 2010](#)].

$$\frac{\tau_{b,x}}{\rho gh} = S_{f,x} = \lambda \frac{\sqrt{U_d^2 + V_d^2} U_d}{8gh} \quad (2.31)$$

$$\frac{\tau_{b,y}}{\rho gh} = S_{f,y} = \lambda \frac{\sqrt{U_d^2 + V_d^2} V_d}{8gh} \quad (2.32)$$

where λ is the Darcy-Weisbach coefficient. This coefficient is a universal coefficient and its calculation takes into account the nature of the flow and the state of its boundary layer [[French \[1985\]](#)].

[Yen \[2002\]](#) proposes an explicit formula for computing λ ; for $Re = U_d \times 4R/\nu > 120000$ and $k_s/R < 0.05$, we have:

$$\frac{1}{\sqrt{\lambda}} = -2 \log \left(\frac{k_s}{12R} + \frac{6.79}{Re^{0.9}} \right) \quad (2.33)$$

Instead of the Darcy-Weisbach's coefficient, the Manning's coefficient n is also commonly used for estimating the friction in the river reach (see §A.2). Nevertheless, this coefficient is only valid for rough turbulent flows [[Proust, 2005](#); [Suzanne, 2005](#)].

To finish, the boundary shear stress in the streamwise direction is also often written as:

$$\tau_b = \rho u_*^2 \quad (2.34)$$

where u_* is called friction velocity and is generally modelled as following:

$$u_* = \sqrt{ghS_{f,x}} \quad (2.35)$$

Expression for u_* can be either used under uniform or non-uniform flow conditions. Under uniform flow conditions it is considered that in Equation 2.32, $S_{o,x} = S_{f,x}$ and $S_{o,y} = S_{f,y}$. For non-uniform flow, it is classically assumed that the friction slope $S_{f,i}$ equals the bed slope $S_{o,i}$ of a channel in which a uniform flow occurs at the same discharge and with the same cross-section area [Bousmar, 2002; French, 1985]. Such approximations of the friction velocity are really useful for evaluating the nature of the boundary layer that develops on the bottom.

All the previous coefficients are “equivalent” following the relationships:

$$\frac{\lambda}{8} = \frac{n^2 g}{h^{1/3}} = \frac{u_*^2}{U_d^2} \quad (2.36)$$

NB – Excepted in flows, with perfectly logarithmic velocity profiles, the use of the coefficients of Darcy-Weisbach or of Manning introduced a bias in the friction modelling. The use of such coefficients as friction coefficients is indeed inappropriate, they rather model a kind of flow resistance which mixes different phenomena (friction + mixing layer...). Errors made by the use of such coefficients may be partly compensated by another modelling, for instance by the dispersion modelling or by the turbulence modelling. The mis-use of such coefficients is mostly the fundamental problem of the 1D-modellings (see §A.2.1).

2.6.2 Turbulence

As for the friction, the depth-averaging of the 3D mean motion equations leads emergence of another term to measure or model: the depth-averaged Reynolds stresses T_{ij} , which is expressed as following:

$$T_{ij} = -\rho \frac{1}{h} \int_{Z_b}^{Z_{ws}} \begin{bmatrix} \overline{u'u'} & \overline{u'v'} & \overline{u'w'} \\ \overline{v'u'} & \overline{v'v'} & \overline{v'w'} \\ \overline{w'u'} & \overline{w'v'} & \overline{w'w'} \end{bmatrix} dz \quad (2.37)$$

$3D \Rightarrow 2D$

$$= -\rho \frac{1}{h} \begin{bmatrix} \int_{Z_b}^{Z_{ws}} \overline{u'u'} dz & \int_{Z_b}^{Z_{ws}} \overline{u'v'} dz \\ \int_{Z_b}^{Z_{ws}} \overline{v'u'} dz & \int_{Z_b}^{Z_{ws}} \overline{v'v'} dz \end{bmatrix}$$

Terms in Equation 2.37 express the additional stresses that the turbulence induces on the mean motion [Chassaing, 2000a]. In this thesis, turbulence was measured using an Acoustic Doppler Velocimeter (see §3.3.4.3).

2.6.2.1 The Boussinesq assumption

In absence of measurements of the turbulence or if measurements are inconsistent, engineers need to use a turbulent closure in order to estimate the Reynolds stresses. The depth-averaged Reynolds shear stresses in the 2D-H Saint-Venant equation (Equations 2.23 and 2.24) are modelled using the Boussinesq eddy viscosity concept [Rodi, 1980]; *i.e.* by analogy with molecular viscosity, the Reynolds stresses are assumed to be proportional to the depth-averaged velocities and they are written as following:

$$T_{ij} = -\rho \begin{bmatrix} 2\nu_t \left(\frac{\partial U_d}{\partial x} \right) - \frac{2}{3} \frac{1}{h} \int_{Z_b}^{Z_{ws}} \overline{k'} dz & \nu_t \left(\frac{\partial U_d}{\partial y} + \frac{\partial V_d}{\partial x} \right) \\ \nu_t \left(\frac{\partial U_d}{\partial y} + \frac{\partial V_d}{\partial x} \right) & 2\nu_t \left(\frac{\partial V_d}{\partial y} \right) - \frac{2}{3} \frac{1}{h} \int_{Z_b}^{Z_{ws}} \overline{k'} dz \end{bmatrix} \quad (2.38)$$

where ν_t is the eddy viscosity and $\int_{Z_b}^{Z_{ws}} \overline{k'} dz$ is the depth-averaged kinetic turbulent energy. The eddy viscosity is either assumed constant or is modelled using an algebraic equation or one or two transport equations.

NB – The turbulent closures that use the Boussinesq assumption belong to the first-order turbulent closures [Chassaing, 2000a], while the second-order closures directly solve transport equations of Reynolds stresses (The Reynolds stress equations result from the ensemble-mean of the equations resulting from the multiplication of Equation 2.7 by the fluctuations (u', v', w')) and model the triple-correlations terms [Estivaleres, 2005]; the Boussinesq assumption is no more used in such modelling. These closures are generally more accurate, but they are also much more complicated than the first-order closures. The Reynolds stress equations are indeed expensive in computation time and difficult to solve. Therefore, they are generally simplified into algebraic expressions by considering assumptions on the convection and the diffusion terms in the Reynolds stress equations. These modelling are called Algebraic Reynolds Stress Model.

2.6.2.2 Constant eddy viscosity

The constant eddy viscosity is often used for 2D-H modelling with weak horizontal momentum transfer. This assumption of constant turbulent viscosity is used when mass exchange and momentum transfer cannot be separated from dispersion effects due to vertical heterogeneity of the velocity and numerical diffusion [Hervouet, 2002; Proust, 2005]. The eddy viscosity is more a kind of effective viscosity which combines the vertical dispersion and the numerical diffusion.

2.6.2.3 Modelling with algebraic equations

Algebraic equations model the main sources of the turbulence in a given channel. The classical mixing length modelling [Prandtl, 1925] is generally adapted for depth-averaged equations. The eddy viscosity is here a function of the transverse shearing and is modelled as:

$$\nu_t = l_m^2 \left| \frac{\partial U_d}{\partial y} \right| \quad (2.39)$$

with l_m the mixing length.

When the flow is governed by the bottom friction, the eddy viscosity is expressed using the Elder modelling. The eddy viscosity is then proportional to the bottom friction and to the water depth:

$$\nu_t = \lambda_E u_* h \quad (2.40)$$

Where λ_E is an empirical calibration coefficient. In the present work [Peltier et al., 2008], we set this coefficient equal to 0.1 for narrowing compound channels, while Bousmar [2002] sets this coefficient within 0.13 and 0.16 for the large experimental flumes. Wark et al. [1990] considers that this coefficient is within 0.6 and 2 for natural rivers.

Under uniform flow conditions [Shiono and Knight, 1991] **or under non-uniform flow conditions** [Rezaei and Knight, 2009] **in compound channels**, some authors consider that the turbulence is mainly due to the planform vortices at the interface between channels (see §1.2.2). The turbulence is therefore linked to the spanwise gradient of the streamwise velocity and to the bottom friction in order to take into account the shallowness of the flow. Nevertheless as brought up by van Prooijen et al. [2005], the contribution of the secondary currents is switched off at the interface between the main channel and the floodplain. Yet the secondary currents play a role in the mixing region in compound channel. This explains why the range of the empirical constant λ_E in the Elder formulation of Shiono and Knight [1991] is too high ($\lambda_E \in [0.07 \ 40]$) and is not in agreement with the usual range $\lambda_E \in [0.6 \ 2]$ [Wark et al., 1990].

According to van Prooijen et al. [2005], **in compound geometries**, secondary currents effects in the mixing layer have to be taken into account in addition to bottom-generated turbulence and horizontal shearing in order to model the turbulence in a compound channel. Based on the physics presented in §1.2, previous authors proposes to split the eddy viscosity into two components; a contribution of the bottom-generated turbulence (ν'_t) and a contribution due to transverse shears at the interface between channels (ν''_t):

$$\nu_t = \nu'_t + \nu''_t \quad (2.41)$$

For the bottom-generated turbulence, the Elder formulation is then adopted (Equation 2.40) and for the transverse shear, the contribution is modelled using a Prandtl's mixing length model. The eddy viscosity is then formulated as follows [van Prooijen et al., 2005]:

$$\nu_t = \lambda_E h(y) u_* + \gamma^2 \delta^2 \frac{H_{mc} H_{fp}}{2h(y)} \left| \frac{\partial U_d}{\partial y} \right| \quad (2.42)$$

where γ is a proportionality constant (in the center of a developing plane mixing layer, $\gamma \in [0.088 \ 0.124]$, Pope [2000]); δ is the width of the mixing layer (Equation 1.5). The compound geometry imposes to the shape and velocity of the macro-vortices in the mixing layer to depend on the water depth (Figure 1.9); as a consequence, the eddy viscosity due to transversal shearing also depends on the water depth.

2.6.2.4 Modelling with one or two transport equations

In the previous algebraic formulations, it is assumed that the turbulence is directly linked to the mean flow characteristics. It is obvious that for flows with strong momentum transfer (due to mass or turbulent exchange), the use of only algebraic modelling may be not sufficient for well describing the turbulence in the flow (see in Peltier et al. [2008]). The consideration of the local modifications of the turbulent agitation linked to the evolution of a transportable quantity should be more appropriate [Chassaing, 2000a]: this is the role of the turbulence transport equations [Bousmar, 2002; Nezu and Nakagawa, 1993; Rodi, 1980].

The most common one-transport equation transports the turbulent kinetic energy. Resulting eddy viscosity is proportional to a length scale l and a time scale $\tau = u'/l$ that are characteristic of the turbulent field; l is linked to the characteristic scale of the macro-structures and $\tau = \sqrt{1/h \int_{Z_b}^{Z_{ws}} \overline{k} dz} / l$ is linked to the turbulent kinetic energy. The eddy viscosity is then written

as:

$$\nu_t = C'_\mu \sqrt{\frac{1}{h} \int_{Z_b}^{Z_{ws}} \overline{k'} dz} \quad (2.43)$$

where C'_μ is related to the dissipation rate ϵ , which according to [Bailly and Marsden \[2009\]](#), is fixed by the macro-structures in the turbulent flow, hence:

$$\epsilon \approx u'^3/l \quad (2.44)$$

The length scale l is empirically determined (similar to the mixing length) [[Launder and Spalding, 1974](#)] or is computed using algebraical formula. The quality of ν_t then depends on the calculation of l .

Since the determination of l may be problematic, additional equations are used for determining the missing turbulent length scale [[Bousmar, 2002](#); [Estivalezes, 2005](#); [Nezu and Nakagawa, 1993](#)].

The k- ϵ modelling

In addition to solving an equation for $1/h \int_{Z_b}^{Z_{ws}} \overline{k'} dz$, a second equation is used for determining the dissipation rate ϵ . With this new system of equations the eddy viscosity is estimated as following (Prandtl-Kolmogorov notation):

$$\nu_t = C_\mu \frac{\frac{1}{h} \int_{Z_b}^{Z_{ws}} \overline{k'} dz^2}{\epsilon} \quad (2.45)$$

where $C_\mu = 0.09$ is a constant.

The system of equations for 2D-H modelling slightly differs from the one proposed by [Launder and Spalding \[1974\]](#). In addition to the omissions of the derivatives with respect to the vertical direction, two generation terms are added (one in each equation) to account for turbulence generation due to the gradient $\partial \bar{u}/\partial z$, which occurs mainly near the bottom. These terms strongly depends on the bottom friction [[Nezu and Nakagawa, 1993](#)]. [Bousmar \[2002, p. 33\]](#) derives the complete formulation of the 2D-H k- ϵ equations.

Although this model is widely used by engineers and scientists, there are plenty of different two-equations modellings. Some examples are given in the following paragraphs.

The k- ϵ RNG modelling

This models is an improvement of the classical k- ϵ modelling. It works in the Fourier space and use the theory of ReNormalization Groups. Velocity field is decomposed into wave-numbers bands and the influence of each band is evaluated using an iterative method. The most influent bands are then conserved (for instance, bands of the mean flow) and by returning in the physical space an analytical model of turbulence is deduced. The deduced models have better answers than the classical k- ϵ in rapidly deforming flows [[Estivalezes, 2005](#)].

The k- ω modelling

This model was first proposed in 1942 by Kolmogorov. Instead of modelling ϵ , this model transports a characteristic turbulent frequency ω . This frequency is the inverse of the characteristic time-scale of the dissipation of the kinetic energy $\omega = \epsilon/k'$ [[Estivalezes, 2005](#)].

NB – Given the measurements we made of the turbulence (see in Chapter 3), only the algebraical modelling could be used for modelling the turbulence of our flows. The question is then to know if these modelling are enough to render the complex evolution of the turbulence that develop in compound channel with a groyne set on the floodplain.

2.6.3 Secondary currents of Prandtl's second kind

Excepted using a vorticity equation, by construction of the 2D shallow water equations, the secondary current of Prandtl's second kind cannot explicitly be described. The vertical component w of the velocity is indeed simplified in Equations 2.23 and 2.24. As a consequence the variations of the couple (v, w) is never modelled. The secondary currents are actually implicitly described in $\partial h U_d V_d / \partial y$ (Equation 2.23), in $\partial h U_d V_d / \partial x$ (Equation 2.24) and in the depth-averaged dispersion on the vertical of the horizontal component velocities X_{xx} , X_{xy} and X_{yy} .

2.6.3.1 The Shiono and Knight Method for compound geometries

Shiono and Knight [1991] proposed a new formulation of the shallow water equations under uniform conditions (Equation 2.46) and proposed an analytical solution to this formulation. This new formulation (the so-called Shiono and Knight Method) only considers the depth-averaged x-wise momentum equation of the 3D mean-motion and can model the effects of the secondary currents on the mean motion through the so-called secondary currents term $\partial h(UV)_d / \partial y = \Gamma$.

$$\frac{\partial h(UV)_d}{\partial y} = \rho g h S_{o,x} - \tau_{b,x} \left(1 + \frac{1}{s^2} \right) + \frac{1}{\rho} \frac{\partial h T_{xy}}{\partial y} \quad (2.46)$$

where s is the side slope of the bank (1:s, vertical:horizontal). After *Shiono and Knight* [1990] and *Ikeda and McEwan* [2009], the secondary currents term actually includes at least two effects: vorticity in the vertical direction at the floodplain/main channel interface and longitudinal vorticity on the floodplain. However, *Ikeda and McEwan* [2009] considers that this term is a good “sink” term representing both vorticity effects and influences. In general, the secondary currents term or “ Γ term” is set as a constant in the main channel or in the floodplain, or at any convenient position in order to solve Equation 2.46.

The SKM is an interesting method and is widely used in England for flood prediction and prevention by the environmental agency. However, this method was developed for flows under uniform flow conditions. This method is then inappropriate for our flows in compound channel with a groyne set on the floodplain.

NB – Recently, *Rezaei and Knight* [2009] has proposed a new formulation for the SKM for non-uniform flow conditions. The slope $S_{o,x}$ is replaced by an energy slope $S_{e,x}$ representing the local measureable non-uniformity.

2.6.3.2 Vertical dispersion on the horizontal components of the velocity

The secondary currents can be also modelled using the dispersion terms in the classical momentum Equations 2.23 and 2.24; $\partial h U_d V_d / \partial y$ or $\partial h U_d V_d / \partial x$ are just term for the momentum transfer due to mass exchange (see §2.5).

The depth-averaged dispersion on the vertical of the horizontal components of the velocity indirectly models the effects of the secondary currents of Prandtl's second kind (see §1.2.4) on the flow and evaluates the error that introduces the depth-averaging of the velocity in 2D-H

equations as well. According to [Bousmar \[2002\]](#), the dispersion terms that appear in the 2D-H Saint-Venant equations indeed takes into account the non-uniformity of the vertical profiles of the component u and v . This non-uniformity results from the bottom friction effect for the longitudinal velocity u ; and from the secondary currents development for the lateral velocity v [[Nezu, 2005](#)].

In absence of good measurements of the vertical dispersion terms, [Bousmar \[2002\]](#) has also shown that the secondary currents cells are proportional to the water depth h and the couple (\bar{u}, \bar{v}) is proportional to U_d . As a consequence, the dispersion terms can be written as following:

$$\begin{aligned} \int_{Z_b}^{Z_{ws}} (\bar{u} - U_d)^2 dz &= D_{xx} h U_d^2 \\ \int_{Z_b}^{Z_{ws}} (\bar{u} - U_d) (\bar{v} - V_d) dz &= D_{xy} h U_d^2 \\ \int_{Z_b}^{Z_{ws}} (\bar{v} - V_d)^2 dz &= D_{yy} h U_d^2 \end{aligned} \quad (2.47)$$

where D_{ij} are the dispersion coefficients. Theoretical values deduced from classical velocity profiles in single channel are $D_{xx} = 0.0080$, $D_{xy} = 0.0014$ and $D_{yy} = 0.0005$ [[Bousmar, 2002](#)].

Nevertheless, the dispersion coefficients are quite a crude approximation of the reality. A more convenient way is to use the vertical momentum coefficient β_{ij}^v in order to directly evaluate the non-uniformity of the velocity and the effects of the secondary-currents on the flow instead of using a modelling:

$$\begin{aligned} \beta_{xx}^v &= 1 + \frac{X_{xx}}{U_d^2} \\ \beta_{xy}^v &= 1 + \frac{X_{xy}}{U_d V_d} \\ \beta_{yy}^v &= 1 + \frac{X_{yy}}{V_d^2} \end{aligned} \quad (2.48)$$

The expression of the β_{ij}^v in Equation 2.48 were identified by injecting the identities proposed by [Bousmar \[2002\]](#) (*i.e.* $\bar{u} = U_d + (\bar{u} - U_d)$ and $\bar{v} = V_d + (\bar{v} - V_d)$) in the classical expression $\int_{Z_b}^{Z_{ws}} \bar{u}_i \bar{u}_j dz = \beta_{ij}^v U_{d,i} U_{d,j} h$ [[Henderson, 1966](#)].

β_{xx}^v and β_{yy}^v give information on the distortion of the streamwise or spanwise velocity profiles, *i.e.* acceleration or deceleration. β_{xy}^v gives information about the secondary cells, since it is a function of V_d .

NB – In this PhD-thesis, the velocity products $(\bar{u} - U_d)^2$, $(\bar{u} - U_d)(\bar{v} - V_d)$ and $(\bar{v} - V_d)^2$ in Equation 2.18 were estimated at each available point of each vertical defined in the measurement mesh. The depth-averaging was made using the trapezoid rule (§4.4); due to the few points available on the vertical, a theoretical velocity profile could not be fitted more accurately to the data to be integrated.

Conclusion of Part I

In the first chapter of this thesis, the particular physics of overbank flows in prismatic compound channel is first presented. The classical vertical profiles of velocity, so as the spanwise profiles of depth-averaged velocity are described. The characteristics of the mixing layer developing at the interface between channels is then given. In the sequel, the resulting profiles of boundary shear stress are detailed. We also show the way secondary currents of Prandtl's second kind distort the flow in both the main channel and the floodplain. To finish, interactions between all the previous processes are discussed.

In the sequel of this chapter, the various types of gradually varied flows in compound channels with a straight main channel are presented: flow in straight compound channel with unbalanced inlet discharge distribution, non prismatic geometry with continuously varying floodplain with a constant overall width for the flume and non prismatic geometry with a variable overall width for the flume. These new types of flows lead emergence to an additional process that superimpose to the other processes usually found in a compound channel flow: mass exchanges between channels and resulting momentum transfers due to mass exchanges. Measurements and data analyses thus emphasize that in such gradually varied flows, mass exchanges between subsections have a tremendous impact on the physical processes usually found in prismatic geometries.

To finish, effects of a transversal and discontinuous variation (*i.e.* groyne, embankment, ...) of the floodplain are discussed. We show that most experiments were conducted in single channel and their results are highly difficult to apply for flows in compound channel given the few existing data in the literature.

This chapter therefore leads us to highlight the two first objectives of this thesis, *i.e.*

1. To build a complete set of data of rapidly varied flows in the vicinity of a groyne set on the floodplain of a compound channel.
2. To understand effects on the hydraulic parameters of the superimposition of the two problems that are (i) flow in compound geometry and (ii) rapidly varied flow in the vicinity of a thin obstacle.

Nevertheless, just measuring and analysing the flow parameters is not sufficient for a complete understanding of the physics of such flows. We need to identify each physical process in the flows in order to assess their weight relative to the other. We then could have an idea of what phenomenon is dominant or not. This therefore defines the last objective of this thesis.

In the second chapter, we then present a 2D-H momentum equation based on the dispersive Saint-Venant equation that uses the flow parameters we measured for identifying the various physical processes that occur in our particular flows. The streamwise variation of the longitudinal kinetic energy thus gives information on the streamwise variation of the mass in the flume, while the momentum transfers due to lateral mass exchanges are estimated using the lateral gradient of the longitudinal velocity. The friction is represented by the boundary shear stress and the gradient of normal Reynolds stresses T_{xx} give information about the additional stress exerted by the turbulence on the mean motion. The Reynolds shear stress T_{xy} emphasizes effects on the flow of a potential lateral velocity/turbulence shear in the flow. The dispersion terms finally either

highlights the non-uniformity on the vertical of the longitudinal velocity \bar{u} or give information about the secondary currents.

In the sequel, we show that some of the parameters coming from the 2D-H momentum equation could be modelled in absence of consistent measurements (friction, turbulence and vertical dispersion). Nevertheless, among all the modelling we present, none of them was developed for flows with recirculation zones. We cannot therefore be sure that they are valid for such rapidly varied flows [[Stansby, 2008](#)]. This conclusion emphasizes once again the need to have a robust set of data for testing these modelling or for developing some new modelling on recirculating flows.

Part II

Material and Method

3

Experimental set-up and metrology

3.1 Introduction

Experiments presented in the main body of this thesis were conducted in an asymmetrical compound open-channel flume located in the Laboratory of Fluids Mechanics and Acoustics (LMFA) of Lyon, France. In Appendix B, additional experiments conducted in the open-laboratory of Ujigawa, in Japan, are briefly presented [Baba *et al.*, 2010]. These experiments aim at investigating the effects on an overbank flow of a groyne set onto the floodplain. First experiments dealt with developing-flows in a straight compound channel, considered as reference flows (Chapter 5). The second experiments dealt with flows with a groyne set on the floodplain. Non-uniform flows are compared together and are compared to reference flows in Chapters 6, 7 and 8.

The settings of the experimental flume and the available measuring devices at the beginning of the PhD-thesis were not sufficient to achieve the measurements we planned to do for understanding flows in the vicinity of an obstacle set in the floodplain. The first year of the PhD-thesis was therefore devoted to the improvement of the experimental flume and to the adaptation of new measuring devices.

In this chapter, the experimental flume and its specific devices are first presented. The characteristics of the measuring devices used for our experiments are then exposed. Finally, the way the data-set was constructed and the main characteristics of this data-set are exposed.

3.2 Experimental flume (LMFA)

3.2.1 Main characteristics of the flume

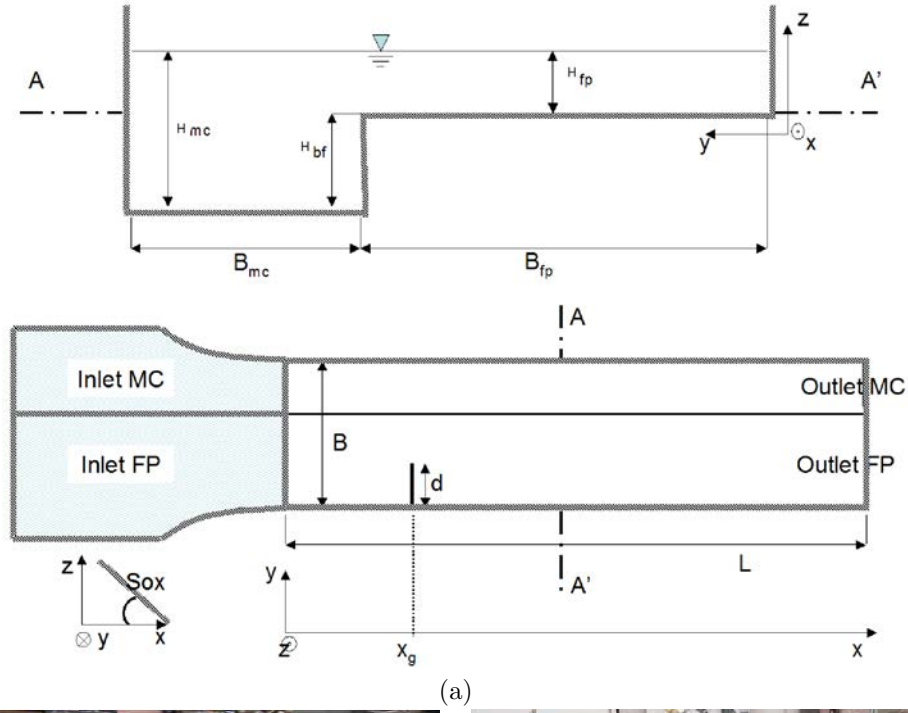
Experiments were conducted in a 8 meters long and 1.2 meter wide experimental flume located at the Laboratoire de Mécanique des Fluides et d'Acoustique (LMFA) of Lyon, France. This flume is straight with an asymmetrical cross-section and has a streamwise mean slope of 0.18 %. The main channel cross-section is rectangular (Figure 3.1.a) and is 0.40 m wide. The floodplain is 0.80 meter wide and the bank-full height is 5.15 cm high. The floodplain and the main channel are PVC made and their surface state is smooth. Geometrical parameters are displayed in Figure 3.1.a and their values are resumed in Table 3.1.

L [m]	B [m]	B_{fp} [m]	B_{mc} [m]	H_{bf} [cm]	$S_{o,x}$ [%]
8.00	1.20	0.80	0.40	5.15	0.18

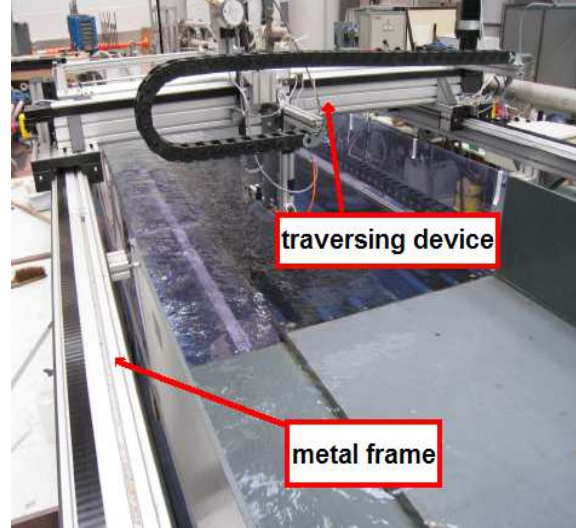
Table 3.1 – Mean characteristics of the experimental flume at the LMFA.

As depicted in Figures 3.1.b and 3.1.c, the flume is surrounded by a metal frame which supports an automatic traversing device. This frame is independent of the channel and follows

the same mean slope as the compound channel. Measuring devices are mounted on the traversing device in order to measure the flow parameters.



(b)



(c)

Figure 3.1 – Definition sketch and photographs of the flume in the LMFA. (a) Cross-sectional and top views (scheme is not to scale). (b) Photograph of the flume (view from upstream to downstream). (c) View of the metal frame surrounding the flume.

3.2.2 Topography of the flume

The longitudinal mean-slope ($S_{o,x}$) of the bottom of the flume was first surveyed using a theodolite: $S_{o,x} = 1.8 \pm 0.36$ mm/m. Afterwards, the slope of the surrounding metal frame was set at the same averaged value in order to avoid any problems of projections between the reference frame attached to the flume and the reference frame attached to the traversing device. The flume topography was then surveyed using an ultrasonic probe (uncertainty: ± 0.3 mm) which measured the distance between the traversing device and the bottom. Measurements were carried out following the mesh displayed in Figure 3.2.b. Then by assuming that both slopes of the flume and metal frame were equal to 1.8 mm/m, this slope was subtracted to measurements. Resulting

data finally represent the variations of the bottom around the mean-slope of the flume and they therefore enable to estimate the positions of possible topographic irregularities (see in Figure 3.2.a).

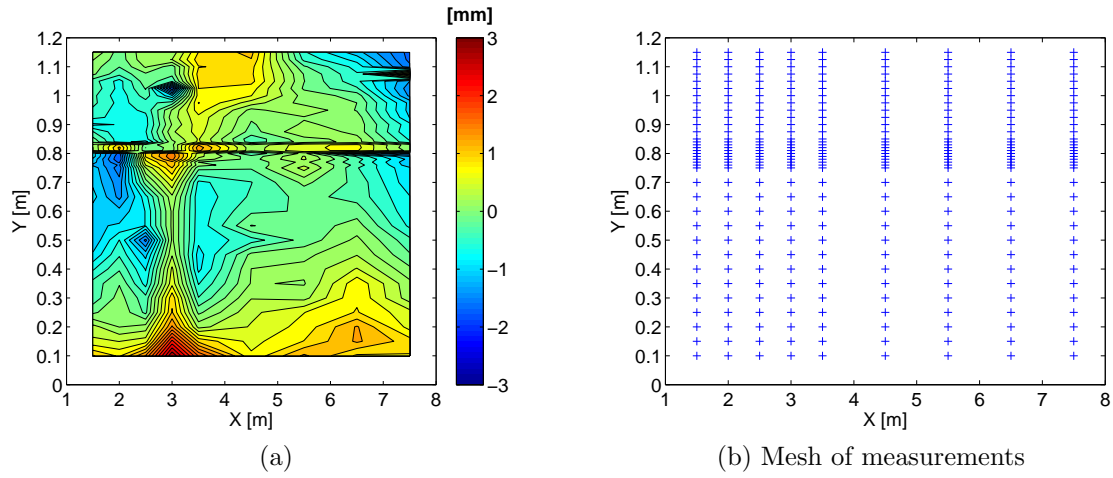


Figure 3.2 – Survey of the flume using an ultrasonic probe; absolute variations of the bottom shape relative to the mean slope of the flume. The interface between the main channel and the floodplain is located at $y = 0.8$.

Figure 3.2.a shows that the floodplain has more bottom variations than the main channel. In the floodplain, maximal differences between irregularities is equal to 5 mm, while this magnitude is only equal to 2 mm in the main channel. At $x = 3$ m in the floodplain, a ridge of 2 mm is observable; in the main channel, the ridge is smaller.

The surface of the floodplain is slightly depressed at its centre, which creates a small basin deep of 2 mm at maximum. As a consequence, a lateral slope is observed in the floodplain (Figure 3.2.a): the variations from the floodplain wall towards $y = 0.48$ m leads to a slope of -4 mm/m, then from $y = 0.48$ towards the interface, the slope is equal to 1.5 mm/m.

3.2.3 Upstream and downstream boundary conditions

According to *Bousmar et al.* [2005], in a compound channel with a unique filling tank and no particular outlet conditions, the flow establishment - for getting an uniform flow - may need a distance at least equal to $35 \times B_{fp}$. In our flume, this distance cannot be reached, since the maximal value of x/B_{fp} in the flume (x measured from the inlet tank) is equal to 24.18 and is then smaller than 35. Without adapted boundary conditions, the quick establishment of a flow is then not possible in the LMFA flume. Separated inlets were therefore set up in the flume (Figure 3.3). Thanks to the separated inlets, each subsection discharge corresponding to the uniform flow was directly injected in each channel. Excess in floodplain discharge, obtained when a single inlet is used, was then minimized and the flow establishment was thus accelerated along each channel.

In each upstream filling tank, where the supply line of each channel ends, an horizontal grid with a square mesh of five centimetres lays down just above the outlet pipe. These grids break the macro-structures generated by the filling of the tank.

For the lowest total discharges $Q_t = 17.3$ l/s and $Q_t = 24.7$ l/s (see in Table 3.3), the upstream boundary conditions consist of a honeycomb followed by a succession of a grillage buffer with a very fine mesh (Figures 3.3.a and 3.3.b, the succession of grids is 1 cm wide). The honeycomb enables to redirect the fluid coming from the tank and is responsible for a decrease of the water depth, while the grillage buffer stabilizes the outflow of the honeycomb in order to avoid the creation of an hydraulic jump due to a too strong diminution in the water depth just in the

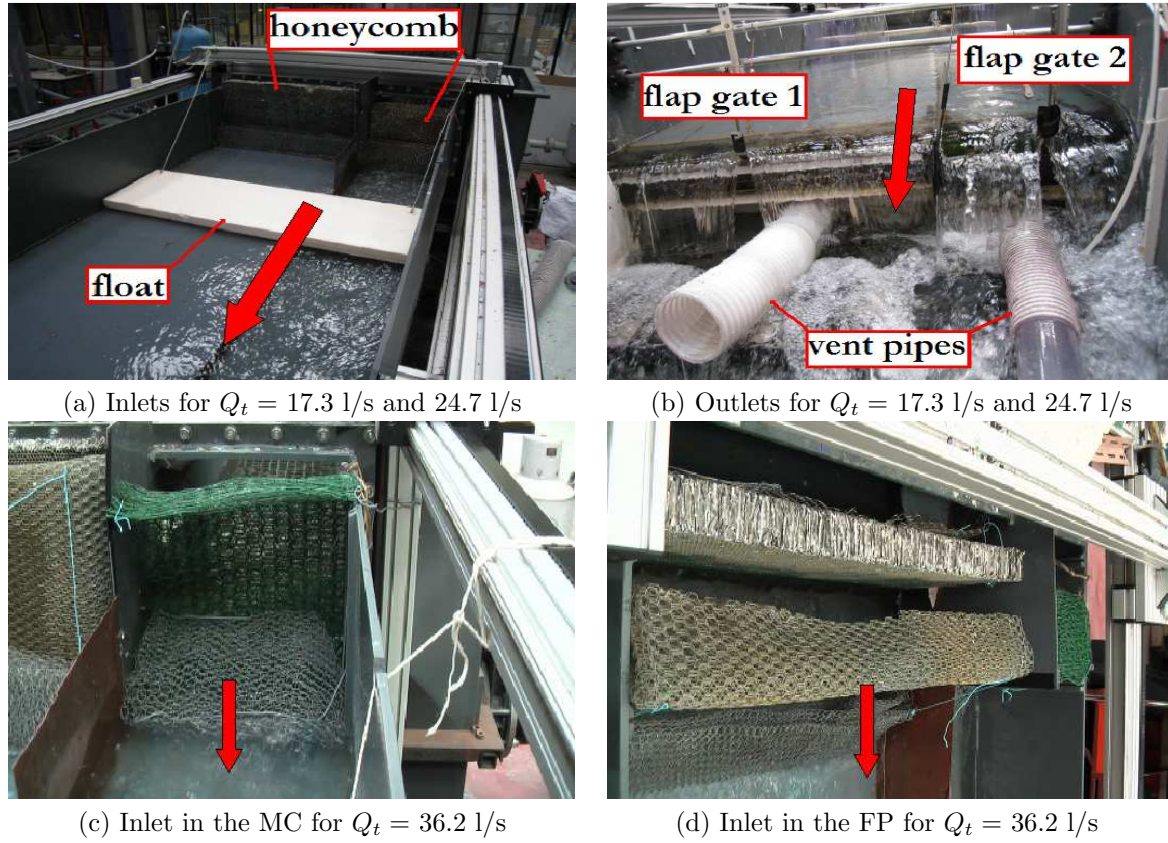


Figure 3.3 – Photograph of the boundary conditions at the LMFA.

output of the honeycomb. Finally, just after the two grids, a float made of extruded polystyrene lays down on the free surface in order to attenuate the free surface oscillations.

For the highest total discharge $Q_t = 36.2$ l/s, an additional grid was installed in the floodplain in order to further reduce the kinetic energy (Figure 3.3.d); the discharge was indeed so powerful, that without the new grid, it was almost impossible to adjust the boundary conditions in order to get a flow nearly uniform in the flume. Contrariwise, in the main channel, the honeycomb was removed (Figure 3.3.c) and a new succession of grids with bigger holes replaced the grids used for $Q_t = 17.3$ l/s and $Q_t = 24.7$ l/s. The size of the holes in the honeycomb was too small and the resulting head-loss was too strong. The flow systematically disconnected just out of the honeycomb. With the new grids, the injection was better and smoother. However, this change in the inlet geometry had some impacts on the flow parameters (see in chapter 5).

The downstream boundary conditions consist of two flap gates, one in each subsection. The height of the gates are referenced using a permanent ruler (uncertainty equal to ± 0.1 mm) fixed between the gate and the frame of the flume: outlet conditions are reproducible (Figure 3.3.b). The separated outlets enabled a better adjustment of the downstream boundary conditions by limiting the mass exchange between subsections at the end of the flume.

NB – When the flume was built in 2000, the aspect ratio L/B of the LMFA flume was chosen slightly greater than the smallest aspect ratio that have been used in the SERC FCF of Wallingford; *i.e.* $L/B = 8/1.2 = 6.66$ for the LMFA and $L/B = 56/10 = 5.6$ for the FCF [Knight, 1992]. Given this ratio and the separated inlets, attempted results in the LMFA could be expected as good as those measured in the FCF, where a simple injection was used and the flow therefore required a great length to establish [Bousmar *et al.*, 2005].

3.2.4 Pumps and flow-meters

3.2.4.1 Pump: Grundfos SP125-1-A

Each channel tank (Figure 3.1) is filled using a submersible helical pump (Grundfos, SP125-1-A; Figure 3.4). These pumps are 400 V three-phased with a nominal power of 7.5 kW, a nominal discharge of 125 m³/h and a nominal manometric head of 13 m.



Figure 3.4 – Pump Grundfos SP125-1-A.

During experiments, the pumps were always used out of their nominal characteristics. Thanks to a regulator (Danfoss FC202P11KT4E55G, maximal intensity of 20 A), the required discharges were directly injected in each channel (Figure 3.5.a) and to ensure that the discharge was constant all along the experiment, a feedback control was set up on the regulator and on the flow-meters using a Proportional-Integral-Derivative controller (constant of time equal to 10 s) to ensure a quick and stable response of the system.

With a fully-open pipe, the engine of the pumps could not properly spin under a frequency of 16 Hz, *i.e.* it could not deliver a discharge smaller than 14.4 m³/h (4 l/s). For flows with low discharge ($Q_{fp} = 2.38$ l/s for RF200L, see Table 3.3), additional head loss was then generated using a valve – one for each filling pipe – in order to change the duty point of the installation. As a consequence, the pump had to spin faster to deliver the required discharge. For small discharges, the valves were closed until the spinning of the engine becomes greater than 20 Hz; this also enabled us to even regulate the small discharge in the flume.

3.2.4.2 Electromagnetic flow-meter

The injected discharge is controlled on each supply line by an electromagnetic flow-meter (Endress Hauser, Promag 10, see in Figure 3.5.b). The uncertainty on the discharge is given by the manufacturer, *i.e.* the uncertainty is equal to 0.5 percent of the maximal working range of the pump: $0.5/100 \times 40$ l/s = 0.2 l/s.



Figure 3.5 – (a) Discharge regulator. (b) Flow-meters.

3.3 Measuring devices

3.3.1 Traversing device, data acquisition and measuring mesh

All measuring devices were mounted on the traversing device moving on the metal frame surrounding the flume. To ensure a good positioning of the measuring devices and to optimize the data-acquisition, measurements were automated using LabVIEW. Thanks to this automation, the experimenter never interacts with devices during the data-collection and collected data can be checked during measurements on the acquisition-computer in order to make adjustments, if necessary. The data acquisition was performed through a cDAQ card driven by LabVIEW and the sampling frequency (F_s) of the card was set to 50 Hz.

The traversing device moves through a stepper motor precise to 0.2 mm in the streamwise direction (x -axis) and in the spanwise direction (y -axis). The motor and the data acquisition is done through LabVIEW. The measurement procedure follows the operation scheme resumed in Figure 3.6. The streamwise and the spanwise positions of measurements and the duration are first defined in a mesh file. This file is then read in the LabVIEW program. After defining the initial position of the automate, it moves in both directions. Once the robot is on position, the data acquisition can start. At the end of the data acquisition, data are written in an excel file and the program checks if it is the end of the measurement mesh. If yes, the program stops. If not, the next line in the mesh file is read and the carriage moves to the new position and the procedure starts again, until the end of the mesh is reached.

NB – The vertical displacement was manual, because we had no more enough time to install a third automatic displacement on the traversing device.

Except for measuring surface velocities (LSPIV method), measuring devices carried out punctual measurements during experiments. These measurements were done using specific meshes along the x - and y -wise directions emphasizing the zones of importance in the flow (Figure 3.7.a: mesh of depth measurements):

- In the floodplain from $y = 0$ m to $y = 0.750$ m, the y -wise mesh-step is 5 or 10 cm wide.
- In a zone of 5 cm of both sides of the centre of the mixing layer developing between the main channel and the floodplain (*i.e.* from $y = 0.750$ m to $y = 0.850$ m, where the velocity gradients are the strongest) the y -wise mesh-step is 1 cm wide.
- Finally in the main channel from $y = 0.850$ m to $y = 1.2$ m, the y -wise mesh step is 2.5 or 5 cm wide.

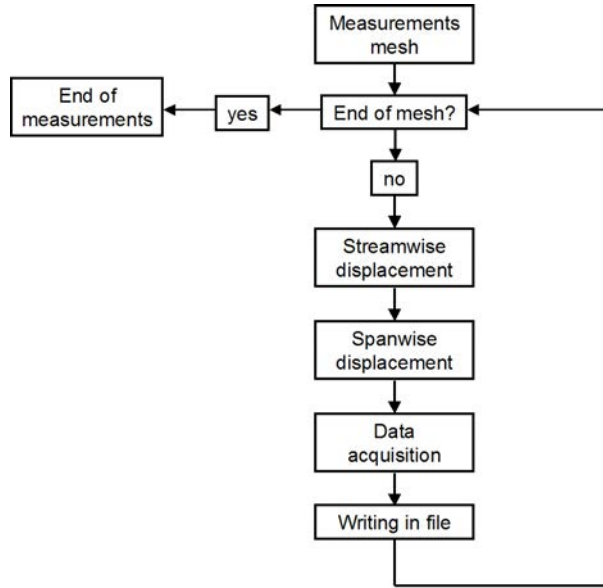


Figure 3.6 – Procedure of data acquisition using LabVIEW.

- In the longitudinal direction the mesh-step is not regular; from $x = 1.5$ m to $x = 3.5$ m, the mesh-step is 0.5 m wide, then the mesh-step is equal to 1 m until the end of the flume.

NB – The mesh in Figure 3.7.a stops 5 cm before the main channel wall and 10 cm for the floodplain, because the traversing device did not allow measurements near the wall. Only measurements with ADV and Preston tube were performed along the solid boundaries. Preston tube was carried by hand and the ADV has a deported sampling volume that allowed us to approach the solid boundaries.

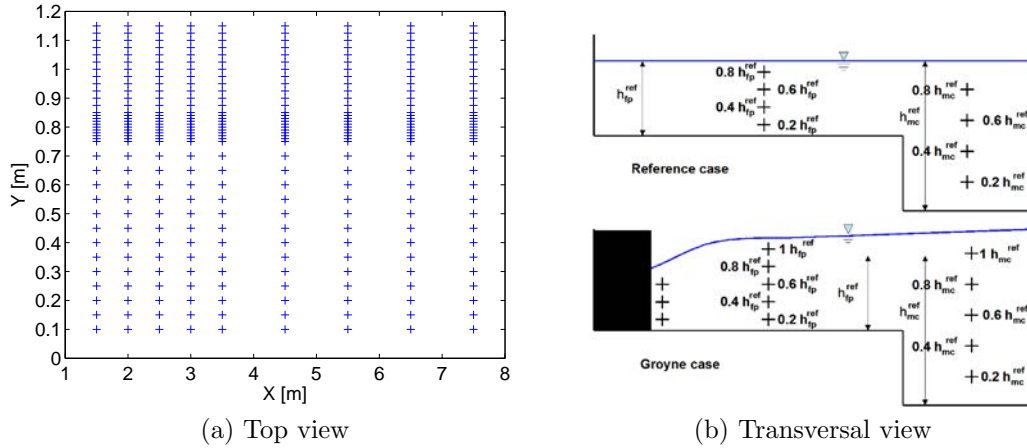


Figure 3.7 – (a) Mesh used for LMFA experiments in order to measure water depths and velocities with the micro-propeller. For groyne-case flows, the groyne is located 2.5 m downstream of the inlet. (b) Vertical meshes for reference and groyne-case flows.

Whether for reference flows or for groyne-case flows, the same reference depths (H_i^{ref} with $i = mc$ or fp) was used for referencing the relative altitude of measurements of mean-velocity and turbulence in the water column. The reference flow depths were calculated from measurements of the water depth under reference flow conditions; they are equal to the x-wise mean of the depths in a subsection between $x = 2$ m and $x = 5.5$ m, *i.e.* where water depths in a subsection were almost constant for reference flows (see Chapter 5).

Velocities were then measured for reference flows at four relative altitudes in comparison with the “reference depth” in the floodplain and in the main channel as shown in Figure 3.7.b: $0.2 \times H_i^{ref}$, $0.4 \times H_i^{ref}$, $0.6 \times H_i^{ref}$, $0.8 \times H_i^{ref}$. For the groyne-case flows, the velocities were measured following the same mesh and the same absolute altitudes as the reference flows. However, depending on the local flow depth, some altitudes have been either removed or added (see Figure 3.7.b: groyne-case flow).

The choice to measure velocity and turbulence at the same absolute altitudes was driven by the vertical axis of the traversing device that could not automatically set alone at a desired relative altitude.

3.3.2 Measurement of water depth

Various techniques enable water depth measurements; in a non-exhaustive manner, we can cite the point gauge, the vibrating point gauge (WAVO Mk-II Precision Liquid Level Meter, see Bousmar [2002]), the resistive probes, the ultrasonic probes and the laser survey. In this PhD-thesis, the free surface level and the bottom level were measured using an ultrasonic probe (Baumer Electric, UNDK 20I 6912 S35A).

The ultrasonic probe was really convenient in the LMFA flume. Although this device is less accurate than a point gauge (manufacturer specifications: point gauge accuracy equal to ± 0.03 mm and ultrasonic probe accuracy equal to ± 0.3 mm), it enabled the acquisition of long times series from which statistics and Fourier analysis could be easily calculated. This device was finally automated through LabVIEW and was attached to the automatic traversing device; a great amount of measurements could be therefore done in a minimum of time with a relatively good accuracy.

Operating principle

The ultrasonic probe (Baumer Electric, UNDK 20I 6912 S35A) is composed of one cylindrical emitter rounded by one receiver (Figure 3.8). The transmitter sends a train of waves that reflects on the object to be detected (bottom or water surface) and then return to the receiver. The time to travel round trip determines the distance of the object relative to the source.

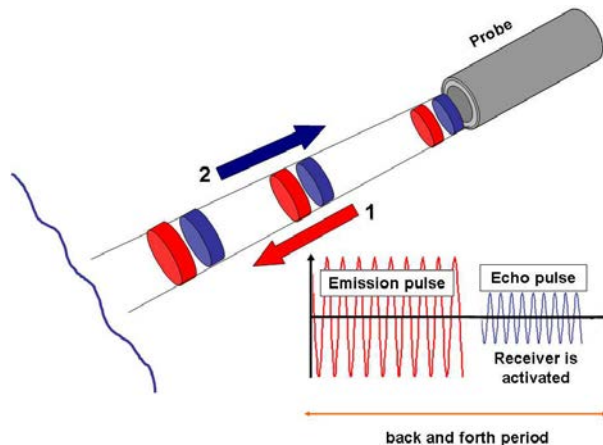


Figure 3.8 – Scheme of operating principle of an ultrasonic probe.

The ultrasonic probe measures the distance between the probe and the bottom or between the probe and the free surface. The depth is equal to the difference of both measured distances relative to the probe.

Measurement characteristics

The emitted signal from the probe is slightly conical. As a consequence the diameter of the patch of the sampling volume varies with the distance relative to the transmitter. It is approximately equal to 5 mm at the free surface level. The accuracy (ACC) of the probe is equal to ± 0.3 mm and the reproducibility between two measurements (RY) is equal to ± 0.5 mm.

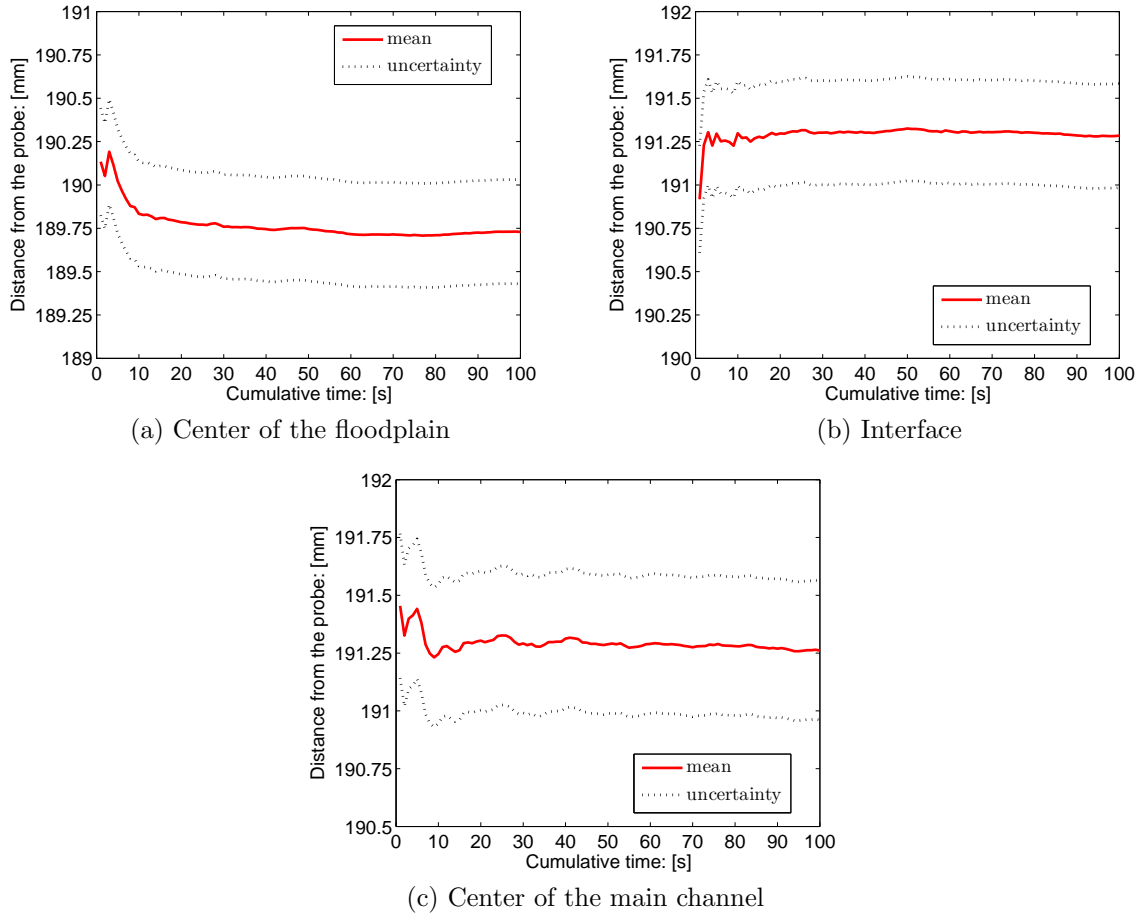


Figure 3.9 – Convergence of the cumulative mean and standard deviation of ultrasonic measurements depending on the position in the compound cross-section.

Long-time measurements can be done with an ultrasonic probe and therefore time-series can be acquired. The measurement of a great number of samples enables the convergence of the cumulative mean of the distance from the probe to the free surface (or bottom) towards a constant value with an uncertainty of ± 0.3 mm (see §4.2 for the uncertainty calculation). As shown in Figure 3.9, the cumulative mean of the measured distance from the ultrasonic probe to the water surface is monotonic and constant from 20 s. As a consequence, we chose to measure levels during 20 s.

3.3.3 Measurements of water level: definition of a reference plan

As previously stated, ultrasonic measurements were referenced relative to the metal from whom mean-slope is equal to the slope of the channel ($S_{o,x} \approx 1.8$ mm/m); this way of measuring enabled measurements of relative parameters such as the water depths. However, in some situations, absolute measurements referenced relative to an horizontal plan were rather needed. To get absolute measurements of the water or bottom elevation, an horizontal reference plan was therefore calculated.

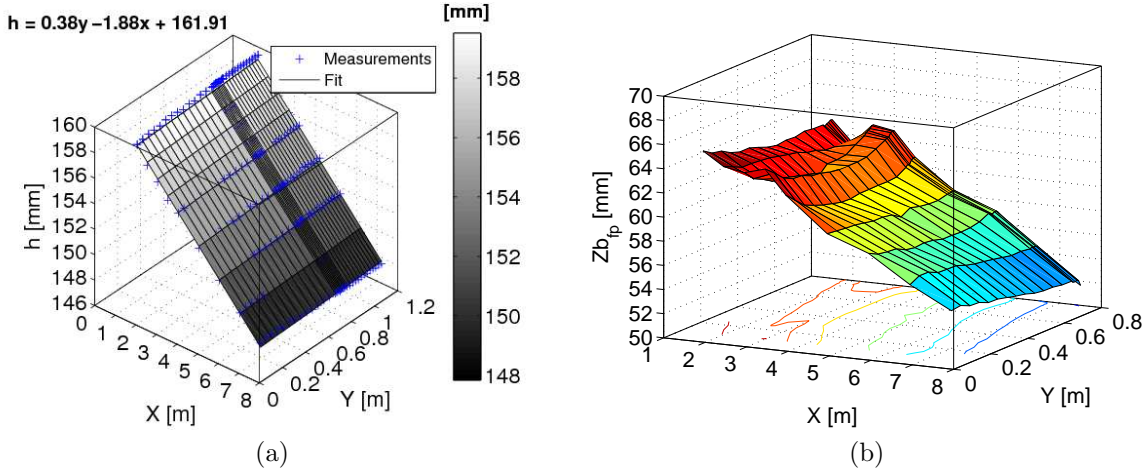


Figure 3.10 – (a) Equation of the plan fitting the free surface relative to the metal frame surrounding the flume. (b) Bottom level in the floodplain referenced to an horizontal plan whom origin is set in the main channel at $x = 7.5$ m and $y = 1.15$ m.

Thanks to the ultrasonic probe mounted on the traversing device, an horizontal plan of water was first surveyed relative to the metal frame. Equation of the plan fitting the free surface relative to the metal frame is displayed in Figure 3.10.a. It emphasizes that the longitudinal slope of the plan is equal to the slope of the metal frame, *i.e.* $S_{o,x} = 1.8 \pm 0.36$ mm/m; this ensures that the plan is well horizontal. A transversal slope of -0.3 mm/m is also observed in Figure 3.10.a. Since the plan of water is horizontal; this slope is probably due to transversal distortions of the metal frame. In the sequel, the subtraction of the ultrasonic measurements to the plan defined in Figure 3.10.a enabled to have bottom levels referenced to an horizontal reference plan whom origin is located at the level of the horizontal free surface. Resulting measurements were finally translated at the lowest level of the flume bottom in order to get $Z_b = 0$ at $x = 7.5$ m and $y = 1.15$ m (*i.e.* at the highest distance between the traversing device and the bottom). This final translation therefore enabled to define all the levels (see bottom level in the floodplain in Figure 3.10.b) referenced to an horizontal plan of reference whom elevation is smaller than the bottom one.

3.3.4 Measurement of mean velocity and turbulence

Depending on the measurement cross-section and on the vertical position in the water column, mean velocities were either measured using a Pitot tube or a micro-propeller.

The Acoustic Doppler Velocimeter (ADV) was first used to measure the Reynolds stresses in the flow, *i.e.* the turbulence. Moreover, it was also used to have redundant measurements of mean-velocities; it then enabled the correction of the micro-propeller and the Pitot tube measurements (§4.8).

3.3.4.1 Micro-propeller coupled to a vane

The micro-propeller (Nixon, Streamflo Velocity Meter 403) was used in most parts of the flume. The micro-propeller was coupled to a vane in order to get the flow direction in the same time as the velocity measurements.

Operating principle

The sensing probe is a measuring head joined by a slim tube to the plug and socket which is connected to the acquisition system. The measuring head comprises a five bladed PVC rotor mounted on a hard stainless steel spindle (Figure 3.11), itself terminating in fine burnished conical pivots which run in jewels mounted in a shrouded frame. Minimum frictional resistance is thus ensured.

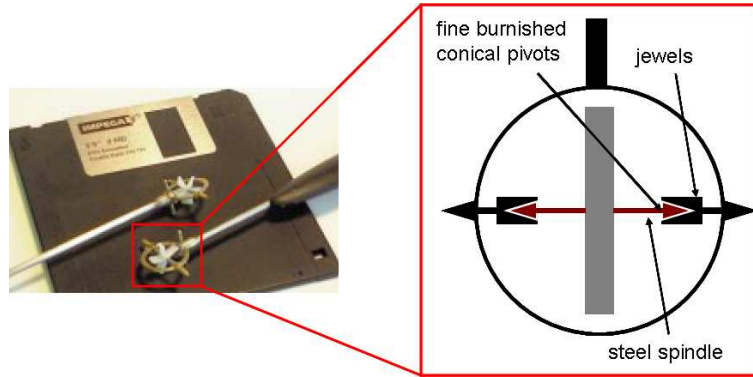


Figure 3.11 – Photograph of a ‘Nixon Flowmeters’ micro-propeller

An insulated gold wire contained within the tube terminates 0.1 mm from the rotor blade tips. When the rotor is revolved by the movement of a conductive liquid, the passage of the rotor blades past the gold wire tip slightly varies the measurable impedance between the tip and the tube. This variation is used to modulate a 15 kHz carrier signal, generated within the indicating instrument which in turn is applied to the electronic detector circuits. Following amplification and filtering out of the carrier frequency, a square wave signal is obtained. In the digital indicator the pulses are counted over a known time period to obtain a digital reading. Via the output slot of the digital reading, the signal is acquired by the general acquisition card (commanded by LabVIEW) at a rate of 50 Hz. Finally, the mean frequency and the standard deviation of the time-series are computed using LabVIEW and are written in file. Mean frequencies and standard deviations are converted into velocities using calibration curves, which linearly link the frequency to the velocity.

NB – The acquired frequency (velocity after calibration) is representative of the flow facing and passing through the probe. In order to get the horizontal components of the velocity in a Cartesian reference frame, the probe is coupled to a vane that orientates the micro-propeller in the main direction of the flow. Then using an angle-encoding device ($\delta\theta = \pm 0.5^\circ$) plugged on the stroke of the micro-propeller, angles of the vane are acquired at the same time as the velocity. The longitudinal and lateral velocities are finally deduced by projecting the micro-propeller velocity according to the measured angle.

Measurement characteristics

The micro-propeller is a robust measurement device. In optimal operating conditions (*i.e.*, well oriented in the flow and no systematic errors), measured time-averaged velocities are acquired with a relative accuracy of $\pm 1.5\%$. Notice that the mean and the standard deviation of the measured time-series (computed using LabVIEW) depend on the intensity of the turbulence and on the velocity magnitude in the sampling volume (Figure 3.12):

- Onto the floodplain the velocity magnitude and the turbulence intensity are low. Therefore the standard deviation of the velocity is low.

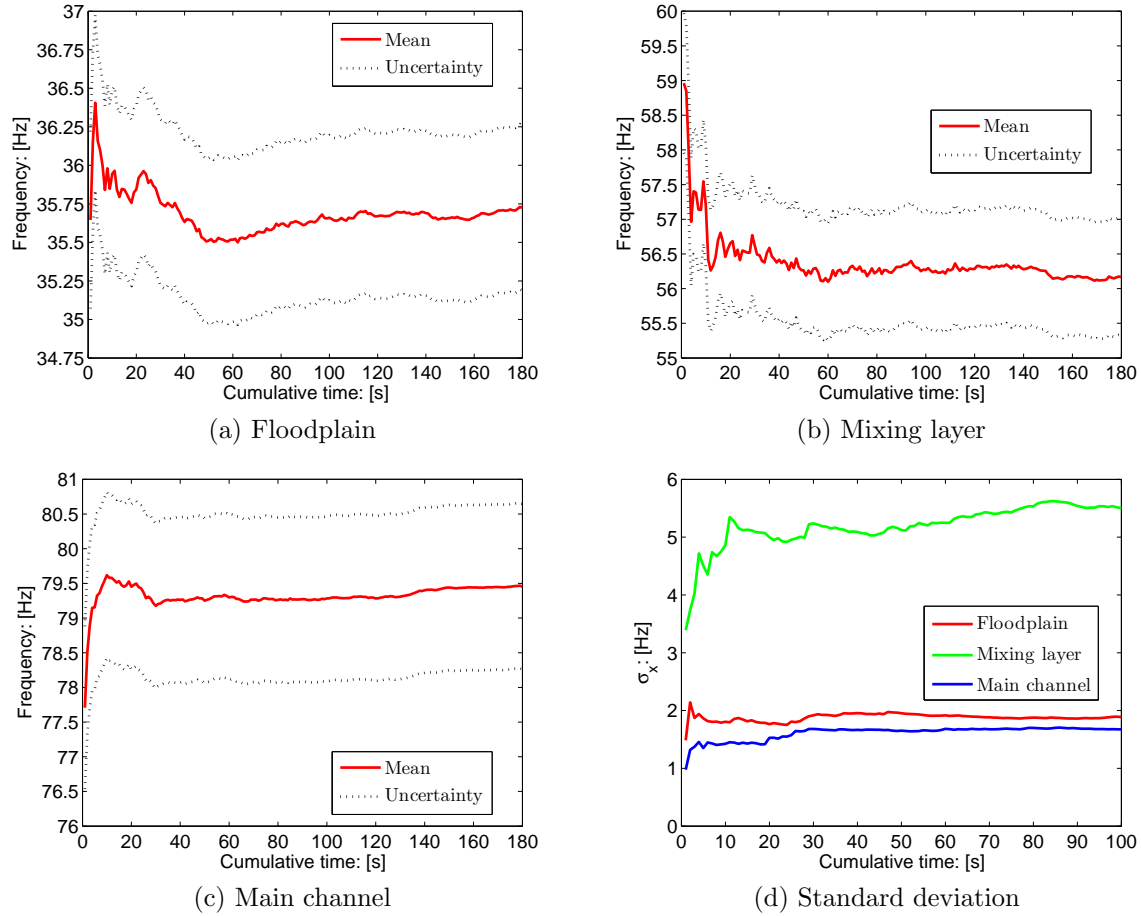


Figure 3.12 – (a-c) Cumulative mean of the micro-propeller measurements (in Hertz) depending on the position in a compound cross-section. (d) Cumulative standard deviation of the micro-propeller measurements (in Hertz).

- In the main channel, far from the mixing layer, velocity magnitudes and turbulent intensity are bigger than the floodplain one. Therefore the standard deviation is bigger than the floodplain one.
- In the mixing layer at the interface, although velocity are lower than in the main channel, the planform vortices developing at the interface make growing up the turbulence intensity. Therefore the micro-propeller signal has a great standard deviation. The mixing layer has the highest standard deviations. (see, Figure 3.12)

As previously said, once the micro-propeller time-averaged frequencies are acquired, the velocities are worked out using the calibration curves. Then thanks to the vane coupled to the micro-propeller, the velocities are projected according to the measured angles in order to get the longitudinal and the lateral velocities in the Cartesian reference frame:

$$\bar{u} = ||(\bar{u}, \bar{v})|| \cos \theta \quad \bar{v} = ||(\bar{u}, \bar{v})|| \sin \theta \quad (3.1)$$

An optimized recording-time has been chosen so that the cumulative mean and the standard deviation of the micro-propeller frequency converges towards a constant value. As shown in Figure 3.12, the cumulative mean and the standard deviation strongly depend on the position in the flume. Whether in the main channel or in the floodplain (Figures 3.12.a and 3.12.c), the cumulative mean begins a plateau from 60 s, while in the mixing layer (Figure 3.12.b), the plateau starts from 100 s. The cumulative standard deviation is constant from 30 s for the floodplain and the main channel and start from 80 s in the mixing layer (Figure 3.12.d). As a

consequence, the minimum acquisition time has been set equal to 60 s (*i.e.* 3000 samples with $F_s = 50$ Hz) in the main channel and in the floodplain and has been set equal to 100 s (5000 samples with $F_s = 50$ Hz) in the mixing layer zone.

3.3.4.2 Pitot tube

The Pitot tube (Kimo, L-type, diameter = 3 mm) was set parallel to the banks and faced therefore the x -wise direction. The Pitot tube was used in shallow configurations, where the measurements cannot be performed using the micro-propeller. Under reference conditions, for RF200L, the Pitot tube was used in the floodplain at every relative altitudes $z/H_{fp}^{ref} = [0.2 - 0.8]$; for RF300L, the Pitot tube was only used at $z/H_{fp}^{ref} = 0.2$. For the groyne-case flows, GC230L and GC250L, measurements with the Pitot tube were done at the same altitudes as the corresponding reference flow (RF200L).

NB – Using the vane mounted on the micro-propeller, angles $|\theta| \geq 10^\circ$ were identified in the flow and the corresponding Pitot-measurements were removed. Measurements where the flow has an angle greater than 10° with the tube are indeed erroneous; below ten degrees, the measured values contrariwise correspond to the streamwise component of the velocity.

Operating principle

The Pitot tube is connected to a differential pressure transducer (druck LP9381, 0-5 mBar \approx 0-10 V). The sampling frequency is 50 Hz as exposed in §3.3.1 and resulting signal is in volts.

The Pitot tube is calibrated using the micro-propeller measurements. Voltages at the output of the pressure transducer are measured in some locations where micro-propeller measurements exist. A calibration law is then deducted from the comparison between the streamwise velocity and the voltage. The calibration law is written as following:

$$\bar{u} = \sqrt{C_1 \cdot V_o + C_2} \quad (3.2)$$

where C_1 and C_2 are the calibration coefficients and V_o the voltage measured at the output of the pressure transducer.

Measurement characteristics

Without considering the calibration, *i.e.* the voltage is not converted in pressure, the uncertainty on the measurements is only due to the electronic in the differential pressure transducer and is equal to ± 0.1 % of the measured voltage.

As shown in Figure 3.13, the signal output of the pressure transducer (in Volt) is wavy whatever the location in the flume. However the peak to peak variations of the cumulative mean are irrelevant (≈ 0.01 V: same order of magnitude as the uncertainty on the voltage). The distribution of the standard deviation (Figure 3.13.d) is more consistent with what we observed for the micro-propeller (Figure 3.12.d). Whether in the main channel or in the floodplain, the standard deviation converges towards a constant from 50 s; in the mixing layer zone, the convergence is obtained after 90 s. As a consequence, it has been decided to choose the same durations as the micro-propeller: 60 s in the main channel and in the floodplain and 100 s in the mixing zone.

Notice that the membrane in the pressure transducer is quite sensitive to a change in pressure. When the Pitot tube is brought back from the floodplain wall towards the main channel wall,

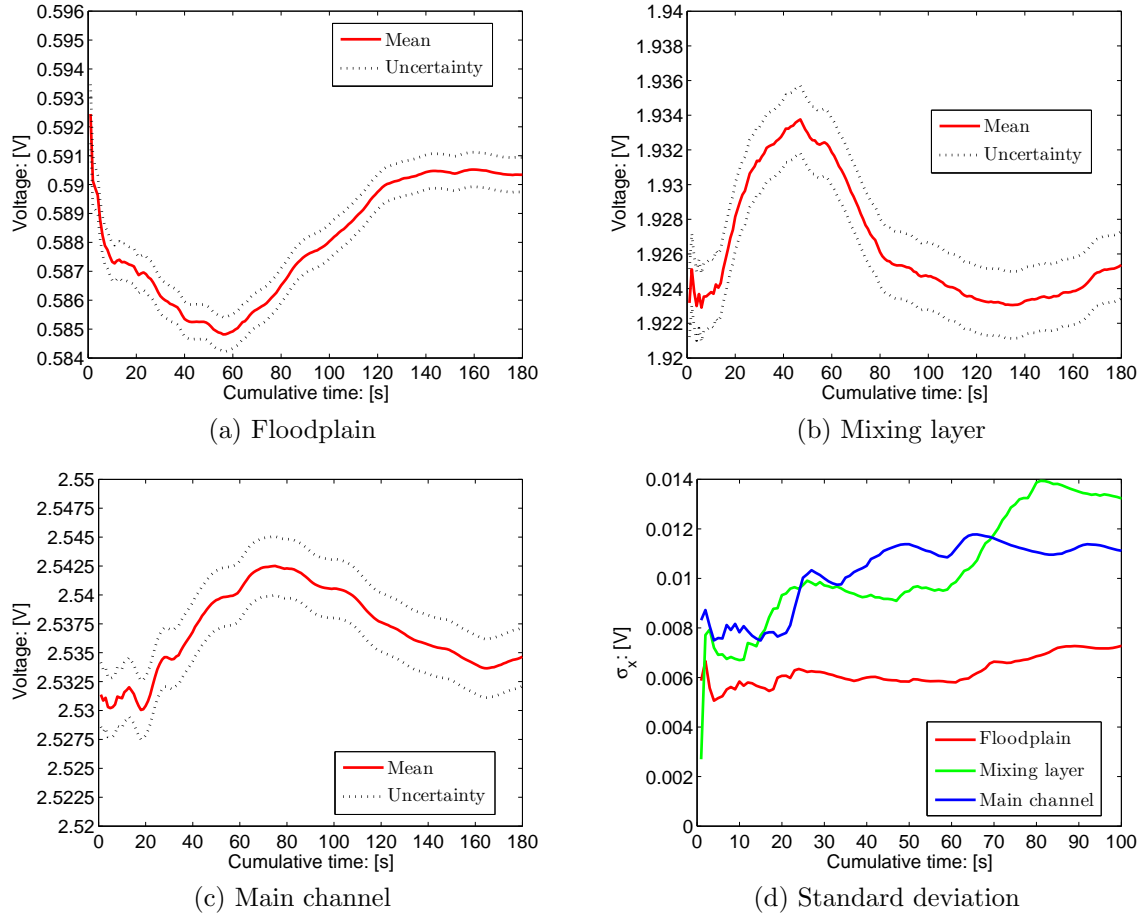


Figure 3.13 – (a-c) Cumulative mean of the Pitot tube measurements (in Volt) depending on the position in a compound cross-section. (d) Cumulative standard deviation of the Pitot tube measurements (in Volt).

or from the mixing layer zone from the floodplain wall, the membrane needs a certain time to reach an equilibrium. If a delay of 100 s between two measurements is not set in the LabVIEW program, the computed mean pressure will be biased.

3.3.4.3 Acoustic Doppler Velocimeter (ADV)

Operating principle

The Acoustic Doppler Velocimeter (Nortek, Vectrino⁺, $F_s = 1-200$ Hz) uses the Doppler effect to measure flow velocity by transmitting a short pulse of sound, listening to its echo and measuring the change in pitch or frequency of the echo (see Figure 3.14). In contrast to standard Doppler profilers and current-meters, the Vectrino is a bistatic sonar; it uses separate transmit and receive beams. It transmits through a central beam and receives through four beams displaced off to the side. The four receivers are all focused on the same volume to obtain the three velocity components from that volume. The beams intersect each other 50 mm from the transmitter (Figure 3.14). The measurement volume is defined by this intersection and by range gating in time. The short pulse, sent by the transmit transducer, covers 3-15 mm vertically (user adjustable), and the receivers listen to an echo that corresponds from this volume. The diameter of the volume is 6 mm.

As displayed in Figure 3.14, the probe is mounted on a fixed stem connected to the main housing through the probe end bell. The four receivers, each mounted inside a receiver arm, and

the transmitter in the centre of the stem are each covered with a hard epoxy and the probe is otherwise titanium made. Depending on the type of the measured flow, the probe can either be “down-looking” (Figure 3.14: Vectrino scheme), or “side-looking” (Figure 3.14: picture). In this PhD-thesis, the side looking ADV was used, as the encountered water depths were quite shallow. The side-looking ADV was mounted on the carriage of the automatic displacement and was moved through LabVIEW. The data acquisition was independent from LabVIEW and was made using the software delivered by the manufacturer. Thanks to the software, the velocity fluctuations can be measured at a maximal frequency of 200 Hz, which is useful for having a well described turbulent spectrum.

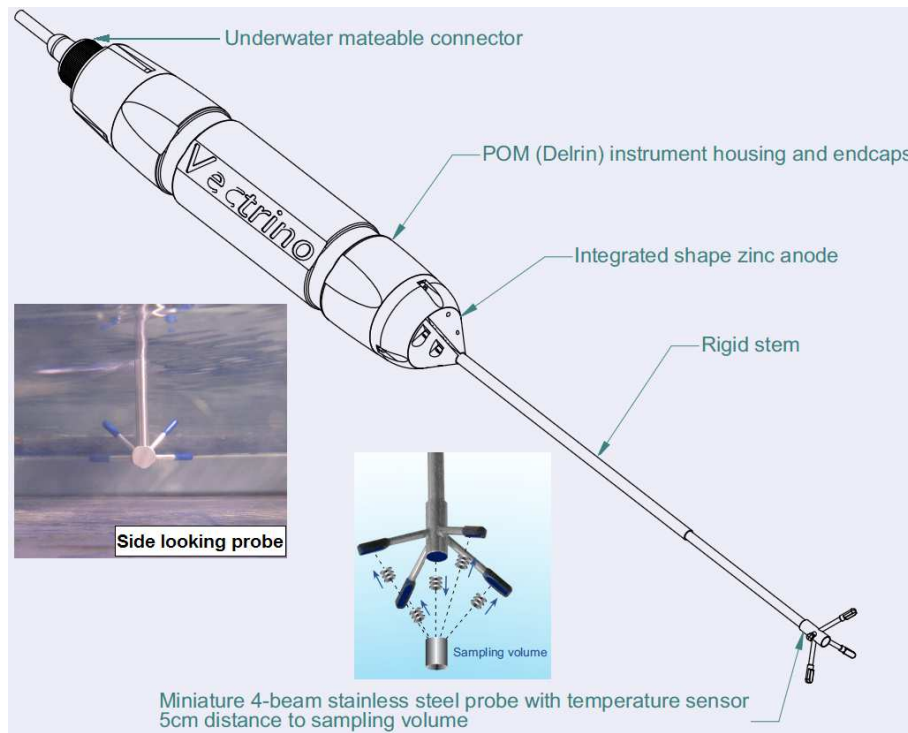


Figure 3.14 – ADV (down-looking) working principle scheme. The side-looking configuration is also displayed on the left-corner picture.

NB – For a question of transparency in the processing of the turbulence, all the turbulent statistics have been worked out with a home-made code based on the paper of [Czernuszenko and Holley \[2007\]](#). In order to avoid an over-estimation of the signal variance (*i.e.* turbulence) due to the large spikes that can be observed in some time-series, the turbulent raw data have been filtered using the algorithm proposed by [Goring and Nikora \[2002\]](#) (see the complete description in §4.5).

Measurement characteristics

As specified in [Nortek \[2004\]](#), the accuracy (ACC) on the measurements is equal to $\pm 0.5 \% \pm 1$ mm/s of the measured instantaneous value and the noise uncertainty is estimated at $\pm 1 \%$ of the velocity range at 25 Hz (in this PhD-thesis the velocity range was 1 m/s, *i.e.* uncertainty = 1 cm/s). Turbulence was measured using the same measurement mesh (Figure 3.6.b) as the micro-propeller for comparing both devices at the same altitudes and at the same spanwise positions.

The level of noise proposed by [Nortek \[2004\]](#) is quite high. [Hurther and Lemmin \[2001\]](#) and [Garcia et al. \[2005\]](#) propose some methods for reducing the effects of this noise. However, those methods are quite long to apply and, given the amount of data, they are almost impossible to

use for our experiments. As a consequence, the noise correction was generally not performed. Fortunately, in this thesis, we were mainly interested in the mean velocity and in the horizontal Reynolds shear stress. After [Strom and Papanicolaou \[2007\]](#) due to the geometry of the ADV probe and the Gaussian nature of the noise, the noise has a negligible effect on the mean velocities (\bar{u}, \bar{v}) , on the component of the Reynolds normal stress parallel to the transmitter τ_{yy} , and on the Reynolds shear stress τ_{xy} . Concerning τ_{xx} , this Reynolds stress is noised, but has low interests in our study; only the general distribution is really considered.

NB – A transmit/receive beam pair is sensitive to velocity in the direction of the angular bisector between the beams. Since the receive beams are slanted at 30° relative to the transmitter, all four receivers measure the velocity that is slanted about 15° from the transmit beam. This means that the Vectrino is more sensitive to the component parallel to the transmit beam than it is to the other directions. Consequently, the parallel component yields a lower measurement uncertainty [[Nortek, 2004](#)].

During experiments, we tried to optimize all the ADV settings in order to minimize the noise and maximize the quality of ADV measurements:

1. The sampling volume was chosen such as the signal-to-noise ratio (SNR) was greater than 20 dB. According to [[McLelland and Nicholas, 2000](#)] the noise has indeed weak influences on the measured signal from a signal-to-noise ratio of 20 dB (the SNR is an indicator of the signal noise and it has to be as great as possible in order to reduce the noise influence). It results that the length of the sampling volume was then set at 7.6 mm and its diameter remained unchanged (6 mm) (see specification device in [Nortek \[2004\]](#)).
2. In order to artificially increase the Doppler signal intensity in the sampling volume, spherical micro-particles of glass (Dantek, HGS 10-20 μm) were injected in the upstream tanks of the flume; they are used to increase the available surfaces in the sampling volume for reflecting the transmitter signal.
3. In order to have satisfactory turbulence measurements (*i.e.* being certain that the major turbulent structures passed in the sampling volume during measurement), sampling frequencies were set from 50 Hz to 100 Hz: $F_s = 100$ Hz for recording time < 10 min and $F_s = 50$ Hz for recording time > 10 min. According to the literature, the most used sampling frequency for ADV is 25 Hz and gives satisfactory results for turbulence measurements [[Bousmar, 2002](#); [Czernuszenko and Rowinski, 2008](#); [Lane et al., 1998](#)].
4. Finally, concerning the length of the recording, [Roy et al. \[2004\]](#) report that for most turbulent statistics, a sufficient recording time is within 60-90 s (see for the convergence of the mean velocity in Figure 3.15.a). In this thesis, we rather chose a recording length of 3 minutes. The purpose of these long records was to get a good convergence of the cross-power spectrum densities in the most productive zone of turbulence in the flume, *i.e.* at the interface between the main channel and the floodplain, as demonstrated in Figure 3.15.d.

NB – The HGS particles have a density of 1.1 and are inert tracers; they are transported by the flow and their settling velocity is equal to $2.1 \times 10^{-5} \text{ m/s}$ (computed using the Stokes formula for spherical particles [Stokes \[1851\]](#)). The multiplication of the settling velocity by the longest time of residence of a particle in the flume (time of residence $L/\min(U_d) = 8/0.1 = 80\text{s}$) leads to the maximum settling height of a particle, *i.e.* 1.6 mm. This height is quite significant, but according to [Rouse \[1938\]](#), the turbulence coming from the bottom keeps in suspension such a particle and counter-balances the fall of the particles. As a consequence, we can consider that such a tracer has no own movement.

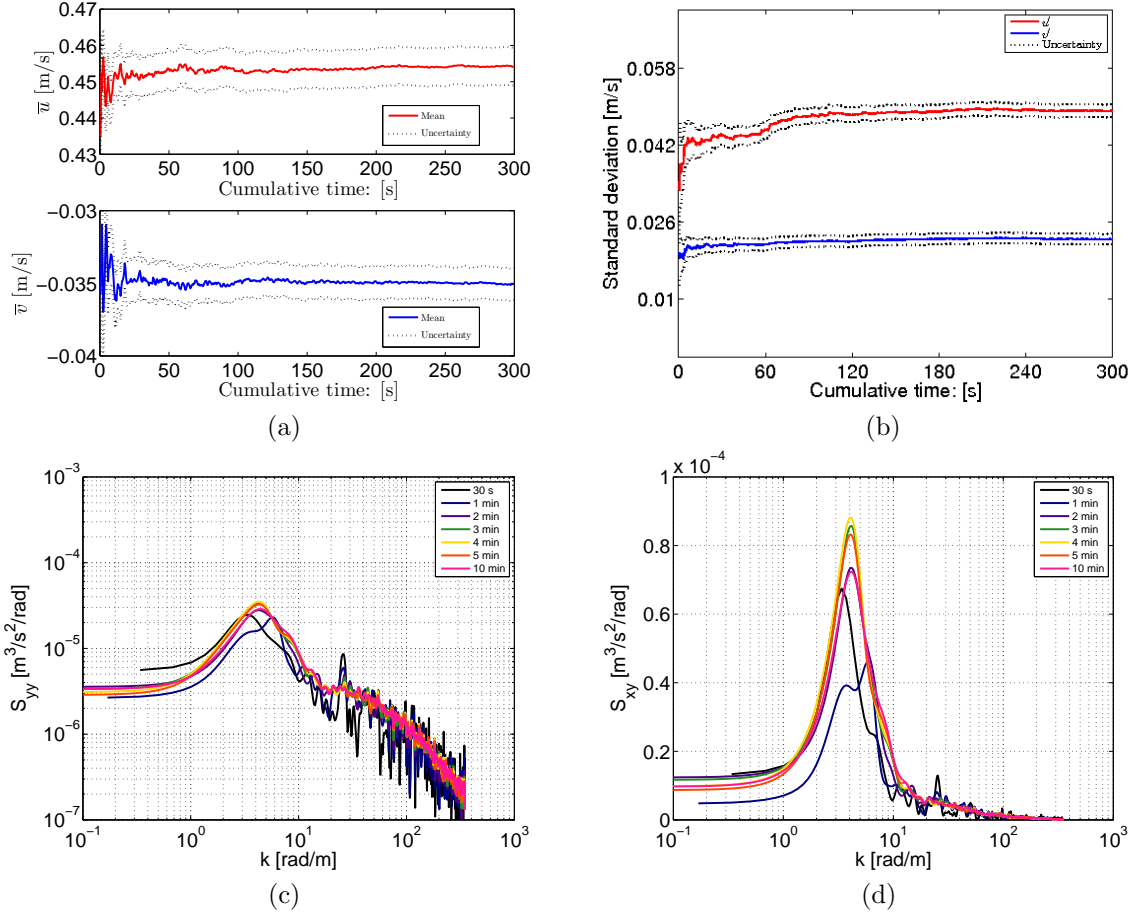


Figure 3.15 – Cumulative mean velocity, standard deviation, power and cross-power spectrum densities of ADV measurements at the interface between the main channel and the floodplain for GC350L ($x = 4.5$ m, $06 \times H_{fp}$, $Q_t = 24.7$ l/s and $d = 0.5$ cm).

The cumulative mean of the horizontal components of the velocity, the cumulative standard deviation, the power spectrum density of the lateral velocity component and the cross-power spectrum density of the horizontal fluctuations (calculated using the Fast Fourier Transform and the algorithm of the short modified periodograms [Welch, 1967]) were computed using a time-series of 1 hour ($F_s = 50$ Hz) measured in the mixing layer at the interface between channels at $x = 4.5$ m and $06 \times H_{fp}$ (Flow case: GC350L). As shown in Figures 3.15.a and 3.15.b, the cumulative mean of the horizontal components of the velocity, so as their standard deviations are converged from 60 s. The power spectrum of the lateral fluctuations are converged from 2 min (Figure 3.15.c). The cross-power spectrum needs more time to be converged; as shown in Figure 3.15.d, the cross-power spectrum starts to be converged from 3 min, hence the decision to use records of 3 min in the mixing layer and in the rest of the flume.

3.3.5 Preston tube

The boundary shear stresses were measured along the mesh defined in Figure 3.7.a and on the vertical boundaries (vertical floodplain and main channel walls, vertical bank-full wall between the floodplain and the main channel) using a Preston tube [Preston, 1954] and the modified calibration laws specified in Patel [1965].

NB – The boundary shear stress τ_b is a general appellation regrouping the bottom shear stresses measured on the horizontal bottom of the flume and the wall shear stresses measured on the vertical walls of the flume.

Operating principles

The Preston tube (Home-made, inner diameter = 2.72 mm), we used in this PhD-thesis, consists of two bent tubes welded together in a particular manner (Figure 3.16.a):

- The upper tube is opened perpendicularly to the flow: the pressure inside the tube is equal to the ambient pressure or static pressure. The orifice of the static pressure is set just above the total pressure orifice;
- The lower pipe is parallel to the flow and is opened on its end facing the flow. The pressure inside, is the total pressure, the sum of static pressure and dynamic pressure.

A Pitot tube could have been used instead of the Preston tube. The only interest of the Preston tube is that the static pressure orifice is placed just above the total pressure orifice. As a consequence it measures the pressures (static and total) in the same water column.

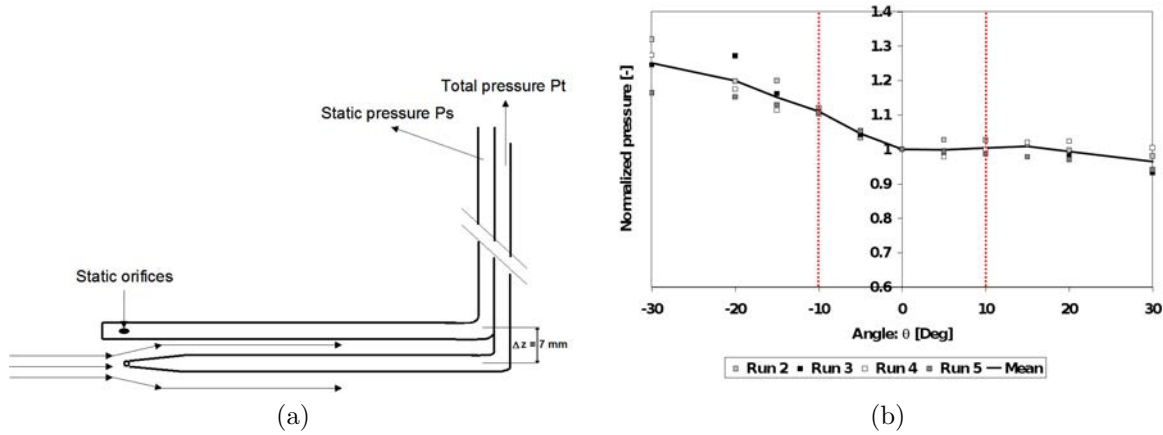


Figure 3.16 – (a) Working principle of the Preston tube. (b) Recalibration of the measured pressure depending on the angle of the flow relative to the Preston orientation.

The differential pressure transducer (druck LP9381, used with the Pitot tube as well) measures the pressure difference between the two tubes and using LabVIEW, the transducer output signal is acquired at a sampling frequency of 50 Hz. The calibration law of Patel [1965] needs a pressure difference for computing the boundary shear stress. By isolating the pressure transducer from the flow, a difference in water depth (*i.e.* in pressure: $\Delta P = \rho g \Delta h$) between the membrane has been injected ($\Delta h \in [0 \text{ cm } 5 \text{ cm}] \approx 0\text{-}5 \text{ mBar}$) and the resulting voltage has been measured (if the gain = 2, $0\text{-}5 \text{ mBar} \equiv 0\text{-}10 \text{ V}$); the gain of the transducer could have been thus estimated. The passage from the voltage to the pressure is a linear function and the gain has been found equal to 2.1:

$$V_o = 2.1 \times \Delta P \quad (3.3)$$

where V_o is the output voltage of the pressure transducer and ΔP is the measured differential pressure.

For each experiment, the Preston tube was always aligned with respect to the streamwise direction. In case of significant lateral velocities, a correction coefficient has been applied on the pressure measurements in order to take into account the fact that the Preston tube is no more aligned with the main flow direction. The correction coefficient has been worked out by measuring the pressure when the Preston tube is turned (following different positive and negative angles) in a uniform flow at various locations in the flume (in the main channel, in the floodplain and near the channels junction). The correction curve is displayed in Figure 3.16.b; it emphasizes that the correction is not symmetrical. For flows with positive angles (from the floodplain towards the main channel), the correction coefficient is almost equal to 1, while for

negative angles, the correction coefficient can reach 1.25 for $\theta = -30^\circ$. This asymmetry comes probably from an asymmetry in the Preston tube construction, notably in the localisations of the two static pressure orifices.

Once the pressure is corrected and the corresponding boundary shear stress is computed using the Patel laws [Patel, 1965], the boundary shear stress is projected in the x -wise or in the y -wise direction in order to get the desired shear component.

Measurement characteristics

In Preston [1954] and Patel [1965] the uncertainty on the Preston tube measurements is estimated to 6 % of the measured value. Like for the Pitot tube, measurements were done during 90 s in the mixing layer zone and during 60 s in the rest of the flume. In order to restabilize the pressure transducer membrane between each measurements, each measurements were doubled and only the second one was retained for the boundary shear stress calculation.

3.3.6 Large Scale Particle Imaging Velocimeter (LSPIV)

To measure the surface flow dynamics (velocity field) under reference conditions or with a groyne set on the floodplain a Large Scale Particle Imaging Velocimetry (LSPIV) was used. This technique was first initiated by Fujita [1994] for monitoring surface flow at a bridge abutment. It was also used in laboratory in order to get very dense surface velocity fields. It was for instance used for measuring recirculating flows in cavities of a groyne field [Weitbrecht et al., 2002, 2008] or for measuring recirculating flows in compound open-channels [Peltier et al., 2009].

The technique used in this thesis is based on the work of Hauet [2006], who improved the technique of Fujita [1994] for monitoring in “continuous” the discharge of a river in the USA. This technique is based on the classical PIV technique reviewed in Adrian [2005] and is now widely used for monitoring surface flows [Hauet et al., 2008; Jodeau et al., 2008].

Main differences between the classical PIV and the LSPIV lies (1) in the size of the studied object, and (2) in the seeding and video-camera used for the flow visualization. While the typical surface for the PIV is 100 cm², the LS-PIV can work with a surface greater than 100 m² [Hauet, 2006]. As a consequence, macro-structures in flows can be observed and large velocity field can be acquired. Moreover, the LSPIV uses macroscopic seeding floating on the free surface (cheap material), while the PIV rather used microscopic seeding in the bulk and requires a laser in order to visualize and localize them. The LSPIV technique is then quite cheap and can be used under most of the flow conditions that we can find on the field or in a laboratory. However these measurements are limited to the free surface.

Operating principles

The video camera (Panasonic, HD-SD9) is a High Definition video camera with 3 CCD sensors (one per primary colour: Red, Green, Blue). The format of sequences is HD Blue-ray (codec: H264), the frame-rate of the video-camera is 25 frames per second and image resolution is 1920 × 1080 which enables to have a good precision on the details even for very large view field. The video-camera was chosen progressive, avoiding the artificial movements generated with interlaced video-camera [Hauet, 2006].

The HD-SD9 was mounted on a tripod which was positioned either on the side of the flume (lateral shooting: recirculating zone) or 3 m above the flume on a wall located 2 m behind the upstream tanks (Figure 3.17). The positioning of the camera was optimized in order to avoid at maximum any lateral parallax in the recorded images. Several Ground Reference Points (GRPs)

were located in the flume at the same elevation (altitude of the floodplain step) to allow further geometrical correction of the pictures. Notice that our GRPs were set at the floodplain bottom level, because we considered that the changes in water depth in our experiments can be neglected in front of the elevation of the video-camera, therefore allowing us to assimilate the level of the free surface to the one of the floodplain bottom.

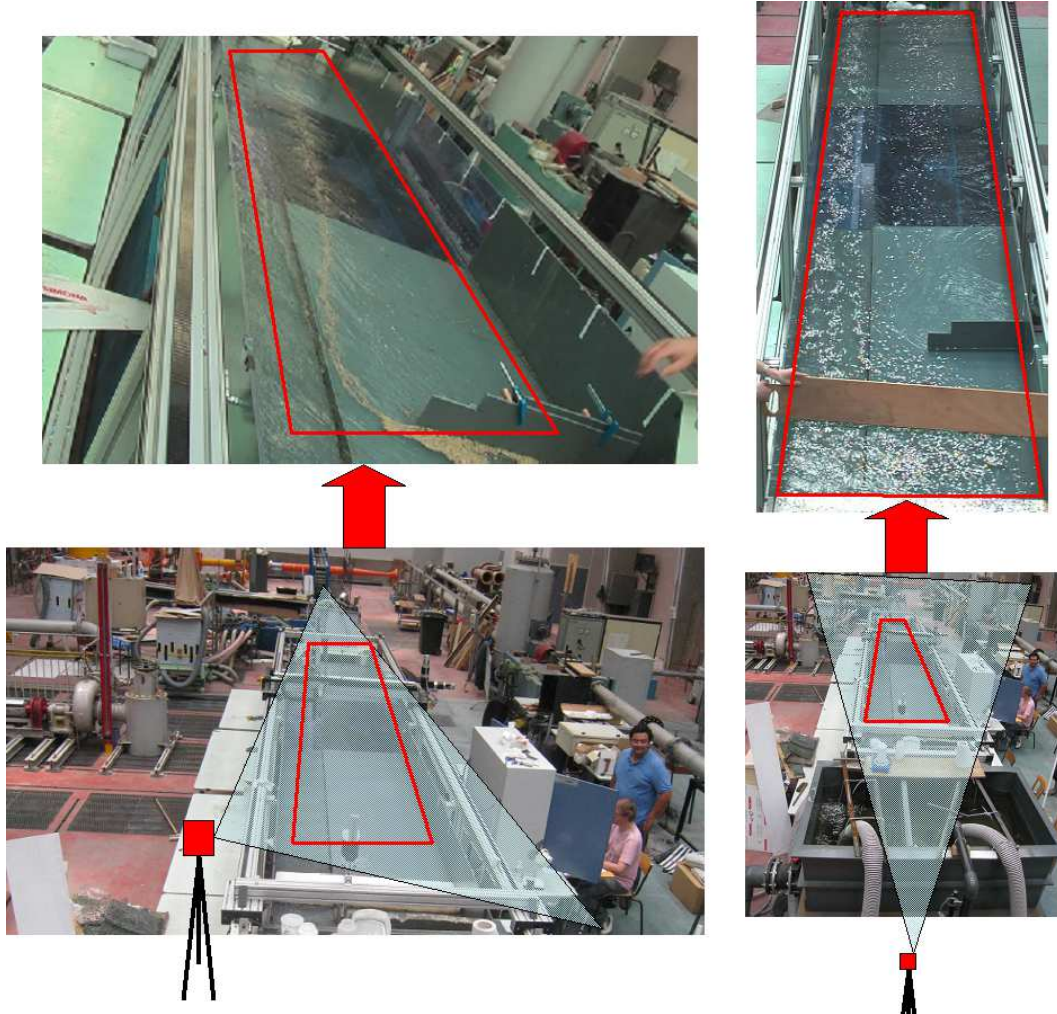


Figure 3.17 – Position of the video-camera for LSPIV measurements.

Once the flow and the video-camera were set up, the flow was seeded either with confetti (5 mm of diameter) or with grass seeds (1-2 mm of length). Seeds were injected on the surface using a wood plate that was shaken above the free surface at 1.5 m downstream of the inlet. For each flow-case (Table 3.3), at least three video-sequences were measured. Thanks to a free software (The KMplayer) that deals with HD-formats, the video sequences were cut in sequences of images; ≈ 400 -1000 images by sequence. The time between two images was optimized in order to reduce the computation-time of the velocity calculations with the software written by [Hauet \[2006\]](#). We found that working at every two images ($\Delta t = 0.08$ s) is a good compromise for avoiding too much sub-pixel displacements and for limiting the size of the interrogation areas and research areas used in the calculation of the velocity.

Thanks to the GRPs located at the floodplain step level (junctions between the PVC plates, or screws), the sequence of images were then orthorectified. The orthorectification is generally a geometrical correction that considers the water surface as a plan of constant elevation, which leads to an 8-parameters plan-to-plan perspective projection that can be solved using at least four GRPs located at the free-surface elevation [[Hauet, 2006](#)]. As shown in Figure 3.18, at the end of the geometrical transformation, each pixel on the image is referenced in a Cartesian ref-

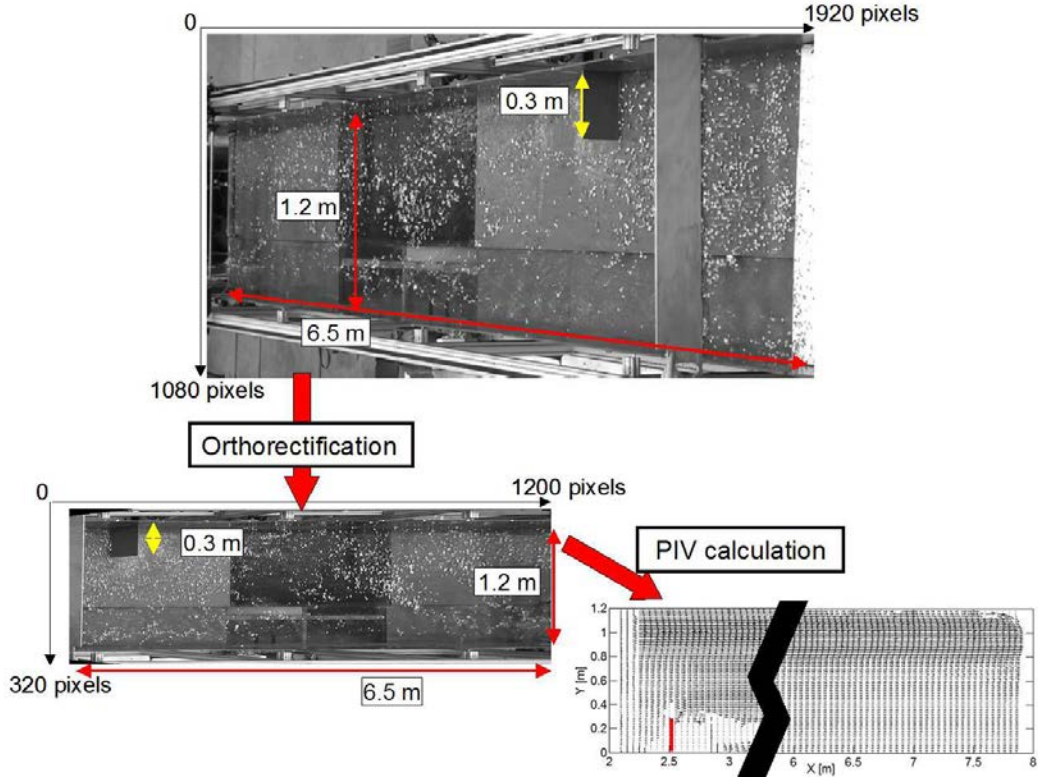


Figure 3.18 – Example of image orthorectification.

erence frame and all the geometrical characteristics that have been distorted by the geometrical perspective are recovered.

A classical cross-correlation algorithm was used to determine the displacement of the flow tracers. In this study, we use a PIV algorithm for large-scale applications with low-resolution images, described by [Hauet \[2006\]](#). It calculates the correlation between the interrogation area (*IA*) centred on a point a_{ij} in the first image (image *A*) and the *IA* centred at point b_{ij} in the second image (image *B*) recorded with a time interval of Δt seconds. The correlation coefficient $COR(a_{ij}, b_{ij})$ is a similarity index for the grey-scale intensity of a group of pixels contained in the two compared *IAs*, expressed as:

$$COR(a_{ij}, b_{ij}) = \frac{\sum_{\substack{1 \leq i \leq M_i \\ 1 \leq j \leq M_j}} (A_{ij} - \bar{A}_{ij})(B_{ij} - \bar{B}_{ij})}{\sqrt{\sum_{\substack{1 \leq i \leq M_i \\ 1 \leq j \leq M_j}} (A_{ij} - \bar{A}_{ij})^2 \sum_{\substack{1 \leq i \leq M_i \\ 1 \leq j \leq M_j}} (B_{ij} - \bar{B}_{ij})^2}} \quad (3.4)$$

where M_i and M_j are the sizes of the interrogation areas (in pixels), and A_{ij} and B_{ij} are the distributions of the grey level intensities in the two interrogation areas (*IAs*). Correlation coefficients are only computed for points b_{ij} within some search area (*SA*). The PIV approach assumes that the most probable displacement of the fluid from point a_{ij} during period Δt is the one corresponding to the maximum correlation coefficient. Sub-pixel displacement accuracy are reached using a parabolic fit. Velocity vectors are finally derived from these displacements by dividing them by Δt . The process is iteratively conducted for the whole image and for the whole sequence of images. The interrogation area was set as covering a physical surface where at least five particles can be observed and the pattern that they form is easily identifiable in the following image. The choice of the search area is detailed in §4.3.

Measurement characteristics

Precision of measurements depends on the physics of the measured flow and therefore on the operating conditions. The best way to get the uncertainty on the measurements is to compare the measured data with an attempted result such as the the total discharge in a cross-section.

It is obvious that to have the best measurement of the mean surface velocity and a good estimation of the standard deviation, a very long video-sequence is needed. In our experiments, the recording time was limited by the seeding. After 2 min, the downstream tank where the water is filtered before coming back in the laboratory tank, was clogged by the seeds and may overflow in the hydraulic hall. As a consequence, the video sequences are rarely greater than 2 min.

3.4 Experimental data-set

As written in the introduction of this chapter, this thesis aims at investigating the impacts on an overbank flow of a groyne set onto the floodplain. More precisely, we want to understand what are the impacts on the flow physics of the strong mass exchange that is induced by the groyne. To achieve this, we need to establish a set of data that covers a wide range of flow conditions with sufficiently strong mass exchange (stronger than in the literature).

In the following section, the method for establishing the data-set is first exposed (resolution of the II-Theorem). Then, the characteristics of the data set are given and discussed.

3.4.1 Method for constructing the data-set

The II-Theorem was used for determining the relationship between the intensity of the mass exchange (L_x/B_{fp}) and the geometrical and mean physical parameters of the experiments.

Variables of the problem

All the geometrical parameters for describing the problem are given in Figure 3.1. The discharge in the floodplain and in the main channel, the water depth, so as the acceleration of the gravity and the viscosity of the water must also be added. Some of these variables are not independent and can be expressed with other. For instance, the water depth in the main channel can be deducted from the sum of the water depth in the floodplain with the bank-full height and the water depth in the floodplain can be deducted from the relationships of the uniform flow regime.

Given the geometry of the flume and the various relationships between the mean physical parameters of the experiments, twelve variables were therefore identified for solving the II-Theorem. They are summarised in Table 3.2.

Number of dimensions in the problem

The parameters can be described using three dimensions: (1) Time, (2) Length and (3) Mass. In the sequel of the resolution, the time is represented by B_{fp}^3/Q_{fp} , the length by B_{fp} and the mass by ρB_{fp}^3 and the II-parameters are calculated using these three variables.

Parameters	Description of the parameters
Q_{fp}	Discharge in the floodplain
L_x	Streamwise length of the downstream recirculation zone
x_g	Position of the groyne relative to the inflows
d	Length of the groyne
ϵ	Roughness
B	Width of the flume
B_{fp}	Width of the floodplain
h_{bf}	Bank-full height
$S_{o,x}$	Streamwise slope of the flume
ρ	Water density
μ	Dynamic viscosity of water
g	Gravitational acceleration

Table 3.2 – Listing of the consistent parameters used for solving the Π -Theorem.**Resulting Π -parameters**

Given the number of parameters, the links between these parameters and the number of dimensions of the problem, **nine Π -parameters** can be established (Equation 3.5).

$$\begin{aligned}
L_x &\Rightarrow \frac{L_x}{B_{fp}} \rightarrow \Pi_1 = \frac{L_x}{B_{fp}} \times \frac{B_{fp}}{d} = \frac{L_x}{d} \\
x_g &\Rightarrow \Pi_2 = \frac{x_g}{B_{fp}} \\
d &\Rightarrow \Pi_3 = \frac{d}{B_{fp}} \\
\epsilon &\Rightarrow \frac{\epsilon}{B_{fp}} = \frac{\epsilon}{h_{fp}^*} \times \frac{h_{fp}^*}{B_{fp}} \rightarrow \Pi_4 = \frac{\epsilon}{h_{fp}^*} \\
B &\Rightarrow \Pi_5 = \frac{B}{B_{fp}} \\
h_{bf} &\Rightarrow \Pi_6 = \frac{h_{bf}}{B_{fp}} \\
S_{o,x} &\Rightarrow \Pi_7 = S_{o,x} \\
\mu &\Rightarrow \frac{\rho Q_{fp}}{\mu B_{fp}} \rightarrow \frac{\rho Q_{fp}}{\mu B_{fp}} = \frac{\rho Q_{fp}}{\mu B_{fp}} \times \frac{(B_{fp} - d) h_{fp}^*}{(B_{fp} - d) h_{fp}^*} \Rightarrow \Pi_8 = \frac{\rho 4 U_{fp}^* h_{fp}^*}{\mu} = Re_{fp}^* \\
g &\Rightarrow \frac{Q_{fp}}{g^{1/2} B_{fp}^{5/2}} \rightarrow \left(\frac{Q_{fp}}{g^{1/2} B_{fp}^{5/2}} \right)^{2/3} = \left(\frac{Q_{fp}}{g^{1/2} (B_{fp} - d)} \right)^{2/3} \times \left(1 - \frac{d}{B_{fp}} \right)^{5/3} \Rightarrow \Pi_9 = \frac{h_{fp}^*}{d}
\end{aligned} \tag{3.5}$$

with

$$h_{fp}^* = \frac{Q_{fp}^{2/3}}{g^{1/3} (B_{fp} - d)^{2/3}} \tag{3.6}$$

the critical depth for $Fr = 1$ calculated with the width $B_{fp} - d$ and

$$U_{fp}^* = \frac{Q_{fp}}{(B_{fp} - d) h_{fp}^*} \tag{3.7}$$

the critical velocity for $Fr = 1$ calculated with the width $B_{fp} - d$.

Intensity of mass exchange

Given the previous results, the intensity of the mass exchange is a function of eight non-dimensional parameters Π_i (see Equation 3.8).

$$\frac{L_x}{d} = f\left(\frac{B}{B_{fp}}, S_{o,x}, \frac{x_g}{B_{fp}}, \frac{h_{bf}}{B_{fp}}, \frac{d}{B_{fp}}, \frac{h_{fp}^*}{d}, Re_{fp}^*, \frac{\epsilon}{h_{fp}^*}\right) \quad (3.8)$$

If we then consider that the Darcy-Weisbach coefficient $\lambda^* = \lambda \left(Re_{fp}^*, \epsilon/h_{fp}^* \right)$ takes into account the influences of Re_{fp}^* and ϵ/h_{fp}^* and the friction number $S = \lambda^* d / 8 h_{fp}^*$ accounts for λ^* and h_{fp}^*/d , Equation 3.8 also writes

$$\frac{L_x}{d} = f\left(\frac{B}{B_{fp}}, S_{o,x}, \frac{x_g}{B_{fp}}, \frac{h_{bf}}{B_{fp}}, \frac{d}{B_{fp}}, S\right) \quad (3.9)$$

Choice of the parameters to make vary

As presented in §.3.2, the geometrical parameters $(B, B_{fp}, S_{o,x}, h_{bf})$ are imposed by construction. Concerning the position of the groyne x_g , it is fixed by the shortness of the flume; x_g was set at $x = 2.5$ m in order (1) to let a slight distance between the inflows and the groyne and (2) to prevent the downstream recirculation zone to spread in the outflows. The groyne length d , the critical depth h_{fp}^* and the Darcy-Weisbach coefficient λ are then the only adjustable parameters that enable to have various intensities of mass exchange. Moreover, the critical depth so as the Darcy-Weisbach coefficient depend on the discharge in the floodplain Q_{fp} . As a consequence, we decide to make vary d and Q_{fp} (then Q_t) in the experiments.

3.4.2 Resulting data-set

Nine flow-cases were then investigated: three flows with various total discharges and no groyne (reference flows) and six with various total discharges and various groyne lengths. Whether for reference-cases or for groyne-cases, the same upstream discharges distributions and the same tailgate settings as the reference flows were used for the groyne-cases. The tailgates were set up such as each reference flow was as close as possible to a uniform flow.

Name	Q_t [l/s]	Q_{fp}/Q_t [%]	d/B_{fp} [-]	S [-]	Re_{fp} [-]	Re_{mc} [-]	H_r [-]
RF200L	17.3	13.9	0	0	1.18×10^4	1.46×10^5	0.18 - 0.23
RF300L	24.7	25.5	0	0	3.16×10^4	1.80×10^5	0.32 - 0.35
RF400L	36.2	38.7	0	0	7.17×10^4	2.29×10^5	0.41 - 0.43
GC230L	17.3	13.9	0.38	2.8	1.47×10^4	1.51×10^5	0.14 - 0.23
GC250L	17.3	13.9	0.63	4.8	1.70×10^4	1.63×10^5	0.12 - 0.3
GC330L	24.7	25.5	0.38	1.7	3.27×10^4	1.77×10^5	0.23 - 0.38
GC350L	24.7	25.5	0.63	3.4	3.77×10^4	1.90×10^5	0.21 - 0.45
GC420L	36.2	38.7	0.25	0.7	7.20×10^4	2.38×10^5	0.31 - 0.5
GC430L	36.2	38.7	0.38	1.2	7.25×10^4	2.49×10^5	0.29 - 0.54

Table 3.3 – Main characteristics of the experimental data-set of experiments at the LMFA: reference flows (RF), groyne-case flows (GC).

The flow conditions are summarized in Table 3.3. The first column indicates the names of the flow-cases. “RF” corresponds to Reference Flow, “GC” to Groyne-Case and “L” to LMFA. The first number refers to the first decimal of the mean relative depth measured under reference flow conditions and the two last numbers correspond to the size of the groyne in centimetres. The second column corresponds to the injected total discharge. The third column corresponds to the

discharge distribution at the inlets. These distributions were measured by [Proust \[2005\]](#) under uniform flow conditions in the same channel as in the present experiments. The fourth column indicates the normalised size of the groyne that is set onto the floodplain. The fifth column gives the value of the friction number calculated in the groyne cross-section. The value of S are well different and this should guarantee that we are scanning a wide range of flow conditions. The sixth and the seventh columns give an idea of what is the mean Reynolds number in the floodplain and in the main channel: friction regime is smooth. The last column indicates how the relative flow depth H_r evolves in the flume between $x = 1.5$ m and $x = 7.5$ m.

4

Data post-processing

4.1 Introduction

In this chapter, we describe the way we evaluated uncertainties, the way we corrected measurements and the way we reduced measurement biases and systematic errors.

The method used for calculating the uncertainty on the various measured data are first exposed. Secondly, criteria for estimating the geometry of recirculation zones using surface velocities and the LSPIV technique are then discussed. Integration schemes for depth-averaging the velocity and calculating discharges are then presented. In the sequel we justify why ADV measurements must be despiked and rotated. Characteristics of the spectral analysis we performed on the corrected turbulence is also given. Finally correction of the micro-propeller data using ADV measurements is presented.

4.2 Uncertainty computation

Uncertainties are useful for quantifying the trueness of measurements. The general theory is first presented, then uncertainties are computed for each device and for the derived quantities (Froude number, ...)

4.2.1 Errors

Definition: When a physical quantity x is measured, the error on measurements is the difference between the measured quantity x and a true value X . X is unknown [Bally and Berroir, 2008]. Two types of errors are generally distinguished.

4.2.1.1 Random error or statistical errors

Definition: A random error is due to discrepancy or uncontrolled variation between an observed (measured) value x and a true value X predicted by a specification, a standard, or a model. If the number of realizations is sufficiently large (a great number of measurements), random errors tend to cancel each other out, and their sum/average goes to zero; the time-series of such measurement are characterized by a probability distribution centred around the true value (supposed unknown).

For instance, in a developed turbulent free shear flow, the punctual measurement of velocity during time has Gaussian probability distribution. The Gaussian is centred on the most probable true value of the velocity and the average of the standard deviation goes to zero [Chassaing, 2000a; Pope, 2000].

4.2.1.2 Systematic error or experimental error

Definition: A systematic error is an error that affects all items comprising a group (such as a production batch) in a similar manner and to a similar magnitude. Systemic errors are caused by a flaw in the system (such as in the calibration of a measuring device), occur in the same direction and, therefore, do not cancel each other out.

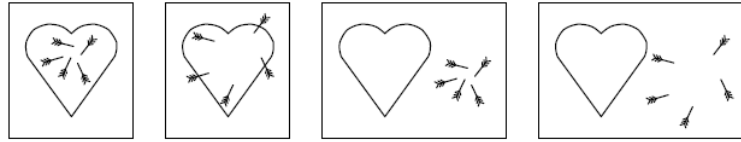


Figure 4.1 – Respective roles of random and systematic errors. [Bally and Berroir, 2008]

Respective roles of random and systematic errors are classically compared with a shoot in a target (Figure 4.1) where the centre represents the true value of the measured quantity:

- if the whole arrows are grouped in the centre of the target, random and systematic errors are weak,
- if arrows are grouped together and are far from the centre, random errors are weak and systematic error are large,
- if arrows are in the target and far from the centre, random errors are large and systematic errors are weak
- If arrows are dispersed and outside of the target, random and systematic errors are large.

NB – This analogy has a major default: the centre of the target is generally unknown!! An another example can be used; if a distance is measured using a flexible ruler, the bending of the ruler introduces some systematic errors and the variability of the bending is a source of random errors.

As previously said, the correction of the systematic errors can be complicated. If the outcome is known (total discharge for instance), the best solution in order to avoid such an error, is to use redundant measurements of a same physical value with two different devices; the best device can be used to correct the bad one. In absence of known outcome, nothing can be done.

4.2.2 Uncertainty estimations

According to [NF ENV 13005 \[1999\]](#), the uncertainty δx is a parameter associated to the result of a measurement, that characterises the dispersion of the values which could be reasonably attributed to the quantity to be measured.

The parameter can be a standard deviation, or the half-length of confidence interval.

The uncertainty has several components. Some can be estimated through the calculation of experimental standard deviations of measurement series. Other components, that are also characterised by standard deviations, are estimated by admitting probability distributions based on observations or coming from other information.

Finally, it is assumed (1) that the result of the measurement is the best estimation of the quantity to be measured, (2) that all the uncertainty components, either coming from systematic errors or random errors, contribute to the dispersion.

4.2.2.1 Statistic estimation of δx

The calculation of the uncertainty δx needs first a characterisation of the probability distribution of the measured quantity x . This quantity is characterised by estimating as well as possible the average value and the standard deviation of the measurement series. Without systematic errors, the estimation of the average value is the best estimation of the true value X while the uncertainty δx , defines an interval in which the true value X is given with a known probability. Let be X the true value, the measured value x of the true value X is written as following (Equation 4.1):

$$x = \bar{x} \pm \delta x \quad (4.1)$$

\bar{x} is the best estimation (without systematic error) of the true value X and δx is the absolute uncertainty on measurements. Without systematic errors, the true value of x is probably within or near the interval $[\bar{x} - \delta x \ \bar{x} + \delta x]$

NB – The relative uncertainty is defined as $\delta x / |\bar{x}|$.

4.2.3 Estimation of random uncertainties

Measurements are generally performed using electronic devices which measure time-series; statistics computations are consequently needed to extract the best estimation of the true value of the measured quantity.

The best estimation (without biases) of the mathematical expectation \bar{x} of the true value X is:

$$\bar{x} = \frac{1}{N} \sum_i^N x_i \quad (4.2)$$

and the best estimation of the standard deviation σ of the true value X is written:

$$\sigma_x = \sqrt{\frac{1}{N-1} \sum_i^N (x_i - \bar{x})^2} \quad (4.3)$$

It is now legitimate to evaluate the accuracy of these estimations, particularly on the mathematical expectation. By repeating several times the measurement of N values of x whom the mean is then calculated, the probability distribution of x is obtained. The mean of this distribution is X and its standard deviation $\sigma_{\bar{x}}$ is equal to:

$$\delta \bar{x} = \sigma_{\bar{x}} = \frac{\sigma}{\sqrt{N}} \approx \frac{\sigma_x}{\sqrt{N}} \quad (4.4)$$

$\sigma_{\bar{x}}$ is called the standard deviation of the mathematical expectation and represents the uncertainty on the determination of the true value X by the mean of N measurements. Generally σ is not known; σ is therefore estimated using σ_x the standard deviation of the true value X .

Finally, using N measurement of x , it finally writes:

$$x = \bar{x} \pm \frac{\sigma_x}{\sqrt{N}} = \bar{x} \pm \delta \bar{x} \quad (4.5)$$

where $\delta \bar{x}$ represents the standard deviation on the mathematical expectation of the true value X .

NB – The uncertainty on the mathematical expectation should be rigorously written using a “Student” coefficient taking into account the number of samples in the measurements: $\lambda_S \frac{\sigma}{\sqrt{N}}$, where λ_S represents the Student coefficient value corresponding to a given quantile and a given sample number. In this thesis, we consider that $\lambda_S = 1$ [Bally and Berroir, 2008], since most of the measurements are done with a great number of samples.

Equation 4.5 means that when the number of samples rises, the uncertainty on the measurements decreases and the estimation of the mean becomes better.

4.2.4 Propagation of uncertainties

The measured quantities might be not directly used and are rather combined to give the required physical parameter (For example, the micro-propeller frequency and the angle encoding device enable the computation of the streamwise and the spanwise velocity). In such a situation, the uncertainty on the new parameter is evaluated using a propagation formula. (Equation 4.6)

Let be q a function ($q = f(x, y)$), assuming the fact that the errors are independent, the uncertainty δq is written as following [Bally and Berroir, 2008]:

$$\delta q = \sqrt{\left| \frac{\partial f}{\partial x} \right|^2 (\delta x)^2 + \left| \frac{\partial f}{\partial y} \right|^2 (\delta y)^2} \quad (4.6)$$

4.2.5 Consideration of the systematic errors in the uncertainty calculation

The reasoning in the previous subsections only considers that uncertainties are due to random errors. The intrinsic errors (systematic errors) of the devices such as the bias on the calibration law. As a consequence, in a practical way, assuming that all the errors are independent, the measurement uncertainty is written in a quadratic formulation and has the following formulation:

$$\delta x = \sqrt{SC^2 + \frac{RM^2 + \sigma_x^2}{N}} \quad (4.7)$$

where SC represents the uncertainty due to systematic errors, σ_x is the standard deviation of the time-series (estimation of the uncertainty on the mathematical expectation) and RM represents the uncertainty of the other sources of random errors.

4.2.6 Device uncertainty

Uncertainties due to systematic errors and random errors are resumed in Table 4.1.

	<i>ACC</i>	<i>RY</i>	N_o	N
Ultrasonic probe	± 0.3 mm	± 0.5 mm	\times	> 1000
Pressure transducer	± 0.1 % of V_o	\times	\times	> 3000
Micro-propeller	± 1.5 % of $ (\bar{u}, \bar{v}) $	\times	\times	> 3000
Angle θ encoder	$\pm 0.5^\circ$	\times	\times	> 3000
ADV	± 0.5 % of (u,v,w) ± 1 mm/s	\times	± 1 cm/s	> 18000
LSPIV	No direct estimations			> 200
Preston tube	± 6 % of τ_b	\times	\times	> 3000

Table 4.1 – Resume of the different sources of devices uncertainties; *ACC*: accuracy, *RY*: reproducibility, N_o : ADV noise and N : number of samples.

The accuracy ACC represents the minimum standard deviation that can be measured with an infinite number of samples. The accuracy is a systematic error and depends on each device.

The reproducibility RY represents the standard deviation of the error included in a single measurement, relative to a reference measurement. The reproducibility of a device includes errors that are systematic with respect to that device, but random with respect to a particular test.

The noise N_o represents an additional variance that the particular setup of the ADV introduces in the measurements. This parameter is therefore a systematic error at a given velocity range (see ADV subsection); if several ranges are used for the same measurement, the Doppler noise becomes a random error.

Using the Table 4.1 and Equations 4.7 and 4.6, device uncertainties are then worked out and are summarised in Table 4.2.

Devices	Parameters	Uncertainty
Ultrasonic measurements	z or Z_i	± 0.42 mm
	h or H_i	± 0.42 mm
Micro-propeller	\bar{u}	$\pm \sqrt{(\cos \theta)^2 (\delta (\bar{u}, \bar{v}))^2 + ((\bar{u}, \bar{v}) \sin \theta)^2 (\delta \theta)^2}$
	\bar{v}	$\pm \sqrt{(\sin \theta)^2 (\delta (\bar{u}, \bar{v}))^2 + ((\bar{u}, \bar{v}) \cos \theta)^2 (\delta \theta)^2}$
Pitot Tube	\bar{u}	$\pm C_1 \delta V_o / 2 \sqrt{C_1 \cdot V_o + C_2}$
ADV	(\bar{u}, \bar{v})	$\pm 0.5\%(\bar{u}, \bar{v}) \pm 1$ mm/s
	Turbulence	see §3.3.4.3
Preston Tube	τ_b	± 6 % of τ_b

Table 4.2 – Resume of the different devices uncertainties.

Details of the computation of uncertainties in Table 4.2 are given in Appendix C. Calculation of uncertainties for derived-quantities such as the Froude number or the dispersion on the vertical of the horizontal components of the velocity X_{ij} (see definition in Equation 2.18).

4.3 Large Scale Image Particles velocimetry

4.3.1 Validity of measurements

The method has been described in the Chapter 3 and can be found in many papers as well [Fujita, 1994; Fujita et al., 1998; Hauet, 2006; Hauet et al., 2007, 2008]. The main interest of this method is that it quickly provides the whole surface velocity field of a flow using a really dense computation mesh. However, if the operating and the computing conditions are not well set, a lot of time can be wasted and computed results can be really bad.

The interrogation area (IA) was chosen such as at least 5 particles can be followed inside the box (a minimum to get enough contrast between the particles and the background). During our experiments, the video-camera was always set at the same position, *i.e.* for one experimental campaign, IA only depends on the image resolution. Given the image resolution we got ($R_{img,i} \approx 5$ mm/pixel), IA was chosen equal to 20 pixels.

Concerning the research area (IB), it was minimized in order to optimize the computation-time. Given a node of a computation mesh, the minimum lengths for IBe , IBw , IBs and IBn of the research area (see Figure 4.2) was computed as a function of the image resolution, of the maximum surface velocity in the considered direction (worked out using a first LSPIV run in

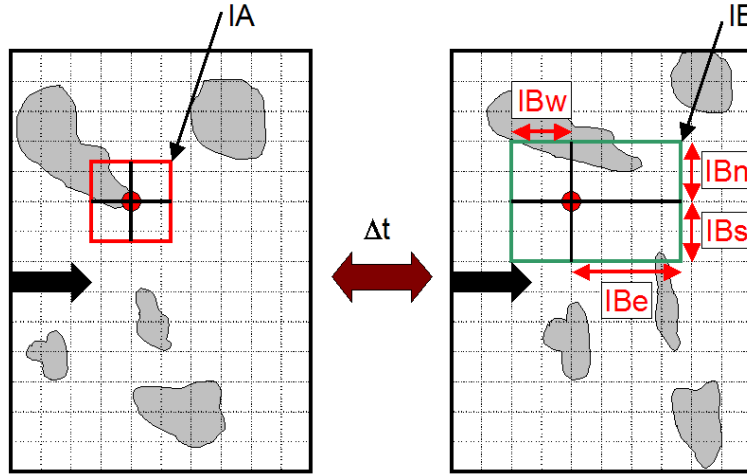


Figure 4.2 – Definition of interrogation and research area size for LSPIV optimization.

some points, or using velocity measuring devices) and of the time lag between two images:

$$MIN(IB_i) = MAX(\text{displacement between two images in the } i \text{ direction}) = \frac{U_s \Delta t}{R_{img,i}} \quad (4.8)$$

where $i = (e, w, n, s)$ (see Figure 4.2) and $R_{img,i}$ is the resolution of the image computed after orthorectification.

4.3.2 Extraction of the geometry of recirculation zones

In this PhD-thesis, the recirculation zones developing in the lee of an obstacle are measured using the surface velocities (U_s, V_s). It is assumed that the recirculation zones are mainly two-dimensional and their geometries can be therefore described with a good accuracy using the surface velocities measured by LSPIV technique.

In this subsection, we propose a method for quickly extracting the geometry of a recirculation zone developing in the lee of an obstacle, this in absence of enough punctual measurements of velocity and turbulence. This method is based on the determination of the separation streamline between the main flow and the recirculating flow in the lee of the obstacle.

4.3.2.1 Spanwise lengths of recirculation zone

According to *Fuchs et al.*, the separation line is the line connecting the separation point at the edge of the groyne and the reattachment point on the floodplain wall. As obstacles are thin in our experiments, the separation point is easily located, *i.e.* at the tip of the groyne. The reattachment point and the separation line are more difficult to be localized.

Through Matlab, the streamlines are calculated using the LSPIV measurements. Some examples are plotted in Figure 4.3 (streamlines are plotted in blue). The recirculating zone is easily recognizable; it is characterized by some spinning streamlines or by an absence of streamlines. The main flow is also easily recognizable; the streamlines have all the same direction (upstream from downstream) and never interact with the walls. The separation line is located between these two types of streamlines. Most of the time, the separation line is not plotted by Matlab. As a consequence we define the separation line as the streamline passing between the last streamline coming from the groyne that turns back near the floodplain and the first streamline coming from

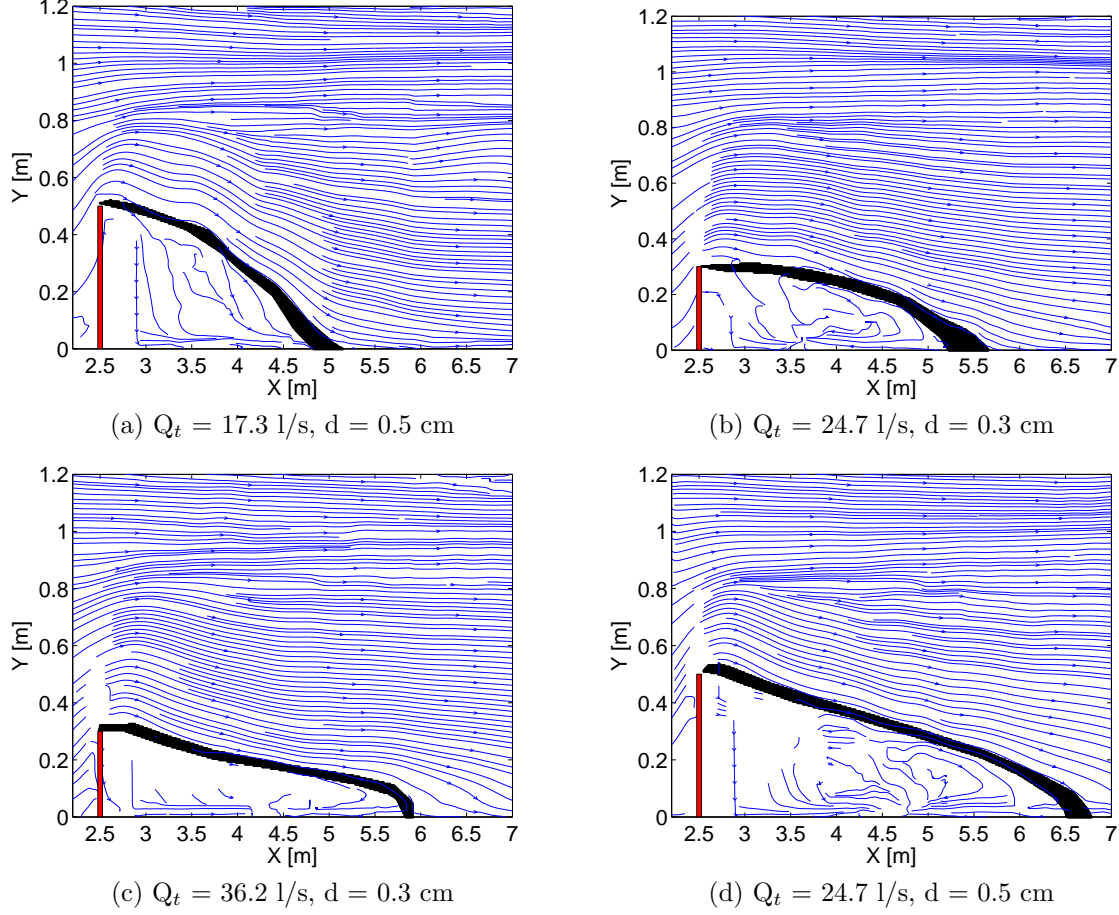


Figure 4.3 – Streamline fields of three groyne-case flows. The black line represents the zone where the separation line should be located. **Uncertainty on the spanwise direction:** ± 1.5 cm. **Uncertainty on the reattachment point location:** $\pm 10 - 15$ cm.

the groyne that does not stop on the floodplain wall. The separation line is determined with an uncertainty of ± 1.5 cm on the spanwise direction and $\pm 10-15$ cm in the streamwise direction.

Notice that the boundary of the upstream recirculation zone is the straight line connecting the separation point (upstream of the groyne) and the stagnation point at the edge of the groyne; the separation point, upstream of the groyne on the main channel wall, is approximately located at a distance equivalent to the groyne length d [Ettema and Muste, 2004; Koken and Constantinescu, 2008].

4.3.2.2 Reattachment points: streamwise length

The reattachment point and therefore the streamwise length L_x of the recirculation is determined using the separation line previously defined. Let be x_r , the reattachment point of the recirculation, (x_0, y_0) the coordinates of the separation streamline and x_g the x-wise location of the groyne. The length L_x is defined as following [Armaly et al., 1983]:

$$\begin{aligned}
 x = x_0(y_0) : \lim_{T \rightarrow \infty} \frac{1}{T} \int_0^T u_s(x_0(y_0), y_0, t) dt &= 0 \\
 \lim_{y_0 \rightarrow 0} x_0(y_0) &= x_r \\
 L_x &= x_r - x_g
 \end{aligned} \tag{4.9}$$

During experiments, the seeding of the free surface was problematic and disabled very long-time measurements; the LSPIV calculations were performed with limited video-sequences (at least 1'30" and maximum 3'). Consequently a bias exists on the recirculation geometry determination. This bias is due to the vortex shedding along the separation line which generates some unsteady movements near the reattachment point; because of the limited recording-time, the reattachment point is rather a "reattachment line". This "line" is a function of the resolution of the computational mesh, the time between two images and the local velocity around the reattachment point. Consequently, L_x has to be written $L_x = \bar{L}_x \pm \delta L_x$.

Using the previous formula (Equation 4.9), the different L_x are resumed in the Table 4.3.

CASE	GC230L	GC250	GC330L	GC350L	GC420	GC430L
\bar{L}_x	1.8 m	2.5 m	2.94 m	4.15 m	3.05 m	3.75 m
δL_x	0.1 m	0.1 m	0.15 m	0.15 m	0.15 m	0.15 m

Table 4.3 – Longitudinal length of the recirculation zones for the six groyne-case flows.

The increase in the uncertainty magnitude for flows at $Q_t = 24.7$ l/s and 36.2 l/s is due to an increase of the parasite movements of the stagnation point. The vortex shedding is more intense for the longer recirculation zones [Rivière et al., 2004] (see in Figure 4.4).

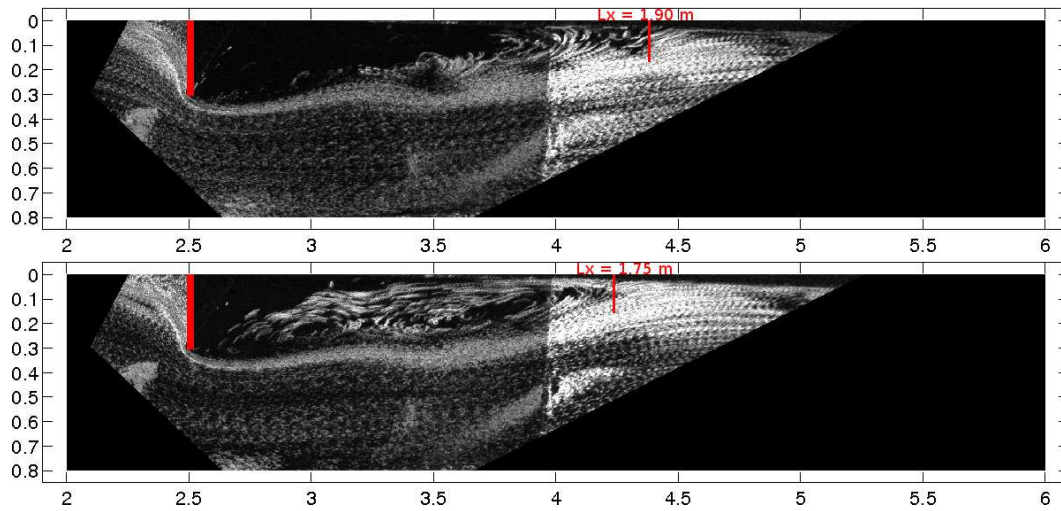


Figure 4.4 – Trajectography of the random motion of the stagnation point for $Q_t = 17.3$ l/s and $d = 0.3$ m. The Trajectographs are calculated with an average of 10 images taken every 0.2 s. Interval between both trajectographs: $\Delta t = 24$ s.

The Figure 4.4 highlights the variability in the position of the stagnation point of groyne-case flow GC230L. Two trajectographs delayed by 24 s, are calculated over ten images. They emphasize a variation of about 15 cm in only 24 s.

4.4 Integration schemes

As introduced in §3.3.1, velocity and turbulence for reference flows were measured at four relative altitudes in the main channel and in the floodplain ($0.2 \times H_i^{ref}$, $0.4 \times H_i^{ref}$, $0.6 \times H_i^{ref}$ and $0.8 \times H_i^{ref}$). For the groyne-case flows, measurements were performed following the same mesh and the same absolute altitudes as the reference flows; nevertheless depending on the local flow depth, some altitudes were removed or added (see Figure 3.7.b: groyne-case flow). It results that six points at maximum were measured on a vertical.

Given the number of measurements on a vertical, the trapezoidal integration scheme was chosen for depth-averaging data. By sake of consistency in the data processing, we decided to as well use a trapezoidal scheme for integrating data in the spanwise direction.

4.4.1 Vertical integration: depth averaging

The depth-averaging of velocity, or turbulent stress is then done using a “trapezoidal scheme” and the following hypotheses:

- The value at the bottom is equal to the value measured at $0.2 \times H_i^{ref}$. The bottom state is smooth and the log-layer in the boundary layer is thin. As a consequence error on the velocity / Reynolds stress distribution between the bottom and $0.2 \times H_i^{ref}$ is weaker than the one when considering the value at the bottom equal to zeros. Such an approximation appears as rather crude. However, due to the few points available on the vertical, a theoretical velocity profile can not be fitted more accurately to the data to be integrated.
- The value at the free surface is equal to the measurement at the highest position in the water column.
- In non-uniform flow conditions, the velocity and the Reynolds stress were measured using the same absolute altitudes as under reference flow conditions (see explanations in §3.3.1). Depending on the local depth, some altitudes may be then added or cancelled (see Figure 3.7.b). In some cross-sections for non-uniform flows, the last accessible measurement may be the one at $0.4 \times H_i^{ref}$ (depth lower than the reference one) or the one at $1.2 \times H_i^{ref}$ (depth higher than the reference one).

The trapezoidal scheme is written as follows (Equation 4.10 and Figure 4.5):

$$\begin{aligned}
 U_d &= \frac{1}{h} \left[0.3 H_k^{ref} u_1 + \sum_{m=2}^{n-1} 0.2 H_k^{ref} u_m + \left(h - \left(0.3 + \sum_{m=2}^{n-1} 0.2 \right) H_k^{ref} \right) u_n \right] \\
 T_{ij} &= \frac{1}{h} \left[0.3 H_k^{ref} \tau_{ij,1} + \sum_{m=2}^{n-1} 0.2 H_k^{ref} \tau_{ij,m} + \left(h - \left(0.3 + \sum_{m=2}^{n-1} 0.2 \right) H_k^{ref} \right) \tau_{ij,n} \right]
 \end{aligned} \tag{4.10}$$

where $k = mc$ or fp .

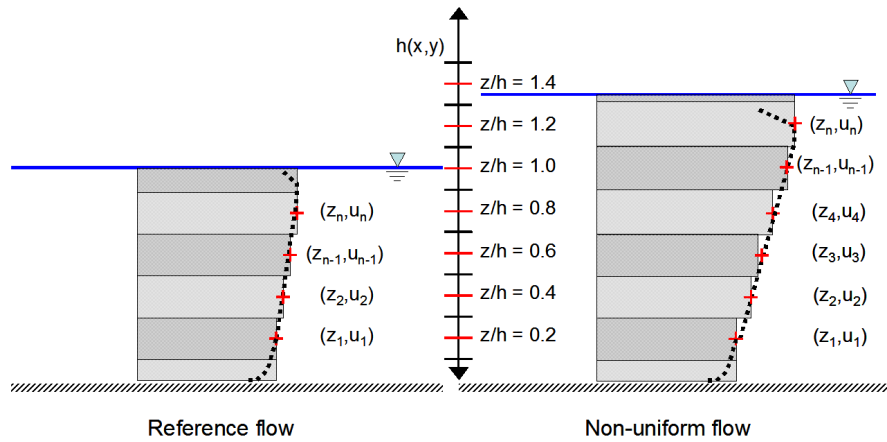


Figure 4.5 – Scheme of the trapezoidal method used for the integration of the depth-averaged velocity.

4.4.2 Lateral integration: discharge computation

The spanwise integration also uses a trapezoidal scheme (Figure 4.6) using the following hypothesis:

- The value at the floodplain bank is equal to the value at y_1 .
- The value at the main channel is equal to the value at y_n .
- At $y = y_i$ (the interface), $dy = (y_i - y_{i-1})/2$.
- At the first point in the main channel-side ($y = y_{i+1}$), $dy = (y_{i+1} - y_i) + (y_{i+2} - y_{i+1})/2$.

The total discharge or the lateral mean depth are then computed using the following formula (Equation 4.11 and Figure 4.6):

$$\begin{aligned}
 Q = & U_d(y_1)h(y_1)\frac{y_2 + y_1}{2} + \sum_{m=2}^{i-1} U_d(y_m)h(y_m)\frac{y_{m+1} - y_{m-1}}{2} \\
 & + U_d(y_i)h(y_i)\frac{y_i - y_{i-1}}{2} + U_d(y_{i+1})h(y_{i+1})\left(\frac{y_{i+2} - y_{i+1}}{2} + y_{i+1} - y_i\right) \\
 & + \sum_{m=i+2}^{n-1} U_d(y_m)h(y_m)\frac{y_{m+1} - y_{m-1}}{2} + U_d(y_n)h(y_n)\left(\frac{y_n - y_{n-1}}{2} + B - y_n\right)
 \end{aligned} \tag{4.11}$$

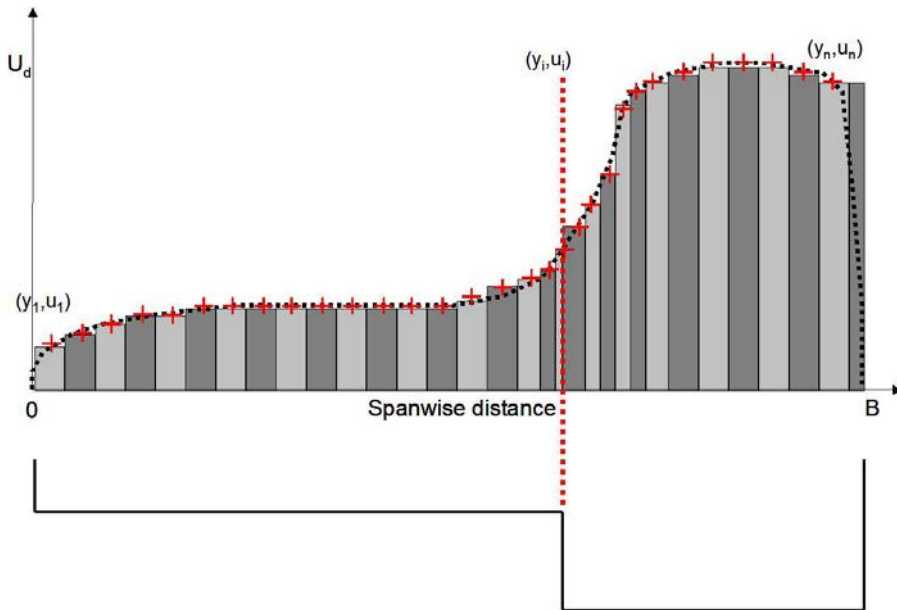


Figure 4.6 – Scheme of the trapezoidal method used for the integration of total discharge.

NB – For groyne-case flows, the discharges are computed without taking into account any measurement in the recirculation zone. Only the flow in the main flow is considered since under steady flow conditions, the mass trapped in the recirculation zone does not participate to the flow. The main flow is the zone between the main channel wall and the separation line defined in the floodplain.

4.5 Despiking the ADV data

Acoustic Doppler velocimeter or ADV is a good choice for measuring velocities and turbulence, where other measurement techniques such as the PIV or LDA are impractical. However the ADV has two disadvantages. The first one is the Doppler noise that appears at high frequency and creates an additional variance that artificially increases the turbulent intensity [Nikora and Goring, 1998; Voulgaris and Trowbridge, 1998]. The second one is due to spikes caused by aliasing of the Doppler signal; the phase-shift between the outgoing and incoming pulse lies outside the range between -180° and $+180^\circ$ and there is ambiguity, causing a spike in the records [Goring and Nikora, 2002]. These spiked signals occur when the velocity is bigger than the measurement range or when there is contamination from previous pulses reflected by a solid boundary.

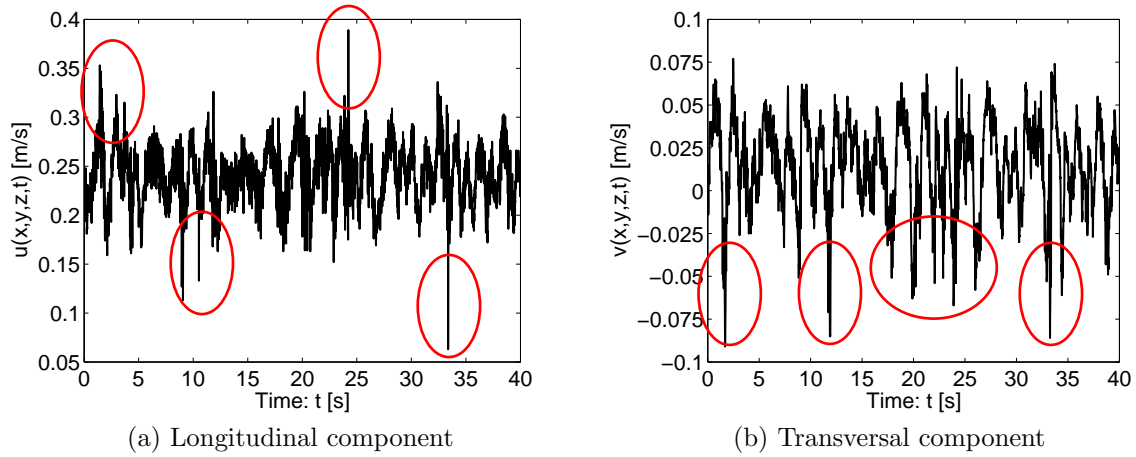


Figure 4.7 – Spiked ADV data: impact of spikes on the variance of the signal.

In Figure 4.7, the red ellipsoids tag some spikes in the time series of the longitudinal and the transversal velocities measured at the point $(2, 0.65, 0.4 \times H_{fp})$ in the flow GC330L. The magnitude of these spikes is twice larger than the average magnitude of the signal; these peaks are not natural and artificially increase the variance of the signal because of their high magnitudes. These peaks have to be removed.

4.5.1 The Phase-Space Thresholding Method

The spikes are removed using a **correction** of the method developed by Goring and Nikora [2002]. This method is called “Phase-Space Thresholding Method” and is used by most of the ADV users.

This method uses the concept of a three-dimensional phase-space plot in which the variable and its derivatives are plotted against each other. The generated scatter plot is enclosed by an ellipsoid defined by the Universal criterion and the points outside the ellipsoid are designated as spikes. The Universal criterion arises from a theoretical result from normal probability distribution theory which says that for N independent, identically distributed, standard, normal, random variables x_i , the expected absolute maximum is $E(|x_i|_{max}) = \sqrt{2 \ln N} = \lambda_U$, λ_U is the universal threshold. For a normal, random variable whose standard deviation is estimated by σ^* and the mean is zero, the expected absolute maximum is $\lambda_U \sigma^* = \sqrt{2 \ln N} \sigma^*$. This last term is the one used in the Phase-Space Thresholding Method. Notice that the expected absolute maximums of the variable and its derivatives define the minor and the major axis of the ellipsoid. Each time a spike is removed, the absolute maximums change. Consequently, the size of the ellipsoid also changes. The method iterates until the number of good data becomes constant (or, equivalently, the number of new points identified as spikes falls to zero). More precisely, in

these experiments, the iteration stops, when between two iterations, the standard deviation of each parameter is equal to the value computed at the previous iteration.

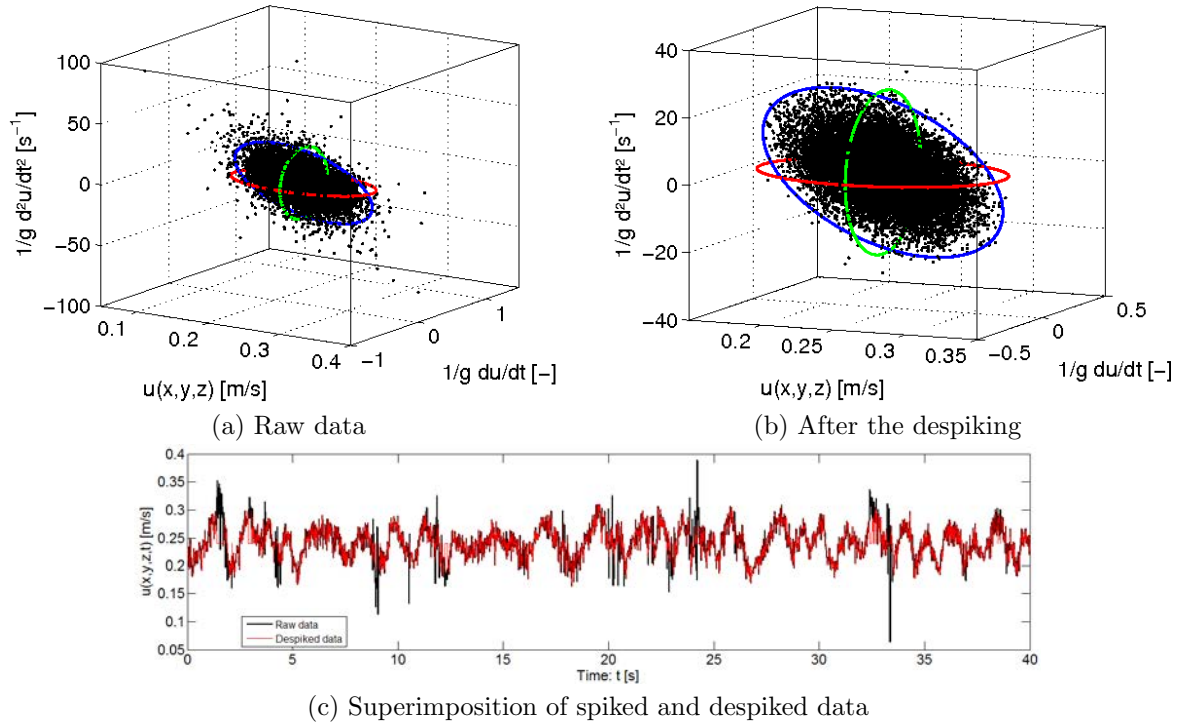


Figure 4.8 – Application of the Phase-Space Thresholding Method: effects on the spikes. The ellipsoids represents the expected maxima of standard deviation for a normal distribution of data.

The Figure 4.8 emphasizes that most of the peaks seen on the raw data are removed by the despiking method. The new time series of the longitudinal velocity is more regular and smooth: high frequency peaks are all gone.

NB – When a bad data is identified, the latter is not simply removed from the time series. Since the data are used to compute Fourier transforms, the time series cannot be filled with holes. [Goring and Nikora \[2002\]](#) propose different methods to replace the removed data and indicate that no replacement method is better than an other. Thus by sake of simplicity, we have chosen to replace the removed data by the mean of the contiguous neighbour data of the spike. If more than 10 % of the time series is spiked, the series is simply invalidated.

4.5.2 Differences with the method developed by Goring and Nikora (2002)

In page 120 in [Goring and Nikora \[2002\]](#), in order to compute the angle θ between the data and their second derivatives, the authors propose that

$$\theta = \tan^{-1} \left(\frac{\sum x_i \cdot d^2 x_i}{\sum x_i^2} \right). \quad (4.12)$$

This assertion is actually wrong. When the second derivative is one order smaller (or more) than the variable, it is impossible to compute the right angle; the angle becomes very small and it is impossible to follow the real slope of the cloud (Figure 4.9.a). In the method used in these

experiments, Equation 4.12 is then replaced by Equation 4.13:

$$\theta = \tan^{-1} \left(\frac{\sum (x_i - \bar{x})(d^2 x_i - \overline{d^2 x})}{\sum (x_i - \bar{x})^2} \right). \quad (4.13)$$

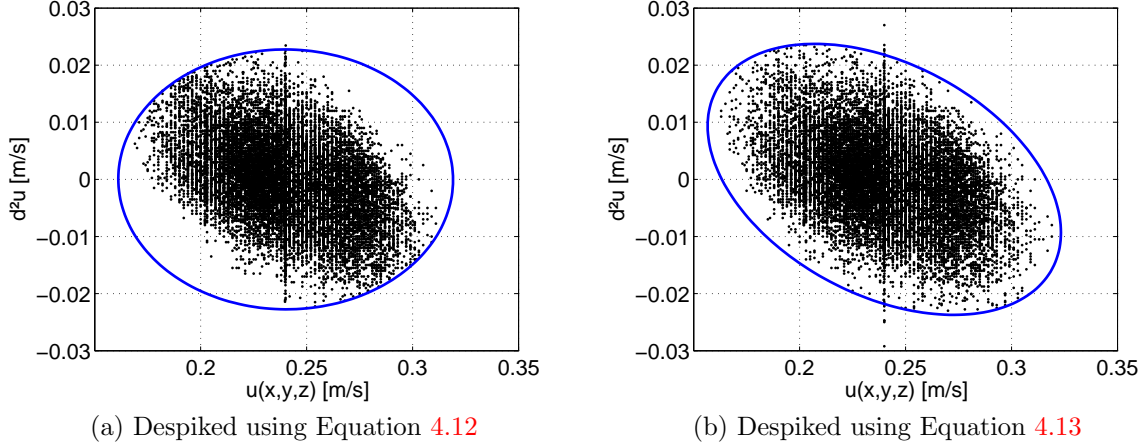


Figure 4.9 – Correction of the method developed by *Goring and Nikora* [2002], impact on the quality of the despiking.

As shown in Figure 4.9.b, the new proposed equation (Equation 4.13) allows the computation of the real slope of the data cloud. The corrected despiking method is less restrictive than the original method. In the original method, since the computed ellipse does not follow the tendency of the cloud, some good data are removed in the left and right corner of the ellipse. The standard deviation is then reduced and more “peaks” can be identified. However, this reduction is not always physical and some removed peaks may be a part of a physical phenomenon. With the correction, the angle of the ellipse matches with the cloud one; all the good data are within the ellipse. The standard deviation of the cloud is therefore higher than the one computed in the original method (Table 4.4), and the probability that the removed peaks are just measurement artifacts and not physical peaks is better.

	$std(u)$	$std(du)$	$std(d^2u)$
Original method [m/s]	0.0244	0.0086	0.0070
Corrected method [m/s]	0.0258	0.0089	0.0073
corrected/original [%]	105.558	103.759	104.294

Table 4.4 – Standard deviation using the original and modified data despiking method.

4.6 Repositioning the angles of ADV data

4.6.1 Problem of the angle repositioning

Because of the size of the ADV transponder and its working principle (side-looking), a part of the flow would not be measurable without turning the probe in the flow. Consequently, the ADV has to be oriented in two directions. Depending on the transversal position in the flume, the probe is oriented either towards the floodplain step or towards the main channel wall. The combination of these two orientations enables the measurement of the velocities throughout the cross-section.

The probe angle is calibrated using the following method. When looking towards the floodplain, the ADV is lowered below the bank-full depth in the main channel and the distances between each receiver and the bank are measured. An equality between all the distances means

that the probe is perfectly perpendicular to the bank. When looking towards the main channel wall, the same procedure is applied. Nevertheless, measuring of those distances is not easy and some biases on the probe angle might remain with this method.

Unfortunately, ADV measurements are very sensitive to the orientation (Figure 4.10); for instance, an error of $\pm 1^\circ$ on the probe orientation creates an additional transversal velocity in the main channel of ± 1 cm/s. Consequently, before any physical interpretations of the data, angles between the ADV reference frame and the flume reference frame have to be checked and corrected to avoid any unwanted effects of wrong projections of the velocity.

NB – This procedure described in the sequel, has to be performed twice in each cross-section, for the probe oriented towards the main channel wall and oriented towards the floodplain wall.

4.6.2 Rotation matrix

Let be (u_0, v_0) the velocities in the ADV reference frame and θ the angle between the flume reference frame and the ADV reference frame. The corrected velocities are computed as following (Equation 4.14):

$$\begin{pmatrix} u_1 \\ v_1 \end{pmatrix} = \begin{pmatrix} \cos\theta & -\sin\theta \\ \sin\theta & \cos\theta \end{pmatrix} \begin{pmatrix} u_0 \\ v_0 \end{pmatrix} \quad (4.14)$$

Using the Reynolds decomposition, velocity correction can also be written as following:

$$\begin{pmatrix} \bar{u}_1 + u'_1 \\ \bar{v}_1 + v'_1 \end{pmatrix} = \begin{pmatrix} \cos\theta & -\sin\theta \\ \sin\theta & \cos\theta \end{pmatrix} \begin{pmatrix} \bar{u}_0 + u'_0 \\ \bar{v}_0 + v'_0 \end{pmatrix} \quad (4.15)$$

Finally considering the fact that,

$$\overline{\bar{u}_1 + u'_1} = \bar{u}_1 \quad \text{and} \quad \overline{\bar{v}_1 + v'_1} = \bar{v}_1 \quad (4.16)$$

the time-averaged velocities and the fluctuation can be treated separately:

$$\begin{pmatrix} \bar{u}_1 \\ \bar{v}_1 \end{pmatrix} = \begin{pmatrix} \cos\theta & -\sin\theta \\ \sin\theta & \cos\theta \end{pmatrix} \begin{pmatrix} \bar{u}_0 \\ \bar{v}_0 \end{pmatrix} \text{ and } \begin{pmatrix} u'_1 \\ v'_1 \end{pmatrix} = \begin{pmatrix} \cos\theta & -\sin\theta \\ \sin\theta & \cos\theta \end{pmatrix} \begin{pmatrix} u'_0 \\ v'_0 \end{pmatrix} \quad (4.17)$$

4.6.3 Impacts of wrong angles on the velocity

Let consider the velocities and the Reynolds stresses stemming from despiked data measured in the cross-section $x = 5.5$ m at seven lateral positions; the flow is taken under uniform conditions at a relative depth of 0.2. The magnitudes of the velocities and of the Reynolds stresses as well as the coordinates of the measurement positions are resumed in Table 4.5.

The impact of the angle orientation strongly depends on the considered component. A wrong angle has very few effects on the streamwise component (less than ± 2 %) compared to the spanwise component (see Figure 4.10.b). Considering the Figure 4.10.a, an increase in the longitudinal velocity decreases the impacts of a wrong angle calibration while an increase in the spanwise velocity increases this impact.

Position	\bar{u}_0 [m/s]	\bar{v}_0 [m/s]	$-\rho \bar{u}_0'^2$ [Pa]	$-\rho \bar{v}_0'^2$ [Pa]	$-\rho \bar{u}_0' \bar{v}_0'$ [Pa]
$y = 0.2$ m and $z/H_i^{ref} = 0.6$	0.227	-0.011	-0.298	-0.087	0.007
$y = 0.7$ m and $z/H_i^{ref} = 0.6$	0.264	-0.026	-1.547	-0.742	0.221
$y = 0.78$ m and $z/H_i^{ref} = 0.6$	0.351	-0.024	-2.813	-1.039	0.889
$y = 0.8$ m and $z/H_i^{ref} = 0.6$	0.426	-0.035	-8.01	-0.793	1.653
$y = 0.85$ m and $z/H_i^{ref} = 0.8$	0.56	-0.035	-2.33	-0.394	0.109
$y = 1$ m and $z/H_i^{ref} = 0.8$	0.658	-0.016	-1.058	-0.417	-0.034
$y = 1.15$ m and $z/H_i^{ref} = 0.8$	0.578	0.017	-0.949	-0.402	-0.115

Table 4.5 – Original values of velocities and Reynolds stresses before rotation. The fourth positions is just located above the interface between the main channel and the floodplain.

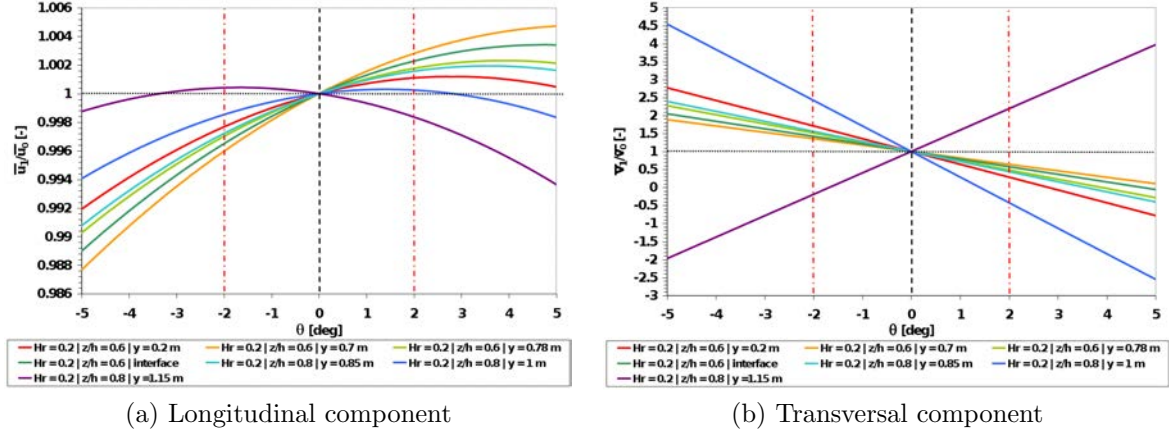


Figure 4.10 – Impacts of wrong angles on ADV measurements. Each rotated velocity is normalized by its corresponding velocity at $\theta = 0^\circ$.

4.6.4 Impacts of wrong angles on Reynolds stresses

Using Equation 4.17, the rotation matrices are applied on the cross-terms $\bar{u}_1'^2$, $\bar{v}_1'^2$ and $\bar{u}_1' \bar{v}_1'$:

$$\begin{aligned}
 \bar{u}_1'^2 &= \bar{u}_0'^2 \cos^2 \theta + \bar{v}_0'^2 \sin^2 \theta - \bar{u}_0' \bar{v}_0' \sin 2\theta \\
 \bar{v}_1'^2 &= \bar{v}_0'^2 \cos^2 \theta + \bar{u}_0'^2 \sin^2 \theta + \bar{u}_0' \bar{v}_0' \sin 2\theta \\
 \bar{u}_1' \bar{v}_1' &= \frac{\sin 2\theta}{2} (\bar{u}_0'^2 - \bar{v}_0'^2) + \bar{u}_0' \bar{v}_0' \cos 2\theta
 \end{aligned} \tag{4.18}$$

Using Equation 4.18 and the flows used for computed the biases on the velocities, impacts of rotations on the Reynolds stresses are then computed. Results are displayed on the Figure 4.11.

Considering the longitudinal auto-covariance (Figure 4.11.a) and the transversal auto-covariance (Figure 4.11.b), impact of the wrong angle increases with increasing $\bar{u}_0'^2$. Moreover an increase in $\bar{u}_0' \bar{v}_0'$ also increases this error; that means, in the zone of great shearing (mixing layer), we have to be careful with the computed turbulent intensity. An error of $\pm 1^\circ$ only leads to an error of $\pm 1\%$ for the longitudinal component, while the error can reach $\pm 10\%$ for the transversal component.

Considering the cross-covariance $\bar{u}_1' \bar{v}_1'$ (Figure 4.12), it strongly depends on $\bar{u}_0' \bar{v}_0'$. If the initial cross-covariance is low, a slight error on the orientation might have a strong influence on the new value. On the other hand, if the initial cross-covariance value is high (at the interface for instance), the rotation will have few impacts on the new value. To resume, in the mixing layer, an error of $\pm 1^\circ$ only leads to an error of $\pm 7\%$, while in the other stations, errors can reach $\pm 50\%$. Nevertheless, an error of $\pm 50\%$ on a value nearly equal to zero is still close to zero, while an error of $\pm 7\%$ on a significant value can leads to a consistent absolute error. Consequently,

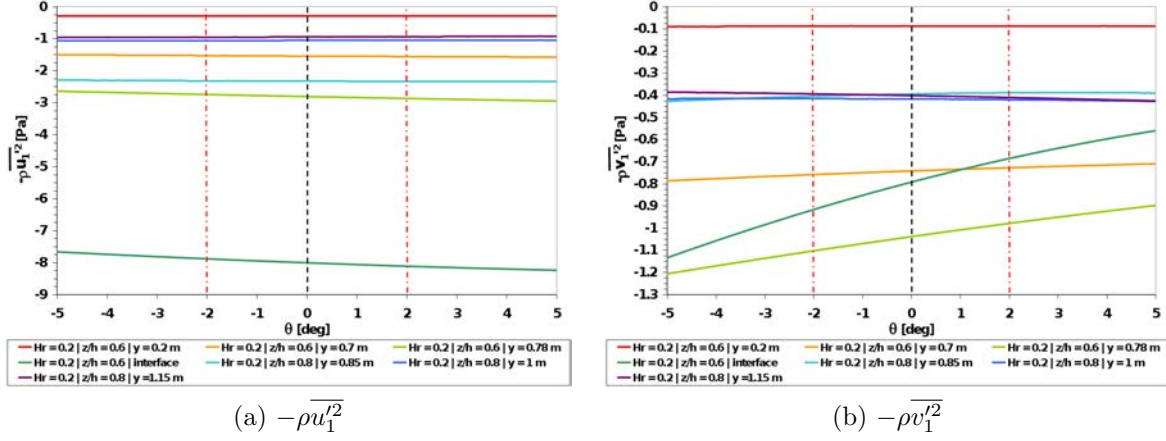


Figure 4.11 – Impacts of wrong angles on ADV measurements: cases of the auto-covariance terms $-\rho \overline{u_i'^2}$ and $-\rho \overline{v_i'^2}$.

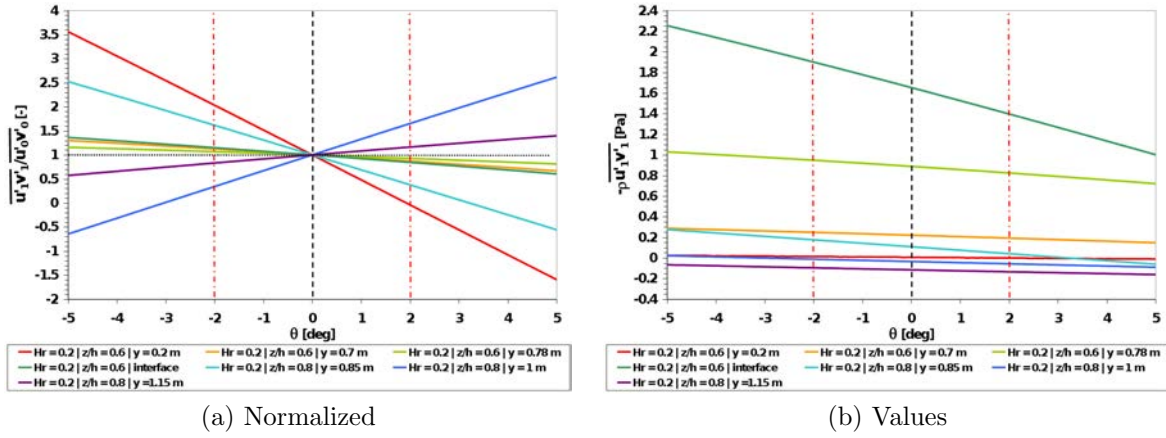


Figure 4.12 – Impacts of wrong angles on ADV measurements: impacts on the cross-covariance term $\overline{u_1'v_1'}$. The Figure (a) is the normalization of the Figure (b).

a bad orientation have a relevant impact on the shear stress component, this, especially at the interface between channels.

4.6.5 Methods to correct a bad angle orientation

The method is based on the assumption that the lateral velocities at $0.4 \times H_i^{ref}$ and $0.6 \times H_i^{ref}$ are nearly equal to zero near a bank (velocities at $0.2 \times H_i^{ref}$ and $0.86 \times H_i^{ref}$ are disturbed by the bottom or the free surface). This assumption is based on the velocity profiles close to the wall displayed in Figure 4.13 for uniform flows [Shiono and Feng, 2003].

As shown in Figure 4.13, the lateral component \bar{v} is nearly equal to zero near the bank separating the main channel and the floodplain. Near the floodplain wall and the main channel wall this behaviour is also observable: this is the non-penetration condition.

We consider that the bad angle – we want to correct – is due to a bad orientation of the probe. That means this angle is unique for each orientation of the probe. The method needs therefore two rotation angles; one for the measurements looking toward the floodplain and one for the other direction (toward the main channel).

The angles are determined using the Equation 4.17 and the fact that the velocities at the positions $y = 0.81$ (≈ 1 cm from the interface between the floodplain and the main channel) and $y = 1.1197$ at the normalized altitudes of $0.4 \times H_i^{ref}$ and $0.6 \times H_i^{ref}$ should be equal to zero. For

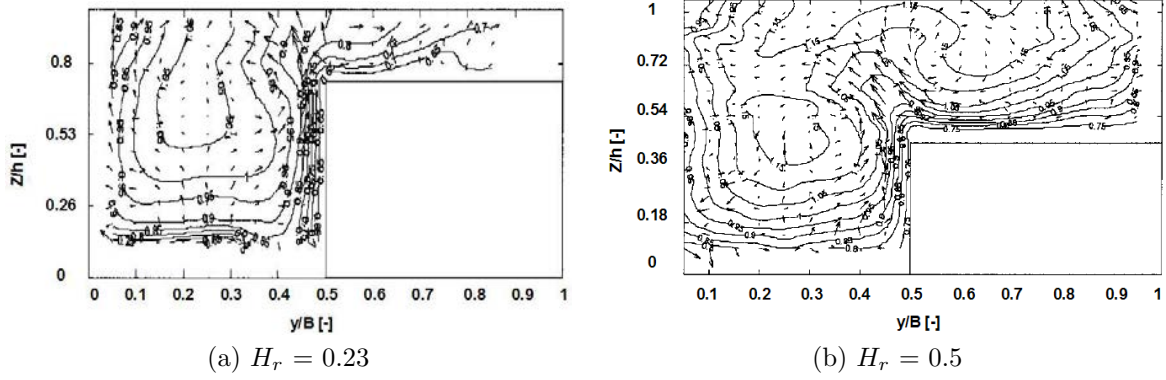


Figure 4.13 – Observation of lateral velocities in a secondary-current cell under uniform flow conditions (After, [Shiono and Feng \[2003\]](#)).

each direction of the probe and each altitude $0.4 \times H_i^{ref}$ and $0.6 \times H_i^{ref}$, velocities are rotated until the lateral velocity reach zero; an averaged angle is then deducted from these measurements for each direction (D_1 is the reorientation angle measured in the direction looking towards the floodplain, D_2 for the direction looking towards the main channel wall); the correction angle should be within $\pm 5^\circ$. If angle is larger than the recommended interval, additional errors might exist and the computed angle has to be invalidated. The ADV setting was indeed done very carefully and an angle bigger than $|\pm 5^\circ|$ is impossible; an error of five degrees in the position of the probe is fairly easy to see during the positioning. On the other hand, there are several other errors of “orientation” that cannot be easily seen. The Doppler effect might introduce a random error that we cannot evaluate. The wake generated around the rod of the probe might also introduce a bias, especially in shallow conditions ($H_r = 0.2$ or downstream of the groyne, where the water depth is really shallow).

	Position	2 m	2.5 m	4.5 m	5.5 m	6.5 m
		[°]				
RF200L	D_1	×	×	×	2.90	×
	D_2	×	×	×	-0.36	×
RF300L	D_1	×	×	×	2.5	×
	D_2	×	×	×	-0.25	×
RF400L	D_1	×	×	×	3.5	×
	D_2	×	×	×	-0.18	×
GC230L	D_1	1.71	1.71	1.71	×	1.71
	D_2	-0.33	-0.33	-0.33	×	-0.33
GC330L	D_1	-2.35	-1.51	-1.73	×	2.4
	D_2	-1.4	-1.58	-1.45	×	-1.43
GC350L	D_1	1.84	1.97	1.97	×	2.4
	D_2	-1.75	-1.83	-0.93	×	-1.15
GC430L	D_1	1.2	2.5	2.5	×	1.87
	D_2	-0.27	-0.38	-0.27	×	-0.31

Table 4.6 – Angles of rotation computed with the method of local rotation. All the flow cases are presented. D_1 (resp. D_2) is the reorientation angle measured in the direction looking towards the floodplain (resp. in the direction looking towards the main channel wall).

The computed correction angles are summarized in Table 4.6; results first emphasize that the angles D_1 and D_2 are all within the $\pm 5^\circ$ interval and the angles in a given probe-direction are nearly the same for the reference cases. On the other hand, some differences appear for the groyne cases. The comparisons between the cross-sections at a given groyne-case flow emphasize that the angles are nearly the same in the direction where D_2 is measured, while there are some big differences in the direction where D_1 is measured. These differences are difficult to explain; it may have some additional effects that are not taken into account when using this method (deformations of the secondary currents due to the mass exchange for instance). Notice that the

D_1 angles are particularly different in the last section ($x = 6.5$ m), we can see here an influence of the downstream boundary condition (located at $x = 8$ m), which interferes with the flow at $x = 6.5$ m.

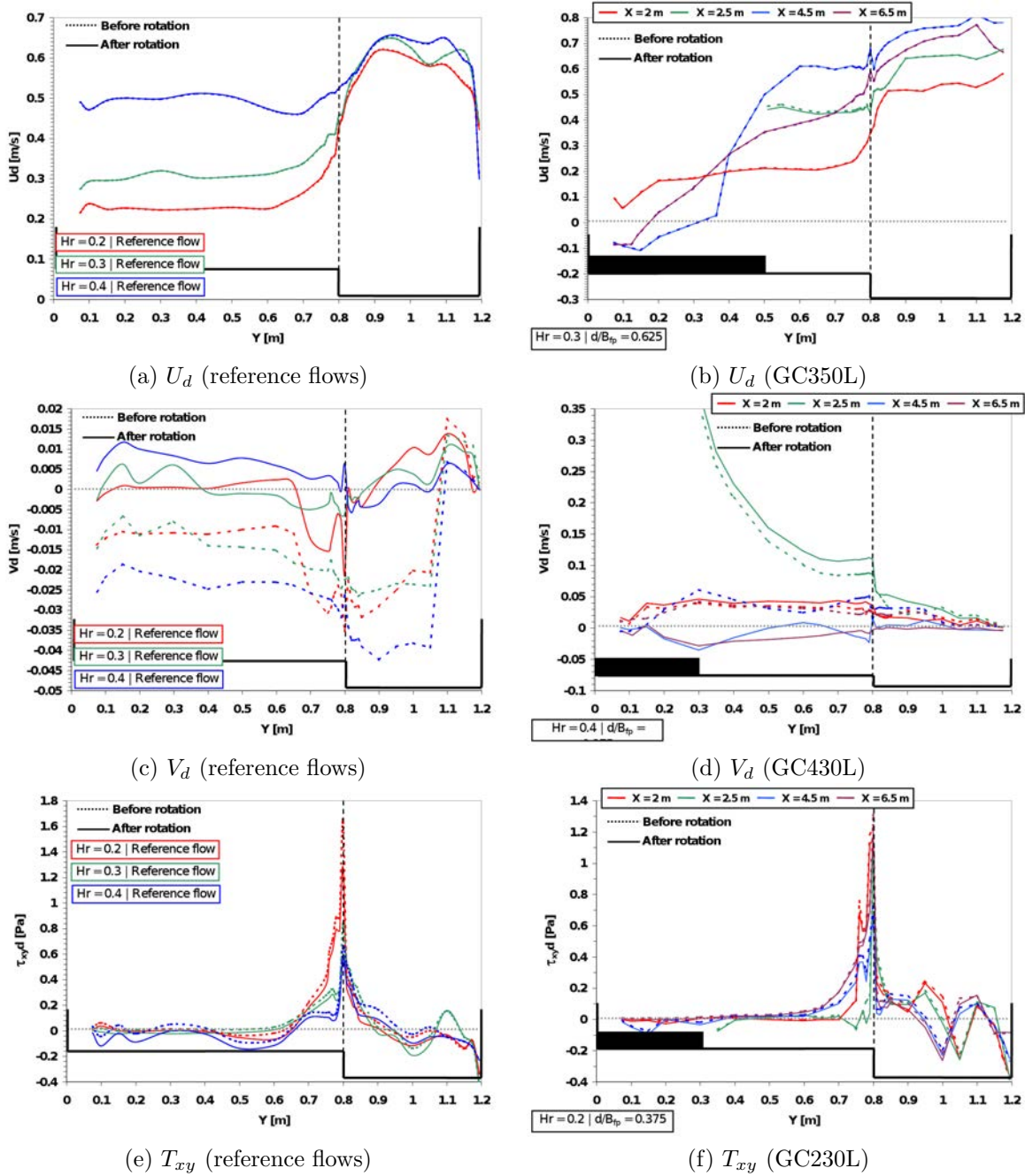


Figure 4.14 – Depth-averaged longitudinal and transversal velocities and depth-averaged lateral Reynolds shear stress for reference flows and for groyne-case flows, after an angle correction using the local method. The raw data (dotted line) and the corrected data are displayed on the same graph.

In Figure 4.14.a, the depth-averaged longitudinal velocities of the three reference flows are displayed and as said in the previous subsection (§4.6.3), the bad orientation has low effects on the streamwise component of the velocity. On the other hand, this correction has a tremendous impact on the depth-averaged lateral velocity (Figure 4.14.c): the local correction enables to get depth-averaged lateral velocities nearly equal to zero as expected under uniform conditions.

The curves in Figure 4.14.e emphasize that the correction has a great impact on the peak magnitude of the depth-averaged Reynolds shear stress T_{xy} . We have to work very carefully

with this parameter, since a slight error in the orientation changes its magnitude. However, the new angle does not change the shape of the stress distribution.

In groyne-case flows, the tendencies observed for reference flows are the same. However, the effects are lessened, because the correction angles are smaller than those of the reference flows. Nevertheless, analysis of the depth-averaged lateral velocities after the rotation is really difficult for the groyne-case flows. The amplitude of the velocity is no more a sufficient criterion to assess if the method is good or not. The only way to assess it, is to look at the sign and the pattern of the lateral velocity. Upstream of the groyne ($x = 2$ m) and in the groyne cross-section ($x = 2.5$ m) the depth-averaged lateral velocities have to be positive, since the floodplain is exchanging mass towards the main channel. Downstream of the groyne, the sign of the velocity depends on the position of the measurement section relative to the recirculation and its contraction (throat). If the section is upstream of the flow contraction, the depth-averaged lateral velocities are mainly positive, while downstream of the contraction the velocities have to be negative, since the main channel returns water to the floodplain.

NB – The corrections have little impacts on the discharge computation in a cross-section, since the corrections have little effects on the longitudinal velocity. Regarding the distribution of the depth-averaged Reynolds shear stress, the correction has no impact on the pattern of the distribution but operates a proportional transformation of the stress amplitude.

4.7 Spectral analysis of the turbulence

The spectral analysis of the turbulence enables to determine the distribution of energy and shear across the various frequencies or wave-numbers of the turbulent structures that passed in the sampling volume of the ADV during measurements. The aim of calculating cross-power spectrum densities in this PhD-thesis was to identify what frequency range contributes to momentum transfer through the mixing layer developing at the interface or in the lee of the groyne and what frequency range is responsible for dissipation. The power spectrum densities were worked out for determining the length-scales of the coherent structures that develop in the mixing layer; they also give information about the nature of the produced turbulence (2D/3D, *i.e.* free shear layer or shallow shear layer).

The spectral analysis was performed using:

1. the power spectrum densities S_{xx} and S_{yy} which give information on the distribution of energy across the various structures present in the flow and also enable to assess the dimension of the characteristic length scales.
2. the cross-power spectrum density S_{xy} which gives information on the momentum that is transferred by the turbulent structures in the flow.
3. the phase relation between the horizontal fluctuating velocities which enables to identify the interval of frequencies or wave-numbers in which the turbulent structures are considered as coherent and participate to the transfer of momentum.

The spectrum densities were calculated using the method of the short modified periodograms [Welch, 1967]: *i.e.* Fast Fourier Transform of several segments (= periodograms), possibly overlapping, of a signal, for calculating the spectral density of despiked time-series. The characteristics of the computations are given below:

1. Using the despiking algorithm presented in §4.5, the spikes were first removed from the velocity time-series we wanted to study and the fluctuating part of the velocity was then extracted from the despiked time-series.
2. With the resulting fluctuating velocities, the average number of samples for time-series was estimated. It was equal to $N \approx 18000$ for 3 min of measurements at $F_s = 100$ Hz (see §3.3.4.3). Nevertheless, since the FFT algorithms need number of samples proportional to a power 2 number [Lemasquerier, 2002], the required number of samples used for our FFT calculations was rather set equal to $NFFT = 32768 = 2^{15}$ ($2^{14} = 16384$ is smaller than the number of samples of 3 a min recording).
3. This higher number of samples compared to the available samples in time-series then indicated that the zero-padding method could be used for improving the discretization of the spectrum density. $NFFT - N$ samples equal to zero completed the time-series (The zeros do not modified information extracted from the time-series).
4. A window of Hanning of 512 samples wide was then applied on the new signal with an overlapping of 50 %, therefore cutting the signal in $K_N = NFFT/512 \times 2 - 1$ segments (the window is used to reduce the aliasing in the spectrum density and it improves the resolution of the spectrum).
5. In the sequel, the FFT of each segment and their periodogram were calculated. The average of all the periodograms finally gave the estimate of the one-sided spectral density.

The phase relation ϕ was easier to compute; it is indeed equal to:

$$\phi = \text{angle}(FT(u') * \text{conj}(FT(v'))) \quad (4.19)$$

where (u', v') are the despiked time-series of the fluctuating velocities and FT is the Fourier transform operator. No window of apodization was applied and the phase was rotated in order to be included between -2π rad and 0 rad. This rotation was operated, because according to Tennekes and Lumley [1972], the phase must be equal to $-\pi$ when turbulence production occurs in the flow.

With the methods previously exposed, the spectral densities as the phase relation are expressed as a function of the frequency. The frequency gives information on the spinning (indirectly the size) of the turbulent structures present in the flow. By convenience, we rather preferred to work with wave-numbers. They give directly information on the size of the turbulent structure and therefore on their ability to transport or diffuse a tracer. The wave number is calculated using the longitudinal mean velocity of the time-series we considered for the spectral analysis: $k = 2\pi f / \bar{u}$ and the spectral density in frequency must be multiplied by $\bar{u} / (2\pi)$.

To finish, as exposed in §3.3.4.3, ADV measurements are noised. In order to have a good interpretation of the distribution of the power spectrum densities, denoising algorithm are required for their calculation (cross-power spectrum densities are independent from the noise [Strom and Papanicolaou, 2007]). According to Hurther and Lemmin [2001], the noise is characterized by (1) the Doppler ambiguity process that is characterized by the amplitude modulation of the backscattered signal related to the transit time of the acoustical targets through the measurement volume. (2) The spatial averaging of the instantaneous velocity field (a large number of targets are present instantaneously), which is taken over the sample volume weighted by the directivity function of the emitter. (3) The effect of the mean flow shear stress present within the sample volume. (4) The phase distortion effect of the emitted front wave. (5) The effect of those turbulent scales that are of the same order of magnitude or smaller than the sample volume's transverse size. (6) The electronic circuitry's sampling errors linked to the A/D conversion. Except for the spatial averaging process (process (2)), all other noise sources enter as additional variance terms in the

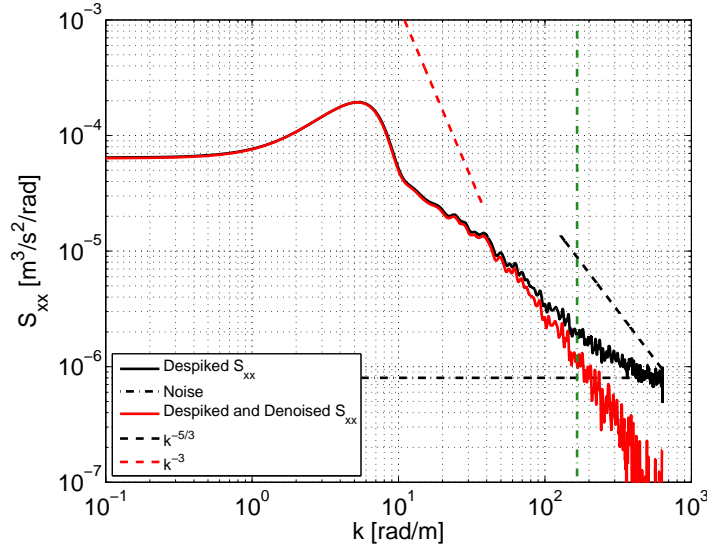


Figure 4.15 – Denoising of a power spectrum density S_{xx} for RF300L.

measured fluctuating velocities variances and therefore are statistically independent. Process 1, 3, 4, 5 and 6 can be minimized using the method proposed by [Voulgaris and Trowbridge \[1998\]](#) or by [Hurther and Lemmin \[2001\]](#):

1. The level of the noise is identified at high frequencies on the power-spectrum (plateau at the end of the despiked signal in Figure 4.15,
2. The noise is considered as a white noise and the level deducted at high frequencies is reproduced for the lower frequencies (N_{xx} in Figure 4.15).
3. The noise is finally subtracted to the despiked signal, therefore giving a despiked and denoised power spectrum density.

Concerning process 2, it is not an additional variance term; it is rather a filtering process of the turbulence due to the non-statistical independency of the multiple targets that are instantaneously used for the velocity calculation in the sampling volume [[Garcia et al., 2005](#)], moreover structures with length scales smaller than the dimensions of the sampling volume are badly detected by the ADV, because the statistical independency of the particles contained in the structures is not achieved. In this thesis, this type of noise was not avoided nor minimized, but we estimated the maximal wave-number beyond which the spectral density is no more significant. The sampling volume for ADV measurements was thus equal to $\approx 0.21 \text{ cm}^3$ (diameter = 6 mm and volume height = 7.6 mm). By adapting a method proposed by [Nezu and Nakagawa \[1993, p30\]](#) in order to assess the maximal wave-number beyond which the spectral calculation is no more significant (*i.e.* $k_{max} \geq 100/h \text{ m}^{-1}$) when using a LDA (sampling volume is considered as infinitesimal), we can calculate the maximal resolution of ADV measurements. In the longitudinal direction, the diameter of the probe (6 mm) is the limiting scale: $k_{max,x} \geq 100/0.006 \approx 166 \text{ m}^{-1}$. In the transversal direction, the height of the sampling volume (7.6 mm) is the limiting scale: $k_{max,y} \geq 100/0.0076 \approx 132 \text{ m}^{-1}$. The cross-power spectrum density is finally limited by the smallest k_{max} , *i.e.* $k_{max,y} \geq 132 \text{ m}^{-1}$.

In addition to the correction of the noise in the power spectrum density S_{xx} , the maximal wave number representing the limit beyond which the spectral density is probably bad is displayed in Figure 4.15 (vertical green line). It results that the spectral density containing the energy is mostly located before the maximal wave-number and few information is lost if we only considered measurements before k_{max} .

4.8 Correction of the systemic error on micro-propeller measurements

The comparison of the velocities stemming from the micro-propeller measurements with the ADV ones emphasizes a systematic bias between measuring devices. The computation of the total discharge in a cross-section using ADV data is indeed equal to 95-100 % of the injected total discharge, while the total discharge deduced from the micro-propeller measurements is rather between 80-90 % of the injected total discharge. As shown in Table 4.7, the computed discharges for reference flows are quite homogeneous; 93 % of the total injected discharge is measured in average using the micro-propeller data, while 100 % is measured using the ADV data. For groyne-case flows a larger bias is observed between ADV and micro-propeller data; some physical phenomena, which are not observed for flows under reference flow conditions, might interact with the micro-propeller and prevent the micro-propeller from properly measuring the physics.

Long. position	RF200L	RF300L	RF400L	GC230L	GC330L	GC350L	GC430L
[m]	[%] of Q_t^{inj}						
Computations done with the micro-propeller data							
1.5 m	92.52	91.56	94.76	90.63	81.85	81.28	93.45
2 m	93.35	90.01	93.53	88.88	82.27	81.76	92.48
2.5 m	92.58	90.11	94.63	88.83	81.51	85.50	89.54
3 m	×	92.58	94.47	90.32	82.59	89.17	89.49
3.5 m	93.05	90.83	94.88	89.34	84.22	89.01	90.70
4.5 m	93.99	92.59	96.05	91.44	85.72	95.07	91.34
5.5 m	92.65	91.92	95.23	92.07	85.21	91.07	93.80
6.5 m	93.11	91.78	95.67	92.00	84.47	88.35	95.84
7.5 m	92.82	91.01	95.67	92.86	86.15	88.48	91.52
Computations done with the ADV data							
2 m	×	×	×	94.87	98.24	100.65	101.90
2.5 m	×	×	×	97.99	96.78	101.33	101.22
4.5 m	×	×	×	100.34	97.88	92.05	92.90
5.5 m	99.76	100.01	99.36	×	×	×	×
6.5 m	×	×	×	100.65	96.64	98.30	97.70

Table 4.7 – Percentage of the injected total discharge computed using the micro-propeller data and the ADV data for the reference flows and the groyne-case flows.

NB – The computed total discharge with the ADV data at section $x = 4.5$ m for GC350L and GC430L are weak. In this section for both flows, the water depth was very shallow; velocities were measured at only one altitude ($0.4 \times H_{fp}^{ref}$) in the floodplain and this impacts the discharge integration since the flow is 3D in this zone.

Biases in the data set are not due to a random error, but are rather due to a systemic error, since there is a tendency in the measurements (see, Table 4.7). These biases can be easily reduced. If one device has more biases than another and if these two devices have measured the same physical value at the same location, we can reduce the bias of the worst device relative to the other one.

4.8.1 Sources of errors

A micro-propeller measures velocity using a propeller spinning in the flow (§3.3.4.1). The rotation frequency directly gives the norm of the velocity of the flow facing the probe; using a vane, the angle of the flow is then deduced and the longitudinal / lateral components of the velocity can be worked out. Depending on the position in the flow, the measurements can be distorted by local

phenomena. In zones of high turbulence production and high turbulent agitation, measurements can be biased by the coherent structures in the flow. The propeller can either be accelerated by lateral structures coming through the sampling volume (wheel effects) or can be decelerated by being misaligned relative to the main flow direction. It results in a higher dispersion in the measurements.

The ADV has no mobile pieces for measuring velocity in the flow and the sampling volume is shifted 5 cm from the transducers, as a consequence transducers have low influences on the sampling volume. Main error sources are due to a bad alignment in the flow or can be due to high Doppler noise. Those two sources were reduced in most experiments. That is why the measurements are better for the ADV.

An other source of bias exists. Depending on the shallowness of the flow, the characteristics of the flow can be partially affected by an obstruction created by the measuring device. This obstruction, induces local changes in depth in the vicinity of the probe and therefore induces changes in the velocity distribution in the whole water column because the Froude number in the LMFA flows are quite high.

The ADV is less affected by this effect of obstruction than the micro-propeller, because the sampling volume is deported out of the distorted zone.

4.8.2 Correction for reference flows

4.8.2.1 Least squares fits

For reference flows, only one complete cross-section was measured using the ADV, while nine cross-sections were measured using a micro-propeller. Analyses of the reference flows using only one cross-section measured by ADV is not realistic. The micro-propeller measurements are also needed to give the characteristics of the flow in the other cross-sections. Nevertheless, since micro-propeller data are biased, they must be first corrected for reducing the bias.

The correction of the micro-propeller data is actually a recalibration of the device. Regardless of the relative depth, ADV and micro-propeller velocity norms are compared and plotted together for each normalized altitude z/H_i^{ref} at $x = 5.5$ m (the only available cross-section for ADV); tendencies are then extracted from these scatter plots using a linear least squares method. For the reference flows, five recalibration laws are worked out (at four normalized altitude and one for all altitudes combined).

NB – To avoid any problem of rotations and bad projections of the velocities, the comparison and the recalibration of the data are done using the norm of the velocity. The rotation matrix is indeed equal to an identity matrix when working with the norm operator.

In Figure 4.16, for each reference flow, ADV velocities are plotted relative to the micro-propeller data. Each resulting scatter plot is fitted using a least squares method. Most of the data are within the 95 % confidence interval (no more than three data are out of bounds) and except at $0.2 \times H_i^{ref}$, where the determination coefficient (R_d^2) is only equal to 0.71, the determination coefficients of the three other fits are larger than 0.92, *i.e.* each linear modelling computed using the least squares method explains at least 92 % of the total dispersion of the scatter plots. The lower value of R_d^2 at $0.2 \times H_i^{ref}$ is due to the lack of data at this altitude (no measurements in the floodplain). Nevertheless, even if the determination coefficient of the fit at $z/H_i^{ref} = 0.2$ is equal to 0.71, the fact that all the points are within the 95 % confidence interval enable to also validate this fit as a possible modelling of the considered data cloud.

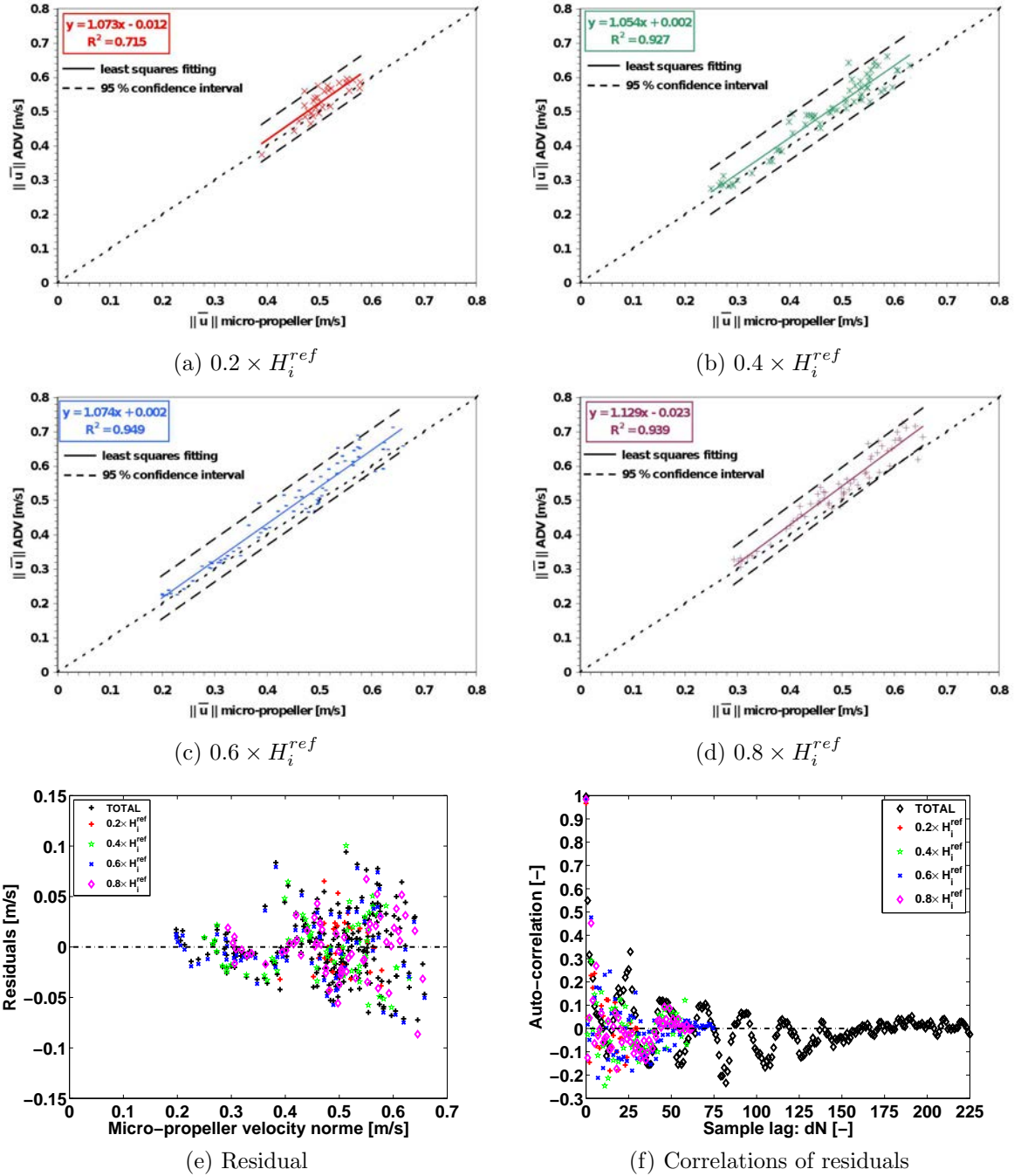


Figure 4.16 – Comparison of ADV and micro-propeller data for the reference flows at different altitude z/H_i^{ref} : new calibration of the Micro-propeller.

In the sequel, in order to know if a fit is good or not, the residuals of the fit and the correlations between the residuals have to be computed. The residuals are the difference between the observed ADV velocities and the computed velocities using the least squares modelling. If the residuals are random around zero and are independent, the fit is acceptable and the least squares fit can be considered as an acceptable modelling of the considered scatter plot. On the two last graphics in Figure 4.16, the residuals and the correlation between the residuals are plotted. For each altitudes, the average of the residuals (Figure 4.16.e and Table 4.8) and the correlations between the residuals are very close to zero: the linear modellings, computed using a least squares method, are acceptable and are a good modelling for the data dispersion.

NB – The recalibration laws by relative altitudes, we used for reference flows, are the equations displayed in Figures 4.16.a, 4.16.b, 4.16.c and 4.16.d. The calibration

	$z/H_i^{ref} = 0.2$	$z/H_i^{ref} = 0.4$	$z/H_i^{ref} = 0.6$	$z/H_i^{ref} = 0.8$
Avg. residuals [m/s]	7.59×10^{-6}	-2.64×10^{-4}	-1.47×10^{-4}	-2.47×10^{-4}
Avg. correlations [-]	3.88×10^{-18}	1.41×10^{-18}	-2.61×10^{-18}	-2.1×10^{-18}

Table 4.8 – Averaged value of residuals and correlations of reference flow fits.

law for the all combined altitudes is the following: $y = 1.076x - 0.003$ with $R_d^2 = 0.93$. x in equations in Figure 4.16 corresponds to the value to recalibrate (micro-propeller) and y then corresponds to the recalibrated value.

4.8.2.2 Impacts of the recalibration

Recalibrations enable a good correction of the micro-propeller data (Figure 4.17). The comparison between ADV and corrected micro-propeller depth-averaged velocities emphasizes that velocities of both devices are now nearly the same in the floodplain for RF200L and RF300L. Concerning RF400L, a difference of $\pm 6\%$ in the floodplain is observed between the ADV and the micro-propeller velocities. This difference is due to the velocity in the floodplain at $H_r = 0.4$ that is nearly equal to the velocity in the mixing layer for RF200L and RF300L, *i.e.* $\approx 0.4 - 0.5$ m/s. The dispersion of the velocity in the mixing layer is higher than in every other part of the flow and this impacts the correction of the velocity in the floodplain for RF400L. In the mixing layer ($y \in [0.6 \text{ m} - 0.85 \text{ m}]$), the corrected velocities and the ADV velocities have the same magnitudes and the distributions have similar shapes whatever the relative depth is. Regarding the main channel, the velocities of both devices follow roughly the same shape, however some differences are observables. These differences might be due to some little changes in the upstream boundary conditions between ADV and micro-propeller measurements, therefore inducing slight changes in the velocity distribution in the main channel. Measurements were indeed not performed the same days and although upstream boundary conditions were perennial, honeycomb in the main channel (§3.2.3) was sometimes blocked off by dirt coming from the tank, therefore generating an additional head loss that changes the shape of the injected velocity in the main channel.

The total discharges calculated with corrected micro-propeller data are given in Table 4.9; they are all within 95 % and 105 % of the injected total discharge. To conclude, the new calibration enables a proper correction of the micro-propeller data measured under reference flow conditions.

Long. position	RF200L	RF300L	RF400L
[m]	[%] of Q_t^{inj}		
1.5	98.58	97.39	101.10
2	99.53	95.84	99.83
2.5	98.75	95.98	101.05
3	×	98.78	100.95
3.5	99.80	96.85	101.37
4.5	100.82	96.91	101.54
5.5	99.35	98.00	101.74
6.5	99.85	97.79	102.20
7.5	99.52	96.89	102.15

Table 4.9 – Percentage of the injected total discharge computed using the corrected micro-propeller data of the reference flows.

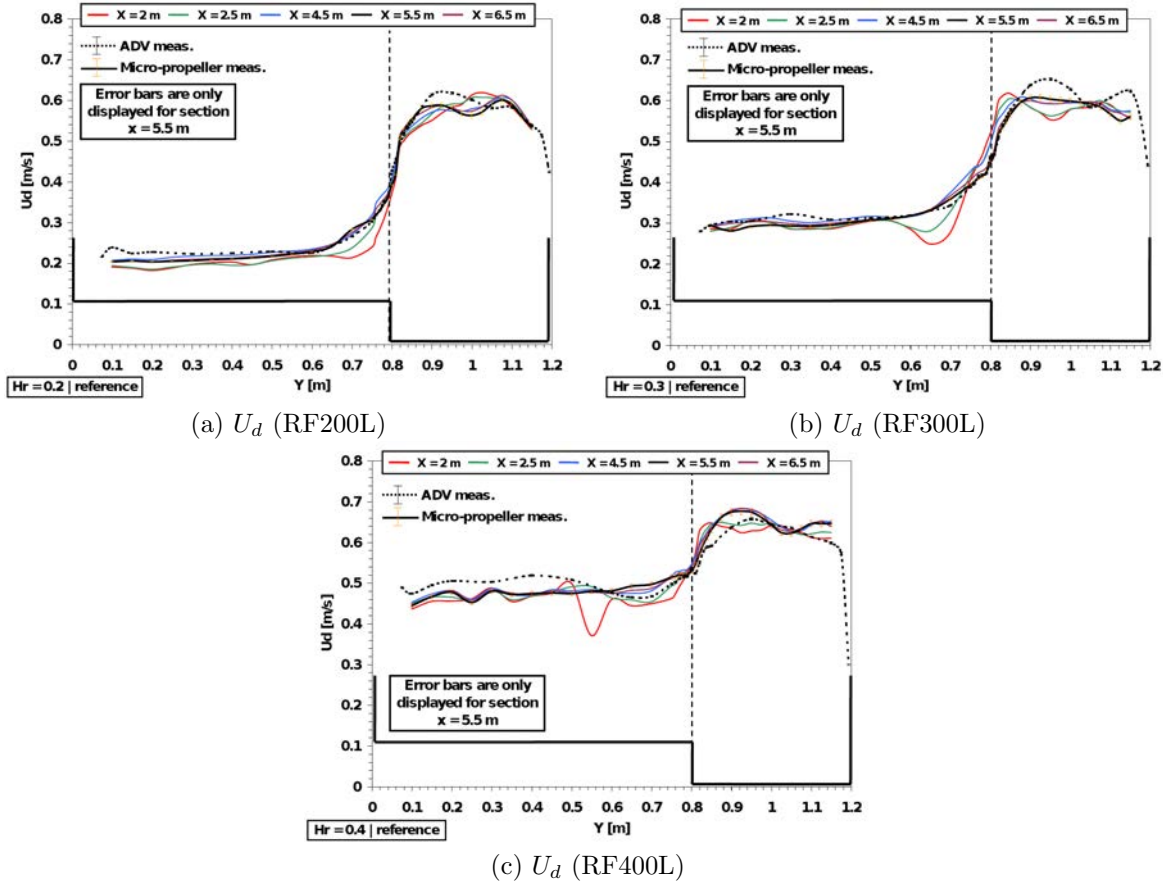


Figure 4.17 – Corrected depth-averaged velocities for reference flows.

4.8.3 Corrections for Groyne-case flows

4.8.3.1 Least squares fits

For each groyne-case flows, four cross-sections were measured using ADV; measurements emphasize that depending on the location of the measurement cross-section, the flow has not the same characteristics. Upstream of the groyne at $x = 2$ m the flow is mainly decelerated and the floodplain exchanges mass towards the main channel. In the groyne cross-section at $x = 2.5$ m until approximately $x = 3$ m (see Chapter 6) the flow is strongly accelerated. Finally downstream of the throat from $x = 3.5$ m, the flow is diverging and mass is exchanged from the main channel towards the floodplain. Three distinct zones, with three distinct behaviours can be therefore identified. As a consequence, we decided to correct the velocity by altitude (the same as reference flows) and by zone, since the physics is different in each identified zone. ADV and micro-propeller velocity norms were then plotted together for each normalized altitude z/H_i^{ref} , this, for each zone we identified. Using a linear least squares method, fifteen recalibration laws were therefore deducted (at four normalized altitude and one at all altitudes combined for each zone, see Table 4.10).

Recalibration coefficients are displayed in Table 4.10. Excepted at $0.2 \times H_i^{ref}$, where there are not enough measurements at low velocities, the fits are good and the recalibration laws are consistent since the determination coefficient R_d^2 are all greater than 0.8; *i.e.* 80 % of the scatter plot dispersion is at least explained by the linear fits represented by equations in Table 4.10. Moreover, most of the data are within the 95 % confidence interval and the residuals are random and centered around zero.

	Total	$0.2 \times H_i^{ref}$	$0.4 \times H_i^{ref}$	$0.6 \times H_i^{ref}$	$0.8 \times H_i^{ref}$
Recalibration coefficients for velocities in the part upstream of the groyne					
a	0.942	0.318	0.959	1.040	0.890
b	0.065	0.381	0.054	0.033	0.095
R_d^2	0.883	0.273	0.918	0.901	0.835
Recalibration coefficients for velocities between $x = 2.5$ m and $x = 3$ m					
a	0.824	0.684	0.817	0.951	0.766
b	0.158	0.219	0.149	0.106	0.202
R_d^2	0.811	0.560	0.835	0.843	0.800
Recalibration coefficients for velocities in the diverging part					
a	0.991	0.819	0.920	1.053	1.024
b	0.062	0.141	0.102	0.029	0.060
R_d^2	0.903	0.788	0.896	0.942	0.809

Table 4.10 – Recalibration coefficients for velocities measured using the micro-propeller under groyne-case flow conditions. Recalibration law is formulate as $y = ax + b$, where y is the corrected data, x is the data to correct, a and b the coefficients of recalibration and R_d^2 is the coefficient of determination that indicates the quality of the recalibration.

NB – Since calibration curves at $0.2 \times H_i^{ref}$ are bad, the calibrations on the whole data set are used for correcting this altitude.

4.8.3.2 Impacts of the recalibration

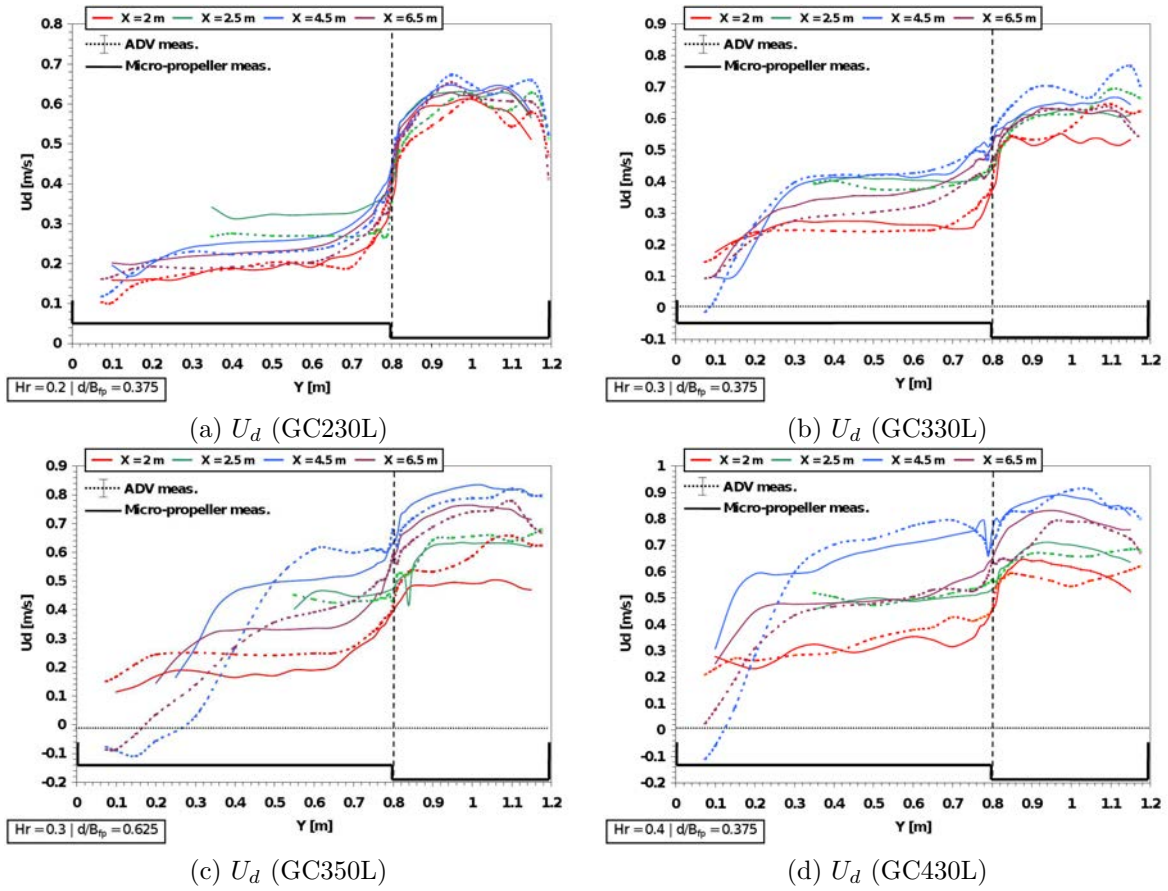


Figure 4.18 – Corrected depth-averaged velocities of the groyne-case flows.

Most of the corrected velocities are $\pm 5\%$ equal to ADV velocities. For the smallest groyne $d = 30$ cm at $Q_t = 17.3$ l/s and $Q_t = 24.7$ l/s (GC230L and GC330L), the ADV profile and the micro-propeller profile match very well. For the two other flows (GC350L and GC430L), the main differences with ADV are observed in the floodplain. In the upstream cross-section at $x =$

2 m for G350L, the recalibrated velocity is 20 % smaller than the ADV one. Those differences are due to the fact that the calibration laws do not cover the range below 0.2 m/s and consequently recalibrated data are more uncertain below this range. Some differences are also present in the floodplain of the downstream cross-sections for GC350L and GC430L. The micro-propeller cannot properly follow the strong decrease in velocity in the vicinity of the recirculation zone; the recalibrated velocity is then lower out of the recirculation zone and is higher inside the recirculation zone. This bad-measurement may be due to the vortex shedding of both sides of the separation line between the recirculation zone and the main flow in the floodplain. The high changes in the flow direction because of the vortex shedding gives bad orientation to the vane. As a consequence micro-propeller measurements are biased (see §4.8.1).

The total discharges computed using the recalibration laws for groyne-case flows are displayed in Table 4.11. Most of the computed total discharges are within 95 % and 105 % which is an acceptable interval for measurements. A flow remains problematic, in some cross-sections of GC330L the computed discharges with corrected velocities are still under-estimate and are below 95 %. This under-estimation is probably a consequence of a defectuous micro-propeller. The micro-propeller we used for GC330L was indeed different from the one used in other experiments. The previous micro-propeller was indeed broken few months before the measurements of GC330L; the new micro-propeller was probably defectuous, especially for the high velocities (> 0.5 m/s).

Long. position	GC230L	GC330L	GC350L	GC430L
[m]	[%] of Q_t^{inj}			
1.5	100.28	92.73	94.90	103.95
2	98.23	92.73	95.27	102.38
2.5	103.47	95.00	97.45	99.94
3	102.85	90.66	96.70	94.37
3.5	104.21	94.06	94.45	94.21
4.5	102.30	92.96	100.61	97.20
5.5	105.05	97.37	101.93	103.64
6.5	105.03	97.33	99.52	106.59
7.5	106.96	99.78	101.02	102.85

Table 4.11 – Percentage of the injected total discharge of the recalibrated micro-propeller data using the calibrations computed with groyne-case data.

To conclude, the recalibration for groyne-case data are acceptable and can be used for correcting the micro-propeller measurements with a groyne set on the floodplain. For GC250L and GC420L, there are no ADV measurements. We assume that the calibration worked out for the four other groyne-cases is consistent and is used for correcting GC250L and GC420L as well.

NB – When the recalibrated velocities of the micro-propeller are calculated, we consider that the calibration laws are unbiased and therefore do not introduce a new uncertainty. After [Bally and Berroir \[2008\]](#), if uncertainties of the data on the y-axis of the calibration law are all equal, the coefficients of the calibration law are independent from the uncertainty. In our situation, uncertainties are almost constant, as a consequence we decide to neglect the uncertainty on the coefficient of the calibration law.

Conclusion of Part II

Objectives of the thesis require measurements of a complete data-set of flows with or without groyne set on the floodplain of a compound channel.

During the first year and a half of the PhD-thesis, we performed several improvements of the flume settings for improving the quality of measurements.

- * The separated inlets and outlets discussed in [Bousmar et al. \[2005\]](#); [Proust \[2005\]](#) were made durable in order to guarantee the reproducibility of our experiments.
- * The filling systems, one by subsection, were then entirely changed and replaced by new pipes, new pumps and new flow-meters. The new pumps are able to deliver regulated discharges thanks to a regulator slaved to the flow-meters.
- * A metal frame was built around the flume to support the measuring devices. The traversing device has been automated and is commanded through the software LabVIEW. Thanks to this automation, measuring devices can be displaced in the horizontal directions through a predefined mesh in the computer, without any external interventions of the experimenter.
- * The flow-meters and the positions of the traversing devices are recorded through an acquisition card also commanded by LabVIEW (sampling frequency of 50 Hz).

Improvements were also made on the available metrology.

- * Water depths were measured using one or two ultrasonic probes fixed on the traversing device instead of using an electronic point gauge.
- * In addition to the micro-propeller, a Pitot tube was used for measuring velocity in shallow flow conditions and an acoustic Doppler velocimeter (ADV) was set up for turbulence measurements.
- * Friction was directly measured using a Preston tube.
- * Geometry of recirculation zones were evaluated using a video-camera and the LSPIV technique.

Excepted for the LSPIV and the ADV, all the measuring devices were commanded by LabVIEW and statistics of the measured times-series were directly recorded using the acquisition cards. Measurements with ADV were manually performed. Thanks to statistics of measurements, uncertainties on measuring devices were first calculated and uncertainties on most of the parameters we need for describing the flow processes in our experiments were then deduced.

Some large uncertainties were identified for some components of the velocity and turbulence (lateral velocities are more uncertain than the longitudinal velocities, ...). We therefore decided to post-process these data in order to limit or reduce these biases.

- * Computation of the surface velocities indicates that the optimised parameters chosen for the LSPIV calculation enable to evaluate with accuracy the geometry of the recirculation zones.

- * Considering the number of velocity measurements in a water column, only the trapezoidal integration scheme can be used for calculating the depth-averaged velocity. For a question of mathematical coherency with the depth-averaged velocity, the discharges are worked out with the same integration scheme.
- * ADV measurements must be corrected before being used for calculating Reynolds stresses. The additional variance in the measured signal which is due to bad reflections in the sampling volume is corrected with a method adapted from *Goring and Nikora* [2002]. In addition, the over-estimation of the lateral velocities must be corrected by rotating the ADV measurements.
- * For spectral analysis, it is recommended to use the method developed by *Hurther and Lemmin* [2001] for correcting the noise at high frequencies.
- * The systematic errors on the micro-propeller velocities must be corrected using the despiked ADV-velocities. Recalibration laws for the micro-propeller are calculated by comparing ADV and micro-propeller velocities together. Resulting recalibration laws enable a physical correction.

Once the bibliography and the metrology are presented, the results of this thesis are then exposed and discussed in the following part.

Part III

Experiments and analyses

5

Reference flows

Developing flows in straight compound channel

5.1 Introduction

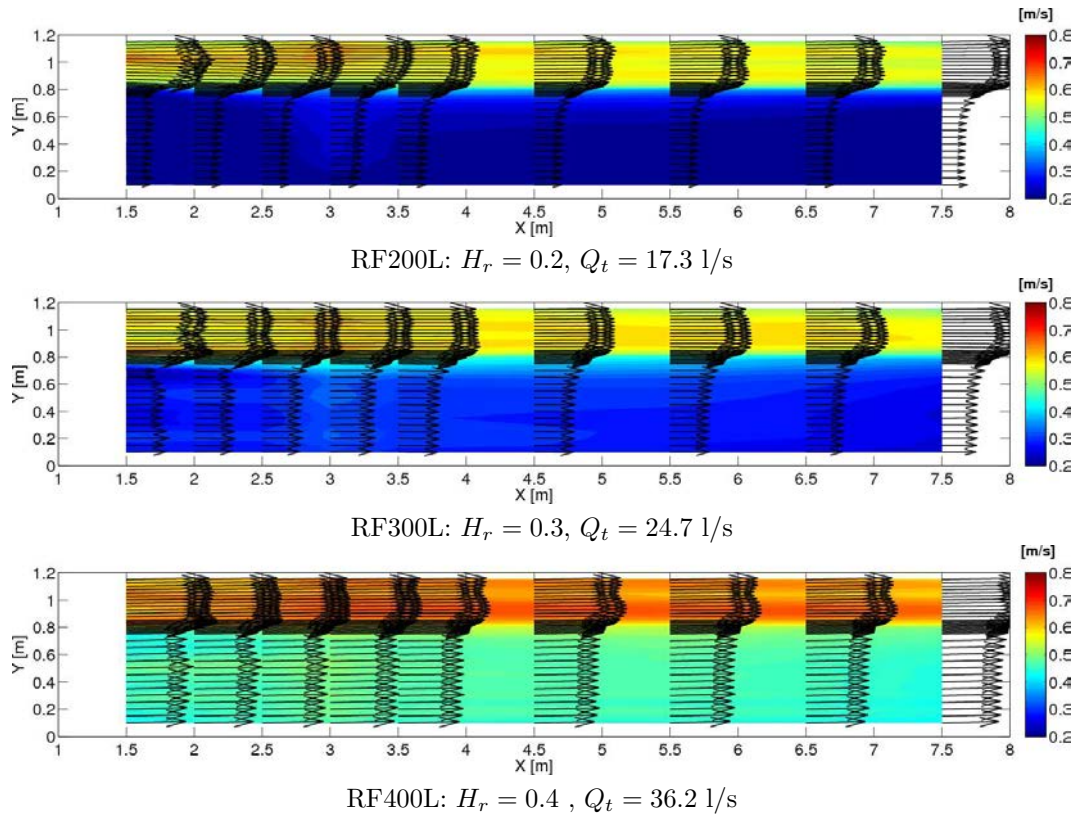


Figure 5.1 – Depth-averaged velocity field (U_d, V_d) and colour map of the velocity norm $\sqrt{U_d^2 + V_d^2}$ of flows measured under reference flow conditions.

This chapter deals with flows without groyne set onto the floodplain, the so-called “reference flows” (see description of the flow setting in Table 3.3). The discharge distributions to inject at the inlets were those measured by Proust [2005] and the tailgates were set up in order to get an equality between the slope of the free surface and the slope of the flume. Resulting relative depths were close to $H_r = 0.2$, 0.3 and 0.4 and mass exchanges between subsections and within subsections were weak (see the direction of the depth-averaged velocity in Figure 5.1 for instance). In Chapters 6, 7 and 8, these flows, close to uniform flow conditions, are used as reference states to be compared to flows with the same boundary conditions but destabilized by a groyne set on the floodplain.

Measurements emphasize that despite the very fine set-up of the upstream and downstream boundary conditions, the three reference flows are developing flows. The shortness of the flume, the inlets, the outlets and the topography of the flume are all responsible for this flow development. Nevertheless, the innovative boundary conditions of the LMFA flume (see §3.2.3) enable for some hydraulic parameters to be established at ± 2.5 % of a particular mean value in some parts of the flow (Table 5.4). We can therefore define various criteria of flow establishment which depend on the complexity of the considered hydraulic parameters.

In this chapter, we first make a detailed description of one reference flow-case: RF300L ($Q_t = 24.7$ l/s, $H_r \approx 0.3$). The effects of the boundary conditions and bottom topography on the development of the depth and velocity in a subsection are first evaluated. Mass exchange is then identified through the discharge measured in the floodplain. The characteristics of the mixing layer developing at the interface are then presented; the link between the geometrical characteristics and the turbulence is discussed. Streamwise and spanwise distributions of the boundary shear stresses are also analysed. Their variations out of the mixing layer are related to the variation of the velocity at the flume bottom, while in the mixing layer, variations are related to the turbulence produced by the shear layer. The effects of the variation in the total discharge are furthermore evaluated for RF200L ($Q_t = 17.3$ l/s, $H_r \approx 0.2$) and RF400L ($Q_t = 36.2$ l/s, $H_r \approx 0.4$). Differences or similarities with RF300L are exposed. To finish, segments of establishment of the various measured flow-parameters are given and a short paragraph is dedicated to the definition of a less restrictive way for defining the uniformity of a flow for field or experimental studies.

5.2 Setting up of the flow conditions for the reference flows

In this section, we show that using the discharge distributions previously measured by [Proust \[2005\]](#) and the appropriate tailgate settings, the distributions of the water depth and of the discharge ratio in the floodplain reach a plateau long of 3.5 meters in both the main channel and the floodplain. By only using these two flow parameters for verifying the uniformity of our reference flows (like generally performed in the literature [[Ancey, 2009](#); [Chow, 1959](#)]), we could be therefore tempted to affirm that our reference flows are established where the plateaus are reached. Nevertheless, we will show in the subsequent sections, that these plateaus in the distributions of the discharge and depth are not a sufficient condition for considering that a flow is plainly established.

NB – In this PhD, we consider that a plateau is reached in a data-cloud, when the dispersion of the considered data is contained within an interval equal to ± 2.5 % of the mean value of the distribution. This interval of $\pm 2.5\%$ corresponds to a low relative error and was arbitrarily chosen. This interval is slightly greater than the relative uncertainties on depth, level and velocity measurements and it enables to have a unique criteria for roughly estimated if a flow parameter is established or not.

The total discharges and the discharge distributions used for our reference flows (see Table 3.3) were previously estimated by [Proust \[2005\]](#) in the same flume as the one used in this PhD-thesis (see §3.2): the total discharges ($Q_t = 17.3$ l/s, 24.7 l/s and 36.2 l/s) and the discharge ratios in the floodplain (13.9 % for RF200L, 25.5 % for RF300L and 38.7 % for RF400L) were chosen such as the relative flow depths, with the appropriate tailgate settings, were equal to $H_r = 0.2$, 0.3 and 0.4 in the most length of the flume.

The tailgates in the present experiments were adjusted such as the streamwise mean-slopes of the water surface ($S_{ws,fp,x}$ and $S_{ws,mc,x}$) – estimated between $x = 2$ m and $x = 5.5$ m – in the floodplain and in the main channel were close to the streamwise mean-slope of the bottom

($S_{o,x} \approx 1.8$ mm/m). Notice that, the levels of the water surface measured at $x = 1.5$ m and downstream of $x = 5.5$ were excluded from the zone to fit because of the inlet conditions (Figures 3.3.a and 3.3.c-d) and because of the backwater effects generated by the tailgates, that induce strong variations in the water depth (Figure 5.2).

The water levels $z(x, y)$ were measured according to the mesh displayed in Figure 3.7.a and they were referenced relative to a reference plan, whom origin was located at $x = 7.5$ m and $y = 1.15$ m in the main channel (see §3.3.3). The levels were then averaged in a subsection in order to estimate the longitudinal mean slope of the free surface in each channel using a linear least-square method. The slopes of the water surface and the coefficients of determination (R^2) are given in Table 5.1. The comparisons with the bottom mean slope ($S_{o,x} \approx 1.8$ mm/m) indicate that the slopes of the free surface for RF200L and RF400L are equal to the bottom slope the uncertainty left aside and the slopes of RF300L are slightly smaller.

Name	Free surface slope $S_{ws,i,x}$ [mm/m]		Coefficient of determination R^2 [-]	
	Floodplain	Main channel	Floodplain	Main channel
RF200L	1.53 ± 0.36	1.70 ± 0.36	0.96	0.96
RF300L	1.34 ± 0.36	1.21 ± 0.36	0.92	0.90
RF400L	1.63 ± 0.36	1.52 ± 0.36	0.90	0.91

Table 5.1 – Comparisons between fits of the water levels and fits of the bottom under reference conditions. Uncertainties on the regression coefficient are calculated using [Bally and Berroir \[2008\]](#).

Once the settings of the tailgates were validated, the mean water depths in a subsection H_i were worked out by subtracting the mean levels of the bottom to the mean levels of the water surface (Figures 5.2.a and 5.2.c). The mean water depths in the floodplain and in the main channel are established between $x = 2$ m and $x = 5.5$ m. They are indeed within ± 2.5 % of $\langle H_i \rangle_{x \in [2 \text{ } 5.5]}$ as highlighted by the relative deviations displayed in Figures 5.2.b and 5.2.d ($100 \times (H_{fp} - \langle H_{fp} \rangle_{x \in [2 \text{ } 5.5]}) / \langle H_{fp} \rangle_{x \in [2 \text{ } 5.5]}$).

The discharge distributions in the flume were finally calculated using the measurements of local water depths and local depth-averaged longitudinal velocities. Discharge ratii in the floodplain are displayed in Figure 5.3.a for the three reference flows. A plateau is reached from $x = 3.5$ m to $x = 7.5$ m (red plain line in Figure 5.3.a). In addition, in Figure 5.3.b (relative deviation of the discharge in the floodplain relative to the mean value calculated from $x = 3.5$ m to $x = 7.5$ m $\langle Q_{fp} \rangle_{x \in [3.5 \text{ } 7.5]}$) the comparisons of the data with the value of the plateau indicate that variations of the discharge in the floodplain is within ± 2.5 % of $\langle Q_{fp} \rangle_{x \in [3.5 \text{ } 7.5]}$ from $x = 3.5$ m to $x = 7.5$ m.

Both results on the water depth and on the discharge confirm that the required distance to have an establishment of these parameters can be reduced by directly injecting the right discharge distribution at the inlet through the use of independent tanks for each subsection in the flume. The minimal length of $35 \times B_{fp}$ [[Bousmar et al., 2005](#)] to ensure that the depth and the discharge distribution are established when using a single tank, is drastically reduced. This new type of inlets therefore enable to study “quasi-established” flows in short compound open-channels: the distance from the inlet of the first “established” cross-section is indeed equal to $2.5 \times B_{fp}$ for the water depth and is equal to $4.4 \times B_{fp}$ for the discharge.

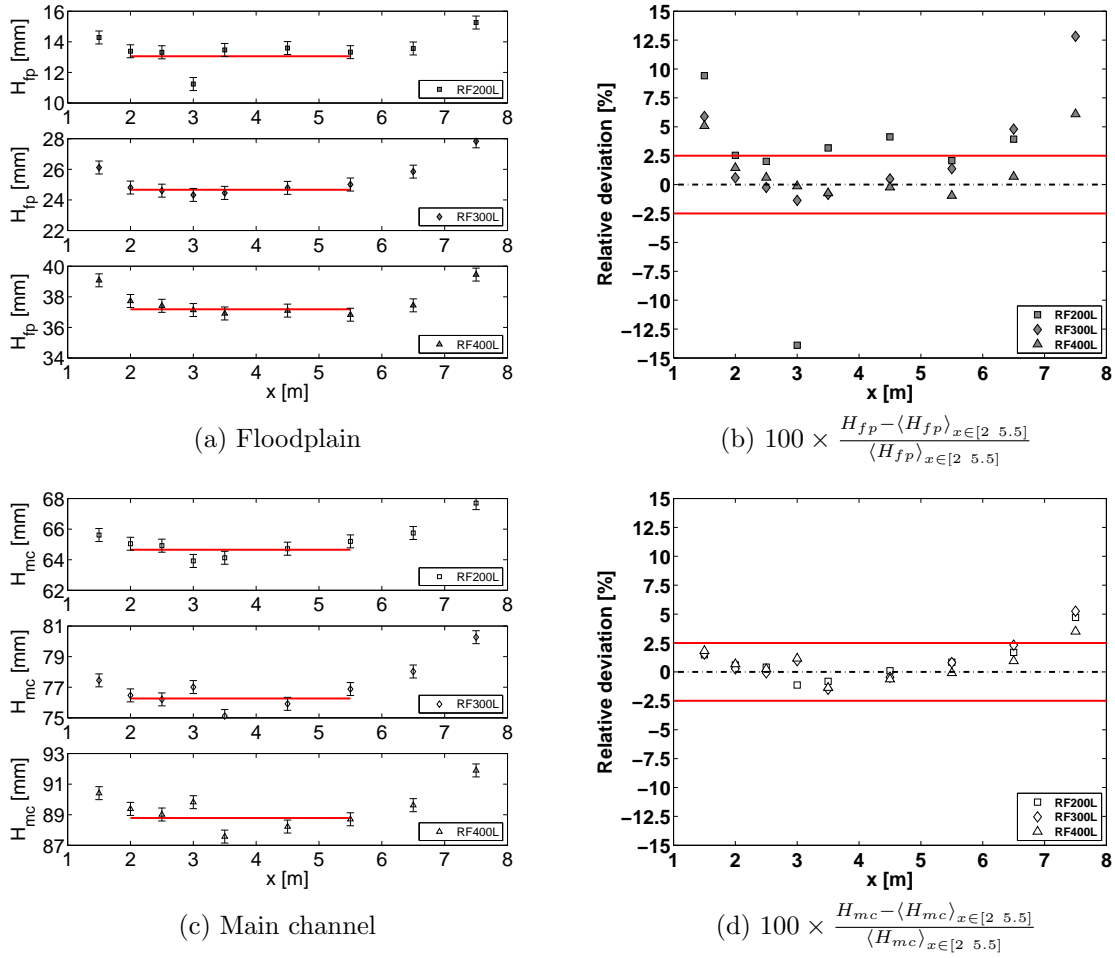


Figure 5.2 – Streamwise variations in mean water depth in a subsection for the three reference flows. Uncertainty on H_i : $\delta H_i = \pm 0.42$ mm. The red plain line represents the mean water depth between $x = 2$ m and $x = 5.5$ m.

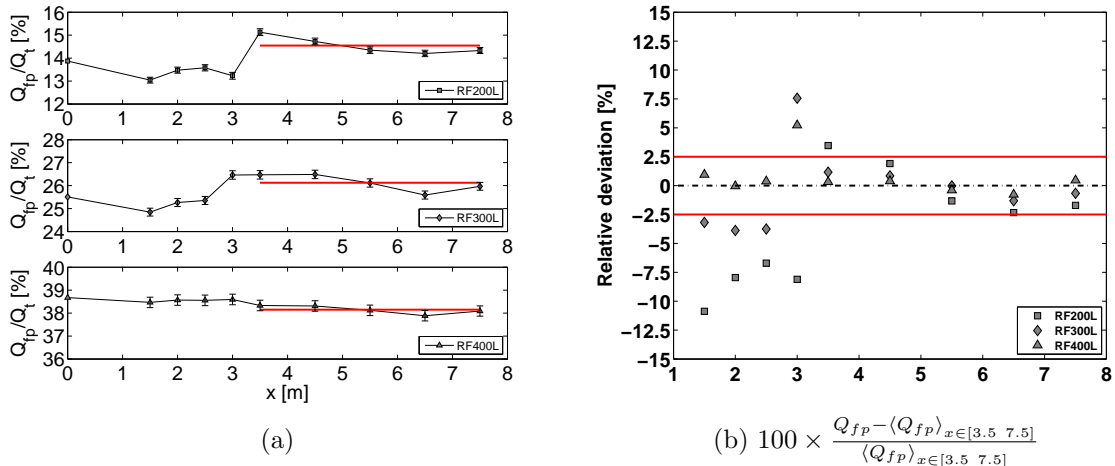


Figure 5.3 – Discharge ratio in the floodplain for reference flows (uncertainty on Q_{fp} : $\delta Q_{fp}/Q_{fp} = \pm 5$ % of Q_{fp}). RF200L: $H_r = 0.2$ and $Q_t = 17.3$ l/s, RF300L: $H_r = 0.3$ and $Q_t = 24.7$ l/s and RF400L: $H_r = 0.4$ and $Q_t = 36.2$ l/s. Red plain lines represent mean values $\langle Q_{fp} \rangle_{x \in [3.5, 7.5]}$.

5.3 Effects on the flow of the flume set-up

5.3.1 Effects of boundary conditions on depths and velocities in a subsection

Despite the attention devoted to boundary conditions, the mean water depths are clearly affected by effects coming from the inlets and outlets. As shown in Figures 5.2.a and 5.2.c (diamond markers), the water depths for in the floodplain H_{fp} and in the main channel H_{mc} at $x = 1.5$ m are indeed in average 1 mm higher than the mean value calculated with data between $x = 2$ m and $x = 5.5$ m, while from $x = 6.5$ m to the end of the flume, the absolute deviation relative to the mean value is in average 4 mm higher. Effects of the backwater curves coming from the two tailgates are thus 4 times greater than the inlet effects.

In addition, considering the relative deviation of the water depth in a subsection relative to the mean value (diamond markers in Figures 5.2.b and 5.2.d), it results that the boundary effects more affect the depths in the floodplain than in the main channel. Thus, excepted at $x = 7.5$ m, depths in the main channel are all within ± 2.5 % of the mean value $\langle H_{mc} \rangle_{x \in [2 \ 5.5]}$, while in the floodplain, only data between $x = 2$ m and $x = 5.5$ m are within ± 2.5 % of $\langle H_{fp} \rangle_{x \in [2 \ 5.5]}$.

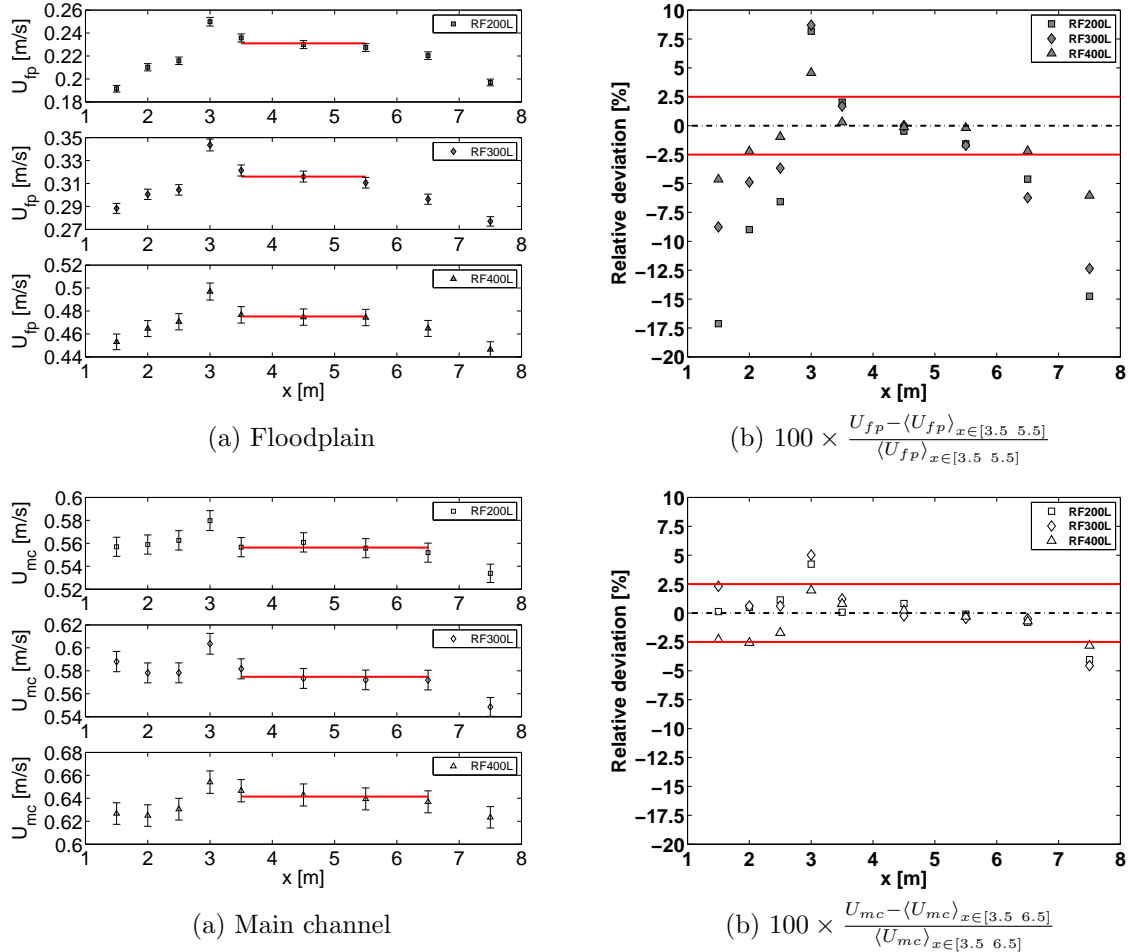


Figure 5.4 – Streamwise variations in mean velocities in a subsection for the three reference flows. Uncertainty on U_i : $\delta U_i/U_i = \pm 1.5$ %. The red plain line represents the mean velocity between $x = 3.5$ m and $x = 5.5$ m in the floodplain and between $x = 3.5$ m and $x = 6.5$ m in the main channel.

Effects of boundary conditions are also felt on the velocity. In Figures 5.4.a and 5.4.c (diamond markers), the mean longitudinal velocities in a subsection are compared with their mean values calculated with data from $x = 3.5$ m to 5.5 m for the floodplain and from $x = 3.5$ m to 6.5 m for

the main channel. In the floodplain, the flow accelerates on the three first meters of the flume ($+0.03$ m/s from $x = 1.5$ m to $x = 3.5$ m), then reaches a plateau of two meters long and finally decelerates until the tailgate (-0.04 m/s from $x = 5.5$ m to $x = 7.5$ m). In the main channel, the flow acceleration is smoother ($+0.01$ m/s from $x = 2$ m to $x = 3.5$) and the plateau is one meter longer than the floodplain one, but the flow deceleration at the end of the main channel is similar to the floodplain one. As for the water depth, effects of the tailgates are more felt than the inlets ones.

Similarly to water depths, the considerations on the relative deviation of the velocities in a subsection relative to their corresponding mean values emphasize that the boundary conditions affect more the flow in the floodplain than in the main channel. In the floodplain, only velocities between $x = 3.5$ m and $x = 5.5$ m are within ± 2.5 % of $\langle U_{fp} \rangle_{x \in [3.5 \ 5.5]}$, while in the main channel only data at $x = 7.5$ m are out of the interval.

As a partial conclusion, the tailgate settings were a bit too high, therefore generating a backwater curve felt until $x = 5.5$ m and because of the shallowness of the floodplain flow, effects of the backwater curve in the floodplain were stronger than in the main channel. Concerning inlets, they introduce less distortions in the flow than tailgates and these distortions are mainly due to:

1. The float laying on the free surface at the entrance of the flume constricts the flow upstream of the float and induces an expansion downstream of the float.
2. As shown by [Proust et al. \[2009\]](#), a slight variation in the water depth is responsible for mass exchange between the main channel and the floodplain (see §5.3.3).
3. The particular inlet and especially the grids at the entrance generate a plunging flow during the first two meters of the flume, resulting in an increase in the boundary shear stress magnitudes (see §5.4.3) and therefore in a rise in water depth.

5.3.2 Effects of the bottom topography

In Figure 5.5, the measurements of the bottom levels – referenced relative to the reference plan defined in §3.3.3 – indicate a ridge of ≈ 2 mm high in the floodplain and a smaller ridge of ≈ 1 mm high between $x = 3$ m and $x = 3.5$ m in the main channel.

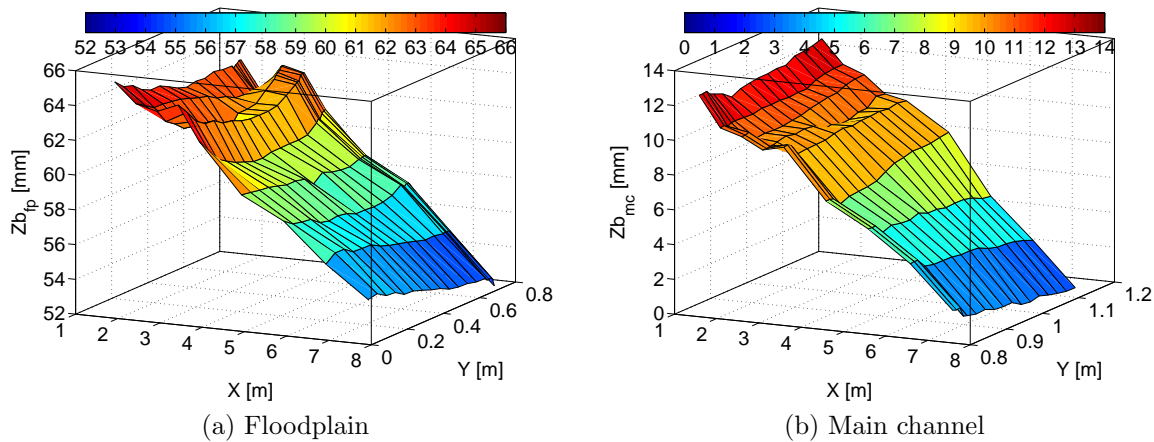


Figure 5.5 – Bottom levels of the LMFA flume. Uncertainty on z : $\delta z = \pm 0.42$ mm.

Effects of the ridge on the water depth and flow velocity is even weaker than the water depth is important. Moreover, the ridge have bigger impact on the velocity than on the depth. As seen in Figure 5.2, water depths for RF300L at $x = 3 - 3.5$ m are 1 mm smaller than the mean

depth in a subsection. Nevertheless, variations in depth are within the interval of ± 2.5 % of $\langle H_i \rangle_{x \in [2.5, 5]}$. By contrast, for the velocity in a subsection, consistent variations are observed. Thus, in Figure 5.4, the velocity in the floodplain (resp. in the main channel) in the ridge cross-section is 7.5 % (resp. 5 %) greater than the mean velocity. This rise in velocity is the consequence of the reduction of the flow section by the ridge. However, the consideration of the upstream flow – the latter accelerates because of (1) the development of the mixing layer at the interface and (2) the establishment of the discharge distribution between channels – prevents from concluding that the ridge is only responsible for the strong rise in velocity.

5.3.3 Mass exchange

The settings of the upstream and downstream boundary conditions, as the ridge at $x = 3$ m, distort the distributions of the depth and velocity, which consequently impact the discharge distribution in the flow because mass exchanges are generated.

Under the reference flow conditions, the lateral velocities are very low ($\bar{v} \approx 0.005$ m/s) and uncertainties (≈ 50 % of \bar{v}) do not enable to have significant observations on the direction and intensity of mass exchange. The discharge ratio in the floodplain is then used to give information about mass exchange.

In Figure 5.3.a, the discharge ratio in the floodplain is displayed for the three reference flows from $x = 0$ m to $x = 7.5$ m. The inlets and the ridge at $x = 3$ m induce mass exchange in the first three meters of the flume. The higher the total discharge is and the lower mass exchange is. The maximum deviation relative to the mean discharge in the floodplain is thus found for RF200L at $x = 1.5$ m, where $Q_{fp} \approx -11$ % of $\langle Q_{fp} \rangle_{x \in [3.5, 7.5]}$ (Figure 5.3.b). Downstream of the ridge, these exchanges then rapidly reduce until the end of the flume. As shown in Figure 5.3.b, from $x = 3.5$ m to the end of the flume, the discharges in the floodplain are all within ± 2.5 % of the mean discharge $\langle Q_{FP} \rangle_{x \in [3.5, 7.5]}$.

NB – The comparison of the injected discharge at the floodplain inlet (see Figure 5.3.a at $x = 0$ m) with the mean discharge in the floodplain between $x = 3.5$ and $x = 7.5$ m indicates some slight differences with the discharge to be injected determined by Proust [2005]. These differences are attributed to the evolution of the flume characteristics with years: different topography in 2005 and tailgates that were not as evolved as in the present experiment (the apron of the tailgate generated recirculations at the upstream face of the tailgates that affected the flow distribution at the end of the flume).

5.4 Detailed description of a reference flow: RF300L

In the following chapters, reference flows are compared with flows with a groyne set on the floodplain. A complete description is therefore needed for defining a state of reference to be compared with.

By just checking levels and discharge ratios in the floodplain, reference flows could be considered as established from at least $x = 3.5$ m to $x = 5.5$ m (see §5.2). Nevertheless, in the following sections, we will show that an establishment of the discharge distribution and water depth is not a sufficient condition for concluding about the uniformity [Ancy, 2009; Chow, 1959] of a flow in a straight compound channel. Despite the good setting up of flows (§5.2), the boundary conditions, the topography variations and the turbulent nature of the flow indeed imply that some hydraulic parameters more evolved than levels or discharge ratios significantly vary between some cross-sections. It then results that reference flows are actually developing flows in most

of the length of the flume and only little segments of flow in the middle of the flume can be considered as established.

In this section, the flow description is focused on one flow-case: RF300L (*i.e.* $H_r = 0.3$, $Q_t = 24.7$ l/s and $Q_{fp}/Q_t = 25.5$ %). Impacts of the boundary conditions and flume topography on the depths and velocities are first resumed using the Froude number. The nature and the development of the turbulence is then discussed. Finally, boundary shear stress distribution is evaluated and the cause of its streamwise evolution is discussed.

5.4.1 Main flow features

In this subsection, we show how the main flow features through the description of the flow in term of Froude number are distorted by the boundary conditions and the ridge on the bottom of the flume at $x = 3$ m, thus preventing the possibility to get an establishment of the flow along the whole length of the compound channel.

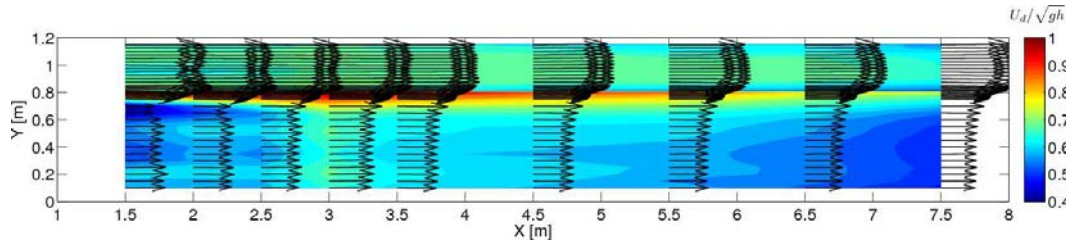


Figure 5.6 – Froude number distribution for RF300L. Maximal uncertainty on the Froude number: $\delta Fr \approx \pm 10$ %.

Analyses are done using the distribution in the flume of the Froude number, which is a quite sensitive parameter (see in Figure 5.6 with $Fr = U_d / \sqrt{gh}$ calculated with the local depth h and the longitudinal depth-averaged velocity U_d). It incorporates both the variations of water depths and flow velocities and amplifies their variations when they are of opposite directions. It results that the Froude number is a good mean for synthesizing the effects of the topography and boundary conditions on the flow.

Whether in the main channel or in the floodplain, because of the rather steep slope of the flume ($S_{o,x} = 1.8$ mm/m), the Froude number is always bigger than 0.50 ($Fr \approx 0.70$ in the main channel, $Fr \approx 0.60$ in the floodplain) and is critical near the interface between the main channel and the floodplain. The critical transition is due to the strong rise in velocity in the floodplain-side of the shear layer developing at the interface separating the main channel and the floodplain.

Study of the streamwise distribution of the Froude number for RF300L also emphasizes three zones where the Froude number significantly varies, therefore pointing out locations where the depth and the velocity are not established. Thus, as shown in Figure 5.6, the Froude number significantly varies in the vicinity of the inlets, outlets and around $x = 3 - 3.5$ m in the floodplain; absolute variations in Froude number within these cross-sections can reach 0.1. Moreover, the floodplain is more affected than the main channel. The zone where the Froude number is nearly constant is shorter in the floodplain (between $x = 3.5$ m and $x = 5.5$ m) than in the main channel (between $x = 3.5$ m and $x = 6.5$ m).

5.4.2 Analysis of the turbulence

5.4.2.1 Geometrical characteristics of the mixing layer developing at the interface between channels

The difference in depth and velocity between channels is responsible for the development of a mixing layer at the interface separating the floodplain and the main channel. An inflection point is indeed present in the lateral profile of longitudinal velocities (Figure 5.7) and induces an instability that results in the generation of planform macro-vortices [van Prooijen *et al.*, 2005]. The mixing layer is then a zone of shear where momentum is transferred from one channel to another, which as for the depth and the velocity needs a certain distance to establish.

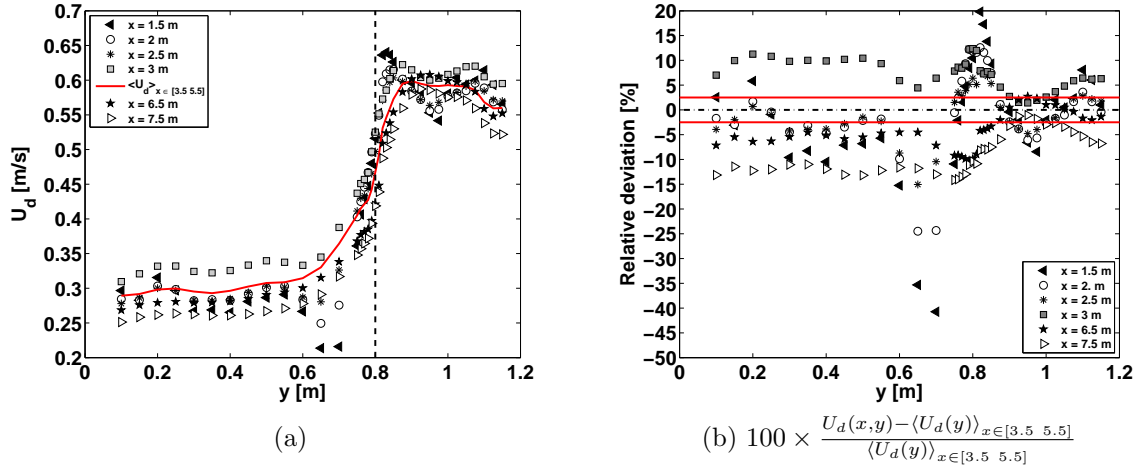


Figure 5.7 – Depth-averaged velocities for RF300L in various cross-sections: mixing layer development. Uncertainty: $\approx 1.5\%$ of the measured value.

Due to the separated discharge injection and the discharge distribution at the inlet, the mixing layer for RF300L only needs 3 meters to be almost developed in term of velocity distribution across the channel. The difference in velocity between channels and the velocity gradient at the interface are almost equilibrated and do not evolve between subsections. Thus, as shown in Figure 5.7.a, the lateral profiles of longitudinal depth-averaged velocity – displayed for cross-sections where $U_d(x, y)$ is not within $\pm 2.5\%$ of $\langle U_d(y) \rangle_{x \in [3.5, 5.5]}$ (Figure 5.7.b) – indicate that the velocity from $y = 0.6$ m to the interface strongly increases from $x = 0$ m to $x = 3$ m, while the velocity from the interface to $y = 0.9$ m decreases. This local behaviour of the velocity emphasizes local mass exchange and transfer of momentum from one channel to another in order to reach an equilibrium in the lateral velocity profile at the interface.

Using measurements of the depth-averaged velocities, the geometrical characteristics of the mixing layer developing at the interface (lateral width δ and location of the centre y_c) are then defined using the classical formulation proposed by Pope [2000] (for other formulations see §1.2.2). The width is worked out as follow:

$$\delta = y_{90\%} - y_{10\%} \quad (5.1)$$

where $U_d(y_{10\%}) = U_2 + 0.10(U_1 - U_2)$ and $U_d(y_{90\%}) = U_2 + 0.90(U_1 - U_2)$ with $U_1(x) = \langle U_d \rangle_{y \in [0.9, 1.15]}$ (resp. $U_2(x) = \langle U_d \rangle_{y \in [0.1, 0.6]}$) the cross-sectional velocity in the main channel (resp. in the floodplain) outside the mixing layer. The centre of the mixing layer y_c corresponds to the location where $U_d(y_c) = U_2 + 0.50(U_1 - U_2)$.

The width of the mixing layer δ for RF300L is displayed in Figure 5.8.a. Results first emphasize that δ strongly rises from the beginning of the flume to $x = 3$ m (*i.e.* the zone where velocity around the interface is equilibrating between subsections) and then, in the zone where weak mass exchange is observed and velocity profiles are well balanced, the width stabilizes until

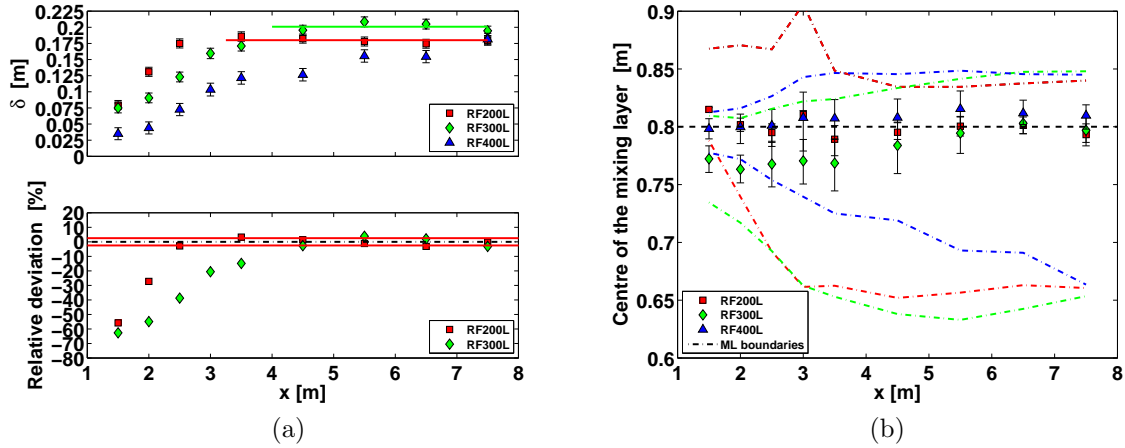


Figure 5.8 – (a) Streamwise evolutions of the mixing layer width δ . (b) Streamwise positions of the centre of the mixing layer y_c .

$x = 7.5$ m. Comparison of $\delta(x)$ with the mean value ($\langle \delta \rangle_{x \in [4.5, 7.5]}$) in Figure 5.8.a indicates that data dispersions is within ± 2.5 % of $\langle \delta \rangle_{x \in [4.5, 7.5]}$ from $x = 4.5$ m to $x = 7.5$ m; *i.e.* the width is established from $x = 4.5$ m to $x = 7.5$ m. Results also highlight that the use of separated inlets and then the injection of the appropriate discharge distribution enable to accelerate the development of the mixing layer in term of velocity distribution in the flume and geometry. Indeed, when considering a single injection, the discharge distribution requires a long distance to equilibrate [Bousmar *et al.*, 2005] and therefore, the mixing layer needs an ever longer distance to establish.

The centre of the mixing layer y_c is displayed in Figure 5.8.b. It is located within an interval of 3 cm at the floodplain-side of the interface, the uncertainties left aside (Figure 5.8.b). Contrarily to mixing layers in single channel [Uijtewaalt and Booij, 2000], in compound channel the centre tends to conserve the same position all along the flume: just above the interface (*i.e.* at $y = 0.8$ m). This difference between single and compound channels is due to the floodplain step that separates the main channel from the floodplain. Thus, in a single channel, with the development of the mixing layer, the centre y_c is deviated towards the zone with the smallest velocity, this, until the velocity distribution in the flume becomes homogeneous, while in a compound channel, the velocity profiles, once established, remain the same because of the floodplain step that imposes the velocity difference between channels and the velocity gradient as well, therefore inducing that $U_d(y_c)$ is constant and localized at the same position all along the flume.

Unlike for y_c which almost has the same position all along the flume, the outer boundaries of the mixing layer (dash-dotted lines in Figure 5.8.b) indicate that the developing and then the developed mixing layer is asymmetrical. The largest part of the mixing layer is located in the floodplain (≈ 70 %) and the biggest growth rate of the outer boundary is found in the floodplain as well: $dy_{90\%}/dx \approx 0.03/7$ m/m in the main channel and $dy_{90\%}/dx \approx 0.1/7$ m/m in the floodplain. This result is consistent with the literature [Sellin, 1964; Tamai *et al.*, 1986] and this asymmetry is a consequence of the difference in depth between the main channel and the floodplain that affects the symmetry of the coherent structures usually observed in mixing layers in single channel. According to van Prooijen *et al.* [2005], the lateral component of the velocity in the back and front of the structure is directly proportional to $1/H_i(y)$: thus *considering the motion within a single vortex in a simplified way, it can be seen that the transverse component of the velocity of the coherent structure at the front (downstream part) is in the direction from the main channel onto the shallow floodplain. In view of continuity the transverse component of the velocity of the coherent structure will therefore increase roughly inversely proportional to the local water depth $1/H_i(y)$. In the same way, it can be argued that the transverse component of the velocity of the coherent structure at the back (upstream-side) of the coherent structure*

will decrease proportionally with $1/H_i(y)$ (the sketch of this concept is given in Figure 1.9 [van Prooijen et al., 2005]).

5.4.2.2 Turbulence in the mixing layer

The Reynolds shear stress was first measured in 5 cross-sections at only one elevation in order to identify the maximum of shear in the flow (Figure 5.9.a; elevation of measurement is referenced relative to the floodplain mean depth). It results that τ_{xy} is maximal in the mixing layer and this extreme value is located in the centre y_c of the mixing layer, the uncertainty left aside.

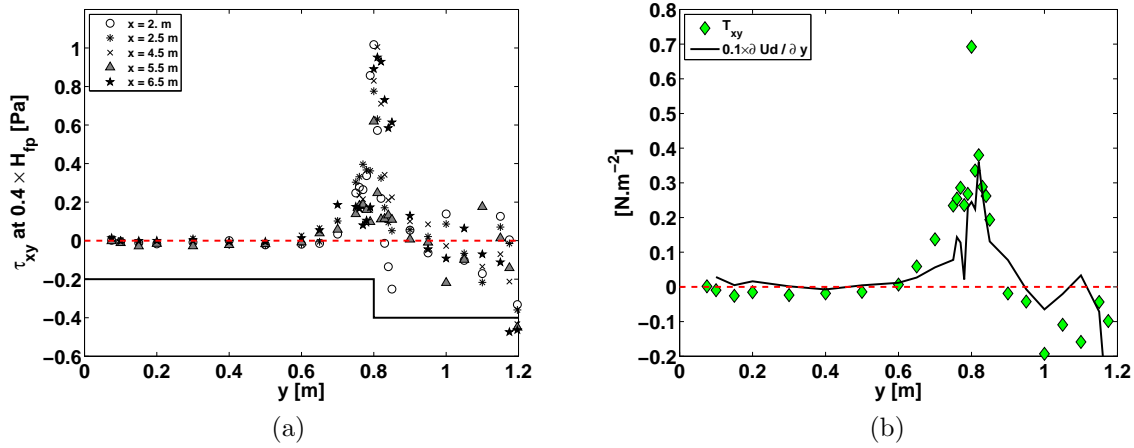


Figure 5.9 – (a) Reynolds shear stress τ_{xy} for RF300L at $0.4 \times H_{fp}$ (uncertainty not estimated). (b) Link between Reynolds shear stress T_{xy} and lateral gradient of longitudinal velocity $a \times \frac{\partial U_d}{\partial y}$ (with $a = 0.1 \text{ m}^2/\text{s}$).

Depth-averaged Reynolds stresses were furthermore assessed in one cross-section at $x = 5.5 \text{ m}$. The cross-section was carefully chosen where the mixing layer is established in term of width calculated with U_d (Figure 5.8.a).

The comparison of T_{xy} with $a \times \partial U_d / \partial y$ ($a = 0.1 \text{ m}^2/\text{s}$) in Figure 5.9.b emphasizes a strong correlation between both parameters. Variations of the gradient confirm that the shear produced in the mixing layer is mostly caused by the local velocity gradient generated by the floodplain step. The Boussinesq hypothesis (Equation 2.38) can be then used for flow in prismatic compound channel; it results that the simple knowledge of the velocity distribution enables to have a first estimation of the turbulence in the flow. It remains now whether this assumption works for flows with an embankment set on the floodplain.

As the shear within the mixing layer is the most powerful in the flume, the depth-averaged Reynolds stresses were measured at y_c for several streamwise positions in order to give consistent information about the establishment of the depth-averaged Reynolds stresses in the flume. The analysis of the depth-averaged Reynolds stresses $T_{xx,int}$, $T_{yy,int}$ and $T_{xy,int}$ (calculated with four points on the vertical) displayed in figure 5.10 thus indicates that they evolve from the beginning of the flume to $x = 3.5 \text{ m}$ and they then stabilize until the last measurement cross-section at $x = 7.5 \text{ m}$. An established segment for the depth-averaged Reynolds stresses can be then defined between $x = 3.5 \text{ m}$ and $x = 6.5 \text{ m}$ (Figure 5.10.d). Nevertheless, since uncertainty on turbulence measurements was not assessed, results about establishment of depth-averaged Reynolds stresses must be considered with care. The ADV probe did not enable a correct estimation of the noise in the turbulence measurements; the fourth probe of the ADV was indeed not operative and the method for denoising the data proposed by Hurther and Lemmin [2001] could not be therefore completely applied on the measured data.

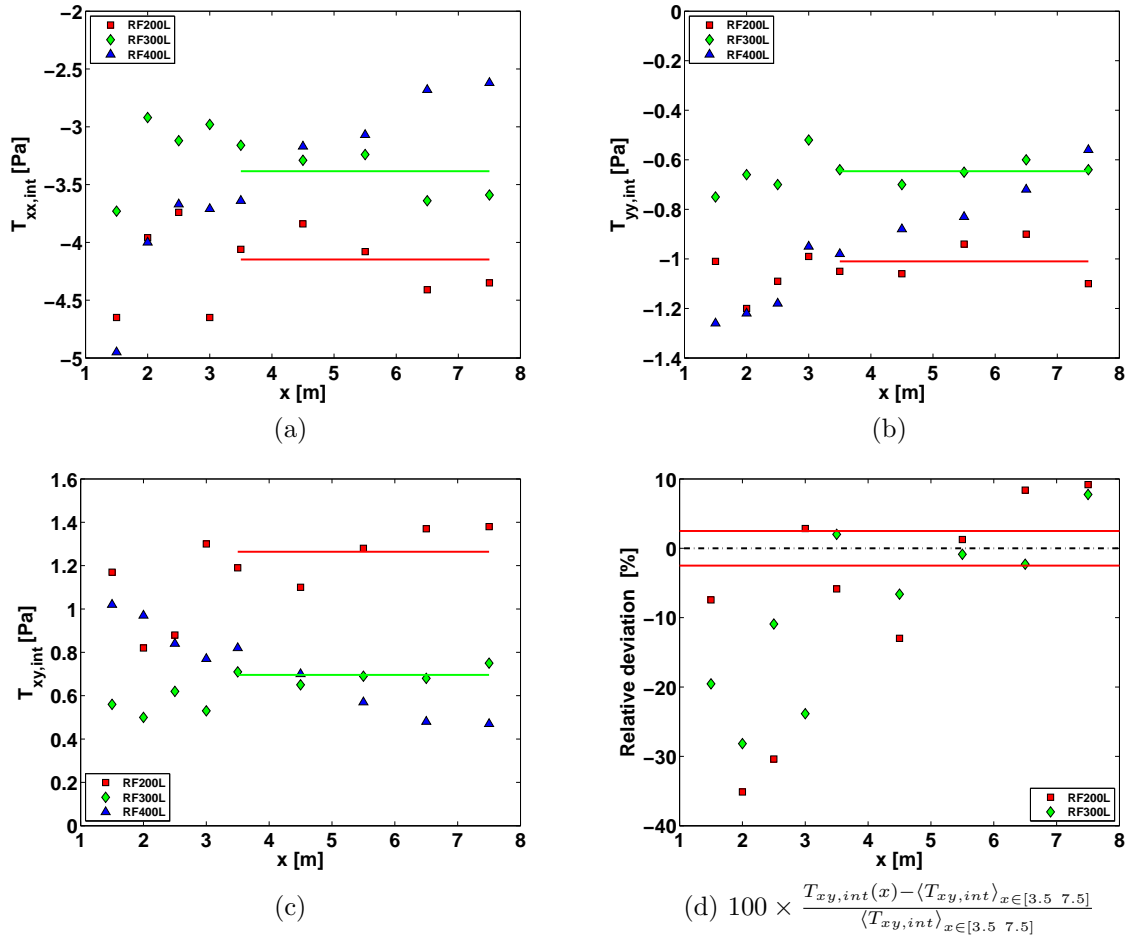


Figure 5.10 – Depth-averaged Reynolds stress at y_c : (a) $T_{xx,int}$, (b) $T_{yy,int}$ and (c) $T_{xy,int}$ for reference flows (RF200L, RF300L and RF400L). Uncertainty is not estimated.

5.4.2.3 Turbulence out of the mixing layer

The spanwise evolutions of the depth-averaged Reynolds shear stress at $x = 5.5$ m are displayed in Figures 5.11.a-c. Out of the mixing layer, in the floodplain, T_{xy} is close to zeros and T_{xx} so as T_{yy} are constant and maximum. In the main channel behaviours are less clear, because two effects are at least present in the channel. The focus on the depth-averaged Reynolds shear stress T_{xy} for RF300L in Figure 5.11.c indeed emphasizes that in addition to the mixing layer at the interface, a boundary layer develops along the main channel side-walls ($y = 1.2$ m). The boundary layer is 5 cm wide and distorts the Reynolds stresses distribution until the centre of the main channel.

The level of turbulence in the flow is then assessed using the “depth-averaged” turbulent intensity I_k (Equation 5.2) [Chassaing, 2000a; Nezu and Nakagawa, 1993]:

$$I_k = \frac{\sqrt{u'^2_d + v'^2_d}}{\sqrt{U_d^2 + V_d^2}} \quad I_x = \frac{\sqrt{u'^2_d}}{U_d} \quad I_y = \frac{\sqrt{v'^2_d}}{U_d} \quad (5.2)$$

As shown in Figure 5.11.d, the turbulent intensity in the mixing layer is between 10 % and 14 % of the depth-averaged velocity. According to Nezu and Nakagawa [1993], such an intensity well indicates an high level of turbulence, as expected in a zone of turbulence production. In the main channel and in the floodplain, the turbulent intensity is equal to 10 % of the depth-averaged velocity in the floodplain and 7 % in the main channel, which is a bit milder than in the

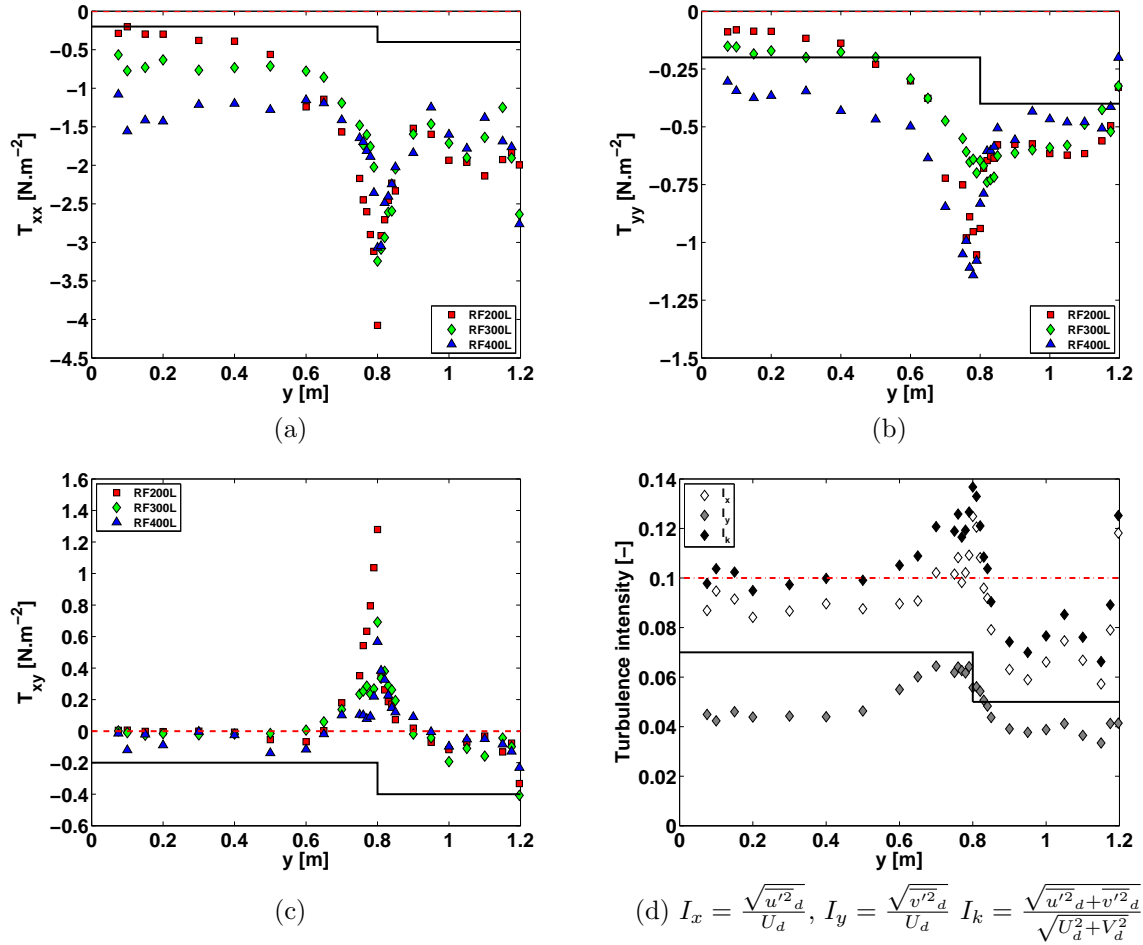


Figure 5.11 – Lateral distribution of depth-averaged Reynolds stresses (a) T_{xx} , (b) T_{yy} and (c) T_{xy} in one cross-section for reference flows. (d) Lateral distribution of depth-averaged turbulent intensity.

mixing layer, but is still considered as an high level of turbulence. This high level of turbulence in the flow is probably generated by the inlet grids (see in §3.2.3), that introduce an additional turbulence compared to a configuration without grids.

The longitudinal “depth-averaged” turbulent intensity I_x and the lateral “depth-averaged” turbulent intensity I_y displayed in Figure 5.11.d finally confirm that the fluctuating velocities in the flow do not contribute to turbulence at the same level; $\overline{u'^2_d}$ (*i.e.* u') indeed contributes in average to 80 % of the turbulence in the flow, while $\overline{v'^2_d}$ (*i.e.* v') only contributes to 20 % since $\overline{w'^2_d} = 0$. This result indicates that the turbulence at $x = 5.5$ m is mostly one-dimensional and is oriented in the x-wise direction.

5.4.2.4 Coherent structures in the mixing layer

In the previous paragraphs, we observed at least two zones of shear in the flow, (1) in the mixing layer at the interface between channels and (2) in the wall-boundary layers at the main channel side-wall. In these shear layers, especially at the interface, the no-slip condition at the bottom leads emergence of a wall-generated turbulence with a characteristic length scale proportional to the water depth, while the transverse motion may contain length scales largely greater than the water depth, resulting in large-scale motion restricted to the horizontal plane and recognised by a correlation that extends over a long time span [Uijtewaal and Booij, 2000] (Figure 5.12). *These planform vortices have significant influence on the transverse mass exchange*

and momentum transfer, which is important for example for the dispersion of pollutants and for sediment transport [van Prooijen and Uijttewaalt, 2002].

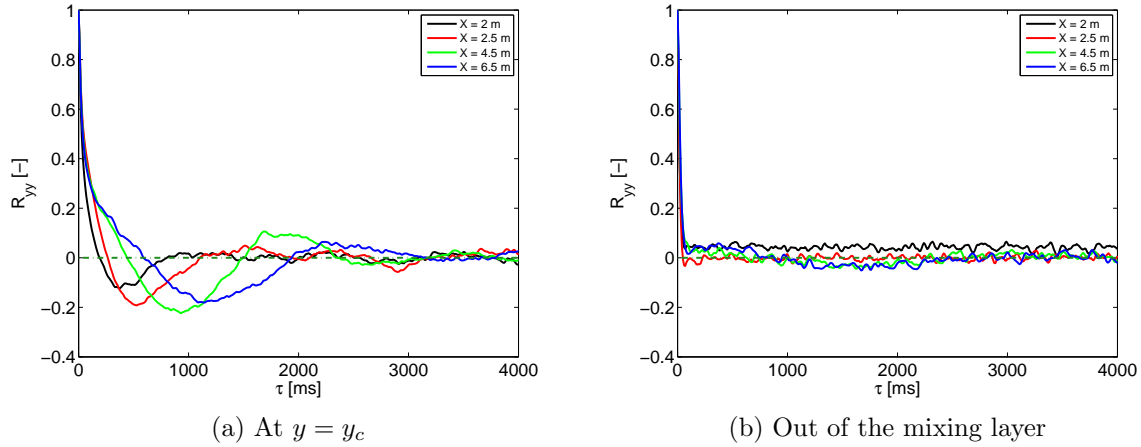


Figure 5.12 – Streamwise evolution of the autocorrelation function of lateral velocity at $0.6 \times H_{fp}$ (a) in the centre of the mixing layer y_c and (b) at $y = 0.3$ m for RF300L.

Due to the 3 minutes long time-series of ADV measurements in the shear layer at the interface (see §3.3.4.3: Measurement characteristics), the autocorrelation function of the lateral velocities at $0.6 \times H_{fp}$ in the centre of the mixing layer y_c and at $y = 0.3$ m were calculated with Equation 5.3 for RF300L:

$$R_{yy}(A, \tau) = \frac{\overline{v(A, t)v(A, t + \tau)}}{\overline{v(A, t)v(A, t)}} \quad (5.3)$$

where A represents the coordinates of the measurements used for calculating the autocorrelation function and τ is the time span.

The comparisons of the autocorrelation functions in and out the mixing layer (Figures 5.12.a and 5.12.b) thus indicate that the correlation extents until 2 s at $x = 2$ m and 3.5 s at $x = 6.5$ m in the mixing layer, while out of the mixing layer, the correlation reaches zero after only 0.1-0.5 s; in addition, the characteristic time of the modulations is equal to 2-3 s in the mixing layer and is not quantifiable outside. The free stream in the floodplain mainly contains small-scale structures, while the mixing layer is mainly settled by large structures. Moreover, while the small scale turbulence does not significantly evolves with increasing downstream positions, the correlation time as the characteristic time of modulation clearly increase in the mixing layer, therefore highlighting a growth of the large-scale structures.

The cross-power spectrum densities S_{xy} and the phase relation ϕ were then calculated for assessing the wave-numbers of the structures that contribute to the shear in the flow. The power spectrum densities S_{xx} and S_{yy} were also worked out for determining the nature of the coherent structures. The methods for calculating the spectral densities are exposed in §4.7.

The power spectrum densities in Figures 5.13.a and 5.13.b are first discussed. Except at $x = 2$ m for S_{xx} , large structures for RF300L yield a peak in both lateral and longitudinal power spectrum densities. Amplitude gradually varies and the wave-number of the maximum is shifted towards low wave-numbers: this confirms that the characteristic length-scale of the large structures increases with increasing downstream direction. Moreover, the high-wave number side of the peaks has a slope of ≈ -3 . According to Batchelor [1969]; Lindborg [1999], the -3 slope indicates that the large-scale structures possess 2D characteristics, therefore indicating low effects on the mixing layer of the turbulence coming from the bottom.

The cross-power spectrum density and phase relation in Figure 5.13.c then confirm that the large 2D structures are mainly responsible for the momentum transfer across the mixing layer. Peaks of S_{xy} and S_{yy} coincides: the motion at low wave-numbers (between $] 5 \text{ m}^{-1} \text{ } 20 \text{ m}^{-1} [$)

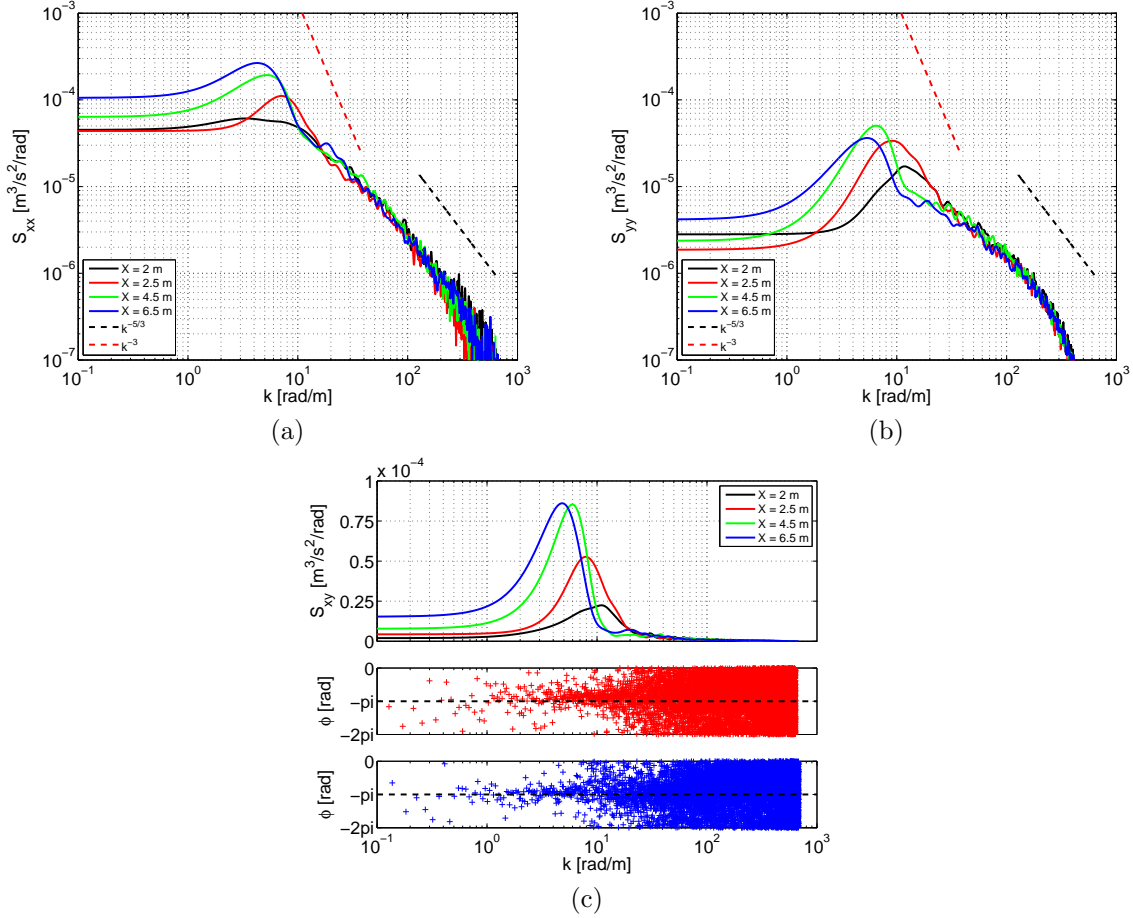


Figure 5.13 – Streamwise evolution of (a) longitudinal power spectrum densities S_{xx} , (b) transversal power spectrum densities S_{yy} and (c) cross-power spectrum density S_{xy} and phase relation ϕ of the instantaneous velocity component u and v measured at $0.6 \times H_{fp}$ in the centre of the mixing layer y_c for RF300L.

is the main contributor to the shear. This result is also confirmed by the phase relation which indicates values of $-\pi$ until the descending edge of the peaks and a random phase beyond. According to *Tennekes and Lumley* [1972], a $-\pi$ phase corresponds to a zone of turbulence production.

5.4.3 Boundary shear stress

Boundary shear stresses were measured using a Preston tube (§3.3.5). We recall that the boundary shear stress is a general appellation regrouping the bottom shear stress measured on the horizontal bottom of the flume and the wall shear stress measured on the lateral walls of the flume. Moreover only solid boundaries are considered for calculating boundary shear stresses in a subsection.

5.4.3.1 Distribution of boundary shear stresses across the flume

Boundary shear stresses for RF300L are displayed in Figure 5.14.a and they are compared to the 2D value $\rho g h S_{o,x}$ in Figure 5.14.b. The particular way of representation of τ_b in Figure 5.14.b was inspired by *Shiono and Knight* [1991]. This enables to evaluate how the flow is retarded or accelerated relative to a uniform flow in a wide single channel of same slope $S_{o,x}$ far from the lateral banks [*Chow*, 1959].

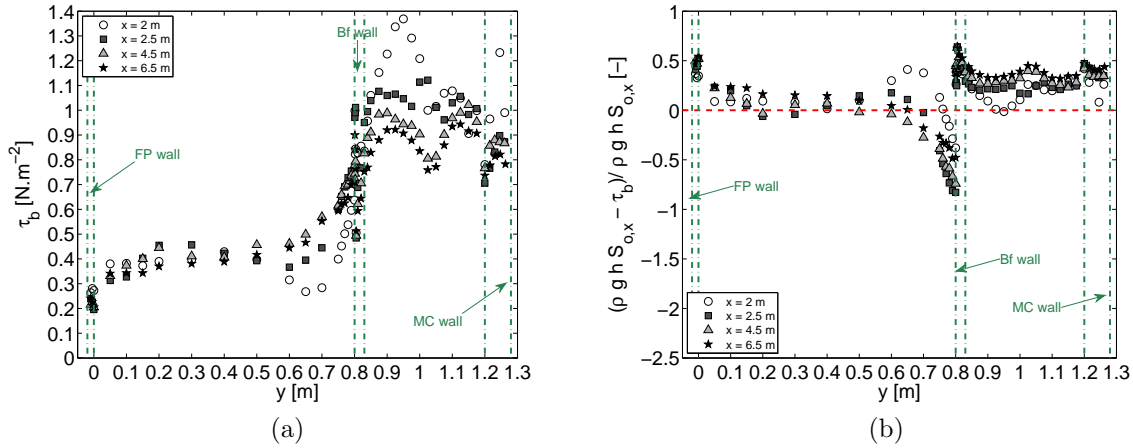


Figure 5.14 – Spanwise distribution of boundary shear stresses for reference flow RF300L. Data within the green lines correspond to measurements on the vertical walls. Uncertainty: $\delta\tau_b/\tau_b = 6\%$.

The spanwise distribution of boundary shear stress is consistent with previous measurements in straight compound channel (§1.2.3). Boundary shear stresses in the floodplain are lower than in the main channel and a local maximum is present in the floodplain-side of the interface between both channels. This local maximum is a consequence of the turbulent shear in the mixing layer that enhances the local turbulence. Moreover, comparison with the 2D value $\rho g h S_{o,x}$ (Figure 5.14.b) indicates that the flow is accelerated in the floodplain-side of the mixing layer and is decelerated in the rest of the cross-section. The flow is globally decelerated relative to a flow in a single channel of same slope $S_{o,x}$ and same hydraulic radius.

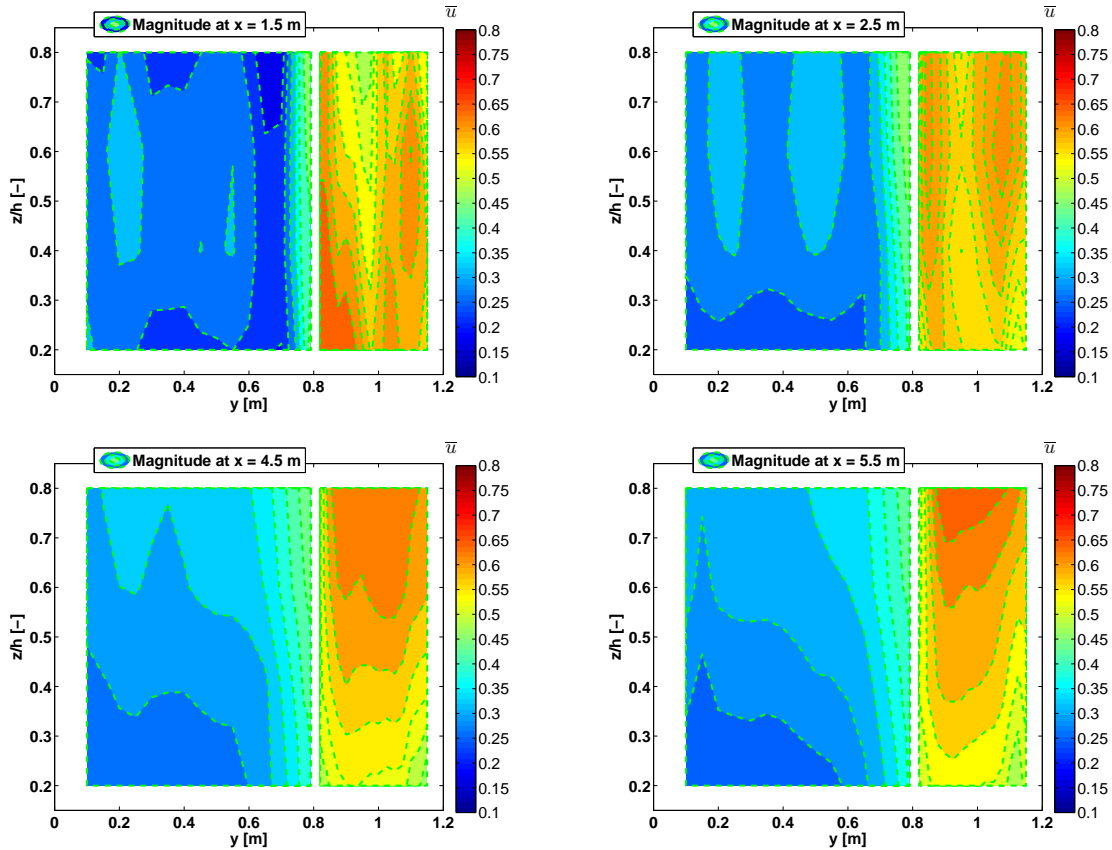


Figure 5.15 – Isolines of longitudinal velocities in four cross-sections ($x = 1.5$ m, 2.5 m, 4.5 m and 5.5 m) for reference flow RF300L ($H_r = 0.3$, $Q_t = 24.7$ l/s).

Concerning the streamwise distribution of boundary shear stress, measurements are quite new and to the author knowledge, no occurrence of a similar work can be found in the literature. Results first emphasize that boundary shear stresses in the floodplain, from $y = 0$ m to $y = 0.6$ m, are stabilized, the uncertainty left aside (Figure 5.14.a), while a deficit in friction, that progressively reduces with increasing downstream position, is present from $y = 0.6$ m to the interface ($y = 0.8$ m). In the main channel, the boundary shear stress reduces by 16 % from $x = 2$ m to $x = 4.5$ m.

The evolution of the boundary shear stress in the vicinity of the interface between channels must be directly linked to the developing mixing layer and especially to the shape of the lateral profile of longitudinal depth-averaged velocity in Figure 5.7.a. By contrast, the variability of the boundary shear stress in the main channel must be rather linked to velocity close to the bottom, where $\bar{u}|_{\text{near the bottom}} \approx u_*$ ($\approx u_*$ the friction velocity), because $\tau_b = \rho u_*^2$. As shown in Figure 5.15, where vertical profiles of \bar{u} are plotted for various streamwise positions, the inlet condition in the main channel initiates a plunging flow and therefore a decreasing in the square of the velocity close to the bottom of 15 % between $x = 2$ m to at least $x = 4.5$ m.

5.4.3.2 Towards an establishment of the boundary shear stresses?

According to [Chow \[1959\]](#), under uniform flow conditions, the boundary shear stress measurements are consistent if the boundary shear force and the gravity force per unit of length are balanced in the total cross-section:

$$\rho g A_t S_{o,x} - \int_0^{P_t} \tau_b \cdot dl = \rho g A_t S_{o,x} - P_t T_{b,t} = 0 \quad (5.4)$$

where A_t is the total wetted area, P_t is the total wetted perimeter, dl is an element of the wetted perimeter and $T_{b,t}$ is the boundary shear stress computed in a total cross-section.

The force balance between gravity force and boundary shear force per unit of length are resumed in Table 5.2:

x	$\rho g A_t S_{o,x}$ [N/m]	$P_t T_{b,t}$ [N/m]	$100 \times \frac{T_{b,t}}{\rho g R_t S_{o,x}}$	$100 \times \frac{T_{b,fp}}{\rho g R_{fp} S_{o,x}}$	$100 \times \frac{T_{b,mc}}{\rho g R_{mc} S_{o,x}}$
2 m	0.89	0.86	96.45	34.65	61.80
2.5 m	0.89	0.86	97.36	38.73	58.63
4.5 m	0.89	0.84	94.34	41.13	53.21
6.5 m	0.92	0.79	86.66	37.14	49.52

Table 5.2 – Boundary shear force (column 3) and gravity force (column 2) per unit of length in a total cross-section for RF300L. Percentage of completion of the force balance in a total cross-section (column 4). Percentage of shear in FP (column 5) and in MC (column 6) without considering the additional shear generated at the interface between channels.

The force balance in Table 5.2 is completed at ≈ 5 % from $x = 2$ m to $x = 4.5$ m and only completed at ≈ 15 % at $x = 6.5$ m. First considerations on these results could indicate that boundary shear stresses are at least established from $x = 2$ m to $x = 4.5$ m. Nevertheless, analysis of the percentages of shear in the floodplain and in the main channel (*i.e.* $100 \times T_{b,i} / \rho g R_i S_{o,x}$, with $i = mc$ or fp) indicates a different result. If the percentage of shear in the floodplain is relatively stable and is similar to the one observed by [Knight and Hamed \[1984\]](#) under uniform flow conditions for an aspect ratio $B/B_{mc} = 3$, a strong decreasing tendency is observed in the main channel. Let see here an effect of the flow deceleration at the bottom main channel and of the increase of the water depth due to the backwater curve coming from the tailgates (Figure 5.2). Boundary shear stresses cannot be considered as established.

5.5 Effects of a change in the total discharge

In the previous sections, we studied in detail the way the reference flow-case RF300L was distorted by the boundary conditions and the flume geometry. We also showed that despite RF300L is a developing flow, some hydraulic parameters can be considered as established in a zone located in the middle of the flume (between $x = 3.5$ m and $x = 5.5$ m).

In this section, effects of a change in the total discharge are analysed using the three reference flows investigated for this PhD-thesis (RF200L, RF300L and RF400L). The purpose is to identify the limiting conditions for generating a quasi-established flow in a short compound channel with separated inlets. The influence of the boundary conditions and flume topography on the Froude distribution are first estimated. The evolution of the turbulence is then discussed. Finally, changes in the boundary shear stress distributions are evaluated and the causes of their streamwise evolution are discussed.

5.5.1 Main flow features

In this subsection, we show how the main flow features (through the Froude number distributions) are impacted by the boundary conditions and bottom topography when increasing the total discharge.

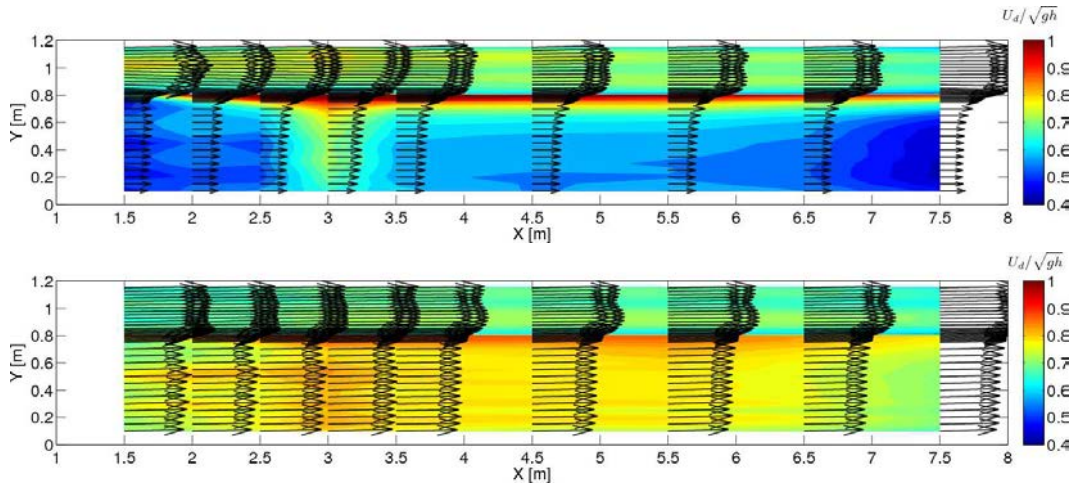


Figure 5.16 – Froude number distribution for RF200L (upper figure) and RF400L. Maximal uncertainty on the Froude number: $\delta Fr \approx \pm 10$ %.

The Froude number distributions in Figure 5.16 indicate that the three distorted zones identified in §5.4.1 for RF300L are also present in the other flow-cases. The absolute variation in Froude number in the vicinity of the inlets and outlets is indeed equal to 0.1 whatever is the total discharge.

The influence of the ridge at $x = 3$ m is inversely proportional to the total discharge. For the shallowest case RF200L ($H_r = 0.2$, $Q_t = 17.3$ l/s) the Froude number in the floodplain is 50 % higher in the vicinity of the ridge than in the other cross-sections. With increasing relative flow depth, the Froude number is 30 % higher for RF300L ($H_r = 0.3$, $Q_t = 24.7$ l/s) and is only 10 % higher for RF400L ($H_r = 0.4$, $Q_t = 36.2$ l/s). In the main channel, the effects of the ridge are weaker.

A zone where the Froude number is established can also be identified for RF200L and RF400L (see in Figure 5.16). This zone is located between $x = 3.5$ m and $x = 5.5$ m in the floodplain and between $x = 3.5$ m and $x = 6.5$ m in the main channel whatever the reference flow.

5.5.2 Analysis of the turbulence

5.5.2.1 Geometrical characteristics of the mixing layer developing at the interface between channels

Similarly to RF300L, the distribution of longitudinal depth-averaged velocities in the mixing layer for RF200L and RF400L needs at least 3.5 meters for equilibrate itself of both sides of the interface (Figure 5.17: between $y = 0.6$ m and $y = 0.9$ m). Momentum transfer is then present in the beginning of the flume and is progressively deleted with increasing streamwise direction.

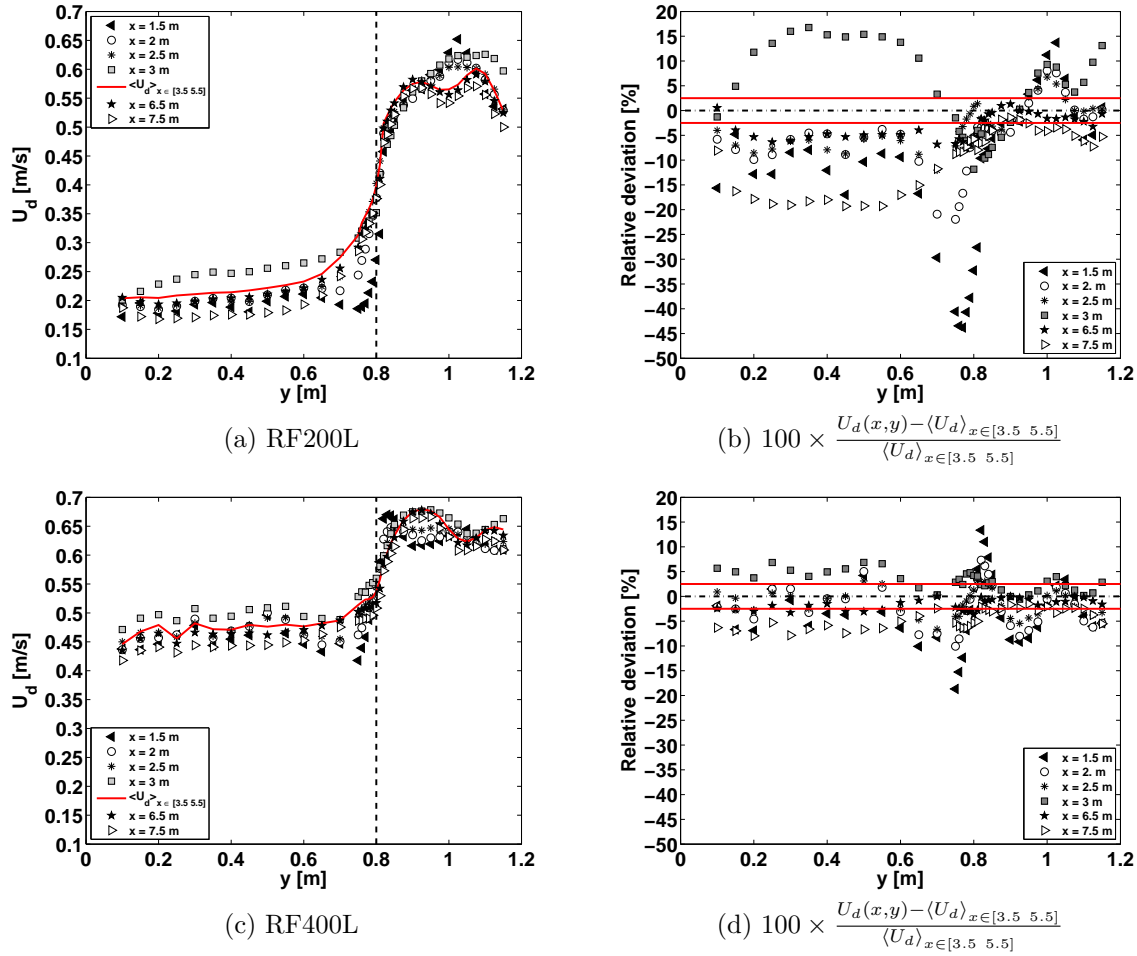


Figure 5.17 – Depth-averaged velocities for RF200L and RF400L in various cross-sections. Uncertainty: $\approx 1.5\%$ of the measured value.

Using the longitudinal depth-averaged velocities and Equation 5.1, the geometrical characteristics of the mixing layers were worked out for RF200L and RF400L (see Figures 5.8.a-b; the mean width of the mixing layer are represented for information in the upper figure in Figure 5.8.a and they are compared with the data in the down figure).

In Figure 5.8.a, the calculation of δ indicates that the mixing layer for RF400L develops until the end of the flume, while for RF200L, it is developed from $x = 3.5$ m. In the first phase of development of the mixing layer, the width of the mixing layer is inversely proportional to the total discharge. In the second phase, where the growth of the mixing layer reduces, the distance of development of the mixing layer gets longer with increasing total discharge. The maximal widths are obtained for RF300L and the smallest for RF400L. *Uijtewaal and Booij [2000]* state that an increase in the shallowness is responsible for a decrease of the characteristic length-scale of the coherent structures in the mixing layer. As RF200L is the shallowest case (see waters in Figure 5.2) the width for RF200L is limited by the shallowness of the floodplain. By contrast,

the fact that the width for RF400L are the smallest is due to the deepness of the flow that induces a small shearing between channels and coherent structures with a smaller characteristic length-scale.

Concerning the centre of the mixing layer y_c in Figure 5.8.b, it is located above the interface between the main channel and the floodplain for each reference flow.

5.5.2.2 Turbulence in the mixing layer

Measurements of the depth-averaged Reynolds shear stresses at the interface $T_{xy,int}$ in Figure 5.10.c finally emphasize that the shear is maximum for RF200L then reduces for RF300L and seems to be minimal at the end of the flume for RF400L. Unlike the relation between the width of the mixing layer and the total discharge (Figure 5.8.a), the relation between the shear and the total discharge is linear. The turbulent shear reduces with increasing total discharge (*i.e.* with increasing relative flow depth).

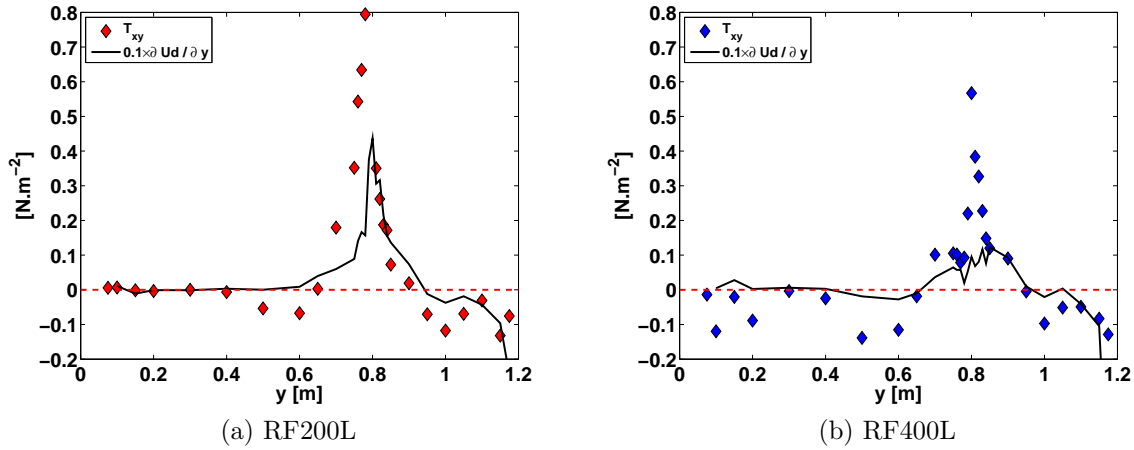


Figure 5.18 – (a-b) Link between Reynolds shear stress and lateral gradient of longitudinal velocity for RF200L and RF400L (T_{xy} vs $a \times \frac{\partial U_d}{\partial y}$ with $a = 1 \text{ m}^2/\text{s}$).

The comparison of the lateral gradient of depth-averaged longitudinal velocity with the depth-averaged Reynolds shear stress for RF200L and RF400L in Figures 5.18.a-b confirms the link between the turbulent shear and the velocity gradient. The turbulent shear can be described using the lateral gradient of the longitudinal velocity.

5.5.2.3 Turbulence out of the mixing layer

The focus on the distribution of depth-averaged Reynolds stress T_{xx} out of the mixing layer for the three reference flows (Figure 5.11.a), indicates that T_{xx} have the same magnitude in the main channel whatever the reference flow is. This must be linked to the depth-averaged velocity in the main channel that weakly evolves with increasing total discharge (Figures 5.7 and 5.17). By contrast, in the floodplain, since the velocity increases with the discharge, the magnitude – in absolute – of the depth-averaged Reynolds stress increases as well.

The analysis of the depth-averaged turbulent intensity I_k (Equation 5.2) of both sides of the mixing layer highlights a decreasing tendency with increasing total discharge (Figures 5.19.a-b and 5.11.d). This result is consistent with the fact that the turbulence production decreases with increasing relative flow depth. Concerning the turbulent intensity out of the mixing layer, it is still high according to the ranges proposed by *Nezu and Nakagawa* [1993]. In the main channel, the turbulent intensity is close to 7 % and does not evolve with increasing total discharge. By

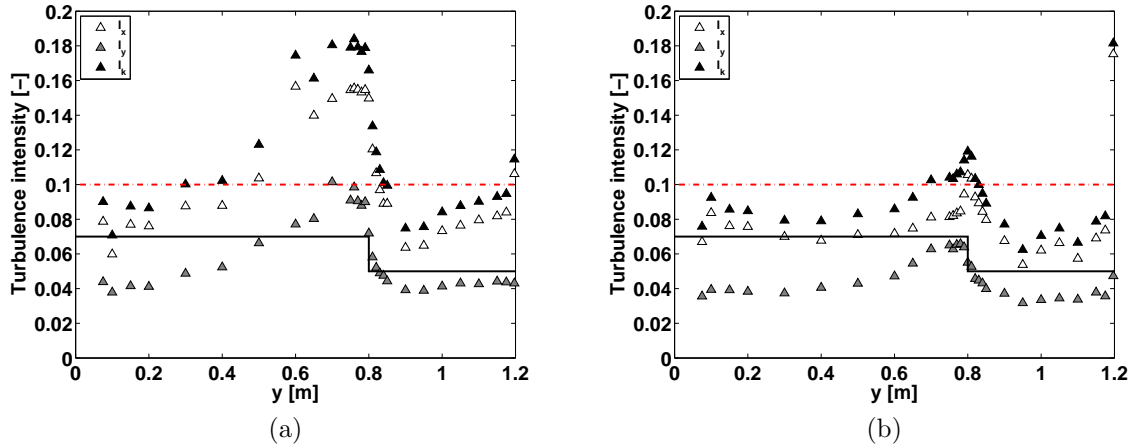


Figure 5.19 – (a-b) Depth-averaged turbulent intensity for RF200L and RF400L.

contrast, in the floodplain, the intensity is inversely proportional to the total discharge (from 12 % in average for RF200L to 8 % for RF400L).

Finally, concerning the weight of the longitudinal turbulence relative to the lateral turbulence, the study of I_x and I_y (see Equation 5.2) indicates that even if I_y remains constant (≈ 4 %) whatever is the reference flow, I_x decreases with increasing total discharge, therefore resulting in an increase in the weight of the lateral turbulence in the flow.

5.5.2.4 Coherent structures in the mixing layer

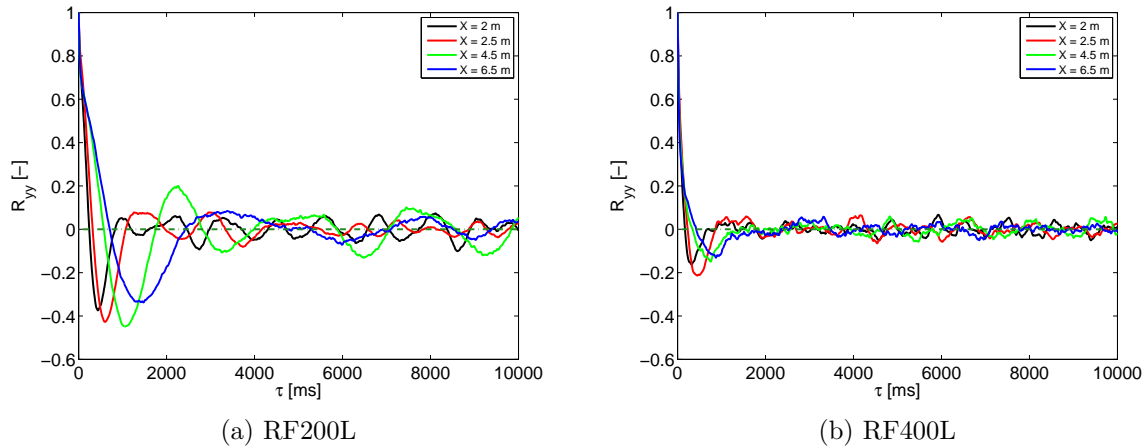


Figure 5.20 – Streamwise evolution of the autocorrelation function of lateral velocity at $0.6 \times H_{fp}$ in the centre of the mixing layer y_c for RF200L and RF400L.

The comparisons of the autocorrelation functions for RF200L and RF400L (Equation 5.3) in Figure 5.20 emphasize that the time span of the autocorrelation function of the lateral velocity reduces with increasing total discharge: *i.e.* the planform vortices reduces in sizes in the flow and are less restricted to develop in the horizontal direction. The spectral analysis in Figures 5.21.c-f confirms this result. The peaks with the -3 slope in the distribution of S_{xx} and S_{yy} indeed tend to disappear with increasing total discharge.

Although, the 2D structures tend to reduce in size with increasing total discharge, the distribution of the cross-power spectrum densities in Figures 5.21.a-b indicate that the shear is still mainly operated by the planform vortices (where $k \in]5 \text{ m}^{-1} 20 \text{ m}^{-1} [$).

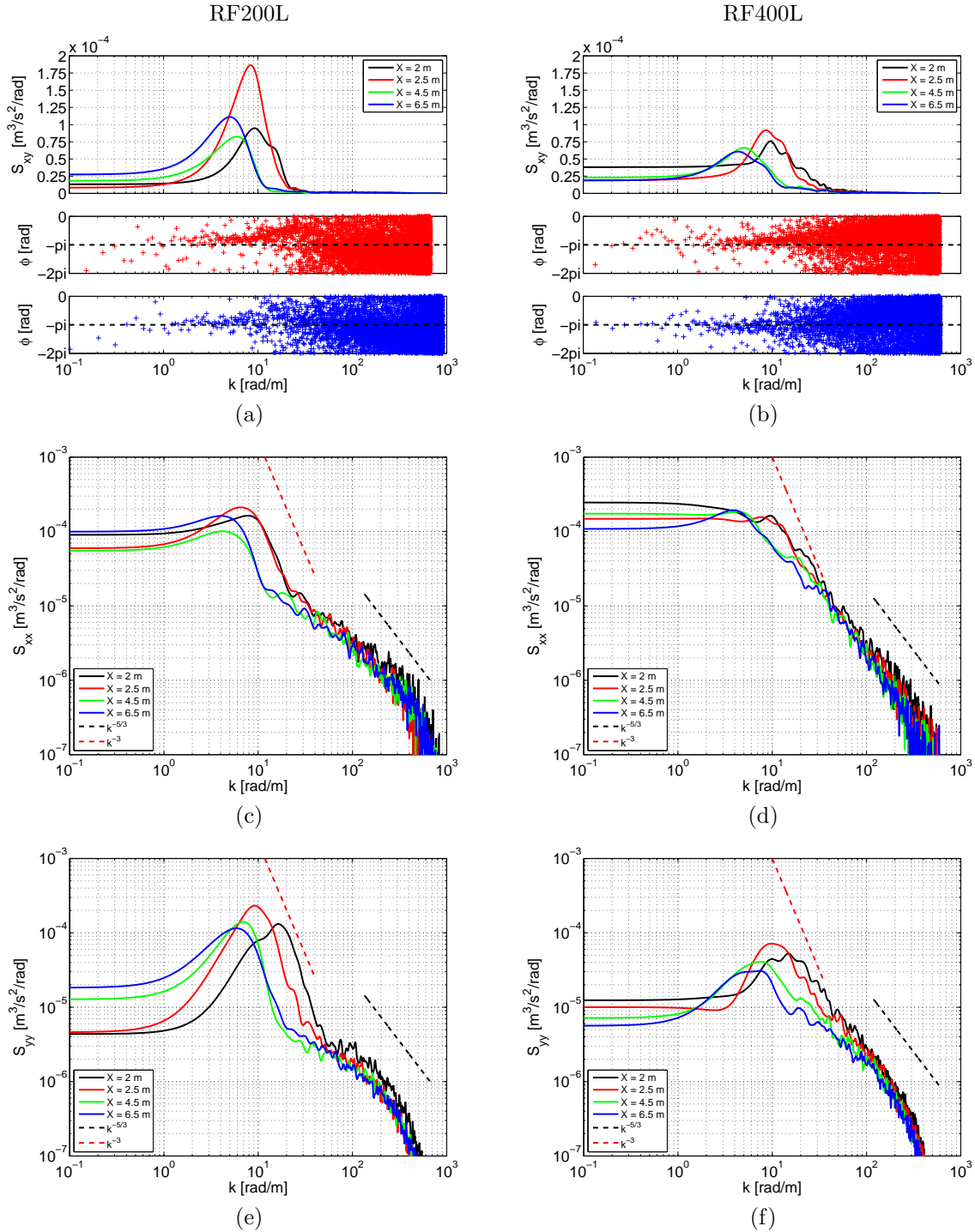


Figure 5.21 – (a-b) Cross-power spectrum density S_{xy} and phase relation ϕ of the instantaneous velocity component u and v . (c-f) Streamwise evolution of the longitudinal and transversal power spectrum densities (S_{xx} and S_{yy}) of the instantaneous velocity component u and v . Measurements are taken at $0.6 \times H_{fp}$ in the centre of the mixing layer y_c for RF200L and RF400L.

5.5.3 Boundary shear stress

5.5.3.1 Distribution of boundary shear stresses across the flume

Boundary shear stresses for RF200L and RF400L are displayed in Figures 5.22.a-b. Boundary shear stress increases with increasing total discharge. This increase is greater in the floodplain than in the main channel, as the increase in velocity in the floodplain is greater than in the main channel when increasing the total discharge. Concerning the local maximum of boundary shear

stress in the floodplain-side of the interface, it tends to reduce with increasing total discharge. This reduction is simply due to the strength of the mixing layer that has also reduced (see §5.5.2.1).

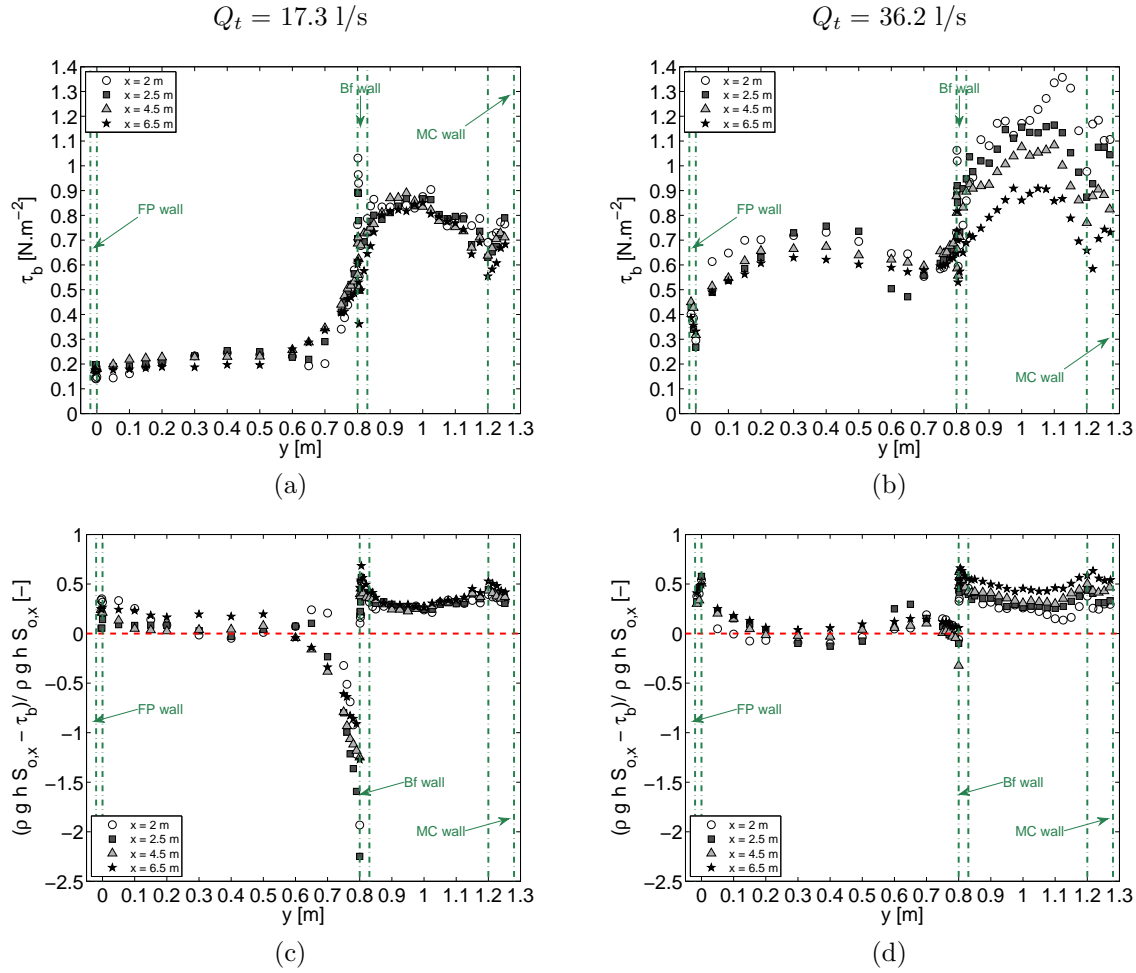


Figure 5.22 – (a-b) Spanwise distribution of boundary shear stresses for reference flows. (c-d) Comparison to the 2D value $\rho g h S_{o,x}$.

Comparison of the boundary shear stress with the 2D value $\rho g h S_{o,x}$ in Figures 5.22.c-d then indicates similar behaviours as for RF300L (Figure 5.14.b). The flow in the centre of the floodplain is almost equilibrated relative to a 2D uniform flow of same slope $S_{o,x}$ (*i.e.* $\tau_b = \rho g h S_{o,x}$), while the flow is decelerated in the main channel (*i.e.* for $Fr < 1$, $\tau_b < \rho g h S_{o,x}$). The flow deceleration in the main channel reduces when increasing the total discharge. Concerning the flow acceleration in the floodplain-side of the mixing layer, it is maximal for RF200L and minimal for RF400L. It results that the global deceleration relative to a flow in a single channel of same slope $S_{o,x}$ and same hydraulic radius reduces with increasing total discharge, as the strength of the mixing layer decrease, therefore limiting the flow dissipation at the interface between channels.

5.5.3.2 Towards an establishment of the boundary shear stresses?

Similarly to RF300L, the force balances (Equation 5.4) between gravity force and boundary shear force per unit of length were calculated for RF200L and RF400L. They are resumed in Table 5.3 and they are displayed in Figure 5.23.

The force balance for RF200L in Table 5.3 is completed at ≈ 5 % from $x = 2$ m to $x = 4.5$ m like for RF300L (Table 5.2) and is only completed at ≈ 13 % at $x = 6.5$ m, while the force

x	$\rho g A S_{o,x}$ [N/m]	$P_t T_{b,t}$ [N/m]	$100 \times \frac{T_{b,t}}{\rho g R_t S_{o,x}}$
RF200L: $H_r = 0.2$ and $Q_t = 17.3$ l/s			
2 m	0.65	0.62	95.00
2.5 m	0.65	0.62	95.15
4.5 m	0.65	0.61	94.56
6.5 m	0.66	0.57	87.32
RF400L: $H_r = 0.4$ and $Q_t = 36.2$ l/s			
2 m	1.16	1.13	97.41
2.5 m	1.16	1.06	91.78
4.5 m	1.15	1.02	88.66
6.5 m	1.16	0.92	78.89

Table 5.3 – Boundary shear force (column 3) and gravity force (column 2) per unit of length in a total cross-section for RF200L and RF400L. Percentage of completion of the force balance in a total cross-section (column 4). Percentage of shear in FP (column 5) and in MC (column 6) without considering the additional shear generated at the interface between channels.

balance continuously decreases for RF400L. Boundary shear stress are clearly not established for RF400L. By contrast for RF200L, as for RF300L, this first result could indicate that boundary shear stresses are established from $x = 2$ m to $x = 4.5$ m.

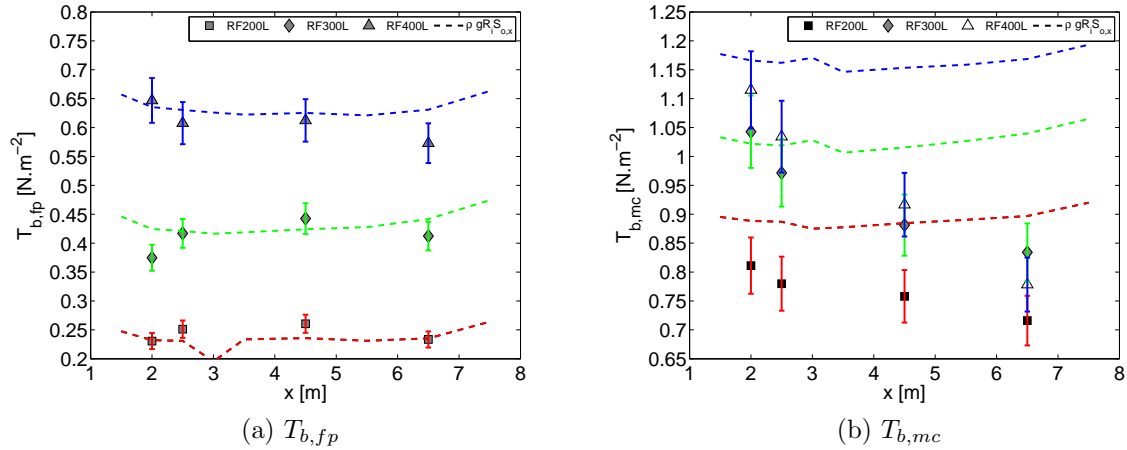


Figure 5.23 – Streamwise distribution of boundary shear stresses in a subsection for reference flows.

Nevertheless, analysis of the percentages of shear in the floodplain and in the main channel for RF200L (*i.e.* $100 \times T_{b,i} / \rho g R_i S_{o,x}$, with $i = mc$ or fp) indicates a different result (see in Figure 5.23). Thus, if with increasing total discharge the percentage of shear in the floodplain is relatively stable and is close to $\rho g R_{fp} S_{o,x}$ (*i.e.* close to equality in Equation 5.4), a strong decreasing tendency is observed for the shear in the main channel. It becomes even steeper with increasing total discharge. As a consequence, boundary shear stresses, whatever is the reference flow, are not established. This is mainly due to the inlet conditions that distort the friction velocity in the beginning of the flume (see velocity close to the bottom in Figures 5.24 and 5.15).

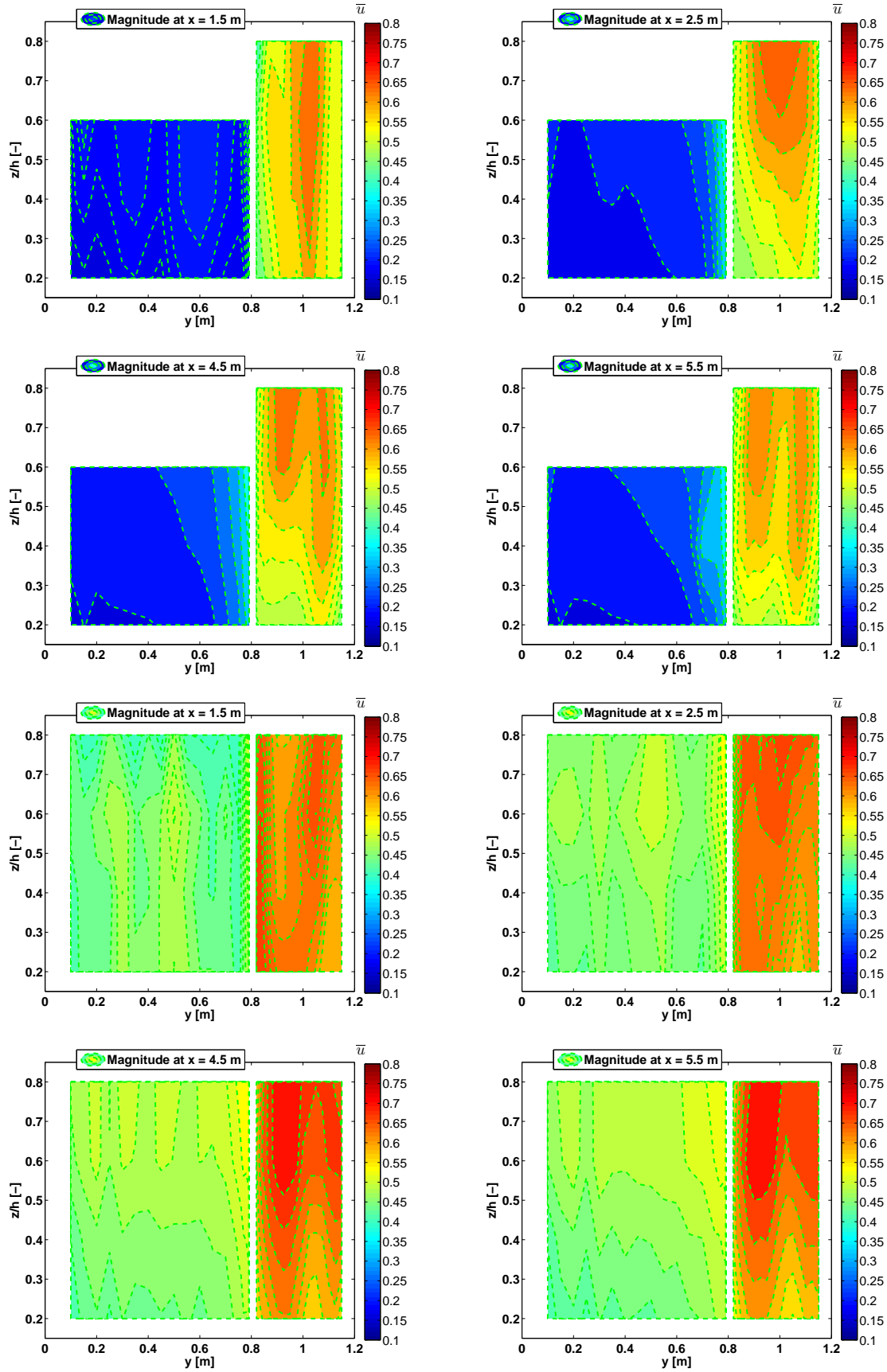


Figure 5.24 – Isolines of longitudinal velocities in four cross-sections ($x = 1.5$ m, 2.5 m, 4.5 m and 5.5 m) for reference flow RF200L (four first figures) and for reference flow RF400L (four last figures).

5.6 Criteria for flow establishment

5.6.1 Segments of establishment

In the previous sections, we have shown that some hydraulic parameters can be considered as established in our experiments. The segments of establishment are summarized in Table 5.4.

	Flow case	Segment of establishment	Criterion of establishment
Z_{fp}	All	$x \in [2 \text{ m } 5.5 \text{ m}]$	$\pm 2.5 \%$ of $\langle Z_{fp} \rangle_{x \in [2 \text{ m } 5.5]}$
Z_{mc}	All	$x \in [2 \text{ m } 5.5 \text{ m}]$	$\pm 2.5 \%$ of $\langle Z_{mc} \rangle_{x \in [2 \text{ m } 5.5]}$
Q_{fp}	All	$x \in [3.5 \text{ m } 7.5 \text{ m}]$	$\pm 2.5 \%$ of $\langle Q_{fp} \rangle_{x \in [3.5 \text{ m } 7.5]}$
H_{fp}	All	$x \in [2 \text{ m } 5.5 \text{ m}]$	$\pm 2.5 \%$ of $\langle H_{fp} \rangle_{x \in [2 \text{ m } 5.5]}$
H_{mc}	All	$x \in [1.5 \text{ m } 6.5 \text{ m}]$	$\pm 2.5 \%$ of $\langle H_{mc} \rangle_{x \in [2 \text{ m } 5.5]}$
U_{fp}	All	$x \in [3.5 \text{ m } 5.5 \text{ m}]$	$\pm 2.5 \%$ of $\langle U_{fp} \rangle_{x \in [3.5 \text{ m } 5.5]}$
U_{mc}	All	$x \in [1.5 \text{ m } 6.5 \text{ m}]$	$\pm 2.5 \%$ of $\langle U_{mc} \rangle_{x \in [3.5 \text{ m } 6.5]}$
$T_{xy,int}$	RF200L	\times	$\pm 2.5 \%$ of $\langle T_{xy,int} \rangle_{x \in [3.5 \text{ m } 7.5]}$
	RF300L	$x \in [3.5 \text{ m } 6.5 \text{ m}]$	$\pm 2.5 \%$ of $\langle T_{xy,int} \rangle_{x \in [3.5 \text{ m } 7.5]}$
	RF400L	\times	\times
$T_{b,fp}$	All	\times	\times
$T_{b,mc}$	All	\times	\times
$h(x, y)$	All	$x \in [3.5 \text{ m } 5.5 \text{ m}]$	$\pm 2.5 \%$ of $\langle h(x, y) \rangle_{x \in [3.5 \text{ m } 5.5]}$
$U_d(x, y)$	All	$x \in [3.5 \text{ m } 5.5 \text{ m}]$	$\pm 2.5 \%$ of $\langle U_d \rangle_{x \in [3.5 \text{ m } 5.5]}$
	RF200L	$x \in [3.5 \text{ m } 7.5 \text{ m}]$	$\pm 2.5 \%$ of $\langle \delta(x) \rangle_{x \in [3.5 \text{ m } 7.5]}$
$\delta(x)$	RF300L	$x \in [4.5 \text{ m } 7.5 \text{ m}]$	$\pm 2.5 \%$ of $\langle \delta(x) \rangle_{x \in [4.5 \text{ m } 7.5]}$
	RF400L	\times	\times
$Fr(x, y)$ in FP	All	$x \in [3.5 \text{ m } 5.5 \text{ m}]$	$\pm 2.5 \%$ of $\langle Fr(x, y) \rangle_{x \in [3.5 \text{ m } 5.5]}$
$Fr(x, y)$ in MC	All	$x \in [3.5 \text{ m } 6.5 \text{ m}]$	$\pm 2.5 \%$ of $\langle Fr(x, y) \rangle_{x \in [3.5 \text{ m } 5.5]}$
$T_{xy}(x, y)$	All	\times	\times
$\tau_b(x, y)$	All	\times	\times
$\bar{u}(x, y, z)$	All	\times	\times
$\tau_{xy}(x, y, z)$	All	\times	\times

Table 5.4 – Definition of the segments where the hydraulic parameters of the reference flows are established ($\langle \rangle_x$ = spatial averaging in the x-wise direction). MC: main channel, FP: floodplain and int: interface

In Table 5.4, the various flow parameters that we considered for the flow establishment, are presented (first column). In the third column of the table, the segment of establishment is given and the fourth column gives the criteria of establishment. It emphasizes that the more the flow parameter is complex to measure and the smaller is the segment of establishment. As a result, none of the turbulent parameters were established, while the depth and the depth-averaged velocity were “constant” between $x = 3.5 \text{ m}$ and $x = 5.5 \text{ m}$.

5.6.2 Definition of the criteria

According to [Chow \[1959\]](#) and [Ancey \[2009\]](#), a flow is considered as established when it is steady and uniform onto the longitudinal direction, *i.e.* $\partial/\partial t = 0$ and $\partial/\partial x = 0$ for the instantaneous depth, velocity and pressure. However, when considering experimental modellings or field measurements, even with very low topographic variations, these criteria are impossible to reach. They are too restrictive. In this subsection we then propose a less restrictive definition for defining the uniformity of a flow.

Using equations in Chapter 2 and assuming a steady flow, we propose to define the degree of uniformity of a flow according to six levels corresponding to six degrees of averaging:

Fifth-order – no streamwise evolution of instantaneous local velocities (original definition of [Chow \[1959\]](#)).

Fourth-order – no streamwise evolution of the local time-averaged velocity and local Reynolds stress: $(\bar{u}, \bar{v}, \bar{w}, \tau_{ij}) = \text{CST}$,

Third-order – no streamwise evolution of the water depth, the depth-averaged velocity, depth-averaged Reynolds stress and boundary shear stress: $(h, U_d, T_{ij}, \tau_b) = \text{CST}$,

Second-order – no streamwise evolution of the water depth, the velocity, the boundary shear stress in a subsection i and the depth-averaged lateral Reynolds shear stress at the interface between the main channel and the floodplain: $(H_i, U_i, T_{b,i}, T_{xy,int}) = \text{CST}$,

First-order – no streamwise evolution of the discharge distribution across the total cross-section and of the water depth in a subsection: $(H_i, Q_i/Q_t) = \text{CST}$ (where Q_i is the discharge in a subsection),

Zero-order – no streamwise variation of the water depth in a subsection i : $H_i = \text{CST}$, *i.e.* the relative depth (H_r) is constant between subsections,

These criteria of establishment are considered as fulfilled when the measured data are at maximum within a range of $\pm 2.5\%$ around a constant value. This constant value can be a mean of the data or a theoretical value.

5.7 Partial conclusion

In this chapter, three reference flows without a groyne were studied. These flows are developing flows, but some hydraulics parameters can be considered as established in the middle of the flume. According to the criteria defined in §5.6.2, we can consider that our reference flows only fulfilled the first order criterion. It results that these flows can be used as reference to compare with flows with a groyne set on the floodplain.

In the sequel of this chapter, flows with a groyne set on the floodplain are then analysed. Differences relative to the reference flows are first discussed. The groyne-cases are then compared together in order to identify effects of the groyne length and of the total discharge.

A general conclusion is finally given for all these chapters.

6

Impacts of the introduction of a groyne in a developing flow in compound channel

6.1 Introduction

This chapter deals with flows in compound channel with a groyne set on the floodplain, perpendicularly to the streamwise direction. The discontinuous variation of the floodplain width generates a non-uniform flow with recirculation zones of both sides of the obstacle. This flow configuration deals therefore with the superimposition of two issues:

- * The interaction between the main channel and the floodplain due to the compound geometry of the flume.
- * The interaction between a flow and a thin obstacle perpendicularly set in the flow.

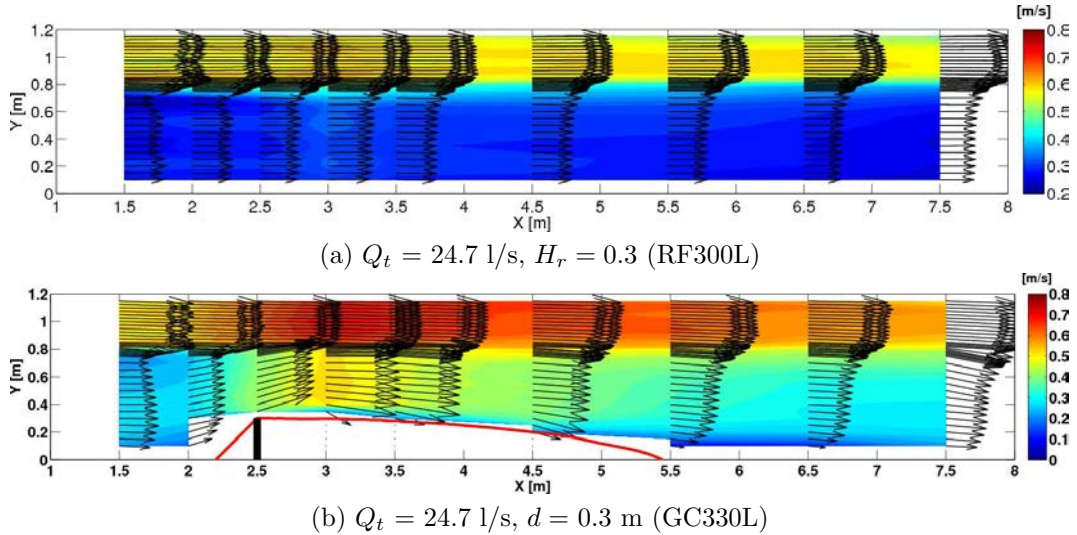


Figure 6.1 – Depth-averaged velocity field (U_d, V_d) for are reference flow (RF300L) and a groyne-case flow (GC330L). d represents the length of the groyne.

In this chapter, we quantify the effects of the introduction of a groyne on the flow parameters that we previously presented under reference flow conditions in Chapter 5. The analyses are focused on the groyne-case flow GC330L (*i.e.* total discharge $Q_t = 24.7$ l/s and groyne length $d = 0.3$ m) relatively to the reference flow RF300L. Moreover, the same discharge distributions and the same tailgate settings as the reference flows were used for the boundary conditions of the groyne-cases. The effects of a change in the groyne length or in the total discharge are analysed in Chapter 7.

A unique groyne was set perpendicularly to the main flow direction in the floodplain (Figure 6.1). The groyne had a negligible relative thickness ($\max(e/d) < 0.1$, with the thickness $e =$

2 cm) and was fixed on the bottom and on the floodplain side-wall, 2.5 m downstream of the inlets.

As shown in Figure 6.1, the flow in the vicinity of the groyne is deviated either from the floodplain towards the main channel or in the opposite direction. It results that the main flow features, as turbulence and boundary shear stresses are strongly impacted and totally new distributions for these parameters are therefore measured. Understanding of such a flow is paramount for engineers and flood modellers.

In this chapter, we describe in detail the geometry of the recirculation zones. The effects on depths and velocities of a groyne introduced in the floodplain are analysed by comparing flow cases RF300L and GC330L. The influences of the boundary conditions and bottom topography on the groyne-case flow are also assessed. Mass exchange is then evaluated through the discharge measured in the floodplain. The characteristics of the mixing layers developing at the interface and along the separation line of the downstream recirculation zone are presented. The effects of mass exchange on the turbulence are then assessed and through a spectral analysis, the nature of the coherent structures developing in mixing layers is discussed. The streamwise and spanwise distributions of the boundary shear stresses are finally analysed.

In this thesis, the groyne-case flows are either referenced using the total injected discharge Q_t and the groyne length d or using the names presented in Table 3.3.

6.2 Geometry of recirculation zones

As shown in Figure 6.1, the groyne in the floodplain promotes two flow separations, therefore resulting in a development of recirculation zones of both sides of the groyne. The groyne induces a reduction in the flow section, which initiates strong mass exchange between channels that strongly impacts the distributions of the flow parameters. In this section, the geometrical characteristics of the downstream recirculation zones are thus exposed for the six groyne-case flows.

The geometry of the downstream recirculation zones was identified using surface velocity fields measured with the LSPIV technique (§3.3.6). The method to identify geometries of recirculation zones is exposed in §4.3.2.

6.2.1 Longitudinal length

The longitudinal length of the downstream recirculation zone (denoted L_x) corresponds to the distance between the groyne and the stagnation point located on the floodplain side-wall. The stagnation point is the point on the floodplain side-wall where stops the velocity streamline coming from the separation point located at the tip of the groyne. The lengths L_x and their uncertainties δL_x are summarized in Table 6.1.

Case	Q_t [l/s]	d [m]	L_x [m]	δL_x [m]	$\delta L_x/L_x$	L_x/d [-]
GC230L	17.30	0.30	1.80	0.10	0.06	6.00
GC250L	17.30	0.50	2.50	0.10	0.04	5.00
GC330L	24.70	0.30	2.94	0.15	0.05	9.80
GC350L	24.70	0.50	4.15	0.15	0.04	8.30
GC420L	36.20	0.20	3.05	0.15	0.05	15.25
GC430L	36.20	0.30	3.75	0.15	0.04	12.50

Table 6.1 – Longitudinal lengths of the downstream recirculation zones for groyne-case flows and uncertainties on the measured lengths.

In Table 6.1, the total discharge and the length of the groyne are reminded in the second and third columns. Even if the uncertainty on the localization of the stagnation points is higher for

the two higher discharges ($\delta L_x = 0.15$ m), results emphasize that the longitudinal length of the downstream recirculation zone increases with the total discharge and the groyne length.

The relatively high uncertainty on measurements of L_x is due to the passage of turbulent structures in the vicinity of the stagnation point that make it moving back and forth around its true position (See Figure 4.4 for an example). Given the limited recording time of the video-sequences (2 min) used for localizing the stagnation point, there are not enough images for better reducing the bias on the measurements of L_x (the recording time is limited by the downstream reservoir, which may overflow after filming more than two minutes, see §4.3.2).

Concerning the upstream recirculation zone, LSPIV measurements emphasize that the separation point is approximately located on the floodplain side-wall at $1 \times d$ (d the groyne length) upstream of the groyne. The stagnation point is located on the upstream face of the groyne close to the tip as observed by *Ettema and Muste* [2004], when obstacle is close to the inlet. No more information were worked out from LSPIV measurements, because we were mainly interested in characterising the downstream recirculation zone.

6.2.2 Spanwise length of the downstream recirculation zone

The spanwise length is the lateral distance between the separation line and the floodplain side-wall. The separation line is the line connecting the separation point at the tip of the groyne and the stagnation point on the floodplain side-wall downstream of the recirculation zone. This line corresponds to the zero-discharge streamline and is defined as the streamline passing between the last streamline coming from the groyne that turns back near the floodplain and the first streamline coming from the groyne that does not stop on the floodplain wall (see §4.3.2).

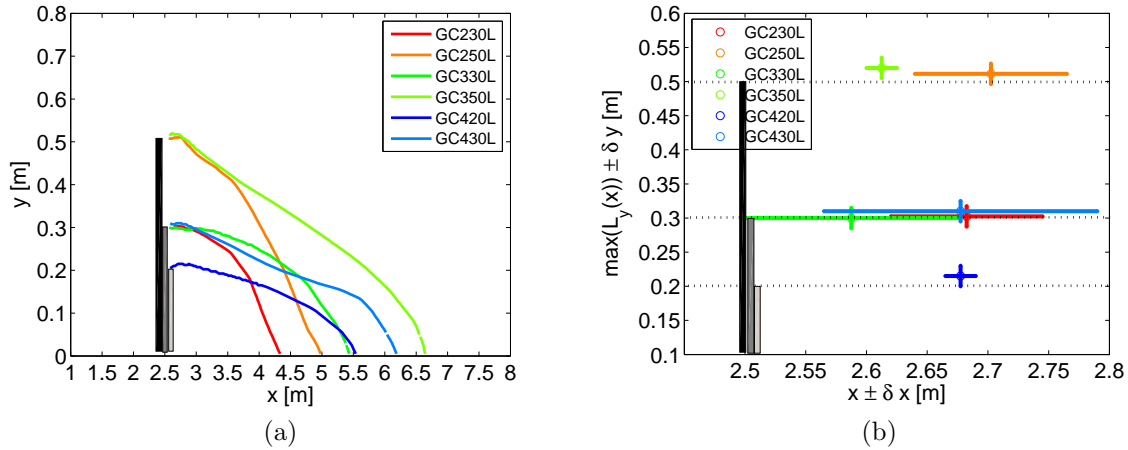


Figure 6.2 – (a) Lateral expansions of the downstream recirculation zones for groyne-case flows. The groyne is located at $x = 2.5$ m (grey bars). Uncertainty on the spanwise direction: ± 1.5 cm and uncertainty on the stagnation point location: $\pm 10 - 15$ cm. (b) Approximative position of the maximal lateral expansion for each groyne-case flow.

In Figure 6.2.a, the shape of the downstream recirculation zones are displayed for each groyne-case flow. The red/orange lines represent the recirculation zones for $Q_t = 17.3$ l/s, the blue ones for $Q_t = 24.7$ l/s and the green ones for $Q_t = 36.2$ l/s. Uncertainty on lateral length measurements is equal to ± 1.5 cm. No particular shapes are observed. As previously mentioned, the spreading of the recirculation zones increases with the total discharge and the groyne length.

The locations of the maximal lateral expansion for the six groyne-case flows are represented in Figure 6.2.b. They are all within $x = 2.50$ m and $x = 2.80$ m and the maximal extent does not exceed $d + 2$ cm ± 1.5 cm. No dependency is observed between the maximal extent and the injected total discharge.

The relatively high uncertainty on the streamwise localization of the maximal expansion is once again a consequence of the limited recording time of the video-sequences (recording time ≤ 2 min, see §4.3.2). The random vortex shedding at the beginning of the separation line (affected by the random movement of the Horse-shoe vortex at the tip of the groyne, [Koken and Constantinescu, 2008]) initiates some random movements of the separation line that may interact with the mixing layer developing at the interface between the main channel and the floodplain. Because of the short video-sequences, these random movements therefore bias the determination of the mean position of the separation line.

6.3 Main flow features

In this section, we analyse the superimposition of the two problems – (i) compound geometry, (ii) recirculating flow – by comparing the flow-case GC330L (*i.e.* $Q_t = 24.7$ l/s and $d = 0.3$ m) with its associated reference flow RF300L. Water level and velocity distributions across the flume are notably depicted. Velocities in the recirculation zones, too weak to be measured with a micro-propeller, are not worked out.

6.3.1 Effects of recirculation zones on the flow

6.3.1.1 Effects on the velocities and water depths

As shown in §6.2, recirculation zones reduce the flow section, therefore inducing high changes in the velocity and the depth.

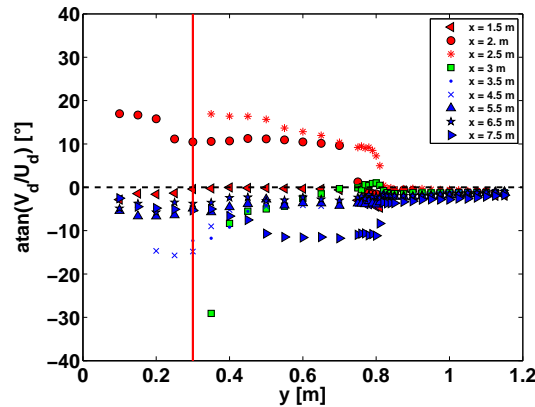


Figure 6.3 – Angle of divergence/convergence for groyne-case flow $Q_t = 24.7$ l/s and $d = 0.3$ m. Uncertainty: $\delta(V_d/U_d)/(V_d/U_d) < 1.5$ %. The red line corresponds to the position of the groyne in the flume.

The flow deflection ($\text{atan}(V_d/U_d)$ in degree) relative to the streamwise direction (Figure 6.3) first emphasizes that the convergence angles of the flow from the floodplain towards the main channel reach a maximal angle of 19° from $x = 0$ m to $x = 2.5$ m, while the main channel is not deflected. The converging flow in the floodplain is laterally confined by the flow in the main channel. From $x \approx 2.6$ m to the stagnation point of the downstream recirculation zone at $x = 5.5$ m (see Table 6.1), the flow diverges from the main channel towards the floodplain with a minimal angle of -30° in the floodplain and a minimal angle of -2.5° in the main channel. Once the recirculation zone has reattached, angles of divergence reduces. The flow in the main channel is less influenced by the recirculation zone than the flow in the floodplain. Notice that the extreme angles of divergence/convergence are greater or equal to those found in the literature for gradually varied flows: $\pm 9.2^\circ$ for skewed floodplains, 22° for converging floodplains [Proust

et al., 2006, 2010] and -5.7° for diverging floodplains [Proust *et al.*, 2010]; as a consequence, mass exchange in our experiments is expected to be at least equal or stronger than the one measured under gradually varied flow conditions.

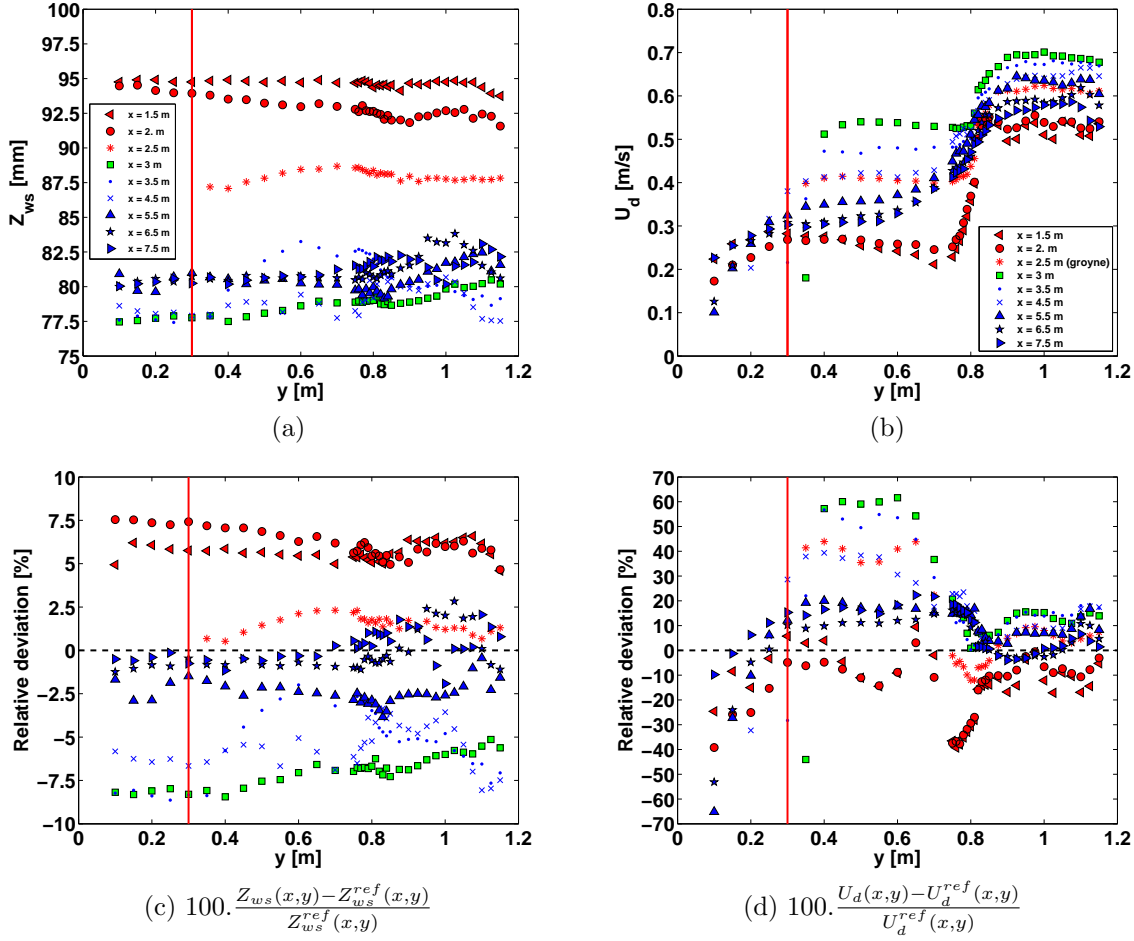


Figure 6.4 – (a-b) Water levels and depth-averaged longitudinal velocity for groyne-case flow $Q_t = 24.7$ l/s and $d = 0.3$ m. Levels are measured relative to a reference plan whom origin is in the main channel at $x = 7.5$ m and $y = 1.15$ m. Uncertainty: $\delta Z_{ws} = 0.42$ mm and $\delta U_d/U_d = 1.5$ %. (c-d) Comparison of GC330L with RF300L. The red line corresponds to the position of the groyne in the flume.

The transversal distribution of water levels is then displayed for GC330L at various downstream stations x in Figures 6.4.a. The longitudinal decrease, so as the lateral decrease in water level are very strong between and within the cross-sections located in the vicinity of the groyne ($x \in [2 \text{ m} - 3 \text{ m}]$). The slope $\partial Z_{ws}/\partial x$ is estimated to ≈ 15 mm/m, while for reference flows this slope is rather close to $S_{o,x} = 1.8$ mm/m (see Chapter 5). The slope $\partial Z_{ws}/\partial y$ is close to ≈ 2.5 mm/m (≈ 0 mm/m for reference flow). The flow then becomes highly three-dimensional in the vicinity of the groyne at $x = 2.5$ m. These gradients of water level are due to mass exchange between the floodplain and the main channel.

The deviations relative to the reference flow of the depth-averaged longitudinal velocity and water level are displayed in Figures 6.4.c-d. The water levels relative to the reference levels are distorted in the same way whether in the main channel or in the floodplain. By contrast, the velocity variations relative to the reference velocities depends on the considered channel. In the floodplain, velocities can be 70 % greater than the reference velocities, while in the main channel, they are all within ± 20 % of the reference velocities. The main channel due to its higher discharge has a greater capacity for absorbing the distortion generated by the groyne.

In addition, water levels in the last cross-section are comparable to -2.5% of the levels of the reference flow, while the velocity is 20% greater in the floodplain and is almost equivalent to the reference in the main channel (Figure 6.4.d). The velocity then needs a longer distance than the water level to reach the reference flow conditions.

6.3.1.2 Identification of a throat

The presence of the groyne in the floodplain has tremendous impacts on the regime of the flow in both channels. The Froude distribution presented in Figure 6.5 emphasizes that the flow becomes supercritical in the floodplain from the contraction induced by the downstream recirculation zone (between $x = 2.5$ m and $x = 2.8$ m, see in Figure 6.2) until at least $x = 3.5 - 4$ m and the highest Froude number is found at $x = 3$ m. By contrast, the main channel is always subcritical. The transition from subcritical to supercritical flow in the floodplain is due to the strong decrease in water depth and flow acceleration in the vicinity of the tip of the groyne (Figure 6.4.a-b).

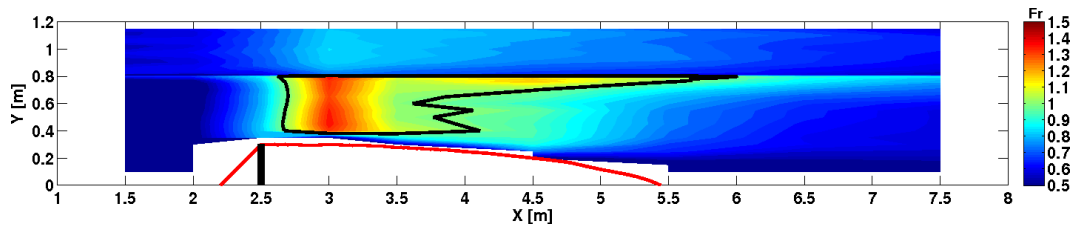


Figure 6.5 – Froude number distribution for groyne-case flow $Q_t = 24.7$ l/s and $d = 0.3$ m. The zone within the plain black line corresponds to a supercritical regime. Uncertainty: $\delta Fr / Fr < 15\%$.

By analogy to the second theorem of Hugoniot [Chassaing, 2000b] which specifies that for isentropic compressible flows, the passage to $Mach = 1$ must be associated to the minimal flow section (*i.e.* a throat), Rivière *et al.* [2007] have shown that a subcritical flow reaches $Fr = 1$ in the contracted cross-section and then becomes supercritical when the flow diverges. For GC330L, the Froude distribution in Figure 6.5 emphasizes that a throat is approximately located at $x = 2.6$ m (see the black plain line perpendicular to the main direction near $x = 2.6$ m). This position for the throat is confirmed by the estimation of the position of the contraction cross-section in Figure 6.2.b.

The position of the throat is between $x = 2.5$ m and $x = 3$ m where the sign of the angles of deflection changes (Figure 6.3). As a result, upstream of the throat, a flow convergence occurs from the floodplain towards the main channel, in the vicinity of the throat the flow is almost aligned with the streamwise direction and downstream, the flow diverges from the main channel towards the floodplain (see in Figure 7.1.c). **Using this flow direction, the part in the flume located upstream of the throat is called converging part and the part downstream is called diverging part.**

6.3.2 Impacts on the flow of backwater effects

A typical groyne case flow is schematized in Figure 6.6 (plan view); the recirculation zones are represented in blue, the supercritical zone is the red hatched zone and the direction of the backwater effects either generated by the throat or by the downstream boundary conditions are represented by green arrows.

In the floodplain, the hydraulic disconnection in the throat induces the creation of two backwater curves. The effects of the first curve are directed from the throat towards the inlets; their influences are difficult to evaluate because effects of the groyne are dominant in this area [Proust,

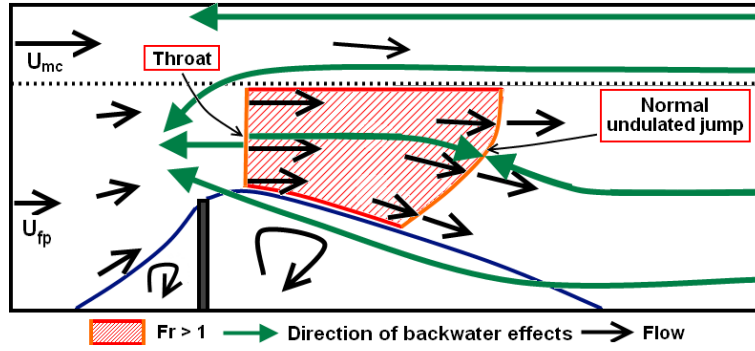


Figure 6.6 – Scheme of the various sources of backwater effects (green arrows) for groyne-case flow GC330L. The scheme is a plan view and is not to scale.

2005, Chapter 9]. The effects of the second backwater curve are easier to identify. They are directed from the throat towards the outlets and their influences are only felt until $x \approx 3 - 3.5$ m, *i.e.* where the velocity is maximal and the depth is minimal (see green data in Figure 6.4). Although the supercritical regime exists until $x \approx 4.5$ m, the backwater effects coming from the throat are actually distorted by other effects that force the flow from $x \approx 3 - 3.5$ m to $x \approx 4.5$ m to decelerate while the flow section is still increasing and the regime is still supercritical (if $Fr > 1$ and $dB/dx > 0$, then $dU/dx > 0$ [Graf and Altinakar, 2000]). These downstream controls from the tailgates cause the appearance of a normal undulated jump in the supercritical zone and are transmitted towards the entrance through the main channel and the recirculation zone.

NB – We did not observed ordinary jump (normal jump) or oblique jump because our Froude numbers were too small ($\max(Fr) < 1.7$) [Graf and Altinakar, 2000].

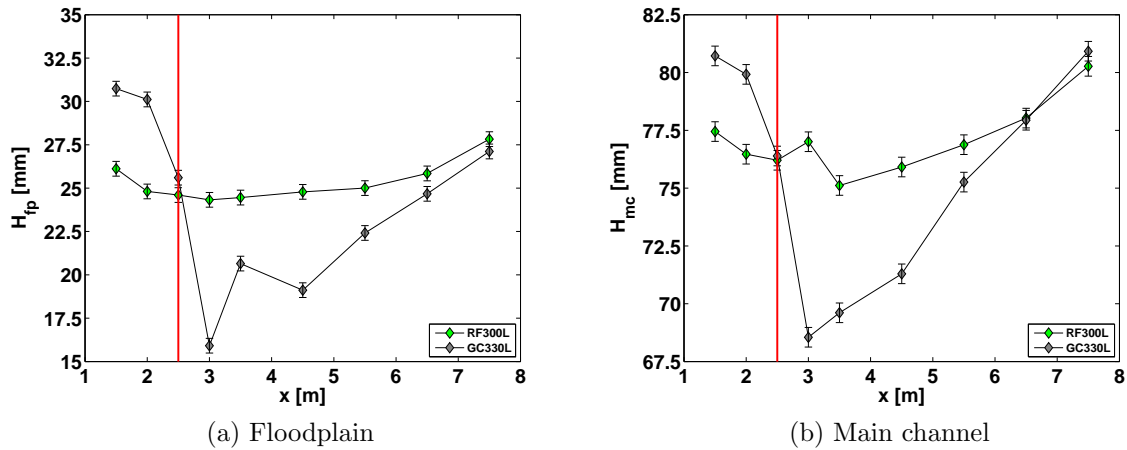


Figure 6.7 – Mean flow depths in a subsection for RF300L and GC330L. The red line corresponds to the position of the groyne in the flume.

The backwater effects generated by the tailgate in the floodplain and in the main channel are highlighted using the evolution of the water depths in a subsection for groyne-case flow GC330L and reference flow RF300L in Figure 6.7.a-b. The comparison emphasizes a similar rising tendency from $x = 6.5 - 7.5$ m to the end of the flume. As the tailgate settings for GC330L was the same as for RF300L, this similar behaviours of the water depth at the end of the flume is only due to backwater effects generated by the tailgates. Thus, while for the reference flow the backwater effects are only felt over the last two meters of the flume, for the groyne-case flow, effects are felt until at least $x = 3 - 3.5$ m, where the minimum of water depth is reached. Variations upstream of $x = 3$ m are probably due to the groyne itself.

Finally, according to Proust [2005], the groyne has more influence on the discharge distribution in the flow than the initial discharge distribution. The groyne locally limits the floodplain conveyance, therefore resulting in an increase in mass exchange between channels (see §6.4). As a consequence, the inlets have few influences on the groyne-case flows.

6.4 Mass exchange

In the previous section, we showed that the groyne strongly distorts the flow distribution between the main channel and the floodplain and therefore induces mass exchange. In this section, we quantify the mass exchange between channels.

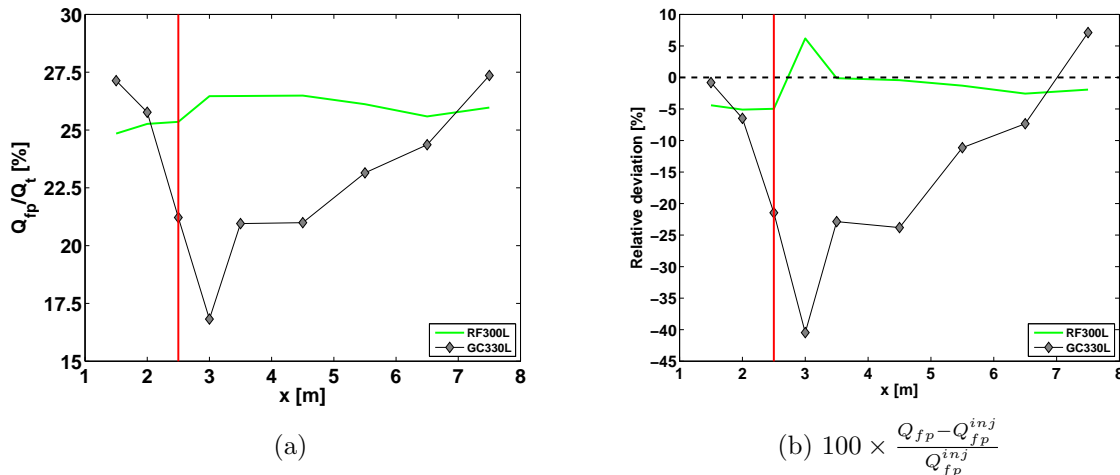


Figure 6.8 – (a) Discharge distribution in the floodplain for GC330L compared to the reference flow-case. Uncertainty: $\delta(Q_{fp}/Q_t)/(Q_{fp}/Q_t) < 1$ %. (b) Comparison to the injected total discharge. The red line corresponds to the position of the groyne in the flume.

Direction of mass exchange in Figure 6.8.a is in accordance with the values of spanwise velocity V_d presented in Figure 6.3. Upstream of the throat at $x \approx 2.6$ m – in the converging part of the flow –, deflection angles are positive and mass is therefore exchanged from the floodplain towards the main channel. Downstream of the throat – in the diverging part of the flow –, the main channel exchanges mass with the floodplain and the negative V_d are observed in the whole cross-section.

Intensity of mass exchange for GC330L is highlighted by the discharge distribution in the floodplain compared to the injected discharge at the inlet of the floodplain (see Figure 6.8.b). Results confirm what was observed with lateral velocities. Like in the converging part, lateral velocities are strong, mass exchange is strong as well; discharge ratio in the floodplain reduces by 40 % in only 1.5 m (from $x = 1.5$ m to the throat cross-section at $x = 3$ m). By contrast, in the diverging part, the strength of the mass exchange is lower. The discharge ratio in the floodplain indeed increases by 45 % on a 5 m length.

6.5 Analysis of the turbulence

In this section we are interested in the study of the turbulence developing (1) in the mixing layer located at the interface between the main channel and the floodplain, (2) along the downstream separation line separating the main flow and the downstream recirculation zone and (3) out of the mixing layers.

6.5.1 Geometrical characteristics of the mixing layer developing at the interface between channels

Similarly to reference flow RF300L, the difference in depth and velocity between channels for GC330L is responsible for the development of a mixing layer at the interface between the main channel and the floodplain. As observed in Chapter 5 for RF300L, an inflection point is present in most lateral profiles of longitudinal velocities for GC330L in Figure 6.4.b, therefore inducing an instability responsible for the generation of planform macro-vortices [van Prooijen *et al.*, 2005]. The mixing layer, here, is still a zone where momentum due to turbulence is transferred from one channel to another, but the strong lateral mass exchange distorts the horizontal vortices, therefore reducing or increasing the mixing relative to the reference case.

Despite the same inlet settings as for RF300L, the groyne and the resulting mass exchange for GC330L (§6.4) are responsible for the non-establishment of the mixing layer in term of velocity distribution across the channel. Indeed, while the longitudinal depth-averaged velocity only needs three meters to establish for RF300L (see §5.4.2.1), the longitudinal depth-averaged velocity for GC330L is never established (see in Figure 6.4.b).

Using the measurements of the depth-averaged velocities, the geometrical characteristics of the mixing layer at the interface for GC330L (lateral width δ and location of the centre y_c) are then worked out using Equation 5.1, where $U_d(y_{10\%}) = U_2 + 0.10(U_1 - U_2)$ and $U_d(y_{90\%}) = U_2 + 0.90(U_1 - U_2)$ with $U_1(x) = \langle U_d \rangle_{y \in [0.9 \ 1.15]}$ and $U_2(x) = \langle U_d \rangle_{y \in [L_y(x)+0.1 \ 0.6]}$ ($L_y(x)$ the y-wise coordinate of the separation line).

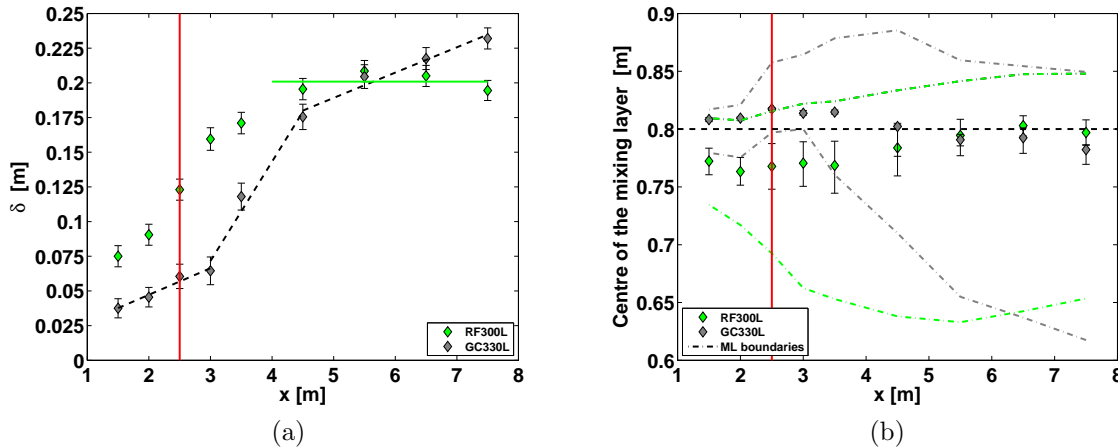


Figure 6.9 – (a) Streamwise evolution of the width δ of the mixing layer. (b) Streamwise positions of the centre of the mixing layer y_c for RF300L and GC330L ($Q_t = 24.7$ l/s, $d = 0.3$ m). The vertical red line represents the position of the groyne in the flume.

The width of the mixing layer at the interface between the main channel and the floodplain is displayed for GC330L in Figure 6.9.a. The width increases from the beginning to the end of the flume ($\langle \delta \rangle_{x \in [1.5 \ 3]} \approx 5$ cm, then $\langle \delta \rangle_{x \in [3 \ 4.5]} \approx 12.5$ cm and finally $\langle \delta \rangle_{x \in [4.5 \ 7.5]} \approx 21$ cm), but the growth rate ($\Delta\delta/\Delta x$) of the mixing layer is not constant. In the converging part of the flow (*i.e.* from the beginning of the flume to $x = 3$ m), the growth rate is indeed equal to 0.033. Then, from $x = 3$ m to $x = 4.5$ m (*i.e.* diverging part, upstream of the stagnation point of the downstream recirculation zone), the growth rate strongly increases and is equal to 0.065. Finally, from the vicinity of the stagnation point at $x = 5.5$ m to the end of the flume, the growth rate reduces to 0.022.

The evolutions of the width and growth rate of the mixing layer must be related to the variations in the flow section and to mass exchange between channels. The reduction in the flow section in the beginning of the converging part of the flume and the low mass exchange relative to the reference flow (Figure 6.8) thus induce a rise in water depth, which results in a

velocity dip in the floodplain-side of the interface (from $y = 0.7$ m to the interface in Figure 6.4.b). This velocity dip prevents the mixing layer to laterally spread too far in the floodplain. Moreover, the position of the dip is almost the same between cross-sections of the converging part, hence the low growth rate of the mixing layer between $x = 1.5$ m and $x = 3$ m. In the sequel, the steep increase in width in the diverging part of the flow (from $x = 3$ m to $x = 4.5$ m) is due to the increasing flow section and to the large mass exchange from the main channel towards the floodplain (Figure 6.8). They both enable to rebalance the velocity profile in the floodplain by cancelling the velocity deficit in the floodplain-side of the interface. This rebalance therefore enable to find $U_d(y_{10\%})$ beyond $y = 0.7$ m: the more the flow deficit in the floodplain reduces and the larger is the width of the mixing layer. Finally once the recirculation zone has reattached (downstream of $x = 5.5$ m), mass exchange from the main channel towards the floodplain is low and changes in the velocity profiles are low. The growth rate then reduces, therefore indicating that the growth rate in the diverging part of the flow is inversely proportional to the strength of the mass exchange.

The comparison of mixing layer widths for GC330L with RF300L in Figure 6.9.a highlights the role played by the groyne and the recirculation zone in the development of the mixing layer. While the recirculation zone has not reattached, the width of the mixing layer is smaller than the one for RF300L and once the flow has reattached, the contrary is observed. The recirculation zone reduces the lateral spreading of the mixing layer.

The position y_c of the centre of the mixing layer for GC330L is then displayed in Figure 6.9.b. Comparison with RF300L indicates that mass exchange changes the position of y_c , the uncertainty left aside. In the converging part, the mixing layer centre is pushed in the main channel, while in the diverging part, the centre is pushed in the floodplain. Nevertheless changes relative to RF300L are low and mixing layer centre is still close to the interface at $y = 0.8$ m.

Considering the outer boundaries of the mixing layer displayed in Figure 6.9 for GC330L, their behaviours in the diverging part of the flow are relatively similar to those for RF300L (*i.e.* the mixing layer is asymmetrical and is mainly contained by the floodplain), while in the converging part, the mixing layer is mainly contained by the main channel.

6.5.2 Turbulence in the mixing layer at the interface between channels

The depth-averaged Reynolds stresses for groyne-cases were assessed in four remarkable cross-sections; (1) upstream of the groyne at $x = 2$ m, (2) in the groyne cross-section at $x = 2.5$ m, (3) 1.5 m downstream of the throat at $x = 4.5$ m – far from the ridge influences – and (4) downstream of the stagnation point of the downstream recirculation zone at the floodplain side-wall. Depending on the local water depth, depth-averaged Reynolds stresses were calculated with at least one measurements and at maximum six measurements on the vertical in the floodplain and between three and five in the main channel (see depth-averaging in §4.4).

Similarly to RF300L, the maximum of T_{xy} is located in the centre y_c of the mixing layer, the uncertainty left aside (Figure 6.10.a). In addition, the peaks of T_{xy} have the same order of magnitude than the reference value at $x = 5.5$ m (the cross-section where the flow is almost developed, see Chapter 5). The maximum of T_{xy} is obtained at $x = 4.5$ m (1/3 greater than the reference value for RF300L), the minimum at $x = 6.5$ m is similar to the reference value. The magnitude of T_{xy} at the interface decreases with increasing water depth (see effects on T_{xy} in Figure 5.10.c) and rises with an increase in the floodplain under-feeding (Figure 6.8.b).

The comparison of T_{xy} with $a \times \partial U_d / \partial y$ ($a = 0.1$ m²/s) in Figure 6.10.b emphasizes a strong correlation between both parameters for data in the mixing layer at the interface. Like for RF300L, variations of the gradient at the interface confirms that the shear produced in the mixing layer at the interface is caused by the velocity gradient generated by the floodplain step.

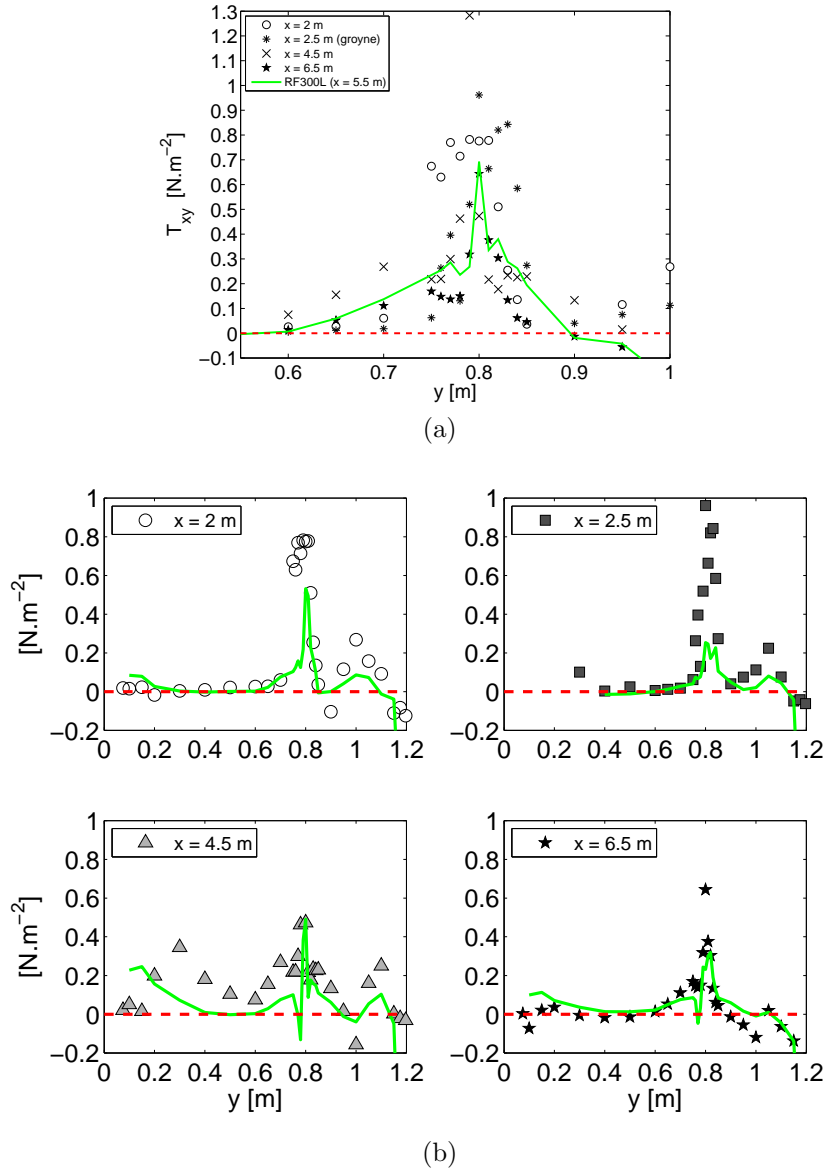


Figure 6.10 – (a) Distribution of depth-averaged Reynolds shear stresses T_{xy} in the vicinity of the interface for GC330L (uncertainty not estimated). (b) Link between Reynolds shear stress and lateral gradient of longitudinal velocity: markers = T_{xy} and lines = $0.1 \times \partial U_d / \partial y$. Uncertainty is not estimated.

By contrast, the correlation between T_{xy} and $a \times \partial U_d / \partial y$ is weak for data located in the mixing layer developing in the lee of the groyne (see at $x = 4.5$ m around $y = 0.3$ m). This bad correlation is probably due to the low resolution of the mesh of measurements which does not enable to correctly assess the velocity gradient in the floodplain. Given these results, it results that the Boussinesq hypothesis (Equation 2.38) can be used for modelling turbulence far from the recirculation zone. Close to the recirculation zone, measuring mesh must be quite dense in order to have a good estimation of the velocity gradient and to use the Boussinesq hypothesis.

6.5.3 Mixing layer developing at the tip of the groyne in the floodplain

Because of the flow separation at the tip of the groyne, a mixing layer develops in the lee of the groyne. This mixing layer exists until the recirculation zone reattaches and then degenerates into a wake (see in Babarutsi et al. [1989]; Chu et al. [2004], recirculation zone in sudden enlargement and behind an isle).

Unlike the mixing layer at the interface between the main channel and the floodplain, the geometrical characteristics of the mixing layer developing in the lee of the groyne were not assessed. In such a mixing layer, the condition of self-similarity of the velocity is indeed not achieved because of the returning flow in the recirculation zone; a self-similar hyperbolic tangent profile used for jet mixing [Chu *et al.*, 1991; Pope, 2000; Uijttewaal and Booij, 2000] cannot fit the velocity in the vicinity of the separation line. As a consequence, the use of a formalism similar to the one proposed in Equation 5.1 could not be used for determining the width of the mixing layer. Direct observation were also not possible, because velocities inside the recirculation zone could not be accurately measured during experiments. Concerning the centre of the mixing layer, Uijttewaal and Booij [2000] showed that in a free mixing layer, it is located along the zero-discharge streamline ($y(x) = L_y(x) : \int_0^{L_y(x)} h \times U_d(x, y) dy = 0$). In our case, the non observance of the self-similarity condition does not enable to locate the centre of the mixing layer: *i.e.* we cannot affirm that the separation line (streamline of zero-discharge) represents the centre of the mixing layer.

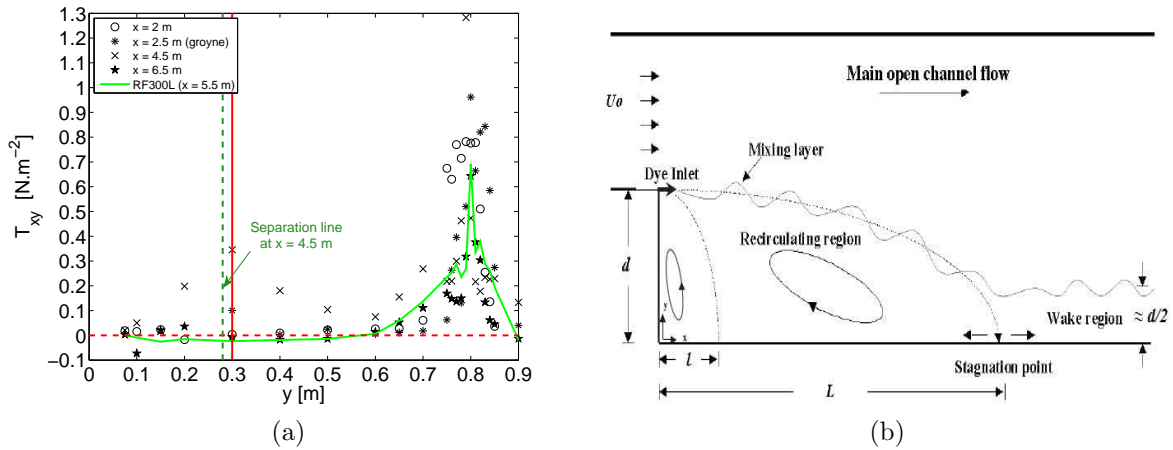


Figure 6.11 – (a) Depth-averaged Reynolds shear stress in the vicinity of the recirculation zone for GC330L ($Q_t = 24.7$ l/s and $d = 0.3$ m). Uncertainty is not estimated. (b) Scheme of a wake developing in the lee of the stagnation point [Chu *et al.*, 2004].

Nevertheless, the analysis of the depth-averaged Reynolds shear stress in the vicinity of the recirculation zone enables to get information about effects of the mixing layer on the surrounding flow. Depth-averaged Reynolds shear stress T_{xy} in the vicinity of the recirculation zone is thus displayed in Figure 6.11.a. The turbulent production along and 20 cm around the separation line is quite strong. A local maximum for T_{xy} is identified in the vicinity of the separation line at $x = 4.5$ m; it is 3 times smaller than the maximum observed at the interface. Once the stagnation point of the recirculation zone is passed, the turbulence magnitude largely decreases and reaches in most parts of the floodplain the reference values of RF300L. At $x = 6.5$ m (*i.e.* 1 m downstream of the stagnation point), T_{xy} is close to the reference value from $y \approx 0.2$ m to $y \approx 0.6$ m, but from the floodplain side-wall to $y \approx 0.5d$ (d the size of the groyne), a local minimum of T_{xy} is measured. As observed by Chu *et al.* [2004] in sudden enlargement in single channel and schematized in Figure 6.11.b, let see here the influence of the wake that develops downstream of the stagnation point until the end of the flume. This wake is induced by the advection of the vortices generated in the mixing layer that have met the floodplain side-wall in the vicinity of the stagnation point.

6.5.4 Turbulence out of the mixing layers

In this paragraph, we are focused on the distribution of the depth-averaged Reynolds stresses out of the mixing layers for GC330L with comparison to the turbulence for reference flow RF300L.

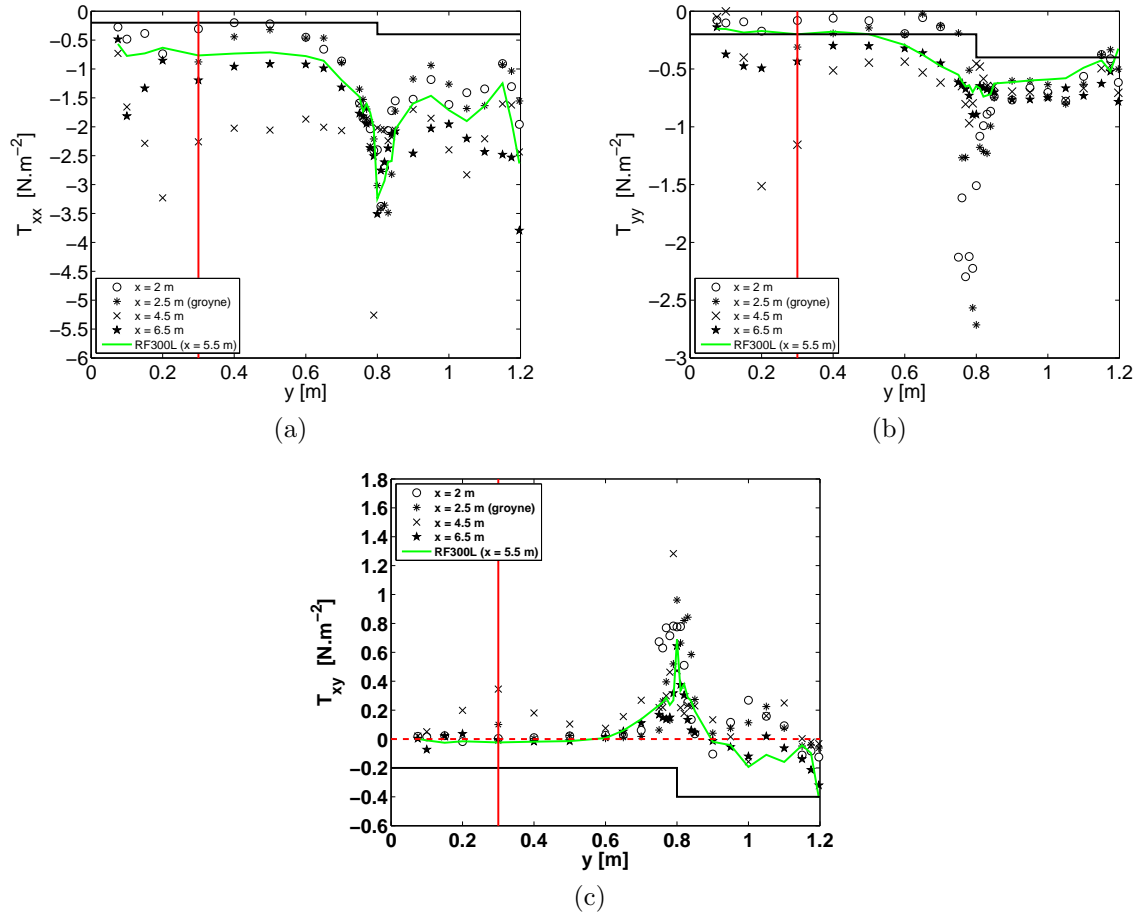


Figure 6.12 – (a-c) Distribution of depth-averaged Reynolds stress for GC330L ($Q_t = 24.7$ l/s and $d = 0.3$ m).

Depth-averaged Reynolds stresses T_{xx} , T_{yy} and T_{xy} are displayed in Figures 6.12.a-c and they are also compared to measurements at $x = 5.5$ m for reference flow RF300L (measurements of T_{ij} in cross-section at $x = 5.5$ m are the closest to what would be found under uniform flow conditions, see Chapter 5). Reynolds stresses have the same orders of magnitude as those measured under reference flow conditions (green line): T_{xx} has a magnitude of $O(1$ Pa), while T_{yy} and T_{xy} are rather close to $O(0.1$ Pa). T_{xy} in the floodplain is close to zero and T_{xx} as T_{yy} are constant and maximum. The measurements at the four cross-sections for GC330L enable to observe that T_{xx} decreases (resp. increases) with increasing (resp. decreasing) depth-averaged velocity. Variations of T_{yy} must be related to variations of depth-averaged lateral velocities (Figure 6.3). T_{yy} increases with positive lateral velocities and decreases with the negative ones. In the zone where lateral velocities are close to zero, T_{yy} is close to the value measured under reference conditions. Concerning the turbulence in the main channel, it is less easy to find a tendency. The boundary layer initiated at the main channel wall interacts with the mixing layer at the interface, hence the various shapes of the T_{xy} distribution.

Turbulence intensity (Equation 5.2) is finally assessed in Figure 6.13. The depth-averaged turbulent intensity (I_k [Chassaing, 2000a; Nezu and Nakagawa, 1993]) is plotted for the four cross-sections previously studied and is compared to the depth-averaged turbulent intensity worked out for RF300L at $x = 5.5$ m. For $y > d$ (d the length of the groyne), the turbulent intensity is equivalent to the one of RF300L (7 % in the main channel, 10 % in floodplain and 14 % at the interface between channels). Contrariwise, the turbulent intensity is far more important for $y < d$, reaching 20 % of the depth-averaged velocity in average and can reach 70 % in the recirculation zone at $x = 4.5$ m. The recirculation zone is then a highly turbulent zone. In addition, the calculation of the lateral depth-averaged turbulent intensity (Figure 6.13.b)

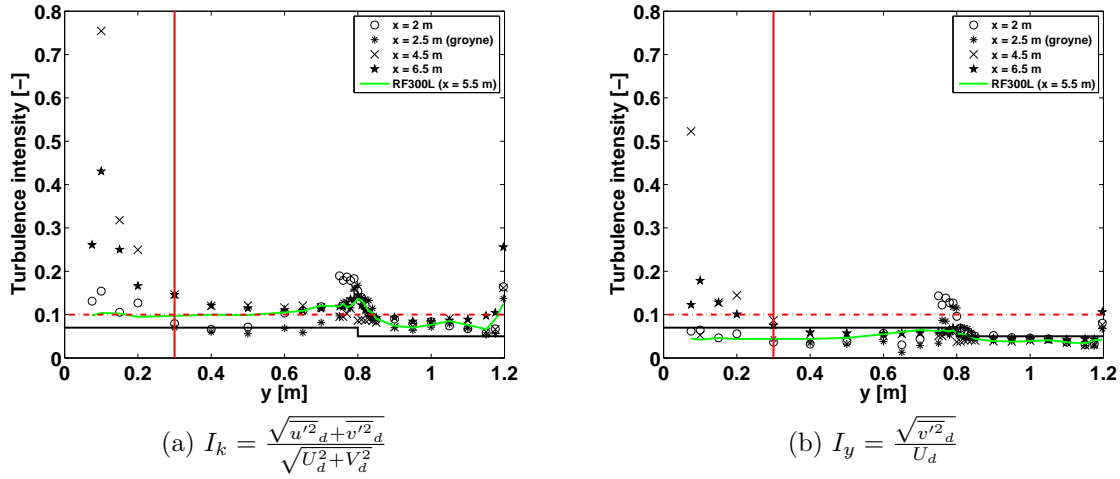


Figure 6.13 – Distribution of depth-averaged turbulence intensity. Uncertainty is not estimated.

emphasizes that in mixing layers and in the recirculation zone, the lateral fluctuating velocity highly contributes to the turbulence, this, because of lateral exchanges for mixing layers and because of the returning flow in the recirculation zone.

6.5.5 Coherent structures in the two mixing layers

Depending on the shallowness of the flow, the coherent structures that develops in mixing layers may be confined by the water depth, as highlighted in §5.4.2.4 and §5.5.2.4 for reference flows. It then results that the 2D horizontal coherent structures are forced by the bottom friction to reduce in size and they can even become 3D [van Prooijen and Uijttewaal, 2002].

The horizontal planform vortices were first recognised through the calculation of the autocorrelation function of the lateral component of the velocity R_{yy} (see Equation 5.3). The cross-power spectrum densities S_{xy} and the associated phase relation ϕ were then calculated for assessing the wave-numbers of the structures that contribute to the shear in the flow. The power spectrum densities S_{yy} were also worked out for determining the nature of the produced turbulence (2D/3D). The methods for calculating the spectral densities are exposed in §4.7.

6.5.5.1 In the mixing layer at the interface

For mixing layers developing at the interface between channels, spectral analyses were performed using data taken at the elevation $z = 0.6 \times H_{fp}$ (*i.e.* a constant distance below the free surface as used in the study of Uijttewaal and Booij [2000]) in the centre of the mixing layer (*i.e.* at $y = y_c$).

The comparisons of autocorrelation functions in the mixing layer at the interface for RF300L and GC330L in Figures 6.14.a and 6.14.b first highlight similar time extents of correlation at $x = 2$ m, $x = 2.5$ and $x = 6.5$ m (*i.e.* in cross-sections which are not containing the downstream recirculation zone), while at $x = 4.5$ m, the correlation for GC330L reaches zero after only 0.5 s, therefore indicating that structures have weak 2D characteristics. Considerations on the characteristic time of the modulations – 2-3 s for RF300L and < 2 s for GC330L – finally highlight that the mixing layer for RF300L is mainly settled by structures larger than in GC330L.

The power spectrum densities S_{yy} for RF300L and GC330L are displayed in Figures 6.15.a-b. Unlike to RF300L, the coherent structures developing in the mixing layer at the interface for GC330L do not systematically yield to a peak in both power spectrum densities. Peaks are

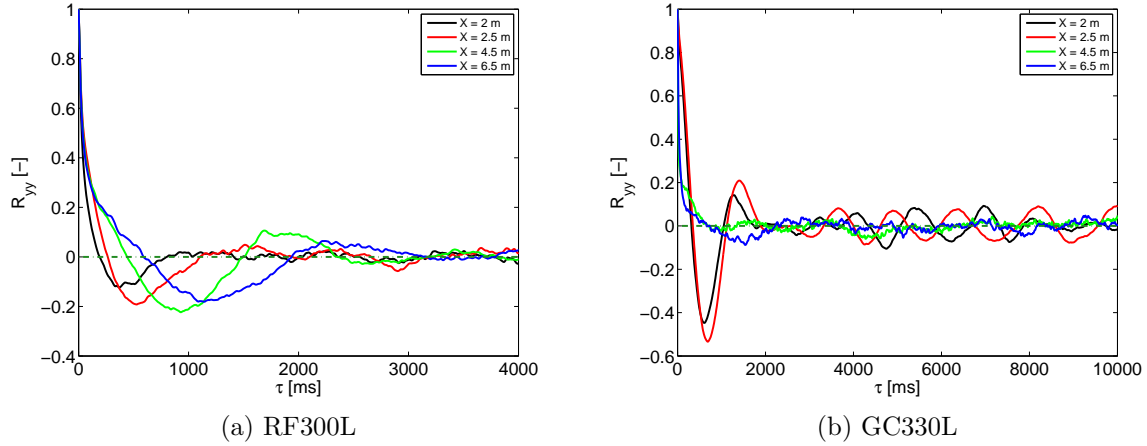


Figure 6.14 – Streamwise evolution of the autocorrelation function of lateral velocity at $0.6 \times H_{fp}$ in the centre of the mixing layer y_c for RF300L and GC330L.

only observed in power spectrum densities worked out with data taken in the converging part of the flow (upstream of the throat at $x = 2.6$ m) and in the diverging part of the flow once the downstream recirculation zone has reattached (downstream of $x = 5.5$ m, Table 6.1). Upstream of the stagnation point, in the diverging part of the flow, the power spectrum densities have a monotonic shape; the energy cascade is operated from the low wave-numbers towards the high wave-numbers.

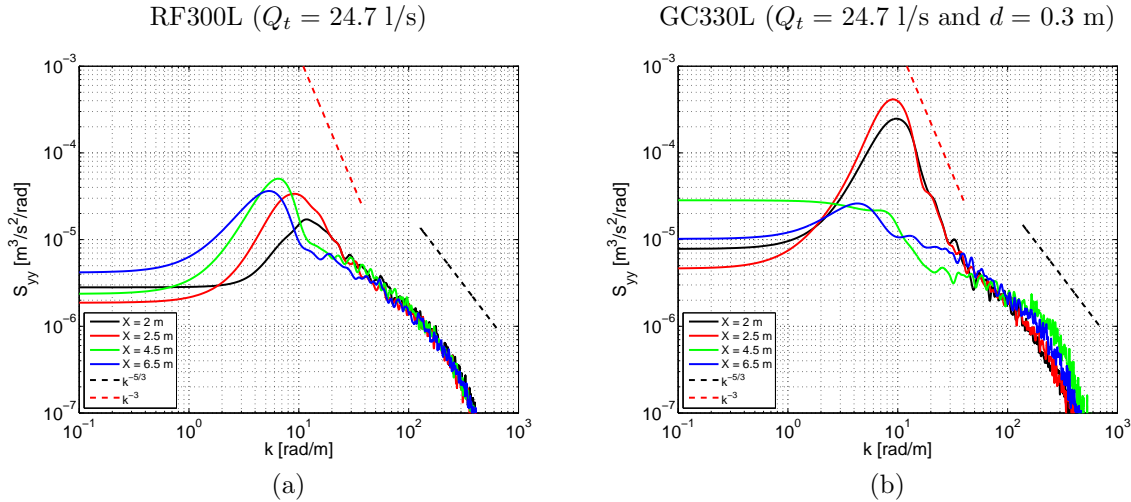


Figure 6.15 – (a-b) Streamwise evolution of transversal power spectrum densities S_{yy} for RF300L (left figure) and GC330L (right figure). Measurements are taken in the centre of the mixing layer ($y = y_c$) at the elevation $z = 0.6 \times H_{fp}$.

In the groyne-case flow, the nature of the coherent structures then depends on the position in the flow relative to the downstream recirculation zone. Descending edges of the observed peaks at low wave-numbers follow a -3 slope, therefore emphasizing that some large-scale structures are restricted to develop in an horizontal plan [Batchelor, 1969; Lindborg, 1999]. By contrast, this absence of peak in the power spectrum densities of data located in the cross-sections containing the recirculation zone highlights that the structures in this area are 3D and are confined by the water depth in the floodplain: the bottom-generated turbulence weakens the turbulence of vertical axis.

The analysis of the cross-power spectrum densities for GC330L in Figure 6.16.b finally indicates that peak of S_{yy} (Figure 6.15.b) in the converging part of the flow and downstream of the stagnation point of the recirculation zone coincides with the peak of S_{xy} . As observed for RF300L, the main contributors to momentum transfer through the interface are the planform vor-

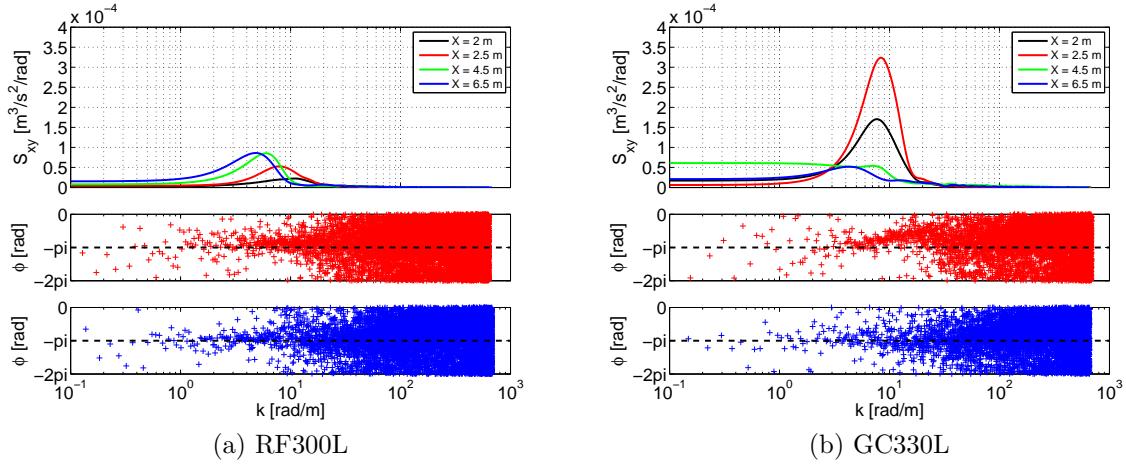


Figure 6.16 – Streamwise evolution of cross power spectrum density S_{xy} and phase relation for RF300L (left figures) and GC330L (right figures). Measurements are taken in the centre of the mixing layer ($y = y_c$ m) at the elevation $z = 0.6 \times H_{fp}$.

tices whom wave-numbers are within $] 5 \text{ m}^{-1} \text{ } 20 \text{ m}^{-1}]$. This result is also confirmed by the phase relation which is equal to $-\pi$ until the descending edge of the peaks at 20 m^{-1} ($\phi = -\pi \Rightarrow$ positive turbulent production [Tennekes and Lumley, 1972]). Concerning measurements at $x = 4.5$ m in the confined shear layer, calculation of S_{xy} and ϕ indicates that contributors to momentum transfer are the vortices whom wave-numbers are within $] 0 \text{ m}^{-1} \text{ } 10 \text{ m}^{-1}]$; within this interval, the level of shear is indeed constant.

6.5.5.2 In the mixing layer developing downstream of the groyne

Like for the mixing layer at the interface, autocorrelation functions, power spectrum densities, cross-power spectrum densities and phase relations are used for characterising the mixing layer that develops at the tip of the groyne. Measurements were performed at $z = 0.6 \times H_{fp}$ in four points (see in Figure 6.17 and in the list below):

- ($x = 2, y = d$), upstream of the groyne at a lateral distance from the floodplain side-wall equivalent to the groyne length d ,
- ($x = 2.5, y = d$), at the tip of the groyne in the groyne cross-section,
- ($x = 4.5, y = 0.2$), on the separation line,
- ($x = 6.5, y = 0.1$), downstream of the stagnation point, approximately in the middle of the wake zone ($y < d/2$).

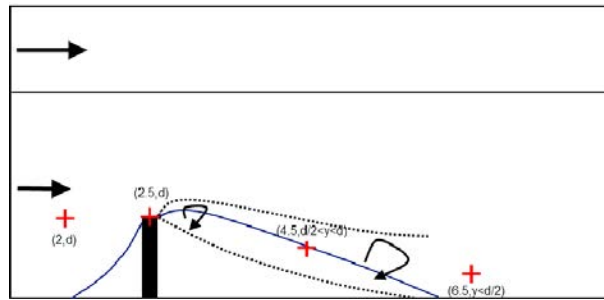


Figure 6.17 – Scheme representing the location of the data used for the spectral analysis in the vicinity of the recirculation zone for GC330L.

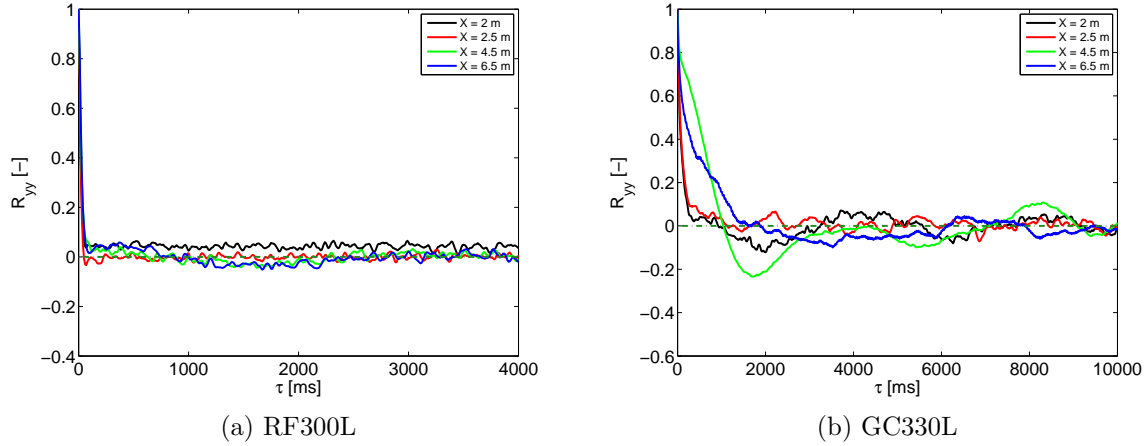


Figure 6.18 – Streamwise evolution of the autocorrelation function of lateral velocity at $0.6 \times H_{fp}$ in the mixing layer developing of both sides of the separation line for GC330L and at $y = 0.3$ m for RF300L.

Autocorrelation functions of the lateral component of the velocity are first analysed. The measurements for GC330L in Figure 6.18.b are compared to data of RF300L at $y = 0.3$ (Figure 6.18.a). Under reference flow conditions, time extents of autocorrelations are equal to zeros, therefore indicating that in the floodplain – far from the mixing layer developing at the interface between channels – turbulence is mainly 3D. By contrast, the time extent of autocorrelations for GC330L may reach 3-4 seconds at $x = 2$ m and in the diverging part of the flow (at $x = 4.5$ m upstream of the stagnation point and at $x = 6.5$ m downstream of the stagnation point), therefore highlighting the presence of some horizontal planform vortices in the flow that develops around the groyne and the recirculation zones. The planform vortices at $x = 2$ m, are a consequence of the upstream recirculation zone which initiates the creation of various 2D and 3D turbulent structures close to the upstream face of the groyne. The planform vortices at $x = 4.5$ m are directly created in the mixing layer developing around the separation line of the downstream recirculation zone, while vortices at $x = 6.5$ are advected by the flow from the upstream cross-sections; the mixing layer at $x = 6.5$ has indeed vanished, because the recirculation zone has reattached one meter upstream.

The comparison of S_{xy} for RF300L and GC330L in Figures 6.19.a-b confirms that the groyne is responsible for the generation of coherent structures that transfers momentum through the separation line of the downstream recirculation zone. Indeed, while no shearing is observed in the floodplain of RF300L, high level of S_{xy} and phase relation equal to $-\pi$ are measured at low wave-numbers ($k \in]0 \text{ m}^{-1} 10 \text{ m}^{-1}[$) along the separation line of the downstream recirculation zone at $x = 4.5$ m.

Concerning measurements at $x = 6.5$ m for GC330L (downstream of the recirculation zone), a small shear and a phase relation equal to $-\pi/2$ is measured at low wave-numbers. This phase of $-\pi/2$ is characteristic of a wake [Tennekes and Lumley, 1972] and means that the coherent structures are degenerating and do no more transfer momentum. The measured low shear is probably due to residual coherent structures that have not completely degenerated and therefore still transfer momentum.

The analysis of S_{yy} in Figure 6.19 then emphasizes that coherent structures generated at the tip of the groyne are first 3D and then becomes partially 2D in the vicinity of the recirculation zone. The power spectrum densities S_{yy} indeed exhibit a -3 slope at the descending edge of the peak observed at low wave-numbers ($k \approx 10 \text{ m}^{-1}$) at $x = 4.5$ m [Kraichnan, 1967]. Nevertheless, unlike mixing layer at the interface, the peak in the distribution of S_{yy} at $x = 4.5$ is not one order of magnitude greater than the rest of the spectrum at low wave-number. As a consequence, 3D structures of wave-numbers within $]0 \text{ m}^{-1} 10 \text{ m}^{-1}[$ must also participate to momentum transfer,

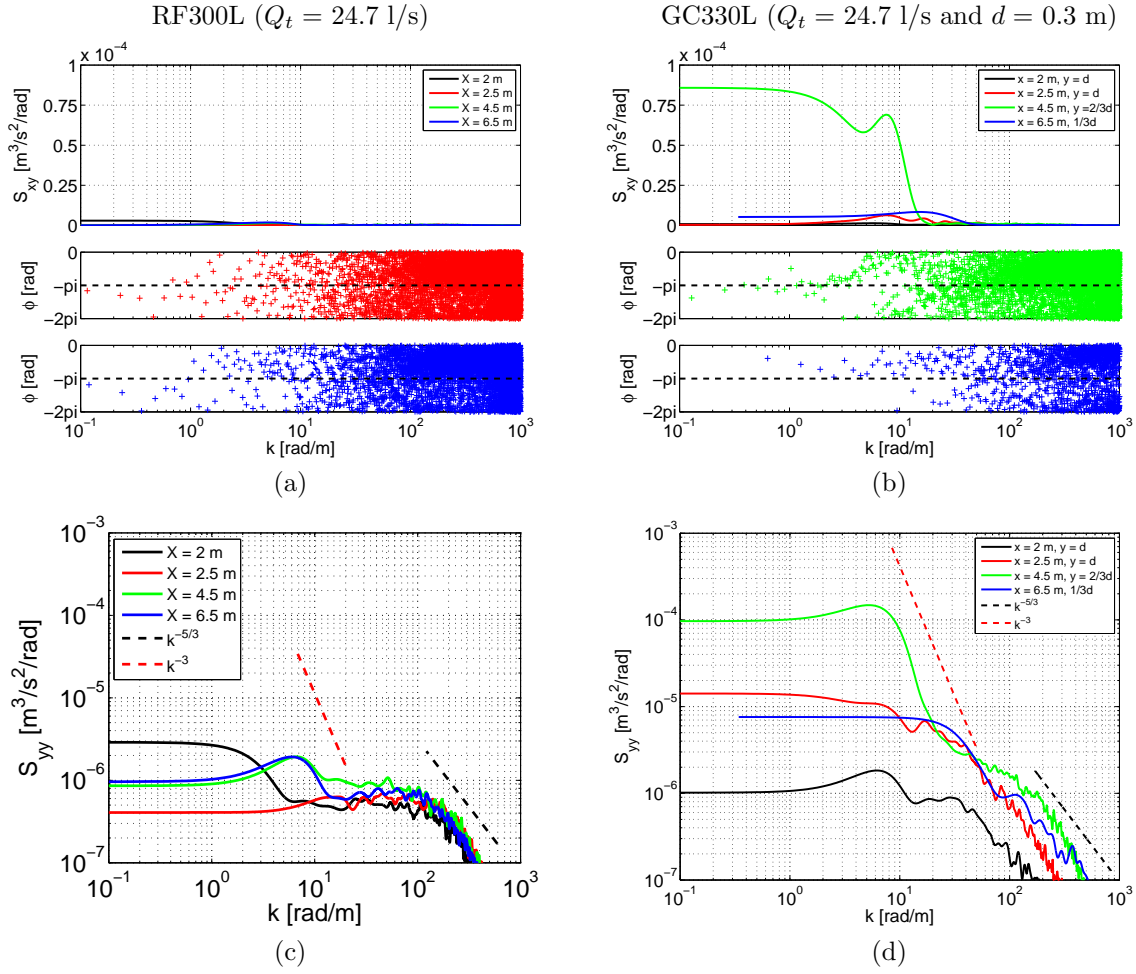


Figure 6.19 – Power spectrum density S_{yy} , cross-power spectrum densities S_{xy} and phase relations for GC330L in the vicinity of the recirculation zone and at $y = 0.3$ m for RF300L. Measurements are taken at the elevation $z = 0.6 \times H_{fp}$.

hence the plateau at low wave-numbers in the distribution of S_{xy} (see at $x = 4.5$ m in Figure 6.19.b); the bottom friction has here a great influence on the length-scale of the turbulence (destruction of the 2D turbulence). Finally, once the recirculation zone has reattached, power spectrum density S_{yy} at $x = 6.5$ m also exhibits a -3 slope, but the sizes of the planform vortices are smaller than at $x = 4.5$ m, since its corresponding wave-number is equal to 20 m^{-1} instead of 10 m^{-1} at $x = 4.5$ m. This behaviour well emphasizes that in the wake zone, the coherent planform vortices degenerate into 3D structures.

6.6 Distribution of boundary shear stress

Introducing a groyne in the floodplain of a compound channel also impacts the distribution of boundary shear stresses in the flow. As shown in Figure 6.20, boundary shear stresses for GC330L compared to RF300L are notably enhanced in the vicinity of the groyne ($x = 2.5$ m) and in the supercritical zone developing downstream of the throat in the floodplain ($x = 4.5$ m). By contrast, they are drastically weakened upstream of the groyne ($x = 2$ m). Understanding the way boundary shear stresses are affected by the presence of the groyne in the flow is paramount for studies on sediment transport and scour counter-measures.

In this section, the distribution of boundary shear stress out of the mixing layers is first studied. In the sequel, distribution in both mixing layers are discussed. Similarly to water levels,

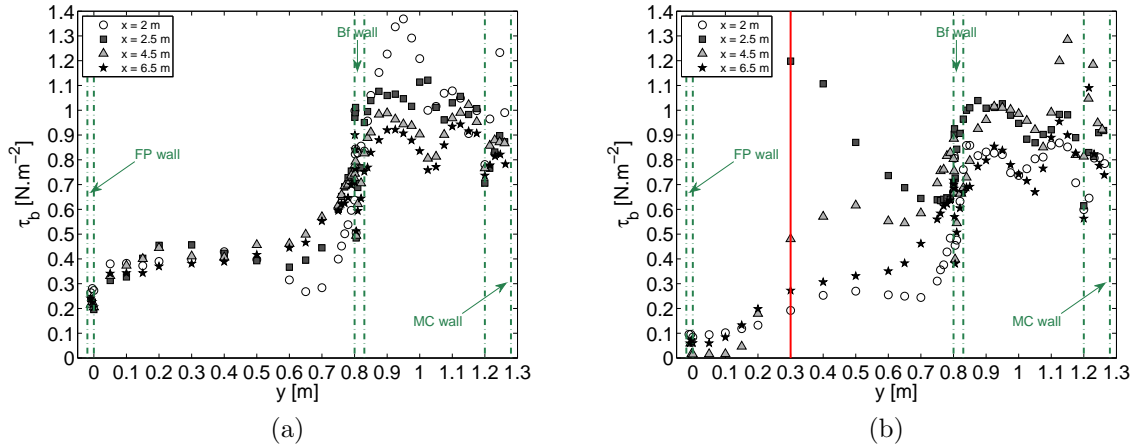


Figure 6.20 – Boundary shear stress distribution for (a) RF300L and (b) GC330L.

velocities and turbulence, the groyne-case flow GC330L ($Q_t = 24.7$ l/s and $d = 0.3$ m) is used for describing the general evolution of boundary shear stress in the flume.

6.6.1 Boundary shear stress out of the mixing layers

Boundary shear stress are first compared to reference flow RF300L in Figure 6.21.a. Excepted upstream of the groyne cross-section at $x = 2$ m, the groyne has low influence on the boundary shear stress in the main channel; boundary shear stresses are only 10 % smaller than the ones for RF300L. For measurements at $x = 2$ m, boundary shear stresses are 25 % smaller. This reduction is due to the upstream rise in water level that impacts the velocity near the bottom ($\tau_b \equiv \rho u_{\text{close to the bottom}}^2$). As shown in Figure 6.21.b, the velocity close to the bottom is indeed equal to 0.5 m/s in average, while for RF300L, this velocity is rather close to 0.6 m/s.

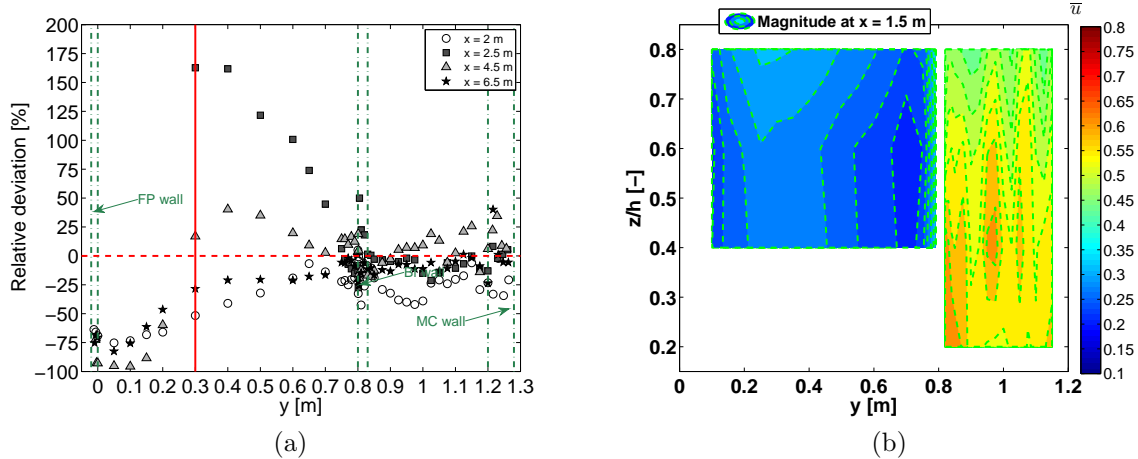


Figure 6.21 – (a) Boundary shear stress distribution for GC330L ($Q_t = 24.7$ l/s and $d = 0.3$ m) compared to RF300L. Uncertainty: $\delta\tau_b/\tau_b \approx 6$ %. (b) Isolines of longitudinal velocity $\bar{u}(x, y, z)$ close to the inlets at $x = 1.5$ m.

Boundary shear stresses in the floodplain decrease upstream of the groyne at $x = 2$ m, in the recirculation zone (see at $x = 4.5$ m and $y < d$) and downstream of the recirculation zone at $x = 6.5$ m. The decrease at $x = 2$ m and at $x = 6.5$ m is mainly due to the rise in water depth in these cross-sections (Figure 6.4.c). Regarding the decrease inside the recirculation zone, it is rather due to the position of the Preston tube in the flow, which did not enable the correct measurements of boundary shear stress in the returning flow (see method of measurements using a Preston tube in §3.3.5). By contrast, boundary shear stresses increase in the groyne

cross-section (at $x = 2.5$ m) and in cross-sections located downstream of the throat (at $x = 4.5$ m). The strong rise in boundary shear stress in the groyne cross-section is due to the plunging flow along the upstream face of the groyne that initiates low water depth and high velocity in this area. This increase may also be due to the so-called horse-shoe vortex system, which increases the bottom-generated turbulence at the tip of the groyne [*Koken and Constantinescu, 2008*] (also see in §1.4.2), but this vortex was not measured in our experiments. The rise in boundary shear stress at $x = 4.5$ m is due to the supercritical regime and the resulting low water depth (Figure 6.4.a) that enhances the friction.

6.6.2 Boundary shear stress in mixing layers

The presence of a groyne set on the floodplain impacts the boundary shear stress distributions in the mixing layer developing at the interface between the main channel and the floodplain. The comparison with the reference flow in Figure 6.21 thus highlights that boundary shear stresses at the interface of cross-sections at $x = 2$ m and $x = 6.5$ m are in average 25 % smaller than the ones for RF300L, while in the groyne cross-section, they are 50 % greater and they are 25 % greater at $x = 4.5$ m. Notice that the higher values of boundary shear stress at $x = 2.5$ m and $x = 4.5$ m confirm why the coherent structures in the mixing layer at the interface have lost their 2D characteristics.

Focus is finally done on boundary shear stresses in the vicinity of the recirculation zone that develops downstream of the groyne. Comparison with RF300L (Figure 6.20 and 6.21.a) indicates that boundary shear stresses are maximal in the vicinity of the tip of the groyne. Local maxima are also measured in the main flow-side of the separation line at $x = 4.5$ m. By contrast, once the stagnation point of the recirculation zone is passed, boundary shear stress are minimal. The strong increase of boundary shear stress in the vicinity of the tip of the groyne is due to the plunging flow at the tip of the groyne and probably due to the horse shoe vortex system that generates additional bottom turbulence. The local maximum in the vicinity of the recirculation zone is due to the mixing layer that develops along the separation line therefore generating an additional source of turbulent production. Finally the difference in boundary shear stress magnitude between $x = 4.5$ m and $x = 6.5$ m are due to the change in flow regime between both sections, which results in a rise in water depth (Figure 6.4.a).

Impacts of a change in the groyne length or total discharge in a groyne-case flow

7.1 Introduction

This chapter also deals with the superimposition of the two issues that are:

- * The interaction between the main channel and the floodplain due to the compound geometry of the flume,
- * The interaction between a flow and a thin obstacle perpendicularly set in the floodplain.

However, after studying in Chapter 6 the differences between the reference flow RF300L and the groyne-case flow GC330L, in this chapter, we are interested in the quantification of the effects on the flow in compound channel of an increase in both the groyne length and the total discharge.

The analysis of the flows with various groyne lengths or total discharges is done with experiments performed in the LMFA laboratory. In Figure 7.1, the vectors and the norm (colour bar) of the depth-averaged velocity field of the groyne-case flows are displayed. It results that the length of the recirculation zones, so as the streamwise variations in velocity, increase with both the length and the total discharge. The turbulence and the boundary shear stress distributions are as well distorted.

In this chapter, we first characterise evolution of the shape of the recirculation zones developing of both sides of the groyne. The main flow features are then studied through the description of the depth-averaged velocity and water level. Mass exchange is therefore evaluated. The impacts on the turbulence and on the boundary shear stress distributions (1) out of the mixing layers, (2) in the mixing layer developing at the interface between the main channel and the floodplain and (3) along the separation line of the downstream recirculation zone are analysed. A quantitative study on coherent structures that develops in such a flow is finally performed.

7.2 Influence of the groyne length

In this section, we quantify the impacts on the flow of a change in the groyne length for a fixed total discharge. The total discharge Q_t is equal to 24.7 l/s and the groyne lengths d are equal to 0.3 m and 0.5 m. We recall that groyne-cases GC330L and GC350L have the same discharge distribution at the inlet and the same outlet settings as the reference flow RF300L (see in Table 3.3).

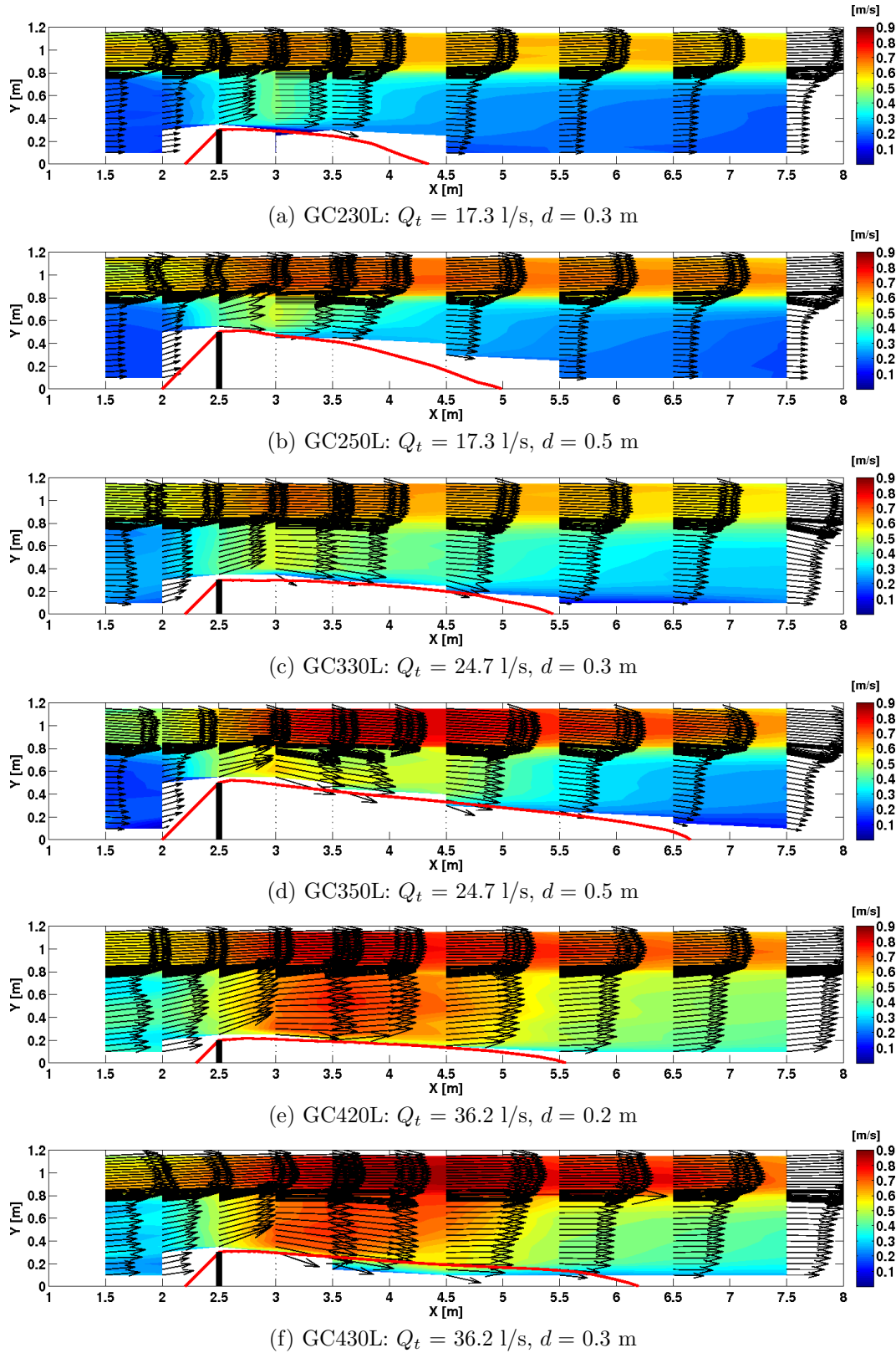


Figure 7.1 – Depth-averaged velocity field (U_d, V_d) of flows measured with a groyne set on the floodplain.

7.2.1 Main flow features

7.2.1.1 Effects on the velocities and depths

The characteristics of the downstream recirculation zones are presented in Figure 7.1. Measurements first emphasize that the longitudinal length of the recirculation zones increases with increasing groyne length ($L_x \approx 3$ m for GC330L and $L_x \approx 4.15$ m for GC350L). This results is consistent with the literature [Rivière *et al.*, 2004]; the increase in the ratio d/B is indeed responsible for the reduction in the ability of the main flow to put along the dead water in the recirculation zone (hence the longer recirculation zone). Moreover, the decrease in L_x/d with increasing groyne length indicates an higher effect of the friction and a lower effect of the groyne length on the turbulence developing in the recirculation zone. Finally, the maximal lateral extent of the downstream recirculation zones occur between $x = 2.5$ m and $x = 2.8$ m.

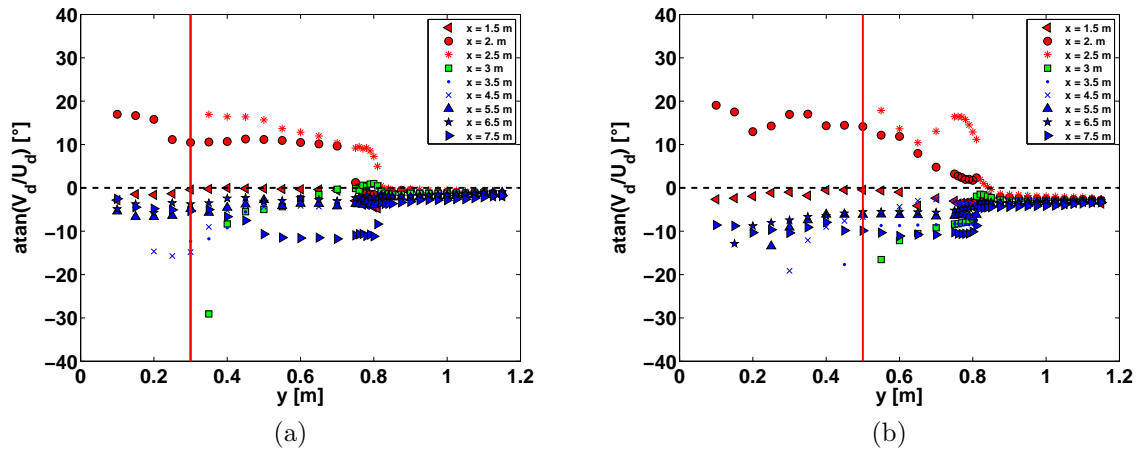


Figure 7.2 – Angle of divergence/convergence for groyne length (a) $d = 0.3$ m and (b) $d = 0.5$ m. Uncertainty: $\delta(V_d/U_d)/(V_d/U_d) < 1.5$ %.

The flow deflection relative to the streamwise direction first emphasizes (Figures 7.2.a and 7.2.b) that the maximal angles of convergence (red markers) are the same whatever the length of the groyne (maximal angle $\approx 19^\circ$); only their distribution in the cross-section changes with the groyne length. The low variations in the value of the convergence angle is directly a consequence of the upstream recirculation zone. According to Koken and Constantinescu [2008], the longitudinal length L_x so as the maximal extent $L_y(x)$ of the upstream recirculation zone are approximately equal to the groyne length d . As a consequence the angle between the separation line of the upstream recirculation zone and the streamwise direction is almost the same whatever the groyne length, hence the relatively similar angles of convergence. By contrast, as the length of the downstream recirculation zone depends on the groyne length, the angles of divergence (green and blue markers) evolve as well, this, even in the main channel. As shown in Figures 7.2.a and 7.2.b, angles of divergence rise with increasing groyne lengths.

The transversal distribution of water levels and the depth-averaged longitudinal velocities are displayed for GC350L at various streamwise cross-sections in Figures 7.3.a-b. With increasing groyne length, the streamwise and spanwise variations in water level are enhanced, this, especially between cross-sections located in the vicinity of the groyne ($x \in [2 \text{ m} - 3 \text{ m}]$). The slope $\partial Z_{ws}/\partial x$ in the vicinity of the groyne is indeed estimated to ≈ 30 mm/m and is twice higher than for GC330L. This steep slope highlights that the contraction initiated by the longer groyne is responsible for a stronger acceleration and plunging flow in the vicinity of the tip of the groyne (data in red at $x = 2.5$ m and green at $x = 3$ m in Figures 6.4.b and 7.3.b). The slope $\partial Z_{ws}/\partial y \approx 2.5$ mm/m for GC330L and ≈ 10 mm/m for GC350L. The groyne blocking off the floodplain increases three-dimensional effects at the tip of the groyne.

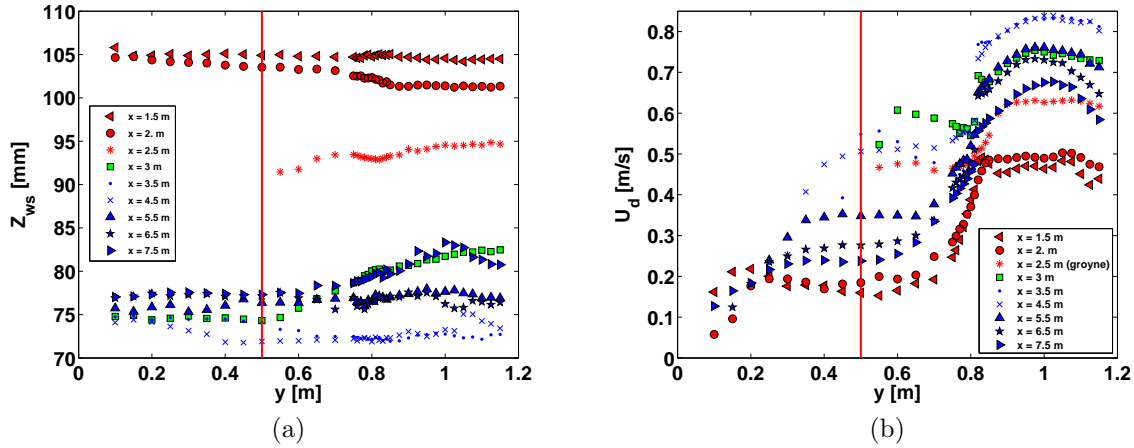


Figure 7.3 – Water levels and depth-averaged longitudinal velocity for groyne-case flow $Q_t = 24.7$ l/s and $d = 0.5$ m. Levels are measured relative to a reference plan whose origin is in the main channel at $x = 7.5$ m and $y = 1.15$ m. Uncertainty: $\delta Z_{ws} = 0.42$ mm and $\delta U_d/U_d = 1.5$ %.

7.2.1.2 Effects on the throat

The Froude distribution for GC350L in Figure 7.4 emphasizes that the flow in the floodplain is supercritical on a greater longitudinal distance than for GC330L: from the flow contraction induced by the downstream recirculation zone until at least $x = 5$ m. In addition, unlike GC330L, the flow in the main channel becomes supercritical between $x = 3.5$ m to $x = 4.5$ m. The transition from supercritical regime to subcritical regime for GC350L is due to the stronger decrease in water depth and flow acceleration in the vicinity of the tip of the groyne relative to GC330L.

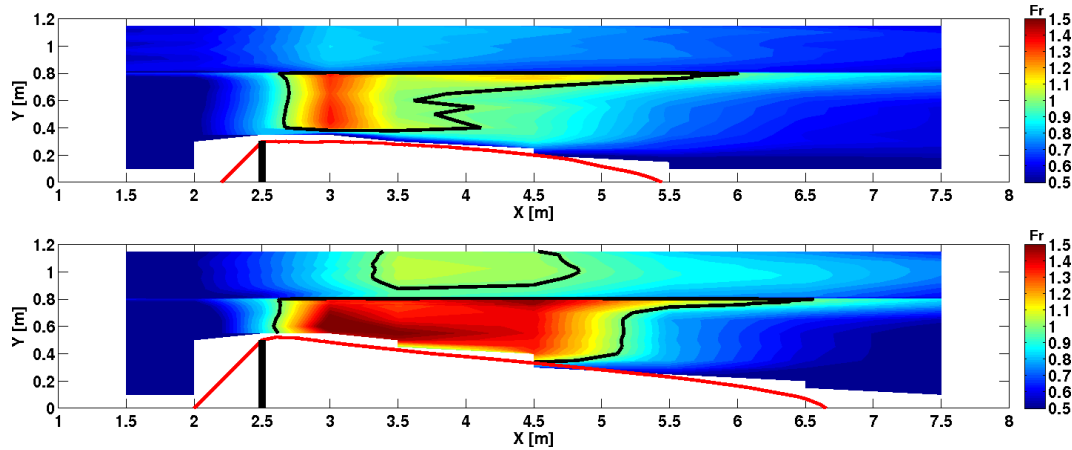


Figure 7.4 – Froude number distribution for $Q_t = 24.7$ l/s, with $d = 0.3$ m (upper image) and $d = 0.5$ m. Uncertainty: $\delta Fr/Fr < 15$ %.

As depicted in Figure 7.4, the analogy to the second theorem of Hugoniot [Chassaing, 2000b] enables to identify a throat at $x \approx 2.6$ m (see the black plain line perpendicular to the main direction near $x = 2.5$ m). Similarly to GC330L, the throat coincides with the maximal expansion of the recirculation zone (Figure 6.2.b).

Regarding, the transition from subcritical to supercritical regime in the main channel, it is not a throat. As the main channel section does not reduce, the theorem of Hugoniot cannot be applied here.

7.2.1.3 Impacts of backwater effects

With increasing groyne length, the hydraulic disconnection in the floodplain generates two backwater curves (see Figure 6.6). The effects of the curve directed from the throat towards the inlets are still difficult to evaluate because of the groyne effects that superimpose on them [Proust, 2005, Chapter 9]. By contrast, due to the supercritical zone in the main channel, effects of the second backwater curve can be better identified than in §6.3.2. The supercritical zone in the main channel indeed indicates that the throat in the floodplain may communicate with the flow in the main channel.

The transition from supercritical to subcritical regime in the floodplain is still a normal undulated jump. This explains the decreasing velocity while the flow section is increasing [Graf and Altinakar, 2000; Rivière et al., 2007].

The backwater effects generated by the tailgate in the floodplain are partially highlighted using the evolution of the water depths in a subsection for groyne-case flows GC330L and GC350L (Figure 7.5.a). Similar rising tendencies of the water depth are measured from $x = 6.5 - 7.5$ m to the end of the flume whatever the flow-case. As the tailgate settings were the same for each flow case, this behaviours of the water depth must be related to the backwater effects generated by the tailgate of the floodplain. But, as the water depth at $x = 7.5$ m differs for GC350L, we cannot conclude that the tailgate is the only responsible for these variations. The smaller depth at $x = 7.5$ m just indicates that the tailgate has enabled to accelerate the return to the reference.

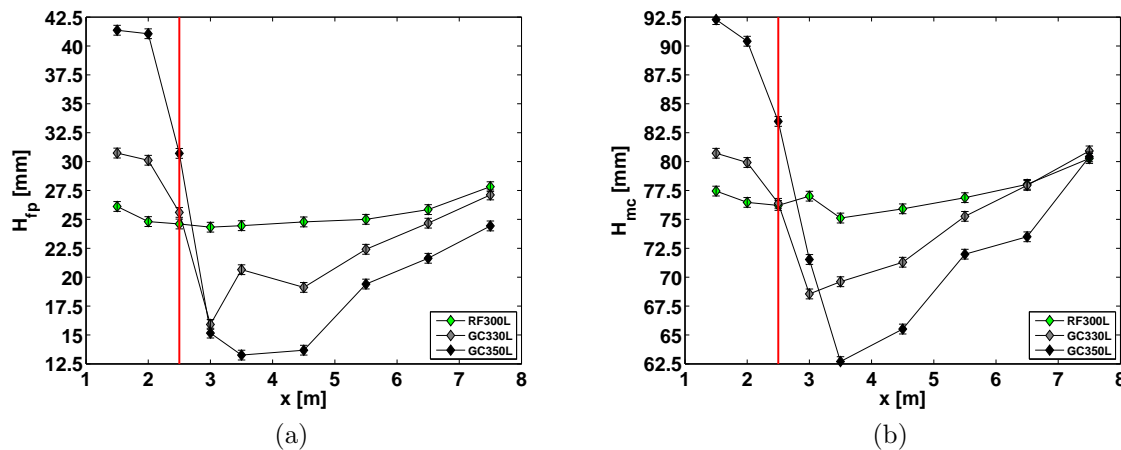


Figure 7.5 – Water levels in a subsection for RF300L, GC330L and GC350L. The groyne is located at $x = 2.5$ m.

Regarding the tailgate effects in the main channel, the water depth in the main channel (Figure 7.5) has the same behaviour as the one in the floodplain. The transition from supercritical to subcritical regime at $x = 4.5$ m then highlights that backwater effects are at least felt until this zone of transition.

Regarding the effects of the discharge distribution at the inlets, measurements of the discharge in the floodplain (Figure 7.7.a) confirm observations of Proust [2005]. If the inlets seem to impose the discharge distribution until $x = 2$ m, downstream of this position, the groyne force the lateral mass exchange to strongly vary when increasing the groyne length. The upstream boundary conditions have few influences in our groyne-case flows.

Accounting for the previous observations on the effects of the backwater curves, the scheme displayed in Figure 6.6 must be therefore corrected as schematized in Figure 7.6:

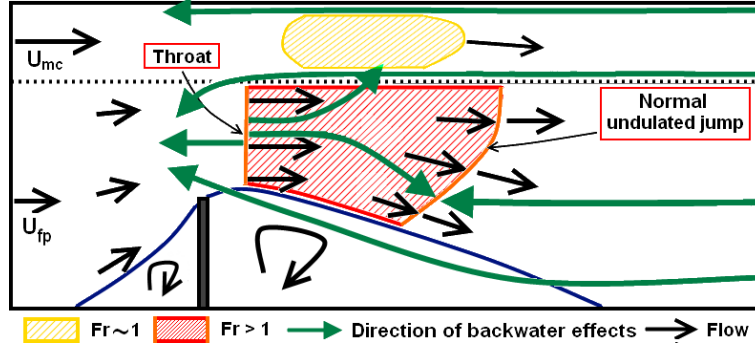


Figure 7.6 – Scheme of the various sources of backwater effects (green arrows) in the presence of a groyne. The scheme is a top view and is not to scale.

7.2.2 Mass exchange

In this section, we quantify the lateral mass exchange between both flume subsections.

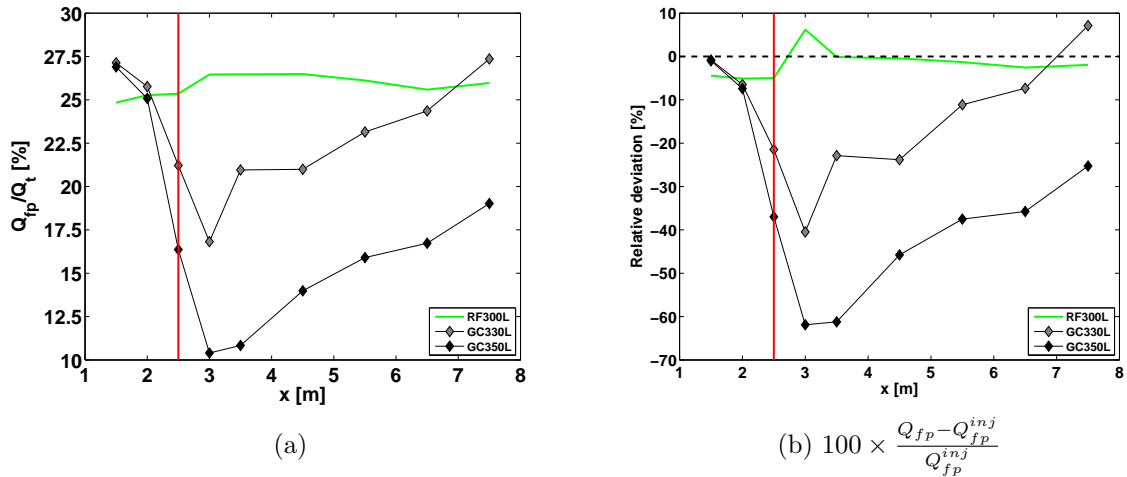


Figure 7.7 – (a) Discharge distribution in the floodplain for $Q_t = 24.7$ l/s. Uncertainty: $\delta(Q_{fp}/Q_t)/(Q_{fp}/Q_t) < 1$ %. (b) Comparison with the injected total discharge.

As shown in Figure 7.7.b, while for GC330L, the discharge in the floodplain Q_{fp} reduces by 40 % in 1.5 m in the converging part, for GC350L, the discharge reduces by 63 %.

In the diverging part, the ratio Q_{fp}/Q_t for GC330L reaches its initial value at the end of the flume (Figure 7.7.a: 27 %, *i.e.* close to the reference value of 25 %), while for GC350L, mass exchange is too strong and discharge ratio in the floodplain is only equal to 19 %. This result is consistent with measurements of water depths (Figure 7.5.a: for $d = 0.5$ m, $H_{fp}(x = 7.5) < H_{fp}^{RF300L}$).

7.2.3 Analysis of the turbulence

In this section we assess the influence of an increase in the groyne length on the turbulence developing (1) in the mixing layer located at the interface between the main channel and the floodplain, (2) along the downstream separation line separating the main flow and the downstream recirculation zone and (3) out of the mixing layers.

7.2.3.1 Geometrical characteristics of the mixing layer developing at the interface between channels

Similarly to GC330L, the longitudinal depth-averaged velocity, for GC350L is never established (see in Figure 7.3.b), so as the mixing layer. Using measurements of the depth-averaged velocities for GC350L, the geometrical characteristics of the mixing layer at the interface (lateral width δ and location of the centre y_c) are worked out using Equation 5.1.

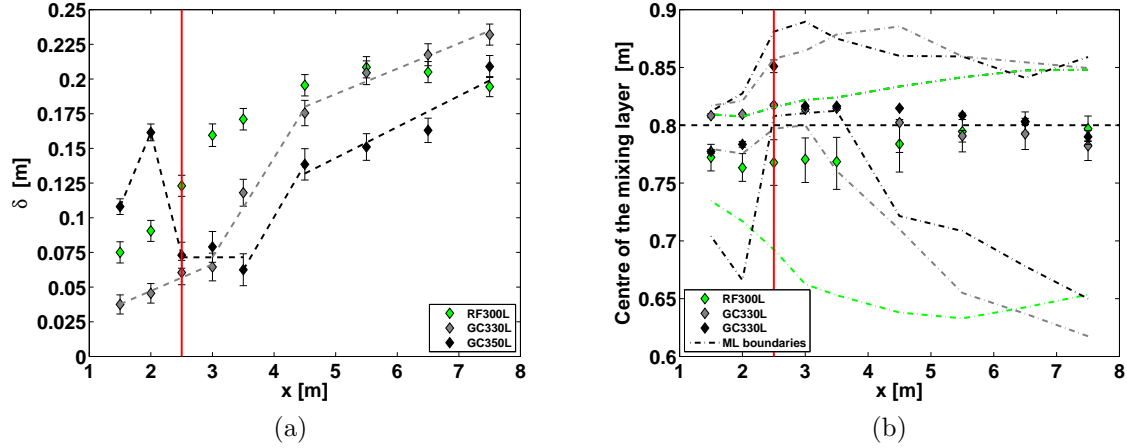


Figure 7.8 – Streamwise evolution of the (a) width δ and (b) centre y_c of the mixing layer for RF300L, GC330L and GC350L.

The streamwise evolution of the mixing layer width for RF300L, GC330L and GC350L is reported in Figure 7.8.a. With increasing groyne length, the width of the mixing layer first increases between $x = 1.5$ m and $x = 2$ m (upstream of the groyne) and is systematically smaller in the rest of the flume. The width of the mixing layer for GC350L is in average 10 cm smaller than for GC330L from the groyne cross-section to the end of the flume. The growth rate strongly rises upstream of the groyne from $x = 1.5$ m to $x = 2$ m ($d\delta/dx = 0.033$ for GC330L and $d\delta/dx = 0.15$ for GC350L), then stabilizes to almost zero in the vicinity of the groyne between $x = 2.5$ and $x = 3.5$, where mass exchange from the floodplain towards the main channel is the strongest. One meter downstream of the throat, the growth rate appears to be similar for both groyne lengths.

When increasing the groyne length, the mixing layer upstream of the groyne can spread in a larger area in the floodplain because of the enlargement of the velocity dip close to the interface in the floodplain (identified from $y = 0.7$ m to the interface for GC330L and from $y = 0.5$ m for GC350L in Figure 7.3.b). The decrease in width and growth rate in the vicinity of the groyne is due to the flow section that is minimal and induces large mass exchange towards the main channel. This mass exchange pushes the mixing layer in the main channel and therefore limits its lateral spreading. The behaviour of the mixing layer in the diverging part of the flow finally indicates that the more the flow deficit in the floodplain reduces and the larger is the width of the mixing layer. Above all, it confirms that the growth rate is inversely proportional to the intensity of the mass exchange.

The position y_c of the centre of the mixing layer for GC350L is then displayed in Figure 7.8.b. With increasing groyne length, the centre of the mixing layer is shifted towards the main channel from the beginning of the flume to the throat cross-section, the uncertainty left aside. The contrary is observed in the diverging part. Moreover, the slight shift observed at $x = 2.5$ m for GC330L in Figure 6.9.b has increased for GC350L: at $x = 2.5$ m, $y_c = 0.815$ m for GC330L and $y_c = 0.85$ m for GC350L. The larger amount of mass to evacuate from the floodplain is larger for GC350L than for GC330L and then pushes the mixing layer in the main channel.

7.2.3.2 Turbulence in the mixing layer at the interface between channels

Similarly to GC330L (Chapter 6), the depth-averaged Reynolds stresses T_{xy} (Figures 7.9.a-b) were measured in 4 cross-sections in the mixing layer for GC350L.

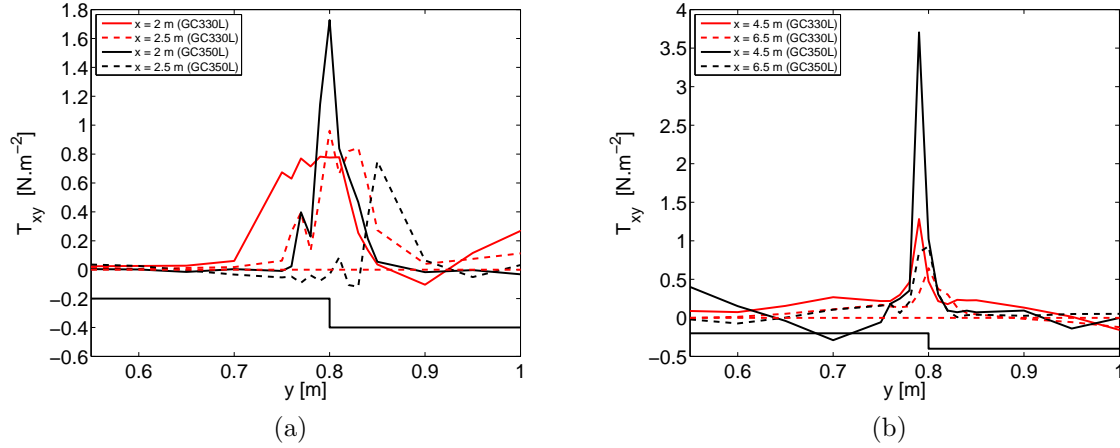


Figure 7.9 – (a-b) Distribution of depth-averaged Reynolds shear stresses T_{xy} in the vicinity of the interface for GC330L and GC350L (uncertainty not estimated).

With increasing groyne length, evolution of depth-averaged Reynolds shear stress between groyne-cases first emphasizes that extreme values are still measured within the mixing layer at the interface and are located at y_c . In the converging part of the flow, mass coming from the floodplain then shifts the peak of Reynolds stresses in the main channel, while in the diverging part, the shift is operated towards the floodplain.

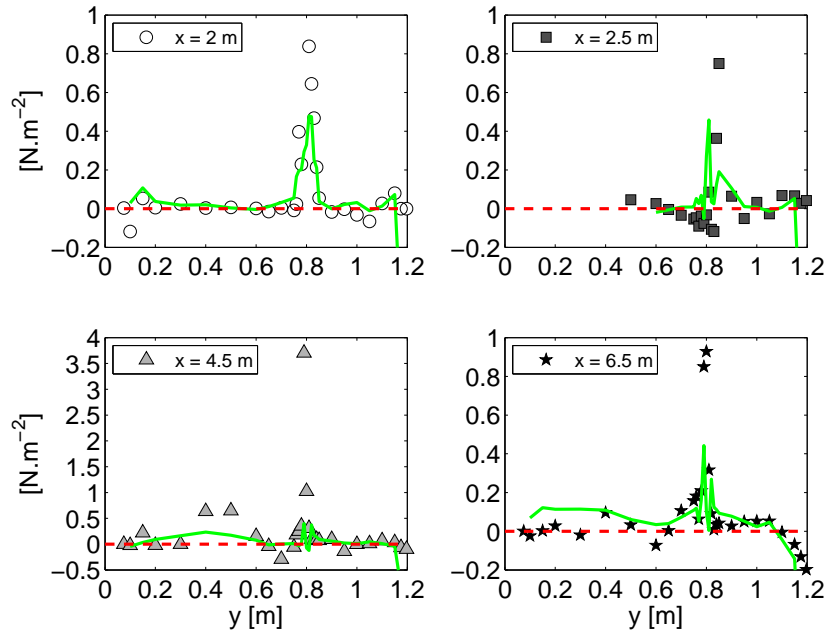


Figure 7.10 – Link between Reynolds shear stress and lateral gradient of longitudinal velocity for GC350L: markers = T_{xy} and lines = $0.1 \times \partial U_d / \partial y$. Uncertainty is not estimated.

Evolution of depth-averaged Reynolds shear stress between groyne-cases then highlights that the magnitude of the peak of T_{xy} increases with the width δ of the mixing layer and the under-feeding of the floodplain. As shown in Figure 7.9.a, T_{xy} at $x = 2$ m increases with the groyne

length, yet the floodplain under-feeding is the same for both cases ($\approx -10\%$ Figure 7.7.b), while the width has increased.

Similarly to GC330L, the comparison of T_{xy} with $a \times \partial U_d / \partial y$ ($a = 0.1 \text{ m}^2/\text{s}$) in Figure 7.10 finally emphasizes a strong correlation between both parameters for data within the mixing layer at the interface. Nevertheless, the maximum of shear is poorly described. Concerning data located in the mixing layer developing in the lee of the groyne (see at $x = 4.5 \text{ m}$), the correlation between T_{xy} and $a \times \partial U_d / \partial y$ is still weak. This bad correlation is once again a consequence of the resolution of the mesh of measurements which does not enable to correctly assess the velocity gradient in the floodplain. Nevertheless, these results confirm that the Boussinesq hypothesis (Equation 2.38) can be used for modelling turbulence far from the recirculation zone.

7.2.3.3 Mixing layer developing at the tip of the groyne

Similarly to GC330L, measurements did not enable the estimation of the geometrical characteristics of the mixing layer at the interface. Only the turbulence is studied.

Peaks of T_{xy} are also observed for GC350L at $x = 4.5 \text{ m}$ along the main flow side of the separation line (Figure 7.11). Peak magnitude increases with increasing groyne length. By contrast, at $x = 6.5 \text{ m}$, the maximum observed for GC350L is not present for GC330L. This difference comes from the fact that for GC330L, the recirculation zone has reattached at $x = 5.5 \text{ m}$ and a wake develops downstream, while for GC350L, the recirculation zone just reattaches and a shear is still felt in the flow.

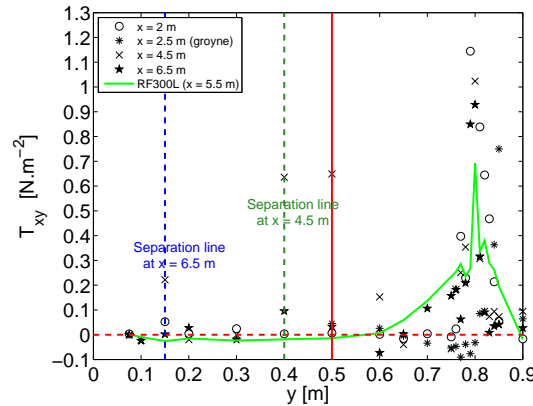


Figure 7.11 – Depth-averaged Reynolds shear stress distribution in the vicinity of the recirculation zone and in the floodplain for GC350L ($Q_t = 24.7 \text{ l/s}$ and $d = 0.5 \text{ m}$). Uncertainty is not estimated.

7.2.3.4 Turbulence out of the mixing layers

Depth-averaged Reynolds stresses T_{xx} and T_{yy} are displayed for GC350L in four cross-sections in Figure 7.12. Comparisons with GC330L (Figure 6.12) emphasize a strong decrease in T_{xx} and T_{yy} in the floodplain of the diverging part (data at $x = 4.5 \text{ m}$ and at $x = 6.5 \text{ m}$); T_{xx} (resp. T_{yy}) for GC350L is in average 150 % (resp. 200 %) smaller than for GC330L. By contrast, changes in the main channel are low. In the converging part (data at $x = 2 \text{ m}$ and at $x = 2.5 \text{ m}$), T_{xx} and T_{yy} slightly increase and are in average 25-50 % greater than those for GC330L. Variations of the normal components of the Reynolds tensor are consistent with variations of longitudinal and lateral velocities in the flume (see in Figure 7.3.b for velocities); T_{xx} gets closer to zeros when the longitudinal velocity decreases and it decreases with increasing velocity. T_{yy} is closer

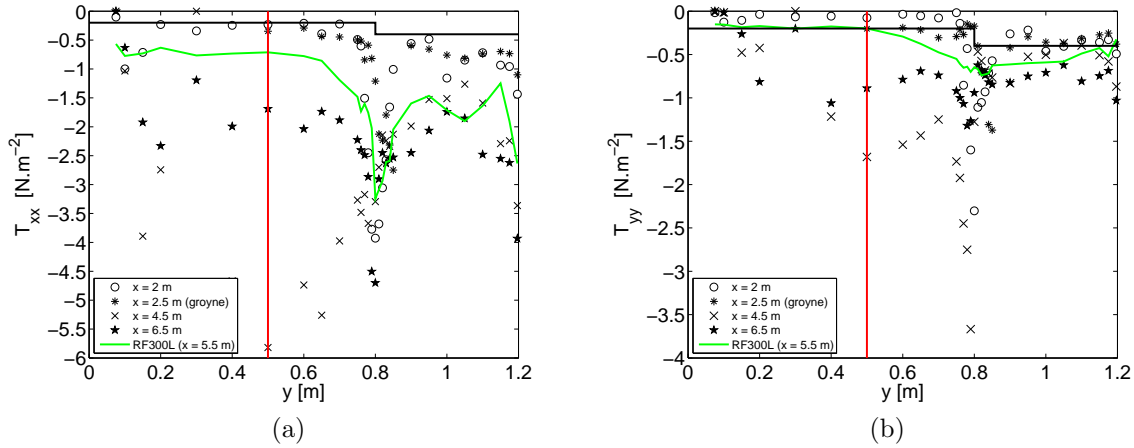


Figure 7.12 – (a-b) Reynolds stresses distribution for GC350L ($Q_t = 24.7$ l/s and $d = 0.5$ m). Uncertainty is not estimated.

to zeros when the flow convergence from the floodplain towards the main channel increases and decreases when the flow divergence from the main channel towards the floodplain increases.

Impact of an increase in the groyne length is finally assessed using the level of turbulence I_k (Equation 5.2). In Figures 7.13.a and 7.13.b, the depth-averaged turbulent intensity (I_k [Chassaing, 2000a; Nezu and Nakagawa, 1993]) is plotted for the four cross-sections we previously studied for GC330L and GC350L. With increasing groyne length, the intensity of turbulence increases upstream of the groyne (from 18-19 % for GC330L to 25 % for GC350L), because of the increase of the turbulent shear. It then decrease in the groyne cross-section, therefore indicating that mass exchange has weakened effects of turbulence. Finally in the diverging part of the flow, the turbulent intensity is weakly influenced by the groyne length and is close to the level measured for reference flow RF300L.

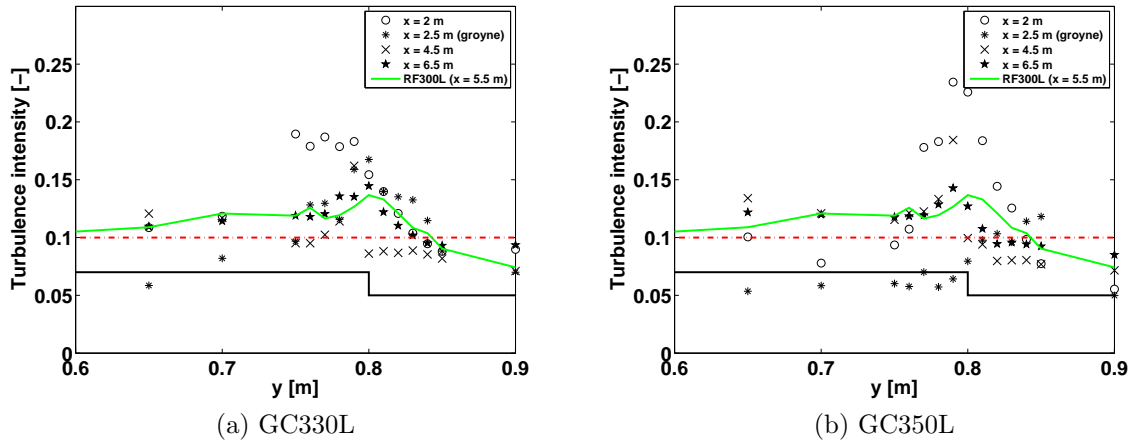


Figure 7.13 – Distribution of depth-averaged turbulent intensity I_k at the interface between channels. Uncertainty is not estimated.

7.2.3.5 Coherent structures in the two mixing layers

Mixing layer at the interface

Spectral analysis for GC330L and GC350L were performed using data at elevation $z = 0.6 \times H_{fp}$ in the centre of the mixing layer (*i.e.* at $y = y_c$).

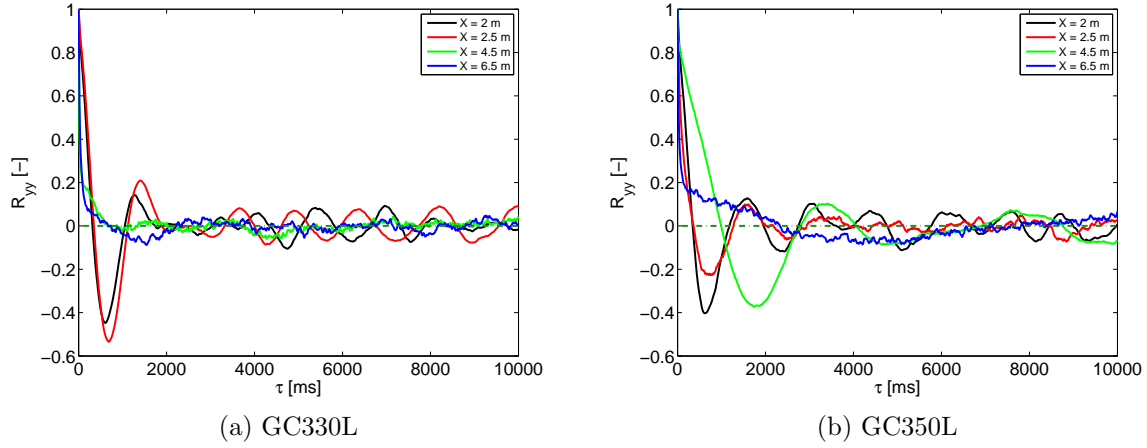


Figure 7.14 – Streamwise evolution of the autocorrelation function of lateral velocity R_{yy} at $0.6 \times H_{fp}$ in the centre of the mixing layer y_c for GC330L and GC350L.

The autocorrelation functions of the lateral velocity for GC330L and GC350L are shown in Figure 7.14. They indicate similar extents of correlation time in the converging part of the flow (2-3 s). By contrast, in cross-sections containing the recirculation zone (between $x > 2.5$ and $x = 5.5$ for GC330L and $x = 6.5$ m for GC350L), the time-extents of the correlation increase with the groyne length, therefore highlighting that structures within the mixing layer have stronger 2D characteristics [Uijtewaal and Booij, 2000].

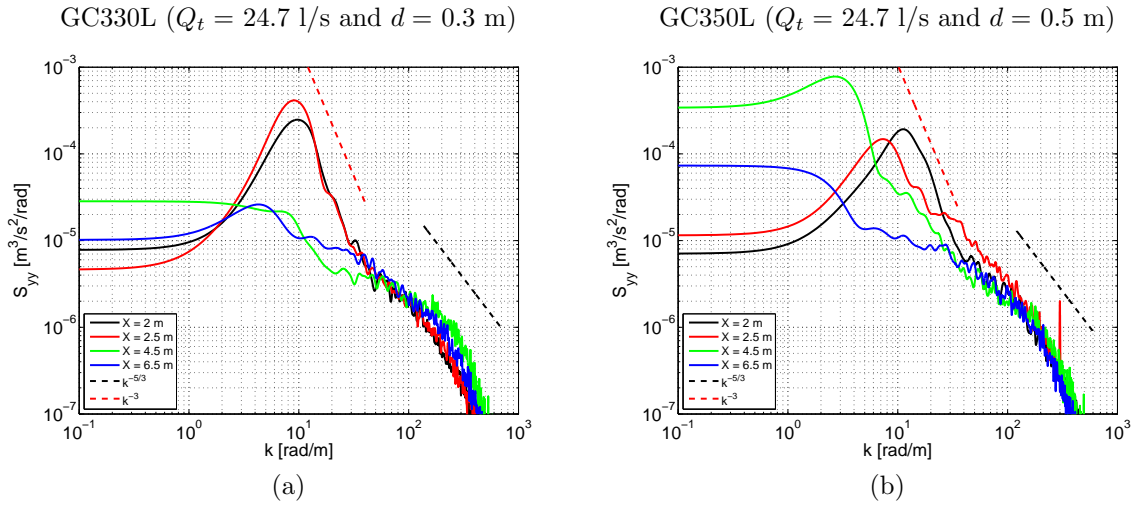


Figure 7.15 – (a-b) Streamwise evolution of transversal power spectrum densities S_{yy} for GC330L (left figure) and GC350L (right figure). Measurements are taken in the centre of the mixing layer ($y = y_c$) at the elevation $z = 0.6 \times H_{fp}$.

Information on the coherent structures generated in the mixing layer at the interface for GC330L and GC350L are then analysed through the use of the cross-power spectrum density S_{xy} , phase relation $\phi(k)$ and power spectrum density S_{yy} .

The power spectrum densities S_{yy} are displayed for GC330L and GC350L in Figure 7.15. The coherent structures in the converging part of the flow are mainly 2D and horizontal whatever the groyne length, because descending edges of the peaks of S_{yy} at low wave-numbers follow a -3 slope. By contrast, while at low groyne length, coherent structures in the diverging part located upstream of the stagnation point ($x < 5.5$) are mainly 3D, with the longest groyne, the spectral densities begin to exhibit a -3 slope at low wave-numbers. Finally downstream of the stagnation point, the mixing layer is settled by 3D structures, whatever the groyne length.

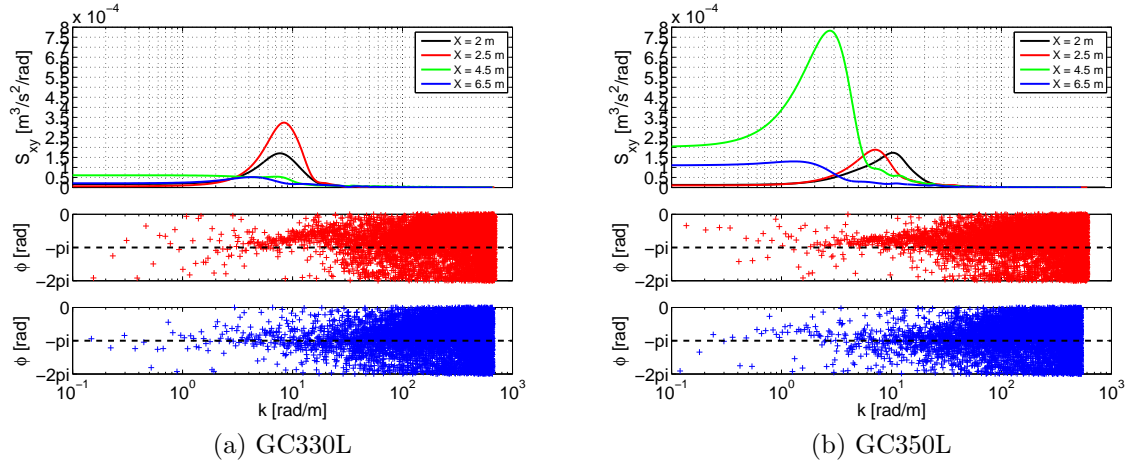


Figure 7.16 – Streamwise evolution of cross power spectrum density S_{xy} and phase relation. Measurements are taken in the centre of the mixing layer ($y = y_c$ m) at the elevation $z = 0.6 \times H_{fp}$.

The analysis of the cross-power spectrum densities in Figures 7.16.a-b indicates that maxima of S_{yy} (Figure 7.15) coincide with maxima of S_{xy} for each groyne-case. With increasing groyne length, the main contributors to the momentum transfer through the interface in the converging part of the flow are the planform vortices whose wave-numbers are within $]5 \text{ m}^{-1} \text{ } 20 \text{ m}^{-1}]$. This result is also confirmed by the phase relation which is equal to $-\pi$ until the descending edge of the peaks ($\phi = -\pi \Rightarrow$ positive turbulent production [Tennekes and Lumley, 1972]). By contrast, measurements in the diverging part indicate that contributors to momentum transfer are first 2D vortices (see at $x = 4.5$ m) and then once the recirculation has reattached, the vortices whose wave-numbers are within $]0 \text{ m}^{-1} \approx 8 - 9 \text{ m}^{-1}]$ (2D+3D).

Mixing layer developing at the tip of the groyne

Information on the nature of the turbulence generated along the separation line are highlighted through the calculation of the autocorrelation functions, of the power spectrum densities, cross-power spectrum densities and phase relations of $u'(z)$ and $v'(z)$ taken in the vicinity of the recirculation zone at $z = 0.6 \times H_{fp}$. For GC350L, the spanwise positions of data used for calculations are as listed below:

- ($x = 2, y = d$), upstream of the groyne at a lateral distance from the floodplain side-wall equivalent to the groyne length d ,
- ($x = 2.5, y = d$), at the tip of the groyne in the groyne cross-section,
- ($x = 4.5, y = 0.4$), on the separation line,
- ($x = 6.5, y = 0.2$), in the vicinity of the stagnation point at $y < d/2$ (approximately in the middle of the wake that develops downstream of this position).

The autocorrelation functions of the lateral component of the velocity are presented in Figure 7.17 for both groyne lengths. Except at $x = 6.5$ m (downstream of the stagnation point), time extents of the correlation are constant whatever the groyne length. Both mixing layers are settled by coherent structures with 2D characteristics. Notice that the large oscillations observed in Figure 7.17.b are due to structures that have been generated in the upstream recirculation zone.

The analysis of S_{yy} in Figure 7.18.a emphasizes the same behaviour as GC330L. Coherent structures are plainly 3D at the tip of the groyne and then become partially 2D along the

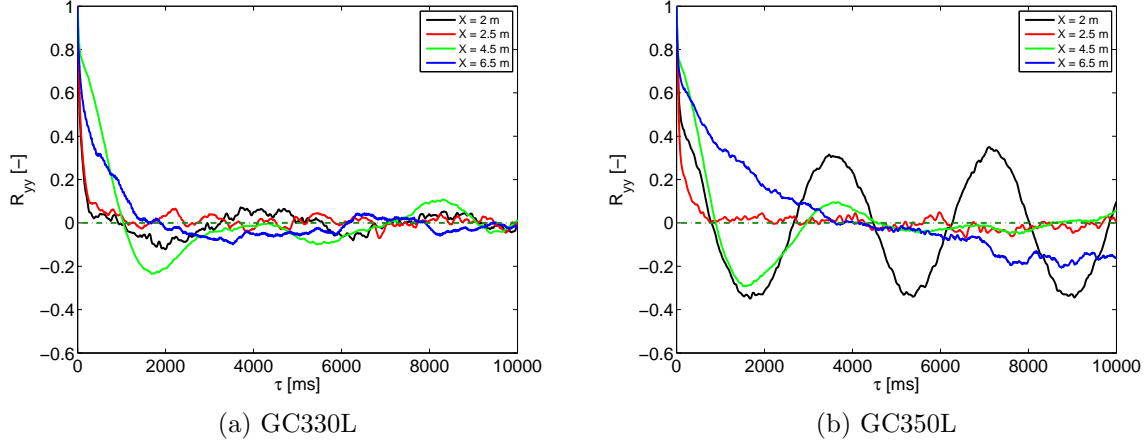


Figure 7.17 – Streamwise evolution of the autocorrelation function of lateral velocity R_{yy} at $0.6 \times H_{fp}$ in the mixing layer developing along the separation line for (a) GC330L and (b) GC350L.

separation line of the downstream recirculation zone (-3 slope at the descending edge of the peak observed at low wave-numbers at $x = 4.5$ m). Moreover, as the peak in the distribution of S_{yy} at $x = 4.5$ is not one order of magnitude greater than the rest of the spectrum at low wave-number, the 3D structures of lower wave-numbers also participate to momentum transfers, hence the plateau at low wave-numbers in the distribution of S_{xy} (see at $x = 4.5$ m in Figure 6.19.b and 7.18.b). Finally, once the recirculation zone has reattached, the coherent planform vortices degenerate into 3D structures.

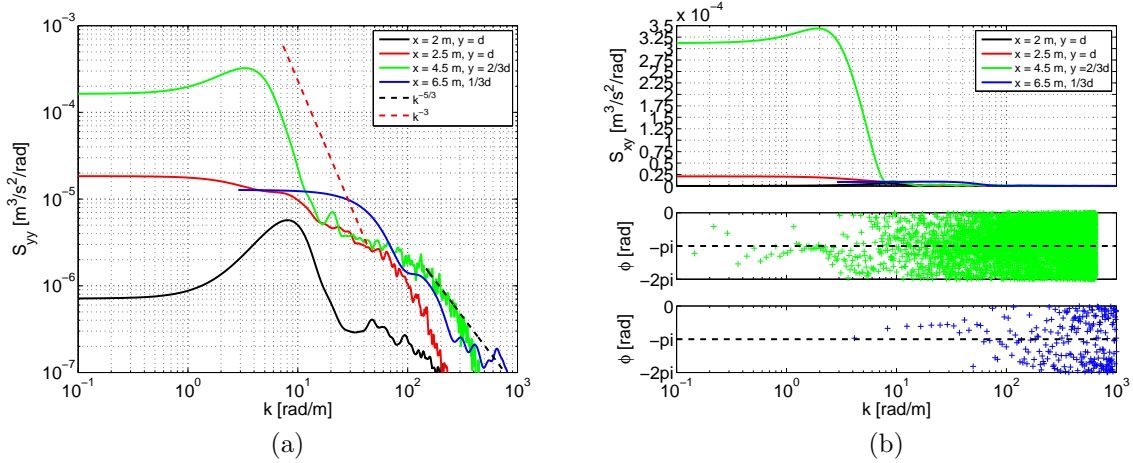


Figure 7.18 – (a) Power spectrum density S_{yy} , (b) cross-power spectrum density S_{xy} and phase relations for GC350L in the vicinity of the recirculation zone. Measurements are taken at the elevation $z = 0.6 \times H_{fp}$.

The comparison of S_{xy} for GC330L and GC350L in Figures 6.19.b and 7.18.b first highlights that the shear along the separation line increases with the groyne length. This momentum transfer is operated by structures whom wave numbers are within $k \in]0 \text{ m}^{-1} 20 \text{ m}^{-1}]$ for GC330L and $k \in]0 \text{ m}^{-1} 8 \text{ m}^{-1}]$ for GC350L. Given the previous interval of wave-numbers, we can moreover say that the sizes of the structures developing along the separation line have increased with d .

Finally, concerning measurements at $x = 6.5$ m for GC350L, a small shear and a phase relation equal to $-\pi/2$ are measured at low wave-numbers, similarly to GC330L. The coherent structures at the end of the downstream recirculation zone have degenerated and do no more transfer momentum.

7.2.4 Distribution of boundary shear stress

The distributions of boundary shear stress out of the mixing layers and within the two mixing layers are studied for two groyne lengths.

The distribution of boundary shear stresses in the floodplain is strongly modified by an increase in the groyne length. Comparing $d = 0.3$ m and $d = 0.5$ m in Figure 7.19, boundary shear stresses are strongly enhanced in the vicinity of the groyne ($x = 2.5$ m) and in the supercritical zone developing downstream of the throat in the floodplain ($x = 4.5$ m). By contrast, they are drastically weakened upstream of the groyne ($x = 2$ m); they are close to zero for GC350L. In the main channel, the distribution is also modified, although to a lesser extent.

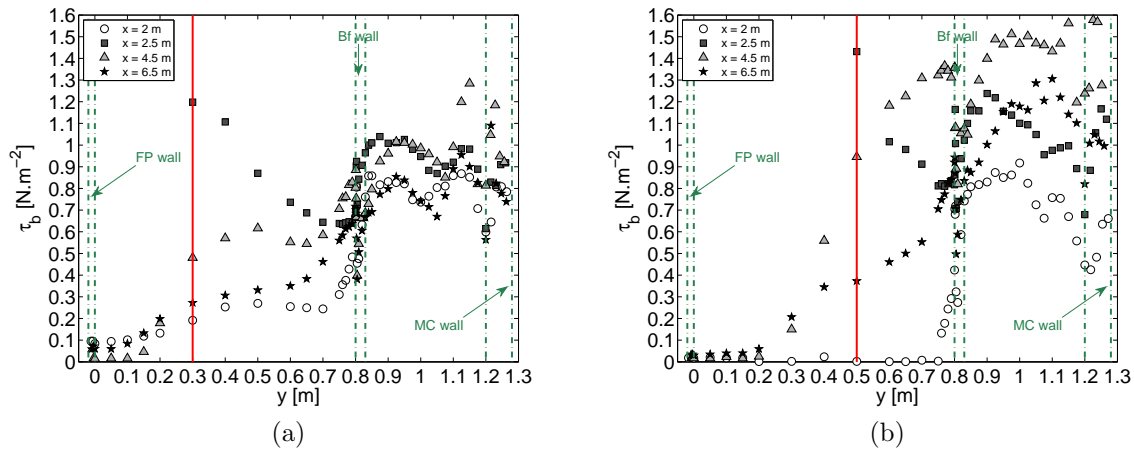


Figure 7.19 – Boundary shear stress distribution for (a) $d = 0.3$ m and (b) $d = 0.5$ m, with $Q_t = 24.7$ l/s.

The relative discrepancy between boundary shear stress for GC350L and GC330L is presented in Figure 7.20.a. When increasing the groyne length, the boundary shear stresses in the floodplain (out of the recirculation zones) increase from the groyne to the end of the flume and decrease upstream of the groyne and in the recirculation zones. The maximum of boundary shear stress is measured in the supercritical zone (see at $x = 4.5$ m and $y > d$), where the water depth is low and the velocity is high (Figures 6.4.a-b and 7.3.a-b). The increase in boundary shear stress at the tip of the groyne (+50 % relative to τ_b of GC330L) is due to the stronger plunging flow at the upstream face of the groyne (probable influence of the Horse Shoe Vortex, but not measured). The decrease in boundary shear stress is maximal upstream of the groyne (−100 % relative to τ_b of GC330L) because of the strong decrease in velocity close to the bottom (see in Figures 6.21.b and 7.20.b). The small values inside the recirculation zones (see at $x = 4.5$ m and $y < d$) are rather due to the position of the Preston tube, which was not facing the returning flow (see method of measurements using a Preston tube in §3.3.5).

Except upstream of the groyne cross-section (see at $x = 2$ m), the boundary shear stresses in the main channel have increased with the groyne length. Boundary shear stress for GC350L can be +75 % higher in the diverging part of the flow. This increase is simply due to the flow acceleration and the lower water depth measured with the longer groyne (Figures 7.3.a-b). By contrast, at $x = 2$ m, they are 25 % smaller than the ones for GC330L. The reduction is due to the low velocity and the high depth in the cross-section (see in Figure 7.3). This reduction is also due to the upstream boundary condition that impacts the velocity near the bottom ($\tau_b \equiv \rho u_{\text{close to the bottom}}^2$). As shown in Figure 7.20.b, the velocity close to the bottom is indeed equal to 0.4 m/s in average, while for GC330L, this velocity is rather close to 0.5 m/s.

The focus is finally done on the boundary shear stresses in the vicinity of the recirculation zone that develops downstream of the groyne (Figure 7.20.a). When increasing the groyne length, the boundary shear stresses increase at the tip of the groyne (plunging flow) and along

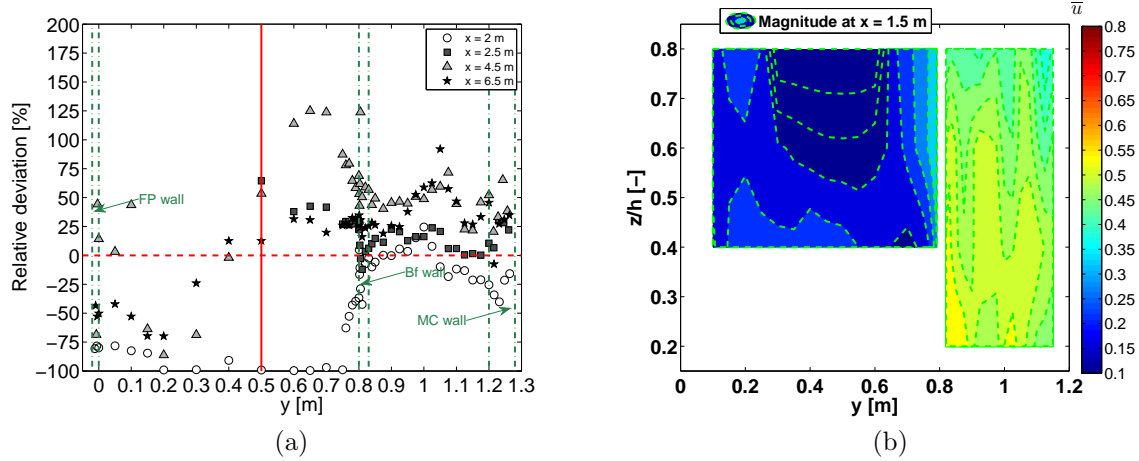


Figure 7.20 – (a) Relative discrepancy of Boundary shear stress between flow cases with $d = 0.5$ m and $d = 0.3$ m. Uncertainty: $\delta\tau_b/\tau_b \approx 6$ %. (b) Isolines of longitudinal velocity close to the inlets.

the separation line (see at $x = 4.5$), because of the stronger shear measured in the mixing layer developing downstream of the groyne (see Figure 7.11.c).

7.3 Influence of the total discharge

7.3.1 Main flow features

In this subsection, the groyne length is fixed ($d = 0.3$ m) and the total discharge is varied ($Q_t = 17.3, 24.7, 36.2$ l/s). The groyne-case flows have the same discharge distribution at the inlet and outlet settings as their corresponding reference flows (see in Table 3.3).

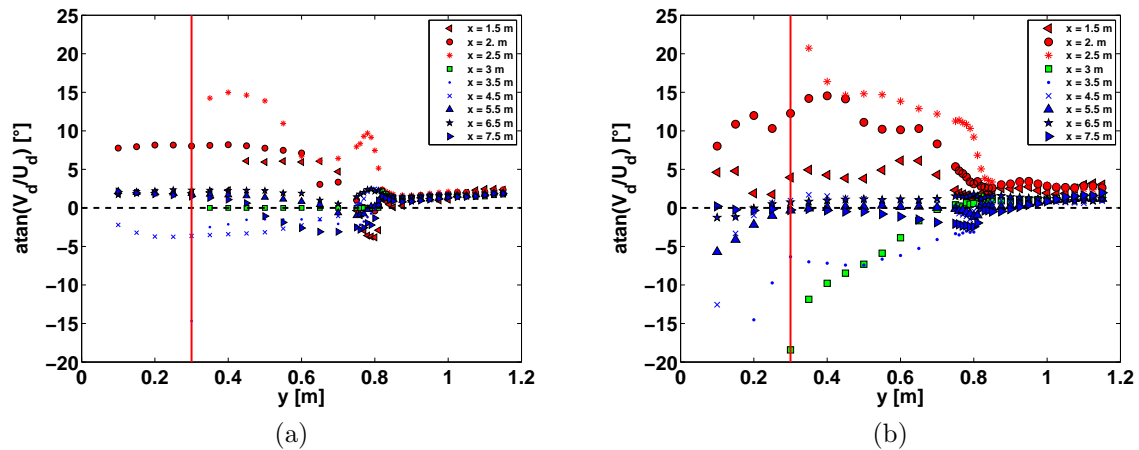


Figure 7.21 – Angle of divergence/convergence for $d = 0.3$ m with (a) $Q_t = 17.3$ l/s and (b) $Q_t = 36.2$ l/s. Uncertainty: $\delta(V_d/U_d)/(V_d/U_d) < 1.5$ %.

7.3.1.1 Effects on the velocities and depths

The characteristics of the downstream recirculation zones are presented in Figure 7.1. The longitudinal length of the recirculation zones increases with the total discharge: ($L_x \approx 1.8$ m for GC230L, $L_x \approx 3$ m for GC330L and $L_x \approx 3.75$ m for GC430L). This result is consistent with the literature; when increasing the total discharge, the water level at the tip of the groyne

increases therefore limiting the influence of the bottom-generated turbulence on the development of the recirculation zone [Babarutsi *et al.*, 1989]. Regarding the lateral maximal extents of the downstream recirculation zones, they are observed downstream of the groyne between $x = 2.5$ m and $x = 2.8$ m.

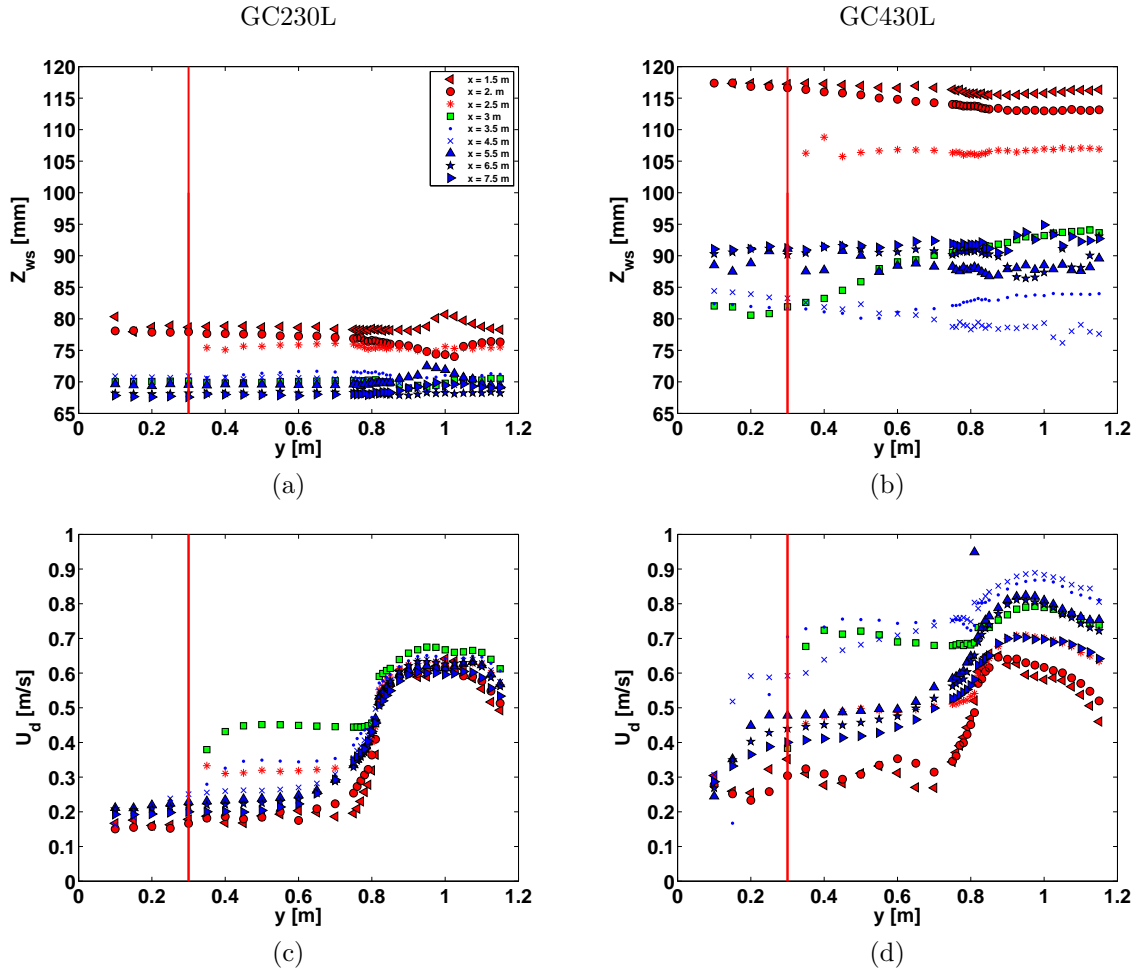


Figure 7.22 – Water levels and depth-averaged longitudinal velocity for groyne-case flows GC230L and GC430L. Levels are measured relative to a reference plan whom origin is in the main channel at $x = 7.5$ m and $y = 1.15$ m. Uncertainty: $\delta Z_{ws} = 0.42$ mm and $\delta U_d/U_d = 1.5$ %.

The flow deflection relative to the streamwise direction is displayed in Figures 6.3 and 7.21.a-b. The maximal angles of convergence (red markers) slowly evolve with the total discharge (from $\approx 15^\circ$ with $Q_t = 17.3$ l/s to $\approx 20^\circ$ at $Q_t = 36.2$ l/s). Similarly to the case of an increase in the groyne length, the low variations in convergence angle are directly a consequence of the upstream recirculation zone, whom lateral and longitudinal extents are proportional to the groyne length d . By contrast, as the length of the downstream recirculation zone depends on the total discharge, the angles of divergence (green and blue markers) evolve, this, even in the main channel (Figure 7.21). The strongest evolution of the flow divergence is felt in the first 1.5 metres of the diverging part of the flow (from $x \approx 2.6$ m to ≈ 4 m), where the flow section is the most reduced.

The transversal distribution of water levels displayed for GC230L and GC430L at various streamwise cross-sections in Figures 7.22.a-b emphasizes that the streamwise, so as the spanwise gradients of water level are enhanced with increasing total discharge, especially between $x = 2$ m and $x = 3$ m in the vicinity of the groyne. The longitudinal gradient $\partial Z_{ws}/\partial x$ close to the groyne is estimated to ≈ 10 mm/m for GC230L, to ≈ 15 mm/m for GC330L (see Chapter 6) and to ≈ 40 mm/m for GC430L and the lateral gradient $\partial Z_{ws}/\partial y$ is close to ≈ 2 mm/m for GC230L, ≈ 2.5 mm/m for GC330L and ≈ 8 mm/m for GC430L. The groyne blocking off the floodplain then increases three-dimensional motions at the tip of the groyne. Moreover, since

the flow acceleration close to the groyne increases with the total discharge (Figures 7.22.c-d), the steep slopes of water levels highlight that the higher available mass at the inlets is responsible for a stronger head loss at the tip of the groyne.

7.3.1.2 Effects on the throat

The Froude distribution for the three total discharges is presented in Figure 7.23. The supercritical zone in the floodplain gets longer with an increase in the total discharge. For the higher total discharge $Q_t = 36.2$ l/s, the main channel also becomes supercritical between $x = 3.5$ m to $x = 4.5$ m like GC350L (see in Figure 7.4). These transitions from subcritical regime to supercritical regime are due to the stronger decrease in water depth and flow acceleration in the main channel.

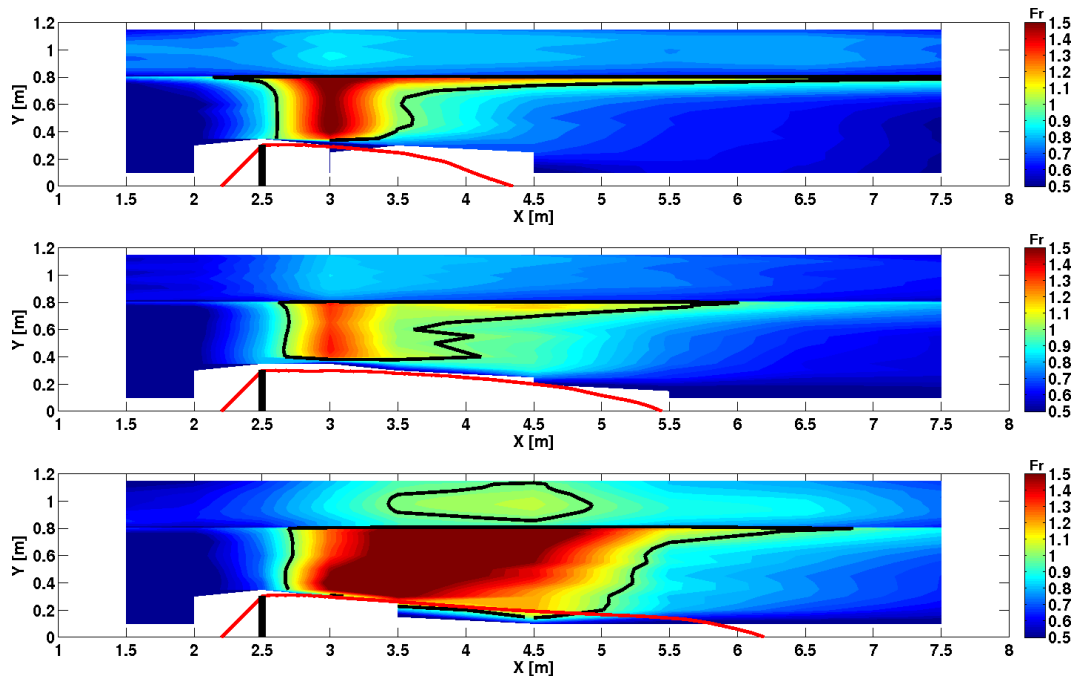


Figure 7.23 – Froude number distribution for $d = 0.3$ and $Q_t = 17.3$ l/s (upper image), $Q_t = 24.7$ l/s (middle image) and $Q_t = 36.2$ l/s. Uncertainty: $\delta Fr / Fr < 15$ %.

A throat is once again identified at $x \approx 2.6$ m in the floodplain (see the black plain line perpendicular to the main direction close to $x = 2.5$ m). Similarly to GC330L, The throat coincides with the maximal expansion of the recirculation zone (Figure 6.2.b), the uncertainty left aside.

The transition from subcritical to supercritical regime in the main channel is not a throat. As the main channel section does not reduce, the theorem of Hugoniot cannot be applied here and this zone is a consequence of the flow acceleration.

7.3.1.3 Impacts of backwater effects

Concerning impacts of an increase in the total discharge on the backwater effects in the flow, no changes relative to §7.2.1.3 were found. As a consequence, the scheme displayed in Figure 7.6 can still be used for explaining the various interactions of backwater curves in the flow.

7.3.2 Mass exchange

In the previous subsection, we have studied the way an increase in the total discharge distorts the flow distribution between channels, therefore inducing mass exchange. In this section, we are interesting in their quantification.

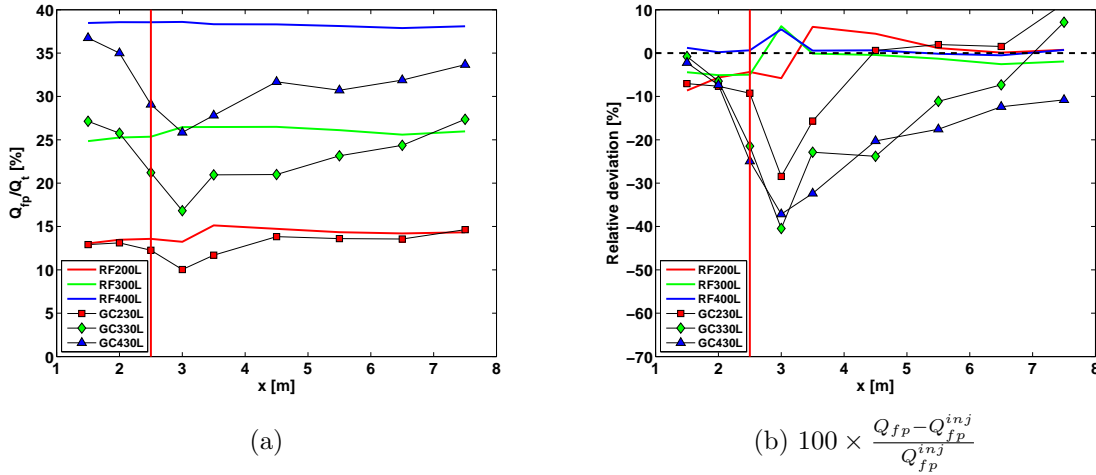


Figure 7.24 – (a) Discharge distribution in the floodplain for GC230L, GC330L and GC430L compared to the references. Uncertainty: $\delta(Q_{fp}/Q_t)/(Q_{fp}/Q_t) < 1$ %. (b) Comparison with the injected total discharge.

The discharge distribution in the floodplain Q_{fp}/Q_t is displayed in Figure 7.24.a. Only the flow with the lower discharge reaches the discharge distribution of its corresponding reference flow. For the two other flows, the higher discharges and therefore the larger amounts of exchanged mass need a greater distance to re-establish.

Nevertheless, despite the larger amount of mass to exchange when increasing the total discharge, the maximal under-feeding of the floodplain reaches a ceiling. As highlighted by the comparison of the measured discharge in the floodplain with the injected discharge at the inlet in Figure 7.24.b, the floodplain is underfed at 40 % maximum, whether for $Q_t = 24.7$ l/s or $Q_t = 36.2$ l/s, the two higher discharges we studied.

7.3.3 Analysis of the turbulence

In this section we assess the influence of an increase in the total discharge on the turbulence developing (1) in the mixing layer located at the interface between the main channel and the floodplain, (2) along the downstream separation line separating the main flow and the downstream recirculation zone and (3) out of the mixing layers.

7.3.3.1 Geometrical characteristics of the mixing layer developing at the interface between channels

Similarly to GC330L, the groyne and the resulting mass exchange whether at low total discharge ($Q_t = 17.3$ l/s) or at high total discharge ($Q_t = 36.2$ l/s, see in §7.3.2), are responsible for the non-establishment of the mixing layer in term of velocity distribution across the channel (Figure 7.22.c-d).

Using measurements of the depth-averaged velocities for GC230L and GC430L, the geometrical characteristics of the mixing layer at the interface (lateral width δ and location of the centre y_c) are then worked out using Equation 5.1.

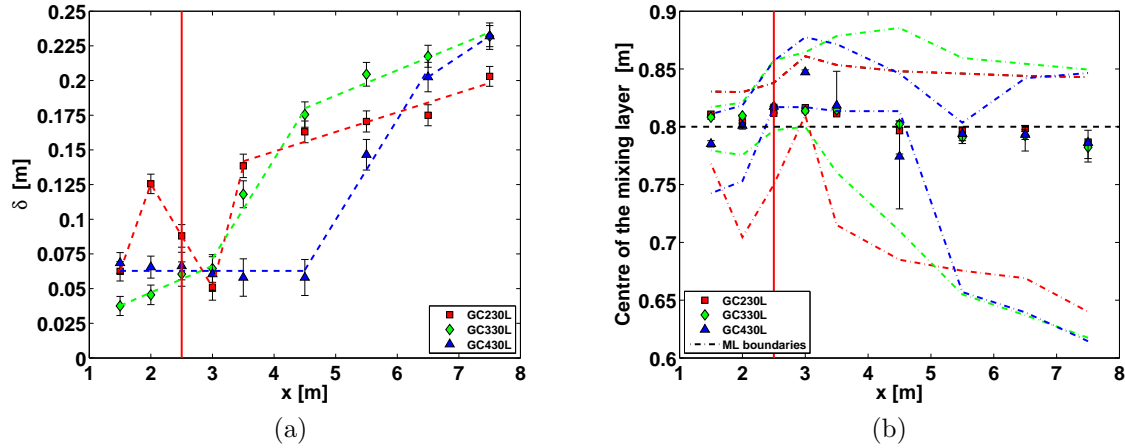


Figure 7.25 – Streamwise evolution of the Width and centre of the mixing layer for $d = 0.3$ and $Q_t = 17.3$ l/s, 24.7 l/s and 36.2 l/s.

The streamwise evolution of the mixing layer width for the three studied discharges (and fixed d) is reported in Figure 7.25.a. The width is constrained upstream of the groyne when increasing the total discharge. This is due to appearance of a velocity dip in the vicinity of the interface in the spanwise profile of the longitudinal velocity, which prevents the mixing layer to spread too far in the floodplain (Figures 6.4.b and 7.22.c-d). Downstream of the groyne, the width depends on the lengths of the recirculation zone. Moreover, while the recirculation zone has not reattached, the width of the mixing layer at the interface is reaching a ceiling. This ceiling is also due to dips in the velocity profiles close to the interface. Finally, when approaching the position of the stagnation point, the widths have the same rising tendencies as observed under reference flow conditions. Thus, from $x = 4.5$ m to the $x = 6.5$ m, the width of the mixing layer for the flow with the intermediate discharge ($Q_t = 24.7$ l/s) is greater than in the other cases (see in Chapter 5: effects of the shallowness).

The growth rate is also impacted by the total discharge, especially at the highest total discharge ($Q_t = 36.2$ l/s). Upstream of the groyne from $x = 1.5$ m to $x = 2$ m, the growth rate decreases with increasing total discharge ($d\delta/dx = 0.12$ for GC230L, $d\delta/dx = 0.033$ for GC330L and $d\delta/dx \approx 0$ for GC430L), then stabilizes to almost zero in the vicinity of the groyne between $x = 2.5$ and $x = 3$, where mass exchange from the floodplain towards the main channel is the strongest. Once the throat is passed the growth rate is equivalent for all cases, excepted between $x = 3$ m and $x = 4.5$ m for GC430L where the growth rate is still equal to zero.

The position y_c of the centre of the mixing layer is then displayed in Figure 7.25.b. With increasing total discharge, the centre of the mixing layer is literally pushed towards the main channel from the beginning of the flume to the throat cross-section, the uncertainty left aside. The contrary is observed in the diverging part, but in a lesser extent.

7.3.3.2 Turbulence in the mixing layer at the interface between channels

The width and the position of the centre of the mixing layers for the three discharges are then compared to distributions in 4 cross-sections of depth-averaged Reynolds shear stress T_{xy} in Figure 7.26.

Evolution of depth-averaged Reynolds shear stress between groyne-cases emphasizes that extreme values are still located in the mixing layer at the interface and are located at y_c . Moreover, with increasing total discharge, the maximum of T_{xy} decreases in the converging part of the flow and beyond the cross-section where the downstream recirculation zones have reattached (*i.e.* at $x \geq 6.5$ m, in the diverging part of the flow). The strongest decrease occurs between GC330L

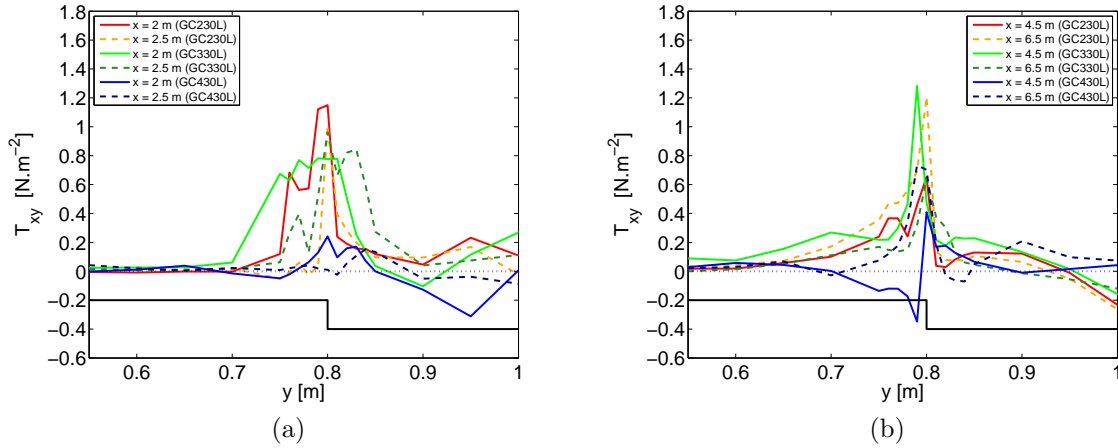


Figure 7.26 – Distribution of depth-averaged Reynolds shear stresses T_{xy} in the vicinity of the interface for GC230L, GC330L and GC430L (uncertainty not estimated).

and GC430L; the peak at the interface is almost divided by ten. By contrast, in cross-sections containing the recirculation zone (between $x > 2.5$ m and $x = 4.5$ m for GC230L, $x = 5.5$ m for GC330L and $x = 6$ m for GC430L), the maximum of T_{xy} does not monotonously evolve with increasing total discharge. Like in §7.2.3.1, an increase in T_{xy} between groyne-cases in Figure 7.26 must be correlated to an increase in the width of the mixing layer, to an higher under-feeding of the floodplain and to a small relative flow depth.

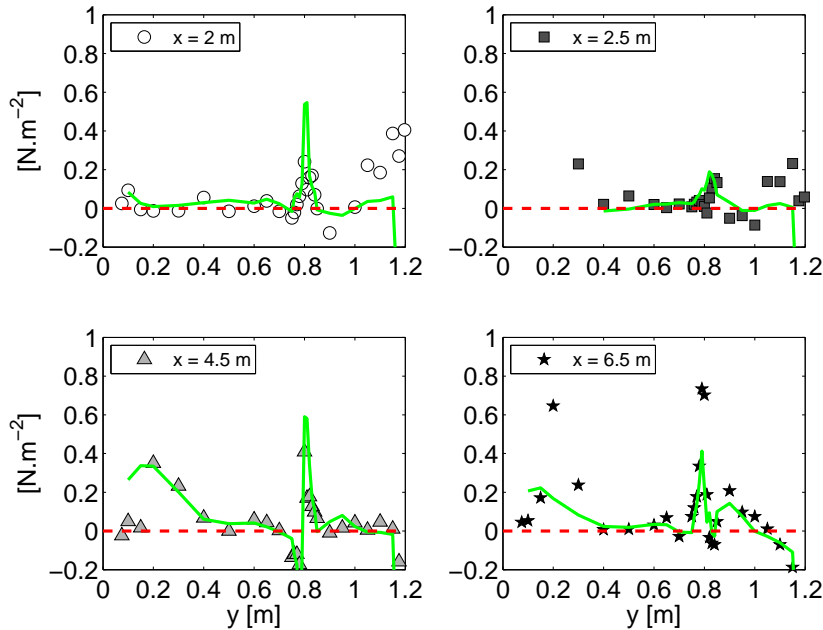


Figure 7.27 – Link between Reynolds shear stress and lateral gradient of longitudinal velocity: markers = T_{xy} and lines = $0.1 \times \partial U_d / \partial y$. Uncertainty is not estimated.

Similarly to GC330L, the comparison of T_{xy} with $a \times \partial U_d / \partial y$ ($a = 0.1 \text{ m}^2/\text{s}$) in Figure 7.27 finally emphasizes a strong correlation between both parameters for data out of the recirculation zone, thus even at high total discharge. These results confirm that the Boussinesq hypothesis (Equation 2.38) can be used for modelling turbulence far from the recirculation zone.

7.3.3.3 Mixing layer developing at the tip of the groyne

Similarly to GC330L, measurements did not enable the estimation of the geometrical characteristics of the mixing layer at the interface. Only the turbulence is studied.

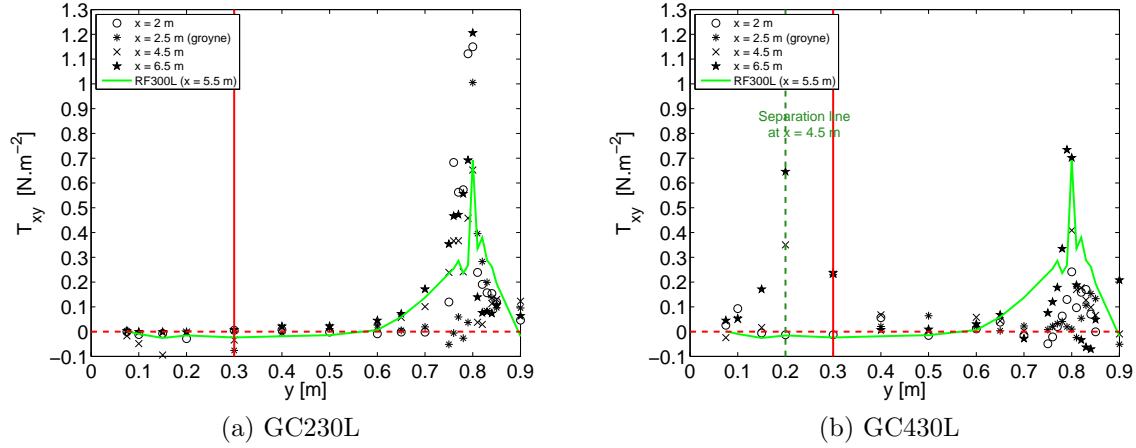


Figure 7.28 – Reynolds stresses distribution in the vicinity of the recirculation zone and in the floodplain. Uncertainty is not estimated.

The distribution of T_{xy} in the floodplain for GC230L and GC430L is displayed in Figures 7.28.a-b (for GC330L see in Figure 6.11.a). It highlights different behaviours depending on the total discharge and therefore depending on the length of the recirculation zone (Table 6.1). For GC230L, a negative peak is observed at $x = 4.5$ m and the distribution of T_{xy} at $x = 6.5$ m is flat and equal to 0 Pa. For GC330L a maximum of T_{xy} is observed at $x = 4.5$ m on the separation line and a negative peak is observed at $x = 6.5$ m. And finally for GC430L, a maximum of T_{xy} is measured at $x = 4.5$ m and $x = 6.5$ m; these peaks are equivalent to those measured along the interface between the main channel and the floodplain. These observations emphasize that the shear between the main flow and the recirculation zone increases with increasing total discharge. Regarding the negative peak of T_{xy} for GC230L and GC330L, they must be related to a wake that develops directly downstream of the stagnation point [Chu et al., 2004].

7.3.3.4 Turbulence out of the mixing layers

The Impact of an increase in the total discharge at a given groyne length is finally assessed using the level of the turbulence in the flow. The depth-averaged turbulent intensity (I_k , Equation 5.2 [Chassaing, 2000a; Nezu and Nakagawa, 1993]) is plotted for GC230L and GC430L in Figure 7.29. With an increase in the total discharge, the turbulent intensity increases in the recirculation zone and remains stable in the rest of the flow, but decreases in the mixing layer at the interface. The decrease in turbulent intensity in the mixing layer at the interface is maybe due to the higher amount of exchanged mass that could weaken the turbulence.

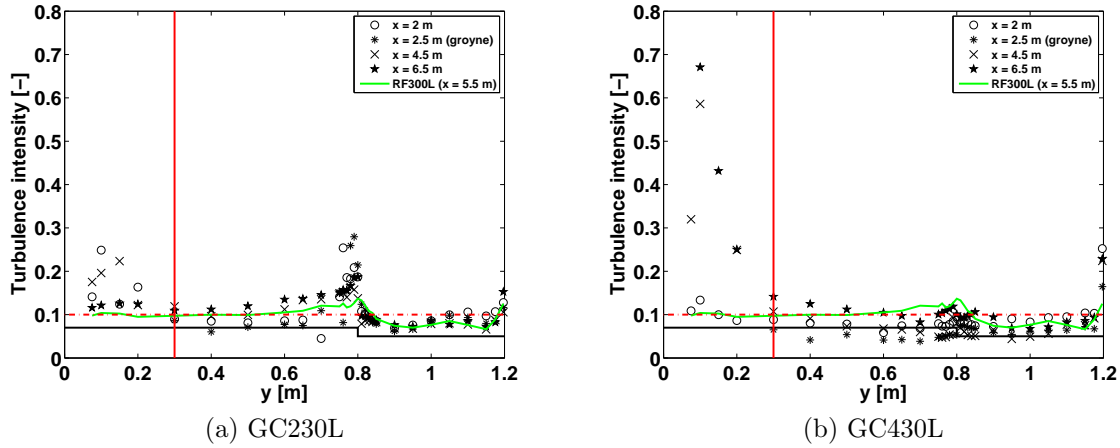


Figure 7.29 – Distribution of depth-averaged turbulent intensity I_k . Uncertainty is not estimated.

7.3.3.5 Coherent structures in mixing layers

Mixing layers at the interface

Spectral analysis for GC230L and GC430L were performed using data at $z = 0.6 \times H_{fp}$ in the centre of the mixing layer (*i.e.* at $y = y_c$).

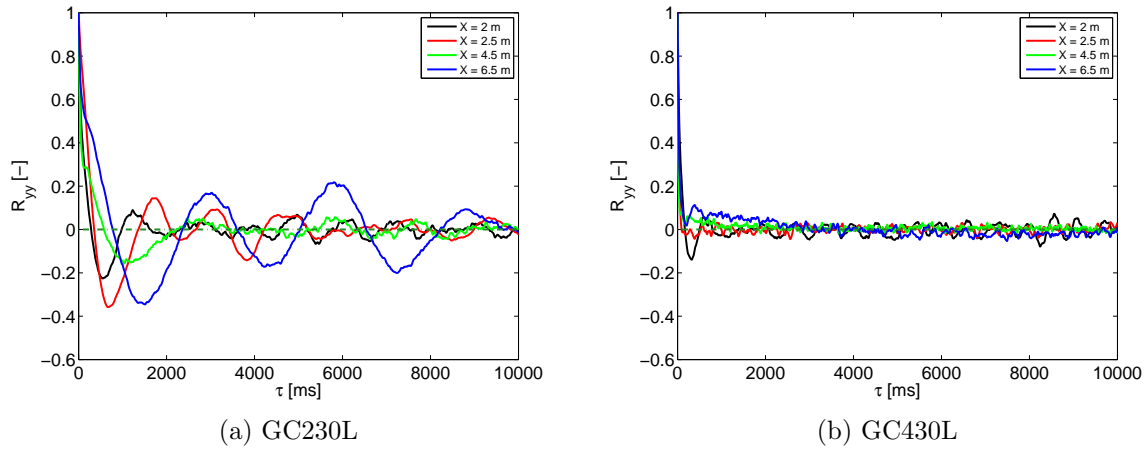


Figure 7.30 – Streamwise evolution of the autocorrelation function of lateral velocity at $0.6 \times H_{fp}$ in the centre of the mixing layer y_c for GC330L and GC350L.

The autocorrelation functions of the lateral velocity is displayed in Figure 7.30. They indicate a decrease in the time extents of the correlation with increasing total discharge (2-10 s for GC230L and less than 1 s for GC430L): the coherent structures inside the mixing layer lose their 2D characteristics [Uijtewaal and Booij, 2000].

Information on the coherent structures generated in the mixing layers for GC230L and GC430L are then analysed through the use of the power spectrum density S_{yy} (Figures 7.31.a-b), the cross-power spectrum density S_{xy} and phase relation $\phi(k)$ (Figure 7.32).

Even at high total discharge, the coherent structures in the converging part of the flow still have 2D characteristics, because peaks of S_{yy} exhibit a -3 slope at their descending edges. Nevertheless these structures are less energetic than at low discharge. By contrast, structures in the diverging part of the flow become 3D, therefore emphasising that the turbulence coming from the bottom have increased.

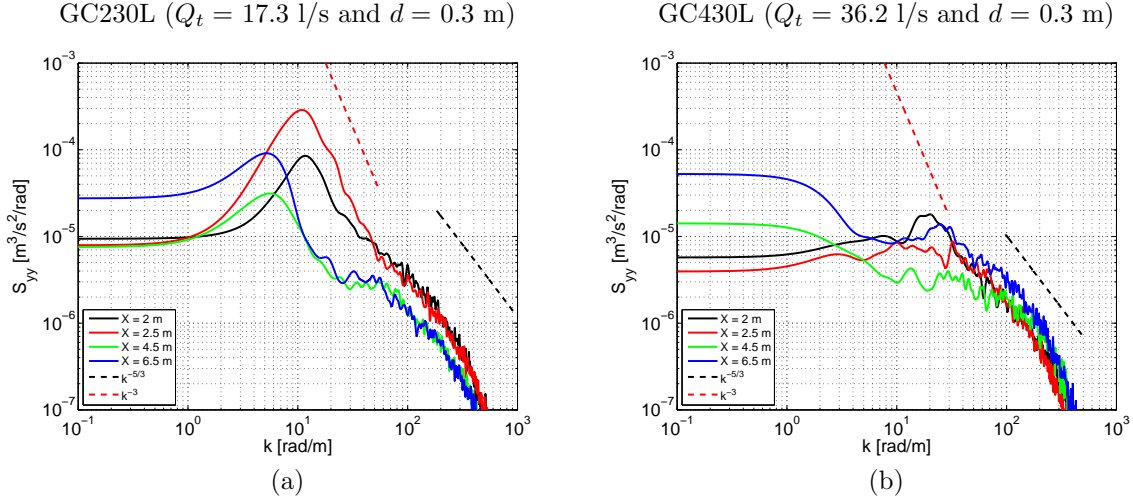


Figure 7.31 – (a-b) Streamwise evolution of transversal power spectrum densities S_{yy} for GC230L (left figure) and GC430L (right figure). Measurements are taken in the centre of the mixing layer ($y = y_c$) at the elevation $z = 0.6 \times H_{fp}$.

The analysis of the cross-power spectrum densities in Figures 7.32.a-b finally indicates that maxima of S_{yy} collapse with the maxima of S_{xy} for each groyne-case. Nevertheless, whether in the converging part or in the diverging part of the flow, with increasing total discharge, the horizontal planform vortices are not the only contributors to the momentum transfer through the interface, because the shear at low wave-numbers has the same order of magnitude as the peak.

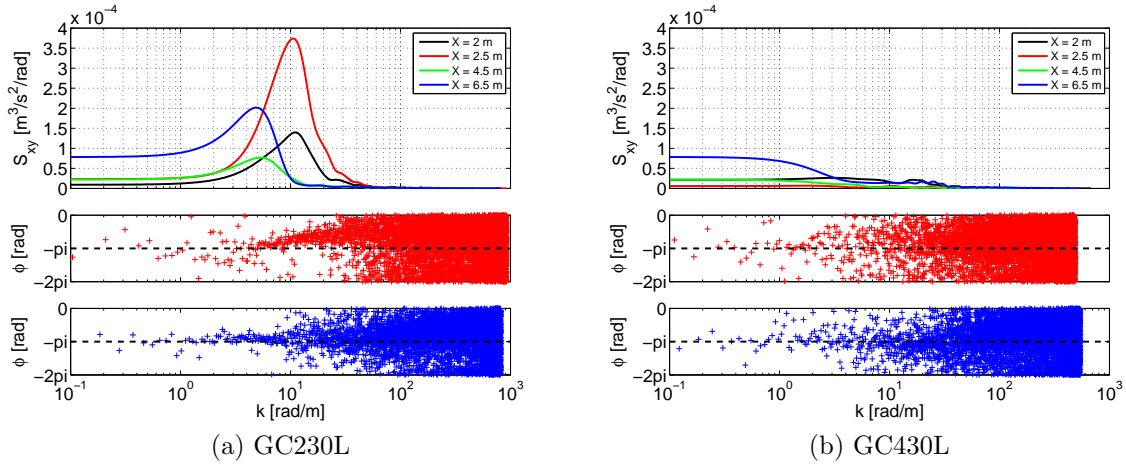


Figure 7.32 – Streamwise evolution of cross power spectrum density S_{xy} and phase relation. Measurements are performed in the centre of the mixing layer ($y = y_c$ m) at the elevation $z = 0.6 \times H_{fp}$.

Mixing layer developing at the tip of the groyne

Information on the nature of the turbulence generated along the separation line are highlighted through the calculation of the power spectrum densities, cross-power spectrum densities and phase relations of $u'(z)$ and $v'(z)$ taken in the vicinity of the recirculation zone at $z = 0.6 \times H_{fp}$. For GC230L and GC430L, spanwise positions of data used for calculation are as follow:

- ($x = 2, y = d$), upstream of the groyne at a lateral distance from the floodplain side-wall equivalent to the groyne length d ,
- ($x = 2.5, y = d$), at the tip of the groyne,

- GC230L: ($x = 4.5, y = 0.1$), in the middle of the wake developing downstream of the stagnation point. GC430L: ($x = 4.5, y = 0.2$), at $x = 4.5$ m on the separation line,
- GC230L: ($x = 6.5, y = 0.1$), 2 m downstream of the stagnation point. GC430L: ($x = 6.5, y = 0.2$), in the vicinity of the stagnation point. At $y < d/2$ approximately in the middle of the wake zone.

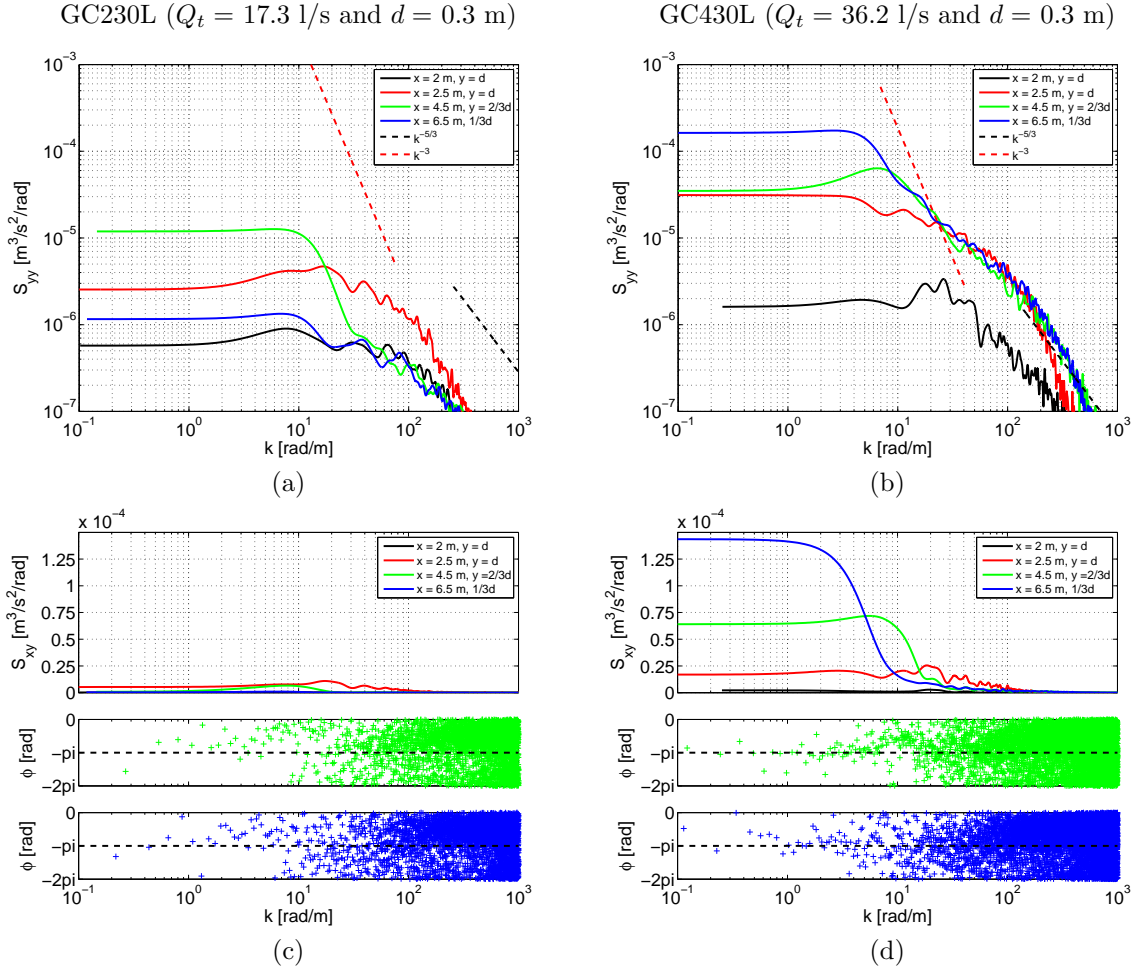


Figure 7.33 – (a-b) Power spectrum density S_{yy} , (c-d) cross-power spectrum densities S_{xy} and phase relations for GC230L and GC430L in the vicinity of the recirculation zone. Measurements are performed at the elevation $z = 0.6 \times H_{fp}$.

The analysis of S_{yy} in Figures 7.33.a-b emphasizes that coherent structures along the separation line acquire 2D characteristics when increasing the total discharge (see at $x = 4.5$ m). The power-spectrum density indeed exhibit a small peak at low wave numbers with a slope of -3 (descending edges). Once the recirculation zone has reattached, power spectrum densities at $x = 6.5$ m lose the -3 slope, which indicates that in the wake zone, the few existing coherent planform vortices coming from the separation line have degenerated into 3D structures.

Comparison of S_{xy} for GC230L, GC330L and GC430L in Figures 7.33.c, 6.19.b and 7.33.d finally highlights that even if 2D structures are observed, they are not the only contributor to the momentum transfer. Whether at low or at high total discharge, momentum transfer is operated by structures whose wave numbers are within $k \in]0 \text{ m}^{-1} \approx 10 \text{ m}^{-1}]$.

7.3.4 Distribution of boundary shear stress

The distribution of boundary shear stresses in the floodplain is strongly influenced by an increase in the total discharge. As displayed in Figures 7.34.a-b for GC230L and GC430L, boundary shear stresses are enhanced in the vicinity of the groyne ($x = 2.5$ m) and in the supercritical zone developing downstream of the throat in the floodplain ($x = 4.5$ m). The contrary is observed upstream of the groyne ($x = 2$ m). Regarding the distribution in the main channels, changes are lower than in the floodplain.

The boundary shear stresses for GC230L and GC430L are then directly compared to GC330L in Figures 7.34.c-d; only distributions between $y = d$ and the main channel wall are considered (for $y < d$, comparisons cannot be done as the downstream recirculation zones have not the same lengths). When increasing the total discharge, the boundary shear stresses in the floodplain (out of the recirculation zones) increase from the groyne to the end of flume and decrease upstream of the groyne. The variations in boundary shear stresses are mainly due to the variations in depths and velocities within and between the flow-cases.

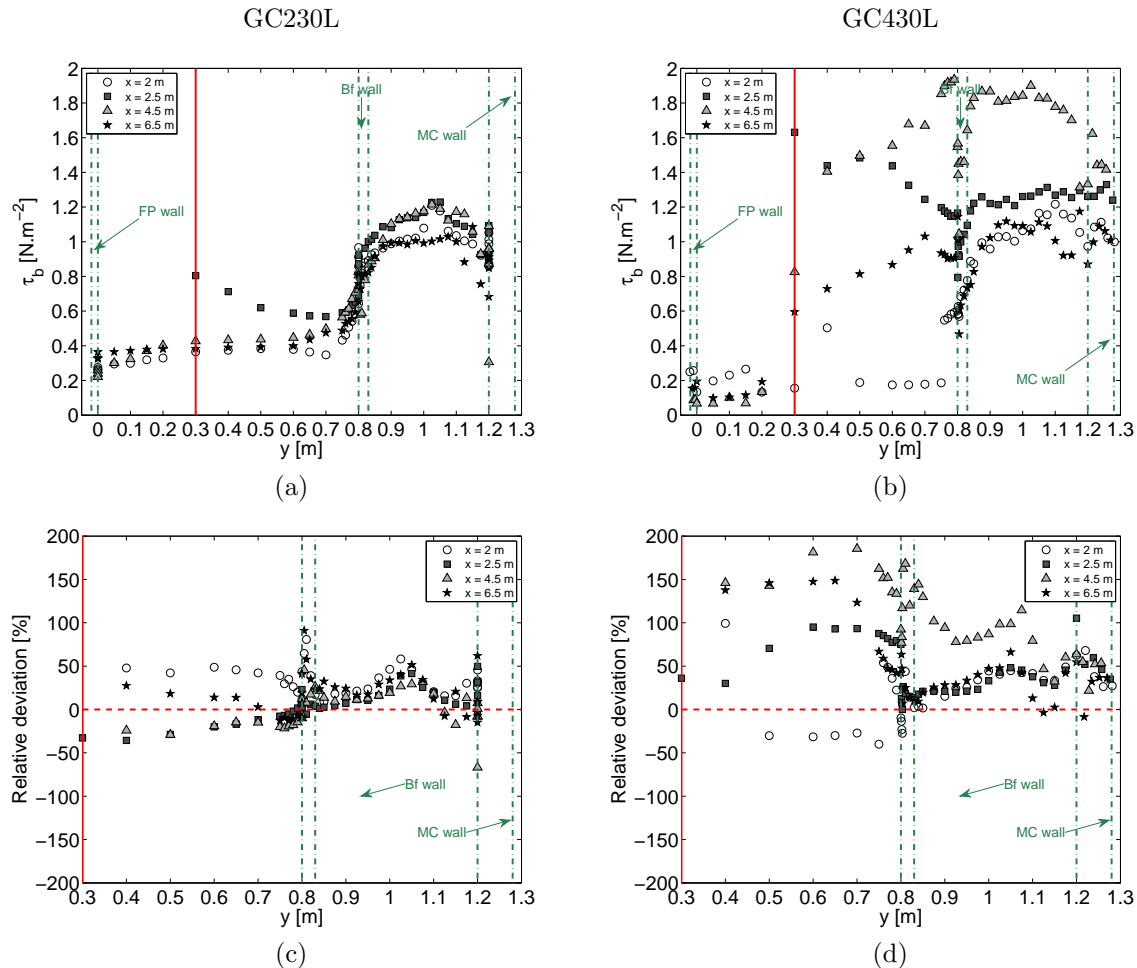


Figure 7.34 – (a-b) Boundary shear stress distribution for GC230L and GC430L. (c-d) Boundary shear stress distribution compared to GC330L. Uncertainty: $\delta\tau_b/\tau_b \approx 6$ %.

Regarding the distribution of boundary shear stress in the main channel, it strongly increases at $x = 4.5$ m for $Q_t = 36.2$ l/s because of the supercritical transition that occurs in this cross-section. In the remaining cross-sections, boundary shear stresses for GC330L are the smallest with comparison to GC230L and GC430L. Effects of the groyne at intermediate discharge ($Q_t = 24.7$ l/s) are then weaker than at low ($Q_t = 17.3$ l/s) or high total discharge ($Q_t = 36.2$ l/s). At low discharge, the shallow depths and the flow acceleration induce strong changes in the boundary shear stress distribution. At high discharge, mass exchange is strong and variation in

water depth between cross-sections is strong as well. The water depth can then become shallow and boundary shear stresses are enhanced. At intermediate discharge, the depth is not enough shallow and the mass exchange is not enough strong, hence the lower changes in boundary shear stresses.

Focus is finally done on boundary shear stresses in the vicinity of the recirculation zone that develops downstream of the groyne (Figure 7.34). With increasing total discharge, boundary shear stresses increase at the tip of the groyne (plunging flow) and along the separation line of the downstream recirculation zone. The strong increase in boundary shear stress in the diverging part of the flow (at $x = 4.5$ m) is due to the mixing layer along the separation line which is stronger with increasing total discharge (see in Figure 7.28).

8

Discussion on momentum transfer in compound channel

8.1 Introduction

In the Chapters 6 and 7, we showed that the flow separation at the tip of the groyne is responsible for the development of a recirculation zone of both sides of the obstacle. In addition, we showed that these recirculation zones operate a flow constriction leading to a reduction in the flow section. As a consequence, the flow, initially unidirectional, is deviated relative to the streamwise direction and mass is exchanged between the main channel and the floodplain. These exchanges between channels strongly impact the distributions of turbulence, boundary shear stress, velocity and depth in the flume. Nevertheless, the analyses of these changes are not sufficient for well evaluating what physical process – we previously identified in Chapters 1 and 2 – becomes dominant or negligible in front of the others in flows with a groyne set on the floodplain. To achieve this, reasoning on a momentum equation is required.

The weight of the various physical processes that occur in the reference flows and in the groyne-case flows is estimated from measurements exposed in Chapters 5, 6 and 7. The physical processes are modelled using Equation 2.28, which stems from the 2D equations of Saint-Venant.

In an operational point view, we first assess if the different types of recirculation regimes proposed by the McGill University [Babarutsi *et al.*, 1989; Chu *et al.*, 2004] can be identified in our specific flows. The aim is to have a first idea of what phenomena between friction and turbulence dominates the development of the downstream recirculation zone, this, depending on the groyne length and on the total discharge and without calculating a momentum balance.

Second, we are interested in the dispersion on the vertical of the horizontal components of the velocity. Bousmar [2002] showed that the dispersion must be taken into account in the 2D Saint-Venant equations for correctly assessing the presence of the secondary currents that partly contribute to the transversal momentum transfer in a prismatic compound channel. Through momentum coefficients that compare quadratic velocities to the dispersion terms, we first analyse the relative weight of the dispersion under our reference flow conditions. The same method is then used for the groyne-case flows.

Finally, through a dispersive 2D x-wise momentum equation, we evaluate the weight of each process in the reference flows and in the groyne-case flows. We compare together the weight of (1) mass exchange, (2) momentum transfers due to turbulence and due to mass exchange, (3) the pressure, (4) the secondary currents and (5) the friction, this, for the various lengths of groyne and total discharges. To term, these comparisons enable to define zone of dominance in the flow for certain processes that modellers should then treat or model with care for producing robust flood mappings or predetermination model.

8.2 Asymptotic regimes for recirculation zones?

In this section, we discuss the possibility to determine the regime of the downstream recirculation zones we measured and we presented in §6.2. The knowledge, *a priori*, of the recirculating flow regime would enable the flow modeller to choose the appropriate hypotheses for modelling the considered groyne-case flow. The regime gives indeed information about the dominant processes that have generated the shape of the recirculation zone. Under frictional regime, the development of the downstream recirculation zone is led by the turbulence coming from the bottom, while under non-frictional regime, its length is only due to the horizontal turbulence generated by the groyne (see §1.4.1).

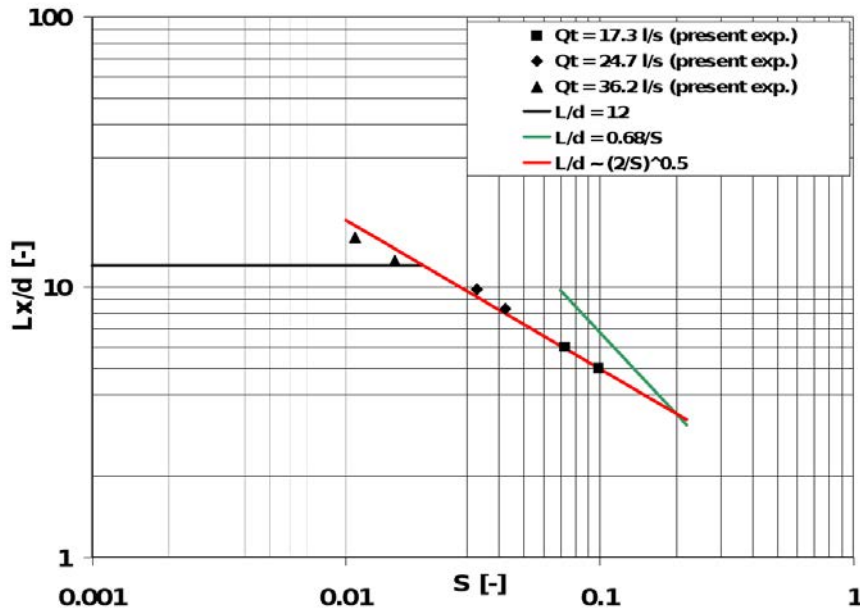


Figure 8.1 – normalised length L_x/d of the downstream recirculation zone displayed as a function of the friction number S ; comparisons of present experiments with the fits found by [Rivière et al. \[2004\]](#) for flows with a groyne in a single channel.

In Figure 8.1, the normalised lengths of recirculation zones of the present experiments are displayed as a function of the friction number $S = \lambda d / 8H$ (see in §1.4.1). The friction number S is computed with the cross-sectional water depth taken in the floodplain of the groyne cross-section. The Darcy-Weisbach coefficient in S is calculated using the Blasius law and the Reynolds number worked out in the floodplain of the groyne cross-section (λ is then the friction coefficient that should have a uniform flow of same Reynolds number, but different mean slope $S_{o,x}$, as the considered groyne-case). The black line ($L_x/d = 12$) and the green line $L_x/d = 0.68/S$ represents the asymptotic regimes (black: non-frictional regime, green: frictional regime) obtained by [Rivière et al. \[2004\]](#) for recirculation zones developing downstream of a unique groyne set perpendicularly to the main flow direction in a single channel.

It results that that the normalised lengths for the present experiments are fitted by none of the asymptotic laws proposed by [Rivière et al. \[2004\]](#). The normalised lengths are rather fitted by a unique function:

$$\frac{L_x}{d} = \sqrt{\frac{2}{S}} \quad (8.1)$$

Because of the root-square ($1/\sqrt{S}$), Equation 8.1 has an expression that is not similar to that of the frictional regime (proportional to $1/S$) nor equal to that of the non-frictional regime (independent from S). As a consequence, assuming that the asymptotic regimes truly exist, we can

affirm that the recirculating regime for the present experiments is transitional and no turbulent length-scale is dominant. The length and the shape of the recirculation zone is influenced by both the bottom-generated turbulence and the groyne length. The particular flow conditions in our experiments are probably responsible for this situation. Nevertheless, given the various calculated friction factors S , for flows at $Q_t = 17.3$ l/s, friction effects are stronger than for $Q_t = 36.2$ l/s.

8.3 Dispersion on the vertical of the horizontal velocities

Physical processes that occur in a compound channel were expressed using Equation 2.28, which is derived from the 2D equations of Saint-Venant. As exposed in the Chapter 2 of this PhD-thesis, the passage from the 3D-equations to the Saint-venant equations explicitly leads emergence of (1) the turbulence, (2) the friction and (3) the secondary-currents. During experiments, the turbulence, so as the friction were directly measured. The secondary-currents were assimilated to the dispersion on the vertical of the horizontal components of the velocity [Bousmar, 2002].

The depth-averaged dispersion on the vertical of the horizontal components of the velocity is first presented in this section. Then using Equation 2.48, the momentum coefficients β_{ij}^v are calculated and their distribution is commented. The momentum coefficients are convenient for evaluating the weight of the vertical dispersion on the vertical relative to the depth-averaged velocity. It enables to know if the depth-averaged velocity is representative or not of the velocity distribution in the water column.

8.3.1 Dispersion for reference flows

Since estimation of the weight of the phenomena occurring in our experiments is done using an x-wise momentum equation (Equation 2.28), only the depth-averaged dispersion on the vertical of the horizontal components of the velocity X_{xx} and X_{xy} are presented. In Figure 8.2, only cross-sections between $x = 3.5$ m and $x = 6.5$ m are displayed. These cross-sections are the ones where an establishment of the depth and of the depth-averaged longitudinal velocities is reached, see Chapter 5. The dispersion terms were calculated with at least 2 points and at maximum 4 points on the vertical (except for the floodplain for RF200L).

First observations emphasize that except near the main channel side-wall and around the interface between the main channel and the floodplain, the shapes of the X_{ij} distributions are similar between $x = 3.5$ m and $x = 6.5$ m and few changes are observed with increasing relative depth. In addition, comparison of the dispersion terms highlights that X_{xx} is one order of magnitude greater than X_{xy} . This difference comes from the fact that the magnitudes of the lateral velocities are one order of magnitude smaller than those for the longitudinal velocities.

The average values of X_{xx} in the floodplain ($y < 0.8$ m) is close to 0.25×10^{-3} m²/s² for $Q_t = 17.3$ l/s, 0.75×10^{-3} m²/s² for $Q_t = 24.7$ l/s and 0.5×10^{-3} m²/s² for $Q_t = 36.2$ l/s. In the floodplain-side of the interface between channels, the dispersion is equal to zero since the isolines of velocity are vertical (see Figures 5.24 and 5.15). In the main channel, the dispersion is higher and variations are less monotonous than in the floodplain. The differences between the floodplain and the main channel for X_{xx} may be due to the different shapes that have the vertical profiles of longitudinal velocity in each subsection. The low values of X_{xx} in the floodplain could either mean that the depth-averaging of the velocity introduces less biases than in the main channel, or that the number of points on the vertical for depth-averaging is not enough for well calculating the dispersion on the vertical.

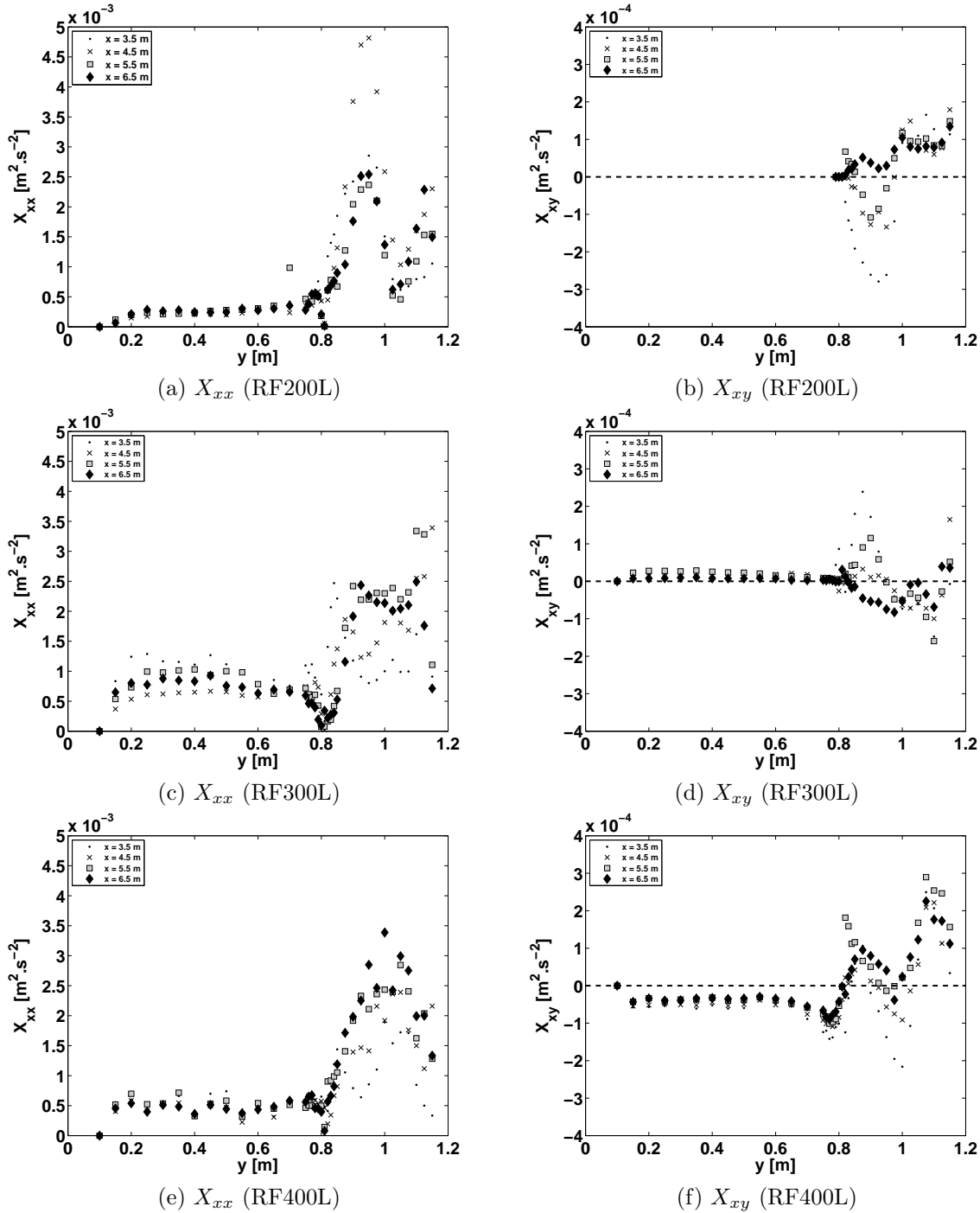


Figure 8.2 – Depth-averaged vertical dispersion X_{xx} and X_{xy} for reference flows at $Q_t = 17.3$ l/s, 24.7 l/s and 36.2 l/s. Uncertainty: $\delta X_{xx}/X_{xx} < 20\%$ and $\delta X_{xy}/X_{xy} < 50\%$.

Regarding X_{xy} , it is close to $\pm 0.1 - 0.5 \times 10^{-4} \text{ m}^2/\text{s}^2$ in the floodplain and it increases with the total discharge. In the main channel, X_{xy} is close to $\pm 1 \times 10^{-4} \text{ m}^2/\text{s}^2$ and it oscillates around the mean value (especially see at $x = 5.5 \text{ m}$ and $x = 6.5 \text{ m}$ in Figures 8.2.b and 8.2.d). X_{xy} is maximum (resp. minimum) at $y = 0.9 \text{ m}$, then passes by the mean value close to the centre of the main channel at $y = 1 \text{ m}$ and then is minimum (resp. maximum) at $y = 1.1 \text{ m}$. These oscillations of X_{xy} in the main channel could indicate the presence of two counter-rotative secondary-current cells in the main channel [Nezu and Nakagawa, 1993]. Notice that as shown in Tominaga and Nezu [1991] and in Ikeda and McEwan [2009], it should also exist at least two secondary-current cells in the floodplain. However, the fineness of the mesh do not allow the capture of such structures.

8.3.2 Dispersion for groyne-case flows

In this paragraph, vertical dispersion terms X_{xx} and X_{xy} are displayed for the 6 groyne-cases in Figures 8.3 and 8.4, respectively. The dispersion terms were calculated with at least 2 points and at maximum 5 points on the vertical. In zones with very shallow depths (in the floodplain at $x = 4.5$ m for GC350L for instance), the dispersion terms could not be calculated, since only one point on the vertical was available.

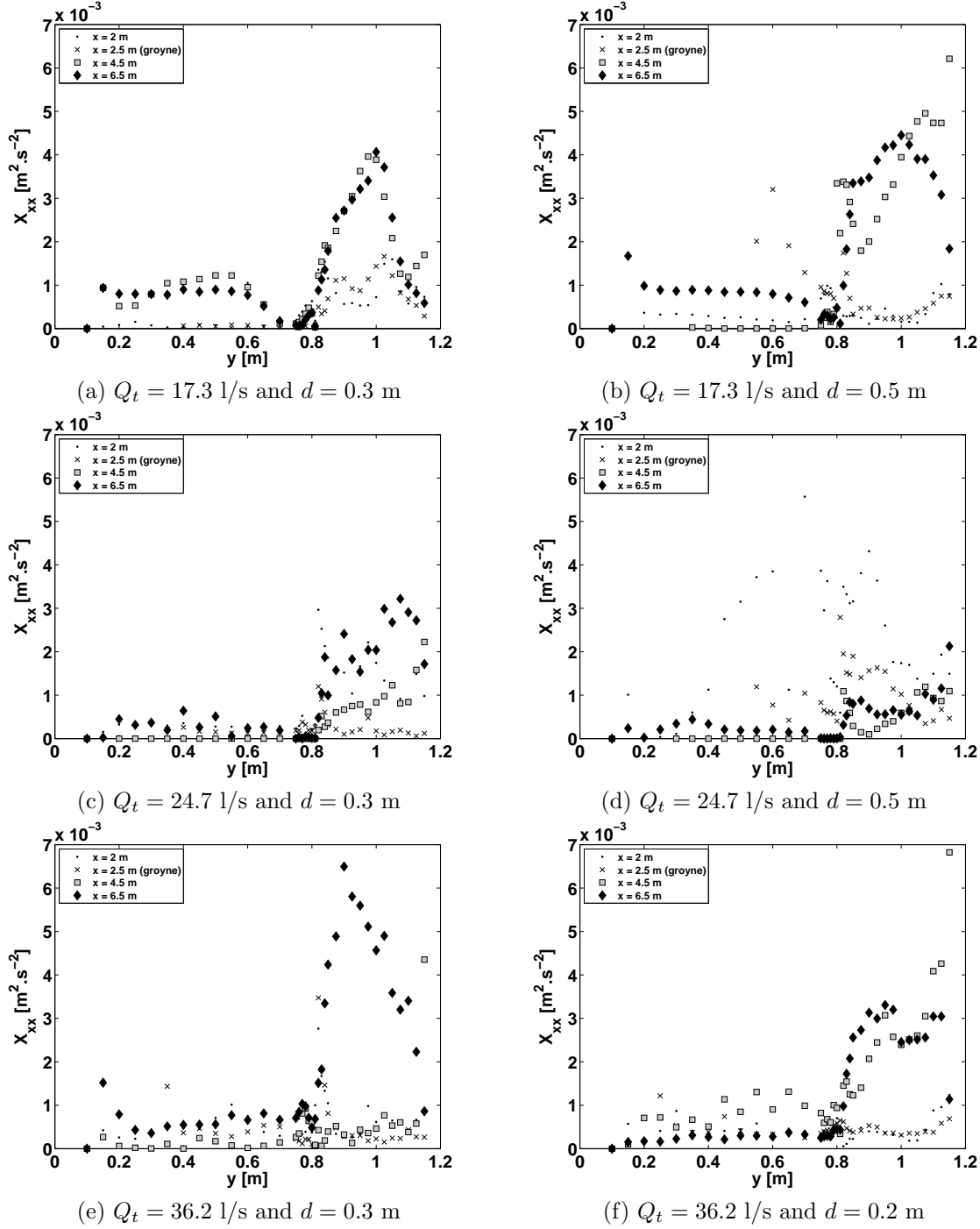


Figure 8.3 – Depth-averaged vertical dispersion X_{xx} for groyne-case flows. Uncertainty: $\delta X_{xx}/X_{xx} < 20$ %.

The comparison of groyne-case flows (Figure 8.3) with their corresponding reference flows emphasizes a reduction in X_{xx} upstream of the groyne in both the main channel and the floodplain. By contrast, in the diverging part of the flow (*i.e.* downstream of the throat cross-section), the

dispersion has increased. The vertical profile of the longitudinal velocity is thus more distorted downstream of the groyne than upstream.

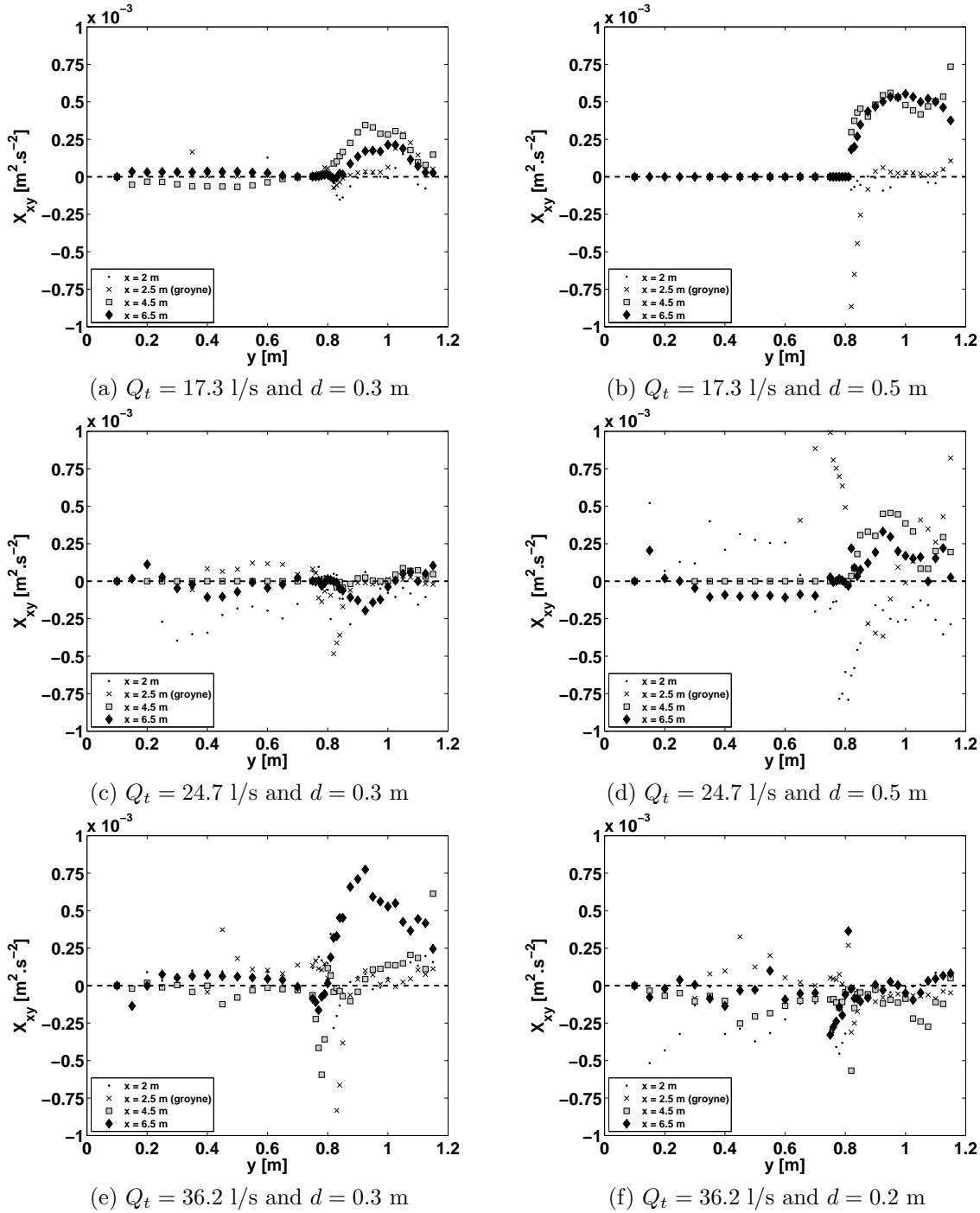


Figure 8.4 – Depth-averaged vertical dispersion X_{xy} for groyne-case flows. Uncertainty: $\delta X_{xy}/X_{xy} < 50$ %.

The comparison of groyne-cases together does not enable to find a real tendency with increasing groyne length and total discharge. The probable explanation for this failure comes from the mesh of measurements for groyne-cases that is based on the mesh for reference cases (see vertical mesh in §4.4). Because of the automatic displacement, the measurement mesh indeed uses the mean water depth under reference conditions as a reference for determining measurement points on the vertical, as a consequence, depending on the real water depth in the considered groyne-case flow, measurements are not taken at the same vertical position on the velocity profile and measurements are more or less dense:

- If $H^{groyne-case} \approx H^{ref}$, measurements for groyne-case flows are vertically well spaced on the velocity profile ($z_{measurements} = [0.2 \dots 0.8] \times H^{ref}$).
- If $H^{groyne-case} > H^{ref}$, more measurements are performed on the vertical ($z_{measurements} = [0.2 \dots 1 \text{ or } 1.2] \times H^{ref}$),
- If $H^{groyne-case} < H^{ref}$, less measurements are performed on the vertical ($z_{measurements} = [0.2, 0.4] \times H^{ref}$).

The comparison of the groyne-cases with reference flows for X_{xy} emphasizes that the dispersion in the main channel is strongly enhanced in the diverging part of the flow (downstream of the throat cross-section) and the lateral gradient of X_{xy} gets stronger. The dispersion is one order of magnitude greater than the reference one. Secondary currents in the diverging part should be probably enhanced by lateral exchanges from the main channel towards the floodplain. By contrast, in the converging part of the flow, the dispersion is similar to the one measured under reference conditions, whatever the subsection.

With increasing groyne length at a given total discharge, the cross-dispersion term X_{xy} increases so as its lateral gradient. This increase can be related to an increase in the lateral velocity with increasing mass exchange. By contrast, no clear tendency can be found when considering an increase in the total discharge. Let see here once again a problem due to the measurement mesh that does not enable a correct comparisons between cases with various total discharge.

8.3.3 Momentum coefficients for reference flows

The vertical momentum coefficients β_{ij}^v were calculated under reference flow conditions, results emphasize that β_{xx}^v is smaller than 1.01 (*i.e.* $X_{xx} \approx 1$ % of U_d^2). The depth-averaged longitudinal velocity accurately represents the velocity distribution in the water column and the x-wise dispersion on the vertical can be therefore neglected.

By contrast, the calculation of β_{xy}^v for reference flows highlights that in some part of the flow – especially at the interface between the main channel and the floodplain or in the floodplain – the momentum coefficient can be smaller than 0.9 and greater than 1.1; *i.e.* the depth-averaged dispersion is equivalent to ± 10 % of the product $U_d V_d$. This result is consistent with observations of [Bousmar \[2002, chapter 9\]](#).

8.3.4 Momentum coefficients for groyne-case flows

The vertical momentum coefficient β_{xx}^v worked out for groyne-case flows is close to 1 in both the main channel and the floodplain, whether in the converging part or in the diverging part of the flow. Given these values, we can consider that although X_{xx} is two times greater for groyne-case flows than for reference flows, we can neglect the term containing the longitudinal dispersion in the momentum equation, because X_{xx} is at maximum equal to 2 % of the square depth-averaged longitudinal velocity U_d^2 .

Regarding β_{xy}^v , it is smaller than those calculated under reference conditions. β_{xy}^v is at maximum equal to 1.05 and at minimum equal to 0.95. Nevertheless, some strong lateral gradients can be identified in the vicinity of the interface between channels. The non-consideration of these lateral gradients could impact the momentum balances.

8.4 Dominance of physical processes: momentum calculations

The first purpose, here, is to identify the dominance of the various flow processes that occur in the flow. The second purpose is to identify the flow configuration and the zones in the flow where momentum transfer due to turbulence is dominant or not in front of momentum fluxes due to mass exchange. We want to answer to the question: can we neglect the role of the turbulence for flows with a groyne set on the floodplain of a compound channel?

Momentum balances in this section are performed using an x-wise dispersive momentum equation (Equation 2.28, see in Chapter 2), which is deduced from the equations of Saint-Venant. In the following section, this equation is normalised by the slope $S_{o,x}$ (the weight component) and writes:

$$\frac{1}{S_{o,x}} \left[\frac{\partial h}{\partial x} + \frac{1}{2g} \frac{\partial U_d^2}{\partial x} + \frac{q_y}{gh} \frac{\partial U_d}{\partial y} = 1 - \frac{\tau_{b,x}}{\rho gh} + \frac{1}{\rho gh} \frac{\partial h T_{xx}}{\partial x} + \frac{1}{\rho gh} \frac{\partial h T_{xy}}{\partial y} - \frac{1}{gh} \frac{\partial h X_{xx}}{\partial x} - \frac{1}{gh} \frac{\partial h X_{xy}}{\partial y} \right] \quad (8.2)$$

where:

- $\frac{\partial h}{\partial x}$ is the gradient of hydrostatic pressure,
- $\frac{1}{2g} \frac{\partial U_d^2}{\partial x}$ is the gradient of the longitudinal kinetic energy; it results from the streamwise variation in mass in the flume,
- $\frac{q_y}{gh} \frac{\partial U_d}{\partial y}$ represents the momentum transfer due to lateral mass exchange,
- $-\frac{\tau_{b,x}}{\rho gh}$ represents the friction,
- $\frac{1}{\rho gh} \frac{\partial h T_{xx}}{\partial x}$ is the momentum transfer due to the longitudinal turbulent exchange; it gives information about the effects on the mean flow of the additional stress creating by the fluctuation of the longitudinal component of the velocity,
- $\frac{1}{\rho gh} \frac{\partial h T_{xy}}{\partial y}$ is the momentum transfer due to turbulent shear; it accounts for the effects on the flow of a potential turbulent shear in the flow,
- $-\frac{1}{gh} \frac{\partial h X_{xx}}{\partial x}$ is the gradient of the dispersion on the vertical of the longitudinal component of the velocity; this dispersion is due to the bottom friction that is responsible for the non-uniformity on the vertical of the longitudinal velocity \bar{u} ,
- $-\frac{1}{gh} \frac{\partial h X_{xy}}{\partial y}$ is the gradient of the dispersion on the vertical of the longitudinal and lateral components of the velocity.

All the terms in Equation 8.2 were calculated using the experimental data we measured. For stability reasons of the terms containing gradients, calculations were performed using a centred scheme. The gradients, so as the other terms were therefore calculated between two subsequent cross-sections and spanwise locations as showed in Figure 8.5, where the black, the red, the green and the blue lines correspond to the cross-sections of measurements and the pink ones to the cross-sections of the momentum calculations. Moreover, the calculation of the gradients were only performed between cross-sections of same flow characteristics (*i.e.* in the converging part or in the diverging part, but not between both parts).

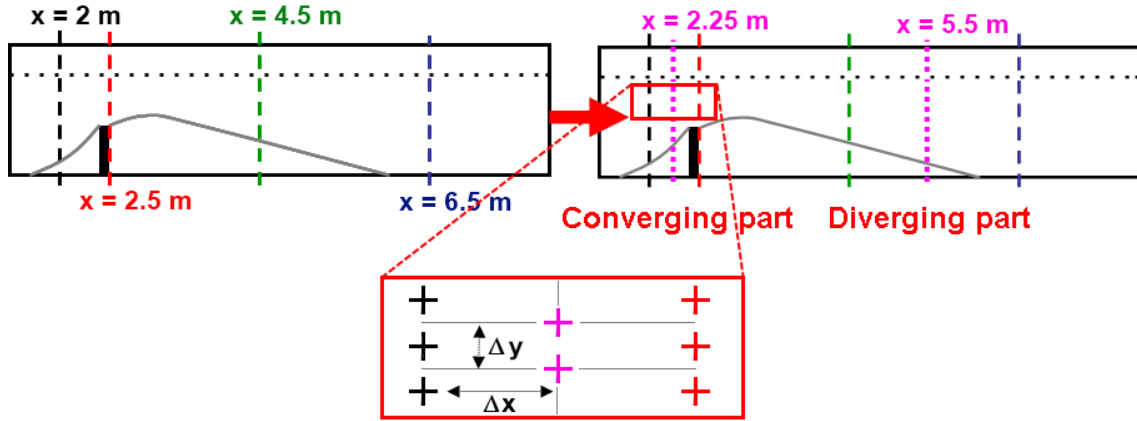


Figure 8.5 – Scheme of the mesh for calculating the gradients of the momentum balances.

NB – Given the density of the grid of measurements in our experiments (see Figures 3.7.a and 8.5), the lateral gradients are certainly more accurate than the longitudinal gradients, because the lateral spacing of the mesh ($\Delta y \in [1 \text{ cm } 5 \text{ cm}]$) is more dense than the longitudinal one ($\Delta x = 50 \text{ cm}$ in the converging part and $\Delta x = 100 \text{ cm}$ in the diverging part). As a consequence, if the net of all the terms of the momentum equation 8.2 is not equal to zero, it is very likely that this is due to the low density of the longitudinal grid and the inaccuracy of the longitudinal gradients.

8.4.1 Reference flows

The calculations of the terms of Equation 8.2 were carried out at $x = 5.5 \text{ m}$ where the flow is established at $\pm 2.5 \%$ of $\langle h(x, y) \rangle_{x \in [3.5 \text{ } 5.5]}$ for the depth and at $\pm 2.5 \%$ of $\langle U_d \rangle_{x \in [3.5 \text{ } 5.5]}$ for the depth-averaged velocity (see chapter 5). Results of calculations are displayed in Figure 8.6 for the three reference flows. The left figures represent the spanwise evolution of the terms of the momentum equation 8.2 normalised by the mean slope of the flume $S_{o,x}$. Each term is thus compared to the gravity – the motive force – that initiates the motion in the flow. The right figures are a zoom of the left figures between $y = 0.6 \text{ m}$ and $y = 1 \text{ m}$. Each figure is divided into three subplots:

- The upper figure represents the evolution of the terms of the left hand-side member of the momentum equation.
- The middle one represents the evolution of the right hand-side member.
- The bottom figure represents spanwise evolution of the net of the momentum balances. Zero then correspond to a balanced momentum balance.

First of all, regarding the net of the momentum balances, its magnitude is almost equal to zero, except near the interface between channels, where it increases with increasing total discharge. The non-zero value of the net is mostly influenced by (1) the gradient of hydrostatic pressure, (2) the gradient of longitudinal kinetic energy and (3) the momentum transfer due to lateral mass exchange. These three terms are indeed less accurate than the other terms of the momentum equation because of the low density of the grid used for working out the longitudinal gradients and because of the high uncertainties on $q_y = hV_d$.

Figure 8.6 secondly highlights that the normalised terms of the momentum equation are mostly within the range $[-1 \times S_{o,x} \text{ } 0.5 \times S_{o,x}]$. This range of values means that the gravity is still the dominant motive force in the flow.

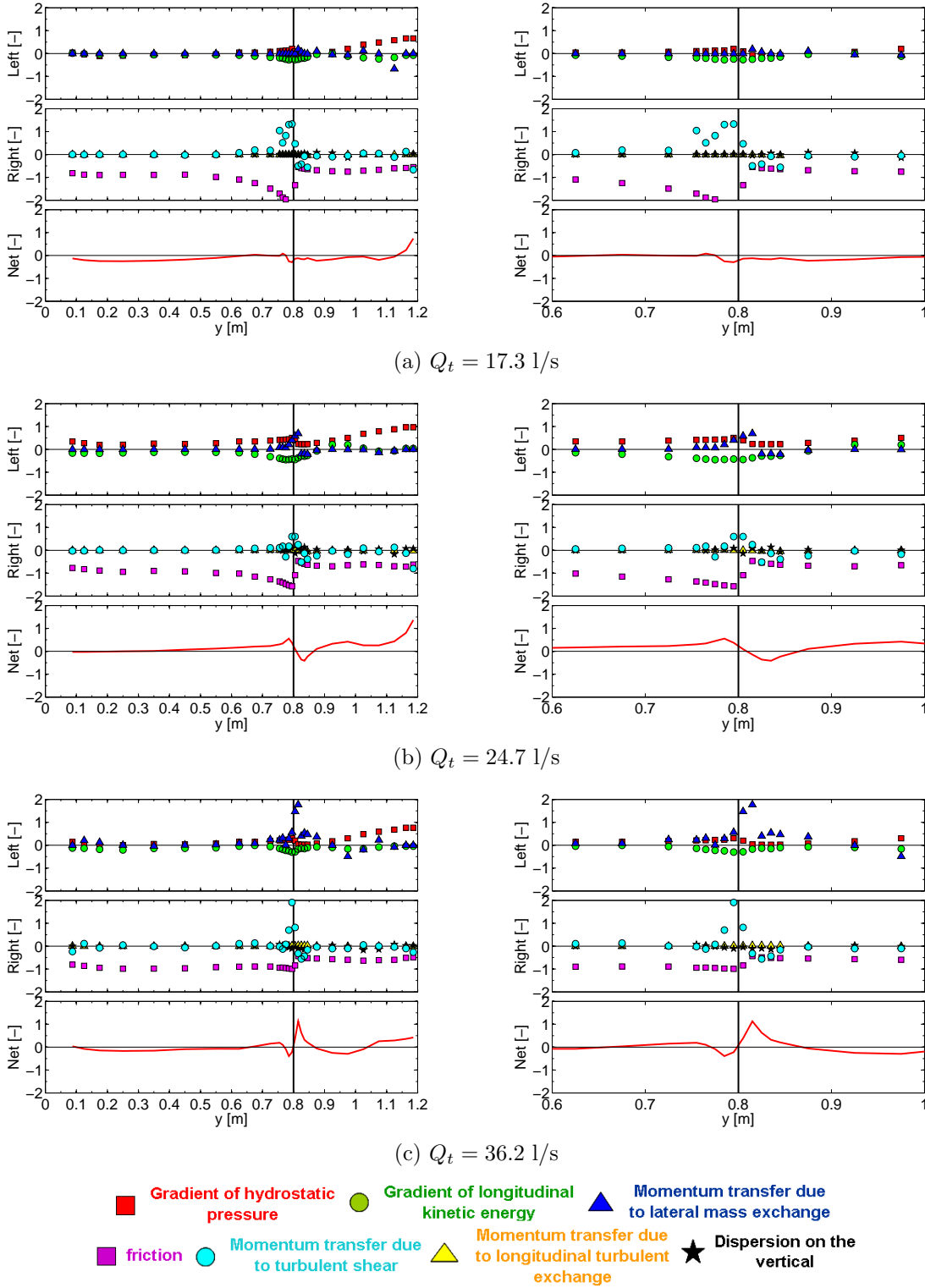


Figure 8.6 – Momentum balances for reference flows. The right figures are a zoom of the left figures between $y = 0.6 \text{ m}$ and $y = 1 \text{ m}$. Uncertainty is not estimated.

Some values greater than $|\pm 1| \times S_{o,x}$ are also identified in the flow. They are located at the interface between the main channel and the floodplain and in the vicinity of the main channel side-wall. These maxima emphasize the zone where momentum transfer due to turbulent exchange occurs: in the mixing layer developing between channels and in the boundary layer of the main channel side-wall.

The focus on the left hand-side member (upper figures in Figure 8.6) then indicates that except at the interface between channels, momentum transfer due to lateral mass exchange is negligible. In the mixing layer, it increase with the total discharge, therefore pointing out that the flow establishment is more difficult to reach at high discharge, because of the presence of local lateral mass exchange within the mixing layer. Nevertheless, the previous result must be considered with care as the net at the interface gets stronger with the discharge and seems to partly follow the distribution of the momentum transfer due to lateral mass exchange.

The focus on the right hand-side member finally leads to a classical result for flows in compound channel close to uniform flow conditions. In the floodplain, momentum transfer due to turbulent shear is negligible and friction counter-balances the gravity. In the floodplain-side of the interface, the friction slope ($S_{f,x} = \tau_b/\rho gh$) is greater than the mean slope: the flow is locally accelerated. This result is confirmed by the momentum transfer due to turbulent exchange in this area that is positive and is close to 70 % of the friction. By contrast, in the main channel, momentum transfer due to turbulence is negative or close to zero and the friction slope is smaller than the mean slope of the flume: the flow is globally decelerated in the main channel.

To resume, the momentum transfer due to turbulent shear in the mixing layer between channel so as the friction in the flume have the same order of magnitude or are greater (2 times in absolute) than both the gradient of hydrostatic pressure and the gradient of longitudinal kinetic energy.

8.4.2 Groyne-case flows

In this subsection, the effects of the introduction of the groyne in the flow in compound channel are analysed through the calculation of the terms of the momentum equation 8.2. A groyne-case flow is first detailed and compared to its corresponding reference flow. Afterwards, the influence of the groyne length or of the total discharge is discussed.

8.4.2.1 Detailed study of groyne-case GC330L

The groyne-case flow GC330L ($Q_t = 24.7$ l/s and $d = 0.3$ m) is analysed in details hereafter. Calculations are performed in two cross-sections: one upstream of the groyne at $x = 2.25$ m in the converging part of the flow and one at $x = 5.5$ m in the vicinity of the stagnation point of the downstream recirculation zone (diverging part of the flow). The streamwise and the spanwise evolutions of the terms of the momentum equation 8.2 for both cross-sections are displayed in Figure 8.7.

The net of the momentum balances is largely greater than zero in the mixing layer and close to the main channel side-wall of the cross-section located at $x = 2.25$ m (*i.e.* in the converging part of the flume). In the other cross-section the net is close to zero. The difference between both cross-sections stems from (1) the gradient of hydrostatic pressure, (2) the gradient of longitudinal kinetic energy and (3) the momentum transfer due to lateral mass exchange that are stronger in the converging part than in the diverging part of the flume. As previously specified, these three terms are less accurate than the other terms of the momentum equation because of the low density of the grid used for working out the longitudinal gradients and because of the high uncertainties on $q_y = hV_d$.

In the converging part of the flow, the gradient of hydrostatic pressure and the gradient of kinetic energy are the greatest terms of the momentum balance. They are from 2.5 to 12.5 in absolute greater than the terms of the right hand-side member of Equation 8.2. The comparison with the reference flow RF300L gives the same result. This strong increase is due to the groyne that initiates a strong decrease in velocity and a strong increase in depth at $x = 2.25$ m.

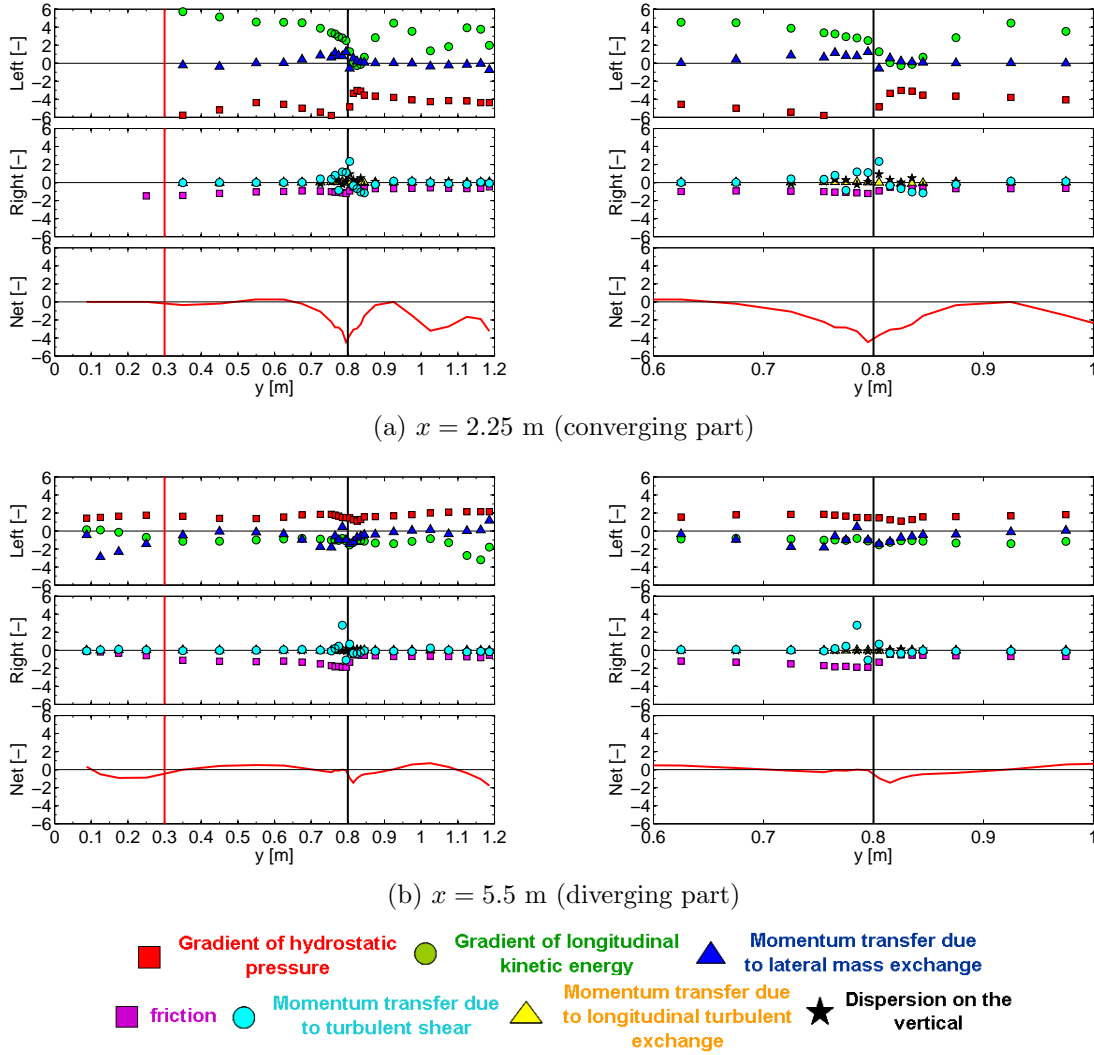


Figure 8.7 – Momentum balances for $Q_t = 24.7$ l/s and $d = 0.3$ m in two cross-sections ($x = 2.25$ m and $x = 5.5$ m). The right figures are a zoom of the left figures between $y = 0.6$ m and $y = 1$ m. The vertical red line indicates the lateral position of the groyne in the flume and the vertical black line gives the location of the interface between channels. Uncertainty is not estimated.

Once the throat is passed, the gradient of hydrostatic pressure and the gradient of kinetic energy strongly reduce. This difference between the converging part and the diverging part is due to the flow divergence that is smoother than the flow convergence (see in Chapter 6).

The focus on the momentum transfer due to lateral mass exchange then emphasizes that it has the same order of magnitude in the converging part and in the diverging part of the flow. It is equivalent to the two other terms of the left hand-side member of Equation 8.2 in the mixing layer at the interface between channels. In the rest of the flume, this momentum transfer is negligible. The almost-constant value for momentum transfer due to mass exchange is due to the decrease in the lateral velocity with the reduction of the floodplain under-feeding that is compensated by the increase in the lateral gradient of the longitudinal velocity.

The average magnitude of the terms of the right hand-side member of the momentum equation 8.2 is similar to the reference flow one, *i.e.* $\pm 0.5 \times S_{o,x}$ (see Figure 8.6). Similarly to the reference flow, the momentum transfer due to turbulent shear is stronger at the interface between the main channel and the floodplain; its magnitude can be 2.5 greater than the mean slope of the flume. By contrast, the behaviour of the friction is less monotonous than under reference flow conditions.

The friction in the main channel is greater than $-1 \times S_{o,x}$; the boundary shear stress in the main channel are indeed still smaller than the gravity stress $\rho gh S_{o,x}$ (*i.e.* the flow in the main channel is decelerated). Regarding the floodplain, the friction increases with approaching the throat and can be 100-150 % greater than under reference flow conditions: the flow is accelerated. Once the throat is passed, the flow in the floodplain globally decelerates and the friction is increased in the vicinity of the interface between the main channel and the floodplain because of the presence of the mixing layer.

Concerning the other terms of the right hand-side member of the momentum equation, the momentum transfer due to the longitudinal turbulent exchange T_{xx} is always negligible and the terms containing the dispersion on the vertical of the horizontal components of the velocity are generally negligible except:

- In the main channel of the converging part of the flow (Figure 8.7.a-b), where the longitudinal gradient of the dispersion on the vertical X_{xx} is equal to $0.2 \times S_{o,x}$ because of the plunging flow in the groyne cross-section that distorts the vertical profile of the longitudinal velocity.
- In the mixing layer between channels where the lateral gradient of X_{xy} can be equal to $|\pm 1| \times S_{o,x}$.

The following table (Table 8.1) resumes the differences in the momentum balance between a reference flow and a groyne-case flow.

	In the converging part	In the diverging part
Gradient of hydrostatic pressure	++	+
Gradient of longitudinal kinetic energy	++	+
Momentum transfer due to lateral mass exchange	+ (shear layer only)	+ (shear layer only)
Friction	-	+
Momentum transfer due to turbulent shear	+ (shear layer only)	+ (shear layer only)
Momentum transfer due to longitudinal turbulent exchange	=	=
Dispersion on the vertical	+	+

Table 8.1 – Listing of the various effects of the groyne on the momentum balance with comparison to the reference. + \Rightarrow increase in absolute, - \Rightarrow decrease in absolute, = \Rightarrow no changes.

NB – The measurements in the vicinity of the separation line in the floodplain were not enough accurate. As a result, we cannot discussed about the weight of the physical processes in this area.

8.4.2.2 Influence of the groyne length

The impacts of an increase in the groyne length at a given total discharge are analysed by comparing GC330L ($Q_t = 24.7$ l/s and $d = 0.3$ m, Figure 8.7) to GC350L ($Q_t = 24.7$ l/s and $d = 0.5$ m, Figure 8.8).

The first observations emphasize that the momentum transfer due to mass exchange increases with an increase in the groyne length; it is almost six times higher than for the smallest groyne. The larger increase is observed upstream of the groyne. By contrast, the momentum transfer due to turbulent exchange is more impacted in the diverging part of the flow.

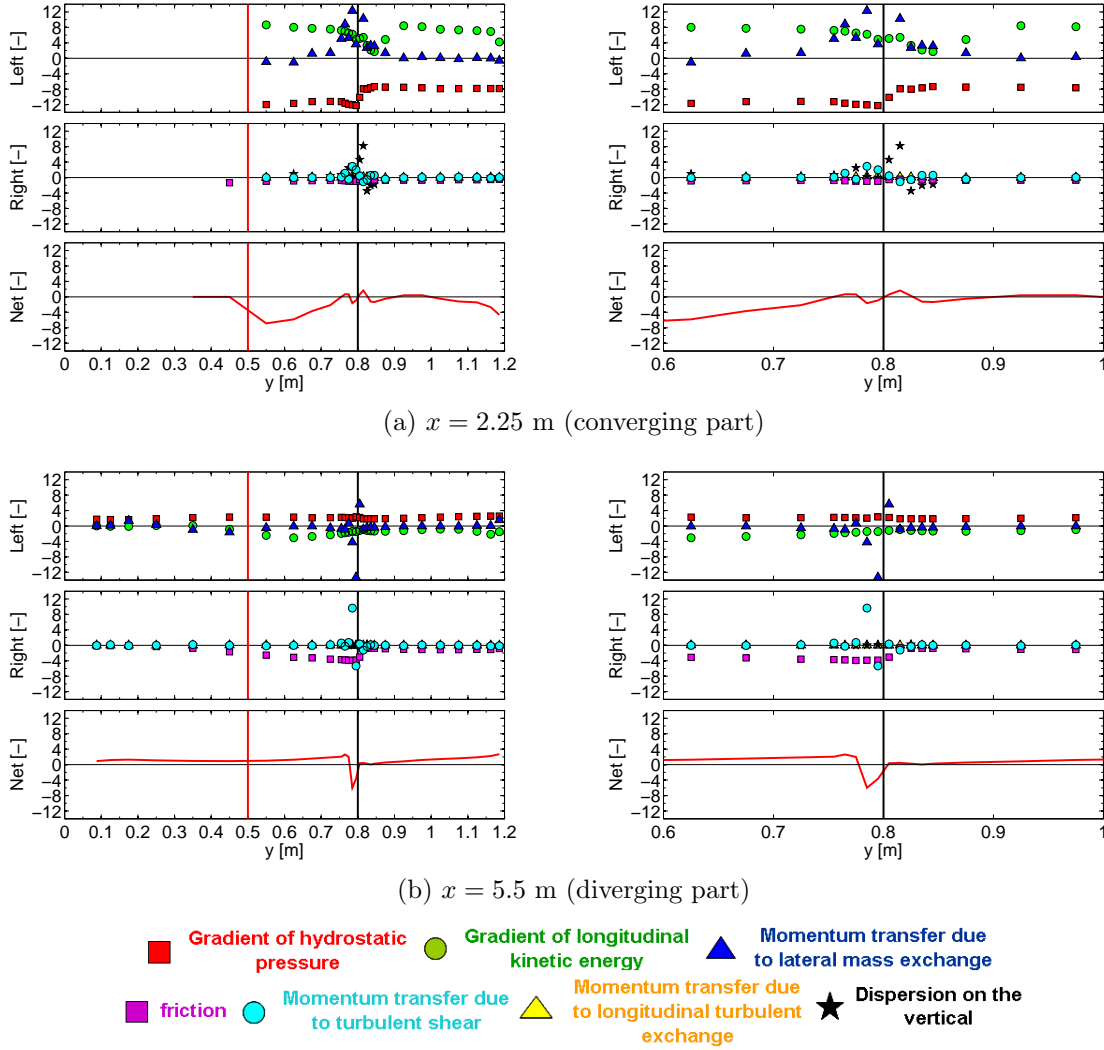


Figure 8.8 – Momentum balances for $Q_t = 24.7$ l/s and $d = 0.5$ m at two cross-sections ($x = 2.25$ m and $x = 5.5$ m). The right figures are a zoom of the left figures between $y = 0.6$ m and $y = 1$ m. The vertical red line indicates the lateral position of the groyne in the flume and the vertical black line gives the location of the interface between channels. Uncertainty is not estimated.

The role played by the boundary shear stresses is enhanced in both the main channel and the floodplain. The flow acceleration in the diverging part of the flow indeed induces a strong increase in the boundary shear stress. It results that the friction almost counter-balance the gravity in the main channel and is 2.5 times greater in the floodplain. Upstream of the groyne, the friction has reduced and has low influences in the floodplain.

Finally notice that the lateral derivative of the dispersion term X_{xy} gets larger in the vicinity of the interface with increasing groyne length. Let see here the effects of the lateral mass exchange that strongly distorts the velocity profiles.

8.4.2.3 Influence of the total discharge

In this paragraph, the impacts of an increase in the total discharge at a given groyne length are analysed by comparing GC330L ($Q_t = 24.7$ l/s and $d = 0.3$ m, Figure 8.7) to GC230L ($Q_t = 17.3$ l/s and $d = 0.3$ m, Figure 8.9) and to GC430L ($Q_t = 36.2$ l/s and $d = 0.3$ m, Figure 8.10).

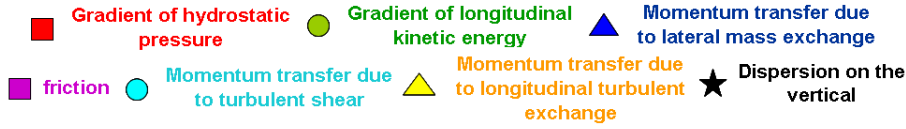
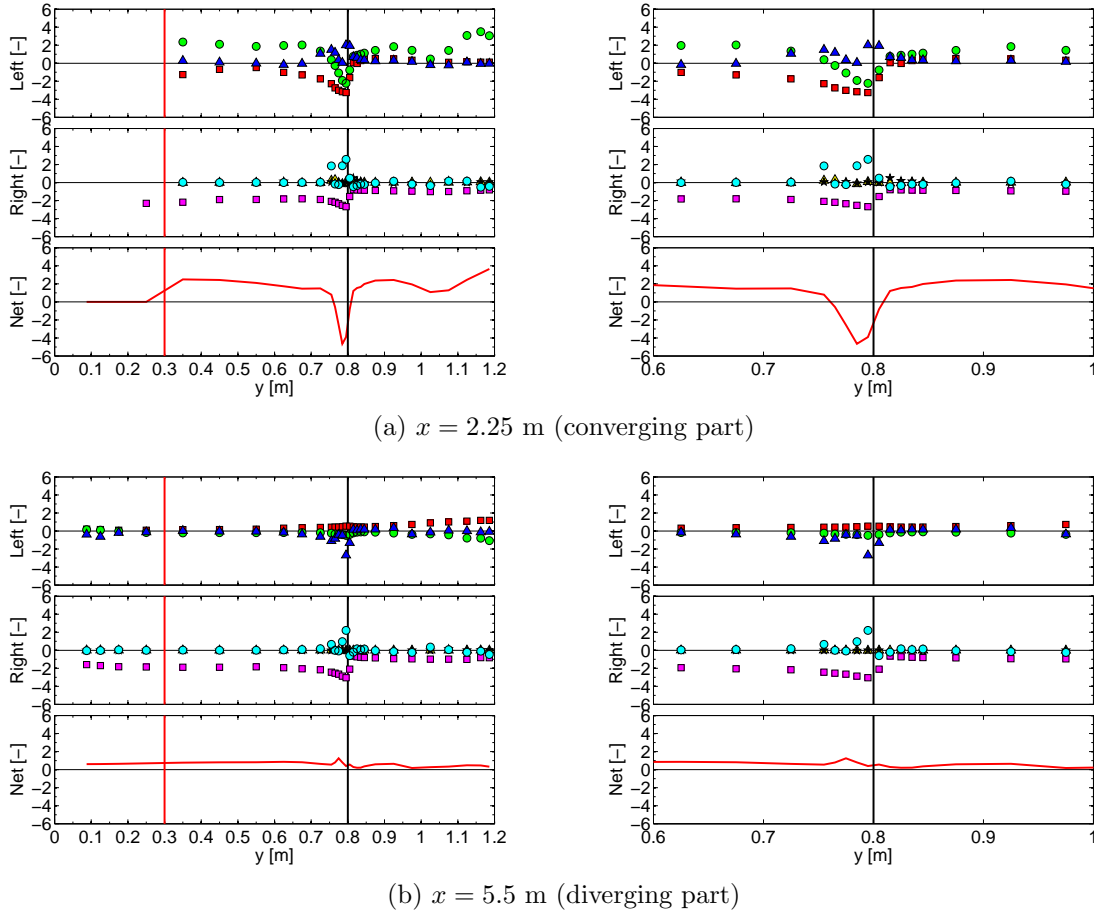


Figure 8.9 – Momentum balances for $Q_t = 17.3$ l/s and $d = 0.3$ m at two cross-sections ($x = 2.25$ m and $x = 5.5$ m). The right figures are a zoom of the left figures between $y = 0.6$ m and $y = 1$ m. The vertical red line indicates the lateral position of the groyne in the flume and the vertical black line gives the location of the interface between channels. Uncertainty is not estimated.

The momentum transfer due to mass exchange, so as the gradients of hydrostatic pressure and kinetic energy have increased in absolute with the total discharge. In the converging (resp. in the diverging) part of the flow, they can be 15 times (resp. 6 times) greater than the right hand-side member of the momentum equation 8.2. Contrariwise, momentum transfer due to turbulent shear at the interface slightly decreases as the total discharge increases whatever the part in the flow.

Concerning the other terms of the right hand-side member of the momentum equation, friction is not negligible. At low discharge, boundary shear stresses in the main channel are equivalent to the gravity stress and with increasing total discharge, they become at maximum 25 % smaller than the gravity stress (upstream of the groyne). In the floodplain, upstream of the groyne, the friction is enhanced by the shallow depth observed at low discharge (Figure 8.9.a-b). Then with increasing total discharge, friction reduces and equilibrate with the gravity at high discharge (Figure 8.10.a-b). In the diverging part of the flow, the magnitude of the friction depends on the shallowness and on the flow regime. Without supercritical zone in the reattachment zone, the friction decreases as the total discharge increases; for the highest total discharge $Q_t = 36.2$ l/s, a super-critical zone is present in the vicinity of the recirculation zone, it results that friction is

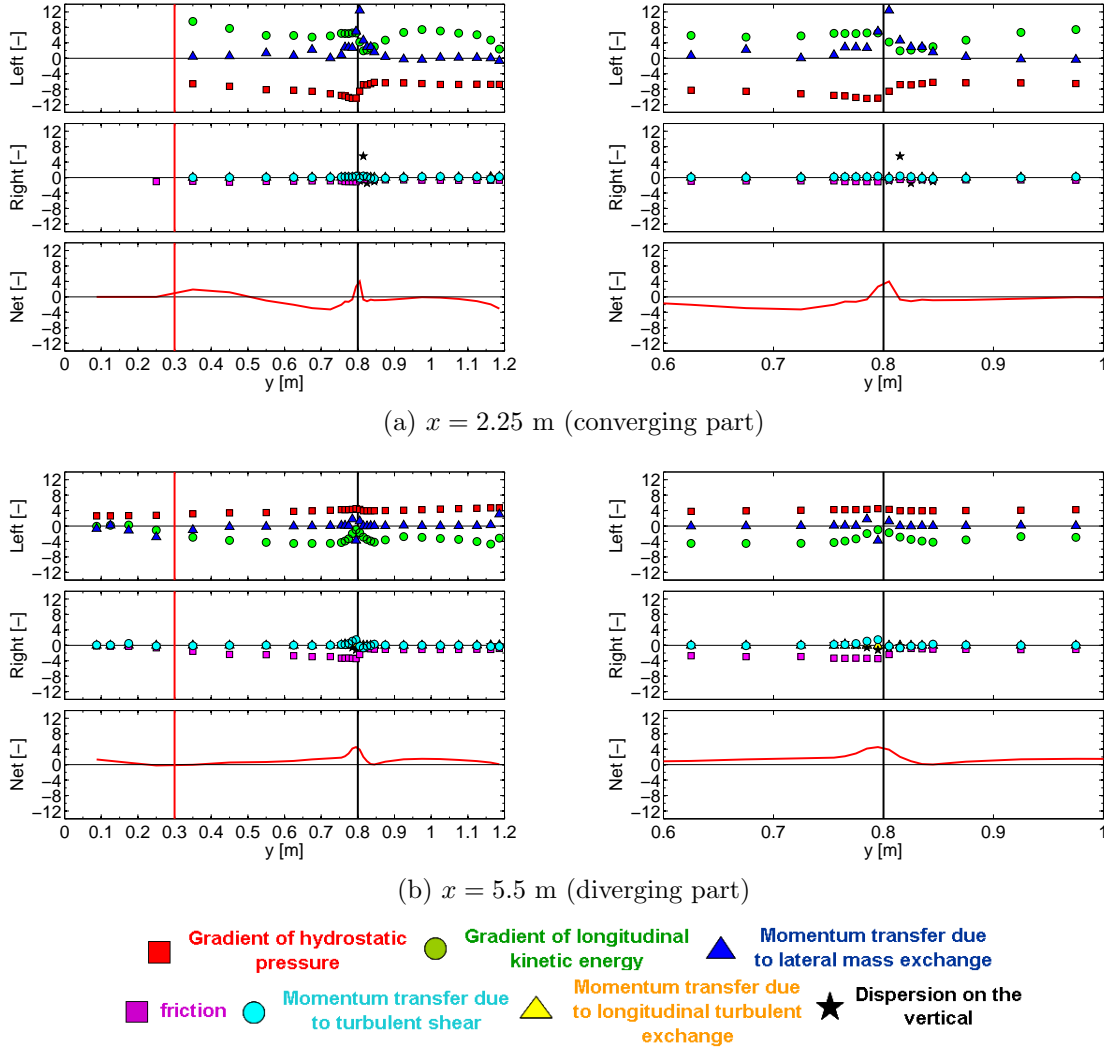


Figure 8.10 – Momentum balances for $Q_t = 36.2$ l/s and $d = 0.3$ m at two cross-sections ($x = 2.25$ m and $x = 5.5$ m). The right figures are a zoom of the left figures between $y = 0.6$ m and $y = 1$ m. The vertical red line indicates the lateral position of the groyne in the flume and the vertical black line gives the location of the interface between channels. Uncertainty is not estimated.

enhanced and is therefore greater than for the two smaller discharges (Figures 8.9.c-d, 8.7.c-d and 8.10.c-d).

Finally, the lateral derivative of the dispersion term X_{xy} gets larger in the vicinity of the interface with increasing total discharge. Let see here once again the impacts of the lateral mass exchange that strongly distorts the velocity profiles.

The following table (Table 8.2) resumes the effects of an increase in the groyne length or in the total discharge on the momentum balance.

	In the converging part	In the diverging part
Gradient of hydrostatic pressure	++	++
Gradient of longitudinal kinetic energy	++	++
Momentum transfer due to lateral mass exchange	++ (shear layer only)	++ (shear layer only)
Friction	--	++
Momentum transfer due to turbulent shear	$-(Q_t) + (d)$ (shear layer only)	$-(Q_t) ++ (d)$ (shear layer only)
Momentum transfer due to longitudinal turbulent exchange	=	=
Dispersion on the vertical	+	+

Table 8.2 – Listing of the various effects of an increase in the groyne length or in the total discharge on the momentum balance with comparison to GC330L. + \Rightarrow increase in absolute, - \Rightarrow decrease in absolute, = \Rightarrow no changes.

8.4.3 Advices to flow modellers

By first considering the reference flows, it results that the modeller can choose to neglect $-\frac{1}{gh} \frac{\partial h X_{xx}}{\partial x}$ and $-\frac{1}{gh} \frac{\partial h X_{xy}}{\partial y}$ in the momentum equation 8.2 for modelling the flow in compound channel without any obstacle in the floodplain. It is interesting to notice that this result differ from the one of *Bousmar and Zech* [2002] who advised to model the dispersion on the vertical in the floodplain in order to take into account the effects of secondary currents on the conveyance of the floodplain. The calculation of the dispersion term in this thesis is maybe not enough accurate. So neglecting the dispersion should be performed with care.

The considerations on the flow modelling with a groyne set on the floodplain then emphasize that although the mass fluxes, the gradient of hydrostatic pressure and the momentum transfer due to lateral mass exchange are dominant, a special care must be taken for modelling the turbulence at the interface between channels and the friction in the flume. They still have a consistent role in the flow resolution.

Finally, regarding the behaviour of the dispersion on the vertical, it is preferable to conserve both dispersive terms of the momentum equation. By contrast, the term containing T_{xx} can be neglected as under reference flow conditions.

Conclusion of Part III

Developing flows in straight compound channel

Using measurements of the flow parameters defined in Equation 2.28, we have shown that the reference flows RF200L ($Q_t = 17.3$ l/s, $H_r \approx 0.2$), RF300L ($Q_t = 24.7$ l/s, $H_r \approx 0.3$) and RF400L ($Q_t = 36.2$ l/s, $H_r \approx 0.4$) are actually developing flows. Nevertheless depending on an establishment criterion based on the comparison of the measured data with an appropriate mean value, a segment of 2 meters can be defined in which the water depths, the depth-averaged velocities and the discharge distribution in the flow are established (see Table 5.4).

The establishment of the depth and velocity in the flume is affected by (1) the inlets over the two first meters, (2) the topography accident (ridge) at $x = 3$ m and (3) the backwater curves coming from the tailgates, which are felt from $x \approx 5.5 - 6.5$ m to the end of the flume.

Mass exchange between subsections is limited and is rather weak for each reference flows.

Distance of establishment of the mixing layer increases with increasing total discharge; as a result, the mixing layer for RF400L (higher discharge) is not plainly established in the flow.

The width of the established mixing layer depends on the shallowness of the flow and on the velocity shear between channel. At low discharge (RF200L), the mixing layer is limited by the turbulence coming from the bottom, because of the shallowness of the depth in the floodplain; the width of the mixing layer is then reduced compared to a deeper configuration with the same velocity shear between channels. By contrast, at higher discharge (RF400L), the width is limited by the weak intensity of the velocity shear. It results that the widest mixing layer is obtained for RF300L, where the shear is relatively high and the shallowness intermediate.

Spectral analysis of the turbulence in the mixing layer shows, that 2D horizontal planform vortices have settled the shear layer whatever the total discharge. These structures are responsible for momentum transfers in the mixing layer.

Analyses of the boundary shear stresses finally indicate that they cannot establish because of the inlets and outlets. The inlets induce a plunging flow near the bottom, which results in strong variations in the friction velocity. The downstream boundary conditions impose a rise in the water depth at the end of the flume, which weakens the boundary shear stress. These distortions increase with the total discharge.

Impacts of the introduction of a groyne in a developing flow in compound channel

In this chapter, we assessed the impacts on the flow parameters of the introduction of a groyne in the floodplain of a flow in compound channel. The comparisons were performed between the reference flow RF300L ($Q_t = 24.7$ l/s, $H_r \approx 0.3$; see in Chapter 5) and the groyne-case flow GC330L ($Q_t = 24.7$ l/s, $d = 0.3$ m). The groyne was perpendicularly set to the streamwise direction. The discharge distribution to inject in the flume for GC330L was the one proposed

by Proust [2005] (*i.e.* $Q_{fp}/Q_t = 25.5\%$) and was the same as for RF300L. For the outlets, the tailgates were set up at the same elevation as for RF300L (see §5.2).

The groyne promotes two flow separations and two recirculation zones develop of both sides of the groyne. The longitudinal length of the recirculation zone located upstream of the groyne is equivalent to the groyne length and its lateral expansion is always smaller than the groyne length. By contrast, the longitudinal length of the downstream recirculation zone is 10 times greater than the groyne length and its lateral extent can be greater than the groyne length, therefore initiating a contraction of the flow in the floodplain slightly downstream of the groyne.

The groyne impact the flow by reducing the flow section, but this reduction is not homogeneously felt in the flow. Depths and velocities in the main channel are weakly influenced, while in the floodplain, they behave like in a venturi-shaped flume. Convergence (*resp.* divergence) angle of the flow in the floodplain can thus reach 20° (*resp.* -30°) close to the recirculation zones and the slope of the free surface close to the tip of the groyne is one order of magnitude greater than the slope of the flume $S_{o,x}$.

The flow contraction in the floodplain at $x = 2.6$ m added to the behaviour of the depths and velocities is responsible for the creation of a throat in the floodplain. Downstream of this throat, the flow regime is supercritical, which has for effects to increase influences of the groyne in the floodplain. The supercritical zone extents over 2 meters in the floodplain and then ends through a normal undulated jump induced by the backwater effects coming from the tailgates. The groyne obviously affects the discharge distribution in the flume. The floodplain is underfed in the whole flume. The minimum of discharge in the floodplain is reached in the throat cross-section.

The impacts of the groyne on the turbulence is then analysed. Geometrical Characteristics of the mixing layer developing at the interface were first discussed. The width of the mixing layer developing at the interface, its growth rate and the position of its centre depend on the position in the flow relative to the throat and to the stagnation point of the downstream recirculation zone. Moreover, while the downstream recirculation zone has not reattached, the mixing layer is smaller than the one for RF300L.

The turbulent shear in the mixing layer at the interface depends on the direction of mass exchange and reduces with increasing relative flow depth.

The analysis of the turbulence also emphasizes that a mixing layer develops along the separation line of the downstream recirculation zone. Once the downstream recirculation zone has reattached, this mixing layer degenerates into a wake.

The spectral analysis of the turbulence emphasizes the presence of 3D vortices in both mixing layers developing in the vicinity of the separation line of the downstream recirculation zone or at the interface between channels between the throat and the cross-section containing the stagnation point of the downstream recirculation zones. These vortices are mainly responsible for the momentum transfers in the mixing layers and emphasize the great role of the turbulence coming from the bottom.

To finish, analyses of the boundary shear stresses indicate great changes relative to the reference flow. The plunging flow at the upstream face of the groyne is responsible for a strong increase in the boundary shear stress in the groyne-cross section. The passage to supercritical regime is also responsible for an increase in the boundary shear stress in the floodplain.

Impacts of a change in the groyne length or total discharge in a groyne-case flow

In this chapter, we have assessed the impacts on the flow parameters (defined in Equation 2.28) of the increase of the length of the groyne or of the injected total discharge. For impacts of the groyne length, comparisons were performed between the groyne-case flow GC330L ($Q_t = 24.7$ l/s, $d = 0.3$ m) and the groyne-case flow GC350L ($Q_t = 24.7$ l/s, $d = 0.5$ m). For impacts of the total discharge, comparisons were performed between the groyne-case flow GC330L ($Q_t = 24.7$ l/s, $d = 0.3$ m) and the groyne-case flows GC230L ($Q_t = 17.3$ l/s, $d = 0.3$ m) and GC430L ($Q_t = 36.2$ l/s, $d = 0.3$ m). The groyne was set perpendicular to the streamwise direction. The discharge distributions to inject in the flume were the ones proposed by Proust [2005] (*i.e.* see in Table 3.3) and were the same as for the reference flows. For the outlets, the tailgates were set up at the same elevation as their corresponding reference flow (see §5.2).

The length of the downstream recirculation zone increases with the groyne length and the total discharge. As a consequence the flow section reduces and the water depth so as the velocity are more impacted. These variations are also responsible for an increase in mass exchange between channels and lead emergence to a supercritical zone in the main channel parallel to the supercritical zone in the floodplain.

Turbulence in the mixing layer at the interface is analysed. The width of the mixing layer as its growth rate depend on the main flow section and on the mass exchange. In the converging part of the flow, they are proportional to the groyne length and are inversely proportional to the total discharge. In the diverging part, they are inversely proportional to both the groyne length and the total discharge. Concerning the centre of the mixing layer, it is literally pushed in the main channel at high total discharge and large groyne in the vicinity of the groyne cross-section.

Reynolds shear stresses at the interface increase with the width of the mixing layer and the under-feeding of the floodplain. By contrast, they are inversely proportional to the water depth.

The coherent structures that develop inside the mixing layer at the interface are also characterised. In the converging part of the flow, dominant structures are mainly planform horizontal vortices and they are the main contributor to momentum transfers through the mixing layer. In the diverging part of the flow, while the recirculation zone has not reattached, coherent structures lose their 2D characteristics with increasing total discharge and acquire 2D characteristics with larger groyne lengths.

When increasing both the groyne length and the total discharge, the measurements of the turbulence along the separation line emphasize that the shear becomes stronger and momentum transfer are operated by structures with 3D characteristics. Once the recirculation zone has reattached, the coherent structures coming from the separation line degenerate into a wake.

To finish, the study of the boundary shear stresses indicate that differences relative to reference flows increase with increasing groyne length and total discharge.

Discussion on momentum transfers in compound channel

In this chapter, the discussion deals with the assessment of the dominant physical phenomena that are observed in flows with a groyne set on the floodplain of an asymmetrical compound channel.

We first showed that considerations on the regime of the recirculation zones through the use of the stability number S do not enable to determine, which from the bottom-generated turbulence

and the groyne-generated turbulence is responsible for the development of the recirculation zones. Considerations on physical processes must be done using a x-wise momentum equation.

Second, the evaluation of the dispersion on the vertical of the horizontal components of the velocity emphasizes that the lateral gradients of X_{xy} can be significant in the vicinity of the interface between channels for groyne-case flows. The dispersion on the vertical must be then taken into account in the calculation of the 2D-momentum balances.

In the sequel, calculation of momentum balances first indicates that reference flows are mainly driven by the friction, the gravity and the momentum transfers due to the turbulent shear at the interface.

By contrast, calculations of momentum balances for groyne-case flows emphasize that the streamwise gradients of hydrostatic pressure and longitudinal kinetic energy are the dominant processes in the flow. They can be 15 times greater than the friction, the dispersion and the turbulent flux. Moreover, with increasing total discharge and groyne length, the momentum transfer due to mass exchange increases at the interface between the main channel and the floodplain. It can be six times greater than the friction, the dispersion and the turbulent flux.

Nevertheless, friction and momentum transfers due to the turbulent exchange, especially at the interface between channels, are not cancelled by mass exchange and have the same order of magnitude as under reference flow conditions. Advices for modellers could be therefore: without correctly considering friction and turbulence, the dominant process that is mass exchange cannot be well rendered. The good estimation of the turbulence and friction is indeed necessary for assessing the depth and the velocity in order to compute the discharge distribution across the flume.

Part IV

General conclusions and prospects

General conclusion

In the present work, steady developing flows in straight compound channel and rapidly varied flows in compound channel with a groyne set on the floodplain were investigated. The first purpose of this work was to compare the hydraulic parameters of the rapidly varied flows with the ones of the developing flows that are close to uniform flow conditions. The second purpose consisted in identifying the weight of each physical process that occurs in rapidly varied flows in order to give advices to modeller regarding the modelling of flows in the vicinity of a groyne. The PhD work relies on experimental modelling performed in the LMFA laboratory (Lyon, France) and on theoretical considerations on momentum transfer.

Experiments were performed in a 8 m long and 1.2 m wide flume with an asymmetrical compound channel (LMFA, Lyon, France). Three developing flows close to uniform flow conditions and six rapidly varied flows with a groyne set on the floodplain, perpendicularly to the streamwise direction were analysed. The impacts on physical processes of an increase in the total discharge were first investigated for developing flows. Then, using the same upstream and downstream boundary conditions as developing flows, the impacts of a groyne introduced in the floodplain of a developing flow were investigated varying the total discharge and the groyne length. Finally, the dominance of physical processes were assessed using experimental data and an 2D-H x-wise momentum equation.

Developing flows in compound channel

The study of the developing flows first emphasizes that thanks to the separated inlets that enable to inject the uniform discharge distribution, mass exchange between channels is mainly limited to the three first meters of the flume and the development of the mixing layer at the interface between the main channel and the floodplain is accelerated relative to a flume with a single inlet. As a result, the depth and the depth-averaged velocity are constant along x-axis within a zone of 2.5 meters in the middle of the flume (between $x = 3.5$ m and $x = 5.5 - 6$ m). By contrast – given the shortness of the flume and the flow injection at the inlets – the boundary shear stresses and the Reynolds stresses evolve all along the flume. This evolution is stronger when increasing the total discharge. Nevertheless, despite these longitudinal evolutions, the lateral mass exchange between the main channel and the floodplain is weak compared to flows with a groyne. Accordingly, they are considered as reference flows.

Flows with a groyne set on the floodplain

Recirculation zone

The study of the rapidly varied flows first highlights that the obstacle promotes two flow separations resulting in two recirculation zones on both sides of the groyne. The recirculation zones are separated from the main flow by a separation line along which a mixing layer develops. The separation line is the streamline linking the separation point at the tip of the groyne and the stagnation point on the floodplain side-wall, which defines the longitudinal extent of the

recirculation zone. The shape of the recirculation zones depends on (1) the water depth h along the separation line, (2) the groyne length d , and (3) the protrusion ratio d/B (B the width of the flume). The streamwise length of the recirculation zone normalized by the groyne length decreases with a decrease in the water depth and an increase in the groyne length. In addition, as the maximal lateral expansion of the recirculation zone is limited by the presence of the interface between the main channel and the floodplain, the maximal expansion is only 2 centimetres greater than the groyne length.

Supercritical transition

The groyne induces a reduction in the flow section, leading therefore to (1) mass exchange between channels, (2) the creation of a throat (hydraulic disconnection) in the floodplain and (3) the transition to a supercritical regime in the floodplain from the throat to at least one meter upstream of the stagnation point. The throat is located ten centimetres downstream of the groyne, where the lateral expansion of the recirculation zone is maximal. This throat separates the flume in two parts: in the converging part, the mass is exchanged from the floodplain towards the main channel and in the diverging part, the mass is exchanged from the main channel towards the floodplain. With increasing the total discharge and the groyne length, the throat remains at the same location in the floodplain and partly affects the flow in the main channel.

The analysis of the various backwater effects in the floodplain emphasizes that the transition to supercritical regime to subcritical regime – close to the cross-section where the downstream recirculation zone reattaches – is characterized by a normal undulated jump.

Mixing layer between the main channel and the floodplain

Considering the impacts of the groyne on the mixing layer between channels. The centre of the mixing layer is pushed in the main channel in the converging part of the flume and is pushed in the floodplain in the diverging part. The width of the mixing layer relative to reference flows is enhanced in the converging part of the flow with increasing groyne length and is respectively lowered with increasing total discharge. The width is limited in the main channel as long as the recirculation zone has not reattached.

Regarding the magnitude of T_{xy} at the interface, it decreases with increasing water depth and rises (1) with the floodplain under-feeding and (2) the width of the mixing layer. As a result, the turbulent shear globally increases with increasing groyne length, while it reduces with increasing total discharge. Notice that a local maximum of T_{xy} is located on the separation line of the recirculation zone: two zones of turbulent momentum transfer are then present in the flow and interact at large groyne length and total discharge.

The study of coherent structures in the mixing layer at the interface between the main channel and the floodplain indicates that planform horizontal vortices are mainly responsible for momentum transfer inside the mixing layer. When increasing the total discharge, planform vortices disappear and are replaced by 3D structures and the width of the mixing layer is restricted by the bottom-generated turbulence. By contrast, with increasing groyne length, planform vortices are generated and reduces the role of the 3D structures.

Mixing layer along the recirculation zone

Measurements of the coherent structures developing along the separation line indicate that they acquire some 2D characteristics when increasing both the groyne length and the total discharge, which therefore point out that the turbulence coming from the bottom is weakened.

Once the recirculation zone has reattached, the coherent structures coming from the separation line degenerate into a wake and therefore become 3D.

Boundary shear stress

The maximum of boundary shear stresses is still located on the floodplain-side of the interface, but a second local maximum is measured (1) at the tip of the groyne because of the strong plunging flow that occurs here and (2) along the separation line separating the recirculation zone and the main flow. The supercritical flow regime in the floodplain located downstream of the throat and the resulting low water depths and high velocities are also responsible for an increase in boundary shear stress. These effects are enhanced by an increase in the groyne length and total discharge.

Momentum balances

Finally, once the non-uniform flows were characterised, the dominance of physical processes was discussed in the last chapter of the thesis.

The calculations of the momentum balances for the developing flows in straight compound channel indicate that the friction, the momentum transfer due to the turbulent shear at the interface between channels and the gravity are the dominant physical processes.

In the sequel, calculations of momentum balances for rapidly varied flows with a groyne set onto the floodplain emphasize that the dominant process in the flow is the mass exchange within a cross-section and the momentum transfer due to mass exchange in the mixing layer between channels. They can be 6 times greater than the friction, the dispersion and the turbulent flux when increasing the groyne length and the total discharge. Nevertheless, friction and momentum transfer due to the turbulent shear at the interface are never cancelled and have the same order of magnitude as the gravity.

Advices for modellers could be therefore: without considering friction and turbulence in rapidly varied flows with a groyne in the floodplain, the dominant process that is mass exchange, cannot be well rendered. The good estimation of the turbulence and friction is indeed necessary for the calculation of the water depth and velocity across the flume that are necessary for computing the discharge distribution in the flow.

Prospects

Despite the great amount of data in this PhD-Thesis, several questions still need answers because of a lack of information. The groyne-case measurements could have been done in a different way. Some zones with few interests are indeed well described (the main flow), while some interesting zones - like the recirculation - zone are not enough detailed.

In the following paragraphs, some prospects to this thesis are presented.

Considering the physical modelling of uniform flows in a short compound channel

In the chapter 5 of this thesis, we showed that the reference flows are almost developed in the middle of the flume according to the depth and the depth-averaged velocities, but the turbulence and the boundary shear stresses evolve until the end of the flume. We found that boundary shear stresses evolve because of the plunging flow at the inlet that increases the velocity at the bottom and the turbulence evolves because of the lateral momentum transfers in the mixing layer.

The distance of establishment for the boundary shear stress could be reduced using a perennial solution for the upstream boundary conditions. Further experiments are needed for reducing the influence of the inlet conditions.

The distance of establishment of the turbulence in the mixing layer could be reduced using the principles exposed in *Proust et al.* [2011] (dependency of the turbulent shear at the interface to the discharge distribution). Thus, with a slight under-feeding of the floodplain (≥ -19 % of the uniform discharge in the floodplain) we could force the establishment of the turbulence.

About of the position of the groyne relative to the boundary conditions

As exposed in Chapter 3, the flume at the LMFA laboratory is short, as a consequence, the boundary conditions, especially the outlets have tremendous effects on longitudinal extents of the recirculation zones. In the Ujigawa experiments (Appendix B), the groyne was set far from any boundary conditions and the length of the recirculation zone are greater than in the LMFA experiments. Further experiments in long compound channels could be performed in order to evaluate the role of the outlets on the development of the recirculation zones.

About a better characterisation of the turbulence in recirculation zones

As said in the introduction of this chapter, some parts of the flow where not enough detailed during measurements. The separation line and the recirculation zone belong to these zones. In Chapters 6 and 7, we showed that the few density-spectra we have along the separation line

give not enough information about the growth of the mixing layer along the separation line and about the sizes of the coherent structures inside, moreover, measurements were not performed at the same positions along the separation line, since we use a regularly spaced mesh. It could be interesting to measure cross-sections in the recirculation zone as we performed at the open-laboratory of Ujigawa (see Appendix B); in the groyne cross-section, in the cross-section of the maximal expansion (\approx throat cross-section), in the middle of the recirculation zone, at the stagnation point and one meter downstream of the stagnation point. We consequently would have a denser mesh and the same mesh for all cases for comparing the spectral densities. We could therefore clearly compare cases together.

About flows with a unique groyne in a symmetrical compound channel

In our flows, we have shown that the opposite wall to the groyne operate a lateral confinement on the flow and on the recirculation zone. It could be interested to performed a study similar to ours with a unique groyne set in the floodplain of a symmetrical compound channel. We could then compare the effects of having a mixing layer in the opposite to the groyne instead of having a solid wall.

Effect of the slope

As exposed in Appendix B experiments in Japan were done with a smaller slope than the one in the LMFA. It could be interested to investigate the effects of the slope on the momentum transfers due to mass and turbulent exchanges. Indeed, the low slope of 0.8/1000 m/m at the Ujigawa laboratory has a big influence on the flow deflection at the tip of the groyne, resulting in longer recirculation zones relative to those we measured in the LMFA flume.

Effect of a difference in roughness between channels

To the author knowledge no experiment deals with measurements in the vicinity of a groyne in compound channel with a difference in roughness between channels. These experiments could be interesting since they will be closer to the reality than those performed for this thesis. It is expected that the higher friction on floodplain inhibits the spread of the recirculation zone and therefore enhances the size of the coherent structures in the mixed layer developing along the separation line.

About sediment transport in the vicinity of a groyne

As exposed in Carrasco and Vionnet [2004] and in Zhang and Nakagawa [2008]; Zhang et al. [2009] some studies deal with sediment transport in the vicinity of a groyne in single channel. A further development could be done in compound channel. Understanding how sediments are transported in such a flow configuration is paramount for reducing scours or for reducing aggradation of river banks in the lee of an obstacle set on the floodplain of a compound geometry. As observed at the Ujigawa laboratory (Appendix B), “a local scour still exists around the permeable spur dyke. However, the magnitude of the scouring and the eroded area is smaller than those in the impermeable case. This result indicates low probability of severe erosion around the

permeable spur dyke, and the permeable spur dyke appears to be a more interesting alternative as the impermeable spur dyke in term of morphodynamics” [Baba et al., 2010].

About the numerical modelling of groyne-case flows

Finally a paramount point has not been analysed in this thesis, because we rather preferred to take time to have good measurements and good physical analyses of the physical processes; thus what about the numerical modelling of such groyne-case flows?

The answer is not simple. Thanks to the robust measurements of this PhD-thesis, the data set could be tested on the existing modelling. Nevertheless the momentum balances in this thesis show that an adapted modelling is necessary for simulating such flow configurations. Indeed, given our results, additional questions have emerged:

1. How can we consider the role of the recirculation zones in the flow in 1D-modelling?
2. What type of turbulence modelling should be used for taking into account the turbulence in the recirculation zone when working with 2D and 3D modelling?
3. Is there any 1D or 2D-modelling which consider the dispersion of the horizontal components of the velocity relative to the depth averaged velocities?

1. The measurements in this thesis highlight that recirculation zones cannot be considered as a non viscous walls with a no-slip condition, since the boundary shear stresses and the Reynolds stresses increased around the separation line. In addition, we have shown that the theory of the McGill University [Babarutsi et al., 1989; Rivière et al., 2004] for predicting the shape of the recirculation zone in single channel does not work very well for flows in compound channel (see chapter 8), and the other existing modelling do not work better [Molinas et al., 1998; Ouillon and Dartus, 1997; Stansby, 2008].

2. According to Koken and Constantinescu [2008] LES is the best way for modelling the turbulence inside the recirculation zone. As the turbulence out of recirculation zones can be modelled using a simple turbulent closure [Peltier et al., 2008], we could therefore use an hybrid modelling using RANS turbulence in the main flow and the LES in the recirculation zone for reducing the computing time. The question is to know if such modelling is possible in compound channel and especially is possible using 2D-H modelling. Indeed, in an operational point of view, 3D modelling demand too much computing time.

3. If 1D and 2D modelling are used in an operational point of view. As highlighted in Chapter 8, we have shown that the dispersion of the horizontal components of the velocity relative to the depth averaged velocities must be taken into account in modelling for reducing the bias that introduces the depth-averaging of the flow parameters. To the author knowledge, only the model proposed by Bousmar and Zech [2002], partially takes into account the flow dispersion. Further development of the dispersion modelling are required.

To close this chapter on the prospects and finally this thesis, I cite Rouse [1961] who said a cruel truth:

“One of several persistent paradoxes in hydraulics is the fact that the flow phenomena that seem to be the least well understood are those that have been the most familiar for the longest time”

Bibliography

- Ackers, P. (1993), Flow formulae for straight two-stage channels, *Journal of Hydraulic Research*, 31, 504–531. 3, 229
- Adrian, R. J. (2005), Twenty years of particle image velocimetry, *Experiments in Fluids*, 39, 159–169, doi:DOI10.1007/s00348-005-0991-7. 63
- Afzalimehr, H., and C. D. Rennie (2009), Determination of bed shear stress in gravel-bed rivers using boundary-layer parameters, *Journal of Hydrological sciences*, 54(1), 147–159. 13
- Alavian, V., and V. H. Chu (1985), Turbulent exchange flow in shallow compound channel, in *21st IAHR Congress, 19-23 August 1985, Melbourne, Australia*. 8
- Ancey, C. (2009), *Introduction à l'hydraulique pour les ingénieurs civils et environmentalistes: notes de cours de mécanique des fluide de l'Ecole Polytechnique Fédérale de Lausanne*, Ecole Polytechnique Fédérale de Lausanne, Lausanne, Suisse. XXIII, 5, 17, 104, 109, 128, 234
- Armaly, B. F., F. Durst, J. C. F. Pereira, and B. Shoenung (1983), Experimental and theoretical investigation of backward-facing step flow, *Journal of Fluid Mechanics*, 127, 473–496. 77
- Arnould, M. (2005), Pour le 21e siècle, réapprendre à vivre avec les crues. pour chacun et tous, faire la part du risque dans nos villes, nos villages, notre pays., *Tech. rep.*, Etablissement Public Loire - WWF. XXI
- Asano, T., H. Hashimoto, and K. Fujita (1985), Characteristics of variation of manning's roughness coefficient in a compound cross section, in *21st IAHR Congress, Melbourne, Australia*. 12
- Baba, Y., B. Camenen, Y. Peltier, F. Thollet, H. Zhang, and H. Nakagawa (2010), Flows and bedload dynamics around spur dike in a compound channel, in *11th International Symposium On River Sedimentation, 6-9 September 2010, Cape Town, South Africa*. XXVI, 45, 207
- Babarutsi, S., J. Ganoulis, and V. H. Chu (1989), Experimental investigation of shallow recirculating flows, *Journal of Hydraulic Engineering*, 115(7), 906–924. XXIII, XXVI, 17, 18, 21, 141, 166, 177, 207
- Babarutsi, S., M. Nassiri, and V. H. Chu (1996), Computation of shallow recirculating flow dominated by friction, *Journal of Hydraulic Engineering*, 122(7), 367–372. 17, 18
- Bailly, C., and O. Marsden (2009), *Turbulence: description physique and modélisation. Module ouvert 3A, ECL'09 et école doctorale MEGA*, Ecole Centrale Lyon, Lyon France. 38
- Bally, F. X., and J. M. Berroir (2008), *Incertitudes expérimentales*, centre de préparation interuniversitaire à l'agrégation de physique de Montrouge ed., Ecole Normale Supérieure de Cachan. 71, 72, 74, 98, 105
- Barré de Saint-Venant, A. J. C. (1871a), Théorie du mouvement non permanent des eaux , avec applications aux crues des rivières et à l'introduction des marées dans leur lits., *Comptes-rendus hebdomadaires des séances de l'Académie des Sciences*, 73, 147–154. 221

- Barré de Saint-Venant, A. J. C. (1871b), Théorie du mouvement non permanent des eaux , avec applications aux crues des rivières et à l'introduction des marées dans leur lits [2e note], *Comptes-rendus hebdomadaires des séances de l'Académie des Sciences*, 73, 237–250. 221
- Batchelor, G. K. (1969), Computation of the energy spectrum in homogeneous two-dimensional turbulence, *The Physics of Fluids Supplement II*, 12(12), 233–239. 5, 9, 116, 145
- Bourdat, A. (2007), Débordements des cours d'eau en présence de remblais routiers dans les lits majeurs, Master's thesis, Projet de fin d'études, ENSHMG de Grenoble, Cemagref, France 48p. 17, 22
- Bousmar, D. (2002), Flow modelling in compound channels / momentum transfer between main channel and prismatic or non-prismatic floodplains, Ph.D. thesis, Université catholique de Louvain, faculté des sciences appliquées. XXII, XXIII, 10, 12, 16, 25, 27, 29, 30, 33, 35, 37, 38, 40, 52, 60, 177, 179, 183, 226, 227, 228, 230, 231
- Bousmar, D., and Y. Zech (1999), Momentum transfer for practical flow computation, *Journal of Hydraulic Engineering*, 125(7), 696–706. 12, 230, 231
- Bousmar, D., and Y. Zech (2002), Periodical turbulent structures in compound channels, in *River Flow 2002: 1st International Conference on Fluvial Hydraulics, 4-6 September 2002, Louvain la Neuve, Belgium*. 193, 207
- Bousmar, D., N. Wilkin, J. H. Jacquemart, , and Y. Zech (2004), Overbank flow in symmetrically narrowing floodplains, *Journal of Hydraulic Engineering*, 130(4), 305–312. XXII, 15, 16, 34
- Bousmar, D., N. Rivière, S. Proust, A. Paquier, R. Morel, and Y. Zech (2005), Upstream discharge distribution in compound-channel flumes, *Journal of Hydraulic Engineering, ASCE*, 131, 408–412. XXII, 15, 47, 48, 99, 105, 112
- Bousmar, D., S. Proust, and Y. Zech (2006), Experiments on the flow in a enlarging compound channel, in *River Flow 2006: 3rd International Conference on Fluvial Hydraulics, 6-8 September, Lisbon, Portugal*. XXIII, 15
- Camenen, B., and M. Larson (2005), A bed-load transport formula for the nearshorevol, *Estuarine Coastal and Shelf Science*, 63, 249–260. 239
- Carrasco, A., and C. A. Vionnet (2004), Separation of scales on a broad, shallow turbulent flow, *Journal of Hydraulic Research*, 42(6), 630–638. XXIII, 19, 206
- Chassaing, P. (2000a), *Turbulence en mécanique des fluides : Analyse du phénomène en vue de sa modélisation par l'ingénieur*, Collection POLYTECH, Cépaduès-éditions, Toulouse, France. 5, 27, 28, 34, 35, 36, 37, 71, 114, 143, 160, 171
- Chassaing, P. (2000b), *Mécanique des fluides: éléments d'un premier parcours*, Collection POLYTECH, Cépaduès-éditions, Toulouse, France. 136, 154
- Cheng, H., and I. P. Castro (2002), Near wall flow over urban-like roughness, *Boundary Layer Meteorology*, 104, 229–259. 34
- Chlebek, J., and D. W. Knight (2008), Observations on flow in channels with skewed floodplains, in *River Flow 2008: 4th International Conference on Fluvial Hydraulics, 3-5 September 2008, Cesme-Izmir, Turkey*. XXII, 15
- Chow, V. T. (1959), *Open-Channels Hydraulics*, McGraw Hill Book Co., New York, USA. XXIII, 4, 17, 22, 104, 109, 117, 119, 128, 129, 234
- Chu, V. H., and S. Babarutsi (1988), Confinement and bed-friction effects in shallow turbulent mixing layers, *Journal of Hydraulic Engineering*, 114, 1257–1274. 8

- Chu, V. H., J. H. Wu, and R. E. Khayat (1983), Stability of turbulent shear flows in shallow channel, in *20th IAHR Congress, Moscow, USSR*. 8, 17, 18, 22
- Chu, V. H., J. H. Wu, and R. E. Khayat (1991), Stability of the transverse shear flow in shallow open channels, *Journal of Hydraulic Engineering, ASCE*, 117, 1371. 6, 7, 8, 22, 142, 227
- Chu, V. H., F. Liu, and W. Altai (2004), Friction and confinement effects on a shallow recirculating flow, *Journal of Environmental and Engineering Sciences*, 3, 463–475. XXIII, 17, 18, 141, 142, 171, 177
- Czernuszenko, W., and E. R. Holley (2007), Open-channel turbulence measurements with a three-component acoustic doppler velocimeter, *Institute of Geophysics, Polish Academy of Sciences, E-7 (401)*. 59
- Czernuszenko, W., and P. M. Rowinski (2008), Shear stress statistics in a compound channel flow, *Archives of Hydro-Engineering and Environmental Mechanics*, 55(1-2), 3–27. 60
- Dimitrov, C., and V. Pin (2006), Les outils de l'action publique face aux aléas, *La Houille Blanche*, 6, 67–72. XXIV
- Einstein, H. A., and H. Li (1958), Secondary currents in straight channels, *American Geophysical Union Transcriptions*, 39, 1085–1088. 14
- Elliot, S. C. A., and R. H. J. Sellin (1990), Serc flood channel facility: skewed flow experiments, *Journal of Hydraulic Research*, 28(2), 197–214. XXII, 15
- Estivalezes, J. L. (2005), *Notes de cours de turbulence*, Polycopié de cours ENSEEIHT, Toulouse, France. 26, 28, 36, 38
- Ettema, R., and M. Muste (2004), Scale effects in flume experiments on flow around a spur dike in flatbed channel, *Journal of Hydraulic Engineering*, 7, 635–646. 19, 20, 21, 22, 77, 133
- Francis, J. R. D., A. B. Pattanaik, and S. H. Wearne (1969), Observations of flow patterns around some simplified groyne structures in channels, *Proceedings of Institute of Civil Engineerings*, 41, technical note 8, 829–837. 21, 22
- French, R. H. (1985), *Open Channel Hydraulics*, 680 pp., McGraw-Hill, New-York, USA. 34, 35, 234
- Fuchs, H., H. Katsher, and J. Lengrecht (), Dissipation due to obstacles in supercritical flow, source unknown. 76
- Fujita, I. (1994), Surface flow measurement of flood by image correlation, in *Third Asian Symposium on Visualization, Chiba, Japan*. 63, 75
- Fujita, I., M. Muste, and A. Kruger (1998), Large-scale particle image velocimetry for flow analysis in hydraulic engineering applications, *Journal of Hydraulic Research*, 36(3), 397–414. 75, 236
- Garcia, C. M., M. I. Cantero, Y. Niño, and M. H. Garcia (2005), Turbulence measurements with acoustic doppler velocimeters, *Journal of Hydraulic Engineering*, 131(12), 1062–1073, doi:10.1061/(ASCE)0733-9429(2005)131:12(1062). 59, 91
- Ghosh, S. N., and S. B. Jena (1971), Boundary shear distribution in open channel compound, *Proceedings of the Institution of Civil Engineers*, 49, 417–430. 12
- Goring, D. G., and V. I. Nikora (2002), Despiking acoustic doppler velocimeter data, *Journal of Hydraulic Engineering*, 128(1), 117–126. 59, 81, 82, 83, 100

- Graf, W. H., and M. S. Altinakar (2000), *Hydraulique fluviale: écoulement et phénomènes de transport dans les canaux à géométrie simple*, PPUR presses polytechniques. 137, 155
- Hauet, A. (2006), Estimation de débit et mesure de vitesse en rivière par large-scale particle image velocimetry, Ph.D. thesis, Institut National Polytechnique de Grenoble. 63, 64, 65, 75
- Hauet, A., J. D. Creutin, and P. Belleudy (2007), Sensitivity analysis of large-scale particle image velocimetry measurement of river discharge using numerical simulation, *Journal of Hydrology*, 349(1-2), 178–190. 75, 236, 237
- Hauet, A., A. Kruger, W. F. Krajewski, A. Bradley, M. Muste, J. D. Creutin, and M. Wilson (2008), Experimental system for real-time discharge estimation using an image-based methodn, *Journal of Hydrologic Engineering*, 13(2), 105–110, doi:10.1061/ASCE1084-06992008132105. 63, 75
- Henderson, F. M. (1966), *Open Channel Flow*, Macmillan, New York, USA. 30, 40
- Hervouet, J. M. (2002), *Les équations de Navier-Stokes à surface libre et leurs formes simplifiées en eau peu profonde. Support de cours, Problèmes non-linéaires appliqués, Ecoulements peu profonds à surface libre*, INRIA, Rocquencourt, France. 36
- Holden, A. P., and C. S. James (1989), Boundary shear distribution on floodplains, *Journal of Hydraulic Research*, 27(1), 75–89. 13, 14
- Hurther, D., and U. Lemmin (2001), A correction method for turbulence measurements with a 3d acoustic doppler velocity profiler, *Journal of Atmospheric and Oceanic Technology*, 18, 446–458. 59, 90, 91, 100, 113, 249
- Ikeda, S., and I. K. McEwan (2009), *IAHR monograph series: Flow and sediment transport in compound channels: the experiences of japanese and UK research*, IAHR, Madrid, Spain. 3, 6, 11, 13, 14, 15, 39, 180
- Jirka, G. H., and W. S. J. Uijtewaal (2003), Shallow flows: a definition, in *International Symposium On Shallow flows, 16-18 June 2003, Delft, the Netherlands*. 5, 28
- Jodeau, M., A. Hauet, A. Paquier, J. L. Coz, and G. Dramais (2008), Application and evaluation of ls-piv technique for the monitoring of river surface velocities in high flow conditions, *Flow measurement and Instrumentation*, 19, 117–127. 63
- Knight, D. W. (1992), Serc flood channel facility experimental data-phase a. report sr314, *Tech. rep.*, HR Wallingford, UK. 12, 48
- Knight, D. W., and J. D. Demetriou (1983), Floodplain and main channel flow interaction, *ASCE, Journal of Hydraulic Engineering*, 109(8), 1073–1092. XXII, 3, 12
- Knight, D. W., and M. E. Hamed (1984), Boundary shear in symmetrical compound channels, *Journal of Hydraulic Engineering*, 110 (10), 1412–1430. 12, 13, 33, 119
- Knight, D. W., J. D. Demetriou, and M. E. Hamed (1984), Boundary shear in smooth rectangular channels, *Journal of Hydraulic Engineering*, 110 (4), 405–422. 12
- Knight, D. W., K. W. H. Yuen, and A. A. I. Alhamid (1994), *Physical mechanisms of mixing and transport in the environment*, chap. 4: Boundary shear stress distributions in open channel flow, pp. 51–87, J. Wiley (Eds K. Beven, B. Chatin and J. Millbank). 13
- Koken, M., and G. Constantinescu (2008), An investigation of the flow and scour mechanisms around isolated spur dikes in a shallow open channel: 1. conditions corresponding to the initiation of the erosion and deposition process, *Water Resource Research*, 44, 1–19. XXIII, 19, 20, 77, 134, 150, 153, 207

- Kraichman, R. H. (1967), Inertial ranges in two-dimensional turbulence, *The Physics of Fluids*, 10(7), 1417–1423. 5, 147
- Lane, S. N., P. M. Biron, K. F. Bradbrook, J. B. Butler, J. H. Chandler, M. D. Crowell, S. J. McLelland, K. S. Richards, and A. G. Roy (1998), Three dimensional measurement of river channel flow processes using acoustic doppler velocimetry, *Earth Surface Processes and Landforms*, 23, 1247–1267. 60
- Lauder, B. E., and D. B. Spalding (1974), The numerical computation of turbulent flows, *Computation Methods in Applied Mechanical Engineering*, 3, 269–289. 38
- Le Coz, J., A. Hauet, G. Dramais, and G. Pierrefeu (), Performance of image-based velocimetry (lspiv) applied to flash-flood discharge measurements in mediterranean rivers, submitted to Journal of Hydrology (subm. 1 September 2009, revised Jan. 2010, Special Issue Flash-floods). 237
- Lefort, P., and J. M. Tanguy (2009), *De la goutte de pluie jusqu'à la mer: traité d'hydraulique environnementale. Tome 1: Processus hydrologiques et fluviaux*, chap. 9: Mécanisme de l'écoulement à surface libre, pp. 207–265, Lavoisier, Paris France (Ed J. M. Tanguy). XXI, XXIV
- Lemasquerier, J. M. (2002), *Calcul numérique de la Transformée de Fourier*, IPEST, Tunis, Tunisia. 90
- Lindborg, E. (1999), Can the atmospheric kinetic energy spectrum be explained by two-dimensional turbulence, *Journal of Fluid Mechanics*, 388, 259–288. 116, 145
- Lotter, G. K. (1933), Considerations on hydraulic design of channels with different roughness of walls, *Transactions, All-Union Scientific Research Institute of Hydraulic Engineering*, 9, 238–241. 226
- Manning, R. (1889), On the flow of water in open channels and pipes, *Transactions, Institution of Civil Engineers of Ireland*, 20, 161–207. 226
- Martin-Vide, J. P., and P. J. M. Moreta (2008), Formulae for apparent shear stress in straight compound channels with smooth floodplains, in *4th International Symposium of River Flow, 3-5 September 2008, Cesme-Izmir, Turkey*. 228
- Martinez-Monclus, J. (2005), Etude des longueurs des recirculations en lit simple et lit composé en utilisant la technique de velocimétrie par intercorrélation d'images de particules, Master's thesis, INSA de Lyon, LMFA. 19, 21, 22
- McLelland, S. J., and A. P. Nicholas (2000), A new method for evaluating errors in high-frequency adv measurements, *Hydrological Processes*, 14, 351–366. 60
- Melville, B., S. van Ballegooy, S. Coleman, and B. Barkdoll (2006), Countermeasure toe protection at spill-through abutments, *Journal of Hydraulic Engineering*, 132(3), 235–245. XXIII, 19
- Molinas, A., K. Kheireldin, and W. U. Baosheng (1998), Shear stress around vertical wall abutments, *Journal of Hydraulic Engineering*, 124(8), 822–830. 19, 207
- Morvan, H., G. Pender, N. G. Wright, and D. A. Ervine (2002), Three-dimensional hydrodynamics of meandering compound channels, *Journal of Hydraulic Engineering*, 128(7), 674–682. 14
- Morvan, H., D. W. Knight, N. Wright, X. Tang, and A. Crossley (2008), The concept of roughness in fluvial hydraulics and its formulation in 1d, 2d and 3d numerical simulation models, *Journal of Hydraulic Research*, 46(2), 191–208. 225

- Myers, W. R. C. (1978), Momentum transfer in a compound channel, *Journal of Hydraulic Research*, 16(2), 139–150. 228
- Myers, W. R. C., and J. D. Elsayy (1975), Boundary shear in channel with floodplain, *Journal of the Hydraulics Division, ASCE*, 101, 933–946. 227
- Nezu, I. (2005), Open-channel flow turbulence and its research prospect in the 21st century, *Journal of Hydraulic Engineering*, pp. 229–246. 40
- Nezu, I., and H. Nakagawa (1993), *IAHR monograph series: Turbulence in open-channel flows*, A. A. Balkema Publishers, Rotterdam, The Netherlands. 14, 37, 38, 91, 114, 122, 143, 160, 171, 180
- Nezu, I., K. Onitsuka, and K. Iketani (1999), *Hydraulic modeling*, chap. Coherent horizontal vortices in compound open channel flows, pp. 17–32, Water Ressources Publications, Colorado, USA (Eds V. P. Singh, I. W. Seo and J. H. Sonu). 10, 11, 14, 15
- NF ENV 13005 (1999), Guide pour l’expression des incertitudes de mesure, iso, 120 p, *Tech. rep.*, AFNOR. 72
- Nicollet, G., and M. Uan (1979), Ecoulements permanents à surface libre en lit composés, *La Houille Blanche*, pp. 21–30. 4, 228
- Nikora, V. I., and D. G. Goring (1998), Adv measurements of turbulence: can we improve their interpretation, *Journal of Hydraulic Engineering*, 124(6), 630–634. 81
- Nortek (2004), Vectrino velocimeter: user guide (rev. c), *Tech. rep.*, NORTEK AS. 59, 60, 248, 249
- Ouillon, S., and D. Dartus (1997), Three-dimensional computation of flow around groyne, *Journal of Hydraulic Engineering*, 123(11), 962–970. 207
- Paquier, A. (1995), Modélisation et simulation de la propagation de l’onde de rupture de barrage = modelling and simulating the propagation of dam-break wave, Ph.D. thesis, Université de Saint-Etienne. XXIII
- Patel, V. C. (1965), Calibration of the preston tube and limitations on its use in pressure gradients, *Journal of Fluid Mechanics*, 23, 185–208. 61, 62, 63, 249
- Peltier, Y., S. Proust, A. Bourdat, F. Thollet, N. Rivière, and A. Paquier (2008), Physical and numerical modeling of overbank flow with a groyne on the floodplain, in *River Flow 2008: 4th International Conference on Fluvial Hydraulics, 3-5 September 2008, Cesme-Izmir, Turkey*. 22, 37, 207, 236, 239, 240, 245
- Peltier, Y., S. Proust, F. Thollet, N. Rivière, and A. Paquier (2009), Measurement of momentum transfer caused by a groyne in compound channel, in *33rd IAHR Congress: Water Engineering for a Sustainable Environment, 9-14 August 2009, Vancouver, Canada*. 63
- Pope, S. B. (2000), *Turbulent flows*, Cambridge University Press, New York, USA. 10, 37, 71, 111, 142
- Prandtl, L. (1925), Ueber die ausgebildete turbulenz, *Zeitschrift fuer Angewandte Mathematik und Mechanik*, 5(2), 136–139. 36
- Preston, J. H. (1954), The determination of turbulent skin frictions by means of pitot tubes, *Journal of the Royal Aeronautical Society*, 58, 109–121. 61, 63
- Programme associé de gestion des crues (2004), Gestion intégrée des crues: document de fond, *Tech. rep.*, Organisation Météorologique Mondiale - Globale Water Partnership. XXII

- Proust, S. (2005), Ecoulements non-uniformes en lits composés : effets de variations de largeur du lit majeur, Ph.D. thesis, INSA de Lyon. [XXIII](#), [15](#), [17](#), [21](#), [22](#), [23](#), [34](#), [36](#), [69](#), [99](#), [103](#), [104](#), [109](#), [136](#), [138](#), [155](#), [196](#), [197](#), [225](#), [227](#), [233](#)
- Proust, S., N. Rivière, D. Bousmar, A. Paquier, Y. Zech, and R. Morel (2006), Flow in compound channel with abrupt floodplain contraction, *Journal of Hydraulic Engineering*, *132*(9), 958–970, doi:10.1061/(ASCE)0733-9429(2006)132:9(958). [XXIII](#), [15](#), [134](#), [233](#)
- Proust, S., D. Bousmar, N. Rivière, A. Paquier, and Y. Zech (2009), Non-uniform flow in compound channel: a 1d method for assessing water level and discharge distribution, *Water Ressource Research*, *45*(12), 411–424, doi:10.1029/2009WR008202. [108](#), [225](#), [231](#), [232](#), [233](#), [234](#)
- Proust, S., D. Bousmar, N. Rivière, A. Paquier, and Y. Zech (2010), Energy losses in compound open channels, *Advances in Water Ressources*, *33*(1), 1–16. [XXIII](#), [15](#), [16](#), [34](#), [135](#), [230](#), [231](#), [232](#)
- Proust, S., Y. Peltier, J. Fernandes, J. Leal, F. Thollet, M. Lagouy, and N. Rivière (2011), Effect of different inlet flow conditions on turbulence in a straight compound open channel, in *34th IAHR Congress: Balance and Uncertainty; Water in a Changing World, 26 June - 01 July 2011, Brisbane, Australia*. [XXII](#), [15](#), [16](#), [205](#)
- Rezaei, B., and D. W. Knight (2009), Application of the shiono and knight method in compound open channels with non-prismatic floodplains, *Journal of Hydraulic Research*, *47*(6), 716–726. [37](#), [39](#)
- Rhodes, D. G., and D. W. Knight (1994), Velocity and boundary shear in a wide compound duct, *Journal of Hydraulic Research*, *32*(5), 743–764. [14](#)
- Rivière, N., S. Proust, and A. Paquier (2004), Recirculating flow behind groynes for compound channel geometries, in *River Flow 2004: 2nd International Conference on Fluvial Hydraulics, 23-25 june 2004, Napolly, Italy*. [XXVI](#), [19](#), [21](#), [22](#), [23](#), [78](#), [153](#), [178](#), [207](#), [239](#)
- Rivière, N., G. Travin, and R. J. Perkins (2007), Transcritical flows in open channel intersections, in *Proceeding Of the 32st IAHR Congress (CD-Rom-paper SS05-11), 1-5 July 2007, Venice, Italy*. [136](#), [155](#)
- Rivière, N., B. Badin, Y. Bomchil, and S. Proust (2008), Recirculation zones downstream open channel expansions, in *River Flow 2008: 4th International Conference on Fluvial Hydraulics, 3-5 September 2008, Cesme-Izmir, Turkey*, pp. 2233–2238. [17](#), [18](#), [21](#), [240](#)
- Rivière, N., S. Gautier, and E. Mignot (2011), Experimental characterization of flow reattachment downstream open channel expansions, in *34th IAHR Congress: Balance and Uncertainty; Water in a Changing World, 26 June - 01 July 2011, Brisbane, Australia*. [18](#), [19](#), [22](#)
- Rodi, W. (1980), *Turbulence models and their application in hydraulics:a state of the art review.*, IAHR book publications, Delft, the Netherlands. [36](#), [37](#)
- Rouse, H. (1938), Experiments on the mechanics of sediment suspension, in *Proceedings of the 5th International Congress in Applied Mechanics, John Wiley and sons, New York, USA*, vol. 55. [60](#)
- Rouse, H. (1961), Energy transformation in zones of separation general, in *9th IAHR Congr., Dubrovnick, Yugoslavia*, pp. 1291–1302, Dubrovnik. [207](#)
- Rouse, H. (1965), Critical analysis of open-channel resistance, *ASCE, Journal of the Hydraulics Division*, *91*(4), 1–25. [225](#)

- Roy, A. G., T. Buffin-Belanger, H. Lamarre, and A. D. Kirkbride (2004), Size, shape and dynamics of large scale turbulent flow structures in a gravel-bed river, *Journal of Fluid Mechanics*, 500, 1–27. 60
- Schlichting, H., and K. Gersten (2000), *8th Revised and Enlarged Edition: Boundary Layer Theory*, Springer-Verlag, Berlin Heidelberg, Germany. 34, 223
- Sellin, R. H. J. (1964), A laboratory investigation into the interaction between the flow in the channel of a river and that over its flood plain, *La Houille Blanche*, pp. 793–802. 3, 7, 11, 112, 227
- Sellin, R. H. J. (1993), Serc flood channel facility: Experimental data – phase a: Skewed floodplain boundaries, *Tech. rep.*, Report Bristol BS8 1TR, University of Bristol, Bristol, UK. XXII, 15
- Shiono, K., and T. Feng (2003), Turbulence measurements of dye concentration and effects of secondary flow on distribution in open channel flows, *Journal of Hydraulic Engineering*, 129(5), 373–384. 14, 86, 87
- Shiono, K., and D. W. Knight (1989), Two dimensional analytical solution for a compound channel, in *3rd International Symposium on refined flow modeling and turbulence measurements, 1989, Tokyo, Japan*. 31
- Shiono, K., and D. W. Knight (1990), Mathematical models of flow in two or multi stage straight channels, in *Proceeding of the International Conference on River Flood Hydraulics, Wallingford, UK*, vol. G1, edited by W. R. White, pp. 229–238, Wiley paper. 39
- Shiono, K., and D. W. Knight (1991), Turbulent open channel flows with variable depth across the channel, *Journal of Fluid Mechanics*, 222, 617–646. 5, 7, 11, 12, 13, 14, 25, 37, 39, 117
- Shiono, K., and Y. Muto (1998), Complex flow mechanisms in compound meandering channels with overbank flows, *Journal of Fluid Mechanics*, 376, 221–261. XXII, 14, 15
- Song, T., and Y. M. Chiew (2001), Turbulence measurement in non-uniform open-channel flow using acoustic doppler velocimeter (adv), *Journal of Engineering Mechanics*, 127(3), 219–232. 226
- Stansby, P. K. (2008), Limitations of depth-averaged modelings of shallow flow with recirculations, *Numerical Modeling of Hydrodynamics for Water Ressources*, pp. 115–126. 42, 207
- Stokes, G. (1851), On the effect of internal friction of fluids on the motion of pendulums, *Transactions of the Cambridge Philosophical Society*, IX, 8–106. 60
- Strom, K. B., and A. N. Papanicolaou (2007), Adv measurements around a cluster microform in a shallow mountain stream, *Journal of Hydraulic Engineering*, 133(12), 1379–1389, doi: 10.1061/(ASCE)0733-9429(2007)133:12(1379). 60, 90
- Suzanne, C. (2005), *Ecoulements à surface libre*, Polycopié de cours ENSEEIHT, Toulouse, France. 34
- Tamai, N., T. Asaeda, and H. Ikeda (1986), Study on generation of periodical large surface eddies in a composite channel flow, *Water Resources Research*, 22(7), 1129–1138. 112
- Tennekes, H., and J. L. Lumley (1972), *A first course in turbulence*, chap. The statistical description of turbulence, pp. 197–222, The MIT press, USA. 10, 90, 117, 146, 147, 162
- Tominaga, A., and I. Nezu (1991), Turbulent structure in compound open channel flow, *Journal of Hydraulic Engineering, ASCE*, 117(1), 21–41. 14, 15, 180

- Uijtewaal, W. S. J., and R. Booij (2000), Effects of shallowness on the development of free-surface mixing layers., *Physics of Fluids*, 12, 392–402. 8, 9, 10, 112, 115, 121, 142, 144, 161, 172
- van Prooijen, B. C., and W. S. J. Uijtewaal (2002), A linear approach for the evolution of coherent structures in shallow mixing layers, *Physics of Fluids*, 14(12), 4105–4114. 116, 144
- van Prooijen, B. C., R. Booij, and W. S. J. Uijtewaal (2000), Measurement and analysis methods of large scale horizontal coherent structures in a wide shallow channel, in *10th International Symposium on Applications of Laser Techniques to Fluid Mechanics*, 10-13 July 2000, Lisboa, Portugal. 10, 11
- van Prooijen, B. C., J. A. Battjes, and W. S. J. Uijtewaal (2005), Momentum exchange in straight uniform compound channel flow, *Journal of Hydraulic Engineering*, 131(3), 175–183. 8, 10, 11, 25, 37, 111, 112, 113, 139
- Voulgaris, G., and J. H. Trowbridge (1998), Evaluation of the acoustic doppler velocimeter (adv) for turbulence measurements, *AMS, Journal of Atmospheric and Oceanic Technology*, 15, 272–289. 81, 91, 249
- Wark, J. B., P. G. Samuels, and D. A. Ervine (1990), A practical method of estimating velocity and discharge in compounds channels, in *International Conference on River Flood Hydraulics*, 17-20 Sept. 1990, Wallingford, England, edited by W.R.White, John Wiley & Sons Ltd, Chichester. 37
- Weitbrecht, V., G. Kuehn, and G. H. Jirka (2002), Large scale piv-measurements at the surface of shallow water flows, *Flow Measurement and Instrumentation*, 13, 237–245. 63
- Weitbrecht, V., S. A. Socolofsky, and G. H. Jirka (2008), Experiments on mass exchange between groin fields and main stream in rivers, *Journal of Hydraulic Engineering*, 134(2), 173–183, doi: 10.1061/ASCE0733-9429(2008)134:2(173). 19, 63
- Welch, P. D. (1967), The use of fast fourier transform for the estimation of power spectra: a method based on time-averaging over short, modified periodograms, *Reprinted from IEEE, transactions of Audio and Electroacoustics*, AU15, 70–73. 61, 89
- Wormleaton, P. R., J. Allen, and P. Hadjipanous (1982), Discharge assessment in compound channel flow, *Journal of the Hydraulics Division, ASCE*, 108(9), 975–994. 12
- Yen, B. C. (2002), Open channel flow resistance, *Journal of Hydraulic Engineering*, 128(1), 20–39. 34, 225, 227
- Zhang, H., and H. Nakagawa (2008), Scour around spur dyke: recent advances and future researches, *Annals of Disaster Prevention Research Institute, Kyoto University*, 51B, 633–652. XXIII, 19, 206, 244, 245
- Zhang, H., H. Nakagawa, K. Kawaike, and Y. Baba (2009), Experiment and simulation of turbulent flow in local scour around a spur dyke, *International Journal of Sediment Research*, 24(1), 33–45. XXIII, 19, 206, 235, 239, 244

Part V

Appendices

1D St-Venant Equations and conveyance modelling

The 1D expression of the St-Venant Equations is obtained by integrating the 2D-H St-Venant equations in the spanwise direction. In this appendix, a new formulation of the 1D-shallow water equation is presented for flow in compound channels. In this new formulation, no hazardous simplifications have been done; the dispersive terms, previously identified, are retained and an expression linking the momentum coefficient with the flow parameters is proposed. In the sequel, the modelling of the parameters coming from the simplification of the 2D-H equations are presented: the dispersion on the spanwise direction and the lateral momentum transfers between subsections. Finally, using the 1D formulation of the St-Venant equations, the various one-dimensional modellings of the conveyance in the total cross-section or in a subsection of a compound channel are described; hypotheses of each modelling are discussed.

The purpose of this appendix is to show that although 1D equation is well appropriate for calculating the conveyance in a compound channel, this equation is too integrated for enabling the consistent description of 2D phenomena in a compound channel flow.

In an engineering point of view, 1D equation is used for large-scale numerical model (typically at the scale of the watershed) and must be as accurate as possible. This accuracy required that physical phenomena must be first well identified, described and theorised in 2D or in 3D modelling for then being simplified into 1D modelling in order to be integrated in the 1D equation.

A.1 One-dimensional equations

The 1D Saint-Venant equations were first deduced by mathematical demonstration by [Barré de Saint-Venant](#) [1871a,b]. In this section, the 1D-shallow water equations are deduced from the 2D-H shallow water equations by integrating the latter on the transversal direction (y-wise direction).

In the following paragraphs, the continuity equations and the momentum equations are distinctly developed in a total cross-section and in a subsection of a flume. It is assumed that:

- $S_{o,x} = CST$ and $S_{o,y} = 0$

And the following notations are used:

- $\chi_{xx} = \int_{Z_b}^{Z_{ws}} (\bar{u} - U_d)^2 dz$ and $\chi_{xy} = \int_{Z_b}^{Z_{ws}} (\bar{u} - U_d) (\bar{v} - V_d) dz$
- $\langle hU_d \rangle_{y,i} = Q_i$ and $\langle U_d \rangle_{y,i} = U_i$
- $\langle h \rangle_{y,i} = A_i$ and $\langle h \rangle_{y,i} / B_i = H_i$

- $\langle \tau_{b,x} \rangle_{y,i} = T_{b,i} = \rho g A_i S_{f,x,i}$
- The lateral unit discharge $(hV_d)_y = q_y$

A.1.1 Equations in a subsection

Let consider a cross-section of section A_t perpendicular to the main flow direction; this section is cut in several sub-sections of section A_i . The general equations of the mass conservation and momentum in a characterless sub-section bounded by $[y_0(x, t) \ y_1(x, t)]$ are written as following:

A.1.1.1 Mass conservation in subsection i

$$\begin{aligned} & \frac{\partial \langle h \rangle_y}{\partial t} + \frac{\partial \langle hU_d \rangle_y}{\partial x} + (hV_d)_{y_1} - (hV_d)_{y_0} \\ & + h(x, y_0, t) \frac{\partial y_0(x, t)}{\partial t} + (hU_d)_{y_0} \frac{\partial y_0(x, t)}{\partial x} - h(x, y_1, t) \frac{\partial y_1(x, t)}{\partial t} - (hU_d)_{y_1} \frac{\partial y_1(x, t)}{\partial x} = 0 \end{aligned} \quad (\text{A.1})$$

Using notations presented in the beginning of this section, Equation A.1 can also be written:

$$\begin{aligned} & \frac{\partial A_i}{\partial t} + \frac{\partial Q_i}{\partial x} + q_{y_1} - q_{y_0} \\ & + h(x, y_0, t) \frac{\partial y_0(x, t)}{\partial t} + (hU_d)_{y_0} \frac{\partial y_0(x, t)}{\partial x} - h(x, y_1, t) \frac{\partial y_1(x, t)}{\partial t} - (hU_d)_{y_1} \frac{\partial y_1(x, t)}{\partial x} = 0 \end{aligned} \quad (\text{A.2})$$

Notice that hypotheses are needed to solve / to simplify the second line of Equation A.2. Most of the time, the integration bounds are chosen constant in time and space.

A.1.1.2 Momentum in subsection i

$$\begin{aligned} & \frac{\partial \langle hU_d \rangle_y}{\partial t} + \frac{\partial}{\partial x} \langle hU_d^2 + 0.5gh^2 \rangle_y + (hV_dU_d)_{y_1} - (hV_dU_d)_{y_0} = \\ & + gA_iS_{o,x} - \frac{\langle \tau_{b,x} \rangle_y}{\rho} + \frac{1}{\rho} \frac{\partial \langle hT_{xx} \rangle_y}{\partial x} + \frac{1}{\rho} (hT_{xy})_{y_1} - \frac{1}{\rho} (hT_{xy})_{y_0} \\ & - \frac{\partial}{\partial x} \langle \chi_{xx} \rangle_y - (\chi_{xy})_{y_1} + (\chi_{xy})_{y_0} \\ & - \left[(hU_d^2)_{y_0} + (0.5h^2)_{y_0} + (\chi_{xx})_{y_0} - \frac{(hT_{xx})_{y_0}}{\rho} \right] \frac{\partial y_0(x, t)}{\partial x} - (hU_d)_{y_0} \frac{\partial y_0(x, t)}{\partial t} \\ & + \left[(hU_d^2)_{y_1} + (0.5h^2)_{y_1} + (\chi_{xx})_{y_1} - \frac{(hT_{xx})_{y_1}}{\rho} \right] \frac{\partial y_1(x, t)}{\partial x} + (hU_d)_{y_1} \frac{\partial y_1(x, t)}{\partial t} \end{aligned} \quad (\text{A.3})$$

Like for the integration on the vertical of the 3D-mean motion, the transversal integration of the 2D-water shallow equations leads to the emergence of dispersion terms: lateral dispersion term. In order to avoid the use of any kind of momentum or Coriolis coefficient, the identities $U_d = U_i + (U_d - U_i)$ and $h = H_i + (h - H_i)$ are injected in Equation A.3. Using those identities

and the notations presented in the beginning of this section, Equation A.3 is then written:

$$\begin{aligned}
& \frac{\partial Q_i}{\partial t} + \frac{\partial A_i U_i^2}{\partial x} + 0.5gH_i^2 \frac{\partial y_1 - y_0}{\partial x} + gA_i \frac{\partial H_i}{\partial x} + q_{y_1}(U_d)_{y_1} - q_{y_0}(U_d)_{y_0} = \\
& + gA_i(S_{o,x} - S_{f,x,i}) + \frac{1}{\rho} \frac{\partial \langle hT_{xx} \rangle_y}{\partial x} + \frac{1}{\rho} (hT_{xy})_{y_1} - \frac{1}{\rho} (hT_{xy})_{y_0} \\
& - \frac{\partial}{\partial x} \left\langle h(U_d - U_i)^2 + 0.5g(h - H_i)^2 + \chi_{xx} \right\rangle_y - (\chi_{xy})_{y_1} + (\chi_{xy})_{y_0} \\
& - \left[(hU_d^2)_{y_0} + (0.5h^2)_{y_0} + (\chi_{xx})_{y_0} - \frac{(hT_{xx})_{y_0}}{\rho} \right] \frac{\partial y_0(x, t)}{\partial x} - (hU_d)_{y_0} \frac{\partial y_0(x, t)}{\partial t} \\
& + \left[(hU_d^2)_{y_1} + (0.5h^2)_{y_1} + (\chi_{xx})_{y_1} - \frac{(hT_{xx})_{y_1}}{\rho} \right] \frac{\partial y_1(x, t)}{\partial x} + (hU_d)_{y_1} \frac{\partial y_1(x, t)}{\partial t}
\end{aligned} \tag{A.4}$$

In Equation A.4, the third line corresponds to all the dispersion terms that the double-integration of the mean-motion equation has created. The fourth and the fifth lines models the behaviour of integration boundaries; this is similar to the mass conservation. Hypotheses on y_0 and y_1 are needed to solve the momentum equation. The modellings previously presented like the friction or the turbulence have to be used in order to solve the 1D-momentum equations.

In addition to the dispersion dispersion terms, the lateral integration of the 2D-shallow water equations in a subsections leads to emergence of new terms:

- The momentum transfers due to turbulent interactions between subsections; represented by $\frac{1}{\rho} (hT_{xy})_{y_i}$
- The momentum transfers due to mass exchanges toward the interface; represented by $q_{y_i}(U_d)_{y_i}$

NB – On the solid lateral bank, $(hT_{xy})_{bank}$ does not appear in equation. This term is included in the measurement of the boundary shear stress, since the latter is also measured on the bank.

A.1.2 Equations in the total cross-section

On the total cross-section, the 1D-shallow water equations defined in a subsection can be simplified. The total cross-section is delimited by a solid boundary, *i.e.* the velocities on the boundary are null and in the viscous sub-layer of the horizontal boundary layer developing on the lateral bank, T_{xy} has to be equal to zero [Schlichting and Gersten, 2000]. Moreover, those boundaries are considered as not erodible, *i.e.* y_1 and y_0 only depends on space. The equations in the total cross-section are then:

A.1.2.1 Mass conservation:

$$\frac{\partial A_t}{\partial t} + \frac{\partial Q_t}{\partial x} = 0 \tag{A.5}$$

A.1.2.2 Momentum

$$\begin{aligned}
\frac{\partial Q_t}{\partial t} + \frac{\partial A_t U_t^2}{\partial x} + 0.5gH_t^2 \frac{\partial y_1 - y_0}{\partial x} + gA_t \frac{\partial H_t}{\partial x} = & +gA_t(S_{o,x} - S_{f,x}) + \frac{1}{\rho} \frac{\partial \langle hT_{xx} \rangle_y}{\partial x} \\
- \frac{\partial}{\partial x} \langle h(U_d - U_t)^2 + 0.5g(h - H_t)^2 + \chi_{xx} \rangle_y & \\
- \left[(0.5h^2)_{y_0} - \frac{(hT_{xx})_{y_0}}{\rho} \right] \frac{\partial y_0(x)}{\partial x} + \left[(0.5h^2)_{y_1} - \frac{(hT_{xx})_{y_1}}{\rho} \right] \frac{\partial y_1(x)}{\partial x} &
\end{aligned} \tag{A.6}$$

NB – On the total cross-section, the momentum transfers terms cancel each other. The only remaining effects are the frictions on the solid boundaries (wall and bottom) and the gravity force.

A.1.3 The momentum coefficient

In the momentum equation in a subsection or in the total cross-section (Equation A.4 and A.6), the deviation of the depth-averaged velocity or of the vertical dispersion in comparison with the velocity in the subsection (resp. in the total cross-section) is explicitly expressed with the parameter of the flow. Like for the 2D equations, it is interesting to link this result with the classical momentum coefficient for 1D-modelling which is often used in Engineering for expressing the uniformity of the transversal profile of the velocity. The momentum coefficient is easily expressed as a function of the dispersion terms:

$$\beta_i = 1 + \frac{\langle h(U_d - U_i) \rangle_y}{A_i U_i^2} + \frac{\langle hX X_{xx} \rangle_y}{A_i U_i^2} \tag{A.7}$$

NB – The momentum coefficient of a uniform flow, computed on the total cross-section in a compound channel, cannot be equal to the unity. The momentum coefficient tends to unity when the relative depth is increasing, *i.e.* when the velocity gradient at the interface between the main channel and the floodplain is decreasing. The value of the momentum coefficient in a subsection for a uniform flow depends on the width of the subsection; the wider the flume is and the less the velocity gradient has influence, therefore the momentum coefficient in a subsection tends to unity.

A.2 1D-modelling of flows: conveyance modellings

While the 2D-shallow water equations give information about the lateral distribution of the velocity in a cross-section, the 1D-shallow water equations give information about the conveyance of a channel. However, the use of equations developed in §A.1 can be costly as it requires the complete resolution of a set of partial derivative equations. Since the 19th century, many simplified sets of equations were therefore proposed for evaluating the conveyance of a channel, however, these equations are much more simplified than equations in §A.1. The phenomena are less precisely described and therefore these formulations use a “sink parameter” (the so-called resistance coefficient) in order to be solved.

A.2.1 The concept of resistance to flow

The coefficient of resistance is a mathematical artefact which takes into account various phenomena. The most common represented phenomena are:

- Bottom friction
- Drag force
- Free surface distortion
- Unsteadiness of flow

[Rouse \[1965\]](#) has been the first who defined the resistance to flow using the Π -Theorem. He demonstrated that the flow resistance is a function of several hydraulics parameters and it is represented by the so-called Darcy-Weisbach coefficient, *i.e.* $\lambda = F(Re, Fr, ks/R, \eta, \beta, \phi)$, where η characterizes the cross-section, β characterizes the non-uniformity of the flow and ϕ represents the unsteadiness of the free surface.

More recently, [Yen \[2002\]](#) proposed a new formulation of the flow resistance in composite geometry, *i.e.* $\lambda = F(Re, Fr, ks/R, \eta, \beta, \phi, ks_i/ks)$. The relative roughness of each channel has been taken into account in the term ks_i/ks . In order to reduce the sink character of this resistance coefficient, [Proust \[2005\]](#) showed the interest to consider homogeneous cross-sections (main channel or floodplain) and explicit modelling of mass exchanges [[Proust et al., 2009](#)]. As a consequence, in such flow configurations, the resistance coefficient reduces to $\lambda = F(Re, Fr, ks/R)$ and becomes more or less a friction coefficient, since the other effects are explicitly modelled.

Notice that [Morvan et al. \[2008\]](#) and several other authors have done an excellent review on the concept on resistance to flow.

A.2.1.1 1D-modelling of flow resistance

Using boundary shear stress measurements for one-dimensional flows, the friction modellings are roughly the same as those used in 2D-modellings. The depth averaged velocity is replaced by the velocity in a subsection U_i or in the total cross-section and the water depth by the hydraulic radius R . The boundary shear stress $T_{b,x,i}$ in a subsection i and the friction slope $S_{f,x,i}$ in a subsection i are thus written:

$$T_{b,x,i} = \frac{\lambda}{8} \rho U_i^2 \quad (\text{A.8})$$

$$S_{f,x,i} = \lambda \frac{U_i^2}{8gR_i} = \frac{T_{b,i}}{\rho g R_i} \quad (\text{A.9})$$

where λ is the Darcy-Weisbach coefficient in a sub- or in a total cross-section (see §2.6.1 for computing the Darcy-Weisbach coefficient). If λ is computed using the boundary shear stress, it can be considered as a friction coefficient taken into account the effects of the bottom and of the walls. On the other hand, if λ is worked out using the other hydraulic parameters, it can just be considered as a resistance coefficient.

The Darcy-Weisbach coefficient is linked to the other resistance coefficient by the following relationship:

$$\frac{\lambda_i}{8} = \frac{n_i^2 g}{R_i^{1/3}} = \frac{U_{*,i}^2}{U_i^2} \quad (\text{A.10})$$

NB – Once again, the validity of the Manning’s coefficient has to be discussed. The latter should only be used in rough conditions.

It should be noticed that the friction velocity, under uniform conditions, is generally computed as following:

$$U_{*,i} = \sqrt{gR_i S_{o,x}} \quad (\text{A.11})$$

Under non-uniform flow conditions, [Song and Chiew \[2001\]](#) states that the friction velocity can be written, for 1D-modelling, as a function of the momentum coefficient defined in a subsection or in a cross-section:

$$U_{*,i} = \sqrt{\rho g R_i \left[S_{o,x} - \frac{dH_i}{dx} \left(1 - \beta \frac{U_i^2}{gH_i} \right) \right]} \quad (\text{A.12})$$

A.2.2 The single channel method (SCM): Manning (1889)

A.2.2.1 Conveyance formula

One of the first formula was proposed by [Manning \[1889\]](#). The conveyance is computed on the total cross-section and is therefore a function of the shape, the slope and the “roughness” - the so-called Manning’s coefficient n - of the channel.

$$Q_t = A_t U_t = \frac{A_t R_t^{2/3}}{n_t} S_{o,x}^{1/2} \quad (\text{A.13})$$

The use of the Manning’s formula has to be limited to homogeneous situation, with uniform velocity distributions, as the Manning’s coefficient is considered as an homogeneous parameter on the whole cross-section. The use of a global Manning’s coefficient in heterogeneous situations leads to mis-estimations of the channel conveyances [[Bousmar, 2002](#)]. This assertion is especially true in compound geometries. When the flow has just overflowed in the floodplain the sudden increase in the width of the river (due to the overflow) implies a strong reduction in the hydraulic radius. Consequently the total conveyance is under-estimated if the Manning’s coefficient is taken as a constant in the whole total cross-section.

A.2.2.2 Resistance modelling

The Manning’s coefficient in such a modelling is a sink parameter. There are no real equivalence between the boundary shear stress and the Manning’s coefficient. The latter is a real resistance coefficient and takes into account many different phenomena.

A.2.3 The divided channel method (DCM): Lotter (1933)

A.2.3.1 Conveyance formula

To avoid the mis-estimation due to the use of a unique Manning’s coefficient in a compound geometry, [Lotter \[1933\]](#) has suggested to divide the channel total cross-section in subsections where the velocities are more homogeneous: the main channel and the floodplains. The conveyance in each channel is estimated using the Manning’s formula (Equation [A.13](#)) and the total

conveyance is then equal to the sum of the conveyance in each channel.

$$Q_t = \sum Q_i = \sum \frac{A_i R_i^{2/3}}{n_i} S_{o,x}^{1/2} \quad (\text{A.14})$$

where subscript i stands for subsection i .

The limits between subsections can be either vertical, diagonal or horizontal [Bousmar, 2002]. The most common separation remains the vertical one. It should be noticed that the formula of Lotter leads to the creation of a composite roughness coefficient:

$$n_t = A_t R_t^{2/3} / \sum \frac{A_i R_i^{2/3}}{n_i} \quad (\text{A.15})$$

where head losses between channel are supposed equal and the division limits perimeter are not taken into account in the computation of the hydraulic radius in a subsection. Yen [2002] cites other methods for computing composite roughness, all based on the scheme $n_t = \sum w_i n_i$, where w_i are weighted functions related to n_i and are linked to the geometry and the flow parameters in the subsection or in the total cross-section.

While the SCM under-estimates the conveyance because of the use of a global Manning's coefficient, Sellin [1964] showed that the DCM overestimates conveyance of compound channels at a given water depth, because of the forget of an important phenomenon at the division limits between channels. Macro-vortices are indeed developing between the floodplains and the main channel. These macro-vortices are due to the shear between fast and slow motions in the subsections. In this shear layer, a momentum transfer due to turbulence is operated from the main channel toward the floodplain. The velocity in the main channel is thus reduced and is increased in the floodplain [Bousmar, 2002; Chu et al., 1991; Proust, 2005]. Moreover, the shear layer is also a source of dissipation, consequently the energy transferred from the main channel toward the floodplain is partly dissipated by the micro-structures in the shear layer. As a result, the total conveyance capacity is reduced.

A.2.3.2 Resistance modelling

Once again, the Manning's coefficient here is a resistance coefficient and has not real physical meanings. Although the division into sub-section provides a kind of homogeneity of hydraulic parameters, the resistance coefficient in a sub-section still takes into account different phenomena, *i.e.* at least friction and mixing layer at the interface between the main channel and the floodplain.

A.2.4 The corrected DCM

In the previous methods, authors supposed that the conveyance in subsections only depends on a "friction coefficient" and on hydraulic parameters. They proposed many kind of roughness coefficients for predicting the good conveyance and the good repartition between subsections. However, they have not taken into account the effects of the mixing layer developing at the interface between channels.

A.2.4.1 Correction with the apparent shear stress

In the Seventies, the investigation of the boundary shear stress distribution in compound channel emphasized that the latter is not linear. The shear stress locally presents a maximum value on the floodplain near the interface with the main channel [Myers and Elsaywy, 1975]. This local

maximum is a consequence of the momentum transfer (shearing) at the interface between both subsections.

Thanks to a momentum balance analysis of each subsections (using a DCM approach) and on the basis of the boundary shear stress measurements, [Myers \[1978\]](#) defined an “apparent shear stress” acting on the vertical interface between the main channel and its contiguous floodplain. This apparent shear stress expresses the momentum transfer through the interface between main channel and floodplain. After [Bousmar \[2002\]](#), *for the lower relative depth (H_r), the apparent shear stress was found to be as great as 25 % of the main channel subsection weight component and as 200 % of the floodplain weight component. This clearly discards the DCM approach.*

The corrected DCM models the effect of the mixing layer on the velocity, *i.e.* increase in the velocity in the floodplain and the decrease in the latter in the main channel. The corrected discharges/velocities in an asymmetrical flume are written (under uniform conditions):

$$Q_{mc} = A_{mc}U_{mc} = A_{mc} \frac{R_{mc}^{2/3}}{n_i} S_{o,x}^{1/2} \sqrt{1 - \left(\frac{\tau_a P_a}{\rho g A_{mc} S_{o,x}} \right)} \quad (\text{A.16})$$

$$Q_{fp} = A_{fp}U_{fp} = A_{fp} \frac{R_{fp}^{2/3}}{n_i} S_{o,x}^{1/2} \sqrt{1 + \left(\frac{\tau_a P_a}{\rho g A_{fp} S_{o,x}} \right)} \quad (\text{A.17})$$

where P_a is the wetted perimeter of the interface, *i.e.* the water depth just above the bank-full at the interface. τ_a is the apparent shear stress at the interface. The apparent shear stress generally follows the form: $\tau_a = K(\Delta U)^2$. You can find in the article of [Martin-Vide and Moreta \[2008\]](#) the different forms of the apparent shear stress.

NB – Like for the classical DCM, the wetted perimeters used in the corrected DCM do not take into account the perimeter of the interface.

A.2.4.2 Debord method: Nicollet and Uan (1979)

The Debord Method is a corrected Divided Channel Method using an apparent shear stress formula to take into account dissipation phenomena at the interface, depending on the relative depth H_r [[Nicollet and Uan, 1979](#)]; this formula describes the decrease in conveyance in the main channel and the growth of it in the floodplain. Considering that $R_r = R_{fp}/R_{mc}$ (R_i : the “wetted” hydraulic radius in a subsection without counting the division limits perimeter), flow discharge in a subsection can be written as following:

$$\begin{aligned} Q_{mc} &= \phi K_{mc} R_{mc}^{2/3} A_{mc} S_{o,x}^{1/2} \\ Q_{fp} &= K_{fp} R_{fp}^{2/3} S_{o,x}^{1/2} \sqrt{A_{fp}^2 + A_{mc} A_{fp} (1 - \phi^2)} \end{aligned}$$

where

$$\begin{aligned} \text{if } R_r \geq 0.3 \quad \phi &= 0.9 (n_{mc}/n_{fp})^{1/6} \equiv \phi_0 \\ \text{if } R_r < 0.3 \quad \phi &= 0.5 \left[(1 - \phi_0) \cos \left(\frac{R_r \pi}{0.3} \right) + 1 + \phi_0 \right] \end{aligned} \quad (\text{A.18})$$

A.2.4.3 The Ackers's Method: Ackers (1993)

Using the data the SERC Flood Channel Facility of H.R. Wallingford [Ackers \[1993\]](#) proposed a modified DCM which uses empirical considerations for correcting the calculations of the conveyance.

He first defined the COH factor (Coherence factor), which is the ratio of the conveyance calculated a single cross-section to that calculated by summing the conveyances of the separate flow zones, *i.e.* $COH = Q_t(SCM)/Q_t(DCM)$. Then he defined the DISADF coefficient which is the ratio of the measured total discharge to that calculated using the DCM method, *i.e.* $DISADF = Q_t(measured)/Q_t(DCM)$. The plot of the relative depth relative of the COH and the $DISADF$ factors is given in Figure A.1.

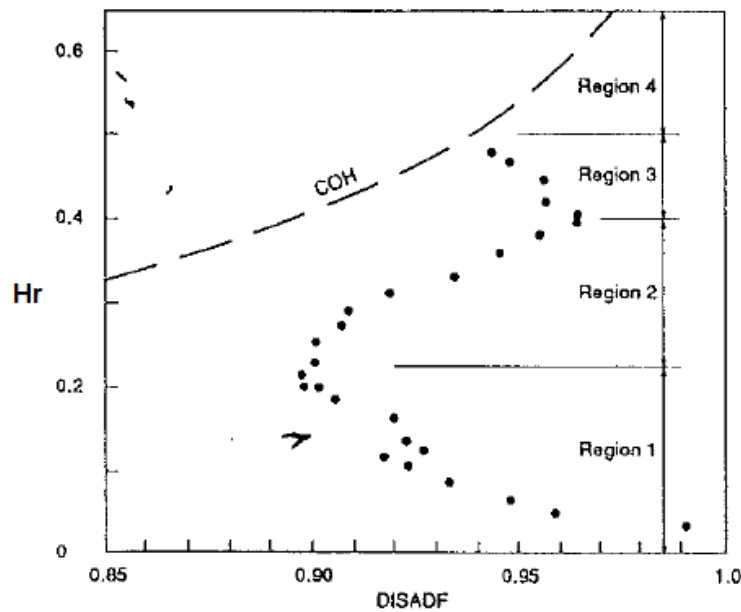


Figure A.1 – Discharge adjustment factor and coherence factor versus relative flow depth, SERC FCF series 02 [\[Ackers, 1993\]](#)

The comparisons of the $DISADF$ and the COH versus the relative depth in Figure A.1 show different region of interest for overbank flows with smooth conditions and a ratio $B/B_{mc} = 4.2$. In the region 1, the flow is relatively shallow and the loss of conveyance ($DISADF$) due to the mixing layer reaches 10 % at $H_r = 0.2$. The COH is quite low, *i.e.* the flow is far from a single channel flow configuration. In the region 2, the $DISADF$ coefficient increases until $H_r = 0.4$, the mixing effects are weaker. As a result, the loss in conveyance is reduced. In the region 3, the Loss in conveyance increases again, this may be due to the boils that appear at high relative depth or is maybe due to changes in the secondary current behaviors. In the last region (region 4) the COH factor is close to 1, *i.e.* the flows can be approximated as single channel flows.

Using such a graphic (COH , $DISADF$), [Ackers \[1993\]](#) studied the impacts of different changes in the hydraulic parameters (width of the floodplain, roughness, ...) and proposed depending on the considered hydraulic parameters and on the region defined by the $DISADF$, different empirical laws in order to correct the flow computation using a DCM model. He especially defined the discharge deficit $Q_{*2} = (Q_t(measured) - Q_t(DCM)) / ((U_{mc} - U_{fp}) H_{mc} H_{fp})$ in each region of the $DISADF$ vs H_r graphics which is a correction coefficient. Using these empirical laws, he evaluated the errors using his method on all the flow of the SERC FCF and found a maximum average discrepancy between prediction and experiments of 0.721 %.

NB – The three previous methods for computing the conveyance assume that the flow is taken under uniform conditions (the steadiness is implicit). The momentum transfers due to mass exchanges are neglected.

A.2.4.4 Resistance modelling

The Manning's coefficient is often computed using a DCM formulation. The apparent shear stress is therefore the complement value that is injected in the momentum balance in order to get the good discharge distribution. In such operating conditions, the Manning is a resistance coefficient. As a consequence, the uncertain physics that the resistance coefficient models, propagates to the apparent shear stress as well. The apparent shear stress is not equal to the shear at the interface between channels. It is a sink parameter that models the interfacial shear and the error that the resistance coefficient has created.

If correct boundary shear stress measurements are used to worked out a “friction coefficient”, under uniform conditions, the apparent shear stress should be equal to the real interfacial shear.

A.2.5 The Exchange Discharge Model (EDM): Bousmar and Zech (1999)

This model is implemented in the code “AxeRiv” and solves the Bernoulli equation on the whole cross-section. The Exchange Discharge Model developed by *Bousmar and Zech [1999]*, is the first model which models the momentum transfer due to turbulence and the momentum transfers due to mass exchanges, *i.e.* this modelling solves the non-uniform flows. It calculates additional head losses due to the momentum effect in the subsections and in the total cross-section. The complete set of equations is exposed in the PhD-thesis of *Bousmar [2002]*.

NB – The EDM, as well as the SCM or the DCM, assume the equality of subsection head loss gradients, which is a restrictive hypothesis [*Proust et al., 2010*].

The Bernoulli equations can be deduced from a simplified form of the 1D-shallow water equations; in Equation A.4, using the following simplifications:

- Steady flow
- $\frac{\partial h T_{xx}}{\partial x} \ll \frac{\partial h T_{xy}}{\partial y}$
- The dispersive effects are neglected: the third line of Equation A.4 is equal to zero, *i.e.* $\beta_i = 1$
- $y_0 = \pm y_0(x)$ corresponds to the floodplain banks
- $y_1 = \pm y_{int}$ corresponds to the interfacial limit between the main channel and the floodplain
- $q_{y_i} = q_{in} - q_{out}$
- $\pm q_{y_{int}}(U_d)_{int} = -q_{in}U_j + q_{out}U_i$

the new equations in a subsection are then:

$$\frac{dQ_i}{dx} - q_{in} + q_{out} = 0 \quad (\text{A.19})$$

$$\frac{dA_i U_i^2}{dx} - q_{in}U_j + q_{out}U_i + gA_i \frac{dH_i}{dx} - gA_i(S_{o,x} - S_{f,x,i}) \pm \frac{1}{\rho}(hT_{xy})_{int} = 0 \quad (\text{A.20})$$

where the subscript i designs the considered subsection and the subscript j , the contiguous subsection. The combination of those two equations leads then to the Bernoulli equation in a subsection:

$$S_{f,x,i} = -\frac{d}{dx} \left(Z_{ws} + \frac{U_i^2}{2g} \right) + \frac{q_{in}}{gA_i} (U_j - U_i) \pm \frac{(hT_{xy})_{int}}{\rho g A_i} \quad (\text{A.21})$$

Where the two last terms represent the head loss due to momentum transfers through the interface and are written Sa_i . The term $-\frac{d}{dx} \left(Z_{ws} + \frac{U_i^2}{2g} \right)$ is written $S_{H,x,i}$ and is the total head loss in a subsection i .

A.2.5.1 Modelling of the friction

The friction slope is solved using the DCM formula.

$$S_{f,x,i} = \left(\frac{n_i Q_i}{A_i R^{2/3}} \right)^2 \quad (\text{A.22})$$

A.2.5.2 Modelling of momentum transfers due to mass exchanges

The term $q_{in}(U_j - U_i)/gA_i$ in Equation A.21 represents the additional head loss that creates mass exchanges through the interface. It is modelled as following when a subsection gains water:

$$q_{in} = \psi^m \frac{dQ_i}{dx} = \psi^m \frac{d}{dx} \left(\frac{A_i R_i^{2/3} S_{f,x,i}^{1/2}}{n_i} \right) \quad (\text{A.23})$$

and $q_{in} = 0$ when the subsection is loosing water.

NB – ψ^m has to be calibrated. *Bousmar and Zech* [1999] calibrates ψ^m at 0.5.

A.2.5.3 Modelling of momentum transfers due to turbulence

The term $\pm(hT_{xy})_{int}/\rho g A_i$ in Equation A.21 represents the additional head loss that creates turbulent exchanges through the interface. It is modelled using the mixing length concept:

$$T_{xy,int} = \psi^t \rho (U_j - U_i)^2 \quad (\text{A.24})$$

where ψ^t is a mixing length to be calibrated. *Bousmar* [2002] recommends to set this parameter at 0.16, while *Proust et al.* [2009] rather set the parameter at 0.02; this parameter depends on the geometry of the flume.

A.2.5.4 Resolution of EDM

The complete resolution procedure of those equations can be found in *Bousmar* [2002]; *Bousmar and Zech* [1999]. The use of the EDM instead of the DCM enables the improvement of the total discharge previsions. Using the calibrated values of ψ^t for flows in straight compound channel the maximal errors on the total discharges estimation relative to the measurements reach 15 %, while for the DCM, this error can reach 50 % [*Bousmar*, 2002]. Using the calibrated ψ^t , ψ^m and the skewed flows of the FCF skewed-channel (max skewed-angle 9 degrees), *Bousmar and Zech* [1999] shows that the prevision are also in good agreement with measurement. However *Proust et al.* [2009] shows that for a skewed angle larger than 9 degrees, the results are not good. The errors come from three main sources [*Proust et al.*, 2009, 2010] :

- the backwater surface profile are computed using a dynamic equation on the overall cross-section area
- an equality is assumed between the subsections head losses and the total head losses
- uniform flow conditions are imposed as downstream boundary conditions

A.2.6 The Independent Subsection Method (ISM): Proust *et al.* (2009)

This model is still experimental and has been only tested for subcritical flows. It solves the momentum equations in a each subsection of a compound channel and links each subsection by a mass conservation relation [Proust *et al.*, 2009]. It enables to solve flow in prismatic channels and gradually varied flows in continuous geometry (diverging or converging floodplain, skewed floodplains, ...). It should be noticed that for the moment, only flows in rectangular subsections can be solved using this method.

NB – Unlike the previous methods, this method do not use the hypothesis of head loss equality between subsections [Proust *et al.*, 2010].

The ISM equations is based on the same equations as the EDM, *i.e.* Equation A.19 and Equation A.23. In a symmetrical compound channel, q_{in} and q_{out} take the following values depending on the position in the compound geometry:

$$\begin{aligned}
 &\text{In the left floodplain, } q_{out} = -\frac{dA_{fp,l}U_{fp,l}}{dx} \text{ and } q_{in} = 0 \\
 &\text{In the right floodplain, } q_{out} = -\frac{dA_{fp,r}U_{fp,r}}{dx} \text{ and } q_{in} = 0 \\
 &\text{In the main channel, } q_{out} = 0 \text{ and } q_{in} = \frac{dA_{mc}U_{mc}}{dx} = -\frac{dA_{fp,l}U_{fp,l}}{dx} - \frac{dA_{fp,r}U_{fp,r}}{dx}
 \end{aligned} \tag{A.25}$$

Resulting on the previous notation, the mass conservation in the total cross-section is written:

$$\frac{dA_{mc}U_{mc}}{dx} + \frac{dA_{fp,l}U_{fp,l}}{dx} + \frac{dA_{fp,r}U_{fp,r}}{dx} = 0 \tag{A.26}$$

and isolating the flow depth in Equation A.23, leads to the ISM formulation in rectangular geometry (l = left floodplain, r = right floodplain, mc = main channel):

$$\begin{aligned}
 (1 + Fr_l^2) \frac{dH_l}{dx} &= S_{o,x} - S_{f,x,l} + \frac{U_l^2}{gB_l} \frac{dB_l}{dx} + \frac{T_{xy,l}H_l}{\rho g A_l} - \frac{dA_l U_l}{dx} \frac{2U_l - U_{int,l}}{g A_l} \\
 (1 + Fr_r^2) \frac{dH_r}{dx} &= S_{o,x} - S_{f,x,r} + \frac{U_r^2}{gB_r} \frac{dB_r}{dx} + \frac{T_{xy,r}H_r}{\rho g A_r} - \frac{dA_r U_r}{dx} \frac{2U_r - U_{int,r}}{g A_r} \\
 (1 + Fr_{mc}^2) \frac{dH_{mc}}{dx} &= S_{o,x} - S_{f,x,mc} + \frac{U_{mc}^2}{gB_{mc}} \frac{dB_{mc}}{dx} - \frac{T_{xy,l}H_l}{\rho g A_l} - \frac{T_{xy,r}H_r}{\rho g A_r} - \frac{dA_l U_l}{dx} \frac{2U_l - U_{int,l}}{g A_l} \\
 &+ \frac{dA_l U_l}{dx} \frac{2U_l - U_{int,l}}{g A_l} + \frac{dA_r U_r}{dx} \frac{2U_r - U_{int,r}}{g A_r}
 \end{aligned} \tag{A.27}$$

The six main unknowns of the ISM are the three depths H_i and the three velocity U_i . The six secondary unknowns are the two shear stresses $T_{xy,i}$, the two interfacial velocities $U_{int,i}$ and the two lateral discharges $-dA_l U_l/dx$ and $-dA_r U_r/dx$. With Equations A.27 and A.25, six closures relations are needed. It is assumed that $Z_{mc} = Z_l = Z_r$, *i.e.* $H_l = H_r = H_{mc} - H_{bf}$

and $dH_l/dx = dH_r/dx = dH_{mc}/dx$. After [Proust et al. \[2006\]](#), this hypothesis is true when the free surface is not distorted; in a sudden contraction for instance this hypothesis leads to an under-estimation of - 9 % of the floodplain velocity in the control cross-section. The four other closures are allighted in the following sub-subsections.

A.2.6.1 Modelling of the friction

The friction slope (S_f) are modelled using the Darcy-Weisbach coefficient. The latter has been estimated by isolating each channel with a plate and by using various experimental discharges. The formulation of S_f is classical (Equation [A.28](#)):

$$S_{f,x,i} = \frac{\lambda_i U_i^2}{8gR_i} \quad (\text{A.28})$$

A.2.6.2 Modelling of momentum transfers due to mass exchanges

The momentum transfers due to mass exchanges are explicit in Equation [A.27](#) (terms with U_{int} inside). The term to be modelled is the depth-averaged velocity at the interface U_{int} . [Proust et al. \[2009\]](#) has found that the velocity at the interface strongly depends on the direction of the mass exchanges.

- When the channel is prismatic and mass exchanges occur from the subsection i towards the subsection j: $U_{int} = U_i$
- When the compound geometry is non-prismatic and the overall width of the channel is a constant: $U_{int} = U_i$ if $dB_i/dx < 0$ and $U_{int} = U_j$ if $dB_i/dx > 0$
- When the compound geometry is non-prismatic and the overall channel width is variable: $U_{int,l} = \phi_l U_l + (1 - \phi_l) U_{mc}$ and $U_{int,r} = \phi_r U_r + (1 - \phi_r) U_{mc}$, where ϕ_i is a weighting coefficient depending on the geometry.

A.2.6.3 Modelling of momentum transfers due to turbulence

Like for the EDM, the turbulent shear stress term $\pm T_{xy,i} H_i / \rho g A_i$ in Equation [A.27](#) is modelled using the mixing length concept:

$$T_{xy,int} = \psi^t \rho (U_j - U_i)^2 \quad (\text{A.29})$$

where ψ^t is a mixing length to be calibrated. [Proust et al. \[2009\]](#) set this parameter at 0.02; this parameter obviously depends on the geometry of the flume.

A.2.6.4 Resolution of ISM

The mass conservation and the three momentum equations are first expressed in matrix form [[Proust, 2005](#)] and the quadruplet $(dH_l/dx; dU_l/dx; dU_r/dx; dU_{mc}/dx)$ is found using an explicit method.

$$\underline{\underline{A}}(\underline{Y}) \cdot \frac{d\underline{Y}}{dx} = \underline{\underline{B}}(\underline{Y}) \quad \text{with} \quad \underline{Y} = \begin{pmatrix} H_l \\ U_l \\ U_r \\ U_{mc} \end{pmatrix} \quad (\text{A.30})$$

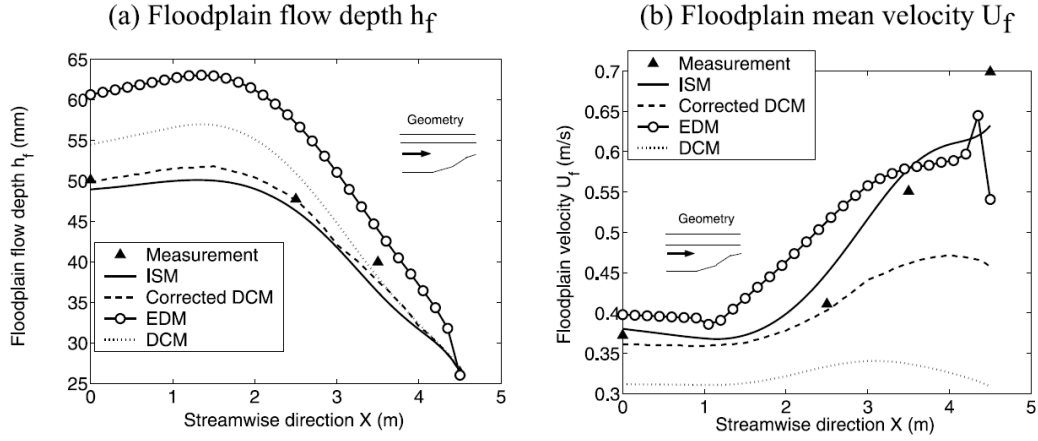


Figure A.2 – Comparisons of 1D-models in a compound channel with an abrupt floodplain contraction [Proust et al., 2009]

where coefficient \underline{A} is a matrix and \underline{B} is a vector and they are non-linear functions of H_l , U_l , U_r , U_{mc} , of geometrical parameters and subsections Darcy-Weisbach resistance coefficients.

For subcritical flows, the solving of Equation A.30 is iterative. The measured upstream discharge distribution and a try of upstream water level is given. A corresponding downstream water level is computed. While the downstream value of the depth is not equal to the appropriate value, the upstream value is adjusted, keeping the upstream discharge distribution constant. This method needs more efficient numerical developments, however the first results are really good compared to all the other methods (Figure A.2).

A.3 Conclusion

Without the usual simplifications proposed in the literature [Ancey, 2009; Chow, 1959; French, 1985], the 1D Saint-Venant equation is quite a complicated equation. Compound channel scientists rather prefer to work with conveyance modelling that are an appropriate and an alternative model for modelling overbank flows. Nevertheless, these modelling become time to time ever better, but complicated and they now require very good modelling of the physical phenomena that occur in flows. 2D or 3D descriptions of flow phenomena are now paramount for then improving 1D modelling.

Experiments at the open-laboratory of Ujigawa

Flows and bed-load dynamics around spur dyke in a compound channel

Y. Baba¹, B. Camenen², Y. Peltier², F. Thollet², H. Zhang¹ and H. Nakagawa¹

1. Disaster Prevention Research Institute, Kyoto University, Yoko-Oji, Fushimi, Kyoto, 612-8235, Japan

2. Cemagref, UR HHLY, 3 bis quai Chauveau, CP 220, 69336 Lyon cedex 09, France

Abstract:

Spur dykes are typical man-made hydraulic structures and widely used in alluvial rivers for a variety of purposes like the bank protection, the maintenance of navigation channel and so on. Spur dykes give some impacts on the flow and bed-load dynamics around itself and cause the variation of flow patten and bottom profile according to the relationship between the flow characteristics and bed configurations. In the case of a compound channel with a spur dyke on the floodplain, the effect of the spur dyke on the flow and bed configuration makes the flow characteristics complicated. In order to investigate the flow characteristics around the spur dyke, some experimental studies have been carried out using the LSPIV technique and an electromagnetic velocimeter. The velocity distributions around spur dykes are discussed in combination with the type of the spur dykes and the relative depth H_r (the ratio of the water depth in the floodplain and main channel). The longitudinal length of the recirculation area is discussed as well. The difference of the flow pattern around the foot of the spur dyke between impermeable and permeable cases also illustrated based on the experimental results, and it is found that the permeable spur dyke appears to be a much more interesting alternative to the impermeable spur dyke in term of morphodynamics around the spur dyke.

B.1 Introduction

Spur dykes are typical man-made hydraulic structures and widely used in alluvial rivers to expect some positive effects for disaster reduction and river restoration. Spur dykes are classified in two types according to its structure, impermeable and permeable types. The existence of the spur dykes brings significant changes of flow patterns and bed configurations around the spur dykes [Zhang *et al.*, 2009]. The change of the flow pattern initiates and controls the bottom profile variation, and the flow pattern adjusts itself according to the bed configurations. The interaction of these processes (flow and bottom profile) develops the river morphology and leads

to an equilibrium stage of flow and bed configurations under certain conditions. Local scour is well-known to be generated around the spur dykes, and it is the result of the combined processes with flow and movable boundaries. It is also well known that an excessive scouring sometimes occurs and causes enormous damage.

This study discusses compound channel flows occurring in a vicinity of a non-submerged spur dyke set on the floodplain. In the case of a compound channel, the interaction between the flow and the bottom profile would be more complicated because the influence of the spur dykes causes the enhancement of the momentum transfer and the mass exchange between the floodplain and the main channel [Peltier *et al.*, 2008]. This means that quantitative information of flow pattern around the spur dykes is strongly required in order to investigate the interaction between the flow characteristics and bed configurations. In this paper, some experimental results on the velocity distributions around the spur dykes are shown, and the effects of the spur dykes (impermeable and permeable) on the flow characteristics is discussed. Additionally some likely impacts of the flow characteristics on the bed configurations, especially bed-load transportation, are also discussed based on the experimental results.

B.2 Presentation of the experiment and measurements

B.2.1 Flume characteristics and experimental set-up

An experimental study was set up in a 20m long straight compound channel (Ujigawa Open laboratory, DPRI, Kyoto University, Japan). The slope was set to $S_{o,x} = 0.8/1000$. The total width (B) of the channel is 1 m with a main channel width (B_{mc}) of 0.35 m (see B.1). A single floodplain was set on the right part of the channel with a step (H_{bf}) of 5.1 cm. Two types of spur dyke set on the floodplain were explored, one is impermeable and the other is permeable (set of piers inducing a permeability of 50 %). The effects on the flow of the length of the spur dyke (d) were studied as well as the ratio $H_r = H_{fp}/H_{mc}$ (where H_{fp} and H_{mc} are the water depth in the floodplain and in the main channel, respectively). The water discharge was set upstream thanks to a gate valve. A honeycomb was used to filter the fluctuations in the infilling tank and constrain the flow. A 1 m long ramp was set at the upstream part of the floodplain; the equilibrium between the main channel and floodplain flows was expected to be obtained after 5 m approximately (see section 2.3). The spur dyke was positioned at $x = 8.5$ m in order to modify a flow assumed in equilibrium. The downstream boundary condition (water depth) was fixed thanks to a tailgate. The description of the compound channel characteristics is presented in Figure B.1 together with a schematic view of the flow around the spur dyke for a typical case with an impermeable spur dyke.

B.2.2 Velocity measurements using LSPIV technique

Velocity measurements were carried out using the Large Scale Particle Image Velocimetry technique [Hauet *et al.*, 2007] and an electromagnetic current meter (ECM). The LSPIV technique used in this study consists of four steps: First, a sequence of time-stamped digital images of the flow free-surface are evenly sampled with a fixed time interval between images. The camera was set on the structure of the laboratory, approximately four meters above the downstream part of the canal for the overall view of the canal. For detailed observations of the recirculation behind the spur dyke, the camera was set on a tripod on the side of the canal. Second, all the images are orthorectified, which consists of correcting perspective and lens distortion effects and of giving metric positions to transformed pixels. Third, the displacement of visible patterns in two successive orthorectified images is quantified using a simple cross-correlation algorithm [Fujita *et al.*, 1998]. Such visible patterns are assumed to be ideal tracers of the surface flow

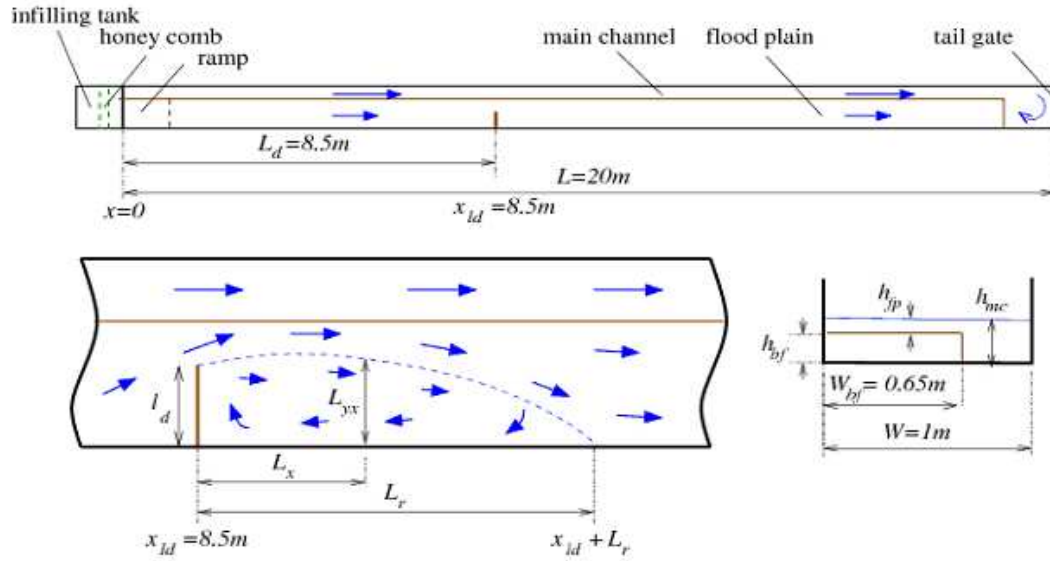


Figure B.1 – Compound channel characteristics and schematic view of the flow around the spur dyke (impermeable case).

velocity with minimal deformation between the two sampled images. For our specific case, artificial tracers (PVC powder, see Figure B.2.a) was injected to seed the flow. The displacements divided by the time step between images yield the surface velocities. The algorithms used for image orthorectification and cross-correlation velocity computation were developed by [Hauet et al. \[2007\]](#). Depth-averaged velocities at each node of canal was computed through (1) interpolation or extrapolation of the surrounding LSPIV surface velocities and (2) multiplication by a float coefficient accounting for the vertical velocity distribution [[Le Coz et al.](#)].

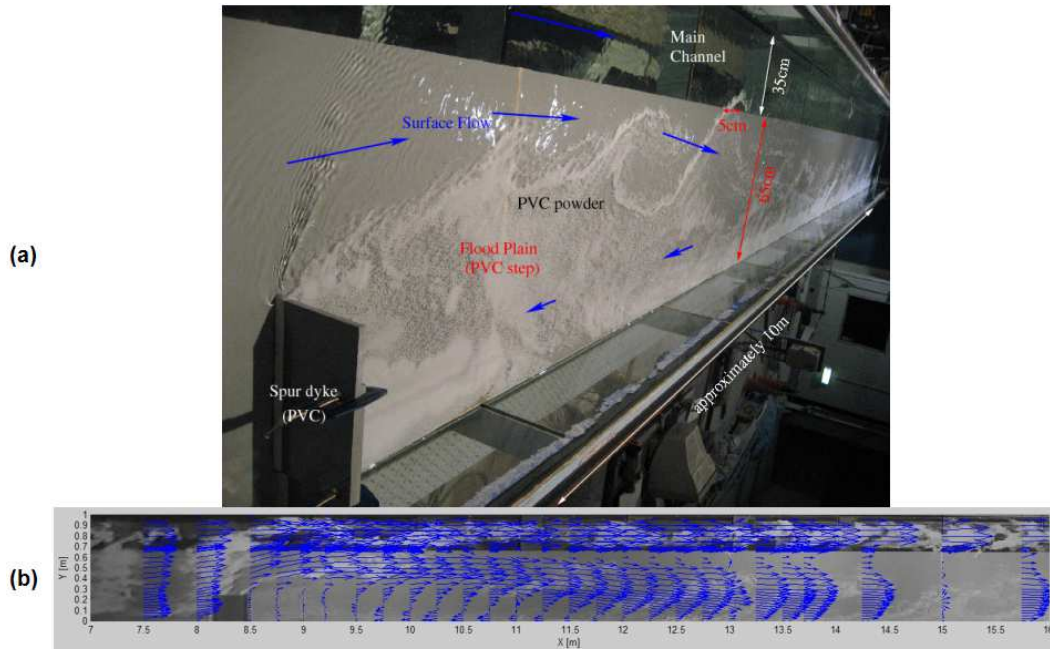


Figure B.2 – (a) Photograph of the experimental set-up. (b) Example of LSPIV results on a orthorectified image of the canal.

The LSPIV allows the determination of the flow field in the channel assuming a relationship between the surface velocity and the mean velocity. The calibration of the LSPIV (float coeffi-

cient) was performed using measurements of the flow carried out with an electromagnetic current meter on four cross-sections along the canal: at $x = x_{sd} = 8.5$ m (section where the spur dyke was fixed), $x = 9.2$ m (section where the width of the recirculation reached its maximum), at $x = x_{sd} + L_x + 1$ (section where the flow in the floodplain is getting back to its equilibrium state) and at $x = x_{sd} + (L_x + 1)/2$ (section in the middle of the recirculation). It appears clearly in Figure B.2.a that the LSPIV method yields good results for the flow description around the spur dike as well as for the description of the recirculation. However, it is performing correctly only if there are enough tracers. Indeed, close to the main channel after the maximum width of the recirculation, the flow is divergent, and very few tracers cover this zone. As a result, the LSPIV method underestimates the surface velocities in this zone. As indicated in Table B.1, the velocity in the main channel is from two to three times larger than the velocity in the floodplain. At the edge of the floodplain, there is a shear flow with the development of vortices. For a typical cross-section, the velocity should increase thus continuously from the middle of the floodplain to the middle of the main channel. Corrections of the results in this zone were undertaken using the results from the sections measured with the ECM.

B.2.3 Test cases carried out

The different cases studied in this paper are presented in Table B.1. Two different lengths of the spur dyke were tested representing one third or one half of the floodplain. Larger length for the spur dyke would induce an interaction between the recirculation and the main channel flow that is too complex to be studied. Three different regimes were studied for $H_r = 0.2, 0.3$, or 0.4 . Totally, 13 experiments were undertaken, 3 cases under flow conditions (no spur dyke), 5 with an impermeable spur dyke and 5 with a permeable spur dyke (using the same conditions as the impermeable cases). The permeability of the permeable spur dykes was of 50 %. For the specific water depth and mean velocities measured from the ECM, this table presents the results at the middle of the floodplain and of the main channel, respectively, for a section measured in the middle of the recirculation approximately, *i.e.* at $x = x_{sd} + (L_x + 1)/2$. For the uniform flow, the chosen section is the one at $x = 12.5$ m. For a permeable spur dyke, as no recirculation was observed, the same sections as the similar impermeable case were chosen for the measurements in order to be able to compare the results.

Test	d [m]	d/B_{fp} [-]	H_r [-]	Q_t [l/s]	H_{fp} [cm]	H_{mc} [cm]	U_{fp} [cm/s]	U_{mc} [cm/s]	L_x [m]
Uni02	×	×	0.2	9.51	1.32	6.36	10.8	42.4	×
Uni03	×	×	0.3	13.25	2.25	7.3	22.2	46.2	×
Uni04	×	×	0.4	20.85	3.57	8.64	33.3	48.9	×
Hr02d24i	0.24	0.37	0.2	9.51	1.04	6.07	3.1	44.2	2.1
Hr02d32i	0.32	0.49	0.2	9.51	0.9	6.06	0.3	44.8	2.4
Hr03d24i	0.24	0.37	0.3	13.25	1.9	7.01	18.4	49.5	4.25
Hr03d32i	0.32	0.49	0.3	13.25	1.62	6.85	9.3	52.4	5
Hr04d24i	0.24	0.37	0.4	20.85	2.79	7.87	30.9	62.6	5.2
Hr02d24p	0.24	0.37	0.2	9.51	1.15	6.26	8.7	40.9	×
Hr02d32p	0.32	0.49	0.2	9.51	1.13	6.2	7.6	42.4	×
Hr03d24p	0.24	0.37	0.3	13.25	2.08	7.22	22.4	43.7	×
Hr03d32p	0.32	0.49	0.3	13.25	2.07	7.17	17.4	47.7	×
Hr04d24p	0.24	0.37	0.4	20.85	3.3	8.47	33.4	49.8	×

Table B.1 – Description of the experiments carried out (H_{fp}, H_{mc} , $U_{d,fp}$, and $U_{d,mc}$ are the mean water depths and velocities measured in the middle of the floodplain, and main channel, respectively at a x-position corresponding to the middle of the recirculation approximately).

B.3 Results from the LSPIV

B.3.1 An estimation of the bed evolution

Using the velocity fields obtained from the LSPIV measurements, an estimation of the potential sediment transport is possible. Assuming bed-load transport proportional to the velocity $V_n = ||\underline{V}|| = \sqrt{U_d^2 + V_d^2}$ to the power 3 (that corresponds to the bed shear stress to the power 1.5 which is commonly used for the bed-load formulas, [Camenen and Larson \[2005\]](#)) with a critical velocity for the inception of transport $V_{n,cr}$, local sediment \underline{q}_s transport may be written as follows:

$$\underline{q}_s = \alpha_s (V_n - V_{n,cr})^3 \frac{V}{V_n} \quad (\text{B.1})$$

where V_n is the velocity magnitude, and α_s a coefficient to be calibrated.

An estimation of the scour and sedimentation locations was suggested using the mass conservation equation:

$$\frac{\partial z}{\partial t} = \frac{1}{1 - p_o} \left(\frac{\partial q_s}{\partial x} + \frac{\partial q_s}{\partial y} \right) \quad (\text{B.2})$$

where $p_o=0.4$ is the porosity of the fictional mobile bed. For our specific case, a simple finite difference scheme was used to obtain an estimation of the bed evolution. As this study remains qualitative, a dimensionless bed evolution z/B will be used hereafter.

Of course, a movable bed made of sediment would influence the flow itself because of a larger roughness height. Considering the impact of a rough bed on the flow homogeneous, it can be assumed that velocity fields obtained from these experiments can give a good approximation of the velocity gradient, and so on the bed evolution. This method allows a macro-scale observation based on mean velocities and does not include local effects such as those due to horse-shoe vortex in front of the structure or wake vortex behind permeable spur dyke [[Zhang et al., 2009](#)].

B.3.2 Results for an impermeable spur dyke

B.3.2.1 Recirculation length

For the impermeable spur dyke, first results confirm the relationship between the ratio L_x/d and the friction number S :

$$S = \frac{\lambda d}{8H_{fp}} \quad (\text{B.3})$$

where L_x is the length of the recirculation behind the spur dyke, d the length of the spur dyke, λ the Darcy-Weisbach friction coefficient with the exception of cases with small H_r and large d where the recirculation was interacting with the main channel flow. Depending on the S values, two asymptotic regimes are distinguished [[Peltier et al., 2008](#); [Rivière et al., 2004](#)]. When $S < 0.01$, the regime is called “non-frictional flow” (DWF), the flow is controlled by the groyne and the length of the recirculation zone L_x is merely proportional to d with $L_x \approx 20 \times d$. When $S > 0.1$, the regime is called “frictional flow” (SWF), the physics is controlled by bed frictions ($L_x \approx 5\lambda/f$). A general equation for the recirculation length writes:

$$\frac{L_x}{d} \approx \begin{cases} 20 & \text{if } S < 0.01 \\ 0.6S^{-1} & \text{if } S > 0.1 \end{cases} \quad (\text{B.4})$$

Figure [B.3](#) presents for different experiments the length of the recirculation behind the spur dyke made dimensionless with the length of the spur dyke L_x/d as a function of the friction

number S . The Darcy-Weisbach friction coefficient was estimated using hydraulic parameters measured in the floodplain for the equivalent uniform flow ($\lambda/8 = gH_{fp}S_{o,x}/U_{fp}^2$ where g is the acceleration of the gravity and $S_{o,x}$ the slope of the floodplain). It appears that the new data set is well described by the theory (Equation B.4) and is in good agreement with previous data from the CNR and LMFA [Peltier *et al.*, 2008]. Most of the present data appear to be in the SWF regime or in an intermediate regime. As observed by Rivière *et al.* [2008] for channel expansions, the recirculation length in the DWF regime appears to be a function of the Froude number and of the ratio B/d where B is the width of the flume. For the case of a compound channel, similar behaviour may be observed. The plateau for L_x/d seems to be not as high for some other experiments especially for $H_r=0.4$.

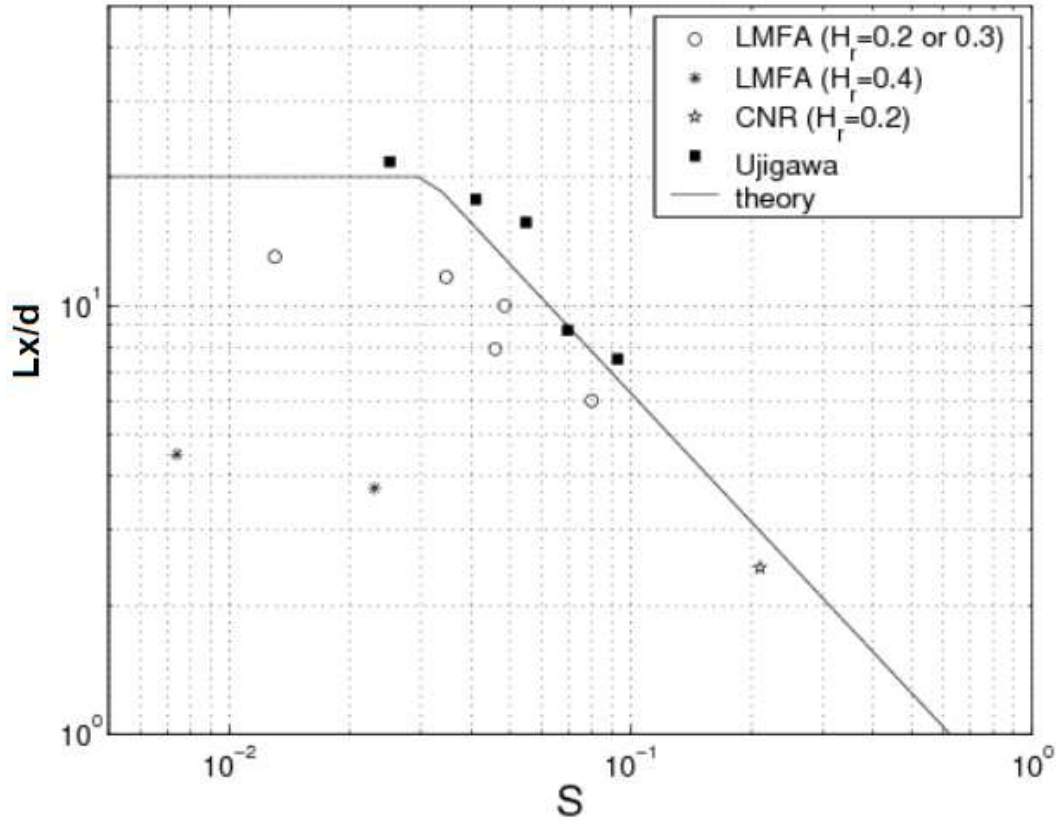


Figure B.3 – Length of the recirculation behind the spur dyke made dimensionless with the length of the spur dyke L_x/d as a function of the friction number S .

B.3.2.2 Main characteristics of the bed evolutions, effect of the critical velocity for the inception of transport

Figure B.4.a presents the results obtained for the velocity field for the test case with $d = 0.24$ m and $H_r = 0.2$ including the corrections of the divergent flow (see section 2.2). The recirculation zone is easily observable with a maximum width at the position $x = 9.2$ m. For this specific case, the velocities in the recirculation zone are very weak. A similar position of this maximum width was observed for all the cases indicating the strong influence of the main channel flow on this value. For a larger length of the spur dyke ($d = 0.40$ was also tested), the lateral expansion of the recirculation zone reached the main channel. A much more complex dynamic of the recirculation was then observed. For $x > 9.2$ m, the flow become divergent until the end of the recirculation zone ($x > x_{sd} + L_x$). The uniform flow (in term of depth-averaged velocities) is reached only after 5 or 6 meters downstream of the end of the recirculating zone.

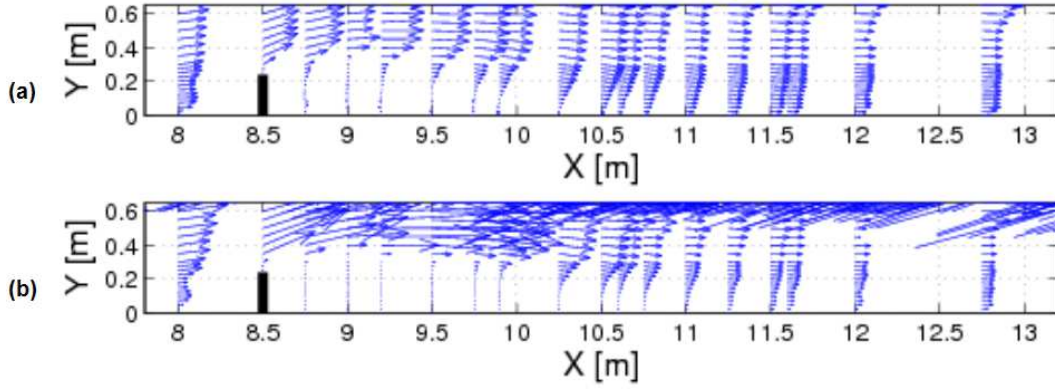


Figure B.4 – (a) Corrected velocity from LSPIV measurements. (b) dimensionless bed-load transport for the test case with $d = 0.24$ m and $H_r = 0.2$

From the velocity field, the estimation of a dimensionless bed-load transport can easily be obtained using Equation B.1. Assuming first that $V_{n,cr} = 0$, it appears that the effect of the recirculation zone on the bed-load transport field is emphasized compared to the velocity field (see Figure B.4.b). From the velocity distributions in Figure B.4, very large spatial variations of the bed-load transport in the floodplain are expected with nearly no transport in the recirculation zone. And the maximum bed-load estimated in the floodplain is generally much lower than the typical values observed in the main channel. For this reason, this study will be more focused on the floodplain.

In Figure B.5.a, the dimensionless bed evolution derived using Equation B.2 is plotted for the test case with $d = 0.24$ m and $H_r = 0.2$ using a critical velocity $V_{n,cr} = 0$ m/s. Significant erosions are estimated in two areas due to the flow acceleration; one is at the foot of the spur dyke and the other above the recirculation area with its maximum lateral expansion ($x = 9.2$ m). On the other hand, large deposition may be observed between two areas mentioned above and the downstream to the maximum width of the recirculation. Some deposition is also observed upstream of the spur dyke because of the decrease of the flow magnitude. Because of the very low dynamics within the recirculation area, nearly no variation of the bed is expected. However, if we consider suspended load and no bed-load transport, this area would be typically a deposition zone for very fine sediments. The shear flow induced by the interaction between the main channel and the floodplain yields also a much more active bed dynamics at this location, which is very sensitive to the modification of the flow induced by the spur dyke. The small erosion observed at the section $x = 11.5$ m seems to be a spurious effect of the LSPIV velocity correction or because of the imperfections of the joints between two PVC plates forming the floodplain (at the section $x = 11.0$ m).

In Figure B.5.b, the dimensionless bed evolution is plotted for the test case with $d = 0.24$ m and $H_r = 0.2$ using a critical velocity $V_{n,cr} = 0.1$ m/s. This critical value affects mainly the recirculation area where very low dynamics were observed. Because of this critical value, the area is now motionless. A value $V_{n,cr} = 0$ m/s will be fixed hereafter.

B.3.2.3 Effect of the size of the spur dyke

In Figure B.6, the dimensionless bed evolution was plotted for the case with a longer spur dyke ($d = 0.32$ m). The length of the spur dyke does not affect significantly the deposition/erosion distribution and amplitude. Compared to the case with a shorter spur dyke (see Figure B.5.a), Very similar results are obtained. Only the width of the main erosion and deposition zones is lower as the distance between the spur dyke foot and the main channel is shorter. As observed

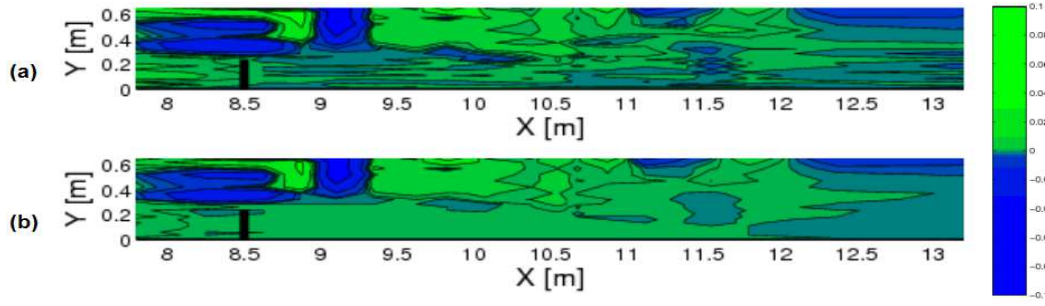


Figure B.5 – Dimensionless bed evolution for the test case with $d = 0.24$ m and $H_r = 0.2$ using a critical velocity $V_{n,cr} = 0$ m/s (a) or $V_{n,cr} = 0.1$ m/s (b).

before, the length of the spur dyke has also a minor effect on the length of the recirculation (see Table B.1).

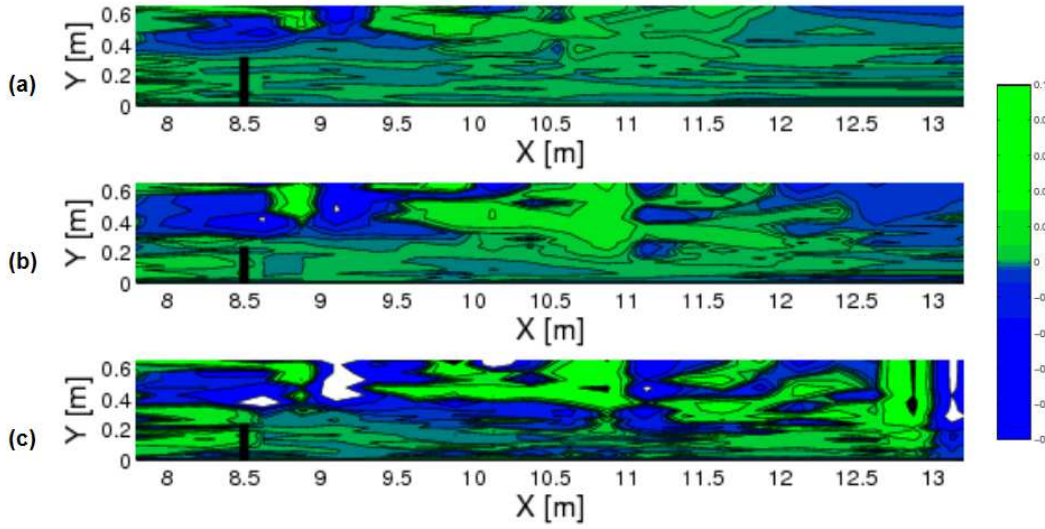


Figure B.6 – Dimensionless bed evolution for three test cases. (a) $d = 0.32$ m and $H_r = 0.2$, (b) $d = 0.32$ m and $H_r = 0.3$ and (c) $d = 0.24$ m and $H_r = 0.4$. $V_{n,cr} = 0$ m/s.

B.3.2.4 Effect of the discharge or water depth ratio H_r

In Figure B.6.b and B.6.c, the dimensionless bed evolution was plotted for cases with water depth ratios ($H_r = 0.3$ and $H_r = 0.4$, respectively). In the same way as for the length of the spur dyke, the water depth ratio does not affect significantly the deposition/erosion distribution. As the length of the recirculation seems to be sensitive to H_r (see Table B.1), the deposition area in the convergent flow is getting larger with the ratio H_r . Also, flow velocities in the floodplain are getting larger for $H_r = 0.3$ and $H_r = 0.4$ especially. Bedload transport and induced bed evolution have thus much larger magnitude (areas in white and black correspond to values smaller than -0.1 and higher than 0.1, respectively).

For the case with $H_r = 0.4$, the erosion area develops all around the recirculation area. Moreover, as the flow in the recirculation is getting faster (development of a return flow close to the wall, see Figure 7), bed-load transport is not negligible anymore and some erosion/deposition areas appears within the recirculation zone.

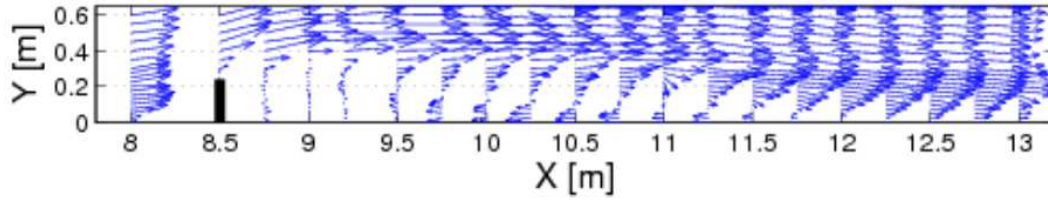


Figure B.7 – Corrected velocity from LSPIV measurements for the test case with $ld = 0.24\text{m}$ and $H_r = 0.4$.

B.3.3 Results for an permeable spur dyke

In case of the permeable spur dyke, effects are roughly similar to those of the impermeable spur dyke but their magnitude are weaker. A weak erosion may be observed at the foot of the spur dyke. However, it is partly due to spurious effects by the vortices developing from the foot of the spur dyke. ECM measurements show continuous increase of flow velocity from the right bank to the left bank (floodplain to main channel) in the cross-section at the spur dyke. The deposition area upstream to the obstacle is also wider than for the case with an impermeable spur dyke. Downstream of the obstacle, there is no recirculation, but a gradual increase in flow velocity is observed, inducing some small erosion. In the same way as for the previous cases, the imperfections of the joints between two PVC plates forming the floodplain at the section $x = 11\text{ m}$ seems to affect the results of the LSPIV, inducing spurious effects in the velocity fields and so in the bed evolution. As a consequence the permeable spur dyke appears to be a more interesting alternative as the impermeable spur dyke in term of morphodynamics.

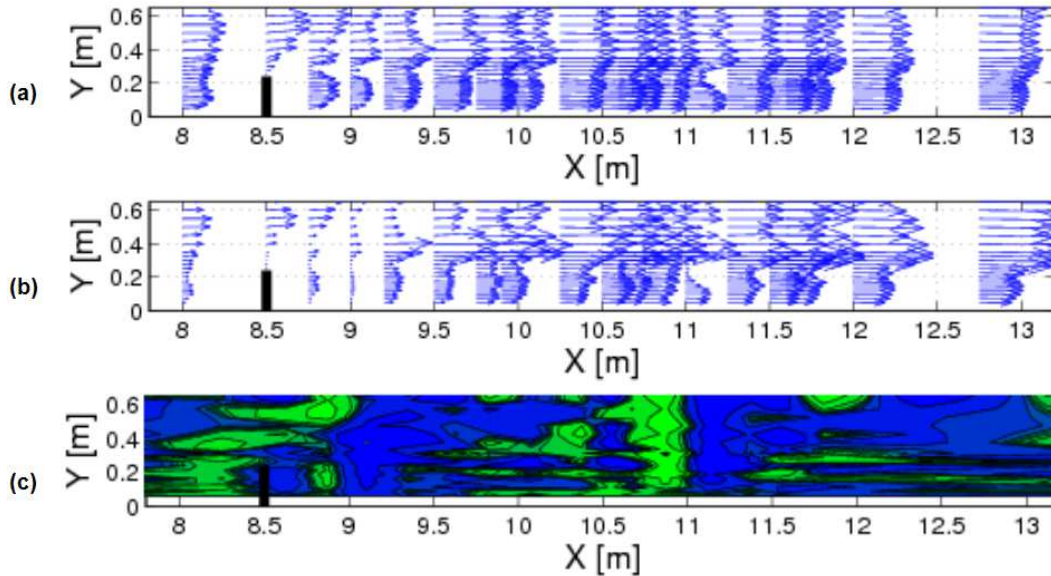


Figure B.8 – (a) Corrected velocity from LSPIV measurements, (b) dimensionless bed-load transport and (c) dimensionless bed evolution, using a permeable spur dyke for the test case with $d = 0.32\text{ m}$ and $H_r = 0.2$.

B.4 Discussion

The main effects of an impermeable spur dyke on the flow are the following:

- o Relative weak magnitude of the velocity in the upstream part of the spur dyke

- o Large velocities around the obstacle with a strong shear flow at the foot of the spur dyke
- o Nearly no velocities in the recirculation area

The weak velocities in the recirculation area downstream of the spur dyke as well as in the upstream part of the spur dyke yield a considerable potential of deposition in both areas.

On the other hand, the strong magnitude of the velocity is observed around the foot of the spur dyke due to the convergence of the flow in each experimental condition. The shear flow induced by the interaction between main flow and recirculation area would yields a much more active bed dynamics at this location. These flow characteristics illustrate the potential bottom profile change, which would lead to generate local scour and deposition. Figures B.5 and B.6 display the contour of the estimated bed evolution derived by Equations B.1 and B.2. It is obvious from these figures that erosion and deposition areas would be generated around the spur dyke and the recirculation area.

In the experimental result around a non-submerged spur dyke with movable bed condition (for example, *Zhang et al.* [2009]), locally bed deformation (local scour around the spur dyke and the deposition downstream of it) is clearly observed around the spur dyke. These typical bed evolutions (local scour and deposition) are produced as a result of the interaction between flow characteristics and bed evolution, including 3D flow characteristics like horse-shoe vortex upstream the obstacle and wake vortex downstream the obstacle (These 3D flow structures are not observed by the LSPIV measurements). The experimental results in Figures B.5 and B.6 indicate the development of the scouring and deposition around the spur dyke although those don't provide full explanation for the bed evolutions under movable bed condition.

In case of the permeable spur dyke, the flow patterns around the spur dyke are completely different from those of the impermeable cases. The effects of the spur dyke on the flow are roughly similar to those of the impermeable case;

- o Relative weak magnitude of the velocity in the upstream and downstream of the spur dyke
- o A weak shear flow around the foot of the spur dyke

No recirculation area is observed downstream of the spur dyke and the velocity downstream of the spur dyke increase gradually in the downstream of the spur dyke. These results are confirmed by other experimental results (for example, *Zhang and Nakagawa* [2008]). In case of the permeable spur dyke, a local scour still exists around the spur dyke. However, the magnitude of the scouring and the eroded area is generally smaller than those in the impermeable cases. This result indicates low probability of a severe erosion around the permeable spur dyke, and the permeable spur dyke appears to be a more interesting alternative as the impermeable spur dyke in term of morphodynamics.

B.5 Conclusion

This paper presents some experimental results with the non-submerged impermeable and permeable spur dyke and discusses the influence of the spur dyke on the flow characteristics and the estimated bed evolutions based on the potential sediment transport. The spur dyke is set on the floodplain of a compound channel, which was installed in a 20 m long straight experimental flume. Two types of spur dyke set on the floodplain were used in the experiments, one is impermeable and the other permeable (pile groin with a permeability of 50%). Totally, 13 experiments were undertaken with some different conditions of the length of the spur dyke, the ratio of the water depth in the floodplain and main channel H_r and the type of spur dyke.

The main results are as follows:

The relationship between the ratio L_x/d and the friction number given by Equation B.3 is confirmed with the exception of cases with small H_r and large d , for which an interaction between the recirculation and the main channel was observed. It is found from the experimental results that the new data set presented here is well described by the previous theory (Equation B.4) and is in good agreement with previous data from *Peltier et al.* [2008]. Most of the present data appear to be in the SWF regime or in an intermediate regime.

In case of the impermeable spur dyke, the velocity distributions in the recirculation area downstream of the spur dyke have relative weak magnitude as well as in the upstream part of the spur dyke. On the other hand, the flow with high velocities was observed around the foot of the spur dyke due to the convergence of the flow in each experimental condition. Using the measured results of velocity distributions, the bed evolutions around the spur dyke are estimated with a simple relationship between the flow velocity and the potential sediment transport (Equations B.1 and B.2). The estimated bed evolutions indicate the development of the scouring and deposition around the spur dyke although the experimental results presented here don't provide full explanation for the bed evolutions under movable bed condition as they don't include 3D flow effects.

In case of the permeable spur dyke, the flow patterns around the spur dyke present completely different behaviour compared to those of the impermeable spur dyke. The results in the bed evolution are in good agreement with other experimental results (for example, *Zhang and Nakagawa* [2008]). A local scour still exists around the permeable spur dyke. However, the magnitude of the scouring and the eroded area is smaller than those in the impermeable case. This result indicates low probability of severe erosion around the permeable spur dyke, and the permeable spur dyke appears to be a more interesting alternative as the impermeable spur dyke in term of morphodynamics.

B.6 Acknowledgement

The authors express their appreciation for the support of all members joining this joint research program. These experiments were partially supported by the bilateral program Sakura from the Japan Society for the Promotion of Science (JSPS) and Hubert Curien Partnership (PHC).

references

- B. Camenen and M. Larson (2005). A bed-load transport formula for the nearshore, *Estuarine Coastal and Shelf Science*, vol. 63, pp. 249-260.
- I. Fujita, M. Muste, and A. Kruger (1998). Large-scale particle image velocimetry for flow analysis in hydraulic engineering applications. *Journal of Hydraulic Research* 36 (3), 397-414.
- A Hauet, JD Creutin and P Belleudy (2007). Sensitivity analysis of large-scale particle image velocimetry measurement of river discharge using numerical simulation, *Journal of Hydrology*, 349(1-2), 178-190.
- Le Coz, J., Hauet, A., Dramais, and G., Pierrefeu, G., 2010. Performance of image-based velocimetry (LSPIV) applied to flash-flood discharge measurements in Mediterranean rivers, submitted to *Journal of Hydrology* (subm. 1 September 2009, revised Jan. 2010, Special Issue Flash-floods).

Y Peltier, S Proust, A Bourdat, F Thollet, N Rivière, and A Paquier (2008). Physical and numerical modelling of overbank flows with a groyne on the floodplain. Proc. of the International Conference on Fluvial Hydraulics, River Flow, Cesme-Izmir, Turkey, September 3-5, 2008, Altinakar, Kokpinar, Aydin, Cokgor and Kirkgoz (eds), 1, 447-456.

N. Rivière, B. Badin, Y. Bomchil, and S. Proust (2008). Recirculation zones downstream open channel expansions. Proc. of the 4th Int. Conf. on Fluvial hydraulics, River flow 2008, Sept. 3-5, Cesme-Izmir, Turkey, pp. 2233-2238.

N. Rivière, S. Proust and A. Paquier (2004). Recirculating flow behind groynes for compound channel geometries. Proc. of the 2nd Int. Conf. on Fluvial hydraulics, River flow 2004, June 23-25, Napoly, Italy, Greco, Carravetta and Della Morte (eds.), pp. 437-442.

H. Zhang and H Nakagawa (2008). Investigation on morphological consequences of spur dyke with experimental and numerical methods, Proc. 8th Int. Conf. on Hydrosience and Eng., pp.1490-1499.

H. Zhang, H Nakagawa, K Kawaike, and Y Baba (2009). Experiment and simulation of turbulent flow in local scour around a spur dyke. Int. J. Sediment Res., 24(1) 33-45.

C

Devices uncertainties

In this appendix, the details of the calculations of uncertainties in Table 4.2 using equations defined in §4.2 are given.

C.1 Water depth and water level: ultrasonic probe

Thanks to Equation 4.7 and Table 4.1, the uncertainty on the distance between the probe and the surface to be measured (δz_i) is written:

$$\delta D_{p,i} = \sqrt{\left(\sqrt{ACC^2 + \frac{RY^2 + \sigma_z^2}{N}}\right)^2}_i \quad (C.1)$$

with $D_{p,i}$ the distance to be measured, $N = F_s \times \Delta t$ the number of samples, and $i = b$ (bottom) or $i = ws$ (water surface).

The Water and the bottom level are both calculated using the reference plan defined in §3.3.3 and the distance between the probe and the bottom or the distance between the probe and the water surface. As a consequence the propagation formula 4.6 is needed for computing the water and the bottom level uncertainties:

$$\begin{aligned} \delta z_i &= \sqrt{(\delta D_{p,hpr})^2 + (\delta D_{p,i})^2} \\ &= \sqrt{\left(\sqrt{ACC^2 + \frac{RY^2 + \sigma_z^2}{N}}\right)^2_{hpr} + \left(\sqrt{ACC^2 + \frac{RY^2 + \sigma_z^2}{N}}\right)^2_i} \end{aligned} \quad (C.2)$$

with N the number of samples, $D_{p,hpr}$ the distance between the horizontal plan of reference and the probe and $D_{p,i}$ the distance from the probe and the surface i ($i = ws$ or $i = b$).

Since, the water depth is obtained by subtracting the distance between the probe and the bottom and the distance between the probe and the water surface, the propagation Equation 4.6 is also needed to compute the water depth uncertainty:

$$\begin{aligned} \delta h &= \sqrt{(\delta D_{p,b})^2 + (\delta D_{p,ws})^2} \\ &= \sqrt{\left(\sqrt{ACC^2 + \frac{RY^2 + \sigma_z^2}{N}}\right)^2_{Z_b} + \left(\sqrt{ACC^2 + \frac{RY^2 + \sigma_z^2}{N}}\right)^2_{Z_{ws}}} \end{aligned} \quad (C.3)$$

with N the number of samples, Z_b the bottom level and Z_{ws} the water surface level.

Thanks to the quite long recording time (20 s, *i.e.* 1000 samples at 50 Hz, see Table 4.1), the random uncertainties can be neglected. Uncertainty on the distance from the probe and the surface i is finally equal to:

$$\delta D p_i = 0.3 \text{ mm} \quad (\text{C.4})$$

and the uncertainty on the water depth and on the level (bottom and water surface) is equal to

$$\delta Z_i = \delta h = \sqrt{2(\delta D p_i)^2} = 0.42 \text{ mm} \quad (\text{C.5})$$

C.2 Mean velocity and turbulence

C.2.1 Micro-propeller:

Thanks to the long recording times and to the sampling frequency, the uncertainty on the mathematical expectation (see in Equation 4.5) is neglected (great number of samples, > 3000). As a consequence, the uncertainty on the micro-propeller only depends on the accuracy, *i.e.* $\delta||(\bar{u}, \bar{v})||/||(\bar{u}, \bar{v})|| = 1.5\%$.

Thanks to Equations 3.1 and 4.6, uncertainties on the streamwise and spanwise velocities are then:

$$\delta \bar{u} = \sqrt{(\cos \theta)^2 (\delta||(\bar{u}, \bar{v})||)^2 + (||(\bar{u}, \bar{v})|| \sin \theta)^2 (\delta \theta)^2} \quad (\text{C.6})$$

$$\delta \bar{v} = \sqrt{(\sin \theta)^2 (\delta||(\bar{u}, \bar{v})||)^2 + (||(\bar{u}, \bar{v})|| \cos \theta)^2 (\delta \theta)^2}$$

C.2.2 Pitot tube:

Given Equation 3.2 and the accuracy of the pressure transducer (Table 4.1), the uncertainty on the velocity measured through the Pitot tube should be written:

$$\delta \bar{u} = \frac{C_1 \delta V_o}{2\sqrt{C_1 V_o + C_2}} \quad (\text{C.7})$$

where C_1 and C_2 are calibration coefficients and V_o is the mean output voltage of the pressure transducer. However, as said in the presentation of the Pitot tube, the calibration of the latter is done using the micro-propeller data that have an uncertainty much larger than the pressure transducer. As a consequence we decided to not use Equation C.7 for computing the Pitot uncertainty and we rather set the uncertainty equal to the same uncertainty as the micro-propeller, *i.e.* $\delta||(\bar{u}, \bar{v})||/||(\bar{u}, \bar{v})|| = 1.5\%$ with $\bar{v} = 0$ (not measured).

C.2.3 ADV:

Uncertainties on the instantaneous velocity (u, v) are specified by the manufacturer ([Nortek \[2004\]](#) and Table 4.1):

$$\delta(u, v) = \pm 0.5 \% (u, v) \pm 1 \text{ mm/s} \quad (\text{C.8})$$

As shown in Equation C.8, the formulation of the ADV uncertainty uses an upper bound. Consequently, the estimation of the uncertainty on the mean velocity cannot use Equation 4.7. We rather consider that the upper bound of the uncertainty on the mean velocity can be formulated as following:

$$\delta(\bar{u}, \bar{v}) = \pm 0.5\%(\bar{u}, \bar{v}) \pm 1 \text{ mm/s} \quad (\text{C.9})$$

NB – After *Hurther and Lemmin* [2001], the mean velocity is independent from the noise.

The fluctuations, after correction of the big spikes (see §4.5) only depend on the noise level (*i.e.* 1 cm/s after *Nortek* [2004]). In order to get a better estimation of the noise and of its impact on the turbulent statistics, some special treatments must be applied on the turbulent data as explained in §3.3.4.3. However, after *Hurther and Lemmin* [2001] and several other authors, the lateral Reynolds shear stress and the horizontal lateral Reynolds normal stress are unbiased (they are the most used parameters in this thesis). The horizontal longitudinal Reynolds normal stress is contrariwise biased; the noise variance must be estimated using the method of *Voulgaris and Trowbridge* [1998].

C.3 Preston tube

As said in the Preston tube presentation, in operating conditions, after using the calibration laws, *Patel* [1965] defines an uncertainty of 6 % of the measured boundary shear stress. Since we have not redundant measurements of boundary shear stress using another device, we considered that the value of 6 % was also acceptable for our measurements.

C.4 LS-PIV

As explained in the LS-PIV subsection, the uncertainty cannot be easily estimated without a good knowledge of the physics that is measured. Without considering the physics of the flow, a partial uncertainty can be calculated using the characteristics of the video-camera and the characteristics of the PIV calculation: the density of the computation-mesh gives for instance an uncertainty on the determination of the length of the recirculation developing in the lee of an obstacle.

C.5 Derived quantities

Thanks to the measurement devices, various physical parameters has been measured. Their combinations lead to the creation of new parameters that are useful for the analysis of the flows. Like for the basic parameters, uncertainties on the new parameters must be computed as well using the propagation formula 4.6. Resulting uncertainties for the Froude number, the dispersion on the vertical of the horizontal components of the velocity and the momentum coefficient are presented below.

C.5.1 Froude number

The Froude number compares the velocity of the fluid and the velocity of the long waves (gravity waves) and is written as following:

$$Fr_i = \frac{U_i}{\sqrt{gH_i}} \text{ and } Fr(x, y) = \frac{U_d}{\sqrt{gh}} \quad (\text{C.10})$$

where Fr_i is the Froude number in a cross-section, $Fr(x, y)$ is the Froude number at the position (x, y) , H_i is the water depth in the subsection i, U_i is the velocity in the subsection i, h the depth at the position (x, y) and U_d the depth-averaged velocity at (x, y) . and its uncertainty has the

form:

$$\begin{aligned}\delta Fr_i &= \sqrt{\left(\frac{Fr_i}{2H_i}\right)^2 (\delta h)^2 + \left(\frac{1}{\sqrt{gH_i}}\right)^2 (\delta U_d)^2} \\ \delta Fr(x, y) &= \sqrt{\left(\frac{Fr}{2h}\right)^2 (\delta h)^2 + \left(\frac{1}{\sqrt{gh}}\right)^2 (\delta U_d)^2}\end{aligned}\tag{C.11}$$

C.5.2 Dispersion on the vertical of the horizontal components of the velocity

The dispersion on the vertical of the horizontal components of the velocity is a mathematical artefact that represents the integral of the deviation of the local velocity relative to the depth-averaged velocity in a water column, *i.e.* shows if the depth-averaged velocity is representative of the local distribution of the velocity.

Assuming that $X_{xx} = \frac{1}{N} \sum_{i=1}^N (\bar{u}_i - U_d)^2$, $X_{yy} = \frac{1}{N} \sum_{i=1}^N (\bar{v}_i - V_d)^2$ and $X_{xy} = \frac{1}{N} \sum_{i=1}^N (\bar{u}_i - U_d)(\bar{v}_i - V_d)$ (trapezoidal sum \approx arithmetic sum), the uncertainty on the dispersion is written:

$$\begin{aligned}\delta X_{xx} &= \frac{2}{N} \sqrt{\sum_{i=1}^N \left[(\bar{u}_i - U_d)^2 \left((\delta \bar{u}_i)^2 + (\delta U_d)^2 \right) \right]} \\ \delta X_{yy} &= \frac{2}{N} \sqrt{\sum_{i=1}^N \left[(\bar{v}_i - V_d)^2 \left((\delta \bar{v}_i)^2 + (\delta V_d)^2 \right) \right]} \\ \delta X_{xy} &= \frac{1}{N} \sqrt{\sum_{i=1}^N \left[(\bar{u}_i - U_d)^2 \left((\delta \bar{v}_i)^2 + (\delta V_d)^2 \right) + (\bar{v}_i - V_d)^2 \left((\delta \bar{u}_i)^2 + (\delta U_d)^2 \right) \right]}\end{aligned}\tag{C.12}$$

C.5.3 Vertical momentum coefficient

The vertical momentum coefficient compares the square of the velocity to the dispersion as shown in Equation 2.48. The uncertainty of this coefficient is worked out hereafter:

$$\begin{aligned}\delta \beta_{xx}^v &= \sqrt{\left(\frac{2X_{xx}}{U_d^3}\right) (\delta U_d)^2 + \left(\frac{1}{U_d^2}\right) (\delta X_{xx})^2} \\ \delta \beta_{yy}^v &= \sqrt{\left(\frac{2X_{yy}}{V_d^3}\right) (\delta V_d)^2 + \left(\frac{1}{V_d^2}\right) (\delta X_{yy})^2} \\ \delta \beta_{xy}^v &= \sqrt{\left(\frac{X_{xy}}{U_d V_d^2}\right) (\delta V_d)^2 + \left(\frac{X_{xy}}{U_d^2 V_d}\right) (\delta U_d)^2 + \left(\frac{1}{U_d V_d}\right) (\delta X_{xy})^2}\end{aligned}\tag{C.13}$$

where β_{ij} represents the vertical momentum coefficient.

MODÉLISATION PHYSIQUE DES ÉCOULEMENTS DÉBORDANTS EN PRÉSENCE D'UN ÉPI PLACÉ DANS LA PLAINE D'INONDATION

Résumé : Si généralement, les variations de sections en travers des rivières naturelles ou anthropisées sont progressives et continues, au droit de certains biefs, des obstacles transversaux et discontinus (naturels ou artificiels) peuvent partiellement ou totalement bloquer les plaines d'inondation. L'écoulement dans la plaine d'inondation est dès lors contracté par l'obstacle, qui promeut le développement de zones de recirculation de part et d'autre de l'obstacle, entraînant une réduction de la section d'écoulement et la génération d'échanges de masse entre lits qui viennent se superposer aux interactions turbulentes. Nous nous sommes intéressés à la modélisation physique de ces écoulements et nous avons particulièrement étudié les distorsions introduites par l'obstacle sur la turbulence dans l'écoulement. Ce travail est basé sur de nouvelles expériences menées dans deux canaux à lit composé. Un jeu complet de données d'écoulements rapidement variés en présence d'un épi dans la plaine d'inondation. Les effets sur les paramètres hydrauliques de la superposition des deux problématiques que sont (i) les écoulements en géométries composées et (ii) les écoulements rapidement variés au voisinage d'un obstacle ont ensuite été analysés. Finalement, les processus physiques dominant dans ces écoulements ont été identifiés.

Mots-clés : inondations, lit composé, écoulement rapidement varié, obstacle, zones de recirculation, turbulence, transferts de quantité de mouvement.

PHYSICAL MODELLING OF OVERBANK FLOWS WITH A GROUYNE SET ON THE FLOODPLAIN

Abstract: If in natural or anthropized rivers, the river cross-section generally gradually and continuously varies, transversal and discontinuous obstacles either natural or artificial may partially or totally block off floodplains. The flow overbanking in the floodplain is therefore contracted by this obstacle which then promotes two recirculation zones of both sides of the obstacle, resulting in a reduction of the flow section and in the generation of strong mass exchange between channels that superimposes to the classical turbulent interactions. New experiments are conducted in two different compound channels: rapidly varied flows in compound channel with a groyne set on the floodplain. Flows with various groyne lengths and total discharges were investigated. Effects on the hydraulic parameters of the superimposition of the two problems that are (i) flow in compound geometry and (ii) rapidly varied flow in the vicinity of a thin obstacle were analysed. Finally, dominance of physical processes in such flow configuration is discussed.

Keywords: flood, compound channel, rapidly varied flows, obstacle, recirculation zones, turbulence, momentum transfer.